NBS SPECIAL PUBLICATION 541

U.S. DEPARTMENT OF COMMERCE / National Bureau of Standards

Laser Induced Damage in Optical Materials: 1978

STP 689

NATIONAL BUREAU OF STANDARDS

The National Bureau of Standards[1] was established by an act of Congress March 3, 1901. The Bureau's overall goal is to strengthen and advance the Nation's science and technology and facilitate their effective application for public benefit. To this end, the Bureau conducts research and provides: (1) a basis for the Nation's physical measurement system, (2) scientific and technological services for industry and government, (3) a technical basis for equity in trade, and (4) technical services to promote public safety. The Bureau's technical work is performed by the National Measurement Laboratory, the National Engineering Laboratory, and the Institute for Computer Sciences and Technology.

THE NATIONAL MEASUREMENT LABORATORY provides the national system of physical and chemical and materials measurement; coordinates the system with measurement systems of other nations and furnishes essential services leading to accurate and uniform physical and chemical measurement throughout the Nation's scientific community, industry, and commerce; conducts materials research leading to improved methods of measurement, standards, and data on the properties of materials needed by industry, commerce, educational institutions, and Government; provides advisory and research services to other Government Agencies; develops, produces, and distributes Standard Reference Materials; and provides calibration services. The Laboratory consists of the following centers:

Absolute Physical Quantities[2] — Radiation Research — Thermodynamics and Molecular Science — Analytical Chemistry — Materials Science.

THE NATIONAL ENGINEERING LABORATORY provides technology and technical services to users in the public and private sectors to address national needs and to solve national problems in the public interest; conducts research in engineering and applied science in support of objectives in these efforts; builds and maintains competence in the necessary disciplines required to carry out this research and technical service; develops engineering data and measurement capabilities; provides engineering measurement traceability services; develops test methods and proposes engineering standards and code changes; develops and proposes new engineering practices; and develops and improves mechanisms to transfer results of its research to the utlimate user. The Laboratory consists of the following centers:

Applied Mathematics — Electronics and Electrical Engineering[2] — Mechanical Engineering and Process Technology[2] — Building Technology — Fire Research — Consumer Product Technology — Field Methods.

THE INSTITUTE FOR COMPUTER SCIENCES AND TECHNOLOGY conducts research and provides scientific and technical services to aid Federal Agencies in the selection, acquisition, application, and use of computer technology to improve effectiveness and economy in Government operations in accordance with Public Law 89-306 (40 U.S.C. 759), relevant Executive Orders, and other directives; carries out this mission by managing the Federal Information Processing Standards Program, developing Federal ADP standards guidelines, and managing Federal participation in ADP voluntary standardization activities; provides scientific and technological advisory services and assistance to Federal Agencies; and provides the technical foundation for computer-related policies of the Federal Government. The Institute consists of the following divisions:

Systems and Software — Computer Systems Engineering — Information Technology.

[1]Headquarters and Laboratories at Gaithersburg, Maryland, unless otherwise noted; mailing address Washington,D.C. 20234.
[2]Some divisions within the center are located at Boulder, Colorado, 80303.

The National Bureau of Standards was reorganized, effective April 9, 1978.

Laser Induced Damage In Optical Materials: 1978

Proceeding of a Symposium Sponsored by:
National Bureau of Standards
American Society for Testing and Materials
Office of Naval Research
Department of Energy
Defense Advanced Research Project Agency

September 12-14, 1978
NBS Boulder, Colorado 80303

Edited by

Alexander J. Glass
Lawrence Livermore Laboratory
Livermore, California 94550

and

Arthur H. Guenther
Air Force Weapons Laboratory
Kirtland AFB, New Mexico 87117

U.S. DEPARTMENT OF COMMERCE, Juanita M. Kreps, Secretary

Jordan J. Baruch, Assistant Secretary for Science and Technology

NATIONAL BUREAU OF STANDARDS, Ernest Ambler, Director

Issued December 1978

Library of Congress Catalog Card Number 79-600050

National Bureau of Standards Special Publication 541
Nat. Bur. Stand. (U.S.), Spec. Publ. 541, 362 pages (Dec. 1978)
CODEN: XNBSAV

U.S. GOVERNMENT PRINTING OFFICE
WASHINGTON: 1979

For sale by the Superintendent of Documents, U.S. Government Printing Office, Washington, D.C. 20402
Stock No. 003-003-02052-4 Price $5.50
(Add 25 percent additional for other than U.S. mailing).

Foreword

The Proceedings contain the papers presented at the Tenth Annual Symposium on Optical Materials for High Power Lasers held at the National Bureau of Standards in Boulder, Colorado, on September 12-14. 1978. The Symposium was jointly sponsored by the National Bureau of Standards, the American Society for Testing and Materials, the Office of Naval Research, the Defense Advanced Research Projects Agency, and the Department of Energy. The Symposium was attended by about 175 scientists from the United States, the United Kingdom, France, Canada, Japan, West Germany, and the Soviet Union. It was divided into sessions devoted to the following topics: the Measurement of Absorption Characteristics, Bulk Material Properties, Mirrors and Surfaces, Thin Film Damage, Coating Materials and Design, and Breakdown Phenomena. The Symposium Co-chairpersons were Dr. Alexander J. Glass of the Lawrence Livermore Laboratory and Dr. Arthur H. Guenther of the Air Force Weapons Laboratory, who also served as editors of this report.

The editors assume full responsibility for the summary, conclusions, and recommendations contained in the report, and for the summaries of discussion found at the end of each paper. The manuscripts of the papers presented at the Symposium have been prepared by the designated authors, and questions pertaining to their content should be addressed to those authors. The interested reader is referred to the bibliography at the end of the summary article for general references to the literature of laser damage studies. The Eleventh Anuual Symposium on this topic will be held in Boulder, Colorado, from October 30 to 31, 1979. A concerted effort is being made to ensure closer liaison between the practitioners of high peak power and the high average power community.

The principal topics to be considered as contributed papers in 1979 do not differ drastically from those enumerated above. We expect to hear more about improved scaling relations as a function of pulse duration, area, and wavelength, and to see a continuing transfer of information from research activities to industrial practice. New sources at shorter wavelengths continue to be developed, and a corresponding shift in emphasis to short wavelength damage problems is anticipated. Fabrication and test procedures will continue to advance, particularly in the micro-machined optics and thin film areas.

The purpose of these symposia is to exchange information about optical materials for high power lasers. The editors will welcome comment and criticism from all interested readers relevant to this purpose, and particularly relative to our plans for the Eleventh Annual Symposium.

A. H. Guenther and A. J. Glass
Co-chairpersons

CONTENTS

Laser Induced Damage in Optical Materials

Tenth ASTM Symposium

September 12-14, 1978

The Tenth Annual Symposium on Optical Materials for High Power Lasers (Boulder Damage Symposium) was held at the National Bureau of Standards in Boulder, Colorado, from 12-14 September 1978. The Symposium was held under the auspices of ASTM Committee F-1, Subcommittee on Laser Standards, with the joint sponsorship of NBS, the Defense Advanced Research Project Agency, the Department of Energy, and the Office of Naval Research. About 175 scientists attended the Symposium, including representatives of the United Kingdom, France, Canada, Japan, West Germany, and the Soviet Union. The Symposium was divided into sessions concerning the Measurement of Absorption Characteristics, Bulk Material Properties, Mirrors and Surfaces, Thin Film Damage, Coating Materials and Design, and Breakdown Phenomena. As in previous years, the emphasis of the papers presented at the Symposium was directed toward new frontiers and new developments. Particular emphasis was given to materials for use from 10.6 μm to the uv region. Highlights included surface characterization, thin film-substrate boundaries, and advances in fundamental laser-matter threshold interactions and mechanisms. The scaling of damage thresholds with pulse duration, focal area, and wavelength was also discussed. In commemoration of the tenth symposium in this series, a number of comprehensive review papers were presented to assess the state of the art in various facets of laser induced damage in optical materials. Alexander J. Glass of Lawrence Livermore Laboratory and Arthur H. Guenther of the Air Force Weapons Laboratory were co-chairpersons of the Symposium. The Eleventh Annual Symposium is scheduled for 30-31 October 1979 at the National Bureau of Standards, Boulder, Colorado.

Key words: Laser damage; laser interaction; optical components; optical fabrication; optical materials and properties; thin film coatings.

1. Introduction

The Tenth Annual Symposium on Optical Materials for High Power Lasers (Boulder Damage Symposium) was held, as in previous years, at the National Bureau of Standards in Boulder, Colorado, from 12 to 14 September 1978. The Symposium was held under the auspices of the ASTM Committee F-1, Subcommittee on Laser Standards, with the joint sponsorship of NBS, the Defense Advanced Research Projects Agency, the Department of Energy, and the Office of Naval Research. Working sessions of the Committee F-1 Subcommittee on Lasers were held on Monday 11 September. About 175 scientists attended the Symposium, including representatives of the United Kingdom, France, Canada, Japan, West Germany, and the Soviet Union. The Symposium was divided into sessions concerning the Measurement of Absorption Characteristics, Bulk Material Properties, Mirrors and Surfaces, Thin Film Damage, Coating Materials and Design, and Breakdown Phenomena. As in previous years, several poster sessions were held. The general consensus of those presenting poster papers and those viewing them was highly favorable. In all, over fifty technical presentations were made. Alexander J. Glass of Lawrence Livermore Laboratory and Arthur H. Guenther of the Air Force Weapons Laboratory were co-chairpersons of the Symposium. At this, our Tenth Annual Symposium, we paused to reflect upon the past ten years' activities in laser induced damage to optical materials. We enlisted the services of fourteen distinguished speakers who are acknowledged to be the principal contributors in the many facets of the laser damage field. They summarized and quantified as well as possible the state of the art and the state of the understanding in their specialized areas. These review or tutorial lectures are being assembled and published as a separate volume on the subject of laser induced damage in optical materials. In addition, round-table discussions were held on those specific subjects in which there is still some question as to the correctness of our understanding to give the participants an opportunity to make recommendations for future research. The purpose of these symposia is to exchange information about optical materials for high power lasers. The authors will welcome comments and criticism from all interested readers relevant to this purpose and particularly relative to our plans for the Eleventh Annual Symposium, scheduled for 30-31 October 1979, at the National Bureau of Standards, Boulder, Colorado.

2. Principal Conclusions

Advances in the field of laser materials are incremental rather than revolutionary. Each year's progress represents a small step forward from the preceding year's position. The advances are also sporadic, unfortunately. New problems or new approaches are often identified in one year's symposium, only to be ignored in succeeding years, possibly to resurface a few years later, or not at all. One reason for this is the reluctance of investigators to report on those methods which failed. We hear only of the new approaches which have succeeded. Because of the incremental nature of advances in this field, the results reported in this summary must be viewed in the context of ten years of laser damage research; thus the significance of many of these results will not be clear for several years to come.

In the realm of operative damage phenomena, thin film damage remains the least well understood. This is to be expected, considering the complexity of the problem and the number of variables required

to characterize fully a thin film system. Most of the advances to date have been empirical, and even for film systems that usually exhibit high damage thresholds, control of the process variables is uncertain. Thus, a coating which performs excellently in one production run may well exhibit a lower threshold on the next run. The identification of the critical process variables has not been made.

There is abundant evidence that damage in thin films is not intrinsic, but arises from defects, impurities, or absorbed materials. The question is, to what degree can multilayer dielectric films be made free of these defects and impurities. The morphology of the film--its grain size, porosity, and crystalline orientation--all depend on a multiplicity of process variables, including deposition method, background pressure, substrate temperature, rate of deposition, and many others.

It is not surprising then that attempts to find simple solutions to thin film damage have not yielded consistent results. Techniques like barrier layer deposition work sometimes, but not always. At pulse durations of several ns and beyond, damage seems to be thermal, originating at highly localized sites. The identity and origin of these sites are still unclear. One does not expect this picture to improve greatly in the near future.

Regarding surface damage, the picture is substantially clearer. Chemical contamination remains the single greatest concern to surface damage. The contaminant can be H_2O, hydroxyl ions, or polishing residue. Surface roughness plays a role in determining the damage threshold, more so at long pulse durations, although the reason for the observed dependence remains open to conjecture. Regarding surface damage, the number of process variables is significantly smaller than for thin films, so the connection between process control and material performance should be much more straightforward.

Thermally induced bulk damage is an area in which great progess has been made. Note that "damage," in this context, includes distortion, birefringence, and other thermal mechanisms, in addition to catastrophic failure. By the sufficient reduction of impurity absorption, bulk absorptions can be reduced below $10^{-4}cm^{-1}$ for specific materials such as SiO_2 and the alkali halides. The intrinsic limit due to multiphonon absorption can be reached at infrared frequencies, and the relevant phonon assignments identified. Thus, both empirical improvement and basic understanding have been achieved for this particular scenario.

The case is quite the opposite for bulk breakdown. There is no consensus regarding the relative role of the several mechanisms which can contribute to dielectric breakdown. These include multiphoton absorption, impurity absorption, electron avalanche, and others. Attempts to link first-principle models to observed damage thresholds are probably futile, given the complexity of the intervening phenomena. Experiments are beginning to be reported in which precursors to damage, like photoconductivity or photocapacitance, are observed. These seem to promise improved correlation with theoretical models.

It is, however, safe to say that dielectric breakdown in bulk materials is not a critical problem for any application currently under investigation. It is important to understand the process and to understand electron behavior in dielectrics, because both surface damage and thin film damage are often accompanied by plasma formation, and so involve related, if not identical, phenomena. However, bulk dielectric breakdown is not on the "critical path" for system development.

Scaling laws provide a general guide to the behavior of damage thresholds as experimental conditions--such as pulse duration, spot size, or surface roughness--are changed. Departures from expected scaling often indicate the onset of some new phenomenon, or the introduction of extrinsic factors. Thus, the $t^{1/2}$ dependence, which is widely observed to apply to surface damage, is often found to describe thin film damage only at very short pulse durations. For pulses larger than a few hundred psec, extrinsic factors may enter, which can result in a departure from the simple scaling law.

The simple scaling relationships which have been reported are empirical and lack full theoretical justification. Nevertheless, they provide a useful guide for exploratory damage results to new conditions and provide a test of consistency for measured threshold values.

Whatever its origin, catastrophic laser damage is a statistical phenomenon, like any other mode of material failure. Failure does not depend on the average properties of the material, but on the strength of the weakest point. The "damage threshold" reported by experimentalists is a statistical concept, representing the intuitive dividing line between power densities at which failure is likely to occur and those at which failure is unlikely. This year, the Weibull statistics, which are widely employed to model failure of electrical components, were applied to laser damage data with gratifying results. Note that this analysis does not presuppose a particular physical model for damage, although the data can be examined, using this analysis, to see if the results are consistent with a particular model. The general approach to laser damage as a generic failure mode appears very promising.

The capability to measure, localize, and identify the dominant source of failure has been greatly advanced in recent years. This year, we heard of greatly increased sensitivity in the measurement of weak absorptions in optical materials. Bulk absorptions of less than $10^{-5}cm^{-1}$ have been measured calorimetrically, both on long bar samples of KCℓ and coated samples of fused silica. Surface absorptions as low as 10^{-6} have also been measured.

Using techniques like long bar calorimetry, the scanning adiabatic film calorimeter and photoacoustic spectroscopy, the contributions of absorption in bulk materials at the surface, at thin film interfaces, or in thin film layers can be separated. This enables one to say where, if not why, the damaging absorption is occurring. Present indications are that surface absorption at the surface-film interface is a common source of absorption-induced damage.

As the pulse length varies, the dominant mechanism changes. Multithreshold analysis allows one to determine which damage process dominates as the pulse length is varied. Again, the root cause of the damage is not identified, but rather the consequence.

Scattering, as a sensitive indicator of damage, has been investigated for some time. This year, a quantitative, sensitive scattering technique was discussed, which should provide a useful addition to the arsenal of sensitive measurement techniques.

Several advances were reported in the realm of materials preparation and fabrication. One such advance is in the isostatic forging of optical elements. The forging of LiF optics, reported this year, is of great interest for short wavelength optics, since very few materials other than LiF are available for high power use at 250 nm or shorter wavelengths. Similarly, forged optics made from other alkali halides and CaF_2 will find use in systems operating in both the uv and IR. At present, forged optics show higher scattering losses than the original crystalline material, but the approach is very promising.

Metal mirrors continue to be attractive, especially where diamond-turning can be used in the fabrication. Molybdenum is a substrate material of considerable interest. As interest shifts to the uv the problem of dielectric coatings for metal mirrors commands increasing attention. The compatibility of coating and substrate will add another dimension to the already complicated problem of mirror design.

Short wavelength systems are beginning to yield data on component damage; and, as expected, laser damage is a limiting factor for uv systems. Two-photon absorption is seen to play a role in damage in both coatings and bulk material, and techniques have been advanced to measure nonlinear absorption. Nonlinear absorption coefficients have only been measured in a few materials, perhaps a dozen in all. The purity of these materials and the sensitivity of the two-photon absorption at various wavelengths to the presence of impurities have not been determined. Clearly, a substantial amount of research is required to bring the state of uv optics up to the required level.

As a consequence of a decade of damage studies, system designers are aware of the limitations imposed on system performance at high power levels, by laser damage. This heightened consciousness of damage problems within the community will undoubtedly spur the improvement of uv optics for high power systems. Additionally, at all wavelengths, techniques for damage avoidance provide a way around the limitations of materials. The term "damage avoidance" refers to methods whereby the total power from an aperture can be increased, while keeping the peak power below the damage-imposed limit. These include spatial filtering, optical relaying, plasma filtering, and phase conjugation. Other techniques undoubtedly remain to be discovered.

Fiber optics and semiconductor lasers seem out of place at a symposium on high power optics, but the power densities achieved in these devices can be high. Because of the commercial importance of these devices, it is important that the optical materials community be aware of the specific problems encountered in their use. This year, in a paper presented on damage in optical fibers, the speaker concluded that surface damage at the edge of the core was the decisive failure mode. Considering the remarkable purity of the core material in low-loss fibers, this is to be expected. This surface damage in fibers thus may be a problem strongly similar to other surface damage phenomena, and knowledge gleaned in the high power laser field may be applicable to its solution.

It is becoming clear that the materials of choice, from the infrared to the ultraviolet, are the light fluorides and oxides, along with NaCℓ and KCℓ. Other materials are under development, especially for use as high index coating materials; but, wherever possible, it seems preferable to use fluoride or fluorite crystalline materials: sapphire, and oxide and fluoride glasses. Except for sapphire, these are all low index materials, which have been developed for optical use over a long period of time. Purified starting materials are available for these materials, and they are chemically stable, which reduces surface contamination.

Given the base of materials identified above, the situation for new optical materials is comparable to that of laser materials in the 60's. At that time, ruby had been refined and developed to the point where it was the standard material for crystalline lasers. There was widespread interest in finding a better material, one with a lower threshold and with comparable, if not better, optical and mechanical properties. Literally hundreds of other crystalline hosts were examined, in small samples, with a "shotgun" approach. It was not until Bell Laboratories undertook the <u>systematic</u> development of YAG that a replacement for ruby was obtained.

The lesson to be learned is twofold. One must identify what characteristics are desirable for a material, and pursue development of those which offer significant promise of exceeding the performance of what is already available. Choices must be made, and a long process of development undertaken, involving purification of starting materials, optimization of the manufacturing process, and development of fabrication and finishing techniques. If these choices are made from materials which provide a reasonable promise of the same or better chemical, mechanical, and optical properties than those materials already available and if a real commitment is made to their development, significant advances will be made.

3. Summary of Papers

The subject matter of the Tenth Symposium broadly consists of six topics, and these proceedings are organized accordingly. The topics are as follows: (1) Measurement of Absorption Characteristics, (2) Bulk Material Properties, (3) Mirrors and Surfaces, (4) Thin Film Damage, (5) Coating Material and Design, and (6) Breakdown Phenomena. In this section, a concise summary of each paper is provided. Closely related papers are discussed together, wherever possible. The interested reader is referred to the complete manuscript of the papers for detail; our intention here is to provide the reader with an overview of the Symposium, and to identify the topics of discussion and the authors of the papers. Each topic is introduced with a brief statement of the underlying problems and the status of understanding within that area of interest.

3.1 Measurement of Absorption Characteristics

Without question, the optical property of ultimate concern in any high average power laser system is absorption. This property, whether present within the bulk of an optical window or at the surface of coated or reflecting elements, can lead to unacceptable thermally induced damage. Thus, it is not surprising that several papers heard at this year's meeting dealt with the measurement and identification of absorption. The papers ranged from a theoretical analysis of rate calorimetry to the comparison of several novel techniques such as total reflection and photoacoustic spectroscopy, with standard calorimetric procedures. Several authors dealt with the particularly pernicious problem of surface absorption in thin films and its separation from bulk absorption. One paper addressed the growing concern for two-photon absorption as interest moves to shorter wavelengths.

A general method for analyzing window characteristics by rate calorimetery, which includes coating absorption, was the subject of a presentation by N. C. Fernelius and G. T. Johnston of the University of Dayton Research Institute. Previous treatments of this procedure were extended to include samples with dissimilar levels of absorption on their faces. The method requires the measurement of temperature rise and reflected power in both orientations to three significant figures. Unfortunately, it is difficult to make reflected power measurements at the levels encountered with AR coated windows to better than two significant figures at the present time. Many other investigators are resorting to long bar substrates or variable thickness coatings to overcome this limitation. However, these approaches require the preparation of special samples to allow one to separate the surface and bulk absorption contributions to the total window absorption.

The increased development of high power, ultraviolet lasers is stimulating the search for and characterization of optical materials, for use both as window materials and as coating components. One promising candidate for use as a low index film material from the uv to the ir is NaF. When assessing a material's utility as a film component, it is necessary to test it in thin film form. To this end, D. L. Burdick of the Naval Weapons Center, employing the powerful technique of Attenuated Total Reflection Spectroscopy, has studied the absorption coefficient of 0.56-μm thick NaF films on ZnSe substrates from the visible to ~3 μm. The spectrum revealed a strong water band at 2.95 μm of very high absorption relative to the substrate. An estimate of the thickness of an adsorbed water layer of 7Å was given. The contribution of scattering to absorption was also investigated in this report. It was observed that coated portions of the test plate tended to scatter less than the uncoated portion at any given wavelength. The scattering difference was about 16 percent of the normal-incidence value observed for the uncoated surface.

With increased emphasis on short wavelength lasers, there is developing a growing interest in techniques for measuring multi-photon absorption coefficients. M. Bass, E. Van Stryland, and A. Stewart of the University of Southern California reported on a calorimetric method for measuring two-photon absorption. In their experiments, a repetitively pulsed, Q-switched Nd:YAG laser was used to illuminate samples of CdSe and CdTe at 1.06 μm. The sample was isolated in a vacuum chamber, and its temperature measured with a thermocouple. The temperature rise was measured as a function of the incident intensity.

The resulting curves were analyzed assuming that there were both an incident wave and a refelcted wave in the sample. Thus, the reflection at the back surface was taken into account. Some deviation from the theoretical prediction was observed, which was ascribed to the presence of free carriers generated in the absorption process (either linear or nonlinear).

This approach to measuring two-photon absorption looks very promising, especially when combined with more sensitive methods of detection, such as photoacoustic spectroscopy. This research also shows

the importance of carrying out a careful and exact analysis of reflected wave effects in optical samples, especially in the presence of nonlinear interactions.

The level of specific absorption is extremely important in assessing the suitability of an optical material for use as a laser window over a given spectral range. H. Vora, M. C. Ohmer, and T. G. Stoebe of the Air Force Materials Laboratory have made a comparison of the bulk and surface absorption in both NaCℓ and KCℓ over the spectral range from 9.2 to 10.8 μm using the long bar technique. The measured bulk absorption in the best RAP-grown NaCℓ was apparently intrinsic at $9 \times 10^{-4} cm^{-1}$ at 10.6 μm and $1.4 \times 10^{-4} cm^{-1}$ at 9.2 μm. By comparison, the best KCℓ showed bulk absorption of 9×10^{-5} at 10.6 μm and $4 \times 10^{-5} cm^{-1}$ at 9.2 μm. These values are probably limited by the presence of some residual ClO_3^- or ClO_4^- impurities.

A variety of samples of NaCℓ and KCℓ from various sources were evaluated together with an investigation of the efficacy of different cleaning and etching procedures to reduce surface absorption. This study has led to a proposed new multiphonon limit for the intrinsic absorption in NaCℓ, lower than Deutsch's reported value of $1.17 \times 10^{-3} cm^{-1}$.

As optical component quality improves, it becomes increasingly imperative that diagnostic instrumentation for the characterization of these elements keeps pace. No where is this more necessary than in the measurement of the absorption in thin films and at interfaces. Thus, it was quite appropriate that T. H. Allen, J. H. Apfel, and C. K. Carniglia of the Optical Coating Laboratory reported on the construction and testing of a 1.06-μm laser absorption calorimeter for thin film coatings. This instrument is quite suitable for routine measurements of coatings deposited on thin discs. Samples, irradiated by a 6 W cw Nd:YAG laser, were usually 2.54 cm in diameter and ranged in thickness between 0.02 and 0.13 cm. The temperature of the coated disc is compared to a similar uncoated element using thermistors, arranged in an AC Wheatstone Bridge, in direct contact with each disc. An ambient pressure of 100 torr is maintained in the sample chamber to reduce thermal variations. The precision of the calorimeter was determined over an absorptance range of 9×10^{-6} to 3.8×10^{-4} and was found to be essentially constant at 2×10^{-6}. Sensitivity for a 0.04-cm thick substrate was 3.8×10^5 μv/watt. Tests on uncoated fused silica discs with thicknesses from 0.04 to 0.13 cm show a surface absorptance of 6×10^{-6} and a bulk value of 5×10^{-5}/cm.

A very elegant technique for isolating the contributions due to interface, bulk, and substrate absorptions in single-layer films was described by P. Temple, D. Decker, T. Donovan, and J. Bethke of the Michelson Laboratory. They prepared samples in the form of a wedge of coating material deposited on a substrate, leaving part of the substrate uncoated. The absorption of this sample was then measured, using the scanning adiabatic calorimeter the authors described in the 1977 Symposium Proceedings. The sample was scanned with a 0.5 W laser, in a spot 500 μm in diameter. A plot of energy absorbed versus film thickness was then generated. The intercept of this plot, corresponding to zero thickness, was generally different from the absorption value obtained on the uncoated portion of the sample. The difference was assumed to represent the sum of the contributions from both the outer and inner interfaces.

The slope of the absorption plot yields the bulk absorption coefficient. By measuring the absorption at the $\lambda/2$ and $\lambda/4$ thicknesses, and taking into account the difference in field configurations, the authors can extract the relative contributions of the air-film and the film-substrate interfaces. Data are presented for NaF and As_2Se_3 films on CaF_2 substrates, measured at 2.87 μm and 2.72 μm. The former wavelength lies within a water band, while the latter does not. For the NaF film, bulk absorption due to water was detected, while for the As_2Se_3 film, the principal effect was due to water absorption at the film-substrate interface.

Photoacoustic spectroscopy (PAS) is a technique for measuring weak absorptions that dates back to Lord Rayleigh and the spectrophone, but is enjoying a revival in current physics. N. Fernelius and D. Walsh of the University of Dayton Research Institute applied this method to the measurement of the absorption spectra of several thin films and bare samples, including samples coated using the discrete graded-index method described in the paper by Moravec and Skogman (see below). PAS provides information concerning the spectral absorptance of the sample and can discriminate between bulk and surface absorption by the variation in the phase of the signal with chopping frequency. It is thus a valuable method for the analysis of optical samples.

In this work, it was found that thin film materials showed different absorption spectra from the same materials in bulk, due either to different crystal forms or to impurities in the coating. The theory of Rosencwaig and Gersho for the chopping frequency dependence of the PAS signal was verified. The PAS method should find wide applicability for investigations of optical materials.

3.2 Bulk Material Properties

Absorption characteristics, discussed in the preceding section, represent only one of the many parameters of interest for the optical materials used in laser systems. Other optical, thermal, and mechanical properties of laser materials are also of importance in determining system performance. At high power, stress-optical and thermo-optical properties can be of great significance for laser window materials, lens materials, substrates, and, in glass lasers, the laser medium itself.

For many years, the National Bureau of Standards has carried out a program of measurement and computation of the optical properties of materials suitable for use in various laser systems. The evaluation of stress-induced birefringence is an important consideration in the mechanical design and thermal performance of high-power laser systems. These changes in refractive index can lead to significant wavefront distortion in actual operation. This year, R. M. Waxler, A. Feldman, and D. Horowitz reported extensive measurements of the piezo-optical coefficients of a wide variety of increasingly important optical materials, including four neodymium phosphate and fluoro-phosphate laser glasses, as well as CaF_2, BaF_2, and SrF_2. Polarimetric and interferometric techniques were employed at the HeNe wavelengths of 0.6328 μm, 1.15 μm, and 3.39 μm. The laser glasses obviously were not measured at 3.39 μm.

Another aspect of the optical materials characterization program at the National Bureau of Standards concerns the measurement of refractive index and dispersion in transparent window materials. M. J. Dodge, of the above organization, reported on the refractive index of fusion cast SrF_2 at 20°C over the spectral range 0.2138 μm to 11.475 μm. SrF_2 and other alkaline earth fluorides, BaF_2 and CaF_2, are candidates for the 2-μm to 6-μm range because of their low index of refraction and dn/dT values as well as their good mechanical stability. These factors, along with others, play an important role in determining optical distortion.

Using a minimum deviation method, 53 data points were fitted to a three-term Sellmeier dispersion equation of the form:

$$n^2 - 1 = \sum_j [A_j \lambda^2(\lambda^2 - \lambda_j^2)^{-1}].$$

The resulting constants for SrF_2 were as follows:

$A_1 = 0.67805894$ $\quad \lambda_1 = 0.05628989$

$A_2 = 0.37140533$ $\quad \lambda_2 = 0.10801027$

$A_3 = 3.3465284$ $\quad \lambda_3 = 39.906666$

Similar results are presented for for BaF_2 and CaF_2, as well.

Wide band-gap materials, especially monovalent and divalent fluorides and cholorides, are of great interest as materials for use in windows and lenses, over the entire range of wavelengths from 10.6 μm to 250 nm. Single-cyrstal materials can be fabricated in large sizes, but these materials exhibit poorer mechanical properties than polycrystalline material. A technique for combining the optical homogeneity and chemical purity of single-crystal materials with the mechanical strength of polycrystalline materials is isostatic forging. Several authors contributed to a status report on this promising fabrication technique.

Addressing the need for improved optical materials with both good ultraviolet transparency and low linear and nonlinear refractive indices, J. F. Ready, H. Vora, R. A. Skogman, K. M. Leung, and E. Bernal G. reported on the development of LiF windows by isostatic forging of single crystal starting material. While the mechanical properties of yield strength and fracture energy were seen to improve, it was found that the ultraviolet transmission of the final product was not appreciably degraded. This is an important observation, since LiF has the widest band gap of any known optical material and can now be made into relatively large, strong, high quality optical elements. The forgings are usually made along the <100> axis at a strain rate of 5×10^{-3}/min under a 2000 ps isostatic helium constraint with temperatures ranging from 300° to 600°C. Resultant grain sizes are in the 10- to 40-μm range. Long-term stability appears to be acceptable. However, whereas the index inhomogeneity of the single crystal starting material was in the range of 4.4 to 8.8 $\times 10^{-6}$ over 2.5 cm diameter samples, the forged materials exhibited Δn values of 17.4 to 22.3 $\times 10^{-6}$.

In a continuing development of forged optics, R. H. Anderson of the Honeywell Corporation and J. M. Bennett of the Naval Weapons Center have investigated the optical properties of plano-plano and plano-concave KCℓ optical elements isostatically forged at 4000 psi between optically polished dies. In this study, the elements were prepared in a two-step forging process. The KCℓ was forged between teflon sheets first, and then water polished, prior to final forging, between fused quartz or pyrex dies at 200 to 275°C under a helium atmosphere. The optical figure, homogeneity, internal strain, scattering, and surface character of these two-step samples were compared with both single-crystal and one-step, press-forged KCℓ samples. It was readily apparent that the two-step process produced a superior element in terms of surface figure, homogeneity, surface roughness, and scattering. The water polishing greatly reduced the occurrence of grain boundaries and thus surface scatter. While the surface topography (roughness) of the die was not replicated exactly, the forged surface compared favorably with state-of-the-art, mechanically polished samples and exhibited lower scatter values.

In a somewhat related paper, R. H. Anderson, R. A. Skogman, and J. F. Ready of the Honeywell Corporation and J. M. Bennett of the Naval Weapons Center presented results of an initial investigation

of the forging of CaF_2. However, in this case, the isostatic forging resulted in considerable veiling (cloudiness) in the polycrystalline CaF_2 windows. Microscopic evaluation suggests that the veiling may result from microvoids formed by the aggregation of vacancies produced by dislocation intersections during plastic deformation, which also results in measurable internal stress. The CaF_2 samples were forged at 750° to 800°C in a helium atmosphere at a pressure of 14.82 MN/m^2. Single crystals having <111>, <100>, <112>, and <113> orientation were deformed approximately 60 percent to ensure a uniform grain size of less than 15 μm. Obviously, much more work needs to be accomplished to assess fully the suitability of isostatic forging for materials such as CaF_2, particularly if their intended use is at shorter wavelengths where scattering is of major concern as a loss mechanism.

In choosing a window material for a high power cw laser, both the power level at which failure occurs and the nature of the damage process are of interest. J. Detrio and R. Petty of the University of Dayton Research Institute conducted an investigation of thermally induced failure in SrF_2 and CaF_2 windows, using the multi-kilowatt DF laser at the Army Chemical Laser Facility. Polycrystalline samples of Raytheon, fusion-cast SrF_2 were irradiated at power levels up to 8.4 kw on a spot size of 0.3 cm^2 area. Failure inevitably occurred at power densities greater than 22 kw/cm^2. All samples were AR-coated at 3.8 μm.

Failure was noncatastrophic and was ascribed to compressive loading in the center of the irradiated area and consequent strain. Plastic deformation was seen to occur in the form of slip along the (100) plane. At the point of failure, the compressive stress was estimated to be 15 Kpsi, and the peak temperature 98°C.

A feature of this investigation was the observation of the sample before, during, and after irradiation using interferometry and a polariscope simultaneously. Comparison of the polariscope patterns with those observed in oriented single crystal specimens of CaF_2 made it possible to identify the crystalline orientation of the polycrystalline samples.

Thermal damage in bulk materials which are used in the region of transparency arises from multiphonon absorption and residual impurities. The latter effect can be reduced by controlling the purity of the raw material, and preventing contamination in the manufacturing process. The chemical vapor deposition process is one means of maintaining the purity of bulk materials during fabrication. However, even in the purest materials, multiphonon absorption must be measured, to obtain the limit of transparency.

As an indication of our progress in achieving an understanding of the properties of one particular material, C. Klein, B. diBenedetto, R. Donadio, T. Kahone, and J. Pappis of the Raytheon Company reported a detailed listing of phonon assignments leading to an excellent prediction of experimental lattice absorption for CVD (chemical vapor deposition) ZnS, a potential window material for use at 2.7 and 3.8 μm. Through an analysis of spectrophotometric data at wavelengths to 25 μm, it was concluded that multiphonon processes dominate the absorptive spectrum at frequencies below 1000 cm^{-1}. As an adjunct to this study, the absorption coefficient was measured for CVD ZnS at laser wavelengths in μm of 2.7 (HF), 3.8 (DF), 5.25 (CO), 9.27 (CO_2), and 10.6 (CO_2). The absorption coefficients in cm^{-1} being $(7.2 \pm 0.5) \times 10^{-3}$, $(2.3 \pm 0.5) \times 10^{-2}$, $(4.5 \pm 1.1) \times 10^{-2}$, $(7.9 \pm 1.3) \times 10^{-2}$, and $(2.4 \pm 0.1) \times 10^{-1}$, respectively. Additional data relating to the utility of CVD ZnS as a window material for infrared imaging applications were also presented.

In the laser fusion program, emphasis is being placed on the construction of very large facilities. CO_2 and Nd glass lasers operating at 100 kJ or more are under construction. The capital cost of these facilities is very large, and the output obtained must be maximized by careful optimization of all components of the systems. Two papers were presented relevant to the choice and development of materials for large, Nd glass lasers.

In an effort to reduce the nonlinear index coefficient of laser glasses, the Lawrence Livermore Laboratory, working with the major laser glass manufacturers, has undertaken the development of fluorophosphate and fluoroberyllate laser glass compositions. S. Stokowski, D. Milam, and M. Weber reported on the status of the damage properties of these fluoride-based laser glasses. Damage measurements were made in both fluorophosphate and fluoroberyllate glasses at 1.06 μm, using pulse durations from 0.1 nsec to 1 nsec. Both bulk and surface damage were observed.

FK-51 is a fluorophosphate composition which has been commercially available for some time. It exhibits a surface damage threshold close to that of BK-7 or fused silica, i.e., 20-25 J/cm^2 at one nsec. Bulk thresholds are greater than 20 J/cm^2 in FK-51. Newer compositions, both fluorophosphate and fluoroberyllate, show surface damage at values of 12-16 J/cm^2, and bulk damage thresholds in excess of 25 J/cm^2. The glass manufacturers are still developing the melting process for these glasses, so further improvements are expected. The newer glasses are still observed to contain bubbles and crystallites, which may be the locus of damage. Development of polishing techniques for these glasses is still under way.

Thus, although low index laser glasses are still in the state of development, preliminary results indicate that surface and bulk damgage thresholds comparable to those achieved in borosilicate glasses should be attainable.

Optical liquids find a variety of uses in glass laser systems operated at moderate or high repetition rates: as coolants, for index matching, and as electrodes. The physical properties of these liquids are of great importance to the laser system designer. A series of measurements in the physical and optical properties of a number of liquids of interest has been carried out by J. Rinefierd, S. Jacobs, D. Brown, J. Abate, O. Lewis, and H. Applebaum of the University of Rochester.

A variety of index matching and coolant liquids was examined. The properties measured were refractive index, dispersion, optical absorption, dn/dT, density, thermal conductivity, and viscosity. An estimate of the electronic portion of the nonlinear index coefficient, n_2, was obtained from the measured values of the index and dispersion. Values of these optical and physical parameters are tabulated for twelve liquids. In general, where comparisons exist with tabulated values, the agreement is satisfactory. Among the liquids examined, H_2O exhibits an attractive combination of properties for a coolant: high thermal conductivity, low dn/dT, low viscosity, and low n_2.

3.3 Mirrors and Surfaces

In most situations, optical surfaces, whether they be on reflecting or transmissive elements, are the bridge between the laser system and the real world and as such are often subjected to hostile environmental conditions. In the heirarchy of damage sensitivity, surfaces fall midway between bulk materials and coatings, and become the critical element in systems forced to use uncoated elements. Thus, there is considerable import associated with raising the damage threshold of uncoated surfaces. One obvious solution, at least for reflecting components, is to use diamond-turned metal mirrors. Papers were presented not only on the physical and optical properties of micro-machined elements but also on the correlation between optical and metallurgical properties.

It seems that the subjects of surface roughness and its influence on damage resistance are still with us. A paper was presented concerning the pulse duration dependence of damage on surfaces of varying roughness. In addition, for the first time, a paper on damage to optical fibers with both nsec and msec pulses was given. We are sure that both of these subjects will be favorite topics for many years to come.

Many diamond-turned metal surfaces are adequate for 10.6 μm applications, but significant improvement is necessary in their quality if they are to be used at shorter wavelengths without additional polishing. D. Decker and D. Grandjean of the Michelson Laboratory reported on their progress in establishing a high precision diamond-turning mechanism. The machine differs from conventional diamond-turning devices in that all components are mounted on a black granite surface plate, isolated from the environment through air suspension. The planar layout minimizes the effects of vertical temperature gradients, and provides a convenient work surface with great flexibility of configuration.

The machine is operational with open-loop control. Surfaces show rms roughness of 10Å (OFHC copper), with slope errors a factor of 2 less than those observed on optics diamond-turned on the Battelle or Y-12 machines. The addition of closed-loop, interferometric controls of slide position is expected to increase the machine precision even further. A contour figure accuracy of 100 Å peak-to-valley over a 0.4-m diameter is expected, when the full servo system is implemented. The authors discuss the design of the machine and the relative roles of tool and machine errors in determining the surface character, and show surface profiles and statistics for pieces turned on this machine as well as for those turned on the Battelle and Y-12 machines.

Molybdenum is a mirror element of potentially great utility because of its good heat conductivity, low thermal expansion, stiffness, and relatively high damage threshold. Unfortunately, it is difficult to fabricate with low-scatter surfaces. In a rather comprehensive study of Mo mirrors, an extensive optical and metallurgical characterization was accomplished by S. M. Wong of Rockwell International, G. Krauss of the Colorado School of Mines, and J. M. Bennett of the Naval Weapons Center. The study attempted to correlate metallurgical process variables and resulting microstructure and surface finish of several samples from different sources. It was determined that there is a close correlation between grain and subgrain structure in the material and structure appearing on polished surfaces, resulting evidently from variations in hardness. As might be expected, little correlation was seen on ground surfaces. Inhomogeneity of the Mo is sufficient to produce measurable variations in surface finish within a given lot, particularly when inhomogeneities are associated with dispersion hardening agents such as Ti or Zr. Guidelines for the selection of optimum raw Mo stock for use as mirror substrates are given.

It is well established that at long pulse durations (~40 ns), there is a strong correlation between surface damage threshold and surface smoothness. At pulse durations of a few ns or less, however, this correlation is not consistently observed, especially as the surface roughness is reduced below 40 Å. It is important to know what the influence of surface roughness on damage threshold is, since this information can influence the procedure used for polishing optical surfaces and the surface quality required for laser components.

D. Milam of the Lawrence Livermore Laboratory investigated the pulse duration dependence of 1.06-μm surface damage on three BK-7 samples and one fused silica sample, with different surface roughnesses. Among the BK-7 samples, one was conventionally polished, grade A material, one was PH-3 material, carefully ground with alumina grits of descending size, and finally polished with commercial CeO_3, and the third had one bowl-feed polished surface. The fused silica sample was conventionally polished.

In general, entrance surface thresholds were observed to be higher than exit surface thresholds, but not as high as predicted from simple Fresnel theory. Cleaning raised the threshold on the conventionally polished BK-7 surface, but not on the others, indicating they were fairly clean initially. The expected scaling with pulse duration ($\sqrt{T}$) was generally observed. No correspondence between surface smoothness and damage threshold was observed in this range of pulse durations, indicating that other factors are dominant. The damage threshold observed at the entrance surfaces were typically 20-25 J/cm^2 in one ns.

Both from the value observed and from the adherence to the root-T scaling law, it appears that the surface damage seen in these experiments may be considered "intrinsic," or at least not dominated by absorbing impurities on the surface. The implication of the research is that super-polished surfaces (roughness ~10 Å) offer no advantages over conventionally polished surfaces for pulse durations of a few nsec, as long as the surfaces are carefully cleaned. It is not obvious why the sensitivities to surface roughness for very smooth surfaces should be so much greater at longer pulse durations.

A welcome addition to this year's Symposium was the report of M. J. Landry of Sandia Laboratories on the subject of laser induced damage to fiber optics including both single and multiple fibers. To our knowledge, this is the first time this subject has been treated at our Symposium and is an indication of both the breadth of the meeting and the coming importance of fiber optics as power transmitting optical elements. In this study, fibers of five manufacturers were subjected to 1.06-μm, 30-nsec pulsed laser exposures as well as unpolarized free-running exposures of a spiked nature for ~100-μs duration. The highest surface damage levels for single and multiple fibers exposed to the Q-switched pulse were 48.2 and 31.6 J/cm^2, respectively. In the case of long duration exposures, single laser exposure levels of 4.66 KJ/cm^2 were the highest achieved. Multifiber bundles initially exhibited damage in the cladding or matrix material. A decrease in the fiber coupling efficiency (ratio of output to input energy) was attributed solely to surface damage. Damage to gamma-irradiated fibers exposed to ~10^6 rad(Si) from a Co^{60} source were also reported. In general little effect was noted on coupling efficiency or damage level due to the irradiation. This result is to be expected since most of the interaction took place at the entrance surface, and thus the remainder of the fiber played little role in these experiments.

3.4 Thin Film Damage

Even though optical materials in thin film form remain the most damage sensitive component of high power laser systems, our efforts to improve their performance are largely empirical, based primarily on parametric studies and go/no go testing of commercially supplied elements, frequently with a short-gain approach characterized by new candidate materials, designs, etc. This situation is made manifest by the exigences of program deadlines and the need for rapid system maintenance. What is needed is a broad-based, fundamental program founded upon the growing wealth of parametric studies and some good sound science and materials engineering. This will be discussed further in the recommendations.

This year's thin film session was again generally a mix of parametric studies and an assessment of the state of the art in coating technology. The first paper was concerned with the current trend to shorter wavelengths (266 nm and 353 nm). Immediately following papers dealt with multithreshold analysis of coating damage at 2.7 μm and 3.8 μm and the role that adsorbed water layers play at the former wavelength.

Continuing their series of short wavelength studies of optical damage in thin film coatings, B. Newman and D. Gill of the Los Alamos Scientific Laboratory measured the damage threshold of fourteen different thin film materials at both 355 nm and 266 nm. The incident light was generated by doubling and tripling the frequency output of an Nd:YAG laser, Q-switched to produce a pulse of 35-ns duration. The 355-nm pulse width was 27 ns, and the 266-nm pulse width was 22 ns.

The film materials were deposited as quarter-wave layers on fused silica substrates, and, in some cases, as binary multilayer dielectric coatings designed for high reflectance. Damage thresholds were obtained as a function of wavelength, coating design, and, in cases where picosecond damage data had previously been taken, pulse duration. Both fluoride and oxide materials were tested.

The single-layer coating with the highest threshold was NaF, the material with the greatest band gap, which exhibited a threshold of 11 J/cm^2 at 355 nm. Fogging of the film due to exposure to a humid atmosphere apparently had no effect on the damage threshold. Of the multilayer reflectors, the NaF/Al_2O_3 film showed the highest thresholds: 3.6 J/cm^2 at 266 nm and 12 J/cm^2 at 355 nm. Al_2O_3 in a single layer showed a lower threshold, presumably because damage was occurring at the coating-substrate interface in the latter case. The wavelength dependence observed was consistent with the linear absorption increase at short wavelengths, for several oxide materials, although the

evidence was not entirely conclusive. Two-photon absorption did not seem to be playing a major role in damage at 20 ns, whereas it was significant for 20-ps pulses. The damage threshold was found to increase with pulse duration more slowly than $t^{1/2}$. This would be expected if the damage were mediated by absorbing impurities. Other scaling laws were also investigated.

This work, providing as it does a broad survey of materials and parameters under well-characterized test conditions, is very valuable in developing a picture of the relevant factors for short wavelength damage in thin films. It also provides a practical guide as to what materials appear most promising.

Pulsed laser damage in NaF, SiO_x Al_2O_3, ZnS, As_2S_3, and Si coatings at 2.7 and 3.8 μm was evaluated via a multithreshold analysis by J. O. Porteus, T. M. Donovan, J. L. Jernigan, and W. N. Faith of the Naval Weapons Center. This type of evaluation is most appropriate at the intermediate pulse length of 100 nsec employed in this study to allow for a greater delineation of damage mechanisms between thermal failure and dielectric breakdown. This type of analysis aids in understanding the role of impurities such as water, which absorbs at one of the two wavelengths employed.

After discussing in some detail the deposition conditions and substrate characteristics, the authors described the experimental variables and multithreshold diagnostic instrumentation including ion and light emission, the onset of delamination, cracking, flow, erosion, or perforation as well as other selective, as opposed to uniform, damage criteria. When appropriate correction factors were applied to convert from incident to internal energy/area values, NaF and Al_2O_3 were seen best at both the DF and HF wavelengths with SiO_x also useful at 3.8 μm. ZnS, As_2S_3 and Si, all higher index materials and SiO_x at 2.7 μm were markedly lower in damage resistance.

Continuing their work on multithreshold damage to films of As_2S_3, As_2Se_3, and NaF, T. M. Donovan, J. O. Porteus, J. L. Jernigan, and E. J. Ashley of the Naval Weapons Center extended their measurements this year to 2.8 μm and 3.8 μm from those reported last year at 10.6 μm. Two principal damage processes were identified. The first is a "uniform" mode associated with the amorphous chalgogenide matrix while the second is a more "selective" phenomena associated with micron-sized crystalline defects. Each type of damage is easily discernable by inspection of the damage morphology of the irradiated area. It was noted that single-layer film (N on 1) conditioning led to an improvement in damage resistance, most probably through gently removing by desorption any adsorbed water layer, which would absorb at 2.7 μm. However, for multilayers of As_2Se_3 and NaF, (N on 1) conditioning led to enhanced crystallite growth, which resulted in a decrease in damage thresholds.

Important results of this study indicated that As_2S_3 first damages at a fluence (areal energy density) of ~50 J/cm^2 while NaF, with a 30 times higher absorption, damaged at ~400 J/cm^2. Thus, absorption alone does not determine the damage sensitivity. For comparison purposes, multilayer films of alternate As_2Se_3 and NaF layers in an enhanced reflection design on polished Mo exhibited a higher threshold than Au-coated, diamond-turned Cu mirrors.

The remaining papers in this session dealt with three diverse areas of coatings, which have been with us a long time. They are a morphological investigation of damage in barrier layers, which emerged last year as a potential means of increasing the damage threshold of antireflection coatings; a significant improvement in the utility of scattering as a quantifiable indication of the onset of damage; and finally, an in-depth analysis of the statistics of absorptive laser damage and its usefulness for identifying the appropriate damage mechanism and as an engineering design tool.

The relatively low damage threshold of antireflection (AR) coatings makes it a limiting factor in the design and achievement of high-power laser systems. Last year the utility of barrier layer coatings to enhance the damage resistance of AR coatings by as much as 50 percent was revealed. C. K. Carniglia and J. H. Apfel of Optical Coating Laboratory, Inc., G. B. Carrier of the Corning Glass Works, and D. Milam of the Lawrence Livermore Laboratory have continued to investigate the role barrier layers play on the damage sensitivity of 1.064-μm AR coatings. The basic coating employed was a standard four-layer silica/titania design on BK-7 glass substrates. Samples were prepared with and without half-wave silica barrier layers. Detailed morphological investigation employing transmission electron microscopy revealed that damage sites were characterized by a 1-μm nuclei which could lead to 3-μm craters. The titania layer seems to fracture while the silica layers appear to melt or tear with evidence of heating in the substrate. The results of this study seem to indicate that damage originates at the interface between the coating and the substrate and may arise as a result of thermal expansion of the material at, or close to, this boundary, most probably resulting from polishing or cleaning residue rather than from absorption in the bulk of the materials themselves.

For many years people have felt that scattering should be both a good indicator of surface or film quality and a useful diagnostic technique to indicate the onset of damage. Unfortunately, to date, proposed laser scattering techniques, while sensitive, have been rather subjective. To increase the utility of scattering procedures and to place them on a quantifiable basis, T. W. Walker and A. H. Guenther of the Air Force Weapons Laboratory and P. E. Nielsen of the Air Force Institute of

Technology reported on new optical techniques for the determination of pulsed, laser-induced damage in thin films. Briefly, this scheme incorporates two fast photo-diodes. The first diode records a reference signal directly proportional to the intensity of the incident laser pulse, as well as a signal due to that fraction of the incident pulse nearly (~5°) back scattered from the target, and a probe signal generated from the incident pulse but delayed up to 55 nsec after the incident exposure of the test film. The delayed probe pulse is reflected from the exposure site into the photo-diode. By appropriate use of delay cables, all three signals can be displayed on a high time resolution transient digitizer. A second photo-diode records the transmitted incident laser pulse through the film and substrate.

By this technique, the relative amplitudes of the signals are compared first at an energy below the damage threshold, second at the damage threshold, and finally at an energy comparable to the first laser exposure by another exposure on the same site. The ratioing of the incident, delayed probe and back scattered signal affords a positive indication of change which can be arrived at by an objective evaluation of the signal amplitudes. The changes in the signal ratios offer, as well, a potential insight into the changes experienced by the thin film-substrate system upon irradiation by pulsed laser radiation. The use of the variable delay probe combined with re-exposure after damage indicates when modification of the film structure takes place and whether or not it is permanent. Films of MgF_2, ThF_4, and ZrO_2 were tested at 0.53 μm with 18-nsec pulses. Interestingly, this technique has indicated damage in films without the observance of either a visible spark or a modification of the transmitted laser pulse. This technique should gain wide acceptance, since it now places sensitive scattering techniques on an objective, but relative, quantitative basis.

It has long been suspected that an appropriate statistical treatment of pulsed laser damage experiments would afford an insight into the physical mechanism of damage and thus allow one to choose between competing theories. To this end, A. B. Budgor and K. F. Luria-Budgor of Lawrence Livermore Laboratory have performed a statistical analysis of absorptive laser damage in dielectric thin films using data supplied by D. Milam of the same organization. They applied a Weibull distribution, which is normally employed to describe both time-to-failure of electrical components and the DC breakdown of insulating materials. The Weibull distribution arises from the theory of extreme values. In this study, the time-to-damage and intensity-to-damage statistics were treated for thin films of ZrO_2, SiO_2, and Al_2O_3. In all cases, correlation greater than 90 percent was achieved. Excluding "over-simplified" statistical theories such as the lucky electron model, it was concluded, based on the pulse length dependence of breakdown and an experimentally nonobserved >2 multiphoton absorption, that the avalanche mechanism is the most likely initiator of the plasma requisite for lattice melting. It was pointed out that statistical confidence bands for material survivability as a function of laser intensity and pulse length can now be constructed, leading to a practical utility of Weibull distributions as engineering design and diagnostic tools.

3.5 Coating Materials and Design

Since thin film coatings remain the Achilles heel of high power laser systems, there is continuing interest in improving their performance. New coating materials continue to be investigated, often in connection with a particular wavelength, or a specialized application. It is well established that not only the coating material but also the design and details of deposition influence the characteristics and performance of a thin film coating.

Among the materials investigated for use as the low-index component of coating systems, fluorides are the most common, since they usually exhibit wide band gaps, and correspondingly low absorption in bulk form.

R. C. Pastor, J. A. Harrington, L. E. Gorre, and R. K. Chew of the Hughes Research Laboratories prepared and evaluated six compounds as candidates for 3.8-μm and 9.3-μm dielectric coatings. They were the rare earth fluorides LaF_3, PrF_3, CeF_3; the tri-halides of Bi, BiF_3, and BiI_3; and the binary salt $KGaF_4$. Using a purification procedure involving RAP (Reactive Atmosphere Process), an intrinsic absorption coefficient of < 0.1 cm^{-1} was sought. Unfortunately, the bulk absorption of the rare earth fluorides ranged between 0.6 and 0.9 cm^{-1}.

Optical transmission studies of single crystals of the rare earth fluorides indicated that only LaF_3 does not exhibit absorption bands in the 3- to 10-μm region. Both CeF_3 and PrF_3 exhibit absorption between 3.5 and 6 μm due to low lying Stark levels. While it was not possible to grow large enough single crystals of BiF_3 or $KGaF_4$ to permit accurate measurements, these materials appeared to have low absorption at 9.2 μm and 3.8 μm. BiI_3 looked the most attractive, due to its featureless spectra between 2.5 and 20 μm.

For a rather specific application, P. Baumeister of Aerojet-General and G. P. Arnold and D. F. Edwards of Los Alamos Scientific Laboratory investigated the deposition and damage thresholds of single-layer PbF_2 films employed as antireflection coatings for a CdSe OPO (optical parametric oscillator) pumped at 2.8 μm with 120-nsec pulses. Reported damage thresholds were as follows: uncoated CdSe, 68.5 MW/cm^2; $\lambda/4$ PbF_2 on CdSe, 50.6 MW/cm^2; $\lambda/1$ $PbF_2/\lambda/8$ ZnS, 50 MW/cm^2 (ZnS, used as an adhesive layer, exhibited no detrimental effects on the damage threshold); commercial PbF_2 coatings on CdSe, 6 MW/cm^2; and finally $\lambda/4$ PbF_2 on Ge at 3 μm, 22 MW/cm^2. Explicit and

complete details as to selection of starting materials, polishing, and deposition conditions are given. The presence of PbOH in the starting material or hydrolized from PbF_2 leads to the production of metalic Pb upon heating, resulting in inferior films.

Thin film coatings are recognized to be the most easily damaged optical elements in a high power laser system. Damage occurs in regions of high electric field and at film-substrate interfaces, where impurities aggregate. Recently, strong interest has developed in ways to eliminate conventional antireflection coatings. One such way is by use of graded-index coatings. In graded-index coatings, two materials are co-deposited on the surface simultaneously, with varying rates, so that the refractive index varies continuously in the desired fashion during the deposition. The control of the graded-index coating process is often difficult. An alternative means to achieve the same end has been proposed by T. Moravec and R. Skogman of the Honeywell Corporate Material Sciences Center. They constructed discrete graded-index films, by alternatively depositing layers of high index material (T&I, n = 2.4 at 10.6 μm) and low index material (PbF_2, n = 1.63 at 10.6 μm) on KCℓ substrates. The thickness of each pair of layers was determined to give a certain value of the average refractive index at that layer. By building up a coating from as many as 50 to 100 layers, a discrete approximation to a continually varying index can be constructed. Individual layers as thin as 100 Å were employed.

T&I normally grows in an orthohombric crystal. On KCℓ, two crystalline orientations develop in T&I, resulting in optical scattering in the film. By growing only thin layers, the T&I is kept in a cubic crystalline form and scattering is reduced. Discrete graded-index films are also free from birefringence, further evidence of cubic crystal structure.

The discrete film method provides a very flexible means of constructing graded-index films. Discrete graded-index films exhibited absorption values similar to those seen in conventional films of the same material. Damage tests have not yet been done, so comparisons with conventional, multilayer films and continuous graded-index films are not available.

The standing-wave pattern formed in a multilayer, dielectric coating creates local maxima and minima of electric field within the coating. The placement of these extrema is an important factor in determining the peak performance of the coating. Thus, the analysis of coating performance is a valuable tool in evaluation of coating designs for high power use.

Although exact calculations of thin film performance are possible using large computers, it is often useful to be able to carry out approximate evaluations of thin film reflectance, transmission, and absorption, using analytic expressions. H. E. Bennett and D. K. Burge of the Michelson Laboratory discussed the general method of obtaining simple analytic expressions for evaluating weakly absorbing, antireflection or high-reflectance coatings. In this age of programmable pocket calculators, the utility of the expressions will be immediately apparent.

In order to employ these expressions, one must know the volume absorption coefficient of the coating materials as deposited, the substrate absorption, and the absorptance at each interface. The indices of all materials must be known. For metal substrates, the effect of surface roughness can be included. All of these parameters can, in principle, be determined experimentally. Their measurement has been discussed in several papers presented at the Symposium this year and in past years. Additionally, these analytic formulae can be used to estimate the effect of absorption, in the volume of the coating materials or at interfaces, on the performance of thin film coatings. In this mode, they provide a useful tool for coating design analysis and for determination of coating specifications.

The analysis of the reflectivity and absorption of a complex dielectric multilayer film, as a function of frequency, generally requires a significant computational effort. M. Sparks and M. Flannery of Xonics, Inc., showed that simple analytical approximations can be obtained in the case of a quarter-wave stack, a design commonly used for high-reflectance mirrors. The authors showed that, to a good approximation, the phase shift can be represented by a linear function of $\omega - \omega_c$, where ω_c is the center frequency for the stack (zero phase shift), and that the absorption can be represented by a quadratic function of $(\omega - \omega_c)$, plus a substrate contribution. The coefficients of the quadratic form can be obtained from analyzing the infinite, quarter-wave stack, and depend only on the absorption constants and refractive indices of the low and high index coating materials.

By varying the operating frequency with respect to ω_c, the field maxima can be shifted into either the high or low index media. Thus, depending on which of these is more susceptible to damage, the coating should be designed to operate off the center frequency, to minimize the field in the more vulnerable material.

Herbert B. Rosenstock of the Naval Research Laboratory reviewed the situation relative to electric fields produced at or near surfaces and in coated elements. He pointed out quite correctly that the use of a coated element at other than design wavelength can either increase or decrease the total electric field depending on the optical constants, thicknesses and specific film design, as well as the wavelength. He also pointed out that it may be useful to coat the exit surface of a transmission element to reduce the field at that point, but that it may introduce a weakness due to increased absorption in the film or at the film/substrate boundary.

3.6 Breakdown Phenomena

The phenomenon of the bulk failure of a transparent dielectric, in the presence of an intense light wave, associated with the formation of a luminous plasma, may be the oldest, and least well understood of the various effects observed under the heading "laser damage." A number of theoretical models have been advanced, each usually stressing one or another aspect of what is ultimately a very complicated process. Indeed, it may not be prudent or even possible to model the breakdown process completely.

Among the competing effects are multiphoton ionization, direct excitation from impurity levels or defect sites, avalanche ionization, thermal ionization of highly absorbing impurities, and phonon-assisted processes. At present, research is directed toward identifying the relative importance of each of these competing effects, as a function of pulse duration, wavelength of illumination, and experimental conditions. It is safe to say that, as yet, no wholly satisfactory model has been developed for dielectric breakdown.

A very preliminary account was given of an attempt to simulate, numerically, the propagation of light through a damage site in a transparent dielectric. P. Kelly and D. Ritchie of the National Research Council and P. Braunlich and A. Schmid of Washington State University are in the process of adapting a "particle-in-a-cell" (PIC) code, originated by D. Henderson of the Los Alamos Scientific Laboratory, to model light propagation in the dielectric in the presence of polarons. The generation of the polarons is assumed to proceed via a four-photon process for NaCℓ, the material initially studied.

Such a computation is necessarily limited by the extent of the physics phenomena which can be included. In reality, the nonlinear optics of the medium, as well as the generation of polarons, must be included; and impurity effects will have to be modeled. The applicability of the PIC method to a strongly convergent focus, especially in the presence of self-focusing, is also open to question.

There has been extensive discussion in the laser damage literature of the relative roles of impact and multiphoton ionization in determining the bulk damage threshold of transparent dielectrics. B. G. Gorshkov, A. S. Epifanov and A. A. Manenkov of the Lebedev Physical Institute in Moscow presented a theoretical analysis of the relative dependence of these two phenomena on optical frequency and laser pulse duration. The dependence of multiphoton ionization on frequency is simply given by the ratio of the ionization potential to the photon energy, for all pulse lengths of interest. For avalanche (impact) ionization, the authors conclude that two different dependencies on photon energy can be observed. In the subnanosecond region, the breakdown field is always expected to show a monotonic increase with frequency, while for pulses several nanoseconds wide, if the photon energy approaches the gap energy, the breakdown field can show an oscillatory dependence on photon energy. Consequently, as the pulse width is varied at fixed frequency, in some cases, the two processes can compete over a wide range of pulse durations.

In a short presentation, S. Brawer and W. Smith of the Lawrence Livermore Laboratory offered a conjecture regarding the modeling of bulk damage in transparent dielectrics. They proposed that electrons near the bottom of the conduction band can be considered as lying in localized states. Transitions between these states are assumed to be dipole allowed. When a conduction electron acquires an energy equal to the band gap in the material, it can excite a valence electron to the bottom of the conduction band by an Auger process. In this way, a population of conduction electrons is built up. Electron energy loss occurs via collisions with the lattice (phonon emission). This process heats the lattice and leads to damage. Avalanche may or may not accompany damage.

The new aspect of the theory is that it assumes localized states in the conduction band and does not require an avalanche for damage to occur. Only preliminary conclusions have been drawn from the theory, and detailed predictions will await further calculation.

A series of investigations of laser induced damage in semiconductor materials was reported by Yu. K. Danileiko, A. A. Manenkov, and A. V. Sidorin of the Lebedev Institute of Moscow. Using three laser probes, a 10.6-μm, CO_2 laser with a 60-ns pulse width, a 2.76-μm, Er:CaF_2 laser with a 90-ns pulse width, and an Er:YAG laser operating at 2.94 μm with a 100-ns pulse width, they measured the dc and microwave photoconductivity induced in Si, Ge, and GaAs. In Ge, no damage was observed, although significant photoconductivity was measured. At the shorter wavelengths, the photoconductivity was attributed to two-photon absorption, with a measured two-photon absorption coefficient of 7.5×10^{-2} cm/MW. At 10.6 μm, the mechanism giving rise to the photoconductivity was unclear. Neither avalanche ionization nor thermal effects could account for the observed dependence of carrier concentration on incident intensity. The absence of damage was attributed to self-defocusing of the incident light by the free carriers generated in the focal region. However, damage was observed in GaAs and Si. The observed damage levels were poorly correlated with measured bulk absorption coefficients. This was probably due to absorbing defects in the material. Defect type of morphology was observed in all cases of damage.

Scaling laws have been useful guides in damage studies, providing estimates of system performance over a range of operating parameters. Additionally, departure from the expected scaling is often evidence of the influence of extrinsic factors. M. J. Soileau of the Michelson Laboratory and M. Bass and E. Van Stryland of the University of Southern California tested the bulk damage threshold of KCℓ and NaCℓ as a function of spot size and of laser frequency. Significant departures from the empirical scaling law proposed by Bettis, et al., for spot-size dependence were observed in both materials. Furthermore, the frequency dependence of the damage threshold, measured at a fixed-spot diameter, contradicted the values obtained earlier for NaCℓ in the infrared, yielding values more in line with those reported last year by Manenkov.

Experiments were carried out at 2.7 μm, in a 140-ns pulse, at 3.8 μm, in a 70- to 100-ns pulse, and at 10.6 μm, in a 60- to 110-ns pulse. Spot sizes varied from 20 μm to 60 μm. In general, the threshold field decreased monotonically with increasing spot size, but no consistent pattern or functional form for the dependence on spot size was evident. In several cases, the spot-size dependence was different at different frequencies.

The authors attribute the lack of a simple set of scaling relations to the effect of impurities, defects, and other extrinsic factors in the materials examined. As Manenkov pointed out in his paper this year, however, the frequency dependence of damage can be quite complicated, even for ideal materials, without invoking any impurity effects. As to the departures of the spot-size dependence from the conjecture of Bettis, et al., uncertainties in the data and the absence of a firm foundation for the scaling law make it difficult to draw any unequivocal conclusion from the result.

A careful study of the surface breakdown mechanism for infrared optical materials was presented by V. I. Kovalev and F. S. Faizullov of the Lebedev Physical Institute in Moscow. They propose as the dominant mechanism in IR material damage a two-step process, consisting first of the boiling off of adsorbed water from the surface, followed by gas breakdown in the evolved water vapor. They carried out experimental tests of five critical predictions of this model. The tests were as follows:

a) The breakdown threshold depends on the ambient gas pressure, but not the gas species, as long as the ambient gas is transparent to the incident light.

b) Since the electron loss in the breakdown region is limited by the depth of the evolved gas rather than the width of the illuminated area, no spot-size dependence is expected.

c) Surface treatment to reduce surface absorption should increase the observed damage threshold.

d) At optical frequencies, the threshold intensity should decrease with increasing wavelength as λ^{-2}.

e) For long pulses (> 1 μs), the threshold should increase with increasing pulse rise time, due to gas-dynamic expansion of the water vapor during the breakdown process.

Good agreement was observed between the predictions of this model and the experimental results. The materials tested included NaCℓ, ZnSe, KRS-5, KRS-6, and Ge.

4.0 Recommendations

As a result of this year's symposium format, it is quite straightforward to cull from the invited papers and round-table discussion an objective summary of the state of the art and understanding in the general area of optical materials exposed to high power lasers. Resulting recommendations are, of necessity, less detailed and specific than normal, but rather are general in nature as appropriate for a ten-year assessment of the field.

Following the order of topics discussed in the section on principal conclusions, we single out those areas which need further attention and note why they are important, whether due to a lack of consensus, inadequate capability or just incomplete data.

The first area appropriately concerns the general subject of laser induced damage to materials, in thin film form, at their surfaces and within the bulk proper. Of interest is not only demonstrated damage resistance but also our understanding of the damage process or mechanism itself. Thin films are at present the most damage sensitive optical feature in any optimally designed system. Optical materials in this form, as compared to surfaces and bulk materials, exhibit their lowest damage resistance. This undoubtedly arises from the presence of absorbing impurities or imperfections in film structure or at interfaces.

The existing data base, correlating the effects of starting material purity (of both films and substrate) and deposition conditions with the resultant structural and optical properties of the prepared optical coating, is grossly inadequate. To obtain a true understanding of why films fail and how to improve their performance, one must follow the road religiously, from describing the selection,

character, and purity of starting materials and substrate, through the fully documented deposition process, to a comprehensive physical and structural characterization of the thin film. Following this, one must determine the film's optical properties and correlate them, if possible, with the early steps. Damage testing and careful morphological investigation to elucidate performance and failure mode can then hopefully lead, after analysis, to an assessment of why films fail and suggest material and process changes which can be recommended to the fabricator. Comprehensive and careful multithreshold analysis will be invaluable at this stage.

The lack of a sufficient capability in this area is leading laser specialists to consider seriously the elimination of coatings, accepting the resultant losses. This is really a very inefficient type of damage avoidance. Other solutions recently rediscovered involve the use of graded-index surfaces which can be achieved by ion implantation. In this case, there is really no film per se but rather a hopefully appropriate index variation from air to bulk. Certainly more work is required in this area to answer the question, "Do these structures exhibit bulk damage levels, damage levels of a reduced index material, or levels typical of thin films." In addition, achievable uniformities, index gradients, optical performance (high and low reflectivity, filtering action), and damage resistance should be determined. One should note that the index change is not only due to the concentration of ions implanted in the base structure but also to the concentration of defects produced as well. Questions on the choice of ions, their energies, rates, angles of incidence, etc., and the utility of annealing, etc., still remain to be answered.

Two years ago, a way around the sensitivity of film/substrate interfaces was proposed. The barrier layer came on the scene with a great hope for materially improving the damage resistance of antireflection coated elements. Up to 50 percent improvement in the damage threshold was reported, and the mechanism for this improvement seemed to be understood. Subsequent studies, however, indicated that improved performance was not always obtained and that the morphology observed was not always consistent with the understanding of the role of barrier layers. Further work is required to reduce the concept to practice reliably.

One last principal recommendation in the thin film area concerns the need for improvements in reflective dielectric coatings for metal mirrors, particularly in the uv. Unstable resonator systems require large aperture mirrors. Metal mirrors must be coated, to obtain a high reflectivity in the uv and to prevent unacceptable levels of thermal distortion. Also, large aperture focusing lenses for uv use will be difficult to fabricate and will be expensive, since the choice of materials is severely constrained by two-photon absorption. There is no question that, at short wavelengths, coated-mirror damage resistance levels will define system design and size. There will be a greater importance attached to scattering in thin films, as a loss mechanism, at these shorter wavelengths.

Even if one either eliminates coatings or can raise their damage resistance to levels comparable to the intermediate values typical of surfaces, there will still be several important areas which will need to be addressed. Certainly, the most important is the further development of metal mirrors and their figuring and finishing to uv required tolerances whether by diamond turning or more conventional methods. The two most important concerns are the reduction of surface absorption (equally true for window surfaces), no matter what its cause, be it plasmon excitation or just plain dirt, and concurrently cleaning, which is particularly important prior to coating. There is no question but that the future bodes well for the further development and employment of metal optics in high power applications from the ir to the uv, if further attention leads to improved surfaces. As metallic optics continues to invade the commercial field, increased attention to environmental degradation will be required to extend the utility and range of application of these components.

This brings us to the last area associated specifically with the laser induced damage process: breakdown mechanisms and phenomena. It has been amply stated that there is no consensus on an analytical or phenomenalogical description of laser induced breakdown in dielectric materials. Thus, scaling relation studies, statistical analysis, and multithreshold investigation are necessary as bench marks to validate and bound proposed theoretical descriptions. For example, roughness scaling may indicate whether an experimental result is indicative of intrinsic behavior or an impurity dominated extrinsic result. The same can be said for the use of statistical analysis as an indicator of probabilistic or deterministic behavior, another measure of intrinsity or extrinsity, similarly so for multithreshold experiments coupled with careful morphological investitgations.

Unfortunately, most morphological assessments are more indicative of the secondary effects of breakdown or of a breakdown plasma interacting with the specimen than the initiation process itself. Thus there was a strong call this year for threshold interaction experiments, to quantify the phenomena of potential precursors before a catastrophic response. Scattering and conductivity, e.g., ellipsometry, were immediately suggested as candidate diagnostics of these pre-breakdown experiments as both are very sensitive indicators of change. This is an excellent area for basic research, and should be closely coupled with scaling studies to insure that mechanisms are not changing, therefore allowing one to bound the applicability of the relation.

The necessity of determining the structural and optical properties of materials, particularly thin films and surfaces, resulting from process variables was mentioned earlier. In order to accomplish this task adequately, improvements in measurement and characterization techniques are

dictated. In concert with developments in these areas, calibration and standardization methods must keep pace to take advantage of the numerous advances in instrumentation. This requirement is best met by the National Bureau of Standards which not only has prime responsibility in the standards area, but should increase its tabulation and documentation efforts as well. To accomplish this task effectively, we must all support the continuation of NBS's activities and encourage their expansion through the acquisition of the latest advances in instrumentation. The desirability and necessity of this course of action is evident to those working in the field of optical materials for high power lasers.

An especially fruitful area of endeavor is the refinement of techniques for measuring nonlinear absorption. One would like to have accurate measurements of two-photon absorption, as a function of frequency, together with a comparison of the spectral dependence of one- and two-photon absorption, as a measure of the density of states accessible by odd and even parity transitions.

In the area of materials and fabrication, there are two principal recommendations, one in each category. Based upon a careful consideration of the numerous and diverse reports presented on thin films over the years during this series of symposia and upon a realization of the almost unlimited number of potential coating materials, it seems particularly propitious to recommend a narrowing of our attention to a reduced set of candidates. We tentatively propose the oxides of aluminum and silicon as well as fluorine containing compounds such as the fluorides and higher fluorine analogues (e.g., PbF_2, CaF_2, CeF_3, ThF_4, ...). It appears that this group provides a reasonable range of refractive indices for the designer (perhaps augmented by a few selected high index materials) and is sufficiently durable and environmentally stable, due to the strength of the chemical bonds in these materials. The thin film community needs to concentrate on perfecting the deposition of these materials. This recommendation will surely meet with some opposition, for everyone has his pet material or design. However, in spite of this expected reluctance, it appears that a concentration on these materials can lead to real improvements in the damage resistance and utility of coated elements.

We are still unsure as to how the hardness of alkali halides contributes to the differences and difficulty of grinding and polishing optical elements fabricated of these materials to required tolerances and figure. Forging may be a solution to this problem. Each year, we see continuted improvements in both understanding and demonstrated quality of forging technology, this year particularly evident with CaF_2. Additional research and develoment are desirable in this area to more fully appreciate the capability and limitations of this technique for fabrication of optical components from crystalline dielectrics. This is an area where additional material characterization is particularly necessary.

The shibboleth of the high power laser systems designer is damage avoidance. He now looks at the overall system performance and asks himself where the critical problems are. For example, can one really expect to achieve diffraction-limited system performance in the uv. Probably not, but then again, it may be necessary. In this uv case, the limit will probably be due to damage levels, unmanageable tolerance requirements, or just plain saturation. The designer instead looks to damage avoidance techniques such as phase conjugation to achieve desired system quality. Other damage avoidance techniques will undoubtedly surface now that our attention has been acutely drawn to this concept.

Phase conjugation is only one of a growing list of new endeavors in the area of laser induced damage to optical materials. Potential solutions usually bring potential problems as well. In this case, phase conjugation devices are subjected to potentially increased damage sensitivity due to the requirement for overlapping high power beams. This is somewhat reminiscent of the different damage sensitivities of intra- and extra-cavity second harmonic generation crystals reported many years ago. In that case, while frequency conversion efficiency was improved for the intra-cavity case, the resistance to damage was much less than for low efficiency extra-cavity elements.

As has been pointed out, this year saw the first report of laser induced damage to optical fibers. It is anticipated that interest in this area will grow as applications for power transmission through fibers increase and the frequency domain of usage extends into the infrared where new materials promise extremely low transmission losses. It is also anticipated that new problems will arise in connection with the continued development of free electron lasers over a wide range of wavelengths. To this we must obviously add the continued movement to shorter wavelengths, which promises increased concern about scattering, more stringent figures and surface tolerances and nonlinear processes.

The revelation that copper optics degrades in industrial CO_2 laser environments is one indication of the important role surface chemistry plays in optical damage phenomena. Environmental stability in general, along with the problems of surface contamination in the preparation of optical elements, needs to be addressed using the analytical tools and diagnostic techniques of surface chemistry. Many diagnostic techniques, such as ATR spectroscopy, and ion, electron, and optical microprobes, are available for this area of investigation.

The laser fusion community is moving to slightly longer pulse durations, in the few to 10 nsec regime. Thus, one would expect more emphasis on thermal mechanisms, especially in thin films, most certainly if systems are repetitively pulsed. It is at these longer pulse durations, compared with the subnanosecond domain, that certain scaling relations, such as surface roughness, become more manifest.

There are two remaining recommendations, both of which we have touched upon earlier. We have matured enough in this field that there should be considerably less excuse for repeating the errors and inefficient approaches characteristic of our earlier years. Through these proceedings, we have tried to transfer information and effectively document in one series the principal efforts and thoughts on laser induced damage to optical materials.

We should now be able to advance in technology by paying careful attention to our history, our tortured and occasionally wandering travels, capitalizing on past successes, and avoiding past pitfalls. This is an appropriate time to assemble our understanding, and to tabulate the results of the past decade's program of measurement of relevant properties of materials. The former will be accomplished through publishing the invited papers given at this, the Tenth Symposium. The latter will probably be best accomplished by the National Bureau of Standards. NBS has maintained a measurements program for optical materials for several years. We should all support the assumption, by NBS, of the responsibility for assembling and cataloguing the parameters of optical materials.

The variety of factors which influence the properties and performance of optical thin films is only matched in number by the fragmented, mostly uncoordinated efforts involving thin films. Unlike the thin film activities of the electronics industry, there is no single incentive for an optical thin film application of comparable magnitude. Rather, there is large diversity of applications, no one of which can justify a comprehensive and fundamental approach to understanding and improving thin films. When this situation arises and is recognized, there is no more appropriate solution than for the problem to be addressed by a government agency or group of agencies collectively. The first alternative is difficult because the problem is so large and multifaceted that, like industry, no one agency can go it alone either. Therefore, the only recourse is a collective attack by interested parties. The group should most logically include the Office of Basic Energy Sciences of the Department of Energy, the various research arms of the Department of Defense, including the Army Research Office, the Office of Naval Research, the Air Force Office of Scientific Research, and, of course, Defense Advanced Research Projects Agency. To these we add the National Bureau of Standards of the Department of Commerce and the National Science Foundation. Industry and education must of necessity play key roles along with government. We must revitalize our depleted thin film physics capability in the academic community. Thin film optics is still largely an art. The development of centers of excellence would not only lead to improvements in understanding and performance but would more importantly establish an open and thus widely available technology base. A concentrated, coordinated, and sound program in optical thin films can lead to tremendous improvements in commerce, communication, defense and energy, as well as many other endeavors. Your support for this approach is solicited.

5. Acknowledgment

The editors would like to acknowledge the invaluable assistance of Dr. Harold S. Boyne, Dr. Aaron Sanders, Ms. Marilee Hood, Ms. Margaret Wooley, Ms. Phyllis O'Rourke, and the other involved staff members of the National Bureau of Standards in Boulder, Colorado, for their interest, support, and untiring efforts in the professional operation of the Symposium and in the preparation and publication of the Proceedings. The continued success of the Damage Symposia would not have been possible without the enthusiastic support of those named above.

6. Bibliography

[1] "Damage in Laser Glass," A. J. Glass and A. H. Guenther, Editors, ASTM Special Technical Publication 469, ASTM, Philadelphia, PA (1969).

[2] "Damage in Laser Materials," A. J. Glass and A. H . Guenther, Editors, NBS Special Publication 341, U.S. Government Printing Office, Washington, D.C. (1970).

[3] "Fundamentals of Damage in Laser Glass," N. Bloembergen, National Materials Advisory Board Publication NMAB-271, National Academy of Sciences, Washington, D.C. (1970).

[4] "High Power Infrared Laser Windows," N. Bloembergen, National Materials Advisory Board Publication NMAB-292, National Academy of Sciences, Washington, D.C. (1972).

[5] "Damage in Laser Materials: 1971," A. J. Glass and A. H. Guenther, Editors, NBS Special Publication 356, U.S. Goverment Printing Office, Washington, D.C. (1971).

[6] "Laser Induced Damage of Optical Materials: 1972," A. J. Glass and A. H. Guenther, Editors, NBS Special Publication 372, U.S. Government Printing Office Washington, D.C. (1972).

[7] "Laser Induced Damage of Optical Elements, A Status Report," A. J. Glass and A. H. Guenther, Applied Optics 12, pp. 637-649 (1973).

[8] "Laser Induced Damage in Optical Material 1973," A. J. Glass and A. H. Guenther, Editors, NBS Special Publication 387, U.S Government Printing Office, Washington, D.C. (1973).

[9] Laser Induced Damage in Optical Materials 1973: A Conference Report," A. J. Glass and A. H. Guenther, Applied Optics 14, pp. 74-88 (1974).

[10] "Laser Induced Damage in Optical Material 1974," A. J. Glass and A. H. Guenther, Editors, NBS Special Publication 414, U.S Government Printing Office, Washington, D.C. (1974).

[11] "Laser Induced Damage in Optical Material 6th ASTM Symposium," A. J. Glass and A. H. Guenther, Applied Optics 14, pp. 698-715 (1975).

[12] "Laser Induced Damage in Optical Materials: 1975," A. J. Glass and A. H. Guenther, Editors, NBS Special Publication 435, U.S Government Printing Office, Washington, D.C. (1975).

[13] "Laser Induced Damage in Optical Materials: 7th ASTM Symposium," A. J. Glass and A. H. Guenther, Applied Optics 15, No. 6, pp. 1510-1529 (1976).

[14] "Laser Induced Damage in Optical Materials: 1976," A. J. Glass and A. H. Guentehr, Editors, NBS Special Publication 462, U.S. Government Printing Office, Washington, D.C. (1976).

[15] "Laser Induced Damage in Optical Materials: 8th ASTM Symposium," A. J. Glass and A. H. Guenther, Applied Optics 16, No. 5, pp. 1214-1231 (1977).

[16] "Laser Induced Damage in Optical Materials: 1977," A. J. Glass and A. H. Guenther, Editors, NBS Special Publication 509, U.S. Government Printing Office, Washington, D.C. (1977).

[17] "Laser Induced Damage in Optical Materials: 9th ASTM Symposium," A. J. Glass and A. H. Guenther, Applied Optics 17, No. 15, pp. 2386-2411 (1978).

S.I. CONVERSION UNITS

In view of present accepted practice in this technological area, U.S. customary units of measurement have been used throughout this report. It should be noted that the United States is a signatory to the General Conference on Weights and Measures which gave official status to the metric S.I. system of S.I. units in 1960. Readers interested in making use of the coherent system of S.I. units will find conversion factors in ASTM Standard Metric Practice Guide, ASTM Designation E 380-76 (available from American Society for Testing and Materials, 1916 Race Street, Philadelphia, Pennsylvania 19103). Conversion factors for units used in this paper are:

Length

1 in = 0.0254* meter

1 ft = 0.3048* meter

1 microinch = 2.5400* x 10^{-8} meter

Area

1 in^2 = 6.4516* x 10^{-4} $meter^2$

1 ft^2 = 9.2903 x 10^{-2} $meter^2$

Force

1 lb (lbf) = 4.448 newton

1 kip = 4448 newton

Pressure Stress

1 psi = 6895 pascal

1 psf = 47.88 pascal

Energy

1 ft-lbf = 1.3558 joule

Moment

1 lbf-ft = 1.3558 newtonmeter

Temperature

$To_C = 5/9\ (To_F - 32)$

Heat

Thermal conductivity,

1 cal (thermochemical) cm.s. ^oC = 418.40* watt/meter kelvin

specific heat, C

1 cal (Thermochemical)/gm.^oC = 4184.00* joule/kilogram kelvin

*Exact value

DOE WELCOME
PRESENTATION OF AWARDS TO DRS. GUENTHER AND GLASS

C. Martin Stickley
Director, Office of Laser Fusion
Department of Energy
Washington, DC 20545

It is both an honor and a privilege to be invited to speak at this tenth anniversary meeting. This symposium has become an established fixture in the laser community, for whom its only title will always be "The Laser Damage Meeting," even though I recommended changing it. As a participant and attendee of many of these meetings over the years, and even as an editor with Art Guenther and Alex Glass for the first one, I must admit that ten years ago few of us expected that our trip to Boulder would become an annual pilgrimage. On the other hand, I doubt that any of us could have appreciated the tenacity with which this group would hold onto the opportunity to spend a week in the Rockies each year!

While preparing these remarks, I was looking back through the proceedings from years past, and I was immediately struck by the progressive size growth of that yearly NBS publication. From barely a hundred pages and a dozen papers in the first years, the proceedings have grown to last year's 561 page tome with some fifty-odd papers.

Another thing I noticed in reviewing the proceedings was the significant maturation of the damage field as evidenced by the kinds of papers submitted. The early meetings, as one might expect, were dominated by empirical papers presenting evidence of damage, principally using glass laser systems. The papers tended to be rather general in nature and more times than not the data in papers by different authors at different laboratories tended to disagree. In recent years the scope of the meeting has broadened significantly to include a large variety of laser sources and optical materials. The basic issues have not changed but the damage thresholds now discussed are appreciably higher and the laser pulses somewhat shorter and more powerful than most were at the early meetings. The titles of the papers tend to sound a bit more erudite than they used to but occasionally one still notices aspects that recall the old days -- things like "scotch tape tests" and "calibrated cheesecloth wipes."

The laser damage field has, in fact, matured to the extent that it is really two rather distinct subfields. On one hand there is the technology community, the laser builders and users (including much of the DOD effort), for whom laser damage is a serious problem which needs to be made less serious but does not necessarily have to be fully understood. On the other hand, many in the research community look upon laser damage as a physical process which ought to be understood in its own right; one which should be well characterized before attempts are made to solve technological issues. This dichotomy in perspective leads at times to an interesting juxtaposition of papers at these damage symposia. Neither of these approaches is totally right or wrong, each has its place in a field as broad as ours. What is necessary is to be able to decide which perspective is appropriate with regard to the situation one has at hand. The desire to find fundamental solutions to problems must be balanced against the needs of technology programs to achieve short term results.

In the laser fusion program most of our present efforts in laser damage are directed at finding short term solutions to improve the performance of our operational systems. However, we are well aware that we must soon begin to address the fundamental issues in the damage field if we ever are going to be able to construct megajoule lasers for power plants of the future. Achieving the proper ratio of technology to fundamental research is always a difficult problem for an R&D program manager and it is not any less so in the laser damage field. As many of us are painfully aware, it is quite possible to throw good money after bad in pursuit of "easy" empirical solutions to damage problems, and, likewise, it is possible to believe that one is investing in a black hole in looking for fundamental solutions to some questions. There is no question but that we are making progress in understanding laser damage mechanisms and improving thresholds, but it is comforting to know that ten years from now we will surely be here celebrating the twentieth anniversary of this symposium.

One other thing that is comforting is the knowledge that when we return here ten years from now, Art Guenther and Alex Glass will still be running this symposium. We all owe a large debt of gratitude to these two young men who not only originated the idea of this meeting but who also have worked each year to put it together and to insure that its deliberations are preserved for posterity. It is probably safe to say that Art and Alex run the most unique conference in the laser business if not in all of physics. This is the only meeting I can think of that is run by a junta, and I can only say that I could wish more meetings were run that way if it would insure as smoothly run a meeting as this conference has always been.

As a symbol of our esteem for this pair of hard working meeting organizers, I would like to take this opportunity to present to them tokens of our appreciation of their efforts. First, on behalf of the ASTM and speaking for Haynes Lee, who could not be here for this meeting, I want to present Alex and Art with this award from the ASTM. The citation on the certificate of appreciation is: "The officers and members of Committee F-1 on electronics express their deep appreciation and gratitude in recognition of the outstanding contributions you have made to the laser industry by serving as Co-Chairman of the Laser Damage Symposium for 10 years." Next on behalf of the Department of Energy, and of the Defense Advanced Research Projects Agency, who is represented here by Captain Harry Winsor, I want to present them with these plaques. The inscription is, "This plaque expresses the appreciation of the Department of Energy and the Defense Advanced Research Projects Agency for leadership in the development of new and improved optical materials over the past decade. Presented to (Alex and Art), Co-Chairman "10th Symposium on Optical Materials for High Power Lasers." Again, my congratulations and thanks to both of them for their outstanding efforts over the past years.

REMARKS TO THE TENTH ANNUAL
BOULDER OPTICAL MATERIALS
FOR
HIGH POWER LASERS SYMPOSIUM

Captain Harry Winsor
Material Science Office
Defense Advanced Research Projects Agency
Washington, D.C.

Let me add DARPA's and my voices to Martin Stickley's welcome to the tenth annual gathering of the Boulder Optical Materials for High Power Lasers Conference. On my meeting papers this has appeared variously as "Boulder Damage Symposium" and "Laser Seminar." You'd think by the tenth time around we would have found a name for this meeting.

The subject of this meeting is components for power optics systems. I say power optics in the same sense that electrical engineers say electrical power handling equipment--the technology, materials, and concerns of optics are fundamentally different, yet strangely the same as those of signal optics. Power optics breaks down into two categories, which are also analogous to the electrical case: pulse optics and high flux (current) optics. Components in both areas have the basic problem of handling large amounts of energy without incurring momentary or permanent loss of function. Let us examine this situation more closely.

The first problem encountered was laser materials. Specifically, I mean ruby and various other laser host materials. This falls under the pulse optics rubric, since the problem was the thermal damage due to inclusions or electric field induced damage in laser rods. The damage occurring in these materials was the subject of many an early session. To a large degree, the problems have been alleviated, as amplified by Dr. Stickley and other contributors at these meetings. The primary remaining problem from DARPA's viewpoint is the generation of materials for miniature lasers for designators and rangefinders.

Other early topics were the investigation of pulse damage of materials introduced in the focus of pulse lasers and the examination of such topical problems as the onset of avalanche breakdown. All research was done in conjunction with the ASTM, since there was a critical need for new standards in this area. You have also heard about this from Dr. Stickley, and you will hear more duing the rest of this Symposium.

Aside from a gain medium, lasers require mirrors and, at times, windows. Both mirrors and windows may use thin films for reflection control. The primary differences between signal and power optics mirrors are the use of water-cooled substrates and the emphasis on absorption as opposed to reflectivity. These concerns emphasize the fact that the parasitic losses are large enough to melt, deform, or fracture the components. Windows are required to separate incompatible environments internal and external to the laser system. (More often, it seems that laboratory high power CW laser systems operate without windows.) The problems of developing window materials with low absorption have been solved at several wavelengths, and can be solved operationally at any other desired wavelengths.

Speaking of wavelengths brings to mind a situation I mentioned last year--every time we solve a material absorption or film deposition problem at one wavelength, the system designers change the wavelength at which they want to operate a system. This has led to a restructuring of DARPA's Laser Window and Coating programs to develop a generic range of experience at a variety of wavelengths rather than to derive solutions for specific wavelengths. We are therefore leaving the problems of optimization of materials and films at most wavelengths to the systems' projects. We have provided documented examples of how the problems may be solved and have performed the necessary survey studies to list the most likely impurity problems that will be encountered at all probable wavelengths.

I would like to reiterate another theme from my remarks last year--the system designers will always want to increase the power handling capacity of the components, so reduced absorption research will be with us until we can show that we have reached intrinsic levels of performance using the best possible materials for the specific job. It is thus very important to list in the technical reports, simply and clearly, whether there is room for further development of the material and what directions that development might take.

In addition to this, there is one other thing the the industrial and commercial concerns represented here should remember: the governmental support available for long-range, fundamental research in power optics materials will be in direct proportion to the requests for this support. For instance, the National Bureau of Standards (NBS) currently wants to hear from industrial and commercial enterprises concerning their needs for basic optical measurements such as index of refraction, optical constants of bulk and thin-film materials, such as strain birefringence and temperature dependence of index of refraction, as well as thermal conductivities and thermal expansion coefficients of optical

materials. Word of new research you want the NBS to conduct is also solicited. Please communicate this information to Bruce Steiner at NBS, Washington, D.C., or even better, call him and follow up with a letter. NBS is trying to restructure its activities, but much of the work of the sort being done by Al Feldman and Marilyn Dodge may be discontinued unless it serves a documented "commercial" need. This documentation may not come directly from the DoD. It must come from prospective DoD contractors and subcontractors. Commercial product needs may also justify such research.

Returning to the power optics problems remaining to be solved, two stand out prominently: (1) anomolously high absorption levels in thin films as compared to the bulk material used for deposition of the films, and (2) survival of power handling components in space and other operating environments. The coating absorption problem appears to be yielding rather rapidly at this time, as will be apparent from Marshall Spark's papers, and the NWC efforts, which were, unfortunately, not cleared in time for presentation here. The space and environmental problems are under attack on a number of fronts and hopefully should yield in the near future. Both these problems combine together for thin films for spaceborne HF laser optics and for mirror coatings for duty in rare gas-halide eximer laser cavities. In the years ahead, they will also be problems for the tunable, free-electron laser. With this latter system, designers have finally devised a system which maximizes the rubber wavelength problem referred to earlier. If this system is developed, as appears nearly certain, we will encounter almost all conceivable adverse internal environmental circumstances in operating power optics components--all on one laser system.

The free-electron laser represents an opportunity as well. Greater than 50 percent wallplug efficiency in photon production opens the possibility of photo-purification of optical materials. The free-electron laser may thus lead to a dramatic improvment in laser component materials. This is lifting oneself up by one's bootstraps. The free-electron laser will also provide isotoptically pure materials for construction of refining machinery and systems. This will allow us to tailor the isotopic mix of the trace impurities left in our optical materials. This may become a major way of improving not only power optics materials but also optical waveguide materials. Other promising isotopic engineering opportunities may well appear as these avenues are explored.

Passing on to some more fundamental problems, the improved scatter required of components for uv power optics systems leads to requirements for improved surface roughness in substrates and films. This means that the long-neglected areas of the polishing of mirror substrates and the nucleation and growth of thin films will require renewed interest. These problem areas lead optical scientists into the unfamiliar (to them) areas of molybdenum metallurgy, wear theory, and surface topographic characterization. Add the problems that arise as one seeks optical coatings which resist impurity absorption, radiation damage, and erosion in adverse environments, and the optical scientists are entering the areas of polymer chemistry, atomic physics, and corrosion rate theories. The point of this is that the area is astonishingly multidisciplinary. Add the problems encountered with repetitively pulsed lasers: material fatigue, thermal conductivity, and interface adhesion theory, and....The problems and interconnections never stop. How will we be able to document this astonishing array of interdisciplinary problems and techniques in a manner that will facilitate their being understood by people who haven't enough time to assimilate all the details. More and more, the complexity of this field inhibits our ability to determine whether more research is needed, and if so, what research. Who will write the book which brings perspective to this field, and how long will it take. How much of this complexity must be mastered by systems designers. How soon. I am sure that the proceedings of this Symposium will play a significant role in answering this need for readable documentation.

SYMPOSIUM WELCOME

Alexander J. Glass
Lawrence Livermore Laboratory
P.O. Box 5508, Livermore, CA 94550

It is my annual hope that each year's Symposium will be the last. Not because I dislike the subject, or because I find Boulder inhospitable, but because I'd like to think that we can solve the problems of laser damage, and move on to new challenges.

Like other speakers addressing you at the beginning of this conference, I asked myself what we have learned in ten years, and what remains to be done. What we have learned in ten years, very simply stated, is how to build high power lasers. Ten years ago we were discussing high power lasers. Now, high power lasers are a reality. According to Aviation Week, there exist high power, cw lasers operating in excess of 100 kilowatts. At the Lawrence Livermore Laboratory, and elsewhere, there exist multi-terawatt systems operating on a relatively routine basis. Gigawatt lasers have become commonplace, and hardly worthy of mention in a high power laser meeting. Lasers with design figures of 100 terawatts or greater are under construction in at least two locations in the United States. The technology of high power lasers has not waited for us to solve the damage problems, and that is the theme I want to discuss.

One of the things we have learned in the last ten years is how important laser damage and optical materials considerations are in the design of high power lasers. We have three papers at this meeting addressed to the influence of materials problems on the design of high power laser systems: one on cw lasers, one on pulsed IR lasers, and one on pulsed neodymium glass lasers.

The failure of optical materials, either transient or permanent, remains the major limit to the performance of high power laser systems. Although there have been great advances, it remains as one of the highest leverage areas for improvement. System designers are now well aware of damage problems, which in itself represents a major achievement. The overall awareness of damage problems on the part of everyone involved, from the people who make the materials to begin with, to the people who apply the materials in the end use, has increased tremendously. We have learned, as we were taught at our mother's knee, that cleanliness and purity are virtues. The cleanliness and purity of the basic materials from which optical components are made are very important. It has been as a consequence of the work of the people attending this symposium that the importance of cleanliness and care in maintenance of operating systems has also come to be realized. Captain Winsor alluded to the importance of keeping in mind the fact that the system must operate in a certain environment. In some of the environments that we anticipate, the maintenance of the necessary cleanliness in the system may be very difficult.

But all of that comes under the heading of consciousness raising. It is not sufficient simply to make people aware of the problems. One must also provide solutions. In the course of the ten years in which this symposium has been going on, we have made significant advances in the quality of optical materials for high power lasers. There is good evidence to believe that for any wavelength desired, low loss window materials can be provided. In the neodymium glass area, the advent of materials with low nonlinear index materials is a reality. We shall be hearing about some of those advances at this symposium. These two things have been very real accomplishments and lead directly to improved system performance. In the coating area, Captain Winsor mentioned that damage thresholds have been significantly increased, to which I would only add the word "occasionally." What are we going to have to learn to avoid having this meeting in ten years? The first thing is to translate research advances into production terms. I am somewhat biased by recent experiences at the Lawrence Livermore Laboratory; but I am sure it is true generally that it is one thing to obtain a research coating which is of extremely good quality and exhibits a very high damage threshold, but it's another thing to get it on a production basis over a large aperture, when you need it. In the materials area, and particularly regarding thin films, we need good materials and components to be available on a regular commercial basis, at reasonable cost, and in reasonable quantity. There is a strong incentive to the manufacturers to pursue this, because there are very large systems under design and on which construction will soon start. These very large systems will carry with them significant orders. It is not only the orders for the first round of components, but for a continuing supply of replacement parts as well. Large lasers are inevitably driven beyond the limit imposed by the onset of damage. The importance of generic studies was mentioned. We clearly have to learn to transfer knowledge from one pulse length to another, and from one wavelength to another. In the laser fusion program, for example, as the lasers get larger, the pulse lengths get longer.

For a while, we were reveling in the relative simplicity of sub-nanosecond damage phenomena. Now we are working with longer pulses. The pulse duration is moving steadily out into the one-to-ten nanosecond regime, where a host of new and fascinating effects enter. It is not sufficient to say we have solved the problem; just operate your system at 100 picoseconds. The end use requirement dictates that we must continue to come to terms with damage phenomena over a range of pulse durations.

Some years ago, Martin Stickley suggested changing the name of the Symposium. He felt that "Laser Damage" was too restrictive and had a negative connotation. We now officially refer to the Symposium on Optical Materials for High Power Lasers. I should like to advocate broadening the scope of the

Symposium a little further, to place increased emphasis on "damage avoidance."

What do I mean by damage avoidance? I mean the following: There is always some level at which the system fails, but in designing the system we try to maintain the minimum ratio of peak-to- average power density. Almost all the phenomena we talk about are either sensitive to the maximum of power density or to the time integrated maximum of power density. If we can reduce the modulation on the beam temporally and spatially, then we can transmit the maximum average power subject to local damage constraints. Examples of the techniques to do this, of damage avoidance techniques, include the following. Spatial filters have been introduced in neodymium glass systems to suppress the growth of spatial modulation. Optical relaying is an application of the imaging character of the spatial filter, which enables us to suppress diffraction effects, and therefore make more efficient use of the aperture to again raise the total power through the system while holding the peak power density below some limiting value. A technique which is showing great promise, especially at 10.6 microns, is phase conjugation, double passing through an amplifier and using a nonlinear element to correct out any phase distortion, which is a very promising technique for maintaining a low peak-to-average ratio. There also is the plasma spatial filter, invented at KMS, in which dithering of the beam provides spatial averaging during the course of the pulse as a way of reducing peak-to-average energy density on any particular spot. Design techniques are also damage avoidance techniques. The best example is designing thin film coatings to minimize the local field maximum. I am sure there are other good ideas for damage avoidance, and I invite you all to extend your thinking beyond the particular problem of a given material or component to this area as well. I think that it is an area of great promise. There are many good ideas which have not been exploited, and we need new approaches quite urgently. We are currently building large systems which must perform well, and the leverage is very great. Improvement in the ability to transmit high power or high energy through the aperture translates directly into more kilojoules or more terawatts per megabuck. In the real world, that is the figure of merit. I know I speak for the preceding speakers when I say there are funds available for good ideas in the area of damage avoidance.

It is fairly certain that we will meet here next fall for the Eleventh Symposium on Optical Materials for High Power Lasers. We still have not solved the problems of laser damage. I sincerely hope, however, that we can broaden the scope of our activity to include not only improved understanding of damage phenomena, but also new ways to avoid damage as well.

In closing, I'd like to acknowledge the continuing support of the Defense Advanced Research Projects Agency, the Office of Naval Research, and the Department of Energy. Both Dr. Guenther and I are personally grateful to Dr. Stickley and Captain Winsor for their kind words on the occasion of the Tenth Symposium. We want to express our gratitude also to Haynes Lee of the American Society of Testing and Materials and to Dr. Boyne and the staff of the National Bureau of Standards for their hospitality and their continuing efforts to make these symposia both pleasant and productive.

DISCUSSION OF A THEORY OF ANALYSIS OF RATE CALORIMETRY WHICH INCLUDES COATING ABSORPTION

Nils C. Fernelius and George T. Johnston
University of Dayton Research Institute
300 College Park Avenue
Dayton, Ohio 45469

A simplified method of analyzing laser rate calorimetry on samples with absorbing coatings is presented. Special cases of rate calorimetry are shown to agree with previously derived cases. Results are given for samples with dissimilar faces in which the temperature rise and the reflected power in both orientations to the laser beam are measured. A computer program was written to reduce data. A sample case shows that the output requires the reflected and transmitted powers to be measured to three significant figures for meaningful results.

Key words: Coating optical absorption; laser calorimetry theory; optical calorimetry theory; surface optical absorption.

1. Introduction

The problem of how to treat rate, or slope, calorimetry in samples with absorbing coatings has appeared from time to time during the course of our work. This paper gives a simplified method to handle more general cases of rate calorimetry and is shown to agree with the results of previous analyses of some special cases. We will first derive basic calorimetric equations for a window sample which includes surface absorption for the case of absorption independent of incident medium and for incident medium dependence. Later these results will be applied to coatings in the approximation that coherence effects may be ignored.

2. Basic Equation Derivation

The basic calorimetric problem is illustrated in figure 1. Each surface of the sample is described by an absorbance, reflectance, and transmittance coefficient subject to these restrictions:

$$A_1 + R_1 + T_1 = 1 \quad \text{and} \quad A_2 + R_2 + T_2 = 1 \ .$$

The bulk absorbance, $A_o \equiv 1 - \exp(-\beta\ell)$, where for small $\beta\ell$, $A_o \simeq \beta\ell$. Likewise, the unit incident power has this restriction: $P_T + P_R + P_B + P_1 + P_2 = 1$,

where

P_T = power transmitted,

P_R = power reflected,

P_B = power absorbed in bulk,

P_1 = power absorbed in front surface,

P_2 = power absorbed in back surface.

Coherent effects in the substrate are neglected, which is acceptable in thick samples with non-optically parallel surfaces. They are also ignored on the surfaces which may be seriously incorrect on coated samples. However, even with these severe assumptions, the resulting simplified treatment is barely tractable. Multiple reflection effects are handled by the use of the binomial expansion,

$$1/(1 - x) = 1 + x + x^2 + x^3 + x^4 + x^5 + \ldots$$

valid for $x^2<1$. For unit incident power, the power transmitted at the exit surface is

$$P_T = (1-A_o)T_1T_2 + (1-A_o)^3T_1T_2R_1R_2 + (1-A_o)^5T_1T_2R_1^2R_2^2 + \ldots.$$

$$P_T = \frac{(1-A_o)T_1T_2}{1 - (1-A_o)^2R_1R_2} \tag{1}$$

The power reflected at the front surface,1, is

$$P_R = R_1 + (1-A_o)^2R_2T_1^2 + (1-A_o)^4R_2^2T_1^2R_1 + (1-A_o)^6T_1^2R_2^3R_1^2 + \ldots.$$

$$P_R = R_1 + \frac{(1-A_o)^2T_1^2R_2}{1 - (1-A_o)^2R_1R_2} = \frac{R_1 + R_2(1-A_o)^2(T_1^2 - R_1^2)}{1 - R_1R_2(1-A_o)^2} \tag{2}$$

The power absorbed at the front surface,1, is

$$P_1 = A_1 + A_1(1-A_o)^2T_1R_2 + A_1(1-A_o)^4T_1R_2^2R_1 + \ldots.$$

$$P_1 = A_1 + \frac{A_1T_1(1-A_o)^2R_2}{1 - (1-A_o)^2R_1R_2} = \frac{A_1[1 + (1-A_o)^2R_2(T_1-R_1)]}{1 - R_1R_2(1-A_o)^2} \tag{3}$$

The power absorbed at the back surface,2, is

$$P_2 = (1-A_o)T_1A_2 + (1-A_o)^3T_1A_2R_1R_2 + (1-A_o)^5T_1A_2R_1^2R_2^2 + \ldots.$$

$$P_2 = \frac{T_1A_2(1-A_o)}{1 - R_1R_2(1-A_o)^2} \tag{4}$$

The power absorbed in the bulk per pass is A_o times the intensity at the beginning of the pass. Thus,

$$P_B = A_o[T_1 + (1-A_o)^2T_1R_1R_2 + (1-A_o)^4T_1R_1^2R_2^2 + (1-A_o)^6T_1R_1^3R_2^3 + \ldots.\ ] +$$
$$A_o[(1-A_o)T_1R_2 + (1-A_o)^3T_1R_1R_2^2 + (1-A_o)^5T_1R_1^3R_2^2 + \ldots.]$$

$$P_B = \frac{A_oT_1}{1-R_1R_2(1-A_o)^2} + \frac{A_o(1-A_o)T_1R_2}{1 - R_1R_2(1-A_o)^2} = \frac{A_oT_1[1 + (1-A_o)R_2]}{1 - R_1R_2(1-A_o)^2} \tag{5}$$

The power absorbed in the sample is $P_A = P_1 + P_2 + P_B$

where

$$P_A = \frac{A_1[1 + (1-A_o)^2R_2(T_1-R_1)] + (1-A_o)T_1A_2 + A_oT_1[1 + (1-A_o)R_2]}{1 - R_1R_2(1-A_o)^2} \tag{6}$$

By going through the algebra, we find that $P_A + P_R + P_T = 1$, as it should for conservation of energy.

Another approach to this problem is presented in Heavens [1][1]. He treats the optical properties by the use of the complex index of refraction, $\tilde{n} = n - ik$. The optical absorption coefficient can be expressed as $\beta = 4\pi k/\lambda_o$, where λ_o is the vacuum wavelength. This yields a reflection coefficient of $R = [(n-1)^2 + k^2]/[(n+1)^2 + k^2]$. Note that for a $\beta \simeq 10^{-3}cm^{-1}$ at 10 μm wavelength, we get $k = \lambda_o\beta/(4\pi) \simeq 10^{-7}$, an insignificantly small number in most cases. Heavens treats the case of an absorbing film on an absorbing substrate and includes coherence effects in the film (pp.76-77). He comments that the reflectance at the film-substrate interface differs according to the direction from which the interface is approached but that the transmittance remains the same. Very complicated formulae are given for the two reflectances. They are identical except for the interchange of two brackets. Unless one is dealing with heavily absorbing films, the two reflectance values are essentially the same in this treatment. Gibbs and Butterfield [2] have used this approach for laser window calorimetry.

Workers in the area of laser damage have consisently observed that a transparent dielectric material traversed by a collimated light beam, always damages on the exit surface at a lower power level than that at which the entrance surface damages. Crisp et al [3,4,5] have proposed that this is explained mainly as an effect of Fresnel reflection. All of their analysis assumes phase coherence. A way of incorporating this effect into laser rate calorimetry has been suggested by Miles [6] and Apfel [7]. It will be given in the following paragraphs.

At each surface as shown in figure 1, the absorbance, reflection and transmission for light approaching from air is A_1, R_1 and T_1; A_2, R_2 and T_2 as before. However when light approaches the surface from inside the substrate, the absorbance and reflectance are different and denoted as A_1', R_1', A_2' and R_2'. This leads to additional conservation conditions, viz. $A_1' + R_1' + T_1 = 1$ and $A_2' + R_2' + T_2 = 1$ where $A_1' = xA_1$ and $A_2' = xA_2$. Thus $R_1' = R_1 + A_1(1 - x)$ and $R_2' = R_2 + A_2(1 - x)$. When coherence is not assumed [6,7] $x = n$, when it is assumed[3,4,5] $x = 4n^2/(n + 1)^2$.

Going through a similar analysis as before, various results are changed. The analogous equations will be numbered as before only primed.

$$P_T = \frac{(1-A_o)T_1T_2}{1 - (1 - A_o)^2R_1'R_2'} \tag{1'}$$

$$P_R = \frac{R_1 + R_2'(1-A_o)^2(T_1^2-R_1R_1')}{1 - (1 - A_o)^2R_1'R_2'} \tag{2'}$$

$$P_1 = \frac{A_1 + (1-A_o)^2R_2'(A_1'T_1-A_1R_1')}{1 - (1 - A_o)^2R_1'R_2'} \tag{3'}$$

$$P_2 = \frac{T_1A_2'(1-A_o)}{1 - (1 - A_o)^2R_1'R_2'} \tag{4'}$$

---

1. Figures in brackets indicate the literature references at the end of this paper.

$$P_B = \frac{A_o T_1[1 + (1-A_o)R_2']}{1 - (1-A_o)^2 R_1' R_2'} \qquad (5')$$

$$P_A = \frac{A_1 + (1-A_o)^2 R_2'(A_1' T_1 - A_1 R_1') + (1-A_o)T_1 A_2' + A_o T_1[1 + (1-A_o)R_2']}{1 - (1-A_o)^2 R_1' R_2'} \qquad (6')$$

Again with the additional conservation equations, conservation of energy is maintained with these new results.

3. Applications of Basic Equations

Now we shall apply these results to some special cases. A few have been obtained previously and are used as a check of the validity of this method. These applications fall into two general classifications--those allowing for large absorptance and those regarding absorptance as a small quantity. The cases treated are summarized as follows:

A. A_o may be large

Case 1- no restrictions on A's or R's
2- $R_2=0$, i.e. side away from laser beam (back side) an AR coating
3- $A_1=0$, assumes no surface absorption on front side
4- $A_1=A_2=0$, bulk absorption only

B. A_o, A_1, A_2 less than 0.1

Case 5- $A_1=A_2=0$, get the often used formula which has the correction for reflection at the rear surface.
6- $R_1=R_2=0$, AR coatings on both sides
7- Measure reflected power as well as transmitted power with window in both orientations with respect to incoming light beam.
8- If both surfaces identical, no new information from second orientation. Find surface and bulk absorption inseparably linked.
9- Before and after measurements when applying AR coatings.

CASE 1: If $A_o \equiv 1 - e^{-\beta\ell}$ with no restrictions on the magnitude of the A, R, and T's, then

$$P_T = T_1 T_2 e^{-\beta\ell}/[1 - R_1' R_2' e^{-\beta\ell}]$$

$$P_R = [R_1 + R_2'(T_1^2 - R_1 R_1')e^{-2\beta\ell}]/[1 - R_1' R_2' e^{-2\beta\ell}]$$

$$P_A = \frac{A_1 + R_2(T_1 A_1' - A_1 R_1')e^{-2\beta\ell} + A_2' T_1 e^{-\beta\ell} + T_1(1 + R_2' e^{-\beta\ell})(1 - e^{-\beta\ell})}{1 - R_1' R_2' e^{-2\beta\ell}}$$

This yields

$$\beta\ell = \ell n[\{T_1 T_2(1 + P_A/P_T) + \sqrt{T_1^2 T_2^2(1 + P_A/P_T)^2 + 4(A_1 + T_1)[R_2(A_1 R_1' - T_1 A_1') + T_1 R_2']}\}/2(A_1 + T_1)]$$

The $-\sqrt{\ }$ solution is unphysical since the argument of the log would be negative. Removing the primes on the above quantities yields the results obtained in the original simple treatment.

CASE 2: If the rear surface is an AR coating, then $R_2 = 0$ and

$$\beta\ell = \ell n[T_1 T_2(1 + P_A/P_T)/(A_1 + T_1)]$$

In the primed case, this equation is true if also $A_2 = 0$.

CASE 3: If we assume that $A_1 = 0$, (i.e., the front surface is bare and not absorbing with the rear side coated), then

$$\beta\ell = \ell n[\{T_2(1 + P_A/P_T) + \sqrt{T_2^2(1 + P_A/P_T)^2 + 4R_2'}\}/2]$$

Again, removing the prime yields the original result.

CASE 4: If $A_1 = A_2 = 0$, $R_1 + T_1 = 1$, and $R_2 + T_2 = 1$, then

$$\beta\ell = \ell n\left[\{(1-R_2)(1+P_A/P_T) + \sqrt{(1-R_2)^2(1 + P_A/P_T)^2 + 4R_2}\}/2\right]$$

This formula has been obtained previously.

In all of the following cases, we shall assume that $A_o = \beta\ell < 0.1$ and that A_1, A_1', A_2, $A_2' < 0.1$; that is, the substrate and coatings are all at least moderately transparent. To first order in the A's, we obtain the following expressions, where the transmittances have been eliminated:

$$P_R = \frac{R_1 + R_2[1 - 2(A_1+R_1) + (x+1)A_1 R_1 - 2A_o(1-2R_1)] - (1-2R_1)(x-1)A_2}{1 - R_1 R_2(1 - 2A_o) + (x-1)(A_1 R_2 + A_2 R_1)}$$

$$P_T = \frac{(1-R_1)(1-R_2)(1-A_o) - A_1(1-R_2) - A_2(1-R_1)}{1 - R_1R_2(1-2A_o) + (x-1)(A_1R_2 + A_2R_1)}$$

$$P_A = \frac{A_1[1+R_2\{x-(x+1)R_1\}] + xA_2(1-R_1) + A_o(1-R_1)(1+R_2)}{1 - R_1R_2(1-2A_o) + (x-1)(A_1R_2 + A_2R_1)}$$

When x = 1, we obtain the results of the original treatment. Again in this approximation, $P_R + P_T + P_A = 1$. Thus,

$$\frac{P_A}{P_T} = \frac{A_1[1+R_2\{x-(x+1)R_1\}] + xA_2(1-R_1) + A_o(1-R_1)(1+R_2)}{(1-R_1)(1-R_2)(1-A_o) - A_1(1-R_2) - (1-R_1)}$$

The calorimetric analysis of optical absorption data used in our laboratory follows the method described in the appendix of M.Hass et al [8]. The method considers the time situations before the laser is turned on, while it is on, and after it is turned off. Before the laser is turned on, while it is on, and after it is turned off. Before the laser is turned on, the sample is at temperature T_o.

When the laser is on, the power absorbed is

$$P_A = m\, C_p(dT_2/dt) + \rho(T_2-T_o).$$

After the laser is turned off, no power is absorbed, so

$$0 = m\, C_p(dT_3/dt) + \rho(T_3-T_o).$$

By measuring slopes where $T_2 = T_3$, we obtain

$$P_A = m\, C_p[(dT_2/dt) - (dT_3/dt)] = m\, C_p\, (\Delta T/\Delta t).$$

Since we measure the power transmitted by the sample, P_T, this equation must be converted to use the expression P_A/P_T derived above:

$$\frac{m\, C_p}{P_T}\frac{\Delta T}{\Delta t} = \frac{P_A}{P_T} = \frac{A_o(1-R_1)(1+R_2) + A_1[1+R_2\{x-(x+1)R_1\}] + xA_2(1-R_1)}{(1-R_1)(1-R_2)(1-A_o) - A_1(1-R_2) - A_2(1-R_1)} \quad .$$

Now we will treat some additional special cases, all of which assume that $\beta\ell$, A_o, A_1', and A_2' < 0.1.

CASE 5: If there is no surface absorption with reflections at each surface, i.e., $A_1 = A_2 = 0$, $A_o = \beta\ell$, then $P_A/P_T = A_o(1+R_2)/[(1-A_o)(1-R_2)] \simeq \beta\ell(1+R_2)/(1-R_2)$

ergo, $P_A/P_T = \beta\ell\,(1+R_b)/(1-R_b)$ where R_b is the reflectivity at the back surface. Note that we may get a different $\beta\ell$ when we reverse the orientation of the window with respect to the laser beam. If the window is uniform with no coatings, $R_b = [(n-1)/(n+1)]^2$, where n is the index of refraction of the substrate and $(1+R_b0/(1-R_b) = (1+n^2)/2n$. This correction factor is used for uncoated samples.

CASE 6: If a window has AR coatings, i.e., $R_1 = R_2 = 0$, then $P_A/P_T = (A_1+xA_2+A_o)/[1-(A_o+A_1+A_2)] \simeq A_1+A+xA_2$ the absorbance of each surface plus the bulk contribution. If in addition $A_1 = A_2 = 0$, then we get $P_A/P_T = A_o/(1-A_o) = \beta\ell/(1-\beta\ell) \simeq \beta\ell = m\, C_p(1/P_T)(\Delta T/\Delta t)$

CASE 7: With all the parameters in the above theory, additional experimental information is needed to evaluate them all. One way to obtain additional data is to measure the power reflected by the sample and the transmitted power. Alternatively, a beamsplitter could be used to measure the incident powers or the sample could be measured with each surface facing the beam. The reflection from each surface can be measured with a spectrophotometer. With the one per cent accuracy obtainable on the Perkin-Elmer 180, obtaining values from it for A_1 and A_2 is probably out of the question, since they may be considerably smaller. The front side of the window is defined as that one facing the incoming laser beam. The following equations are useful when there are unequal surfaces, e.g. one side is AR coated.

The general first order solution for small A's is:

$$\left(\frac{P_A}{P_T}\right)_{\substack{1\text{ in}\\ \text{front}}} = \frac{A_1[1+R_2\{x-(x+1)R_1\}] + xA_2(1-R_1) + A_o(1-R_1)(1+R_2)}{(1-R_1)(1-R_2)(1-A_o) - A_1(1-R_2) - A_2(1-R_1)}$$

$$\left(\frac{P_A}{P_T}\right)_{\substack{2\text{ in}\\ \text{front}}} = \frac{xA_1(1-R_2) + A_2[1+R_1\{x-(1+x)R_1\}] + A_o(1-R_2)(1+R_1)}{(1-R_1)(1-R_2)(1-A_o) - A_1(1-R_2) - A_2(1-R_1)}$$

$$\left(\frac{P_R}{P_T}\right)_{\substack{1\text{ in}\\ \text{front}}} = \frac{R_1 + R_2[1-2(A_1+R_1) + A_1R_1(1+x) - 2A_o(1-2R_1)] - (1-2R_1)(x-1)A_2}{(1-R_1)(1-R_2)(1-A_o) - A_1(1-R_2) - A_2(1-R_1)}$$

$$\left(\frac{P_R}{P_T}\right)_{\substack{2\text{ in}\\ \text{front}}} = \frac{R_2 + R_1[1-2(A_2+R_2)+A_2R_2(1+x) - 2A_o(1-2R_2)] - (1-2R_2)(x-1)A_1}{(1-R_1)(1-R_2)(1-A_o) - A_1(1-R_2) - A_2(1-R_1)}$$

The above equations can be rearranged as linear equations in the A's. A computer program was written to solve them when x = 1. As a test of the computer program, some trial answers were assumed: $A_o = 0.003$, $A_1 = 0.0005$, $A_2 = 0.001$, and an incident power of 25 watts. The quantities P_{R1}, P_{T1}, P_{A1}/P_{T1}, P_{R2}, P_{T2}, and P_{A2}/P_{T2} were calculated by hand to about 5 significant figures. This simulates an ideal case. The results were P_{R1}= 4.29206 watts, P_{T1}= 20.6125 watts, P_{A1}/P_{T1}= 0.0046325, P_{R2}= 4.25803 watts, P_{T2}= 20.61245 watts, and P_{A2}/P_{T2}= 0.0062832. The substrate sample consisted of a ZnSe window with a PbF_2 coating. The measured reflectances on a Perkin-Elmer 180 were R_1 = 0.171 and R_2 = 0.001. The output results were A_1 = 0.00050055, A_2 = 0.00110937, and A_o= 0.00289008, in good agreement with the assumed values. Thus, we are satisfied that the program is working properly. As a check on how sensitive parameters in the program are, various inputs were singly changed by a small amount and the new results were obtained. Table 1 lists some of the inputs used and their corresponding outputs.

Table 1. Results of parameter sensitivity study of computer program

Input quantity changed	New value	Outputs A_1	A_2	A_o
P_{R1}	4.30	.00143	.19246	-.18939
P_{R1}	4.28	-.00091	-.29006	.29547
P_{R2}	4.26	.00050	.00111	.00289
P_{R2}	4.25	.00050	.00111	.00289
P_{R2}	4.20	.00050	.00111	.00289
P_{A1}/P_{T1}	.0050	.00136	-.03639	.03968
P_{A2}/P_{T2}	.0068	-.00053	.00111	.00413

The results of this exercise show that the power absorbed with the AR coating in both orientations shold be measured to three significant figures for reasonable results. The same can be said with the AR coating in the rear. The latter is much more difficult to achieve experimentally. Perhaps with improvements in the precision of power measurements, this treatment will be helpful in using laser rate calorimetry to handle windows with absorbing coatings.

In one experimental test no reflected power was measured when the AR coating faced the beam. Putting numbers in the formulae we find that the power reflected with the AR coating in front and with it in back should be identical to within a few per cent. Apparently the reflected beam was not centered in the power meter entrance window.

CASE 8: An uncoated window with identical front and back surfaces is a commonly encountered case. Here we have $A_1 = A_2 = A$, $R_1 = R_2 = R$, $T_1 = T_2 = T$.

This case yields the same equations whether side 1 or side 2 is in front; thus, no additional information is obtained by taking data in both positions.

$$P_A/P_T = [(1+x)A + A_o](1+R)/[(1-R)(1-A_o) - 2A] \approx [(1+x)A + A_o](1+R)/(1-R)$$

We see that the surface and bulk contributions are inseparably linked together as in the AR coating case.

CASE 9: One experimental situation has been found to be tractable. In this case the uncoated substrate with assumed identical surfaces was measured. Thus, $A_1=A_2=A_u$ and $R_1=R_2=R$, therefore,

$$(P_A/P_T)_o = [A_o + (1+x)A_u](1+R)/(1-R).$$

After applying an AR coating on one side, say 1, we have $R_1=0$, $A_1=A_c$, $R_2=R$, $A_2=A_u$. With the coating facing the beam,

$$(P_A/P_T)_1 = [A_c(1+xR) + xA_u + A_o(1+R)]/(1-R).$$

With the coating away from the incident beam,

$$(P_A/P_T)_2 = [xA_c(1-R) + A_u + A_o(1-R)]/(1-R).$$

Thus $\Delta P_c = (P_A/P_T)_1 - (P_A/P_T)_2 = \{A_c[1-x+2xR] + (x-1)A_u + 2RA_o\}/(1-R)$.

When the substrate is AR coated on both sides, $(P_A/P_T)_{2c} = A_o + (1+x)A_c$.

These equations yield,

$$A_o = [(1-R)(1+x)\Delta P_c - (1-x+2xR)(P_A/P_T)_{2c} - (x-1)(P_A/P_T)_o(1-R)/(1+R)]/2R$$

$$A_c = [\{2R(1+x) - (x-1)\}(P_A/P_T)_{2c} - (x-1)(P_A/P_T)_o(1-R)/(1+R) - (1+x)(1-R)\Delta P_c]/[2R(1+x)]$$

$$A_u = [(1-x+2xR)(P_A/P_T)_{2c} - (x+1)(1-R)\Delta P_c + (2R-1+x)(P_A/P_T)_o(1-R)/(1+R)]/[2R(1+x)] .$$

For the case of x = 1, these results have been applied to PbF_2 coatings on ZnSe, see Fernelius et al [9].

4. Conclusion

When surface absorption occurs, most experimental laser calorimetry situations do not yield data where surface and bulk absorption are solvable. Unequal faces are needed for a solution. The transmitted and reflected power can be measured in both window orientations (three measurements are needed). For a meaningful solution, the reflected power must be measured to better than two significant figures which is currently not viable. Another possibility is to measure uncoated, coated on one side (both ways), and coated on both sides. With equal faces an alternative is to use a long bar sample and/or multi-thickness samples.

5. References

[1] O.S.Heavens, Optical Properties of Thin Solid Films, (Butterworths, London, 1955)

[2] W.E.K.Gibbs and A.W.Butterfield, Appl.Optics 14, 3043 (1975)

[3] M.D.Crisp, N.L.Boling and G.Dubé, Appl. Phys.Lett. 21, 364 (1972)

[4] N.L.Boling, M.D.Crisp and G.Dubé, Appl. Optics, 12, 650 (1973)

[5] M.D.Crisp, IEEE J. Quantum Electronics, QE-10, 57 (1974)

[6] P.A.Miles, Appl.Optics, 16, 2897 (1977)

[7] Joseph A. Apfel, private communication

[8] M.Hass, J.W.Davisson, P.H.Klein and L.L.Boyer, J.Appl.Phys. 45, 3959 (1974)

[9] N.C.Fernelius, J.A.Fox, D.A.Walsh and G.S.Coble, Proc. High Power Laser Window Conference, Denver, 1978

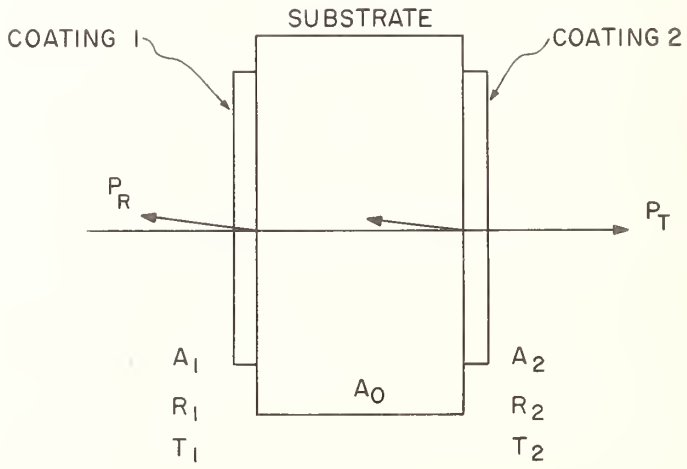

Figure 1. Diagram of Calorimetry Sample

ABSORPTION COEFFICIENT OF NaF BY ATTENUATED TOTAL REFLECTION SPECTROSCOPY*

David L. Burdick
Michelson Laboratory, Physics Division
Naval Weapons Center, China Lake, CA 93555

Attenuated total reflection (ATR) spectroscopy has been employed to measure the absorption coefficient of NaF films from the visible to 3 μm. A 1-mm-thick ZnSe ATR plate (50-mm long) was coated on two sides with NaF (0.55- and 0.57-μm-thick films). By coating half the width of the ATR plate, "sample-in/sample-out" measurements could be performed to reduce substrate effects. The spectra reveal a strong water band in NaF peaking at 2.95 μm with a peak absorption coefficient at 165 cm^{-1} relative to the substrate. Scattering effects are noted at shorter wavelengths, and it is estimated that 7 Å of water are adsorbed onto the bare ATR plate.

Key words: Absorption coefficient; sodium fluoride film; total internal reflection; 0.65 to 3.0 microns.

Introduction

While attenuated total reflection (ATR) or, more appropriately, internal reflection spectroscopy has been used for some time by chemists to study interfaces [1][1], it has only been very recently that ATR has been seriously applied to the study of thin films for optical technology [2-5]. The advantages of the method are rooted in the fact that specially designed film substrates, i.e., the ATR plate, can be either fabricated or purchased to produce many reflections of the probing light beam, thereby increasing the total interaction between film and photon.

We have assembled an optical system for performing ATR measurements using commercially available ATR plates. This system has been tested using NaF films on a ZnSe plate. This paper presents the results of our ATR measurements from 0.8 to 3.0 μm on NaF films, and discusses briefly a scattering phenomenon in the region of 1 μm. Our measurements also permit us to calculate the thickness of the adsorbed water layer on the uncoated ZnSe plate.

Experimental Details

The optical layout of the ATR system is shown in figure 1 and is rather conventional. The light beam exiting the monochromator is split by a mirror splitter (1) into a sample beam and a reference beam. The reference beam is focussed by a mirror (4) onto the detector; this beam is chopped at 104 Hz by a tuning-fork chopper (2). The sample beam is focussed onto the entrance aperture of the ATR plate by mirrors; it is chopped at 150 Hz by the tuning-fork chopper (3). Finally, the beam leaving the ATR plate is focussed by mirrors onto the same detector. The system uses a Perkin-Elmer 98 monochromator, a 100-W tungsten filament source, and a room-temperature PbS photoconductive detector.

The signal is processed by two Princeton Applied Research 124 lock-in amplifiers. The resulting sample and reference signals are ratioed electronically and the ratio is applied to the y-axis of an x-y recorder. The x-axis is driven by the monochromator wavelength drum. The spectra so obtained contain only ATR data; all source and detector factors are eliminated.

A single ATR plate was coated on half of each broad side with NaF deposited in an ultrahigh vacuum system. The films were 0.5523- and 0.5708-μm thick as measured by a Talystep stylus. A diagram of the plate is shown in figure 2. The reason for coating just half of each side is to enable us to make "sample-in/sample-out" measurements. The ATR plate was attached to a vertical translation stage so that it could be raised and lowered relative to the focussed sample beam. As a result, we could scan both the coated and uncoated portions with no changes in the system other than displacing the plate by about 1 cm.

Results

Figure 3 shows the ATR spectra obtained in our measurements. Two spectra, from about 0.8 to 3.0 μm, are shown; the upper line with the large dip near 2.9 μm is for the NaF films, and the lower line with the smaller dip at 2.9 μm is the uncoated ZnSe ATR plate. Each spectrum shows a monotonic increase in

* Work supported by the Defense Advanced Research Projects Agency.

1. Figures in brackets indicate the literature references at the end of this paper.

signal as λ increases, with no structure until the dip at 2.9 μm is reached. Note that the coated portion of the plate is transmitting more energy to the detector at the shorter wavelengths than is the uncoated portion, a seemingly anomalous result. We will discuss each of these spectra in the following sections.

Analysis

We will follow the treatment presented by Harrick [1]. In normal fashion, the reflectance in total internal reflection is reduced by both absorption and scatter so that the intensity of the sample beam is

$$I = I_o(1 - A - S)^N(1 - R)^2 \quad , \tag{1}$$

where I_o is the incident intensity at the ATR plate entrance aperture, R is the reflectivity of the entrance and exit apertures, A and S are the absorption and scatter for one internal reflection, and N is the number of reflections. Under our experimental conditions the ratio of the coated I_c and uncoated I_u intensities is

$$\frac{I_c}{I_u} = \left(\frac{1 - A_c - S_c}{1 - A_u - S_u}\right)^N \quad . \tag{2}$$

We will examine this relationship for three cases.

1) $A_c = A_u = 0$:

In a spectral region where there is no absorption, or the absorption is small compared to the scattering, we have

$$\frac{1 - S_c}{1 - S_u} = \left(\frac{I_c}{I_u}\right)^{1/N} \quad . \tag{3}$$

Assuming that $S << 1$,

$$S_u - S_c = \left(\frac{I_c}{I_u}\right)^{1/N} - 1 \quad . \tag{4}$$

This is the condition which applies in the 0.8- to 2.3-μm region in our NaF films.

2) $S_c, S_u << A_c, A_u$:

In this case,

$$\frac{I_c}{I_u} = \left(\frac{1 - A_c}{1 - A_u}\right)^{1/N} \quad . \tag{5}$$

This condition holds near the absorption band at 2.9 μm in our NaF films. To obtain a value for the absorption coefficient we shall use the effective penetration depth of Harrick [1] and write

$$A_c = \alpha_c d \quad , \tag{6}$$

where α_c is the absorption coefficient of the NaF film (assumed to be the same for both films) and the effective penetration depth d is approximated as

$$d = \frac{1}{2}\left(d_{e_\parallel} + d_{e_\perp}\right) = \frac{\lambda_1 n_{21}\cos\theta}{2\pi(1-n_{21}^2)(\sin^2\theta - n_{21}^2)^{1/2}} \quad \frac{3\sin^2\theta + n_{21}^2\sin^2\theta - 2n_{21}^2}{(1+n_{21}^2)\sin^2\theta - n_{21}^2} \quad , \tag{7}$$

where $\lambda_1 = \lambda/n_{ZnSe}$, $n_{21} = n_{NaF}/n_{ZnSe}$, θ = angle of incidence on interface (45°), and $d_{e_\parallel}$, $d_{e_\perp}$ are the effective penetration depths for the two polarizations of light.

Equation (7) is valid for internal reflection at an interface between two infinite media. Since we are dealing with films about 0.5-μm thick, we must estimate the validity of eq. (7). Thus we have calculated the true penetration depth of the power in the evanescent wave at the 1/e point. This is given by

$$d_p = \frac{\lambda_1}{4\pi(\sin^2\theta - n_{21}^2)^{\frac{1}{2}}} \quad . \tag{8}$$

This depth, which is essentially linear in λ, is plotted in figure 4 together with the film thicknesses. It is clear that the infinite approximation should be valid over the range of our experiments. Our calculations were further modified to include the finite film thickness by introducing a factor of $1-\exp(-L/d_p)$ into the effective penetration depth for each film (L is the film thickness).

Two additional factors were included in our calculations. The first, and simplest to handle, is the fact that the two films on the ATR plate were of different thicknesses. The second is the fact that absorption measurements on the coated portions actually measure a ZnSe surface which has water adsorbed onto it, coated subsequently by NaF. We have attempted to introduce these facts by finally solving this equation:

$$1 - (A_{c_1} + A_u))(1 - (A_{c_2} + A_u) = (1 - A_u)^2 \left(\frac{I_c}{I_u}\right)^{2/N} \quad . \tag{9}$$

Here A_{c_1}, A_{c_2} are the absorptions in the two different films and A_u is the absorption in the ZnSe surface with adsorbed water. Pursuant to our discussion, $A_{c_{1,2}} = \alpha d_{1,2}$, and the factor $1 - A_u$ is obtained below. Our final result is

$$\alpha = (1 - A_u) \frac{d_1 + d_2 - \sqrt{(d_1 + d_2)^2 - 4d_1d_2(1 - (I_c/I_u)^{2/N})}}{2d_1d_2} \quad . \tag{10}$$

3) Thin layer of water:

This is a special case for the uncoated ZnSe ATR plate and corresponds to the small dip at 2.95 μm in figure 3. This spectrum is assumed to be a very thin layer of water adsorbed onto the ATR plate. It is described by the equation

$$(1 - A_u)^N = \left(\frac{I_u}{I_o}\right) \quad , \tag{11}$$

where I_o is represented by the level dashed line (the "bleached" film).

This equation provides direct access to $1 - A_u$ as required in eq. (10) (assuming that the adsorbed water layer is unaffected by the NaF evaporation). A further result is that, by assuming the optical constants of bulk water [6], we can use eq. (11) to estimate the thickness of the adsorbed water layer. Using the thin film approximation of Harrick [1], we have

$$d = \frac{1}{\alpha_w}\left(\frac{I_u}{I_o}\right)^{1/N} \frac{(1 - n_{31}^2)[(1 + n_{31}^2)\sin^2\theta - n_{31}^2]}{2n_{21}\cos\theta[(2 + n_{31}^2 + n_{32}^4) - 2n_{31}^2]} \quad . \tag{12}$$

Here α_w is the absorption coefficient of bulk water, $n_{31} = 1/n_{ZnSe}$, $n_{21} = n_w/n_{ZnSe}$, $n_{32} = 1/n_w$, and the other parameters have been defined earlier.

Since the ATR plate was 50-mm long and 1-mm wide and the angle of incidence θ onto the totally reflecting face is 45°, the number N of bounces is 50. In our calculation we used the refractive index of ZnSe given by Dodge and Malitson [7] and the refractive index of NaF taken from the American Institute of Physics Handbook [8].

Discussion

First consider case 1), that of low absorption but some scattering. In figure 3 this region lies roughly between 0.8 and 2.3 μm. We have some confidence that this region is dominated by surface scattering because of a series of normal-incidence scattering measurements on the uncoated portion of the plate at 0.6471 μm and 1.15 μm. The scattering was 8.2×10^{-3} and 2.6×10^{-3}, respectively, at these two wavelengths, and the ratio of these numbers is 3.2; this is also equal to $(1.15/0.6471)^2$, the square of the wavelength ratio. Thus, we feel that surface scattering is most important here. Applying eq. (4) at 1.15 μm, we find that

$$S_u - S_c = 4 \times 10^{-4}$$

This scattering difference is about 16% of the normal-incidence scattering from the uncoated surface. As one moves toward longer wavelengths the effect persists, but diminishes until absorption in the NaF film finally causes the two spectra to overlap at about 2.4 μm. One can see that the scattering difference is significant by noting figure 5 which shows scattering measurements obtained by placing the detector close to the exit aperture of the ATR plate, without intercepting the exiting beam. Although these rough measurements do not give a measure of the absolute scatter, they do show that the coated portion scatters less than the uncoated portion over the same spectral range as the ATR measurement. The ratio of the scattering curves in figure 5 is nominally independent of λ, a result consistent with a λ^{-m} scattering law.

Turning now to the absorption coefficient of NaF, we note immediately that there is a large absorption peak in figure 3. When analyzed by means of eq. (10), we obtain the absorption coefficient as a function of λ; this is shown in figure 6. It is believed that the peak is due to water incorporated into the NaF film, both during the evaporation process and from the atmosphere prior to the measurement. The peak absorption coefficient is 165 cm^{-1}. This peak is located at 2.923 μm as compared with the bulk water absorption peak at 2.950 μm [6]. The arrow in figure 6 indicates the bulk water absorption peak location. We do not know yet whether this difference in spectral location is real or illusory. Our absorption coefficient is high compared to all the calorimetry data taken at the Naval Weapons Center on NaF films. This is not surprising in view of the fact that the sample has been exposed to the atmosphere for an extended period prior to measurement. Calorimetry samples, on the other hand, are usually measured shortly after removal from the vacuum system. As a check on these ATR measurements, our first, the sample was measured near 3.0 μm on a Perkin-Elmer 180 spectrophotometer. While it is not particularly easy to see a dip on the order of 2%, our measurements at normal incidence through the two NaF films showed a dip which is entirely consistent with about 1.1 μm of material absorbing at 165 cm^{-1}. Thus, although the sample used here cannot be considered a state-of-the-art film, it does seem to verify the techniques and interpretation.

Finally, let us examine the dip at 2.95 μm in the uncoated spectrum. We assume that it is due to adsorbed water, and by using optical constants of bulk water and eq. (12) we have estimated the layer thickness to be about 7 Å. This is about twice the thickness of the adsorbed water layer on CaF_2 ATR plates reported by Palik *et al.* [5]. These calculations, while interesting, must be viewed with caution because of the assumed optical constants of the adsorbed specie.

Conclusions

Attenuated total reflectance measurements of NaF films on a ZnSe plate allow us to determine the absorption coefficient of the film at 2.92 μm (165 cm^{-1}), to estimate the thickness of the adsorbed water layer (7 Å), and to observe a difference in the scattering between a NaF-ZnSe interface and an air-ZnSe interface.

References

[1] See the book by Harrick, N. J., *Internal Reflection Spectroscopy*, Interscience (1967) and the review article by Hansen, Wilford N., in *Advances in Electrochemistry and Electrochemical Engineering*, Vol. 9, John Wiley and Sons, Inc. (1973) for good reviews of the subject.

[2] Holm, R. T., and Palik, E. D., Appl. Opt. 17, 394 (1978).

[3] Willingham, C., Bua, D., Statz, H., and Harrigan, F., "Laser Window Studies," Final Technical Report on Contract DAAHOI-74-C-0719, Raytheon Research Division, Waltham, Mass. (August 1975).

[4] Deutsch, T. F., J. Electron Mater. 4, 663 (1975).

[5] Palik, E. D., Gibson, J. W., Holm, R. T., Hass, M., Braunstein, M., and Garcia, B., Appl. Opt. 17, 1776 (1978).

[6] Downing, H. D., and Williams, D., J. Geophys. Research 80, 1656 (1975).

[7] Dodge, M. J., and Malitson, I. H., in *Laser Induced Damage in Optical Materials: 1975*, A. J. Glass and A. H. Guenther, eds. Washington, D.C., National Bureau of Standards, 1975 (NBS Spec. Publ. 435), p. 170.

[8] American Institute of Physics Handbook, 3rd Edition. (McGraw-Hill Book Co.), 1972, pp. 6-45.

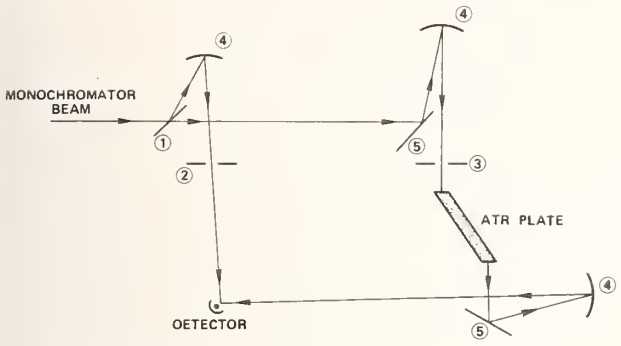

Figure 1. Diagram of ATR optical arrangement. (1) Mirror beam splitter; (2) 104 Hz tuning-fork chopper; (3) 150 Hz tuning-fork chopper; (4) focussing mirrors; (5) plane mirrors.

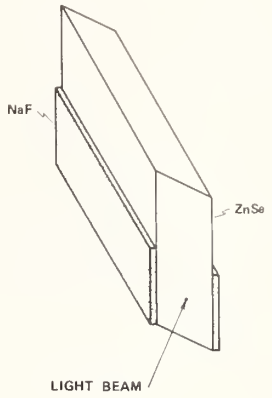

Figure 2. Diagram of ZnSe ATR plate coated on two sides with NaF. The plate is translated vertically in the system to illuminate the coated and uncoated portions in succession.

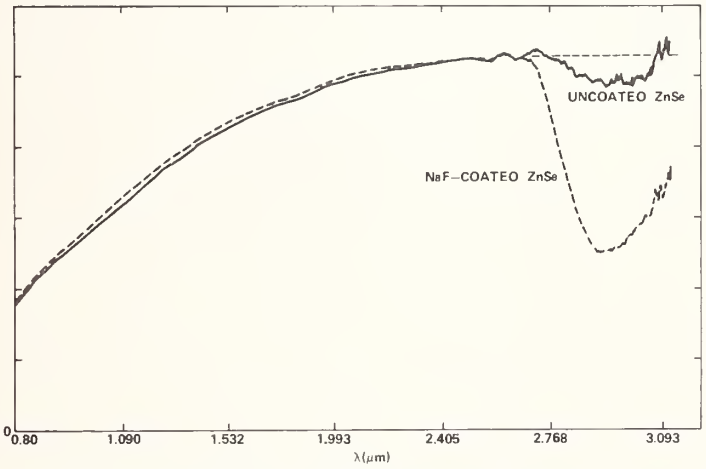

Figure 3. Tracing of ATR spectra. The solid line is the transmission of the uncoated ZnSe plate. The dashed line is the transmission of the NaF-coated poriton of the ZnSe plate; note that it is greater than the uncoated portion from 0.8 to 2.5 μm. The short dashed section from 2.7 to 3.1 μm is the estimated transmission of the "bleached" plate.

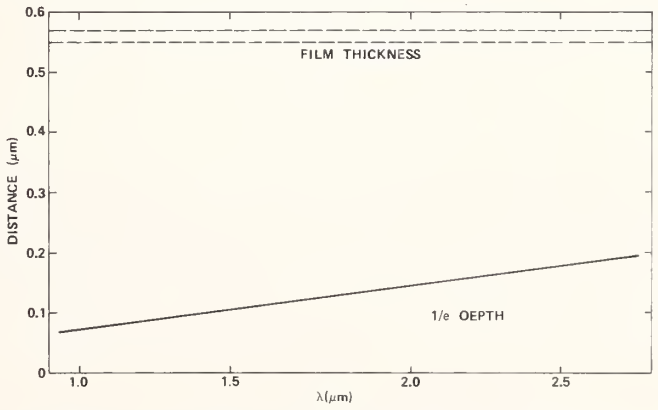

Figure 4. Penetration of power into the NaF films. The solid line shows the 1/e depth of power as caluclated from eq. (8). The dashed lines indicate the physical thickness of the films. At these depths the approximations used in the analysis are valid.

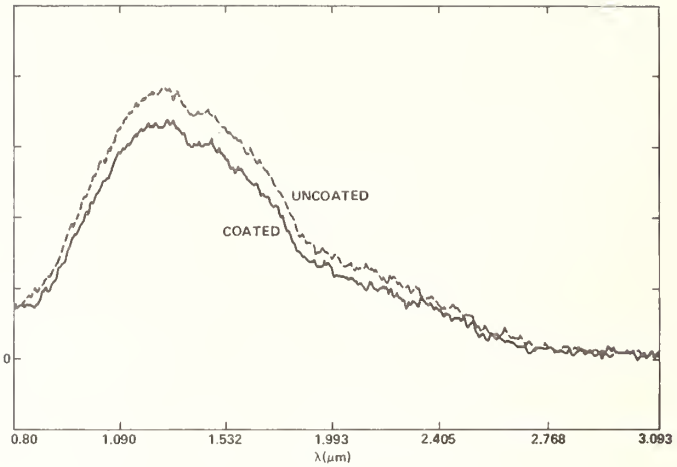

Figure 5. Scattered radiation from both the coated and uncoated portions of ATR plate. The scattering from the uncoated portion is greater than that of the coated portion, a result which tends to explain the "anomalous" difference in the two ATR spectra from 0.8 to 2.3 μm.

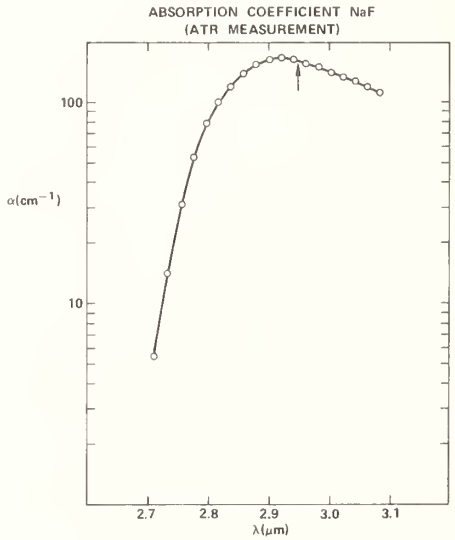

Figure 6. Calculated values of the NaF absorption coefficient. The peak is assumed to be due to water in the films. The arrow indicates the location of the absorption peak in bulk water.

LASER CALORIMETRIC MEASUREMENT OF TWO PHOTON ABSORPTION

Michael Bass, Eric W. Van Stryland and A.F. Stewart
Center for Laser Studies
University of Southern California
Los Angeles, California 90007

A laser calorimeter has been used to measure two photon absorption in solids. This new technique provides greater sensitivity than is possible in nonlinear transmission measurements. The two photon absorption coefficients of CdTe and CdSe at 1.06 μm using ∿ 16 nsec (FWHM) pulses are 0.13 ± 0.04 cm/MW and 0.050 ± 0.014 cm/MW respectively.

Key words: CdSe; CdTe; internal reflections; laser calorimeter; linear absorption; Nd:YAG laser; two photon absorption.

1. Introduction

The laser calorimeter is a device that is widely used to measure small linear absorptions at wavelengths where laser sources are available. Such an instrument can measure absorptions which are less than one part in 10^5 using a 1 W laser.[1] The calorimeter measures the total absorption due to all processes including the intensity dependent phenomenon of two photon absorption (TPA). Thus the experimental technique described in this paper is based on a measurement of the total absorption as a function of the laser intensity. Calorimetric measurements of the total absorption in CdTe and CdSe as functions of 1.06 μm laser intensity were used to obtain both linear and TPA coefficients of these materials. The results can be understood by using a simple model for the attenuation with distance in the presence of TPA and by properly accounting for multiple reflections in the sample.

In 1931, M. Goppert-Mayer presented a theoretical description of TPA in which the transition probability was shown to be proportional to the square of the light intensity[2]. Thus a material having both linear and two photon absorption will transmit light according to the expression

$$\frac{dI}{dz}(x,y,z,t) = -\left[\alpha + \beta I(x,y,x,t)\right] I(x,y,z,t), \qquad (1)$$

(See fig. 1).
Here $I(x,y,z,t)$ is the light intensity in MW/cm^2 and is a function of the space coordinates and time; z is the direction of propagation; α is the linear absorption coefficient in cm^{-1}, and β is the two photon absorption coefficient in cm/MW.
In many materials of interest α will be small, $\alpha \simeq 10^{-2} cm^{-1}$, and $\beta \simeq 10^{-2}$ cm/MW according to transmission measurements at high intensities[3].
Thus a modest intensity of 1 MW/cm^2 will result in a two photon contribution to the total absorption which is equal to the linear term (See eq. (1)). On the other hand, this intensity will result in a change in transmission for samples shorter than 1 cm of less than 1% which is too small to be measured accurately. A comparison of the two techniques can be made by noting that in a transmission experiment one measures a small change (the reduction of transmission due to TPA) in a large quantity (transmitted intensities), whereas using calorimetry one measures a large change (the added absorption due to TPA) in a small quantity (total absorption).

2. Experimental

The experimental procedure is to measure the total absorption as a function of intensity and evaluate the data according to eq. (1), taking into account reflections at the rear surface. A flashlamp pumped, Q-switched, TEM_{00} mode, Nd:YAG laser was the source for the experiments as shown in figure 2. The laser was operated at ∿5 Hz with an output of ∿ 1 mJ/pulse [4]. The pulse temporal waveform was a Gaussian function with full width at 1/e points in intensity of 19 nsec (See fig. 3). A beam scan was used to determine the spatial profile which was Gaussian having a 1/e full width in intensity of 1.2 mm at the focusing lens (See fig. 5). An 8 cm focal length lens was

1. Figures in brackets indicate the literature references at the end of this paper.

used to increase the intensity at the samples, which were placed 4 cm behind the focus. The attenuators and optics in front of the sample limited the maximum peak on axis intensity at the sample to $\sim$30 MW/cm^2 with an average power of approximately $\sim$5 mw. The energy per pulse was measured by averaging the output of over 100 pulses with a pyroelectric joulemeter. The accuracy of the TPA measurements is sensitive to pulse to pulse energy variations which must therefore be kept as low as possible ($\sim$5%) (See fig. 4). The beam intensity at the sample was adjusted using a two polarizer attenuator described in references [5] and [6].

A thermocouple attached to the otherwise thermally isolated sample recorded the sample's temperature change due to the absorption of the laser light. When amplified and recorded, the thermocouple voltage appeared as sketched on the chart recorder in figure 2 and shown in figure 6. While the laser is on the temperature rises. The gentle slopes while the laser is off are due to small thermal losses that are seen with thin samples. The time constant of the calorimeter was long enough so that a 5 Hz laser beam caused no uneveness in the recorded temperature change. Thus the calorimeter responded to the total average power absorbed. The calorimeter was of conventional design and when evacuated had a measured sensitivity to absorption of one part in 10^5 with a 1 W source.

3. Results and Discussion

Data such as in figure 2 was obtained at several laser intensities for room temperature samples of CdTe and CdSe. The samples were single crystals and the CdSe was oriented with its optic axis normal to the entrance (exit) surface. This orientation eliminated the possibility of second harmonic generation at 0.53 μm which could be directly absorbed. The CdTe sample had its optic axis approximately 22^o away from the normal to the entrance surface. Figures 7 and 8 show the intensity dependence of the total absorption of these two materials measured calorimetrically. For a small total absorption (i.e. $(\alpha + \beta I)z << 1$), eq. (1) predicts a straight line for absorption versus intensity. The vertical intercept of this line gives α and its slope determines β. In these experiments which employ a Gaussian beam profile and a Gaussian temporal shape the TPA coefficient would be $2\sqrt{2}$ times the slope in such a plot. The data fits a straight line quite well but the total absorption at the highest intensities used for CdTe was over 20%. Thus eq. (1) must be solved exactly. This was done previously including the effects of Gaussian spatial and temporal profiles but the effects of multiple reflections were neglected [3]. For high index materials the intensity of the reflected beam from the rear surface can significantly affect the computed absorption coefficients. Since TPA results from the imaginary part of the third order optical nonlinear susceptibility, χ [3], the field equations for both the incident and reflected beams were used to obtain the following coupled differential equations for the intensities:

$$\frac{dI}{dz} = -(\alpha + \beta(I + I_R))I; \quad \frac{dI_R}{dz} = +(\alpha + \beta(I + I_R))I_R \qquad (2)$$

where I is the intensity of the incoming beam and I_R is the intensity of the reflected beam. (See fig. 9). Subsequent reflections have been neglected because they contribute still less to the total absorption. Noting that the product $I(z)I_R(z)$ is a constant everywhere in the sample, these equations can be solved in closed form with the constant as a parameter. A rapidly converging numerical iterative procedure for determining the constant from the boundary conditions was used to determine the total absorption integrated over the spatial and temporal beam profiles.

The theoretical fits along with the data are shown in figures 7 and 8. These fits were used to obtain the values for β listed in Table 1. The values given for α were obtained using a cw Nd:YAG laser and the usual calorimetric techniques. These

Table 1. Linear absorption coefficient, α, and two photon absorption coefficient, β at 1.06 μm

Material	α(cm^{-1})	β(cm/MW)
CdSe	.062 $\pm$ .06	.050 $\pm$ .014
CdTe	.335 $\pm$ .03	.130 $\pm$ .036

measured values of α are quite accurate and as such were used in the calculations of β. This means that the values of β given in the table are the result of a one parameter fit. The deviation of the fit from the data at high intensities particularly for CdSe may be due to a contribution from direct absorption by two photon created free carriers as discussed in references [3] and [7]. However, at this time the data is

insufficient and the error bars too large to make any conclusions concerning the possible role of free carriers. Work is continuing in this area seeking a predicted pulse width dependence to TPA if free carrier absorption is significant.

4. Conclusions

The experimental error bars shown in figures 7 and 8 were determined from scatter in the data and uncertainties in determining the heating rate from curves such as shown in figure 6. The laser intensity fluctuations, the accuracy of the laser spot size measurement and temporal profile measurement along with the uncertainties mentioned above combine to give the quoted accuracies in Table 1. The accuracy of TPA measurements using laser calorimetry has the potential for considerable improvement. The initial work presented here has, however, demonstrated the feasibility of the technique.

The inclusion of the reflected beam in the analysis of TPA measurements is essential in high index materials where it has been ignored previously, [3] but may be eliminated in future experiments (thus greatly simplifying the calculations) by using AR coated samples. It should be pointed out that in certain materials the two photon excited level can decay through a combination of radiative and nonradiative processes. Then a part of the total TPA may not register as heat generated in the sample. This means that a simultaneous transmission measurement may make it possible to determine the quantum efficiency of such radiative transitions. This type of quantum efficiency study and measurements of TPA using two different lasers are in progress.

5. Acknowledgments

The partial support of Air Force Office of Scientific Research under Contract No. F49620-78-0065 is gratefully acknowledged. Valuable help in calorimetric measurement techniques was provided by Dr. Susan D. Allen and Dr. Jean-Claude Diels provided a turbine driven Q-switch for the Nd:YAG laser as well as valuable theoretical help.

6. References

[1] A. Hordvik, Appl. Opt. 16, 2827 (1977).

[2] M. Göppert-Mayer, Ann. Phys. (Leipz.) 9, 273 (1931).

[3] J.H. Bechtel, W.L. Smith, Phy. Rev. B, 13, 3515 (1976).

[4] For CdTe the prf was 6.7 Hz and for CdSe the prf was 7 Hz. The CdTe sample was 2.03 mm thick and the CdSe sample was 0.89 mm thick.

[5] Laser-Induced Damage to Nonlinear Crystalline Materials, M. Bass, NBS Special Publication 341, Proc. of 1970, Damage in Laser Materials Conference.

[6] Damage to 10.6 μm Window Materials Due to CO_2 TEA Laser Pulses, K.M. Leung, M. Bass, and A.G.J. Balbin-Villaverde, NBS Special Publication 435, Proc. of 1975, Laser Induced Materials Conference.

[7] F. Brynkner, V.S. Dneprovskii, V.U. Khattatov, Sov. J. Quant. Electron; Vol. 4, No. 6, (12-74).

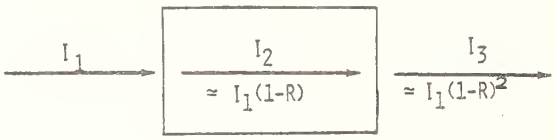

$$\frac{dI_2}{dz} = -(\alpha + \beta I_2) I_2$$

Figure 1. Absorption in a two photon absorbing medium.

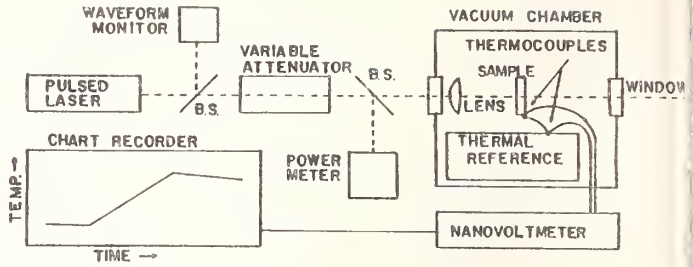

Figure 2. Experimental apparatus for TPA measurements using laser calorimetery.

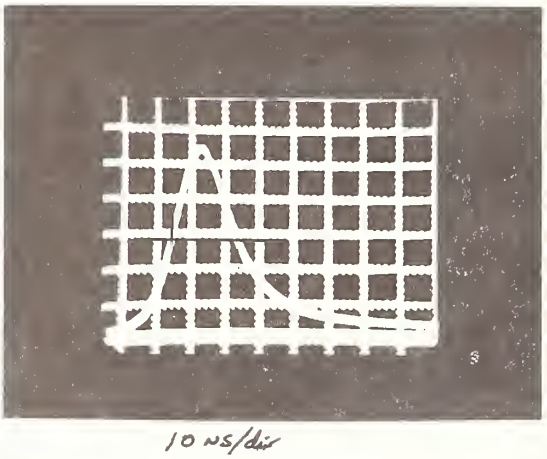

Figure 3. Ten successive laser pulses as detected with a fast photodiode.

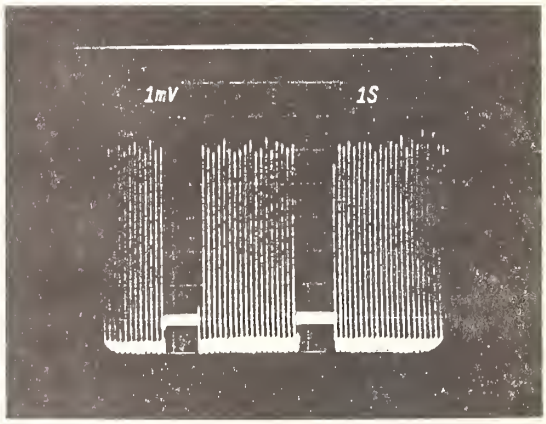

Figure 4. Pulse to pulse energy reproducibility measurement with a slow pyroelectric detector.

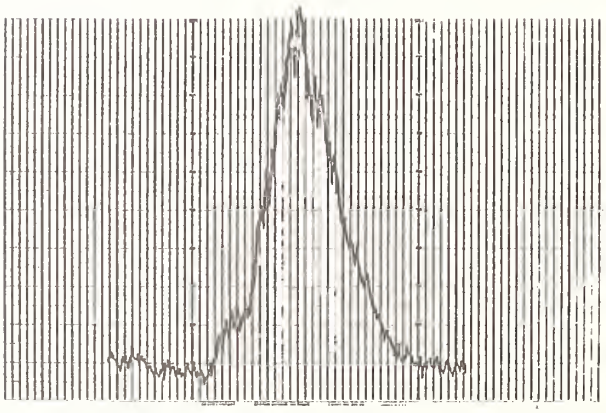

Figure 5. Beam spatial profile generated with a .15 mm slit scanned continuously at 14.6 sec/mm, laser prf ~7 Hz.

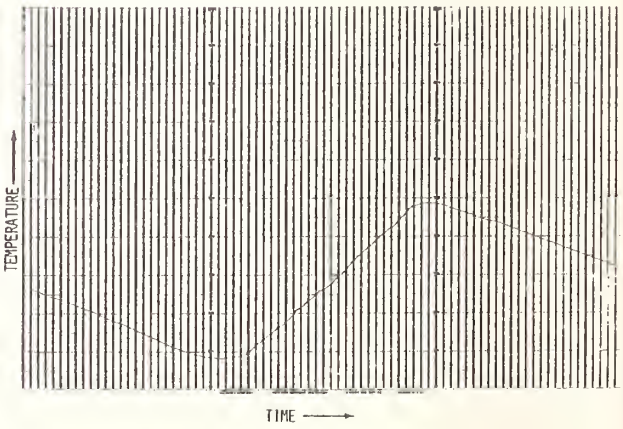

Figure 6. Typical plot of thermocouple voltage vs. time. Laser prf ~7 Hz. Calorimeter not evacuated.

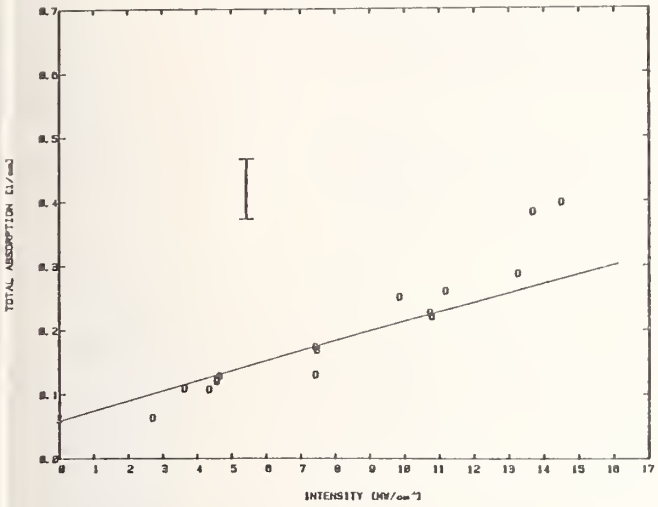

Figure 7. Intensity dependent absorption in CdTe: high intensity data (0's), low intensity (cw) data (X's), theory (—).

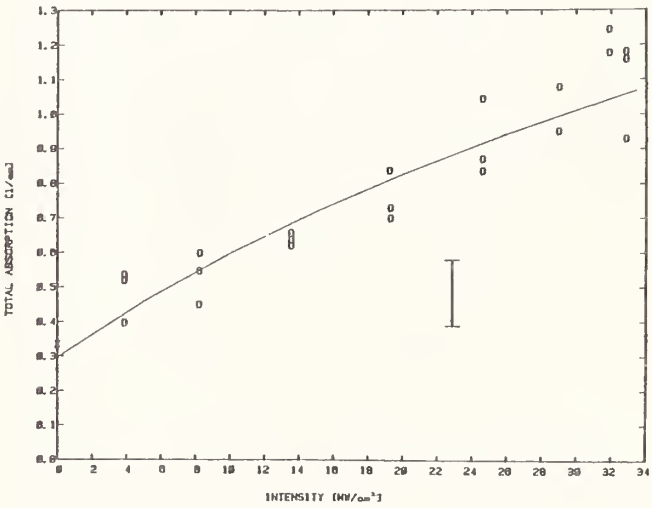

Figure 8. Intensity dependent absorption in CdSe: high intensity data (0's), low intensity (cw) data (X's), theory (—).

INTERNAL REFLECTION ENHANCES TPA

$$I_1 \qquad \boxed{\begin{array}{l} I_2 \approx I_1(1-R) \\ I_3 \approx I_1 R(1-R) \end{array}} \qquad I_4 \approx I_1(1-R)^2$$

$$\frac{dI_2}{dz} = -\left\{\alpha + \beta(I_2 + I_3)\right\} I_2$$

$$\frac{dI_3}{dz} = +\left\{\alpha + \beta(I_2 + I_3)\right\} I_3$$

THESE COUPLED EQUATIONS MAY BE SOLVED NUMERICALLY

THE TOTAL ABSORPTION IS THEN GIVEN BY

$$\alpha + \frac{\beta(I_2 + I_3)}{2\sqrt{2}} = \frac{1}{L}\,\frac{P_{2\,ABS}}{P_2}$$

$$\alpha + \frac{\beta(I_2 + I_3)}{2\sqrt{2}} = \frac{1}{L}\,\frac{P_{3ABS}}{P_3}$$

$I_3 \sim RI_2$ $\qquad P_{ABS} \approx P_{2ABS} + P_{3ABS}$

$P_3 \sim RP_2$

$$\alpha(1+R) + \frac{\beta I_2 (1+R)^2}{2\sqrt{2}} = \frac{1}{L}\,\frac{P_{ABS}}{P_2}$$

Figure 9. Absorption with internal reflection in a two photon absorbing medium.

A COMPARISON OF BULK AND SURFACE ABSORPTIONS IN NaCl AND KCl BETWEEN 9.2 AND 10.8 μm*

H. Vora,[1] M.C. Ohmer and T.G. Stoebe[2]
Air Force Materials Laboratory/LPO
Wright-Patterson AFB, Ohio 45433

Tunable CO_2 laser calorimetry has been used to study the wavelength dependence of optical absorption at 16 different wavelengths between 9.2 and 10.85 μm in NaCl and KCl. Samples prepared on a small scale using the reactive atmosphere process (RAP) growth, as well as samples cut from large diameter ingots prepared commercially for high-power CO_2 laser windows, have been investigated. A differentiation between the bulk and surface absorption has been made in several cases using long bar samples. The measured bulk absorption in the best RAP-grown NaCl crystal is intrinsic over the entire wavelength range from 9.2 to 10.85 μm, showing bulk absorption values near 9×10^{-4} cm^{-1} at 10.6 μm and 1.4×10^{-4} cm^{-1} at 9.2 μm. The best KCl shows bulk absorption values near 9×10^{-5} cm^{-1} at 10.6 μm and 4×10^{-5} cm^{-1} at 9.2 μm; these values are above the expected intrinsic limit due to residual absorption caused by the presence of at least two bulk impurities, possibly ClO_3^- and ClO_2^-.

Key words: Absorption; KCl; NaCl; 9.2 to 10.6 μm; tuneable laser calorimetry.

1. Introduction

Infrared absorption in the 9.2 to 10.8 μm region is critical in determining those materials applicable for use as laser windows in this spectral region. Considerable work has been carried out in both NaCl and in KCl, which have predicted multiphonon absorption limits at 10.6 μm of 1×10^{-3} and 7×10^{-5}, respectively[1][3]. Comparing these intrinsic values of absorption, KCl appears to have an advantage over NaCl in the laser window application with a lower intrinsic absorption coefficient. Further, for equal absorption coefficient

---

* Research supported by the National Research Council (NRC) and conducted during the tenure of H. Vora as an NRC Associate at the Air Force Materials Laboratory.

1. Present address: Honeywell, Inc., Corporate Research Center, 10701 Lyndale Avenue South, Bloomington, MN 55420.

2. Permanent address: Division of Metallurgical Engineering, University of Washington, Seattle, WA 98195.

3. Figures in brackets indicate the literature references at the end of this paper.

values, the figure of merit for the peak stress (the product of Young's modulus and the thermal expansion coefficient) for KCl is approximately one-half that of NaCl[2]. However, NaCl has other advantages in being less soluble and less moisture sensitive than KCl, having a lower intrinsic solubility for absorbing impurities and being apparently harder than KCl[3-6]. Small-grained polycrystalline windows of NaCl are more stable than KCl, and no alloying or doping is required to maintain small grain sizes[7]. NaCl has a higher dielectric strength than KCl, a point of further interest for pulsed applications.

Laser calorimetric measurements of bulk absorption at 10.61μm in RAP-grown KCl[8,9] and total absorption in RAP-grown NaCl and Harshaw NaCl [10] have yielded values in good agreement with those expected on the basis of intrinsic multiphonon processes, $\sim 8 \times 10^{-5}$ cm^{-1} for KCl and $\sim 1 \times 10^{-3}$ cm^{-1} for NaCl. Allen and Harrington[9] recently reported a value of 2×10^{-5} cm^{-1} for the bulk absorption coefficient at 9.27μm of a RAP-grown KCl. While this is the lowest absorption level reported to date at 9.27μm in KCl, it is significantly higher than the expected intrinsic value of $\sim 5 \times 10^{-6}$ cm^{-1} at this wavelength, suggesting that an impurity absorption band is possibly present near 9.27μm even in such high purity KCl. Apparently this absorption band, and/or some other bands, are present at a significantly higher level in KCl prepared using proprietary processes; these materials typically yield total absorption coefficient values in the range of 9×10^{-4} to 1.3×10^{-3} cm^{-1} at 9.27 μm and in the range 5×10^{-4} to 9×10^{-4} cm^{-1} at 10.61μm.

Many molecular impurities, when present in alkali halides, give rise to strong infrared absorptions, as demonstrated by the calculation of Duthler[11]. This calculation indicates that impurities like SO_4^{--} or HCO_3^-, when present in KCl concentration levels in the range 0.01 - 0.03 ppm, will give rise to absorption coefficient levels of $\sim 1 \times 10^{-4}$ cm^{-1}. Studies of absorption in KCl due to ClO_3^- and ClO_4^- impurities [12,13] indicate that these impurities have stronger absorption near 10.61μm than the impurities considered by Duhler; an assumption of incorporation of only 0.001 ppm of chlorate (ClO_3^-) in the KCl lattice is required to account for the residual absorption of 1×10^{-4} cm^{-1} at 10.61μm.

Of the techniques available for the measurements of low absorption coefficient values, the laser calorimetric method has found the widest application [8,14-17]. An attractive feature of this method is that it can be used to differentiate between bulk and surface absorption by employing a long bar sample [8,14]. If the half length of the sample is greater than its radius, the time required for the heat generated by absorption at the two end surfaces to reach the thermocouple will be greater than the corresponding time for the heat generated by bulk absorption near the specimen axis; a time-temperature plot obtained during laser irradiation of a bar sample length L thus exhibits two linear regions. Here the slope of the first linear region is proportional to the value

of $\beta_B L$, the fraction absorbed by the bulk, where β_B is the bulk absorption coefficient, and the slope of the second linear region is proportional to the value of total absorption, $\beta_B L + 2S$ is the fraction absorbed by the two end surfaces[14]. From the known values of specimen mass, length, specific heat and refractive index, the measured transmitted power and the slopes of two linear regions, the values of β_B and 2S can be determined.

In the present paper, results obtained on absorption coefficients in the 9.2 to 10.8μm region are reported, using the technique of tunable CO_2 laser calorimetry, are presented on several NaCl and KCl samples. RAP-grown materials and the long bar technique were used, when samples were available, to determine more information on intrinsic absorption limits and the extent of extrinsic absorption caused by bulk and surface defects in this wavelength region.

2. Experimental

A total of five long bar single-crystal samples were employed in the present study. The sources, materials and dimensions of these samples are indicated in table 1. Absorption measurements were made initially on each of these samples after mechanically polishing their surfaces to remove visible scratches. The RAP-grown NRL (Naval Research Laboratory) NaCl and Hughes KCl crystals were then etched to determine absorption values at the etched surfaces of NaCl and KCl. Etching was done in concentrated HCl (2 min) followed by successive rinsing in ethanol (10 sec), 2-propanol (10 sec) and 2-propanol (10 sec). After final rinsing, each sample was dried in warm air as it was gently pulled from a bath of 2-propanol, then immediately transferred to the calorimetry chamber for absorption measurements. All absorption measurements were made in vacuum.

Table 1. Sources, materials and dimensions of various long bar samples

Source	Material	Dimensions (cm)
Hughes Research Laboratories	RAP-grown KCl	13.0 x 2.5 (dia.)
Naval Research Laboratory (NRL)	RAP-grown KCl	8.2 x 3.3 (dia.)
Naval Research Laboratory (NRL)	RAP-grown KCl	8.3 x 2.5 (dia.)
Harshaw Chemical Company	KCl:Eu	6.6 x 2.5 x 1.6
Harshaw Chemical Company	KCl:Rb, Eu	12.6 x 3.2 x 3.2

Several additional samples of single and poly-crystalline NaCl, 1 cm in thickness and 2.8 cm in diameter, cut from large diameter ingots, were provided by Harshaw. The samples were polished by Harshaw and the absorption measurements at 9.27 and 10.61μm were made both in the as-received condition and after etching. The procedure used for etching was the same as above.

All our laser calorimetric experiments on long bar samples were carried out by placing two copper-constantan foil thermocouples (connected in series) diametrically opposite to one another on the periphery of the sample at the center of its length. Rubber bands were used to keep the thermocouple junctions in intimate contact with the specimen surface. The duration of the scattering region in our

experiments varied from about one-half to less than one-fourth of the time required for the surface heat to reach the temperature sensor. The approximate magnitude of this time is obtained from the relation $t = (L/2)^2/6k$, where L and k are the length and thermal diffusivity of the specimen; for a 6.6 cm long sample of KCl ($k \sim 0.06$ cm^2/sec), t is 30 secs. Since the time required for a long bar sample to reach equilibrium with its surrounding is inconveniently long, the three slope formula [18], which takes into account the cooling rates of the sample both before and after laser irradiation, was used to calculate β_B and 2S from the t-T plots obtained in our study.

3. Results and Discussion

The wavelength dependence of the bulk absorption coefficient for the 9.2-10.8 μm region in four long bar samples of KCl, and the total absorption in an etched 6 mm thick Harshaw KCl:Rb sample, is shown in figure 1. The long bar samples have been characterized in table 1; the Harshaw KCl:Rb sample was selected for the present study because it showed unusually high absorption near 9.3 μm. The magnitude of the error bars represent the standard deviation of absorption, determined from at least three calorimetric measurements at the indicated wavelengths. These results were all obtained with mechanically polished surfaces. The solid line shown in figure 1 was obtained from Deutsch[1]. Absorption coefficient values for the same long bar samples in the etched condition at 9.27 and 10.6μm are reported in table 2.

Table 2. Measured bulk absorption in various KCl crystals (units 10^{-4} cm^{-1}) and ratio of absorption coefficient values at 9.27 to that at 10.6μm

λ	HRL RAP KCl	NRL RAP KCl	Harshaw KCl:Eu	Harshaw KCl:Rb,Eu	Multiphonon
9.27	0.43	1.2	5.4	4.8	0.052
10.6	0.9	1.6	5.6	2.5	0.76
Ratio $\frac{\beta_{9.27}}{\beta_{10.6}}$	0.48	0.75	0.96	1.9	0.068

The ratio of the bulk absorption coefficient β_B at 9.27μm to that at 10.6μm varies randomly from sample to sample, as shown in table 2. This is also seen in the relative inconsistent trends in figure 1 of the absorption coefficient variation with wavelength. This indicates that the residual absorption in the region 9.2-9.7μm is independent of the residual absorption observed in the range 10.1-10.8μm, suggesting that at least two impurities, one with absorption predominating in the region 10.1-10.8μm and the other with absorption predominating in the region 9.2-9.7μm are limiting the transparency of KCl crystals at the CO_2 laser frequencies. The variation in the relative concentrations of these impurities from sample to sample would give rise to the observed variation in the raio β_B at 9.27μm to β_B at 10.61μm.

Since the estimated strength of absorption at 10.61μm per unit concentration of ClO_3^- impurity in KCl [12] is greater by at least an order of magnitude than the corresponding absorption strengths of impurities considered earlier by Duthler [11] the ClO_3^- ion would appear to be a likely impurity to limit the transparency of KCl near 10.61μm.

The ClO_3^- impurity in alkali halides absorbs in the range 10-10.9μm [6,12] compared to the spectral range of 9.2-10.85μm of the observed residual absorption in KCl crystals used in the present work. This suggests that, in addition to ClO_3^-, an impurity with strong absorption in the range 9.2-9.7μm is present in these KCl crystals. This impurity would appear to be ClO_4^-, which has an absorption near 9.27μm which is as strong as the absorption of ClO_3^- near 10.61μm [6].

Two surface absorption (2S) and bulk absorption data for the long bar RAP-grown NRL NaCl and Hughes KCl crystals are shown in figure 2. These data are for chemically etched surfaces, and indicate that the wavelength dependence of the surface absorption increases with decreasing wavelength in both materials. The surface absorption of NaCl appears to be slightly lower than that of KCl, with the surface absorption of NaCl being too small to distinguish in the laser calorimetry results in the 10.8-10.1μm region. The surface absorption component in the Hughes RAP-grown KCl is seen to be greater than the bulk absorption at all wavelengths. This dominance of surface absorption is assumed to be caused by the surface interaction with oxygen ions, forming ClO_3^- and ClO_4^- as discussed above.

Total absorption coefficient data at 9.27 and 10.61μm for single-crystal and polycrystalline Harshaw NaCl are shown in tables 3 and 4, respectively, for both as-received and etched conditions. All twelve samples in table 3 were obtained from large diameter ingots; samples numbered 1 to 6 were cut from near the seed end of Kyropoulos grown ingots, while those number 7 to 12 were cut from near the cone end of Bridgman grown ingots. The polycrystalline samples in table 4 were obtained by forging slices cut from large diameter NaCl crystals grown using the Bridgman technique. The slices were cut from the middle, cone or heel ends of the ingots, as indicated. These data demonstrate the influence of surface preparation on observed absorption coefficient values: The Harshaw single crystal samples (table 3) show a 25% reduction in average absorption coefficient at 10.61μm after surface etching and a 30% reduction at 9.27μm. Similar reductions are seen in the polycrystalline Harshaw samples (table 4). High values of surface absorption also influence the apparent bulk absorption coefficient in polished samples. Comparing results from figures 1 and 2, the observed increase seen in polished vs. etched RAP-grown KCl is 10% at 10.6μm, increasing to 30% at 9.27μm.

Table 3. Absorption coefficient data at 9.27 and 10.61μm on Harshaw NaCl crystals. Sample thickness = 1 cm

Sample No.	β_T 9.27μm ($\times 10^{-3} cm^{-1}$) As Rec'd.	Etched	β_T 10.61μm ($\times 10^{-3} cm^{-1}$) As Rec'd.	Etched
1	1.45	0.73	1.76	1.12
2	1.24	0.84	1.69	1.29
3	1.53	0.92	1.75	1.35
4	1.92	0.80	2.40	1.45
5	0.87	0.83	1.28	1.31
6	1.23	0.75	1.61	1.16
7	1.17	0.78	1.55	1.31
8	1.34	1.05	1.81	1.61
9	1.08	1.00	1.53	1.35
10	1.43	1.04	1.69	1.42
11	1.08	0.85	1.21	1.19
12	1.29	1.06	2.06	1.94
Average	1.30±0.26	0.89± 0.12	1.70±0.32	1.37±0.21

Table 4. Absorption coefficient data at 9.27 and 10.61μm on Harshaw NaCl polycrystalline samples. Sample thickness = 1 cm

Sample No.	Location	β_T9.27μm($\times 10^{-3} cm^{-1}$) As Rec'd	Etched	β_T10.61μm ($\times 10^{-3} cm^{-1}$) As Rec'd	Etched
1	Cone	1.17	0.88	1.80	1.64
2	Cone	1.38	0.87	1.66	1.57
3	Cone	1.01	0.69	1.67	1.34
4	Mid	1.32	1.27	2.17	1.94
5	Mid	1.21	0.89	1.93	1.38
6	Mid	1.22	1.27	1.90	1.90
7	Heel	1.69	1.20	2.53	2.18
8	Heel	1.46	1.31	2.28	2.23
9	Heel	1.81	1.25	2.95	2.49

Taking into account absorption at the exterior surfaces only in the cone section samples of Harshaw polycrystalline NaCl (table 4), bulk absorption values similar to those in Harshaw single crystals are obtained. Higher values in the mid-section and heel of the polycrystalline sample are probably due to higher bulk absorption due to higher impurity concentrations. These results seem to indicate that the interior surfaces in the polycrystalline sample do not contribute to surface absorption under these conditions.

In the cases shown here, the etched surface results in an absorption coefficient of about 10^{-4} cm^{-1}. Workers in this field have often used the absorption coefficient of an etched, 1 cm thick sample as the bulk absorption value. The present results demonstrate that this assumption is not valid for samples with low absorption coefficient.

The bulk absorption data for the NRL RAP-grown NaCl in the 9.2 to 10.6μm range is shown in figure 3, in comparison with the least squares extrapolation of Deutsch's earlier data[1] indicated by the dashed line. The latter is normally taken as the intrinsic multiphonon absorption limit in NaCl, but as can be seen, the present data fall below this line. The total absorption coeffi- at 10.6μm previously determined by Rowe and Harrington[19] for RAP-grown NaCl also fell slightly below the extrapolated value.

Due to this observed discrepancy, the bulk absorption data for RAP-grown NaCl given in figure 3 have been used to operationally define a new multiphonon absorption limit. For an exponential dependence of the absorption coefficient on frequency of the form $\beta=A\exp(-\gamma\omega/\omega_o)$, a least square fit of the nine data points near 10.6μm yields A = 8999.8 cm^{-1} and ω_o/γ = 58,495 cm, with a correlation coefficient of 0.9976. Using this new multiphonon limit, the intrinsic absorption coefficient for 10.6μm is .0009 cm^{-1}, compared to Deutach's value of .00117 cm^{-1}. The measured values for β near 9.3μm in the NRL RAP-grown NaCl lies above this newly define multiphonon limit by a factor of about 4. This may be due to higher scatter caused by the higher surface absorption in this region, or it may be caused by impurities that are more likely to contribute to bulk absorption in this low absorption region. Hence, only those data points in the 10.1 to 10.8μm region are used in the definition of the multiphonon limit.

4. Conclusions

The present study has established a new operationally defined multiphonon limit for intrinsic absorption in NaCl, and has documented the importance of surface absorptions, possibly related to ClO_3^- and ClO_4^-, in determining total absorption coefficients for NaCl and KCl in the 9.27 - 10.8μm region. The measured bulk absorption in RAP-grown NaCl is intrinsic in the 10.1 - 10.8μm region but may be impurity dominated near 9.27μm. Bulk absorption of etched Harshaw NaCl is nearly intrinsic at 10.61μm (table 3) but could be improved by a factor of 4 at 9.27μm by added purification. The bulk absorption of the RAP-grown KCl sample is the lowest measured; it is intrinsic at 10.6μm but increases to a factor of 10 above the extrapolated intrinsic value at 9.27μm. Compared to available KCl laser window material, the availability of RAP-grown KCl laser windows would reduce bulk absorption by an order of magnitude throughout this wavelength range.

5. Acknowledgements

The authors would like to thank Dr. G.E. Kuhl of the Air Force Materials Laboratory for helpful discussions, and Dr. P.H. Klein of the Naval Research Laboratory, Dr. J.A. Harrington of the Hughes Research Laboratories, and Mr. D.J. Krus of the Harshaw Chemical Company for providing the NaCl and KCl samples for the present study. The authors are indebted to Mr. J.A. Fox and Mr. P. Greason of the University of Dayton Research Institute for invaluable technical assistance.

6. References

[1] T.F. Deutsch, J. Phys. Chem. Solids 34, 2091 (1973).

[2] M. Sparks and H.C. Chow, J. Appl. Phys. 45, 1510 (1974).

[3] L.S. Combes, S.S. Ballard and K.A. McCarthy, J. Opt. Soc. Am., 41, 215 (1951).

[4] Harshaw Optical Crystals, A. Smakula, et al, eds., Harshaw Chemical Co., 1967.

[5] Handbook of Chemistry and Physics, 56th ed., R.C. Weast, ed., CRC Press, 1975.

[6] G.N. Krynauw and C.J.H. Schutte, Spectrochim Acta 21, 1947 (1965).

[7] J. Fenter, AFML, private communication.

[8] H.B. Rosenstock, M. Hass, D.A. Gregory and J.A. Harrington, Appl. Opt. 16, 2837 (1977).

[9] S.D. Allen and J.A. Harrington, in Proceedings of the High Power Laser Optical Components and Component Materials Meeting, October 3-4, 1977, Boulder, Colorado, compiled by J.S. Harris and C.L. Strecker (Defense Advanced Research Projects Agency, Arlington, VA, 1977), p. 438.

[10] J.M. Rowe and J.A. Harrington, in Optical Properties of Highly Transparent Solids, S.S. Mitra and B. Bendow, eds. (Plenum, New York, 1975), p. 109.

[11] C.J. Duthler, J. Appl. Phys. 45, 2668 (1974); Proceedings of the Fourth Annual Conference on Laser Window Materials, November 18-20, 1974, Tucson, Arizona, compiled by C.R. Andrews and C.L. Strecker (Advanced Research Projects Agency, Arlington, VA, 1975), p. 166.

[12] H.G. Lipson, J.J. Larkin, B. Bendow, and S.S. Mitra, J. Electron. Mater. 4, 1 (1975).

[13] D. Shim and C. Wittig, Appl. Opt. 15, 1896 (1976).

[14] M. Hass, J.W. Davisson, H.B. Rosenstock, and J. Babiskin, Appl. Opt. 14, 1128 (1975).

[15] L.H. Skolnik, in Optical Properties of Highly Transparent Solids, S.S. Mitra and B. Bendow, Eds. (Plenum, New York, 1975), p. 405.

[16] S.D. Allen and J.E. Rudisill, Appl. Opt. 16, 2914 (1977).

[17] A. Hordvik, Appl. Opt. 16, 2827 (1977).

[18] M. Hass, J.W. Davisson, P.H. Klein and L.L. Boyer, J. Appl. Phys. 45, 3959 (1974).

[19] J.M. Rowe and J.A. Harrington, J. Appl. Phys. 47, 4926 (1976).

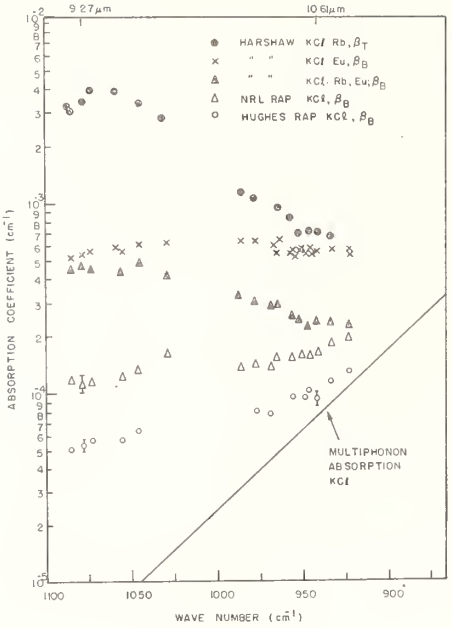

Figure 1. Wavelength dependence of absorption for four long bar samples and one thin KCℓ:Rb sample. Bulk absorption β_B separated from surface contribution using laser calorimetry on long bar samples; total absorption β_T reported in thin sample. Extrapolation of Deutch's KCℓ data, taken as the multiphonon limit, shown for comparison.

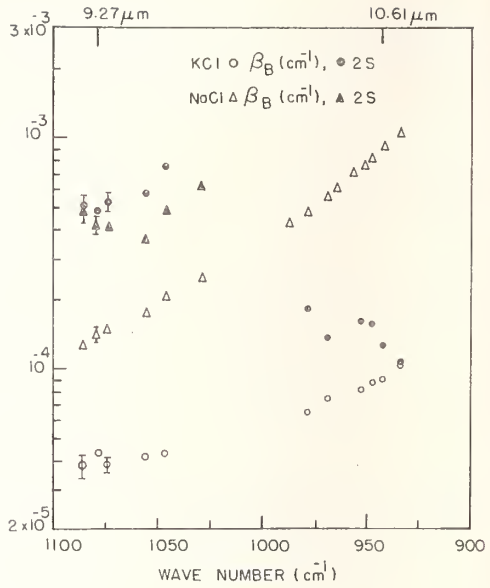

Figure 2. Comparison of bulk (β_B) and two-surface (2S) absorption for long bar NRL NaCℓ and Hughes KCℓ. Chemically etched surfaces. Bulk absorption in cm^{-1}; surface absorption in fraction absorbed per surface.

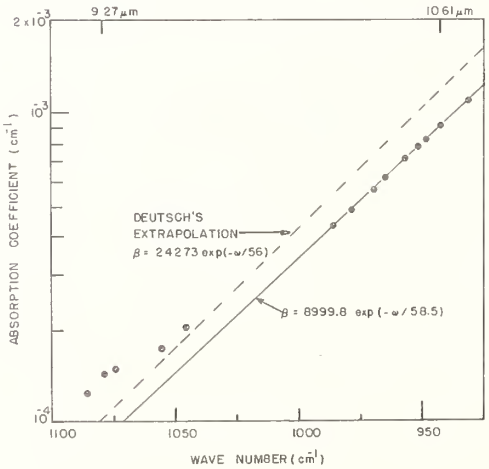

Figure 3. Bulk absorption for NRL RAP-grown NaCℓ with least squares line fit to data near 10.6 μm (solid line). Extrapolation of Deutch's data shown for comparison (dashed line). These data define a new operational multiphonon limit line for NaCℓ.

A 1.06μm LASER ABSORPTION CALORIMETER FOR OPTICAL COATINGS

Thomas H. Allen, Joseph H. Apfel, and C.K. Carniglia
Optical Coating Laboratory, Inc.
Santa Rosa, California 95402

We describe a laser calorimeter for measuring the absorption of an optical coating deposited on a thin disc. The sample with diameter 2.54cm and thickness between 0.02 to 0.13cm is irradiated with 6 watt CW Nd:YAG laser. The temperature of the coated disc is compared to that of a reference disc using thermistors in mechanical contact with the samples. Measurements are made under vacuum (100 torr) to reduce temperature variations caused by convection. The calorimeter was evaluated by measuring coated and uncoated discs of various thicknesses with absorptances from 9×10^{-6} to 5×10^{-3}. These measurements demonstrated a repeatability of ± 2% at an absorptance level of 1×10^{-4} and a sensitivity for a 0.04cm thick substrate of 3.8×10^{5}μV/watt. The lower absorption limit of the calorimeter is 2×10^{-6}. The results of measurements on polished, uncoated fused silica discs with thicknesses from 0.04 to 0.13cm show a surface absorptance of 6×10^{-6} and a bulk value of 5×10^{-5}/cm.

Key words: Absorption; calorimetry; optical coatings.

1. The Laser Calorimeter

A wide range of techniques has been developed for measuring the absorptance of optical materials [1,2]. Of these various techniques, laser calorimetry is the most widely used because of its simplicity and high sensitivity [3]. Laser calorimetry involve measuring the increase in temperature of a sample that results from the irradiation by a known amount of laser energy. In most low level laser absorption calorimeters, including the adiabatic calorimeter described by Decker and Temple [4], the sample and its mounting are assumed to be at essentailly uniform temperature throughout the experiment. For dielectric samples the uniform temperature requirement limits the shape to thick discs or rods for axial illumination [5].

We have choosen to use thin discs for substrates in order to keep the absorption of the disc smaller than that of the coating. This sample geometry results in a large thermal gradient between the central illuminated region and the edge where the temperature measurement is made. Therefore, a new measurement and calibration procedure and thermal analysis are required for this calorimeter.

The optical arrangement of the calorimeter is shown in figure 1. The beam of a 6 watt Nd:YAG laser is transferred by a series of lenses and apertures to provide a well defined spot approximately 5mm in diameter at the sample plane. A He-Ne laser is used for alignment purposes. The intensity of the laser beam is monitored with a silicon detector prior to the all-dielectric turning mirror (M5) which reflects the beam into the sample chamber. A small amount of the incident laser beam is transmitted by this turning mirror (M5) to the beam position monitor. The entrance and exit windows of the sample chamber have been positioned to transmit the laser radiation reflected by the sample and the exit window. The laser power transmitted by the sample is measured by a radiometer. All lenses and windows are multilayer coated to achieve a reflectance of ~.5% at 1.064μm.

The most critical design problems involved supporting the sample disc and measuring its temperature. These problems were solved by the use of thermistors for temperature measurement and the sample mounting arrangement shown in figure 2. The sample is supported by an arrangement of three thin-walled glass tubes to minimize thermal leakage to the support structure. Two thermistor beads are mounted on the tops of the glass tubes to contact the sample. The support was designed so that the temperature sensor is not irradiated by laser radiation scattered by the sample or its support. An unirradiated reference disc is mounted on an identical arrangement of three glass posts and two thermistor beads. The four thermistors are electrically arranged in an AC Wheatstone bridge with an input voltage of 1.600 volts at a frequency of 950Hz. The

output of the bridge is measured with a lock-in amplifier. This electrical arrangement is capable of measuring changes in output voltage as small as 1μV.

Absorption measurements are made by measuring the transmitted laser power and the increase in sample temperature 4 minutes after opening a shutter in the laser beam. These signals are combined with the sensitivity to determine the total absorptance of the sample as discussed in the evaluation section. All absorption measurements on coated samples were made with the coated side away from the incident laser beam. A pressure of 100 microns was used to reduce convection cooling of the sample.

2. Thermal Analysis

We have carried out a computer analysis of the thermal response of our calorimeter using standard numerical methods [6]. The sample was modeled as a thin absorbing disc irradiated in the center by a laser beam. The heat conduction through the sample was assumed to be radially out from the center so that a one dimensional analysis could be used. Radiation losses and gas conduction losses were also included in the model.

The results of the thermal analysis show that the temperature of the disc rises to a limiting value at which the absorbed power is balanced by the radiation and conduction losses. During the heating cycle and at equilibrium, a large thermal gradient exists across the part. For a 0.25mm thick disc, the temperature in the center is approximately 20 times the temperature at the edge. As the thickness increases, the temperature at the center decreases and the temperature at the edge increases. Figure 3 illustrates the heating curves for several thicknesses of fused silica discs. The temperature at the edge of the disc is plotted against time after the laser is turned on. These curves also illustrate that the time required to reach equilibrium increases as the thickness increases.

The major result of the thermal analysis is that the temperature at the edge of the disc is a linear function of the total power absorbed by the sample, in spite of the large thermal gradient across the part. Thus either the equilibrium temperature with constant irradiation of the part, or the maximum temperature after irradiation for a fixed time interval can be used to measure the absorption of the sample. The linearity of the system has been confirmed experimentally as shown in figure 4.

3. Evaluation

The calorimeter sensitivity and linearity were determined by measurements on a sample coated with a slightly absorbing SiO_2-Cr-SiO_2 trilayer. The reflectance and transmittance of the sample were measured with a precision laser photometer [7] whose accuracy is reported to be ±.0005 (±.05%). Its absorptance at 1.06 micron was found to be .0048. The linearity was determined by measuring the signal level as a function of transmitted laser power by inserting attenuators of known transmittance in the laser beam incident on the sample. Figure 4 shows that the signal is a linear function of absorbed power over more than three orders of magnitude. The sensitivity is the slope of the linear relationship between signal and absorbed power , and is 3.8×10^5 μV/watt for this substrate thickness.

The precision was established by repeated measurements on a set of four uncoated glass and fused silica samples choosen to cover an absorptance range 1×10^{-5} to 4×10^{-4}. The results for 0.5mm thick BK7 are shown in figure 5 and are summarized for all samples in table 1.

Table 1. Summary of precision measurements.

Sample	Thickness (mm)	Number of Measurements	Mean Absorptance	Standard Deviation
Fused Silica	.15	10	9×10^{-6}	2×10^{-6}
Fused Silica	.41	13	8×10^{-6}	2×10^{-6}
BK7	.25	12	1.2×10^{-4}	3×10^{-6}
BK7	.51	12	3.8×10^{-4}	5×10^{-6}

These results show that the standard deviation is essentially constant over this absorption range. It is felt that the standard deviation of 2×10^{-6} represents the noise equivalent absorptance inherent to the calorimeter.

4. Total Absorptance of Uncoated Fused Silica

The absorptance of uncoated fused silica has been measured to determine its variation with thickness. Samples were fabricated from synthetic fused silica (Corning 7940) and ranged in thickness from 0.4 to 1.27mm. The total absorptance of an uncoated substrate can be approximated by

$$A = \beta d + A_1 + n A_2$$

where β is the absorption coefficient (cm^{-1}) of the material, d is the substrate thickness, A_1 and A_2 are the absorptances of the entrance and exit surfaces, and n is the refractive index. The factor n results from the increased electric field strength at the exit surface described by Crisp, Boling, and Dubé [8].

The measured absorptance as a function of substrate thickness is shown in figure 6. These results indicate that the fused silica has $\beta = 5 \times 10^{-5} cm^{-1}$ and a total surface absorptance of 6×10^{-6}. If the two surfaces have the same absorptance, $A_1 = A_2 \cong 2.5 \times 10^{-6}$.

5. Summary

A 1.06 micron laser calorimeter has been designed and built for measuring the absorptance of optical coatings. The sample consists of a thin 25.4mm diameter disc whose central portion is irradiated by the laser beam. The temperature of the sample disc is compared to that of an identical but unradiated disc by thermistors in physical contact with both discs. The thermistors are electrically arranged in an AC Wheatstone bridge. The precision of the calorimeter was determined over an absorptance range of 9×10^{-6} to 3.8×10^{-4} and found to be essentially constant at $\sim 2 \times 10^{-6}$. The sensitivity was determined using a SiO_2-Cr-SiO_2 trilayer absorptance standard and found to be $3.8 \times 10^5 \mu V$/watt for a 0.4mm thick substrate. The absorptance standard was also used to show that the measured temperature rise is a linear function of absorbed power as predicted by thermal analysis. Measurements have been made on uncoated fused silica to resolve the bulk and surfaces absorptances.

6. References

[1] Hordvik, A., Appl. Opt. 16, 2827 (1977).

[2] Moravec, T. J. and Bernal G., E., Appl. Opt. 17, 1938 (1978).

[3] Hass, M., Optical Engineering 17, 525 (1978).

[4] Decker, D. L. and Temple, P. A., NBS Special Publication 509, 281 (1977).

[5] Bernal G., E., Appl. Opt. 14, 314 (1975).

[6] Adams, J. A. and Roger, D. F., Computer-Aided Heat Transfer Analysis, McGraw-Hill, 1973.

[7] Anthon, E., Proceedings of the Society of Photo-Optical Instrumentation Engineers, 140 (1978).

[8] Crisp, M. D., Boling, N. L. and Dubé, G., Appl. Phys. Lett. 21, 364 (1972).

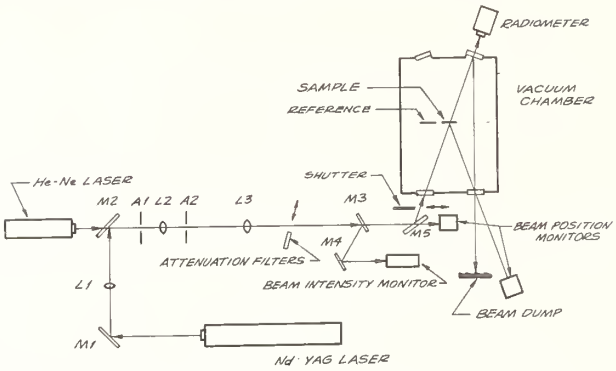

Figure 1. Optical arrangement of the calorimeter.

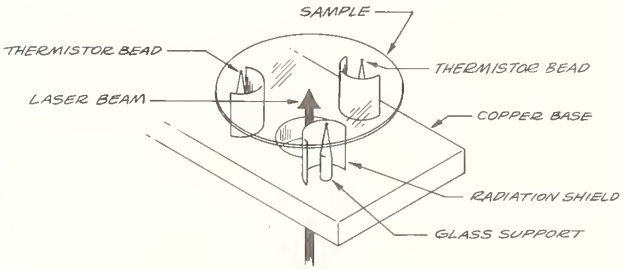

Figure 2. Sample support showing the location of thermistor beads and glass supports.

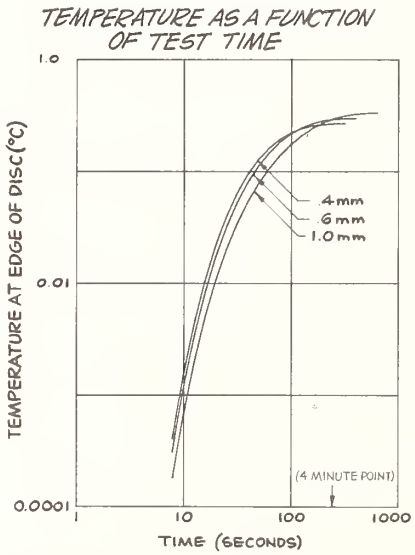

Figure 3. Computed temperature as a function of test time for three different sample thicknesses.

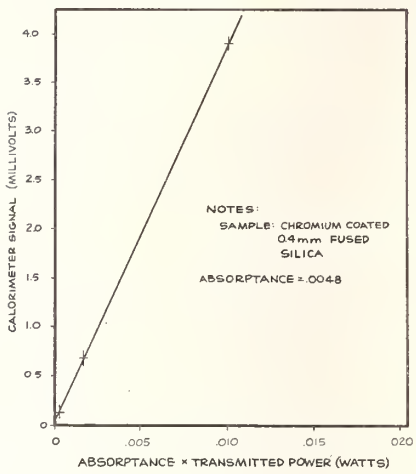

Figure 4. Measured signal as a function of absorbed power used to determine linearity and sensitivity.

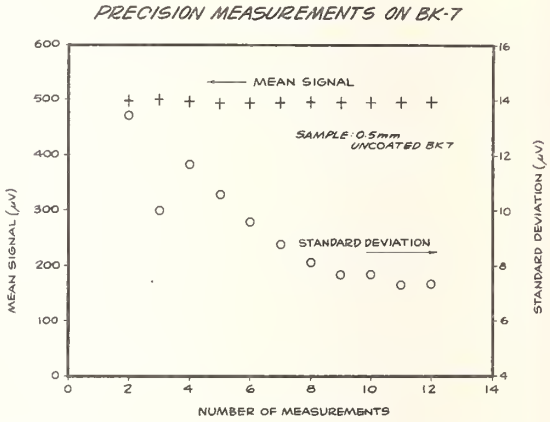

Figure 5. Repeated measurements on BK7 used to determine precision.

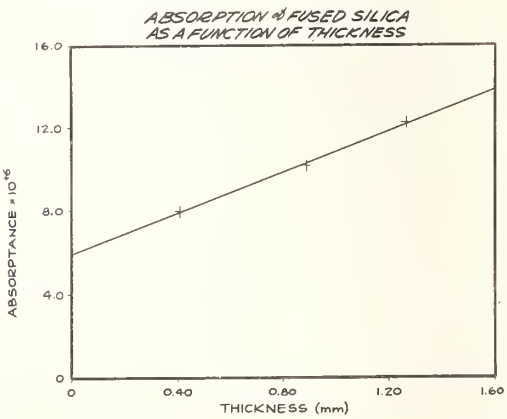

Figure 6. Measured absorptance of fused silica showing the effects of bulk and surface absorption.

MEASURED THIN FILM ABSORPTION AT THE AIR-FILM INTERFACE, THE FILM BULK, AND THE FILM-SUBSTRATE INTERFACE*

P. A. Temple, D. L. Decker, T. M. Donovan, and J. W. Bethke
Michelson Laboratory, Physics Division
Naval Weapons Center, China Lake, CA 93555

A measurement technique is described where the absorption introduced by the addition of a single-layer thin film is separated into three parts: absorption (a) within the bulk of the film; (b) at the air-film interface; and (c) at the film-substrate interface. The technique employs a scanning adiabatic calorimeter to measure substrates which are partially coated on the entrance surface with films of continuously varying thickness. By measuring the absorption on the bare substrate and at various film thicknesses, we have unambiguously determined the film-bulk absorption coefficient. We have also measured the combined absorption due to the two film interfaces. It will be shown that, in some cases, it is possible to distinguish between air-film interface absorption and film-substrate interface absorption and determine the magnitude of each. Data will be presented for 2.9 and 2.7 μm for films made of NaF and As_2Se_3 on CaF_2. These films show the presence of impurities in the film and/or at the film interfaces. The relative magnitude of absorption in the three regions will be discussed.

Key words: Absorption coefficient; adiabatic calorimetry; As_2Se_3; interface absorption; laser calorimetry; NaF; thin film absorption; water absorption; wedged film.

Introduction

In this paper we report the measurement of interface absorptance and the bulk absorption coefficient as a function of frequency of a material in thin film form. This was accomplished by adiabatic calorimeter measurements, using a tunable laser source on a film of varying thickness. This technique was used to determine the presence of water in films as separate from water at film interfaces. The effects of electric field modulation within thin films on the total loss due to film and interface absorptance are also analyzed.

One commonly determines the absorption properties of a material in thin-film form [1][1] by first measuring the absorptance, A_1, of a suitable substrate. A film of known thickness is then deposited on the substrate and the absorptance, A_2, is again measured. The increased absorptance is attributed to the film, and a film absorption coefficient, $\beta = (A_2-A_1)/d$, is calculated. It is generally recognized that the increased absorption is due not only to the bulk of the film, but also to the newly introduced film-substrate interface and the film-air interface.

In order to separate the interface contributions from the bulk contributions and to determine the bulk absorption coefficient of the film, α_f, we have used samples with a film of varying thickness deposited on one face of the sample [2]. This has allowed calorimetric absorptance measurements to be made for various thickness films on the same substrate. As discussed below, this allows us to separate the absorption of a film into three parts: (a) that within the bulk of the film; (b) the absorption at the air-film interface; and (c) the absorption at the film-substrate interface. This technique has been particularly useful in determining the presence of water *in* films as separate from water *on* films.

Experimental

The adiabatic calorimeter used to make these measurements has been described elsewhere [3,4]. In this instrument the sample is surrounded by a temperature-controlled box such that the surroundings are always at the same temperature as the sample. The sample and box are in a vacuum chamber. When the sample temperature is increased due to laser heating, the surrounding temperature is also increased. This adiabatic nature allows us to use a large variety of laser sources since low irradiation laser power is needed. The measurements reported here were made with a laser output power of less than 1/2 watt. The source was an HF chemical laser with a grating as the high reflector cavity element.

A second feature of this instrument is its ability to allow irradiation at various positions on the sample. This is permitted since the absorptance is deduced from the total temperature rise of the sample and not the rate of temperature rise. The beam diameter used was ~ 0.5 mm as measured at the e^{-2} points, and any point on a specified diameter of the sample could be irradiated with spatial resolution of 0.5 mm.

---

* Work supported by the Defense Advanced Research Projects Agency.

1. Figures in brackets indicate the literature references at the end of this paper.

The sample configuration is shown in figure 1. A mask was used to produce the two edges. The wedge shape was produced by slowly obscuring the sample from the deposition source with a shutter. This was done so the film-substrate interface was produced at one instant in the deposition. The film thickness profile was determined by scanning the film edge every 3 mm with a profilometer [5]. A significant advantage of using samples of this configuration is that one substrate and one deposition are involved. Thus, while measurements of the type described here may be made with several depositions of various thicknesses on several substrates, we have eliminated a significant source of experimental error by using one substrate and one deposition. A second advantage is the savings in time used to load and equilibrate one sample rather than several samples.

Calorimetric measurements were then made along the diameter which is indicated in figure 1. This allowed absorptance measurements to be made on the uncoated substrate and at various film thicknesses.

Figure 2 shows data of a typical wedged film. This is a NaF film on a CaF_2 substrate measured at 2.72 and 2.87 μm. The ordinate indicates the measured absorptance, $A = \frac{\text{absorbed power}}{\text{incident power}}$, and the abscissa indicates the film thickness at which the absorptance was measured. The *measured* zero thickness absorptance (bare substrate) is indicated by the two data points at zero thickness. The *extrapolated* zero thickness absorptance is indicated by the ordinate of the left end of the solid curves. The absorptance offset from the measured value is the absorptance due to the film-air interface and the substrate-film interface. These two contributions are always present together in the substrate plus film measurements. We assume that, for the thicknesses measured, the two interface contributions are constant, independent of film thickness.

Determination of α_f

The absorptance of a sample under normal incidence irradiation is given by the expression

$$A = \int_o^L n(x) \frac{|E(x)^2|}{|E_o^2|} \alpha(x) \cdot dx \quad ,$$

where $n(x) \frac{|E(x)^2|}{|E_o^2|}$ is the time averaged relative power density $p(x)$ at position x, and $\alpha(x)$ is the absorption coefficient at x. $|E_o|$ is the time average of the incident electric field. We can then write the absorptance as

$$A = \int_o^L p(x)\alpha(x)dx \quad .$$

For a single film at the incident face we have assumed that the absorptance at the interfaces can be characterized by a specific absorptance $a_{af} = \alpha_{af}\Delta\ell_{af}$, where the air-film interface is of thickness $\Delta\ell_{af}$ and has absorption coefficient α_{af}. Similarly, the film-substrate interface is characterized by $a_{fs} = \alpha_{fs}\Delta\ell_{fs}$. We also assumed that the bulk absorption coefficient of the film, α_f, is constant throughout the thickness of the film. All the relative power densities were calculated from a thin-film computer program [6]. Analytic expressions are given in reference [7]. In all cases we have spoiled Fabry-Perot type interference in the substrate by slightly tilting the sample. This guaranteed that the incident beam and the beam reflected back from the exit surface of the substrate did not intersect at the substrate entrance surface.

Under these conditions, the substrate contribution to the absorptance is very nearly given by $(T/T_o)A_o$, where A_o is the uncoated substrate absorptance, T_o is the uncoated substrate first surface transmittance, and T is the first surface transmittance with the film in place. This is an approximation which ignores the absorption of the back-reflected beam in the film. In the cases reported here, the back-reflected beam is ~ 3% of the transmitted beam.

With the above approximations, the single-film plus substrate absorptance becomes

$$A = p_{af}a_{af} + \bar{p}_f\alpha_f\ell_f + p_{fs}a_{fs} + \frac{T}{T_o} A_o \quad .$$

See figure 3. $\bar{p}_f$ is the spatially averaged relative power density within the film.

In order to determine α_f, the bulk absorption coefficient within the film, we have measured the absorptance at film thicknesses which had the same relative power densities at the interfaces and in the bulk of the film. In this case, the film absorption coefficient is given by

$$\alpha_f = \frac{dA/d\ell}{\bar{p}_f} \quad .$$

Two cases are represented in the data. These are for $n_f \cong n_s$ and $n_f \neq n_s$. The time-averaged (squared) electric field pattern for these two cases is shown in figure 4. In case A, $n_f \cong n_s$, there is no reflection from the film-substrate interface. Interference from the back face of the substrate has been spoiled. Therefore, the relative power density is constant throughout the sample in the region near the front surface. The data in figure 2 were taken in this way.

In case B, $n_f \neq n_s$, the constant relative power density conditions are met for integral half-wave film thicknesses. The data for such a case are shown in figure 5, which is a film of As_2Se_3 on CaF_2. In this material the bulk absorption coefficient of the film is very small with nearly all the absorption being interface absorption.

Determination of a_{af} and a_{fs}

Once α_f was determined, we measured the absorptance at $1/4\lambda$ as well as $1/2\lambda$ film thicknesses. This changed the relative power densities at the various interfaces and within the bulk of the film. By writing the absorptance equations for these two cases (unprimed for $\lambda/2$, primed for $\lambda/4$), with all measured quantities on the right, we see that a_{af} and a_{fs} can be determined by these two measurements:

$$a_{af}p_{af} + a_{fs}p_{fs} = A - \bar{p}_f\alpha_f\ell_f - \frac{T}{T_o} A_o$$

$$a_{af}p'_{af} + a_{fs}p'_{fs} = A' - \bar{p}'_f\alpha_f\ell'_f - \frac{T'}{T_o} A_o \quad .$$

Only the case for $n_f \neq n_s$ is considered. The relative power density plots for this case is shown in figure 6. While it is possible to determine interface properties with an exit surface film, the simple expressions above do not apply and will not be considered here.

Figure 7 shows the absorptance of an As_2Se_3 first surface film on CaF_2 measured at film thicknesses of $\lambda/4$ and $3\lambda/4$, as well as $\lambda/2$ and λ, as shown in figure 5. An analysis as above indicates that all of the interface absorption takes place at the film-substrate interface.

Discussion of Data

Figure 2 shows the absorptance of a NaF film on CaF_2 deposited in a LN_2-trapped oil-pumped system. This is a front surface wedged film and was analyzed only for bulk absorption coefficient. The presence of water in the film is evidenced by the higher absorption coefficient at 2.87 μm which is within the waterband than at 2.72 μm, just outside the waterband. Note that 1/2 μm of NaF on CaF_2 results in equal interface and film bulk absorption.

Figures 5 and 7 show the absorptance of an As_2Se_3 film deposited on CaF_2. In this case, we have determined the absorption coefficient of the film, α_f, and the specific absorptances a_{af} and a_{fs} at the two interfaces. It can be seen that the presence of water in the film is minimal, with essentially all the absorption taking place at the film-substrate interface. Such data are very helpful if one is attempting to reduce the absorption due to the presence of a film.

Concluding Remarks

We have presented a description of a method for determining the absorption coefficient of the bulk of a film and the specific absorptance at the two film interfaces. In addition, we have shown representative data for a film which exhibits substantial bulk absorption within the film and a film which exhibits almost exclusively interface absorption. While not discussed above, this method can be directly extended to investigate the absorption properties of film-film interfaces by depositing a wedged film on a previously deposited constant thickness film.

Finally, we would like to make the point that while much attention has been given to the electric field plots for multilayer coatings in damage resistance discussions, it is the relative power density which must be considered in discussing thermal absorption since the local absorptance is the product of the relative power density and the absorption coefficient at that point. The time-averaged electric field squared and the relative power density in a three-layer AR stack are shown in figure 8.

The requirement that the tangential component of the electric field be continuous across a boundary forces the relative power density to be discontinuous across the boundaries. Once the interfacial specific absorptances and the bulk absorption coefficients are determined, it is possible, from a plot such as in figure 8, to determine the heat deposited within an AR or HR stack.

References

[1] See, for example, Harrington, J. A., Rudisill, J. E., and Braunstein, M., "Thin-Film 2.8 μm and 3.8 μm Absorption in Single-Layer Film," Appl. Opt. 17, 2798 (1978).

[2] Burdick, D. L., "Optical Constants of As_2S_3 by a Wedged-Film Technique," in *Laser Induced Damage in Optical Materials: 1977*, ed. by A. J. Glass and A. H. Guenther. Washington, D.C., National Bureau of Standards, 1977. (NBS Spec. Publ. 509.) P. 352.

[3] Decker, D. L., and Temple, P. A., "The Design and Operation of a Precise, High Sensitivity Adiabatic Laser Calorimeter for Window and Mirror Material Evaluation," *op. cit.*, p. 281.

[4] Temple, P. A., and Decker, D. L., to be published in Rev. Sci. Instrum.

[5] Elson, J. M., and Bennett, J. M., "Relation Between the Angular Dependence of Scattering and the Statistical Properties of Optical Surfaces," J. Opt. Soc. Am. (in press).

[6] Baumeister, P. W., private communication.

[7] Temple, P. A., to be published.

Figures

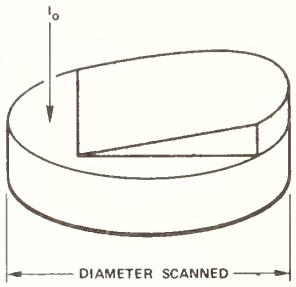

Figure 1. Calorimeter sample configuration showing a thin wedge of material which has been deposited on one face of the substrate. The bare region to the left is used to measure A_0 and the step in the foreground is used to determine the film thickness profile.

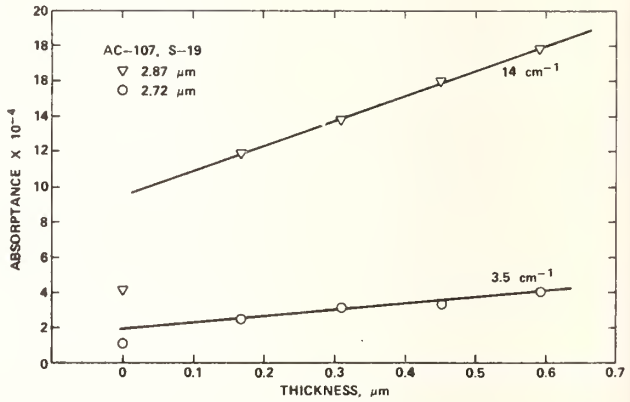

Figure 2. The absorptance of a NaF film on CaF_2 measured at various film thicknesses. The two data points at 0.0 μm thickness are bare substrate absorptances.

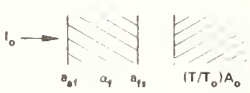

Figure 3. The four absorbing regions of a front surface film. Shown is the incident beam of intensity I_0, the air-film interface, the film bulk, the film-substrate interface, and the substrate whose absorption properties are characterized by a_{af}, α_f, a_{fs}, and $(T/T_0)A_0$, respectively. The film is shown separated from the substrate for clarity.

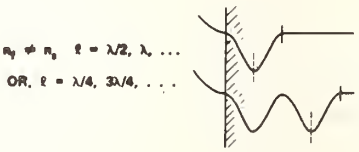

Figure 4. The relative power density pattern (standing wave pattern) for a first surface film used to determine α. The short bars indicate the film-substrate interface.

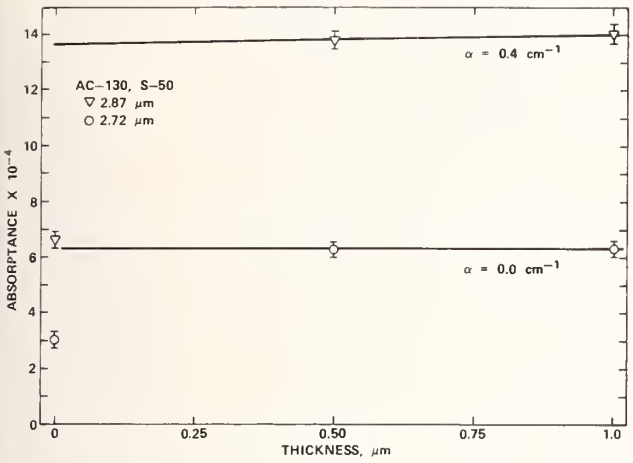

Figure 5. The absorptance of an As_2S_3 first surface film on CaF_2 measured at 2.72 and 2.87 μm wavelength and λ/2 and λ film thickness. The two data points at 0.0 μm thickness are bare substrate absorptances.

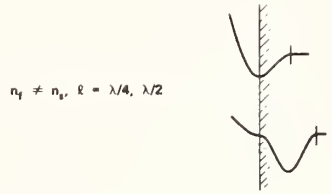

Figure 6. The relative power density pattern (standing wave pattern) for a first surface film used to determine a_{af} and a_{fs}. The short bars indicate the film-substrate interface.

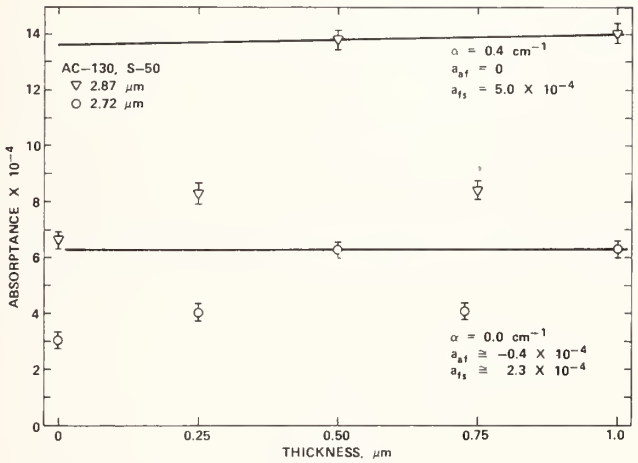

Figure 7. The absorptance of a first surface film of As_2Se_3 on CaF_2. This figure is identical to figure 5 except that the absorptances at λ/4 and 3λ/4 are also shown along with the calculated specific absorptances.

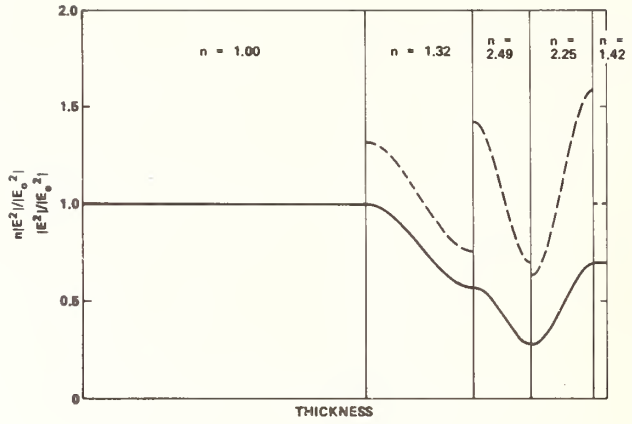

Figure 8. The $|E^2|$ values and relative power densities for a three-layer AR coating. The $|E^2|$ values are continuous at the boundaries by virtue of a boundary condition. This then requires that the relative power densities be discontinuous at all boundaries. The absorptance is the product of the relative power density and the absorption coefficient. The relative power density plot is shown by the dashed line.

Discussion

Two suggestions were made to obtain more information from this procedure: one was to take measurements through the substrate, with the wedged film at the rear of the sample, to obtain an additional measure of substrate surface absorption; and the other was to extend the film to "zero thickness," rather than to end the wedge in a step discontinuity, to confirm the extrapolation to zero depth.

PHOTOACOUSTIC SPECTROSCOPY STUDIES OF THIN FILM COATINGS ON LASER WINDOWS

Nils C. Fernelius and David A. Walsh
University of Dayton Research Institute
300 College Park Avenue
Dayton, Ohio 45469

Photoacoustic spectroscopy (PAS) studies have been made of TlI and graded PbF_2-TlI coatings on KCl. Wavelength dependent PAS studies on the TlI absorption edge indicate impurities in TlI in the graded coating and/or the existence of cubic TlI layers. PAS wavelength studies were made on a solid ZnSe window and various ZnSe coatings on CaF_2. Wavelength dependent studies show poorer stoichiometry as the coating gets thinner. Frequency dependent PAS studies at 440 nm on the solid and thin film ZnSe all showed a signal dependence of $S = Af^{-1}$. Theoretical calculations based on the Rosencwaig-Gersho theory show that these results are consistent if β is greater than 500 cm^{-1} for ZnSe at 440 nm.

Key words: Absorption edge; CaF_2; KCl; optical absorption coefficient; optoacoustic spectroscopy; PbF_2; photoacoustic spectroscopy; TlI; ZnSe.

1. Introduction

Photoacoustic spectroscopy (PAS) is a recently developed technique for studying solids [1-5].[1] A periodically interrupted light beam impinges on a sample and heats it through optical absorption and non-radiative decay. The periodically heated sample heats the gas in contact with its surface creating a sound wave. If the gas volume is enclosed with a sensitive microphone, the sound can be phase sensitively detected with a lock-in amplifier.

There are basically two types of experiments which can be performed. In the first, the wavelength is swept on a monochromator illuminated, for example, by a xenon lamp. The variation in power output with wavelength is normalized by dividing the spectrum of interest with that of carbon black. The second technique operates at a given wavelength and varies the chopping frequency. Elaborate theories have been developed to calculate the magnitude and phase of the PAS signal generated [6-9]. According to these theories in the optically transparent region, the amplitude of the PAS signal from regions near the surface has a chopping frequency dependence of Af^{-1}; from bulk regions $\beta f^{-3/2}$. At low chopping frequencies the bulk contribution should predominate while at higher frequencies the surface contribution is larger. This agrees with the physical intuition that slower chopping frequencies are needed to provide time for the bulk contribution to diffuse to the surface. There is also a saturation effect. When the β of the material is very high, light penetrating the sample is quickly attenuated so only surface absorption contributes to the signal. Thus depending upon the β and f values encountered, a f^{-1} dependence at low f may be seen tapering into a $f^{-3/2}$ at higher frequencies.

A description of the equipment used has been given elsewhere [10]. Here we shall present results from both types of experiments plus theoretical calculations for the special cases studied experimentally.

2. Experimental Results

2.1. TlI and Related Coatings on KCl

One of the earliest samples studied by spectroscopy PAS in our laboratory was UDRI Sample No. 1523 (Honeywell 806) which consisted of a 2.2 μm thick coating of TlI on KCl: 1.75% RbCl. A piece was cut to fit inside the PAS cavity and a wavelength sweep was made. The results were measured with an Ithaco Model 391 lock-in amplifier. The chopping frequency used was 740.4 Hz and the lock-in time constant was 4 s. The signal amplitudes were measured and divided by the amplitude at the same wavelengths of a

1. Figures in brackets indicate the literature references at the end of this paper.

carbon black soot sample. Note in figure 1 that there is a rather sharp absorption edge at around 435 nm and that the transparent region was reached by about 450 nm.

Recently we received some samples from Honeywell consisting of Harshaw single crystal KCℓ coated with an alternate step graded index TℓI-PbF_2 coating on approximately half of the face of each sample. These samples were developed by Honeywell under DARPA contract DAHC-15-73-C-0464. More information on these samples is given in [11] on pp. 54-65.

UDRI Sample No. 2722 (Honeywell No. 801262) had an AR minimum at 10.8 μm. PAS wavelength dependent studies were made between 300-800 nm, which showed some interesting features of the absorption edge. Data was taken with a PARC 5204 Lock-in Analyzer in the bandpass mode using an Ithaco 167 pre-amplifier. The input was A, Float, and x10. The d.c. prefilter had a 1.1 s time constant. The output was x100 with 1 s time constant. The lock-in phase on the coating was set at 400 nm and was 171.7°. The sweep was on high blaze at 50 nm/min. The chopping frequency was 319.6 Hz. The reference signal was obtained from 3M Nextel Velvet Black freshly sprayed on a 1/4 inch thick quartz disc. The lock-in phase was set at 500 nm and was 157.1°. Otherwise the experimental conditions were identical with that of the coating. The data was recorded on a Hewlett-Packard Model 7046A X-Y_1-Y_2 Recorder and digitized on a Tektronix 4954 digitizing tablet. The normalized plot was displayed on a Tektronix 4014-1 graphics terminal. It is shown in figure 2. Again an absorption edge occurred around 430 nm. The main difference from the previous results was the gradual falloff with wavelength to the transparent region which was not reached until about 540 nm. Often a gradual falloff is indicative of impurities in the material or a non-stoichiometric condition. Another possible effect, which may be shown in the curve, is that some TℓI layers may have been deposited in the cubic form. The absorption edge of the cubic form is shifted toward the red end of the spectrum.

ESCA depth profiles of similarly prepared samples ([11], pp. 64-5) indicates that there are alternate layers of PbF_2 and TℓI coating the KCℓ substrate. Sputtering with argon tends to pit a surface, thus the samples may have a more abrupt graduation than shown in the figures. Yet there still were regions where the TℓI had a considerable amount of impurity.

Chopping frequency dependent studies were also made on this sample at 440 nm wavelength. The data between 50 and 400 Hz fell on a straight line in a log-log plot of PAS signal versus chopping frequency. The data fit a signal dependence of $S = Af^{-n}$ where n = 0.85. The thermal diffusion length in PAS is defined as $L_{th} = \sqrt{\alpha/\pi f}$ where α is the thermal diffusivity and f is the chopping frequency. $\alpha = \kappa/\rho C$ where κ is the thermal conductivity, ρ the density, and C the heat capacity of the sample. For TℓI, $L_{th} = 0.039/\sqrt{f}$ cm, using numbers from Ohmer [12]. At 50 Hz it is 55 μm and at 1 kHz it is 12 μm. Thus a 2.5 μm film is a surface absorber at all frequencies studied. For β - PbF_2, $L_{th} = 0.0425/\sqrt{f}$ cm, using numbers from Fernelius, et al. [13]. At 440 nm PbF_2 is transparent so that the model is that of layers of absorbing material interspersed with a thermally similar but inactive material. These nonabsorbing regions contribute no heat generation but do have thermal resistance, thus they lower the frequency dependence slope.

An earlier study on a TℓI/KCℓ/TℓI sandwich on a KCℓ backing (UDRI 1745) gave a value of n = 0.97. The layer thicknesses were TℓI, 1.0 μm; KCℓ, 0.7 μm; and TℓI, 0.5 μm. For KCℓ, $L_{th} = 0.090/\sqrt{f}$ cm, a somewhat larger value than TℓI. This gave good agreement with a surface absorption regime where n = 1.0. Perhaps the optically inactive regions acted as thermal shorts giving essentially the same results as solid TℓI.

2.2. Study of Solid ZnSe and Thin Films on CaF_2

An uncoated ZnSe laser window (UDRI No. 1310) was mounted in PAS tip No. 1. The spectra from the polished surface were noisier than those from a powder, but were still obtainable. The lock-in phase was set at λ = 450 nm. Spectra were run from 300-800 nm. All spectra were digitized on a Tektronix 4954 graphics terminal. Spectra from carbon black soot deposited on an Al_2O_3 platelet were run at 111.6 Hz chopping frequency and digitized as the reference spectrum. The raw data spectrum was divided point-by-point to obtain a spectrum normalized for the variation in light intensity with wavelength of the xenon lamp. Figure 3 and figure 4 show normalized spectra for the solid ZnSe window (UDRI No. 1310) taken at chopping frequencies 316.9 Hz and 407 Hz. Note that there is a sharp absorption edge at 460 nm and that the transparent regime is reached by 490 nm.

UDRI Sample No. 1797 consisted of a 21,300 Å thick ZnSe film deposited on a CaF_2 substrate. A spectrum was run at 317 Hz chopping frequency. The normalized result is shown in figure 5. The absorption edge is at about 470 nm. The absorption curve then falls off more slowly than other solid samples, not reaching the transparent regime until about 590 nm.

UDRI Sample No. 1976 is a 2650 Å thick ZnSe film on CaF_2. Spectra were run at 318 Hz chopping frequency. The normalized result is shown in figure 6. Here the absorption edge is blurred considerably and the transparent regime is reached by about 560 nm. The explanation for these results may be that the deposited thin films did not have the correct stoichiometry or they may contain some argon gas in them.

The chopping frequency dependence studies in addition to studying various thicknesses of ZnSe also involved a comparison of different lock-in amplifiers and operating modes. A typical plot is shown in figure 7. The results of various combinations of experimental arrangements are given in table 1. Above 500 Hz coherent noise corrections were made following the prescription derived in the appendix. As can be seen from inspection of the table, the solid ZnSe and the thin films all have essentially the same chopping frequency dependence at 450 nm wavelength, viz., that of surface absorption.

Table 1. Chopping frequency studies.

Samples	Measurement Mode	n
Solid ZnSe (UDRI 1310)	P-B*	0.99
	P-F†	1.07
	P-B	1.09, 1.09
	P-F	1.12, 1.02
	I-3**	1.02
21,300 Å ZnSe on CaF_2 (UDRI 1797)	P-B	0.99
	P-F	0.99
2650 Å ZnSe on CaF_2 (UDRI 1796)	P-B	1.06
	P-F	1.03

Note: All results except the first two use Ithaco 167 Pre-Amplifier, the frequency range is 50Hz-1kHz, signal = A/f^n, and λ = 450 nm.

*P-B = PARC 5204 Lock-in Crystal-Het Bandpass mode.
†P-F = PARC 5204 Flat mode.
**I-3 = Ithaco 393 Dynatrac 3.

Rosencwaig and Gersho [6,7] give a very complicated complex expression for the magnitude and phase angle of the PAS signal. A complex number computer program was written to calculate this expression and examples corresponding to the ZnSe samples studied above were determined. Figure 8 shows a chopping frequency dependence plot for the 1 cm thick sample. It shows that for β = 1000, there is a f^{-1} dependence with a 90° phase angle similar to surface absorption. Since the ZnSe signal in this region was about 10^{-4}, that of carbon black soot, it was hard to believe that β was so large. This is probably an example of how much greater surface area soot has compared with a polished flat sample. As β decreased, the slope got steeper until n = 1.5 was reached with a 45° phase angle. Results of calculations on the film coatings, figures 9 and 10, all showed an n = 1 throughout the β range indicating surface abosrption. The results are summarized in table 2. Thus the apparent discrepancy between the solid window and thin film results is reconciled for a β greater than 500.

3. Conclusion

Wavelength variation photoacoustic studies around the absorption edge of coating materials can give information about the stoichiometry of the coating, its impurity content, and crystalline phase. Chopping frequency dependent studies in the heavily absorbing region seem to be consistent with the Rosencwaig-Gersho theory. Hopefully the theory will also be valid in the transparent region where the ratio of bulk to surface absorption will be attainable.

4. Acknowledgements

One of us (NCF) wishes to thank the Air Force Office of Scientific Research for financial support.

Table 2. Rosencwaig-Gersho Results for ZnSe.

Thickness Backing	β	Q @1 Hz	ϕ @1 Hz	$Q = Af^{-n}$ n	$Q \times 10^{-6}$ @10 kHz	ϕ @10 kHz
1 cm	1000	0.396	89.7	1.00-1.06	23.5	69.7
	100	0.376	86.8	1.06-1.36	4.41	49.5
air	10	0.235	69.7	1.22-1.49	0.476	45.5
	1	0.0441	49.5	1.467	0.0479	45.1
	0.1	0.00476	45.5		0.0048	45.0
21,300Å	1000	0.0948	89.9	1.00	8.57	84.7
	100	0.0104	89.9	1.00	0.940	84.6
CaF_2	10	0.00105	89.9	1.00	0.0949	84.6
	1	0.0001052	89.9	1.00	0.0095	84.6
2650Å	1000	0.0129	90.0	1.00	1.278	89.3
	100	0.00131	90.0	1.00	0.129	89.3
CaF_2	10	0.000131	90.0	1.00	0.0129	89.3
	1	0.0000131	90.0	1.00	0.0013	89.3

5. References

[1] Rosencwaig, A., Physics Today 28(9), 23 (September 1975).

[2] Rosencwaig, A., Anal. Chem. 17(6), 592A (May 1975).

[3] King, A. A. and Kirkbright, F. F., Laboratory Practice 25, 377 (1976).

[4] Rosencwaig, A., Rev. Sci. Instrum. 48, 1133 (1977).

[5] Rosencwaig, A. Chapter 8 in "Optoacoustic Spectroscopy and Detection", edited by Yoh Han Pao (Academic Press, N.Y., 1977), pp. 193-239.

[6] Rosencwaig, A. and Gersho, A., J. Appl. Optics 47(1), 64 (1976).

[7] Rosencwaig, A., J. Appl. Physics 49, 2905 (1978).

[8] Bennett, H. S. and Forman, R. A., Appl. Optics 14, 3031 (1975); 15, 347, 1313, 2405 (1976); 16, 2834 (1977).

[9] Bennett, H. S. and Forman, R. A., J. Appl. Phys. 48, 1432 (1977).

[10] Fernelius, N., Appl. Spectrosc. 32, Scheduled for Publication Nov.-Dec. 1978.

[11] Bernal G., E., Anderson, R. H., Leung, K. M., Moravec, T. J., Ready, J. F., Skogman, R. A., and Wertman D., Honeywell, Inc., "A Study of Polycrystalline Halides for High Power Laser Applications", HR-78-256:2-59, (March 1978).

[12] Ohmer, M., T&I Coatings for KCℓ for 9.27 μm, AFML-TR-77; 157.

[13] Fernelius, N. C., Fox, J. A., Walsh, D. A., and Coble, G. S., Proc. High Power Laser Window Conference, Denver, 1978.

6. Appendix

Correction Due to Coherent Noise for Lock-In Signals

The input voltages to a lock-in amplifier consist of a reference signal to define a phase angle zero and the signal of interest, which can be written as $V_{in} = A \exp(i\phi) + A_n \exp(i\phi_n)$; where A is the amplitude of the signal and ϕ is the phase angle with respect to the reference signal. A_n and ϕ_n are similar quantities for coherent noise. The lock-in provides an internal phase shift, ϕ_r, which can be applied to the incoming signal before undergoing phase sensitive detection. Some lock-in's provide an in-phase and quadrature output. The in-phase output is

$$I_o = A \cos(\phi - \phi_r) + A_n \cos(\phi_n - \phi_r);$$

and the quadrature output is

$$Q_o = A \sin(\phi - \phi_r) + A_n \sin(\phi_n - \phi_r).$$

When there is no coherent noise, $A_n = 0$, and one varies ϕ_r such that $\phi = \phi_r$. This gives the maximum in-phase output. This is most readily done by varying ϕ_r so that $Q_o = 0$, since it is easier to detect a precise zero crossing than to ascertain the maximum of a cosine function.

When coherent noise is present, one still sets $Q_o = 0$ and thus obtains a ϕ_{ro}, but then corrections have to be made to obtain A. We have $A \sin(\phi - \phi_{ro}) = -A_n \sin(\phi_n - \phi_{ro})$ and $I_o = A \cos(\phi - \phi_{ro}) + A_n \cos(\phi_n - \phi_{ro})$. Having done this, one can block off the light source, say with a shutter, i.e., $A = 0$, and measure $I = A_n \cos(\phi_n - \phi_{ro})$ and $Q = A_n \sin(\phi_n - \phi_{ro})$. From these equations we have $A \sin(\phi - \phi_{ro}) = -Q$ and $I_o = A \cos(\phi - \phi_{ro}) + I$. Squaring and adding, one obtains

$$A = \sqrt{Q^2 + (I_o - I)^2}.$$

Note that $\tan(\phi_n - \phi_{ro}) = Q/I$. Once can also calculate the phase change due to coherent noise. When $A_n = 0$, we have $\phi = \phi_r$.

$$\phi = \phi_{ro} = \phi_r + \delta$$

$$I_o = A \cos\delta + I$$

$$O = A \sin\delta + Q$$

$$\tan \delta = -Q/(I_o - I)$$

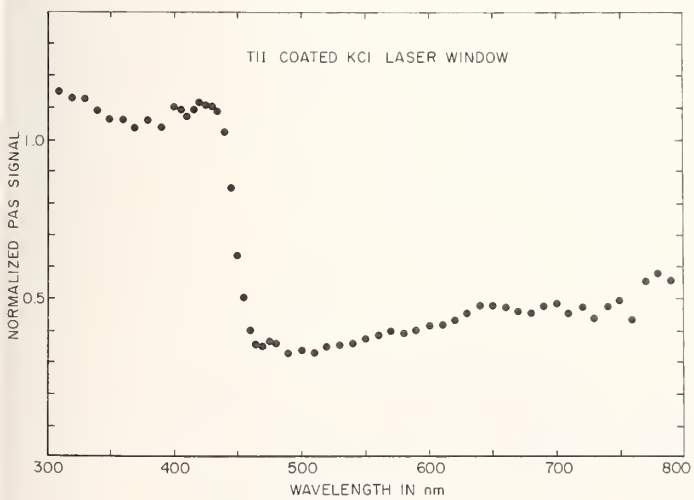

Figure 1. T&I coated KC& laser window.

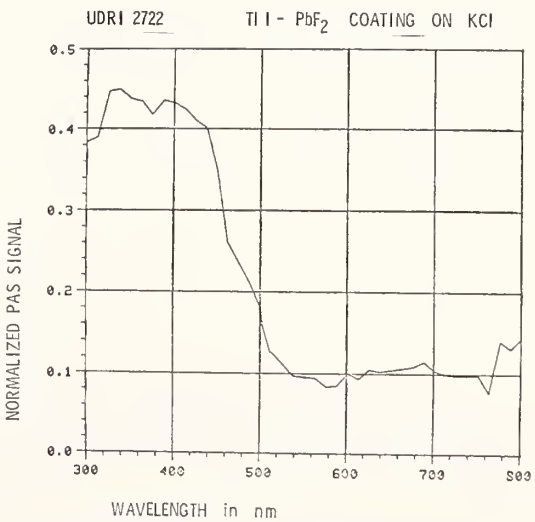

Figure 2. T&I-PbF_2 coating on KC&.

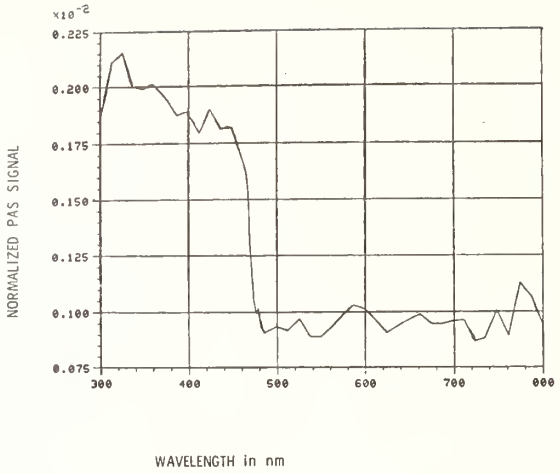

Figure 3. Photoacoustic signal vs. wavelength for solid ZnSe laser window (UDRI 1310) f = 407 Hz.

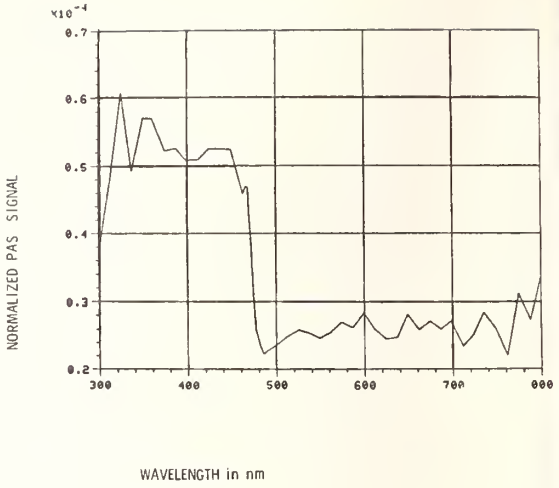

Figure 4. Photoacoustic signal vs. wavelength for solid ZnSe laser window (UDRI 1310) f = 316.9 Hz.

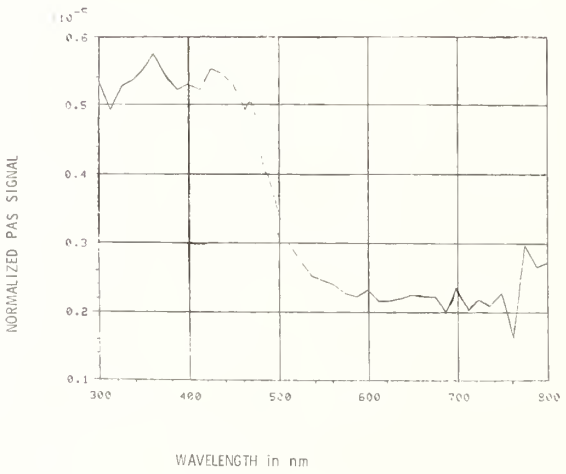

Figure 5. PAS signal from 21,00 Å thick ZnSe on CaF_2 substrate vs. wavelength (UDRI 1797) f = 317 Hz.

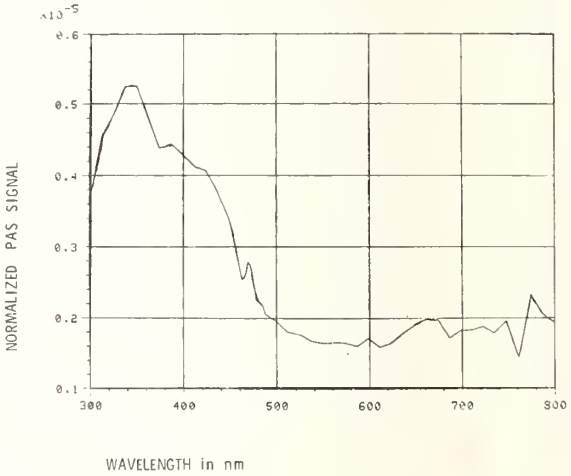

Figure 6. PAS signal from 2650 Å thick ZnSe on CaF_2 substrate vs. wavelength (UDRI 1796) f = 318 Hz.

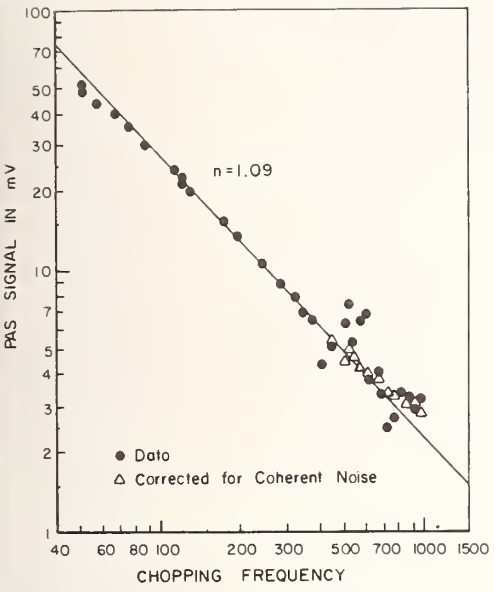

Figure 7. UDRI 1310 ZnSe window, Par 5204 lock-in, crystal-het. bandpass mode, Ithaco 167 pre-amp., output X 100, input X 10, τ = 1 sec.

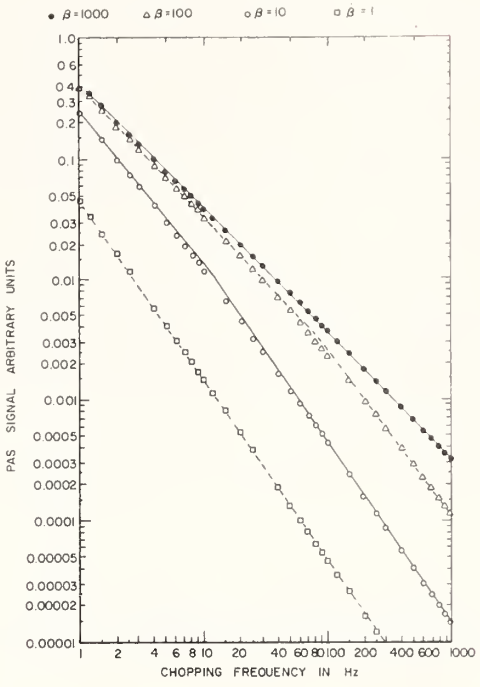

Figure 8. Rosencwaig-Gersho theory, 1 cm thick ZnSe air backing.

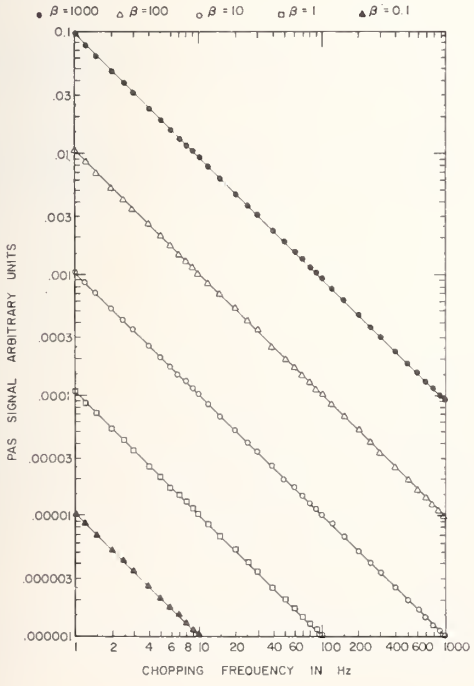

Figure 9. Rosencwaig-Gersho theory, 21,300 Å, ZnSe on CaF_2.

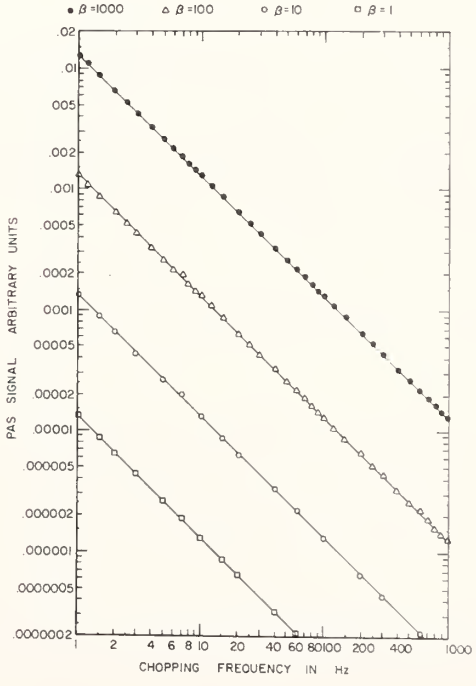

Figure 10. Rosencwaig-Gersho theory, 2650 Å, ZnSe on CaF_2.

PIEZO-OPTIC COEFFICIENTS OF SOME NEODYMIUM DOPED LASER GLASSES AND SINGLE CRYSTALS OF CaF_2, BaF_2 and SrF_2*

R. M. Waxler, A. Feldman and D. Horowitz
Ceramics, Glass and Solid State Science Division
Center for Materials Science
National Bureau of Standards
Washington, D. C. 20234

The piezo-birefringence coefficients of one neodymium doped phosphate laser glass and three neodymium doped fluorophosphate laser glasses have been measured at 0.6328 μm and 1.15 μm. All of the piezo-optic constants have been obtained for two of the glasses. The piezo-optic coefficients, q_{11}, q_{12} and q_{44}, of CaF_2, BaF_2, and SrF_2 have been measured at 0.6328 μm, 1.15 μm, and 3.39 μm. The coefficients were obtained by interferometric and polarimetric techniques.

Key words: BaF_2; CaF_2; laser glass; photoelasticity; piezo-birefringence; piezo-optic constants; SrF_2; stress-optical coefficient.

1. Introduction

Stress in an optical element will produce by way of the piezo-optic effect a change in refractive index that will distort the wavefront of an optical beam propagating through the element. In laser rods and discs stress can be produced by clamping or by thermal gradients produced by flashlamp pumping. In windows and lenses in high average-power laser systems, stress may result from thermal gradients induced by absorption of laser radiation in the element. As part of a continuing program at the National Bureau of Standards to characterize the optical properties of materials, we have measured piezo-birefringence coefficients of one neodymium-doped phosphate laser glass, designated Q-88, three neodymium-doped fluorophosphate glasses, designated LG-812, E-181, and LHG-10, and the alkaline earth fluoride crystalline materials, CaF_2, BaF_2, and SrF_2. In addition the absolute piezo-optic constants of the crystalline materials and glasses LH6-10 and Q-88 were also determined. The measurements on the glasses were performed at 0.6328 μm and 1.15 μm; the measurements on the alkaline earth fluorides were performed at 0.6328 μm, 1.15 μm, and 3.39 μm. The glass specimens were obtained from the Lawrence Livermore Laboratory and the alkaline-earth fluorides were obtained from a commercial source.

The piezo-optic constants have been treated in the literature [1][1], and, hence, will not be described in detail here. The glasses, which are isotropic materials, have two independent piezo-optic constants q_{11} and q_{12} [2], whereas the alkaline-earth fluorides, which belong to the cubic crystal class m3m, have three piezo-optic constants q_{11}, q_{12}, and q_{44} [3,4]. The values of q_{11} and q_{12} can be obtained from a measurement of the absolute change of refractive index with stress, and are found with interferometric techniques. Values of q_{44} and $(q_{11}-q_{12})$ can be found by measuring the stress-induced birefringence with polarimetric techniques. In glasses, it is common to define another coefficient, C, called the stress-optical coefficient.

$$C = -\frac{n_o^3}{2}(q_{11}-q_{12}), \qquad (1)$$

where n_o is the zero stress refractive index.

2. Experimental Methods

All specimens were prepared in the form of rectangular parallelopideds with approximate dimensions 35 x 13 x 13 mm. One specimen of each glass material was prepared; two specimens of each crystalline material were prepared, one specimen with the long dimension along the [001] crystallographic direction for obtaining q_{11}, q_{12} and $(q_{11}-q_{12})$, and the other specimen with the long dimension along the [111] crystallographic direction, for obtaining q_{44}. The crystals were oriented by X-ray techniques and cut to

*This work was supported in part by the Defense Advanced Research Projects Agency and by the Air Force Office of Scientific Research, Air Force Systems Command, USAF, under Grant No. AFOSR-ISSA-78-0026, by the Lawrence Livermore Laboratory of the Department of Energy, and by the National Bureau of Standards. The United State Government is authorized to reproduce and distribute reprints for governmental purposes not withstanding any copyright notation herein.

1. Figures in brackets indicate the literature references at the end of this paper.

within one degree of the appropriate orientation. Two opposite rectangular faces of each prism were polished sufficiently flat and parallel so that about six localized Fizeau-type interference fringes could be observed across the face when illuminated with collimated radiation from a He-Ne laser operating at 0.6328 μm. The method for mounting and stressing the specimens has been described earlier [5].

The absolute coefficients have been measured principally by the method of Fizeau interferometry. This method requires a knowledge of the elastic compliance component, s_{12}, in order to obtain q_{11} and q_{12}. Values for s_{12} can be obtained from the literature or from an independent measurement by the method of Twyman-Green interferometry. The use of Fizeau and Twyman-Green interferometry for obtaining q_{11}, q_{12} and s_{12} has been discussed in the literature [6-9], and hence, will not be described here.

The coefficients $(q_{11}-q_{12})$ and q_{44} can be determined directly by stress-birefringence measurements. Light passes through a polarizer oriented to transmit radiation polarized at 45° with respect to the vertical axis. This polarized radiation propagates through the specimen, oriented with the stress axis vertical, and is reflected back through the specimen and the polarizer. The output intensity will undergo a series of nulls as a function of applied stress and from these data one can calculate C, $(q_{11}-q_{12})$ or q_{44}. For the crystalline materials, $(q_{11}-q_{12})$ is obtained from specimens stressed along the [001] direction and q_{44} is obtained from specimens stressed along the [111] direction. A more detailed analysis of experimental techniques for measuring piezo-birefringence is discussed in the literature [9].

A problem arose in the measurements of q_{11} and q_{12} at 1.15 μm and 3.39 μm for the crystalline materials. The use of the [001] prism was inadequate because of the small shift of interference fringes with applied stress; instead the [111] prism was used. Measurements were made of the change of refractive index for light polarized both parallel and perpendicular to the stress axis. q_{11} and q_{12} were then evaluated by solving simultaneously, the two equations:

$$\Delta n_1 = n_o^3 (q_{11} + 2q_{12} + 2q_{44}) \frac{P}{6}, \qquad (2)$$

$$\Delta n_2 = n_o^3 (q_{11} + 2q_{12} - q_{44}) \frac{P}{6}, \qquad (3)$$

where Δn_1 and Δn_2 are respectively the refractive index changes for light polarized vertically and horizontally and P is the applied stress.

3. Results and Discussion

In order to calculate the q_{ij}, it is necessary to know n_o. Values of n_o for the glasses and crystals are presented in Table 1 together with the literature reference sources.

The results of the study of the neodymium doped glasses are presented in Table 2. It can be seen that the phosphate glass, Q-88, has a value of C much larger than that of the three fluorophosphate glasses. There is relatively little dispersion for the coefficients, but the values of C are consistently higher at the shorter wavelength.

To evaluate the constants, q_{11} and q_{12}, it is necessary to know the elastic compliance, s_{12}, in order to account for the change in thickness of the specimen when it is compressed. Of the four glasses, we have measured s_{12} only for Q-88 and LHG-10 at present, and the q_{ij} are reported here for these two glasses. There is little dispersion shown. From these values, it is possible to calculate the change of refractive index with applied hydrostatic pressure according to the equation,

$$\frac{\Delta n}{\Delta P} = \frac{n_o^3}{2} (q_{11} + 2q_{12}), \qquad (4)$$

and the change of refractive index with density, $\rho\frac{dn}{d\rho}$, may then be found by multiplying $\frac{\Delta n}{\Delta P}$ by the bulk modulus. Because of uncertainty in the value for the bulk modulus, it is not possible to calculate $\rho\, dn/d\rho$ although its sign can be determined. In a poster session at the Symposium*, we indicated that LHG-10 glass had a negative value for $\rho dn/d\rho$. This result was based on erroneous values for the elastic constants, and, hence, is incorrect. Based on the value of s_{12} we have obtained from Fizeau and Twyman-Green interferometer measurements the values of q_{11} and q_{12} have been changed and we find $\rho dn/d\rho$ to be positive.

*The Tenth Symposium on Materials for High Power Lasers (The Damage Symposium), National Bureau of Standards, Boulder, Colorado, September 12-14, 1978.

The data on the alkaline-earth fluorides are shown in Table 3. It can be seen that the errors are greatest at 3.39 μm. Within the experimental error, it appears that there is no significant wavelength dependence in the coefficients.

All errors were calculated from the standard deviations of our data and the errors in the elastic constants obtained from the literature which were on the order of one percent [10,11]. However, there is a question about the accuracy of some of the elastic constant data. For example, in preliminary measurements on SrF_2, it was found that the coefficients q_{11} and q_{12} obtained on the <001> specimen differed from the values obtained on the <111> specimen. The discrepancy was resolved by making Twyman-Green interferometer [6,8,9] measurements in addition to the Fizeau interferometer measurements. Both sets of measurements permitted us to calculate elastic compliance components, and these values differed from the values given in the literature. This suggests that additional Twyman-Green measurements on the CaF_2 and BaF_2 crystals should also be made.

In Table 4, our results at 0.6328 μm are compared with other determinations of q_{ij} for the alkaline-earth fluorides in the visible region. There is good agreement between the sets of data in some cases, but in several instances the disagreement is outside the experimental error. A possible cause for the discrepancies is that different investigators used different values of the elastic constants. In addition values of the elasto-optic constants p_{ij} are frequently given in the literature, as was the case of SrF_2. In order to compare our values with the values in the literature, it was necessary to make the transformation

$$q_{ij} = \sum_k p_{ik} s_{kj} \qquad (5)$$

where k = 1 through 6. Any errors in the elastic constants would result in data disagreement.

4. Summary

The piezo-birefringence coefficients, $(q_{11}-q_{12})$ and C, of one neodymium doped phosphate laser glass and three neodymium doped fluorophosphate laser glasses have been measured at 0.6328 μm and 1.15 μm. The absolute piezo-optic constants q_{11} and q_{12} have also been obtained for two of the fluorophosphate glasses. The piezo-optic constants q_{11}, q_{12} and q_{44} of CaF_2, BaF_2 and SrF_2 have been measured at 0.6328 μm, 1.15 μm and 3.39 μm. The coefficients were obtained by interferometric and polarimetric techniques. The results of the study bring out the importance of having reliable data on the elastic constants in order to calculate the photoelastic constants from the optical measurements. It appears that it is not advisable to accept data on the elastic constants that are reported in the literature. The data on the photoelastic constants are presented in this report only tentatively, and it is planned for future work to make additional interferometric measurements that will permit the evaluation of both elastic and photoelastic constants.

5. References

[1] Nye, J. F., Physical Properties of Crystals (Oxford University Press, London, 1957), pp. 243-254.

[2] Vedam, K., Proc. Ind. Acad. Sci., [A] 31, 450 (1950).

[3] Rao, K. V., Narasimhamurty, T. S., J. Phys. Chem. Solids, 31, 876 (1970).

[4] Dickinson, S. K., Infrared Laser Window Materials Property Data for ZnSe, KCl, NaCl, CaF_2, SrF_2, BaF_2, (ARCRL-TR-75-0318) Physical Sciences Research Papers, No. 635, Solid State Sciences Laboratory, Projects 5620, 3326, Air Force Cambridge Research Laboratories, L. G. Hanscom Field, Bedford, Massachusetts 01730, June 6, 1975), pp. 147-194.

[5] Feldman, A., McKean, W. J., Rev. Sci. Instrum., 46, 1588 (1975).

[6] Feldman, A., Waxler, R. M., Horowitz, D., Optical Properties of Highly Transparent Solids, Ed. by S. S. Mitra and B. Bendow (Plenum Publishing Corp., New York, 1975), pp. 517-525.

[7] Waxler, R. M., Farabaugh, E. N., J. Res. NBS, 74A, 215 (1970).

[8] Feldman, A., Electro-optical Systems Design, 8, 36 (1976).

[9] Feldman, A., Optical Eng. 17, 453 (1978).

[10] Wong, C., Schuele, D. E., J. Phys. Chem. Solids, 29, 1309 (1968).

[11] Gerlich, D., Phys. Rev., 136A, 1366 (1964).

Table 1. Refractive index data used in computing the piezo-optic coefficients.

Material	Refractive Index, n_o .6328 μm	1.15 μm	3.39 μm
Glasses			
LG-812	1.4297[a]	1.425[a]	
E-181	1.4418[a]	1.437[a]	
Q-88	1.5432[a]	1.536[a]	
LHG-10	1.4581[a]	1.453[a]	
Crystals			
CaF_2	1.433[b]	1.427[b]	1.416[b]
SrF_2	1.436[c]	1.432[c]	1.423[c]
BaF_2	1.473[d]	1.468[d]	1.459[d]

[a] Dr. Stanley Stokowski, Lawrence Livermore Laboratory, Livermore, California, Personal Communication.

[b] I. H. Malitson, Appl. Opt. 2, 1103 (1963).

[c] M. J. Dodge, National Bureau of Standards, Data to be published.

[d] I. H. Malitson, J. Opt. Soc. Am., 54, 628 (1964).

Table 2. Piezo-optic coefficients and s_{12} of neodymium doped laser glasses ($10^{-12}Pa^{-1}$)

	λ = 0.6328 μm	λ = 1.15 μm
LG-812		
C	0.92 ±0.03	0.89 ±0.02
$(q_{11}-q_{12})$		
E-181		
C	0.75 ±0.04	0.71 ±0.01
$(q_{11}-q_{12})$		
Q-88		
C	2.17 ±0.04	2.06 ±0.02
$(q_{11}-q_{12})$	-1.18 ±0.03	-1.14 ±0.02
q_{11}	0.74 ±0.08	0.72 ±0.07
q_{12}	1.92 ±0.08	1.86 ±0.07
s_{12} = -4.27 ±0.08		
LHG-10		
C	0.63 ±0.03	0.60 ±0.02
$(q_{11}-q_{12})$	-0.41 ±0.02	-0.39 ±0.02
q_{11}	0.71 ±0.09	0.74 ±0.08
q_{12}	1.12 ±0.09	0.13 ±0.08
s_{12} = -4.14 ±0.08		

Table 3. Piezo-optic coefficients of alkaline-earth fluorides (10^{-12} Pa^{-1})

	λ = 0.6378 μm	λ = 1.15 μm	λ = 3.39 μm
CaF_2			
q_{11}	-0.38 ±0.03	-0.40 ±0.06	-0.52 ±0.11
q_{12}	1.08 ±0.03	1.09 ±0.06	1.00 ±0.11
$(q_{11}-q_{12})$	-1.46 ±0.01	-1.49 ±0.02	-1.51 ±0.03
q_{44}	0.71 ±0.01	0.72 ±0.01	0.87 ±0.06
SrF_2			
q_{11}	-0.64 ±0.04	-0.63 ±0.05	-0.83 ±0.09
q_{12}	1.45 ±0.04	1.50 ±0.06	1.23 ±0.07
$(q_{11}-q_{12})$	-2.08 ±0.01	-2.13 ±0.04	-2.05 ±0.06
q_{44}	0.60 ±0.01	0.62 ±0.02	0.72 ±0.04
BaF_2			
q_{11}	-0.99 ±0.03	-0.91 ±0.07	-0.75 ±0.07
q_{12}	2.07 ±0.04	2.13 ±0.07	2.11 ±0.05
$(q_{11}-q_{12})$	-3.06 ±0.01	-3.03 ±0.02	-2.91 ±0.08
q_{44}	0.95 ±0.01	0.95 ±0.01	0.99 ±0.07

Table 4. Comparison of data in the visible region on piezo-optic coefficients of alkaline-earth fluorides ($10^{-12}Pa^{-1}$)

	NBS	Literature				
CaF_2						
q_{11}	-0.38	-0.29[a]	-0.41[b]			
q_{12}	1.08	1.16[a]	1.04[b]			
$(q_{11}-q_{12})$	-1.46	-1.45[a]	-1.45[b]	-1.48[d]	-1.44[e]	-1.47[f]
q_{44}	0.71	0.70[a]	0.89[b]	0.81[d]		
SrF_2						
q_{11}	-0.64	-0.58[c]				
q_{12}	1.45	1.77[c]				
$(q_{11}-q_{12})$	-2.08	-2.35[c]				
q_{44}	0.60	0.59[c]				
BaF_2						
q_{11}	-0.99	-0.62[b]				
q_{12}	2.07	2.31[b]				
$(q_{11}-q_{12})$	-3.06	-2.93[b]				
q_{44}	0.95	1.06[b]				

[a] F. Pockels, Lehrbuch der Kristallobtik (B.G. Teubner, Leipzig und Berlin, 1906). (λ= 0.5893 μm)

[b] K. V. Rao, T. S. Narasimhamurty, J. Phys. Chem. Solids 31, 876 (1970). (λ= 0.5893 μm)

[c] O. V. Shakin, M. F. Bryzhina, V. V. Lemanov, Sov. Phys. Solid State 13, 3141 (1972). (λ= 0.6328 μm)

[d] K. S. Iyengar, K. G. Bansigar, Current Science 27, 436 (1958). (λ= 0.5890 μm)

[e] A. J. Michael, J. Opt. Soc. Am. 58, 889 (1968). (λ= 0.5461 μm)

[f] V. G. Krishna Murty, Ph.D. Thesis (Osmania University, Hyderabad, India, 1964). (λ = 0.5461 μm)

REFRACTIVE INDEX OF STRONTIUM FLUORIDE*

Marilyn J. Dodge
Ceramics, Glass, and Solid State Science Division
National Bureau of Standards
Washington, D. C. 20234

The refractive index, relative to air, of fusion-cast strontium fluoride was determined from 0.2138μm to 11.475μm by means of the minimum-deviation method. Measurements were made on a precision spectrometer at a controlled room temperature near 20 °C. The experimental data were fitted to a Sellmeier-type dispersion equation which permits refractive index interpolation within several parts in 10^{-5}. The index of SrF_2 is compared graphically with that of BaF_2 and CaF_2.

Key words: Alkaline earth fluorides; refractive index; strontium fluoride.

1. Introduction

The efficiency of a high-power laser system is dependent on the optical and mechanical stability of the optical components within the system. Optical distortion caused by absorptive heating can render a component ineffectual at power levels below what would be required to cause fracture of the component. Predictions of the optical distortion in laser system components depends on the knowledge of the refractive index, temperature coefficient of index, thermal expansion coefficient, and stress-optical constants of the material under consideration. An optical materials characterization program [1][1] is currently in progress at the National Bureau of Standards (NBS) to determine these pertinent properties.

The alkaline earth fluorides, BaF_2, CaF_2, and SrF_2 are excellent candidates for component materials in the 2 to 6μm range because of their low index of refraction and dn/dT values as well as their good mechanical stability. Both the index and dn/dT of CaF_2 and BaF_2 have been well characterized. The dn/dT of SrF_2 has been determined [2,3], but reliable refractive index data over a wide wavelength range is not readily available.

Dr. James Stanford of the Naval Weapons Center provided an optically finished prismatic sample of SrF_2 for index measurements. The material was made by the technique of fusion casting by the Raytheon Corp.[2] The prism had two polished faces 3.0 cm × 1.5 cm, and a refracting angle of approximately 65°.

2. Experimental Technique

The refractive index was determined relative to air by means of the minimum-deviation method on a precision spectrometer shown schematically in figure 1 [4]. Known emission wavelengths of mercury, cadmium, helium, and zinc were used as sources for the measurements from 0.21 to 2μm. Beyond 2μm, a glo-bar was used for the radiant-energy source, and index determinations were made at known absorption bands of water, carbon dioxide, polystyrene, 1,2-4 trichlorobenzene and methylcyclohexane. A series of narrow band interference filters was also used between 3.5 and 10.6μm. A photomultiplier tube was used as the detector from the ultraviolet to 0.55μm in the visible. A thermocouple with a CsI window was used for detection from 0.4 to 11.5μm. Several wavelengths in the visible were measured with both detectors in order to check the consistency in the system alignment. The scale of this spectrometer is considered accurate to within 1.0 second of arc. The refractive index of good optical quality material can be determined to within several parts in 10^{-5} over a wide wavelength range.

The refractive index of fusion cast SrF_2 was measured from 0.2138 to 11.475μm at a controlled room temperature of 20 °C. Fifty-three experimental data points were fitted to a three-term Sellmeier-type dispersion equation [5] of the form

$$n^2-1 = \sum_j [A_j \lambda^2 (\lambda^2-\lambda_j^2)^{-1}],$$

where n is the refractive index, λ is the wavelength of interest, the λ_j's are the calculated wavelength of maximum absorption and the A_j's are the calculated oscillator strengths corresponding to the absorption wavelengths. The λ_j's and A_j's do not necessarily have any physical significance, but are chosen primarily to procure a mathematical fit of the measured data useful for interpolation.

---

* This work was supported in part by the Defense Advanced Research Projects Agency.

1. Figures in brackets indicate the literature references at the end of this paper.
2. The use of company and brand names in this paper are for identification purposes only and in no case does it imply recommendation or endorsement by the National Bureau of Standards and it does not imply that the material used in this study is necessarily the best available.

3. Index Data

The constants calculated for the dispersion equation are given in table 1.

Table 1. Constants for three-term Sellmeier dispersion equation to calculate refractive index of SrF_2 at 20 °C.

$A_1 = 0.67805894$	$\lambda_1 = 0.05628989$
$A_2 = 0.37140533$	$\lambda_2 = 0.10801027$
$A_3 = 3.3485284$	$\lambda_3 = 39.906666$

These parameters refer specifically to one particular sample of fusion-case SrF_2 at 20 °C. Since the variation in index from one sample to another is unknown, care should be taken when applying these constants to another specimen of SrF_2. This is especially true, if the wavelengths of interest are close to the regions of strong infrared or ultraviolet absorption where the discrepancies in index from sample to sample would be the greatest due to impurity absorption band differences. In any case, interpolations using the parameters in table 1 should be limited to the range of experimental data or approximately 0.21 to 11.5μm. The average absolute residual (the average absolute difference between the experimental values and the calculated values) was 2.1×10^{-5}. This average residual is an indication of the overall accuracy of the experimental data.

The parameters in table 1 were used to calculate the refractive index at regular wavelength interval Figure 2 shows a curve of the index of SrF_2 plotted as a function of wavelength. For comparison purposes index curves of BaF_2 [6], CaF_2 [7], and SrF_2 are shown in figure 3. At 4μm the refractive index of SrF_2 is higher than the refractive index of CaF_2 by about 1×10^{-2} and lower than BaF_2 by approximately 4×10

4. Conclusions

The refractive index of fusion cast SrF_2 was measured over the wavelength range 0.21 to 11.5μm and the data was fitted to a Sellmeier dispersion equation. Although the parameters for the Sellmeier equation apply specifically to one specimen they can be used as a guide for calculating the index at any desired wavelength between 0.21μm and 11.5μm of another sample of SrF_2. The refractive properties of strontium fluoride are similar to those of CaF_2, with the index differing at most by 1×10^{-2} from the ultraviolet to about 5μm in the infrared. Because of its superior intrinsic hardness and low absorption [8], SrF_2 is a very good candidate for high-power laser system components.

5. References

[1] Feldman, A., Malitson, I., Horowitz, D., Waxler, R. M., and Dodge, M., Laser Induced Damage in Optical Materials, 1974, NBS Special Pub. 414, 141, (1974).

[2] Feldman, A., Horowitz, D., and Waxler, R.M., Laser Induced Damage in Optical Materials: 1977, NBS Special Pub. 509, 74, (1977).

[3] Lipson, H. G., Isay, Y. F., Bendow, B., and Ligor, P. A., Appl. Optics, 15, 2352 (1976).

[4] Rodney, W. S., and Spindler, R. J., J. Res. Nat'l. Bur. Stds. (US), 51, 123, (1953).

[5] Sulton, L. E. and Stavroudis, O. N., J. Opt. Soc. Am. 51, 901 (1961).

[6] Malitson, I. H., J. O. S. A., 54, 628 (1964).

[7] Dodge, M. J., Laser Induced Damage in Optics Materials: 1976, NBS Special Pub. 462, 64, (1976).

[8] Newberg, R. T., Readey, D. W., Newborn, H. A. and Miles, P. A., Proceedings Fourth Annual Conf. on Infrared Laser Window Materials, p. 445, ARML (Jan. 1975).

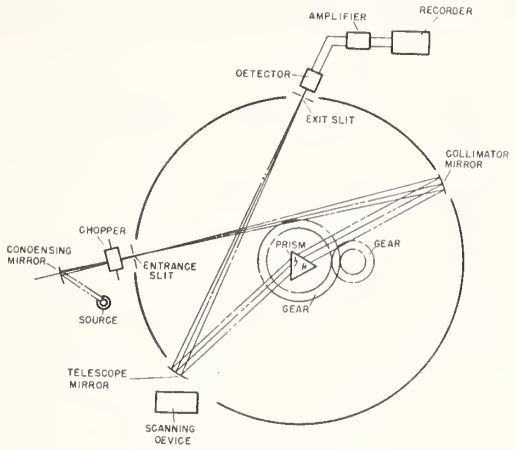

Figure 1. Schematic diagram of the modified Gaertner precision spectrometer showing the optical path. The prism is rotated at one half the rotation rate of the telescope assembly by gear system, thus maintaining the condition of minimum-deviation for any wavelength. The scanning device drives the assembly which scans the spectrum to identify lines or bands and determine their approximate scale positions.

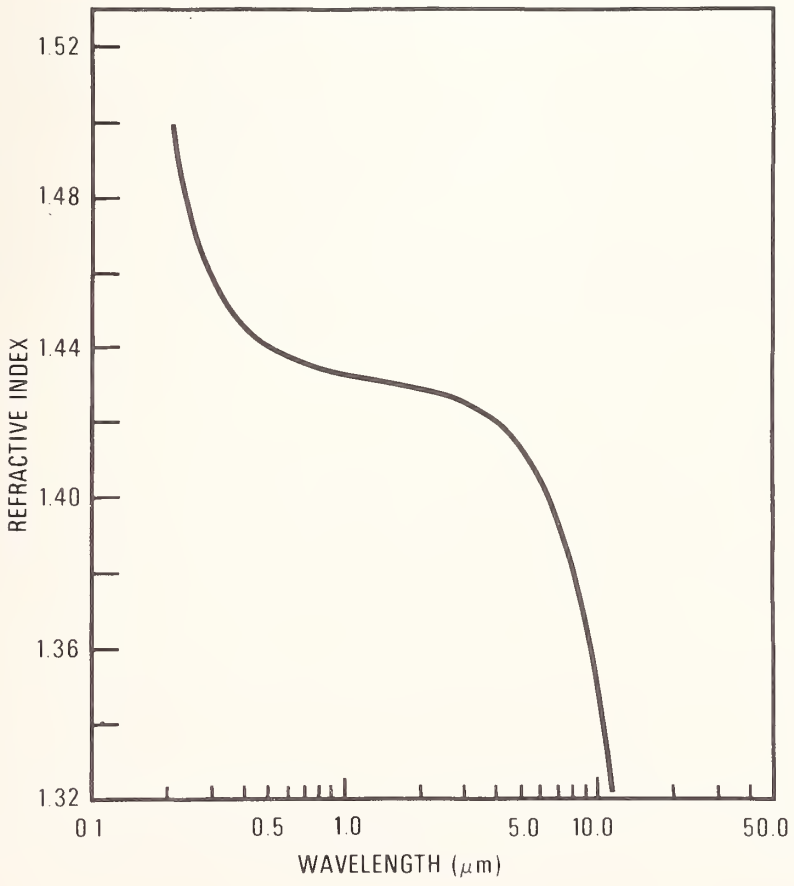

Figure 2. Refractive index of fusion-cast SrF_2 as a function of wavelength (logarithmic scale). Data at 20°C were calculated from the dispersion equation of the form $N^2 - 1 = \Sigma A_j \lambda^2 (\lambda^2 - \lambda_j^2)^{-1}$.

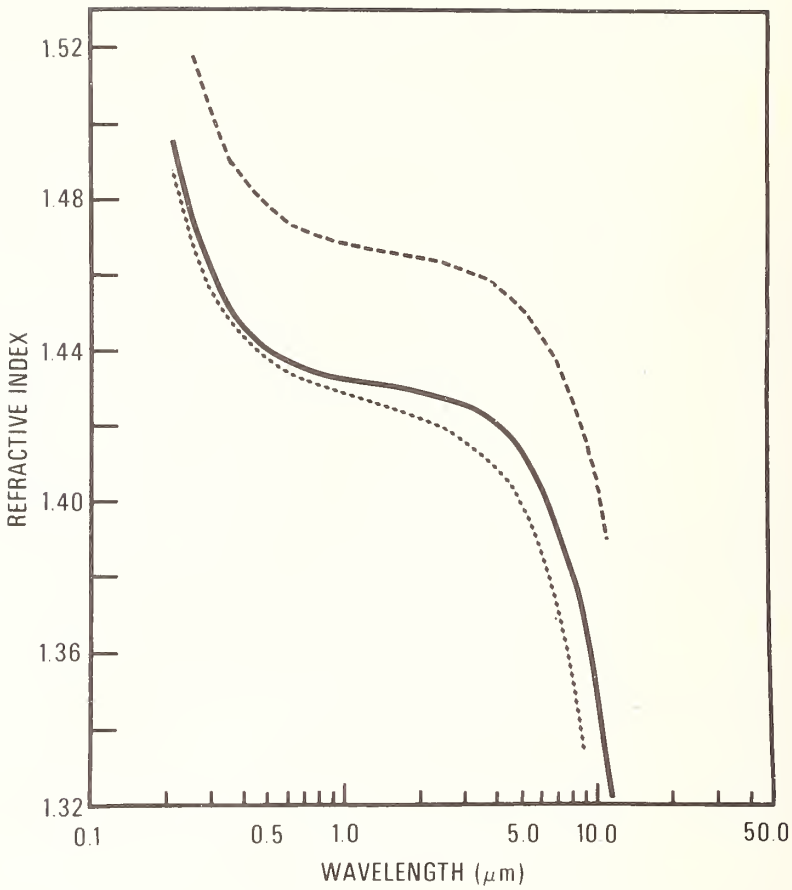

Figure 3. Refractive index of BaF_2, SrF_2 and CaF_2 as a function of wavelength (logarithmic scale).
BaF_2; SrF_2; CaF_2.

THE DEVELOPMENT OF FLUORIDES FOR HIGH POWER LASER OPTICS*

J. F. Ready, H. Vora, R. A. Skogman, K. M. Leung and E. Bernal G.
Honeywell Corporate Material Sciences Center
Bloomington, Minnesota 55420

The development of improved optical materials with low nonlinear refractive index and good vacuum ultraviolet transparency is needed for future laser systems to heat fusion targets. This program has produced lithium fluoride windows through isostatic forging of single crystalline material. For reductions around 60%, forging yields fine-grained material with considerably increased yield strength and fracture energy. The ultraviolet transparency of the material is not degraded by the forging.

This paper will describe the improvement of yield strength and fracture energy as a function of forging parameters. It will discuss measurements of optical homogeneity, optical scattering and visible and ultraviolet transmission for both the original material and the forged material.

Key Words: Fluroides, forging, laser windows, lithium fluoride, mechanical properties, optical properties, ultraviolet transmission

Introduction

The development of improved optical materials with low nonlinear refractive index n_2, and good ultraviolet transparency would simplify the design of future laser systems to generate short intense pulses at short wavelengths to heat targets for laser fusion. The program described in this paper is intended to develop materials having both low nonlinear refractive index and good ultraviolet transparency. In addition, the materials will have good mechanical stability, resistance to environmental degradation and optical uniformity.

The employment of lithium fluoride as a laser window material provides a material with excellent optical transparency, broad spectral transmission, low refractive index so as to have high damage threshold, and very low nonlinear refractive index. For the shorter wavelength lasers being developed, ultraviolet transparency is an essential requirement. Lithium fluoride has excellent ultraviolet transmission; in fact, it is the material with the largest energy band gap known. Fluorides in general and in particular lithium fluoride, have very low nonlinear index of refraction, less than 0.5×10^{-13} esu [1][1]. This means that optical components of lithium fluoride will have relatively low self-focusing and beam breakup and therefore relatively high resistance to the damage associated with self-focusing. In addition, among the halide materials, lithium fluoride is relatively resistant to degradation by environmental water vapor. The combination of these properties makes lithium fluoride an excellent candidate material for use as an optical material in high power, short pulse, short wavelength lasers.

Single crystal LiF, particularly single crystal LiF of the high purity compatible with good ultraviolet transmission, has relatively low mechanical strength. Therefore it is not readily compatible with use as a structural element in laser systems. In our previous work on development of alkali halides for use in high energy laser applications [2], [3], we have demonstrated the value of hot forging for improving the mechanical properties of materials such as KCl, NaCl, KBr and CaF_2. The hot forging process produces fine-grained material with considerably increased fracture energy and yield strength. At the same time, all the good optical properties that these materials possess inherently are maintained.

In the program described in this paper we have been developing LiF for use specifically in high intensity pulsed laser systems. We have placed emphasis on strengthening the LiF with high transparency by forging, so as to achieve a fine-grained polycrystalline material with much improved mechanical properties as compared to the single crystalline starting material. The optical homogeneity and the transparency in the ultraviolet are preserved in the forging process.

The forging process begins with billets of single crystalline material which have been obtained from three sources: Harshaw, Optovac, and the University of Utah. The material obtained from all these sources is of high purity, quoted to be in the parts per million regime for both monovalent and divalent cations. Measurements of ionic conductivity, according to the method described by Stoebe and Pratt [4], indicate that the concentration of divalent cations (largely magnesium) is less than

*This work is supported by the U. S. Department of Energy under Contract No. ED-78-C-08-1555.
1. Figures in brackets indicate the literature references at the end of this paper.

one part per million for both the Harshaw single crystal material and the University of Utah material and is approximately 9 parts per million for the Optovac material. Attempts to measure the impurity concentration of the single crystalline starting material by atomic absorption spectroscopy have been unsuccessful because the impurity concentrations lie below the threshold for detection of cations in the presence of the lithium ion background.

The starting materials have also been tested for optical homogeneity and ultraviolet transmission. These measurements and their comparisons with the results for the similar properties in the forged material will be described in the discussion of optical properties.

Forging

The isostatic forging process for LiF is identical to that described previously for CaF_2[5]. The important feature of the process is the use of isostatic constraint by high pressure (2000 psi) helium gas. This constraint prevents billet fracture and permits lower forging temperatures.

Figure 1 is a schematic representation of the forging chamber. The LiF billet rests between graphite platens on top of the stationary lower ram. The upper ram transmits the forging pressure applied by a hand-operated hydraulic press surrounding the forging chamber. Water cooled O-rings seal the rams against high pressure helium from a compressed gas cylinder. A valve near the inlet vents pressure build-up during the chamber heating. Deformation rates and percentages are monitored with a dial indicator mounted on the press. Forging temperature is monitored by thermocouples located directly in the forging chamber.

All crystals to date have been forged along the LiF <100> axis at a strain rate of 5×10^{-3}/min under 2000 psi isostatic helium constraint. The forging temperature has been varied from 300 to 600°C. Deformation reductions from 15 to 86% have been achieved. All forgings were cooled at approximately 50°C/hr.

Twenty-five single crystal LiF samples have been forged to date. Three of the forgings contained one or two small cracks which occured sometime after the forging operation. All of the other forgings were crack-free.

Grain sizes range from approximitely 10μm for samples forged at 400°C and 74% reduction to approximately 40μm for samples forged at 500°C and 62% reduction. Figure 2 shows photomicrographs of the forged material, indicating grain sizes under these two sets of firging parameters. Large increases in yield strength and fracture toughness were observed in all forged specimens when compared to the single crystal starting material.

The forged samples exhibit good stability against grain growth and recrystallization, even under conditions of high ambient relative humidity.

Optical Properties

Optical absorption measurements in the region 200-650 nm were made on single crystal and polycrystalline specimens using a Cary-14 spectrophotometer. The UV and visible transparency of LiF were not adversely affected by the forging operation, as shown in figure 3. In this figure, curve (d) represents the spectrum of Harshaw LiF single crystal and curve (a) represents that of a forging made using Harshaw material. Also shown in the figure are the spectrum of an Optovac LiF single crystal, curve (c), and that of a forging made using University of Utah LiF starting material, curve (b). Absorption bands in the region 200-400 nm seen in figure 3 (b) are believed to have been present in this starting material. Although the absorption in all LiF samples increases with decreasing wavelength in the ultraviolet, the rate of increase is much greater in Optovac and University of Utah LiF than in Harshaw LiF. Note that the losses due to reflection were taken into account in computing the absorption coefficient (β) values shown in figure 3 for various LiF samples. Because of the high visible transparency of the LiF samples, it was not possible to obtain quantitative information on their relative transparency in the 400-650 nm region with the spectrophotometric technique used in our study.

We also carried out measurements of the scattering produced by forged samples and the single crystalline starting material in a helium-neon laser beam at 0.6328μm. The samples are immersed in index matching fluid (Cargille Laboratories) in order to minimize contributions from surface scattering. The scattering from the fluid cell, which has single crystalline LiF windows, is measured with no sample in the cell. This background level is subtracted from the scattering observed with a sample in the cell. This result gives the volume scattering produced by the presence of the sample. The scattered helium-neon laser radiation is detected by a photomultiplier tube which is rotated along a circular track with its center at the position of the sample. The smallest angle at which measurements could be obtained was approximately 2° from the HeNe beam; at smaller angles the transmitted beam struck the edge of the photomultiplier housing and yielded a spurious signal. The results indicate that the forging process with its associated fine-grained structure does not increase the scattering as compared to the original single crystalline starting material. For both the single crystalline

material and the forged material, the fractional small angle scattering was $\lesssim$0.002/sterdian over the angular range of 2° - 15°.

Optical homogeneity was measured using the technqiue described by Bennett, et al. [6]. The measurements were carried out using coated quartz plates in contact with the sample surfaces to form a Fizeau interferometer. Index matching fluid was used in the contact regions. A 0.6328μm HeNe laser was used as the light source. The fringe pattern was detected with a TV camera and displayed on a TV monitor screen. The interference patterns were photographed with a Polaroid camera.

Analysis of the interferograms was performed by digitizing the fringes and then converting the digitized interferograms to contours of optical path difference through the use of the computer program FRINGE, developed at the Optical Sciences Center, University of Arizona. This method of analyzing interferograms has been described previously[7]. We characterize the inhomogeneity by the maximum span of the optical path difference across the sample. The inhomogeneity Δn in index of refraction for samples of single crystalline material measured to date ranges from $\Delta n = 4.4 \times 10^{-6}$ to $\Delta n = 8.8 \times 10^{-6}$, across samples about 2.5 cm in diameter. For samples of forged material measured to date, Δn ranges from 17.4×10^{-6} to 22.3×10^{-6}. The results indicate that LiF samples can be forged without serious degradation of the excellent optical homogeneity of the single crystalline starting material. Efforts to correlate optical homogeneity with forging parameters are underway.

Mechanical Properties

The modified double-cantilever-beam technique of Freiman, et al. [8] was used to determine the critical fracture energy of forged LiF. Specimens 2.5 cm long, 1 cm wide and 0.5 cm thick were cut from forging U1 (a University of Utah LiF crystal forged to 50% reduction at 500C) such that during testing, the crack propagated parallel to the top and bottom surfaces of the forging along a groove which was cut halfway through the thickness of the specimen to guide the crack. After polishing with 6μm diamond grit in oil, the specimens were chemically polished in fluoroboric acid and rinsed in methanol and ether. Sharp cracks were introduced in each specimen before testing by gently tapping with a blade. The tests were carried out at a crosshead speed of 0.025 cm/minute.

Yield strengths of single-crystal and forged LiF were determined by compression tests on specimens cut to dimensions of 4 x 4 x 10 mm. Single-crystal specimens were cut with surfaces parallel to (100) cleavage planes. Samples were polished with 6μm diamond paste. The single-crystal samples were then annealed in a helium atmosphere at 700°C for 2 hours and furnace cooled and the forged samples were chemically polished as described above to remove any residual stresses that may have been introduced during mechanical polishing.

The results of compression and fracture energy tests on samples from forging U1 are given in table 1, where they are compared with single-crystal data of Ahlquist [9]. Compression tests on University of Utah LiF single crystals yielded a value for yield stress of 1.9 MN/m^2 at 0.2% offset. This value is lower than that reported by Ahlquist, apparently because of the higher purity of this starting material.

The data in table 1 indicate that the yield strength and critical fracture energy of single-crystal LiF can be improved by at least an order of magnitude by the forging operation.

Table 1. Mechanical Properties of Lithium Fluoride

	Yield Stress (MN/m^2)*	Fracture Energy γ_c (J/m^2)	Reference
Single - crystal	2.4	0.64	[8]
Single - crystal	1.9	---	This work
Polycrystalline (forging U1, ~40μm subgrain size)	36.0	6.75	This work

*0.2% offset

Summary

Isostatic forging has produced stable fine-grained polycrystalline material with both yield strength and fracture energy increased by at least an order of magnitude as compared to the single crystalline starting material. The optical properties of the single crystalline LiF, including high transmission in the visible and ultraviolet, good homogeneity and low scattering, are not degraded by the forging operation.

Acknowledgements

The authors are happy to acknowledge the able technial assistance of Dave Woodward in this work. We also thank Dr. Thomas G. Stoebe of the Dept. of Metallurgical Engineering, University of Washington, for the measurements of ionic conductivity.

References

[1] D. Milam, M. J. Weber, and A. J. Glass, Appl. Phys. Lett 31, 822 (1977).

[2] E. Bernal G., et al., A Study of Polycrystalline Halides for High Power Laser Applications, Final Technical Report on Contract DAHC-15-73-C-0464 (May, 1978).

[3] R. H. Anderson and E. Bernal G., Proceedings of the High Power Laser Optical Components and Component Materials Meeting, 3-4 October, 1977, Boulder, Colorado., J. S. Harris and C. L. Strecker, eds. P. 429.

[4] T. G. Stoebe and P. L. Pratt, Proc. Brit. Ceram. Soc. 9, 181 (]967).

[5] R. H. Anderson, B. G. Koepke and E. Bernal G., in Laser Induced Damage in Optical Materials: 1976, A. J. Glass and A. H. Guenther, eds., NBS Special Publication #462.

[6] H. E. Bennett, J. W. Bethke, and W. P. Norris, in Proceedings of the High Power Laser Optical Components and Component Materials meeting, 3-4 October, 1977, Boulder, Colorado, J. S. Harris and C. L. Strecker, eds. P. 328.

[7] E. Bernal G., K. M. Leung, and J. S. Loomis, Interferometric Testing and Analysis of Windows Exposed to CO_2 Laser Irradiation, Final Technical Report for Navy Contract N605-30-77-W-6911, 20 May]977.

[8] S. W.Freiman, D. R. Mulville, and P. W. Mast, J. Mater. Sci. 8, 1527 (1973).

[9] C. N. Ahlquist, Acta Met. 22, 1133 (1974).

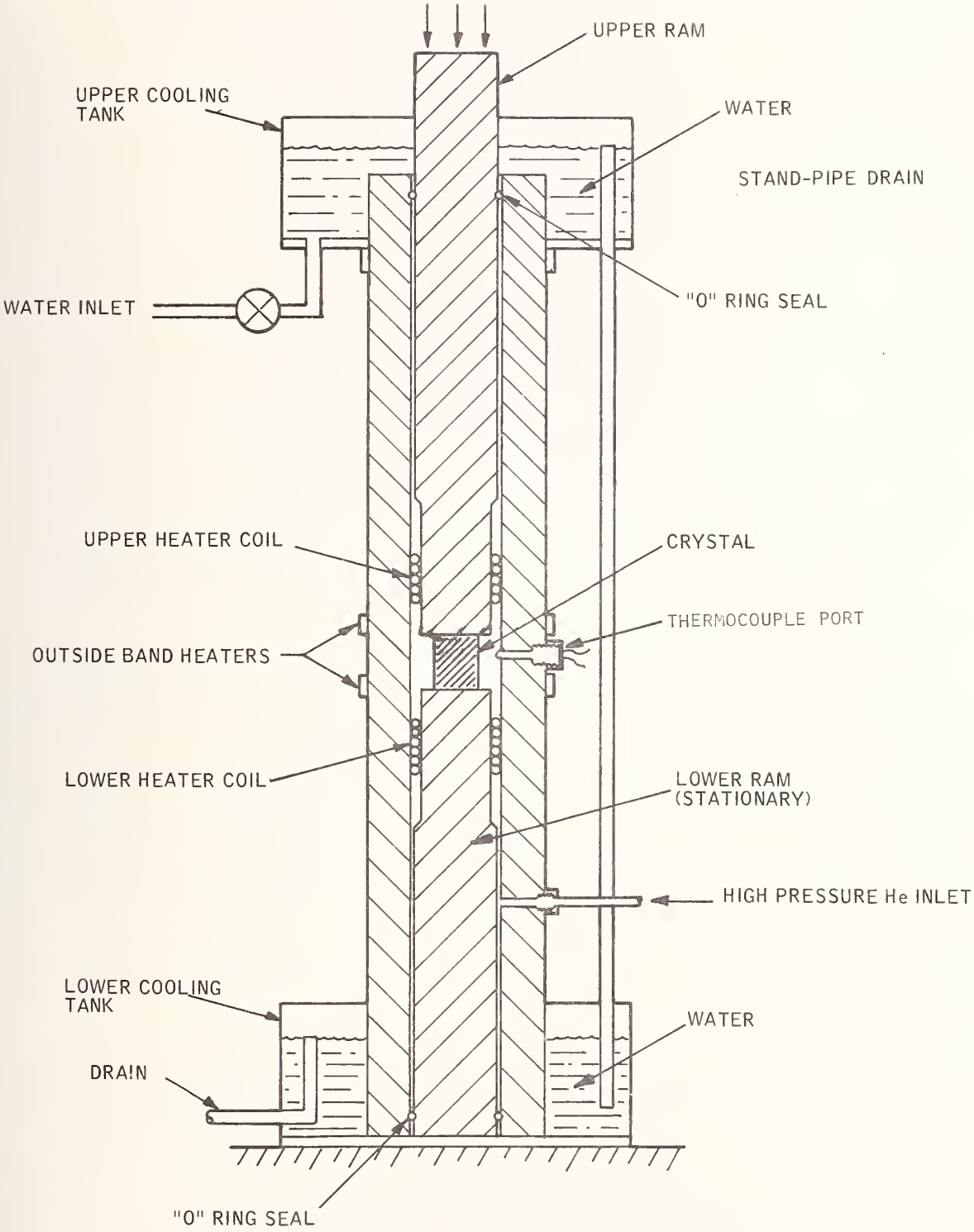

Figure 1. Schematic diagram of isostatic forging apparatus.

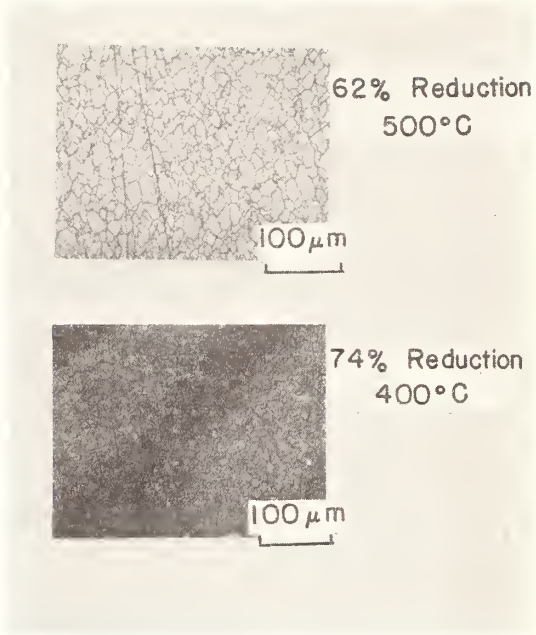

Figure 2 Photomicrographs of fine-grained LiF, forged under the indicated conditions.

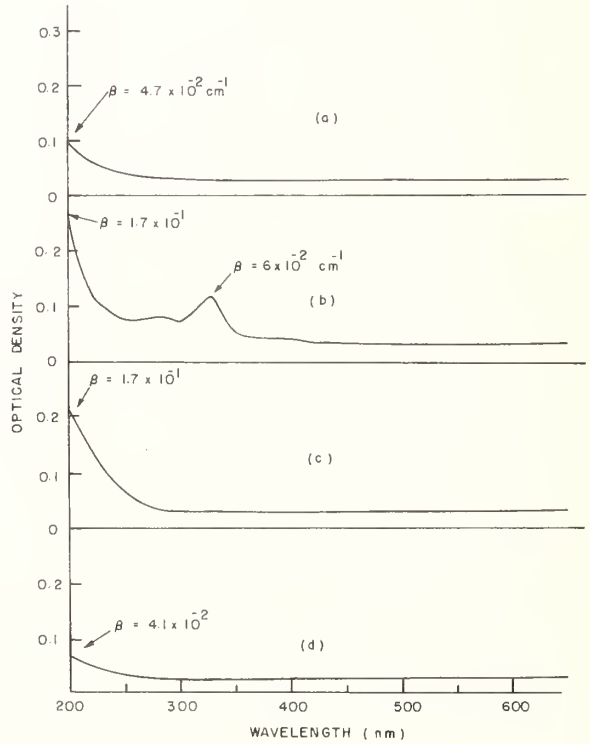

Figure 3 Optical absorption spectra of LiF (a) Forged Harshaw material, thickness t = 3.5 cm; (b) Forged University of Utah material, t = 3.6 cm; (c) Single crystalline Optovac material, t = 2.7 cm; (d) Single crystalline Harshaw material, t = 2.6 cm. Values of absorption coefficient β in cm^{-1} are indicated.

OPTICAL PROPERTIES OF KCl FORGED BETWEEN OPTICALLY POLISHED DIES*

R. H. Anderson
Honeywell
Corporate Material Sciences Center
Bloomington, MN. 55420

and

Jean M. Bennett
Michelson Laboratory, Physics Division
Naval Weapons Center, China Lake, CA 93555

Plano-plano and plano-concave KCl optcial elements have been isostatically forged using a two-step forging process in a closed die. No optical polishing was required for the finished surfaces. The initial forging was performed between teflon sheets, the sample was then water polished, and the final forging was done between optically figured fused quartz or pyrex dies. Forgings were typically done in the 200 to 275°C temperature range in a helium atmosphere at 29.65 MN/m^2 (4000 psi). Measurements on the finished samples include optical figure, homogeneity, internal strain, total integrated forward and backscattering, surface texture (Nomarski microscopy), and surface roughness. The results of these measurements are compared with similar measurements on optically polished single-crystal and press-forged KCl samples.

Key Words: Alkali halides, backward scattering; forward scattering; grain boundaries; isostatic forging; optical homogeneity; optical figure; single crystal; Talystep traces.

Introduction

The unique combination of physical and optical properties possessed by the alkali halides make them potential candidates for infrared windows and many other optical elements. Their broad spectral transmission from the ultra-violet out to 12μm and beyond also contributes to their consideration for very broad band use. One of the physical properties which is hindering the potential development of the alkali halides is their extremely low hardness.

This low hardness contributes to the difficulties which are encountered when conventional optical grinding and polishing techniques are used to produce a desired optical figure and geometric shape. This paper discusses results obtained from a forging process which may be an alternative method for providing the desired optical figure and geometric shape. This technique uses die surfaces which have been optically figured from quartz, pyrex, or metal. The die surface shape and figure is replicated on the halide by forging with these die surfaces. This forging approach should be compatible with spheric as well as aspheric surfaces. The ease with which diamond turning can provide radially symetrical surfaces makes the eventual use of metal dies especially attractive.

The forging process is described and the result of varying a number of the forging parameters on surface roughness, optical figure, scattering and optical homogeneity are discussed.

The Forging Process

To provide mechanical strengthening and eliminate welding of the halide forging to the quartz, pyrex, or metal die surface, the single crystal starting material is forged at a temperature at which the crystal is normally brittle. To prevent fracture during forging and enhance lubrication between the halide forging and the die surface the forging operation takes place in a high pressure gas environment. The gas provides a constraining force which prevents fracture during deformation. This forging method has been named isostatic forging [1][1].

Presently the forging is done in helium at 29.65 MN/m^2 at a temperature from 200° to 250°C. All crystals are now <100> orientation. Quartz, pyrex, and diamond-turned electroless-nickel metal die surfaces have been used for replication. The closed die assembly as used is shown in place in figure 1. Basically, it will be noted, that this is a closed die forging operation done in a heated variable volume, high pressure chamber.

*The forging work was partially supported by Defense Advanced Research Projects Agency under Contract No. DAHC-15-73-C-0464. The optical evaluation was supported by Naval Weapons Center Independent Research Funds.

1. Figures in brackets indicate the literature references at the end of this paper.

Ideally, it would be desireable to forge the halide single crystal to its final shape in a single processing step. The single crystal cylinder is preshaped with water to produce a dome on each end. This shape ensures that the forging operation originates at the center of the die surface and progresses radially outward thereby eliminating the entrapment of gas between the forging and the die surface.

An alternative forging process has also been explored. This is called the two step process. The single crystal cylinder is initially deformed between teflon sheets to at least 60%. This step provides a uniform strain distribution throughout the bulk of the forging while minimizing the development of internal stresses. The forging is then preshaped as in the one step process and re-forged in the same way.

Surface and Optical Evaluation

The surface and optical evaluation of four forgings are discussed in this section and compared with a press forged window that was optically figured using the conventional method and also a single crystal window that was figured using the same method and then chemically polished. Chemical polishing of polycrystalline window surfaces will preferrentially attack the grain boundaries, consequently, is only useable on single crystal materials.

Figure 2 illustrates the optical figures and homogeneity of a one step forging on the left and the press forged mechanically polished window on the right. The optical figure of the one step forging is obviously related to the original crystal orientation and would be difficult to correct by altering the die surfaces. The homogeneity fringes below indicate high internal stress and birefringence. The window on the right is about $\lambda/4$ flat and his low internal stress. This window was press forged and mechanically polished.

A plano-concave sample, shown in figure 3 illustrates the resultant optical figure and homogeneity using the two step process. The plano surface is actually convex but the nearly circular fringes suggest the possibility of improving the figure by making the die surface comparably convex. The fringes show the internal stress to be low. The curvature of the fringes is due to an index mismatch. The method used to determine the homogeneity results utilized a Zygo interferometer and high reflectance quartz flats and index matching fluid [2].

The surface finish produced by the one step forging varies with location on the plano surface. The area on the plano surface represented by the initial single crystal diameter is much smoother than the additional area produced during forging. Figure 4 shows Nomarski photographs illustrating this difference. The Talystep traces vividly emphasize this surface roughness variation.

The plano surface of a plano-concave element produced by the two step process is shown in figure 5. The Taly step traces show a marked reduction in roughness compared to the previous figure. The substitution of a 1 μm radius stylus indicates the surface contains many small, narrow cracks. The major excursions of the trace may be due to grain boundary etching resulting from the preparation for the second forging step.

To determine if these grain boundaries were contributing to the surface roughness and scattering, two plano-plano samples were examined. The element identified as #534 in figure 6 was forged without any attempt to remove the grain boundaries. The other specimen #537 was rubbed gently with paper saturated with methyl alcohol to eliminate the grain boundaries.

One of the die surfaces used to produce both #534 and #537 had a pair of shallow fiduciary marks ground into the forging surface. All of the scans shown in figure 6 were taken between these marks to compare die roughness and the forged halide surface roughness. The trace shown in the lower center is from one of these areas of the die.

Scattering measurements in forward and backward directions were made on all the forgings, as well as, the press forged and the single crystal specimen. These results are summarized in tabular form in figure 7. The identification of each sample is as follows:

Sample	History
Honeywell Window (1)	One Step Forging
Honeywell Window (2)	Two step forging Grain Boundaries Reduced
AFWL Polished	Press Forged Mechanically Polished
E-3 Etched	Single Crystal Mechanically Polished Etched

Sample	History
Honeywell #534	Two Step Forging Grain Boundaries Evident
Honeywell #537	Two Step Forging Grain Boundaries Reduced

It is apparent that in almost all cases the forged materials exhibit lower scattering values. The results in the forward direction were taken from several hundred points and the fiduciary marks do contribute to these scattering results of both windows #534 and #537.

Figure 8 illustrates in tabular form rearrangement of the data shown in figure 7. All values less than 1.0 show the Honeywell forged elements to be superior to the element identified in the denominator of the fraction.

Conclusions

It is apparent that the two step forging process produces a superior element from the standpoint of surface figure, homogeneity, surface roughness, and scattering.

The preparation of the water polished surface prior to the second forging step to reduce or eliminate the grain boundaries also improves the forged element properties. The surface is smoother, consequently the scattering values are lower.

The comparison of the die surface roughness to the halide forged surface does not replicate the die surface exactly. However, the forged surface does compare favorably with the "state of the art" mechanically polished samples and the scattering values are lower than mechanically polished or etched samples.

These forging results are encouraging and efforts are now directed to demonstrate the forging of halide optical elements with satisfactory optical figures.

Acknowledgements

The authors would like to acknowledge the excellent technical assistance provided by Messrs. W. J. Polzin and R. A. Skogman of this laboratory and Messrs. P. C. Archibald and J. W. Bethke of the Michelson Laboratory, Naval Weapons Center, China Lake.

References

[1] R. H. Anderson and J. M. Bennett, Proceedings of the High Power Laser Optical Components and Component Material Meeting, 3-4 October, 1977, Boulder Co. J. B. Harris and C. L Strecker, eds. (Defense Advanced Research Project Agency, Arlington, VA, 1977)

[2] H. E. Bennett, J. W. Bethke, and W. P. Norris ibid. p327-338.

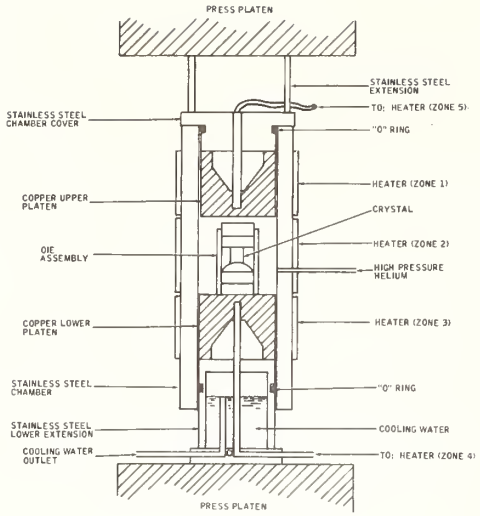

Figure 1. Sectional schematic of the isostatic forging system for producing finished halide optical elements.

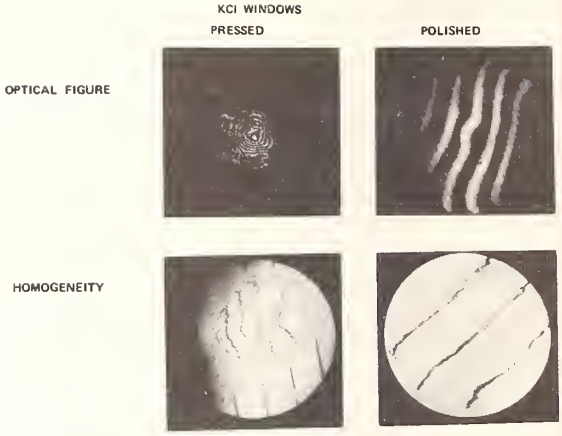

Figure 2. Optical figure and homogeneity of a KCl sample prepared by a one-step forging process (left) and a conventionally polished KCl forging (right).

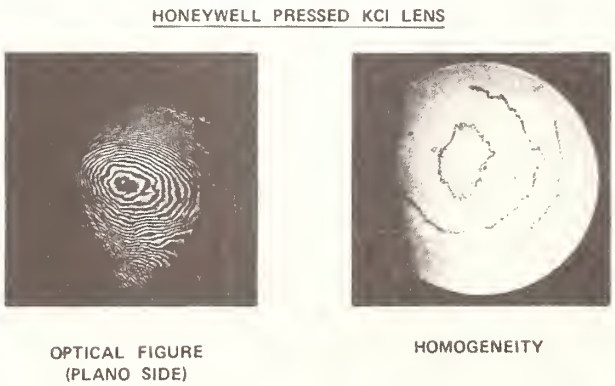

Figure 3. Optical figure and homogeneity of a sample prepared by a two-step forging process.

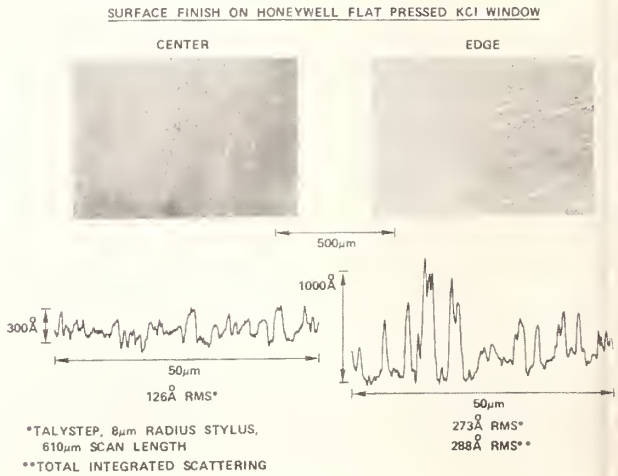

Figure 4. Surface finish of center and edge areas of a one-step forging (Nomarski) and corresponding Talystep traces of surface roughness.

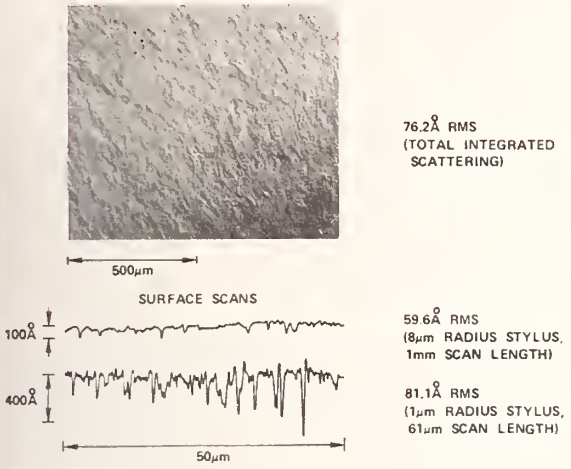

Figure 5. Surface finish of a typical area of a two-step forging (Normarski) and resultant Talystep traces.

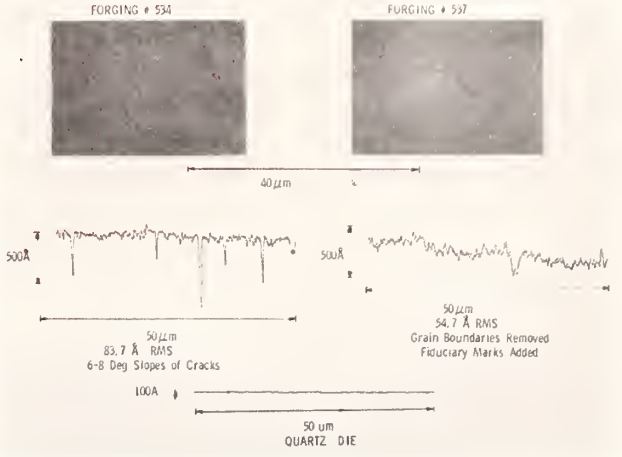

Figure 6. Surface finish of an area between the fiduciary marks (Normaski) with (right) and without (left) surface treatment and Talystep traces of the same area of both forgings and the quartz die.

	0.6471 μm	3.39 μm	10.6 μm
BACKSCATTER			
Honeywell Window Flat Pressed (1)	7.11×10^{-4}	5.20×10^{-5}	1.80×10^{-5}
Honeywell Lens Flat Pressed (2)	4.05×10^{-3}*	8.18×10^{-5}	3.33×10^{-5}
AFWL 6" Diam. Polished	9.98×10^{-3}	2.49×10^{-4}	5.58×10^{-5}
E-3 Etched	2.82×10^{-3}	8.13×10^{-5}	1.02×10^{-4}
		*Wavelength 0.5682 μm	
FORWARD SCATTER			
Honeywell Window Flat Pressed (1)	4.21×10^{-3}	2.19×10^{-4}	6.45×10^{-5}
AFWL 6" Diam. Polished	2.96×10^{-2}	5.90×10^{-4}	6.46×10^{-5}
E-3 Etched	5.42×10^{-3}	4.33×10^{-4}	2.95×10^{-4}
Honeywell Window #534 Flat Pressed (3)	5.91×10^{-3}	2.33×10^{-4}	1.38×10^{-4}
Honeywell Window #537 Flat Pressed (4)	3.39×10^{-3}	2.03×10^{-4}	4.97×10^{-5}

Figure 7. Total integrated scattering results from several KCl samples.

	0.6471 μm	3.39 μm	10.6 μm
BACKSCATTER			
Honeywell (1)/Etched	0.25	0.64	0.18
Honeywell (1)/AFWL	0.07	0.21	0.32
Honeywell (2)/Etched	1.43	1.00	0.32
Honeywell (2)/AFWL	0.41	0.33	0.60
FORWARD SCATTER			
Honeywell (1)/Etched	0.78	0.51	0.22
Honeywell (1)/AFWL	0.14	0.37	1.00
Honeywell (3)/Etched	1.09	0.54	0.47
Honeywell (3)/AFWL	0.20	0.40	2.14
Honeywell (4)/Etched	0.63	0.47	0.17
Honeywell (4)/AFWL	0.11	0.40	0.77

Figure 8. A summary of the scattering results comparing isostatically forged samples to conventionally prepared samples.

BULK OPTICAL PROPERTIES OF FINE GRAINED FORGED CALCIUM FLUORIDE*

R. H. Anderson, R. A. Skogman, and J. F. Ready
Honeywell Corporate Material Sciences Center
Bloomington, MN. 55420

and

Jean M. Bennett
Michelson Laboratory, Physics Division
Naval Weapons Center, China Lake, CA 93555

Single crystals of CaF_2 having <111> . <100>. <112>. and <113> orientations have been routinely isostatically forged in a helium atmosphere at 750°C. The crystals were deformed 60 percent to ensure a uniform grain size of less than 15μm. A fine cloudiness of "veiling" occurs when the forging is done below the recrystallization temperature of about 800°C for CaF_2. Nomarski micrographs show that voids are distributed within the bulk of the forgings. Polariscope photographs show internal stress. Total integrated forward scattering measurements have been made on the sample immersed in a cell containing index matching fluid to eliminate scattering from the sample surfaces. These measurements show variations cannot be definitely correlated with the positions of veils in the CaF_2.

Key Words: Calcium fluoride, forging, laser windows, optical properties, scattering.

Introduction

Calcium fluoride is a prime candidate material for use as a laser window in the chemical laser band from 2.8 to 5.3μm. Its combination of physical and optical properties are most attractive. Unfortunately, its combination of high Young's Modulus, large coefficient of expansion, and extremely low thermal conductivity contribute to its sensitivity to thermal and mechanical shock when CaF_2 is used as single crystal windows.

The strengthening methods that were successfully used with the alkali halides have been applied to CaF_2. [1][1]. Forged CaF_2 with a grain size less than 15 m can be routinely produced. Forged CaF_2 has shown an increase in the critical fracture energy in excess of five times that of single crystals. After the forging operation has been completed, examination of the forging reveals cloudy regions within the bulk of the forging, which is called "veiling".

Efforts to eliminate the veiling have been largely unsuccessful. Several single crystal orientations were forged in an attempt to eliminate the veiling. Many of the forging parameters were varied such as strain rate, reduction, forging temperature and forging sequence. An alloy crystal of CaF_2 with 90 ppm Eu was also forged. All these attempts to eliminate veiling had negative results.

Early efforts to isolate the source of the veiling by optical microscopy, scanning electron microscopy or Auger analysis were unsuccessful. Impurity segregation, which had been observed in the past by Stockbarger [2] in material of much lower purity, was discounted because of the high purity of currently available crystals. Vacancies due to dislocation interaction during deformation appeared the most likely source. Efforts to detect voids by any method were unsuccessful until the development of techniques described later in this paper.

This paper discusses the forging system now used, presents recent birefringence photographs for <111> and <100> orientations, discusses scattering results obtained using a special cell, presents scattering maps of the samples tested in the cell at 0.6471 and 3.39μm, and also discusses the angular and wavelength dependence of the scattering. Some comments are also made about the origin of the veiling

The Isostatic Forging System

To minimize the development of internal stress within the CaF_2 forging, it is vital to maintain isothermal conditions in the region where the forging occurs. Figure 1 illustrates the present isostatic forging system used for forging fine grained CaF_2 and designed to provide isothermal forging

*The forging work was partially supported by Defense Advanced Research Projects Agency under Contract No. DAHC-15-73-C-0464. The optical evaluation was supported by Naval Weapons Center Independent Research Funds and Honeywell Material Sciences research funds.

1. Figures in brackets indicate the literature references at the end of this paper.

Table 2 Data from Scattering Measurements

	6471Å	3.39μm
Test Cell	$5.192 \pm 0.583 \times 10^{-3}$	$2.32 \pm 1.79 \times 10^{-6}$
Test Cell and <111> Crystal	$1.146 \pm 0.652 \times 10^{-2}$	$2.299 \pm 0.848 \times 10^{-4}$
Test Cell	$5.74 \pm 1.87 \times 10^{-3}$	$2.70 \pm 0.51 \times 10^{-5}$
Test Cell and <100> Crystal	$2.55 \pm 1.06 \times 10^{-2}$	$2.72 \pm 0.61 \times 10^{-4}$

The scattering levels for the sample, cell, and index matching fluid were also measured as a function of position on the sample. The scattering from the cell without the <111> sample was approximately equal to the scattering from the sample in the visible. The scattering from the cell without the <100> sample was approximately 1/3 of the scattering from the sample in the visible. In the infrared the <111> sample was two orders of magnitude lower and the <100> sample was one order of magnitude lower. On the average the bulk scattering from each sample is:

$6.27 \pm 6.52 \times 10^{-3}$ at 6471Å bulk scattering <111>

$2.30 \pm 0.85 \times 10^{-4}$ at 3.39 m bulk scattering <111>

$19.76 \pm 10.6 \times 10^{-3}$ at 6471Å bulk scattering <100>

$2.45 \pm 0.61 \times 10^{-4}$ at 3.39 m bulk scattering <100>

From these results the bulk scattering of the <111> sample is nearly 30 times larger in the visible and the <100> is nearly 80 times larger in the visible than in the infrared.

If we assume that the entire scattering levels of the cell plus index matching fluid are caused by the two windows (2 surfaces plus bulk scattering for two windows) then we can compare bulk and surface scattering from single crystal CaF_2 with bulk scattering from isostatically forged <111> CaF_2. For the single crystal CaF_2, the scattering in the visible is over 2000 times larger than in the infrared. The scattering levels for the two types of CaF_2 are comparable in the visible (the press forged sample scattering slightly more), but the press forged sample scatters about 100 times more than the single crystal windows at 3.39 m. It should be emphasized that the comparisons are not strictly valid because the total thickness of the single crystal windows is only about two-thirds that of the press-forged sample. Also, there is scattering from 2 of the 4 surfaces of the single crystal windows and this may be much larger than the bulk scattering in the material.

The spatial distribution of the scattering from the sample was plotted as a contour map with interpolations made from the measured data. Actual data points were taken on concentric circles whose radii differed by 0.05 inch, out to a maximum radius of 0.800 inch (1.6 inch diameter). On each circle data points were spaced 0.05 inch apart. Thus there were a total of 817 points for each case. Averages of these blocks of 817 data points are the values given above.

Figure 5 and figure 6 show the contour plots as a function of orientation and wavelength. All attempts to compare the veiled pattern of the forgings in the visible with the contour maps were fruitless. It is very difficult to compare the measured total integrated scattering from the sample with the position of the veils in the sample. The veils can only be seen when the sample is viewed obliquely, and tend to appear differently as the sample orientation is changed.

In addition measurements were performed on the angular dependence of the scattering. Measurements were performed at four separate wavelengths: 0.4416μm, 0.6328μm, 2.8μm and 3.8μm. The measurements were performed by directing a laser beam through a small area of the sample and observing the scattered light with a photodetector. The photodetector was moved along the circumference of a circle with its center at the point where the laser beam emerged from the sample. The relative signal due to scattered light was measured as a function of the angle between the incident laser beam and the line from the sample to the detector. Care was taken that only light scattered by the sample could reach the detector. The detectors were a S-1 photomultiplier for the two shorter wavelengths and a PbTe detector for the two longer wavelengths. We ensured that the detectors were operating in the linear portion of their response by inserting filters of known attenuation in front of the detector and observing the decrease in signal. In contrast to the measurements of total integrated scattering described above, these measurements were carried out for only a few selected areas on the sample and do not lead to maps for the scattering. They do allow comparison with Mie scattering theory, however.

conditions. If CaF_2 is to remain fine grained after forging, the deformation must occur below its recrystallization temperature, about 800°C. Since CaF_2 behaves in a brittle manner below 800°C a hoop stress or constraining force must be applied to the single crystal throughout the total forging operation. The high pressure helium environment provided by this forging technique provides this constraining force.

The present forgings are done at 750°C in helium at 14.82 MN/m^2. The forging is done sequentially and cooled 25°C per hour.

Figure 2 shows polariscopic photos of a <111> and a <100> oriented forging. The level of internal stress is low but has not been quantitized.

Table 1 presents data on the critical fracture energy (F_c) obtained from several samples and sources. These results have been described previously [1], but are included here to make the present paper self-contained. The strengthening achieved by the forgings done at 750°C is apparent.

An illustration of how "veiling" appears in visible light is shown in figure 3. This is a <111> orientation crystal and it appears that the veiling is related to the 3-fold symmetry of this crystal orientation.

Table 1 Fracture Energies
γ_c of Several CaF_2 Samples

Condition	$\gamma_c (J/m^2)$
Single Crystal (111) 110	0.45, 0.51(1)
Forged at 500°C	1.63
Forged at 515°C Annealed 1 Hr at 720°C	2.00
Forged at 650°C Annealed 24 Hr at 720°C (Large grained)	1.56
Hot worked large Grained (1-10mm)	1.6(2)
Forged Isothermally at 750°C Annealed 24 Hrs. at 700°C	2.6
Kodak Irtran Hot Pressed Powder	3.6(1)

(1) Freiman, et al. NRL
(2) Harshaw Polytran tested by Freiman et al., NRL

Scattering Results

A number of experiments were performed to determine what effect, if any, the veils in the isostatically forged CaF_2 have on the transmittance and forward scattering. The problem was to eliminate scattering from the surface of the sample which tend to mask bulk scattering. This procedure was to immerse the test sample in a cell containing index matching fluid so that there would be no scattering at the sample surface. The total integrated forward scattering for the sample, cell, and index matching fluid was measured. The measurements were performed in the Optical Evaluation Facility at the Naval Weapons Center. The difference between these two measurements gave the effect of the veils or other bulk defects in the sample. Measurements were performed at 6471Å in the visible (krypton laser red line) and at 3.39μm in the infrared (He-Ne laser). Figure 4 illustrates the test cell, which has windows of single crystalline CaF_2.

The data obtained from the scattering measurements are summarized in Table 2. The scattering levels for the cell and the index fluid without the test sample were quite constant at 6471Å. The somewhat larger variations at 3.39μm are because the scattering is close to the noise level of the system, and one count on the digital voltmeter produces a proportionately larger change.

Results are shown in Figure 7 for scattering from a veiled area and in figure 8 for scattering from a clear area. The results in each case are normalized to the on-axis power as unity. This allows us to compare results for different values of laser power and different detector responsivity at the various wavelengths.

The results in figure 7 indicate that the angular dependence is independent of wavelength for 0.4416μm, 0.6328μm, and 2.8μm lasers, but at a given angle the fraction scattered into unit solid angle is much lower at 3.9μm than at other wavelengths. The minimum value of the angle at which measurements could be made (0.9 degrees for the two shorter wavelengths and 1.9 degrees for the two longer wavelengths) was set by the size of the detector housings. When the unscattered beam struck the edge of the housing, reflection of that beam led to a spurious signal.

The results in figure 8 show that at a given angle, the scattering is such less when the beam was incident on a visually clear area of the sample, as compared to a veiled area. This is to be expected, but the relative wavelength dependence is not. In particular, the reason for the relatively large scattering at 2.8μm is not obvious. The measurement at 2.8μm was repeated on another clear area, the clearest area that could be located on the sample. The same relative signals were found as for the first clear area. Figure 8 does not include data at 0.4416μm; the power of the HeCd laser was low, and meaningful measurements could not be obtained for scattering from a clear area.

We attempted to interpret the results of Figure 7 on the basis of Mie scattering theory for transparent spheres, in order to determine whether the scattering arises from spherical voids within the material. For voids with index of refraction 1 embedded in a material with index of refraction n, Mie scattering theory may be applied with an effective index of refraction m = 1/n. For CaF_2 at 0.6328μm, m = 0.698. Tables of the Mie scattering functions are available for m = 0.7 [4]. It did not prove possible to assign the scattering to Mie scattering by spherical voids within the CaF_2. There is no value which can be assumed for the radius of the void which will yield the relative magnitudes of the scattering at 2.8μm and 3.8μm as shown in figure 7. If one assumes voids with a distribution of radii, it will not improve the situation. Thus, the wavelength dependence of the scattering is not amenable to interpretation on this basis.

The results are useful for indicating the relative seriousness of the veiling at various wavelengths. The results of Figure 7 indicate that the scattering at 2.8μm is as great as in the visible; therefore, veiling would presumably be a problem for CaF_2 used with HF lasers. However, the reduced scattering at 3.8μm indicates that veiling should be less of a problem for CaF_2 used with DF lasers.

Both types of scattering measurements indicate a considerable reduction in scattering at infrared wavelengths greater than 3μm, as compared with visible light scattering. They cannot be compared in detail because the angular scattering measurements contain a contribution from surface scattering, whereas the total integrated scattering measurements do not.

Studies of Veiling

CaF_2 single crystals when forged under certain conditions of temperature and strain become visibly "veiled".[2] Microscopic examination identifies the source of the scattering as voids located along grain boundaries in the forged CaF_2. Scanning electron microscopy and EDAX (Energy Dispersive Analysis of X-rays) confirm the existance of voids and identify no detectable impurities. Recent work has shown however, that the voids can be eliminated from forged material.

"Veiling" has been observed for all forging orientations i.e. <111> , <$\bar{1}$10> , and <100>, after the amount of deformation exceeds approximately 45 percent. The extent of veiling however, decreases with increasing forging temperature but still exists in forgings done at 800°C, the temperature limit of the forging chamber. Early attempts to eliminate veiling while maintaining material strength were largely unsuccessful.

Microscopic examination gives a better understanding of the nature and cause of the veiling in CaF_2. The individual scattering points comprising the veils are very small and extremely difficult to locate microscopically. A veiled area intersecting the surface of a mechanically polished CaF_2 forging can, however, be examined microscopically. See figure 9. Careful examination of the underlying volume using a HeNe laser illuminating a scattering defect and a high magnification long working distance Nomarski lens to focus on it enables one to find the scattering source. The laser is turned off and the transmitted light source of the microscope is turned on. The scattering points are now easily brought into focus at depths up to 4 millimeters below the CaF_2 surface.

These defects appear very narrow and are typically only a few microns in length. The needle-like defects lie parallel to one another in the bulk of the CaF_2. When the defects are brought to focus immediately below and on the sample surface, they are seen lying parallell to the boundaries of the elongated grains characteristic of the forging. These defects appear as voids located at the grain boundaries.

Fractured specimens containing veils show both by optical microscopy and SEM the existence of what appear to be voids. EDAX identifies no detectable impurities i.e. precipitates.

The cause of the voids is not precisely known but an explanation has been proposed in previous work [5]. A high vacancy concentration can be expected at elevated temperatures and high deformations because of non conservative dislocation movement and climb. When areas of high vacancy concentration recrystallize the vacancies could be swept along and "precipitated" at the grain boundary.

This phenomenon is not likely to be avoided at temperatures and pressures attainable in conventional hot forging apparati. Recent encouraging work conducted by the Air Force Materials Lab, however, has shown that veiling can be removed from previously veiled specimens [6].

Conclusion

Isostatic forging of several CaF_2 crystal orientations did not succeed in eliminating veiling in polycrystalline windows. Scanning electron microscopic examinations and optical microscopy suggest that veiling may be caused by microvoids formed by the coalescence of vacancies which were produced by dislocation intersections and annihilations as a consequence of plastic deformation. Optical scattering measurements indicate high values at 2.8μm, but reduced scattering at 3.8μm. Contour maps of the total scattering show similar wavelength dependence, but do not show a correspondence to the visual appearance of the windows.

Acknowledgements

The authors wish to acknowledge technical assistance and helpful discussions with many people, including E. Bernal G., K. M. Leung, M. L. Filzen, H. Vora, K. O. Park, W. J. Polzin, D. W. Woodward and R. I. George of the Honeywell Corporate Material Sciences Center and P. C. Archibald of the Naval Weapons Center, China Lake.

References

[1] R. H. Anderson and E. Bernal G., in Proceedings of the High Power Laser Optical Components and Component Materials meeting, Boulder Co. Oct. 3-4, 1977, J. S. Harris and C. L. Strecker, eds.

[2] D. C. Stockbarger, J. Opt. Soc. Am. 39, 731 (1949).

[3] H. E. Bennett, M. J. Soileau and P. C. Archibald, in Laser Induced Damage in Optical Materials: 1975, A. J. Glass and A. H. Guenther, eds., NBS Special Publication 435.

[4] R. H. Boll, et al., Tables of Light Scattering Functions, the University of Michigan Press (1958).

[5] E. Bernal G., et al., A Study of Polycrystalline Halides for High Power Laser Applications Final Technical Report on Contract DAHC-15-73-C-0464, (1978) p. 30.

[6] A. K. Hopkins, AFML, private communication.

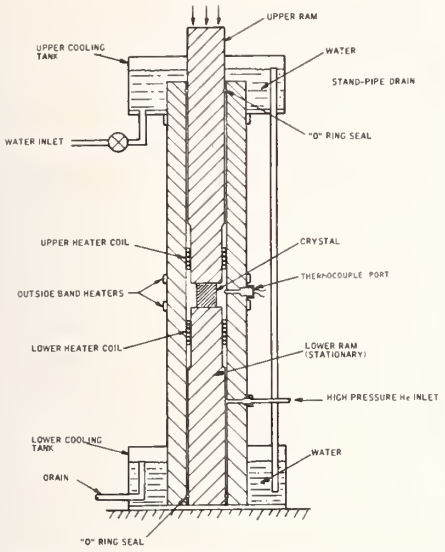

Figure 1. Diagram of forging apparatus.

Figure 3. Veiling in forged CaF_2.

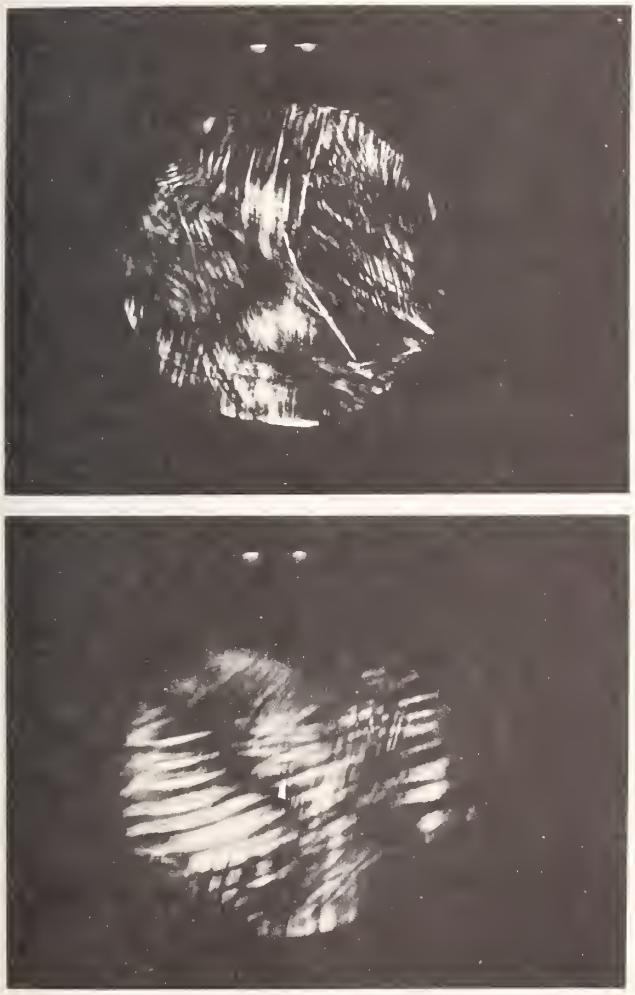

Figure 2. Polariscopic photographs of forged CaF_2. Upper photo: <111> orientation. Lower photo: <100> orientation.

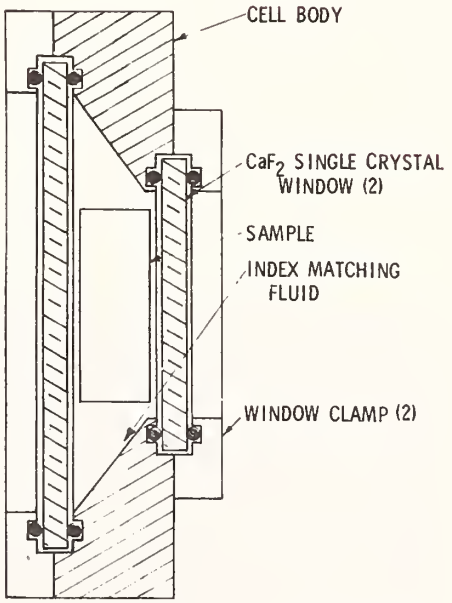

Figure 4. Sample cell for scattering measurements.

<111>ORIENTATION

6471A SCATTERING, CAF2 W/VEILS

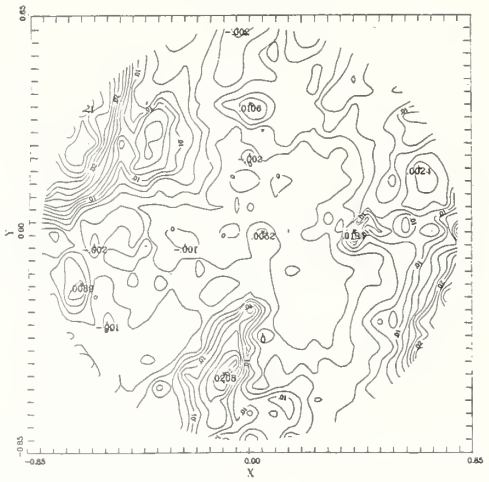

CONTOURS FROM 0 to 0.032
CONTOUR INTERVAL 0.002

<100>ORIENTATION

6471A SCATTERING, CAF2 W/VEILS, 8/78

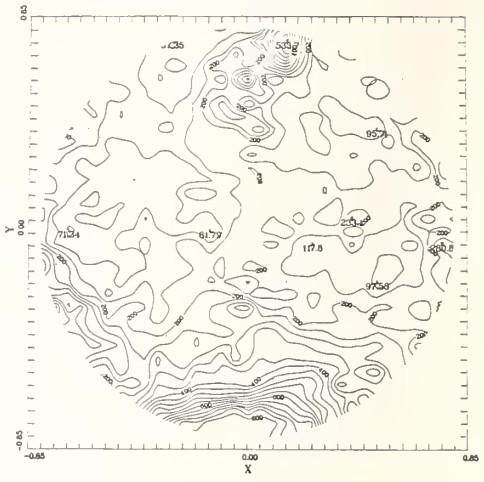

CONTOURS FROM 40 x 10^{-4} TO 800 x 10^{-4}
CONTOUR INTERVAL 40 x 10^{-4}
MULTIPLY ALL VALUES ON GRAPH BY 10^{-4}
TO OBTAIN SCATTERING

<111>ORIENTATION

3.39μM SCATTERING, CAF2 W/ VEILS

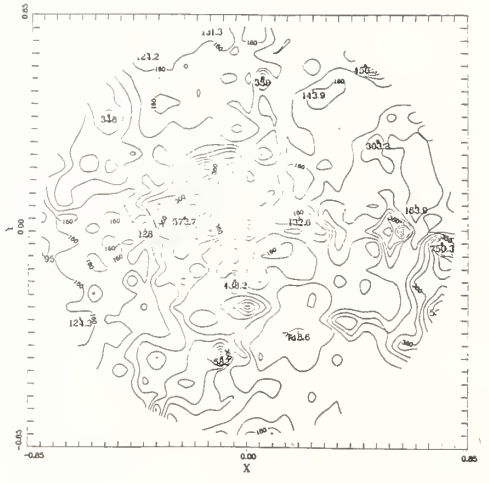

CONTOURS FROM 80 x 10^{-6} TO 720 x 10^{-6}
CONTOUR INTERVAL 40 x 10^{-6}
MULTIPLY ALL VALUES ON GRAPH BY 10^{-6}
TO OBTAIN SCATTERING

<100>ORIENTATION

3.39μM SCATTERING, CAF2 W/VEILS, 8/78

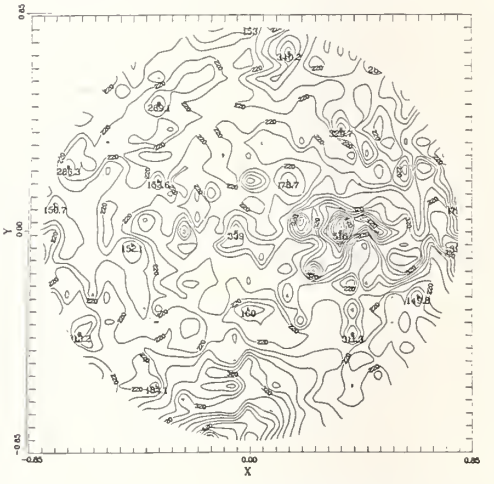

CONTOURS FROM 140 x 10^{-6} TO 520 x 10^{-6}
CONTOUR INTERVAL 20 x 10^{-6}
MULTIPLY ALL VALUES ON GRAPH BY 10^{-6}
TO OBTAIN SCATTERING

Figure 5. Contour maps of scattering from veiled <111> oriented CaF_2. Upper photo: 0.6471μm scattering. Lower photo: 3.39μm scattering.

Figure 6. Contour maps of scattering from veiled <100> oriented CaF_2. Upper photo: 0.6471μm scattering. Lower photo: 3.39μm scattering.

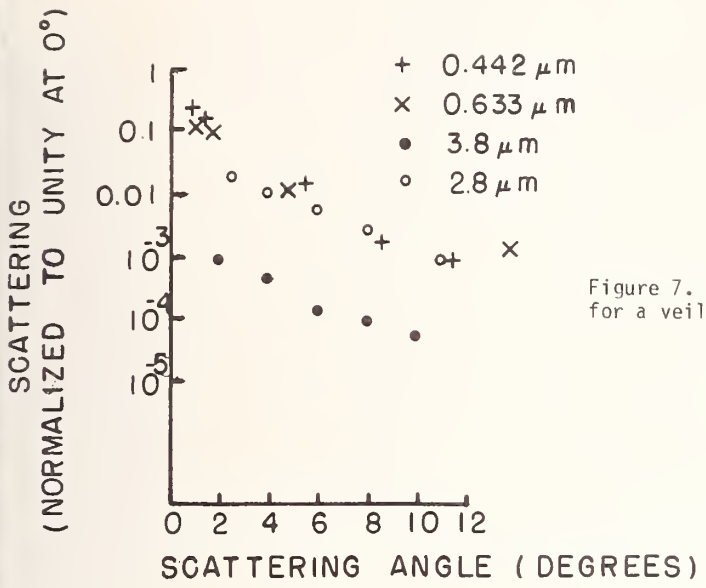

Figure 7. Relative scattering vs. scattering angle for a veiled area on CaF_2.

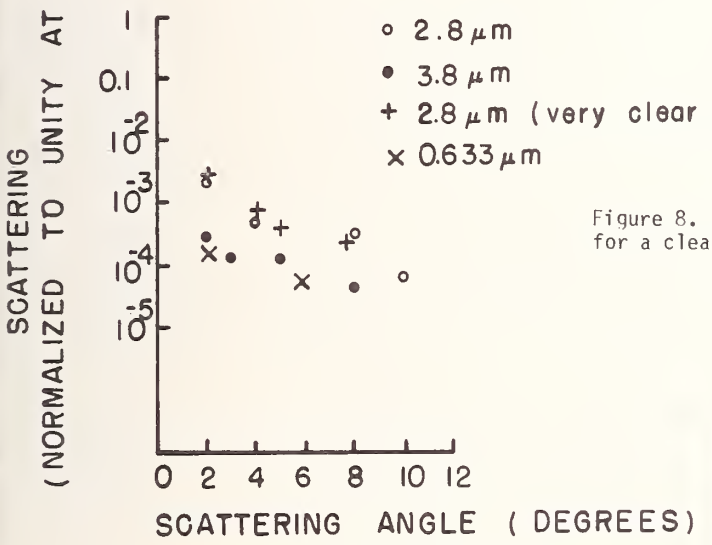

Figure 8. Relative scattering vs. scattering angle for a clear area on CaF_2.

Figure 9. Photograph of voids in a veiled region intersection mechanically polished CaF_2 surface. The width of the area covered by the photograph is about 0.2 mm.

CW LASER DAMAGE IN AR COATED ALKALINE EARTH FLUORIDES AT 3.8 μm*

John A. Detrio and Roger D. Petty
University of Dayton Research Institute
Dayton, Ohio 45469

We have measured the damage threshold of AR coated SrF_2 and oriented single crystals of CaF_2 using a cw chemical laser operating at approximately 3.8 μm. The samples were irradiated for three seconds up to a total power of 8.4 kW. The specimens all failed at a power density of 22 kW/cm^2 over a 0.3 cm^2 area. The failure mode was not catastrophic and is believed to consist of plastic deformation due to compressive loading in the center of the irradiated region on the exit surface. The surface absorption is the dominant contributor to the failures. A novel statistical approach to defining the damage threshold and assessing the confidence level of the data was used.

Key words: Antireflection coatings; calcium fluoride; cw laser damage; DF laser; fusion cast; laser damage; laser window; single crystal; strontium fluoride.

1. Introduction

There have been few material windows used in high power cw laser systems. One factor contributing to the avoidance of material windows is the shortage of engineering data including survival potential, which would permit a systems engineer to design around the materials power handling limitations. The problem of generating engineering quality survival data is complicated by the brittle mechanical behavior of most candidate window materials and by the variability in antireflection coating quality. The objective of the test described in this paper is to demonstrate a method for obtaining statistically significant data on the survival of coated window specimens. Achieving this objective represents a first step in deriving engineering data on which to base a rational window design.

As a test vehicle, we selected polycrystalline SrF_2 (fusion cast by Raytheon) because of the availability of a large, homogeneous batch of substrate specimens. We chose a commercial coating supplier who is not engaged in developing state-of-the-art antireflection coatings for DF laser applications so that we could avoid the variability in quality associated with specimens from a coating research program. For this reason the window performance discussed in this paper does not represent the best available DF laser windows and coatings.

We also examined a systematic aspect of stress birefringence in alkaline earth fluorides by studying the response of oriented single crystals of CaF_2 to DF laser irradiation. The polariscopic images of these materials during irradiation exhibit the predicted response to polarized laser radiation. These results allow one to assess the influence of texturing in the polycrystalline substrates on the propagation of polarized radiation.

2. Apparatus and Experimental Details

2.1. Apparatus

The experimental apparatus is shown in figure 1. The incident power was measured by reflecting the power from the beam switch onto a 0.7 percent rotating mirror chopper and through a CaF_2 beamsplitter into a CRL Model 201 power meter and reflected a portion of the beam into a Laser Precision pyroelectric detector. The pyroelectric detector is capable of very rapid time response which allows the temporal variations in laser output to be monitored. The power transmitted by the specimens was measured with a rapid response cone calorimeter. This device operates as a flow power meter with a thermistor sensing the temperature rise of the water. The water flow rate and temperature rise were measured and converted into a power reading. A series of beam diagnostic test runs were made to calibrate the CRL power meter, cone calorimeter, and pyroelectric detector against one another. In order to maintain internal consistency, all of the power readings are referenced to the CRL meter which had been calibrated against an NBS standard.

*This work was supported by the Air Force Materials Laboratory

The laser beam handling system is also shown in figure 1. The first mirror is mounted atop a concrete pedestal. The beam is then directed to a mirror on a table, then back to a pedestal mounted mirror, and then to a second mirror on the table. By combining the two focusing mirrors in this way the astigmatism in the optics is partially compensated and the required image quality and beam size at the sample is achieved. Before striking the sample the beam passes through or is reflected from the beam switch. When the switch is closed (the normal position), the beam goes to the diagnostic table where the 0.7 percent mirror chopper and CaF_2 beamsplitter sample the pyroelectric detector. When the shutter is open, the beam strikes the center of the sample mounted on the carrousel wheel and, after passing through the sample, is captured in the cone calorimeter.

The Agastat Controller was pre-programmed to control the timing and operation of the various functions required during a test run. The test sequence and typical data are shown in figure 2. The first action is the firing of the solenoid operated 35 mm camera shutter; the beam switch is then activated under the control of a timer set for three seconds. Approximately 2 seconds into the irradiation, the 35 mm camera is again fired. After the beam switch is closed the carrousel clutch is energized and the drive mechanism is engaged to advance the next sample into position. (The first sample is in position at the start of the test.) The next command from the Agastat is to obtain a before-irradiation 35 mm photo. When the beam switch closes the sequence begins again. This program is repeated three times during a given laser run and provides for the test of three samples.

In order to measure the power density on the samples, it was also necessary to measure the beam size. The beam profile was obtained by irradiating Plexiglass specimens located at the sample position with various levels of power for 1/4 second. Castings were made of these burn patterns using a silicon potting compound and the resulting molded pattern was examined with an optical comparator to give the burn depth and full-width at half-maximum depth.

The response of the samples to laser radiation was monitored by the use of an interferometer and a plane polariscope. Both kinds of information were captured on 35 mm film and on video tape.

The interferometer patterns are obtained by interference between HeNe laser light reflected from the front and back of the samples. In most cases, the sample faces were sufficiently parallel so that several fringes could be observed.

The polariscopic view is produced in blue light using a Wratten No. 29 filter in combination with an air-cooled light source (100 W) and a combination of diffuser material and a Fresnel lens.

The recording of the polariscopic and interferometric data is achieved by combining the images in two ways. For video recording the images are formed side by side on a screen that is viewed by a TV camera. The two images are also superimposed and recorded by a 35 mm camera on Kodak Ecktachrome color film. The intensities are balanced by the use of neutral density filters and crossed polarizer attenuators to give an acceptable balance between the two images when a typical strain pattern is present. The images may be color separated (using Wratten No. 29 (red) and No. 46 (blue) filters) for study of either interference or strain pattern.

The Spectro Physics Model 155 HeNe laser source for the interferometer is mounted with a Jodon pinhole spatial filter and beam expander. The light source for the polariscope and the HeNe source are mounted on tripods for ease of adjustment and freedom of placement. The data camera system and carrousel are attached to a 61 x 122 cm optical breadboard from NRC and the breadboard was fastened to a die table which facilitated adjustment of the height of the table to match the laser focusing optics.

2.2. Samples

The samples are listed in table 1. Fusion cast SrF_2 substrates from Raytheon were coated by Valtec (Optical Coating Division) with a SiO/ThF_4 ($\lambda/4$, $\lambda/4$) AR design adapted from one previously used at 5.3 μm on CaF_2. These samples were procured to represent a homogeneous batch of equivalent samples. They were polished to a parallelism of less than twelve arc seconds. Not all of the samples were polished to the same precision; thus, there are differences in the fringe count across the samples. This difference should not affect the test results unless the difference in parallelism is related to differences in polishing and handling which in turn may influence the surface quality and laser absorption. The measured values of absorption and scattering were compared to the fringe count to see if there was any significant correlation between these quantitatives. No correlation was found between either

scattering and fringe count and absorption.

Table 1. Data summary for AR coated SrF_2 samples.

Sample Number	3.8 μm Absorption ($\div 10^{-4}$ cm^{-1})	Scattering at 6328 Å (Ratio $\div 10^{-3}$)	Fringe Count (zero power)
1883	44	9.1	19
1929	41	10.2	21
1930	43	10.8	18
1935	40	11.3	8
1937	42	12.4	9
1942	49	10.2	10
1943	46	8.9	6
1944	38	12.1	11
1949	44	9.4	7
1950	24	10.2	17
1951	37	9.2	9
1955	40	10.7	14
2006	39	9.1	23
2007	50	10.5	--
2008	41	9.8	--
2009	43	10.1	14

Three oriented single crystals of CaF_2 grown by Harshaw Chemical Company were coated at Northrop Research Technology Center by Dr. Sam Holmes. The coating is a two-layer SiO/ThF_4 ($\lambda/4$, $\lambda/4$) AR design for 3.8 μm. These specimens offered an interesting opportunity to test the influence of orientation on the damage threshold of the coated optics. The stress birefringence of the three oriented samples will be different and this difference can be observed in the polariscopic photographs. The pre-test data available for the oriented substrate samples are listed in table 2.

Table 2. Oriented single crystal CaF_2 samples coated by Northrop.

Sample	Orientation	Thickness (cm)	Total Absorption ($\div 10^{-4}$) NRTC	Total Absorption ($\div 10^{-4}$) UDRI	Coating* Absorption (2 Surfaces)	Scattering Ratio ($\div 10^{-3}$)
2409	(100)	0.689	5.28	10.6	4.14	8.1
2410	(110)	0.639	4.41	8.4	3.59	6.9
2411	(111)	0.529	3.57	9.2	2.65	9.3

*Coating: 2-layer SiO/ThF_4 ($\lambda/4$, $\lambda/4$).

3. Data Reduction and Analysis

3.1 Power Measurements

A series of eight calibration runs was performed to relate the power measurements obtained with the three detectors and to correlate these with the burn patterns in plastic discs.

The pyroelectric detector with its rapid time response showed that the laser power was more nearly constant during the entire run than the power meter output would indicate. This is a consequence of the transient reponse of the meter which does not yield a faithful reproduction of the laser's temporal output profile.

The calibration curves for the cone calorimeter and the pyroelectric detector are shown in figures 3 and 4. The CRL meter is used as the primary standard since its calibration history was most complete. The fitted curves are lines contrained to pass through the origin. The assumption was made that zero power output represents a zero reading in all meters. The uncertainties in the prediction of the power from a cone calorimetry measurement or pyroelectric detector signal are no better than 1.5 percent for the cone and 3.2 percent for the pyroelectric detector based on the uncertainty in the determination of the calibration constant. There are other sources of error which can cause a greater uncertainty and which are not well controlled; these are changes in the alignment, principally for the pyroelectric device, and effects due to varying water flow rates or beam displacement and attenuation caused by the samples which influence the cone calorimetry signal. As a practical matter, base line drift produced a noticeable effect on the cone calorimetry readings, especially during the typical three-sample runs. The overall accuracy for a transmitted power measurement is estimated to be not better than ± 15 percent.

The slow time response and alignment problems associated with the CRL meter and the sensitivity of the pyroelectric detector to alignment, made these two devices unsuitable for measuring power. Since most of the samples had very low attenuation, absorption, and reflection losses (less than 1 percent) and the samples were finished to a high degree of parallelism, there was little difference between the incident and transmitted power. Therefore, the cone calorimeter values are used to define the measured power levels.

3.2. Beam Profile

The beam profile, including the cross sectional area, was obtained by measuring silicon rubber castings of the burn pattern in plexiglass. The burn pattern dimensions were measured with an optical comparator. The full width at half-maximum was measured along a major and minor axis (the cross section is elliptical) and found to be 0.58 and 0.46 cm (± 0.036 cm). This represents an area of 0.3 cm^2 ± 13 percent at the equivalent $1/e^2$ diameter.

3.3 Pre- and Post-Test Evaluations

Prior to testing, the samples were characterized with respect to their optical quality by measurements of absorption at 3.8 μm (DF laser), scattering at 6328 Å, surface flatness, optical path difference, spectral reflectance, and transmittance. Visual inspections were also made using a Nomarski microscope, polariscope, and transmission and oblique-incidence surface photographs. Many of these same observations were made after the tests for comparative purposes. A Schlierin optical system was also used to visualize a very subtle change in transmission properties induced by the laser. Schlierin photographs were not made prior to the tests.

4. Discussion and Conclusions

The results of the tests are summarized graphically in figure 5 in which the transmitted power and irradiation history is shown for each sample and the damaged specimens are shown as shaded squares. The interferometer and polariscope photographs are shown in figure 6. Damage is visible at the center of the specimens in these photographs. The relationship between orientation and stress patterns for the randomly oriented test specimens may be correlated by reference to the oriented CaF_2 samples. For example, sample no. 1951 probably has a (111) orientation.

There were 14 specimens tested; four were tested repeatedly at five increasing power levels, (5-on-1); while two samples were tested once at each of the power levels, (1-on-1). All six of the samples tested at the highest power (about 8 kW) suffered a subtle form of permanent damage. There is no "conditioning" effect observable for these samples and the 1-on-1 damage threshold equals the n-on-1 value.

The degradation was observed in the interferometer photographs and in transmission polariscopic or Schlierin observations. The defects were not visible in Nomarski micrographs until the surface was aluminized. A typical damage spot is shown in figure 7.

With the relatively large number of equivalent samples, we can say with better than 80 percent confidence that the damage threshold is 7 kW/0.3 cm^2 for three second irradiation. The uncertainty in this value is about ±15 percent. Since the samples did not fail catastrophically, the damage threshold is conservatively stated.

It is not normally possible to define a single threshold for damage when all possible failure mechanisms are included. It has been our custom to define mechanical damage as the observation of permanent residual strain in the sample (or other physical damage such as fractures or gross failure). The residual strain criteria is good for detecting the onset of mechanical damage in materials which undergo plastic deformation. For brittle materials like SrF_2, residual strains will normally not be observed without some other failure occurring.

It is of questionable value to give a damage threshold in terms of the power or power density, especially when it is desirable to extrapolate the results to large windows. The problem is compounded when one is using a brittle material such as SrF_2 whose failure is described in statistical terms. We would rather specify that the samples failed at a given value of temperature and stress. The failures we observed appear to be due to compression in the center of the sample over such a small area that crack propagation does not occur. The compressive stress at the center of the window was calculated to be approximately 100 Mp; (15 kpsi) with a peak temperature of approximately 98°C at the center.

We believe that the damage morphology is the result of plastic deformation in the form of (100) slip. This conclusion is inferred from x-ray analysis of a CaF_2 window

which had previously failed in service on the ACL. The slip planes, cleavage plane, and crack orientation for the single crystal window CaF_2 are shown in figure 8.

5. Acknowledgements

It is a pleasure to acknowledge the help and support of the Army Chemical Laser Facility personnel. Dr. Tom Barr was especially helpful in the administrative aspects of the tests and in seeing that everything went smoothly. The operation of the laser facility was supervised by Ben Wilson.

The laser operator and test conductor was Ed McCracken, with Tom Witset responsible for optics and laser alignment; Roy Yell was the computer operator and Tom White was responsible for the mechanical details and gas handling. A very special thanks to Ben for his competent and efficient help in every phase of the testing.

The oriented single crystal samples were prepared by Dr. Sam Holmes of Northrop Corporate Research and Technology Center with data supplied by Dr. Paul Kraatz. Dr. Richard Harmer of the University of Dayton provided the x-ray analysis. John Fenter of the Air Force Materials Laboratory was instrumental in obtaining the test time at Redstone and in supporting the conduct of these tests.

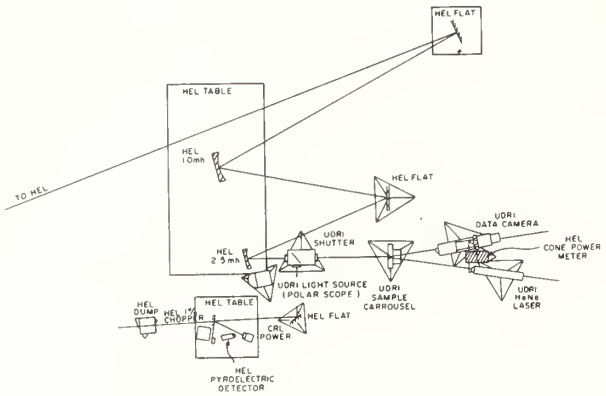

Figure 1. Experimental set-up for DF laser damage tests at the Army chemical laser. The HEL beam handling optical and beam diagnostics and the polariscope and interferometer optics are shown approximately to scale.

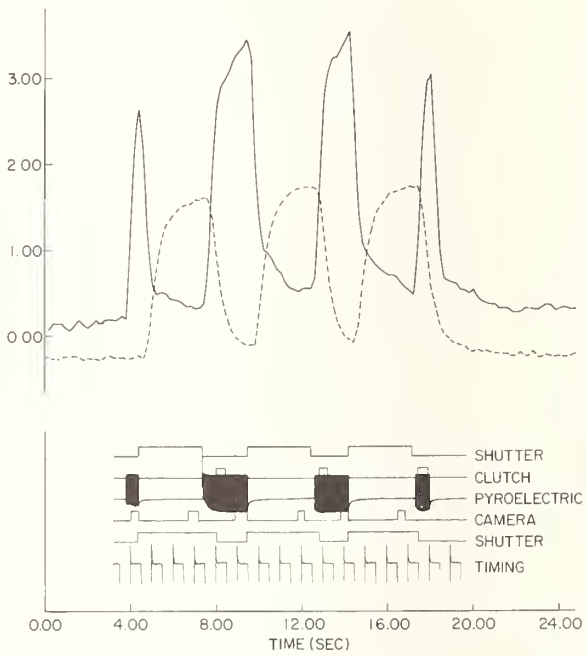

Figure 2. Graphical data output obtained during a typical damage test run. The chart record of cone calorimeter, and CRL power meters output are shown with the oscillographic record of the various timing function and fast pyroelectric detector output. This composite summarizes the quantitative data obtained during the tests and shows the temporal sequence of the significant events occurring during a typical test.

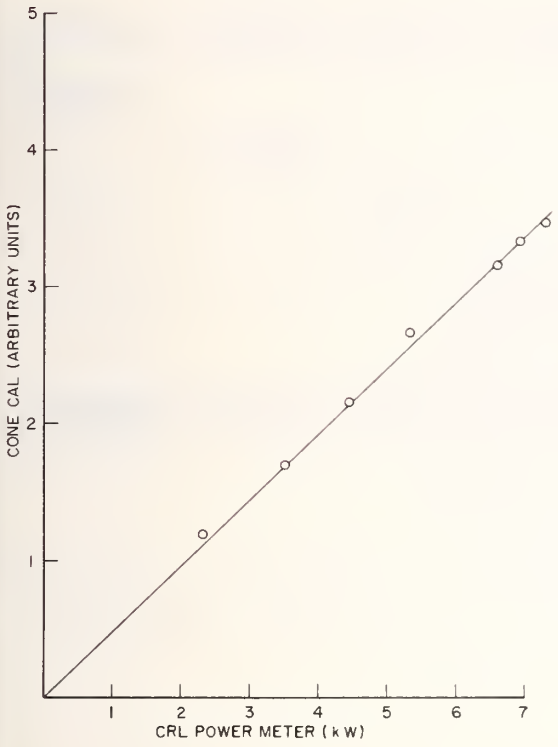

Figure 3. Cone calorimeter calibration data. The power measurements for cone calorimeter are plotted against the calibrated CRL meter readings to permit the arbitrary cone calorimeter signals to be converted to power.

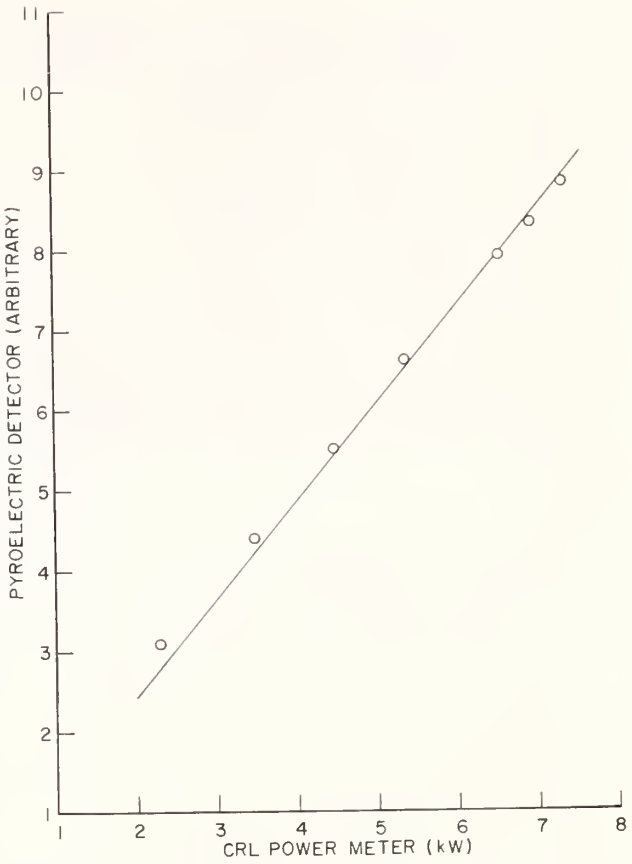

Figure 4. Pyroelectric detector calibration data. The power measurements for the pyroelectric detector are plotted against the calibrated CRL meter to permit the arbitrary pyroelectric detector signals to be converted to power.

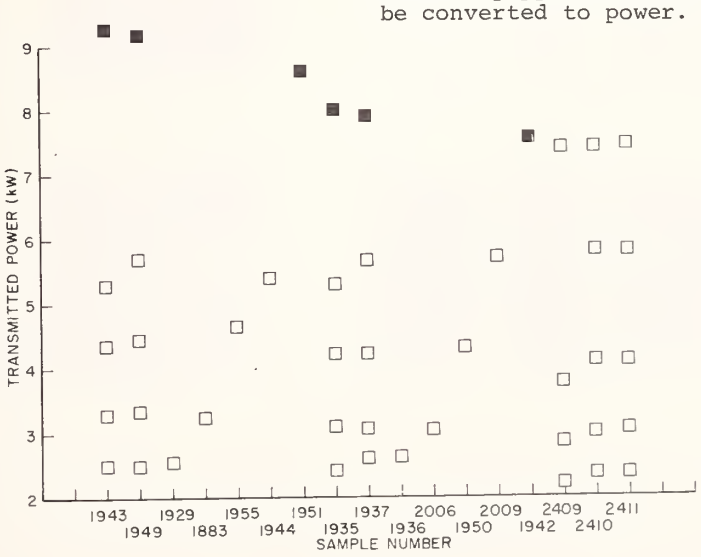

Figure 5. Summary of AR coated SrF_2 sample tests. The transmitted power levels associated with every irradiation on each of the AFML supplied samples are shown as square symbols. The shaded squares represent the observation of permanent mechanical deformation - plastic deformation of the surface for these samples.

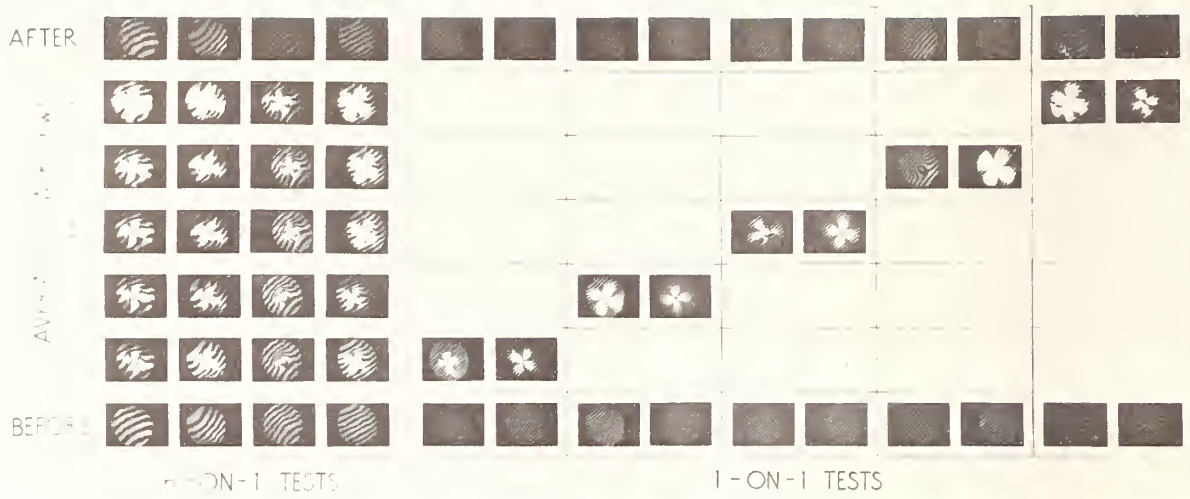

Figure 6a. Composite interferometer-polariscope photographs for the AR coated SrF_2 samples. Permanent deformation near the center of the specimens irradiated at the maximum power level is seen in each of the specimens irradiated at 8 kw. Samples irradiated at lower power levels are not damaged. Although these samples did not fracture - they have been permanently damaged. The third specimen from the right is Sample No. 1951. Note the absence of a strain pattern.

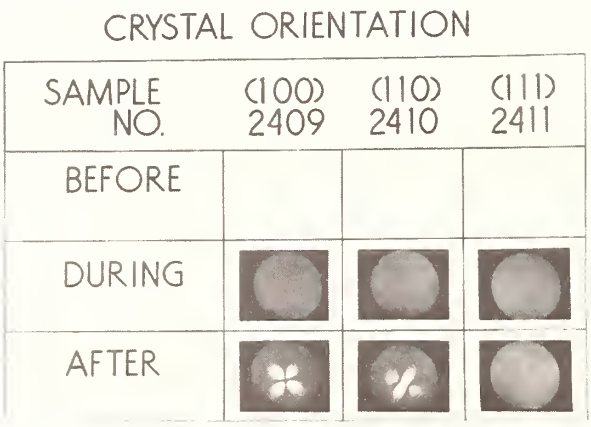

Figure 6b. Composite interferometer-polariscope photographs for oriented single crystals of CaF_2. The relationship between the plane polariscope pattern and the crystal orientation for CaF_2 is clearly shown in these photographs which permit the reader to determine the orientation of the other samples shown in Figure 6a. The interferometer fringes are not visible in these photographs.

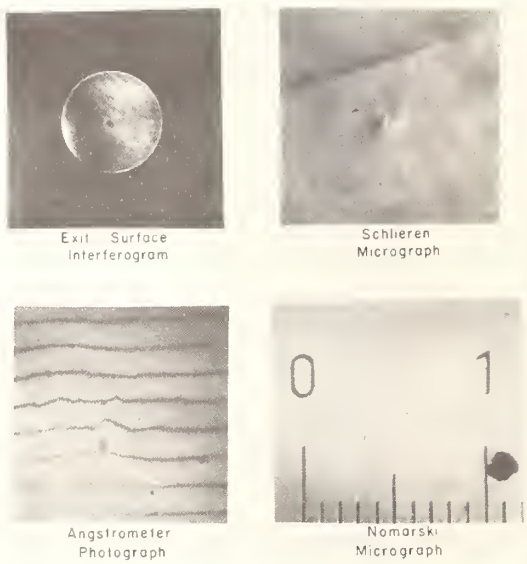

Figure 7. Composite photograph showing the results of several methods applied to make the damage site visible. The scale in the Nomarski micrograph is 1 mm. The Angstrometer photograph is taken with green Hg light. The surface was aluminized in all but the Schlieren image.

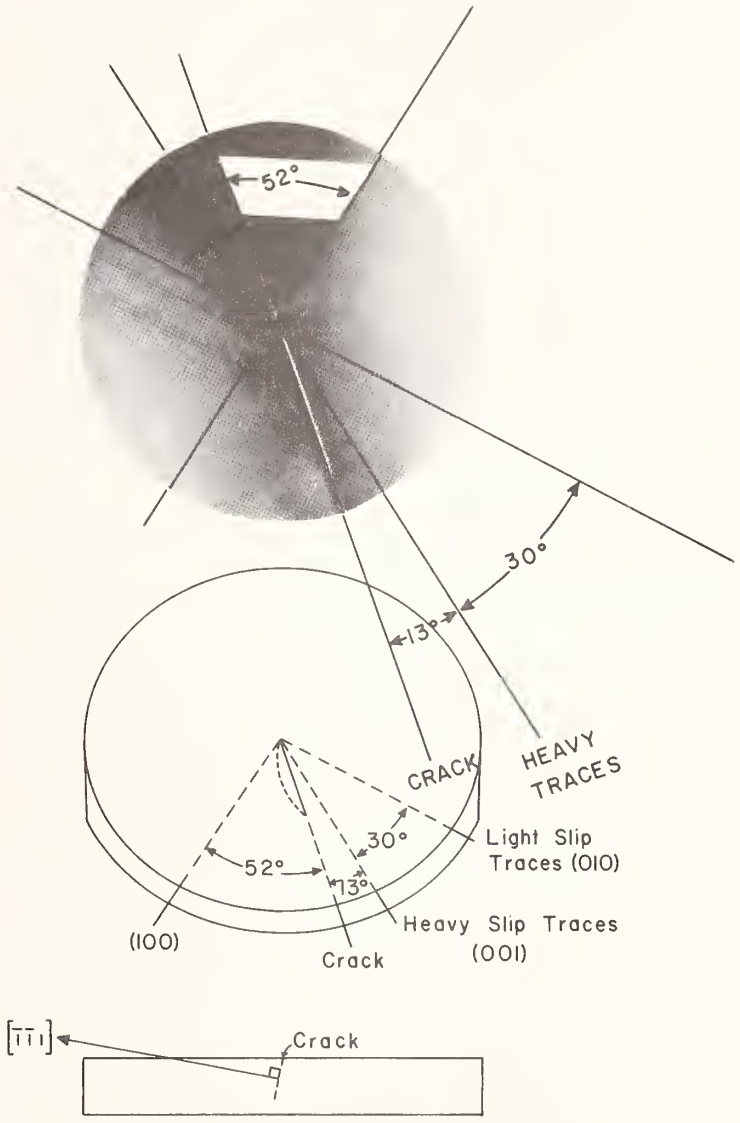

Figure 8. The slip traces and crack orientation for a CaF_2 window are shown superimposed on a photograph of the specimen. The orientations were determined by the analysis of Laue back reflection X-ray photographs. These slip traces cover a larger area than those shown in Figure 7. The specimen image diameter is about 1 cm.

LATTICE ABSORPTION, PHONON ASSIGNMENTS, AND IMAGE SPOILING PROPERTIES OF CVD ZnS IN THE INFRARED

C. Klein, B. diBenedetto, R. Donadio, T. Kohane, and J. Pappis
Research Division, Raytheon Company
Waltham, Massachusetts 02154

Chemical-vapor-deposited zinc sulfide (CVD ZnS) has been established as a highly promising material for advanced infrared imaging applications and is attracting attention as a potential window material at HF/DF laser wavelengths. The present contribution concerns work that has been carried out in the context of assessing the optical characteristics of CVD-ZnS blanks, particularly with regard to: (a) lattice absorption. Careful examination of transmission traces at wavelengths up to 25 μm indicates that multiphonon processes dominate at frequencies below 1000 cm^{-1}; peak-absorption assignments in terms of zone-boundary phonons have been made on the basis of best available inelastic neutron-scattering results for zincblende ZnS. (b) Temperature dependence. Absorption coefficients at temperatures up to 600K have been investigated in light of spectral transmittance and emittance measurements supplemented by calorimetric data at HF, DF, CO, and CO_2-laser wavelengths. (c) Image spoiling. Line-spread functions in conjunction with index-inhomogeneity maps demonstrate that wavefront distortions resulting from the presence of a CVD-ZnS window do not inject any detectable degradation in contrast transmittance.

Key words: Characteristic phonons; chemical-vapor deposition; image spoiling; infrared imaging; lattice absorption; zinc sulfide.

1. Introduction

In recent years, work on chemical-vapor-deposited zinc sulfide (CVD ZnS) has resulted in the development of a material that shows much promise for applications involving windows and domes, in the area of passive infrared systems operating in the 8- to 12-μm spectral passband [1].[1] We note, in particular, that the capability to produce optically finished CVD-ZnS blanks in the sizes required for large-aperture/high-resolution thermal imagers has been demonstrated, and that cost-effective manufacturing techniques have been established. In addition, it has been shown that CVD-ZnS windows capable of satisfying structural requirements stemming from the mechanics of high-speed flight maintain sufficient transmittance to insure that any window-induced degradation in system sensitivity will remain tolerable, over the whole range of anticipated thermal loads.

In a previous paper [2], we have examined how aerodynamically heated windows may affect the thermal sensitivity as a result of gross attenuation of incident signal radiation in addition to enhanced background radiation originating from the window emittance in the wavelength region of system operation. In effect, we have shown that AR-coated CVD-ZnS windows can degrade the electrical signal-to-noise ratio of operational IR systems via two mechanisms: (a) a first-order reduction in target signal reflecting radiation absorption by the window, and (b) a second-order degradation in system detectivity reflecting the additional quantum noise generated by window photons. It was also pointed out that, in order to avoid injecting a significant loss of resolution in the optical image, the window must satisfy strict requirements in terms of spatial-contrast transmittance characteristics.

At this point, it should be said that the degradation in signal-to-noise ratio can be evaluated in rather general terms, as specific features of the optical arrangement other than those relating to the spectral passband do not enter the calculation. In reference [2], we have shown that, for systems operating in a photon-noise limited mode, difficulties arising in evaluating the signal-to-noise ratio (SNR) in the presence of a "hot window" can be avoided by considering an SNR defined as the ratio of H_{eff} and NEI, where H_{eff} represents an effective signal irradiance for extended targets, and NEI is the noise-equivalent irradiance at the peak-response wavelength of the detector. In this manner, we find that the degradation involves a reduction in target signal and an increase in system noise best expressed as follows:

1. Figures in brackets indicate the literature references at the end of this paper.

$$\frac{(H_{eff})_W}{(H_{eff})_0} = \frac{\int_{\lambda_1}^{\lambda_2} \mathbf{T}(\lambda, T_W)\, W_\lambda(T_B)\, d\lambda}{\int_{\lambda_1}^{\lambda_2} W_\lambda(T_B)\, d\lambda} \tag{1}$$

and

$$\frac{(NEI)_W}{(NEI)_0} = \left[\frac{\int_{\lambda_1}^{\lambda_2} \mathbf{E}(\lambda, T_W)\, Q_\lambda(T_W)\, d\lambda + \int_{\lambda_1}^{\lambda_2} \mathbf{T}(\lambda, T_W)\, Q_\lambda(T_B)\, d\lambda}{\int_{\lambda_1}^{\lambda_2} Q_\lambda(T_B)\, d\lambda} \right]^{\frac{1}{2}}, \tag{2}$$

where $\mathbf{T}(\lambda, T_W)$ measures the transmittance of the window and $\mathbf{E}(\lambda, T_W)$ its emittance.[2] In the same vein, and since the modulation-transfer function (MTF) of the system includes contributions originating from all the components [3], it is immediately seen that the MTF of a "bare" system must be multiplied by the transfer function of the window in order to arrive at an overall modulation-transfer function:

$$(MTF)_W = \tilde{r}_W (MTF)_0 . \tag{3}$$

Equation (3) implies that scattering and other image-spoiling properties of IR window material can be characterized by means of a spatial transfer function, $\tilde{r}_W$, which establishes the precise effect of a window blank on the resolution performance of the optical system.

The importance of accurately measuring the optical properties of CVD ZnS becomes evident upon considering eqs. (1, 2, 3) because they involve the emittance, the transmittance, and the transfer function of the window material. With regard to emittance and transmittance, it will be kept in mind that, in the case of AR-coated windows of thickness t, the following holds: $\mathbf{E} = 1 - \exp(-\beta t)$ and $\mathbf{T} = \exp(-\beta t) - \mathbf{R}$, if $\mathbf{R}$ is indicative of the residual surface reflectance and β is the bulk absorption coefficient. For this reason, it will be the primary purpose of this paper to consider information relating to β and to assess in detail some critical features of the absorption spectrum at the multiphonon edge of CVD (or cubic) ZnS. In connection with the matter of transfer functions, we may emphasize that, in the process of creating a new optical material, standard properties such as the spectral transmittance are usually the first to be investigated and form the basis upon which potential applications are to be developed. With high-sensitivity/high-resolution systems, however, image spoiling caused by light scattering, index inhomogeneities, and other imperfections may seriously impact the usefulness of candidate IR transmitting materials [4] and must be carefully assessed from the point of view of their significance relative to aperture-diffraction effects. This is best done by specifying the performance of the blank in terms of a line-spread function (LSF) since LSF yields the transfer function simply by taking the Fourier transform.

In section 2, we first examine some general characteristics of room-temperature transmission spectra for state-of-the-art CVD ZnS and derive absorption coefficients over a wave number range extending from 400 to 1400 cm^{-1}. An analysis of the spectrum is then carried out (sec. 3) on the basis of the best available lattice-dynamics model, that is, on the basis of neutron-scattering data and density-of-states calculations by Vagelatos et al. [5]. Specifically, it will be shown that all significant features of the two-phonon absorption regime can be assigned to summations at critical points in the Brillouin zone, thus yielding accurate frequencies for the phonon modes at high-symmetry locations.[3] In section 4, we present transmittance and emittance data obtained at elevated temperatures and discuss their implications in the light of laser-calorimetry results; it thus will be demonstrated that, beyond 10 μm, structure in the absorption spectrum of CVD ZnS is indeed due to intrinsic multiphonon processes. Information of significance in terms of image spoiling (sec. 5) will be considered from the point of view of IR systems requirements as well as index-inhomogeneity measurements. Finally, section 6 includes the summary and our conclusions.

---

2. This, of course, assumes that both window and background are at uniform temperatures T_W and T_B, respectively.

3. For an elementary discussion of these concepts, see reference [6].

2. Room-Temperature Features

2.1 Spectral Transmittance

Figure 1 shows the infrared transmission profile of three specimens of CVD ZnS ranging in thickness from 0.25 to 1.30 cm; such traces are typical of serial production material deposited at a temperature of 675°C, a furnace pressure of 40 Torr, and a large excess of zinc vapor. These measurements, which were carried out on a carefully calibrated Perkin-Elmer spectrophotometer (model no. 457) operating in the double-beam mode, immediately reveal that there is absorption, or attenuation, at all wavelengths in the infrared. Most prominent is the broad band centered at 1600 cm^{-1}, which is also observed in chemical-vapor-deposited ZnSe, and has been tentatively attributed to vibrational modes associated with residual zinc hydride radicals [7] . In the wavelength region of interest for thermal imaging (8 to 12 μm), we note that, beyond 10 μm, there is a substantial increase in absorptance, which is known to be caused by multiphonon processes [8] and, consequently, imposes intrinsic limitations on the performance of ZnS windows. In effect, the "tailing off" that occurs between 10 and 15 μm may well reflect summations involving three phonons, considering that the high-frequency cutoff for two-phonon absorptions should be at 2 x LO(Γ) = 704 cm^{-1} if the Raman phonon is as indicated by Nilsen [9] . In that case, the structure that emerges in the 900 cm^{-1} wavenumber region emphasizes the role of covalen bonding in ZnS and should be amenable to further interpretation (sec. 3) in the context of a comprehensive investigation of lattice absorption in this material.

For this purpose, we have obtained the transmission profiles of a set of progressively thinner samples in order to extend the range of available CVD-ZnS absorption data into the two-phonon region. Figu 2 displays the far-infrared transmittance trace of our thinnest specimen (0.018 cm), which illustrates the dominance of structure in the absorption at wavelengths above 15 μm. In section 3, it will be shown that this tracing yields appropriate information for initiating a critical point analysis of the phonon spectr in cubic ZnS.

2.2 Absorption Coefficients

For near-normal incidence, and in the absence of interference effects, the classic expression for the transmittance of an optical blank is

$$\mathbf{T} = \frac{(1-R)^2 \exp(-\beta t)}{1-R^2 \exp(-2\beta t)}, \tag{4}$$

which takes multiple internal reflections into account. The absorption coefficient β,

$$\beta = \frac{1}{t} \cdot \ln\left\{\frac{(1-R)^2}{2\mathbf{T}} + \left[R^2 + \frac{(1-R)^4}{4\mathbf{T}^2}\right]^{\frac{1}{2}}\right\}, \tag{5}$$

may thus be derived from the measured transmittance if the single-surface reflectivity R is available as a function of wavenumber. Our work assumes that the reflectivity can be simply expressed in terms of the refractive index, $R = (n-1)^2/(n+1)^2$, with an index as given by Dodge [10] :

$$n = \left[1 + \sum_{j=1}^{3} \frac{A_j \lambda^2}{\lambda^2 - \lambda_j^2}\right]^{\frac{1}{2}}, \tag{6}$$

where the A_j's and λ_j's are empirically determined constants. In this connection, we note that the coefficient of extinction does not enter the calculation because k^2 remains much smaller than $(n-1)^2$ at all relevant wavenumbers, as can be ascertained by referring to figure 3. Furthermore, we may point out that CVD ZnS exhibits maximum transmittance between 8.0 and 8.5 μm, with thin specimens ($t \leq 0.06$ cm) having transmittances of 0.747± 0.001. On assuming zero absorptance, the theoretical transmittance, $\mathbf{T} = 2n/(n^2+1)$, is 0.748± 0.001, which indicates that the losses are almost exactly as expected from Fresnel reflections, thus implying that any form of scattering should play an insignificant role in the wavelength range of interest.

In figure 3, the absorption coefficients are plotted against wavenumber over a frequency range covering the two-, three-, and four-phonon regimes. This spectrum actually represents a "composite" formed by joining the best segments of three data sets derived from eq. (5) on using the transmittances

of three specimens ranging in thickness from 0.018 to 1.59 cm. This procedure has allowed us to map the absorption with great accuracy, especially at the wavelengths of relevance in terms of thermal imaging technology. The spectrum displays a multiphonon-like behavior with structural features that are characteristic of semiconductors [11], up to wavenumbers of about 1000 cm^{-1}. Beyond that point, there is little change with frequency, presumably because of the presence of a weak absorption band at 1100 cm^{-1}, which can be attributed to ZnO impurities. Towards shorter wavelengths ($\lambda < 8$ μm), CVD ZnS invariably shows evidence of increasing absorption, which reflects the dominance of the long-wavelength wing of the zinc hydride impurity.

2.3 Laser Calorimetry

The results of thermocouple-calorimetry measurements conducted at standard laser frequencies on a number of CVD-ZnS samples originating from three different deposition runs are listed in table 1. At both CO_2-laser wavelengths, the calorimetry data are in good agreement with the absorption coefficients

Table 1. Room-temperature laser calorimetry results for CVD ZnS.

Laser wavelength (μm)	Absorption coefficient (cm^{-1})
2.7 (HF)	$(7.2 \pm 0.5) \times 10^{-3}$
3.8 (DF)	$(2.3 \pm 0.5) \times 10^{-2}$
5.25 (CO)	$(4.5 \pm 1.1) \times 10^{-2}$
9.27 (CO_2)	$(7.9 \pm 1.3) \times 10^{-2}$
10.6 (CO_2)	$(2.4 \pm 0.1) \times 10^{-1}$

derived from transmission traces (see fig. 3) and, by the same token, they verify our procedure for interpreting spectrophotometer data. At chemical laser wavelengths, the present results point to substantially lower absorptions compared to those reported by Harrington [12] for an "early" specimen of RAYTRAN ZnS; still, they remain too high from the point of view of establishing CVD ZnS as a credible window-material candidate for high-energy lasers.

At this point, we may emphasize that the absorption coefficients in figure 3 are indicative of state-of-the-art material, even though some non-uniformity has been observed in the impurity-dominated region, for samples cut from similar deposits. It would appear, therefore, that the CVD-ZnS data of Bendow et al. [11] are not quite compatible with experimental evidence outlined here. In this regard, it should be kept in mind that inaccurate assumptions on the wavenumber dependence of the refractive index may lead to relatively large errors in deriving absorption coefficients, since eq. (5) becomes essentially a function of the reflectivity R, for small values of β.

3. Critical-Point Analysis

Chemical-vapor-deposited ZnS crystallizes in the zincblende system. The recent phonon-dispersion data of Vagelatos et al. [5] are therefore applicable and provide highly reliable guidelines from the point of view of doing a critical-point analysis of the two-phonon absorption spectrum displayed in figure 2. Earlier attempts of this nature include the work of Johnson [13] and of Irwin [14] but these authors both rely on the low-temperature data of Deutsch [8]. First, it will be recalled that "critical points" are located at zone-edge positions such as X (1, 0, 0), L(1/2, 1/2, 1/2), and W (1, 1/2, 0), in addition to the position Γ (0, 0, 0) at the center of the Brillouin zone. If allowed by selection rules, frequencies corresponding to multiple-phonon combinations at these points should give rise to "features" in the infrared absorption spectrum, such features reflecting singularities in the multiple-phonon density of states. Both electric-dipole and electric-quadrupole allowed transitions in zincblende have been worked out by Birman [15]; the reader may consult this paper for clarification of concepts and notations used here.

The two tables on the next page (table 2 and table 3) summarize the results of our analysis of two-phonon absorptions in cubic ZnS.

- The strong absorptions centered at 668, 636, and 596 cm^{-1} are assigned to overtones of LO and TO modes, keeping in mind that LO overtones are dipole-forbidden at point X.
- Electric-dipole allowed two-phonon summations at the highest-symmetry zone-edge points (X and L) have all been identified and assigned in accordance with the lattice-dynamics model described in reference [5].
- The features at 662, 612, and 602 cm^{-1} are assigned to quadruple-allowed optical phonon overtones occuring near point W, thus demonstrating the effect of non-linearities in the electric moment on the IR absorption spectrum of ZnS.

Table 2. Critical-point analysis, two-phonon IR spectrum of cubic ZnS.

(k = kink, m = minimum, s = shoulder)

Feature (see fig. 2)	Measured position (cm^{-1})	Phonon assignment	Calculated position (cm^{-1})	Comment (see note)
1 (k)	704	2 LO (Γ)	704	
2 (m)	668	2 LO (L)	668	Raman active
3 (s)	662	2 O_1 (W)	662	Quadrupole
4 (s)	650	LO (X) + TO (X)	650	
5 (m)	636	2 TO (X)	636	LO(L) + TO(L)?
6 (s)	612	2 O_2 (W)	612	Quadrupole
7 (m)	602	2 O_3 (W)	602	Quadrupole
8 (m)	596	2 TO (L)	596	
9 (k)	544	LO (X) + LA (X)	544	
10 (s)	530	TO (X) + LA (X)	530	
11 (s)	526	LO (L) + LA (L)	526	
12 (m)	488	TO (L) + LA (L)	490	
13 (m)	450	O_1(W) + A_2(W)	450	Raman active
14 (k)	420	LO (X) + TA (X)	420	Raman active
15 (s)	406	TO (X) + TA (X)	406	LO(L) + TA(L)
16 (s)	386	2 LA (L)	384	Raman active

Note: Features at 636 and 612 cm^{-1} are also Raman active.

Table 3. Critical-point phonon frequencies (cm^{-1}) in cubic ZnS.
The lattice-dynamics data are those of reference 5.

Critical point	Phonon branch	Lattice dynamics	IR spectrum
Γ	LO	348 ± 5	352
	TO	277 ± 3	---
X	LO	330 ± 3	332
	TO	316 ± 3	318
	LA	212 ± 3	212
	TA	90 ± 1	88
L	LO	337 ± 8	334
	TO	289 ± 3	298
	LA	195 ± 3	192
	TA	70 ± 1	72
K/W	O_1	330 ± 5	331
	O_2	308 ± 5	306
	O_3	302 ± 5	301
	A_1	194 ± 2	---
	A_2	117 ± 2	119
	A_3	87 ± 1	---

- Some of the assignments listed in table 2 also apply to Nilsen's [9] second-order Raman spectrum and do reflect the polarization situation.

- With the possible exception of the TO(L) mode, phonon energies derived from the IR spectrum agree remarkably well with the results of neutron-diffraction work (see table 3) and yield more accurate critical-point frequencies.

- The mode frequencies at point W have not yet been established on a "lattice dynamics" basis; relevant "IR spectrum" assignments rely on point K frequencies as given by Vagelatos et al. [5].

In the three-phonon region (see fig. 4), structural features are seen to be much less prominent, which suggests that, initially, it should be more meaningful to analyze the absorption in terms of characteristic phonons [6] rather than relying on a complete set of critical phonons. For this purpose, we can make use of a recent phonon density-of-states calculation for ZnS [5] and postulate that structural features at the lower levels of absorption relate to four main peaks in the density-of-states curve. In other words, we proceed on the basis that the gross features of the three-phonon absorption process can be interpreted in terms of combinations of the four characteristic phonons listed in table 4. In this

Table 4. Characteristic zone-edge phonons in cubic ZnS.

Phonon branch:	LO	TO	LA	TA
Mode frequency (cm^{-1}):	330	295	193	89

approximation, and in light of some pertinent observations by Bendow et al. [11], it appears reasonable to entirely ignore selection rules and assign each possible combination strictly on the basis of summation energies. The procedure is illustrated in figure 4 and discloses a number of impressive correlations; specifically, we note that the prominent absorption band at 885 cm^{-1} can be attributed to TO overtones, which clearly identifies the phonon branch that is responsible for the loss in transmittance experienced at around 11 μm with CVD-ZnS windows. In addition, it is seen in figure 4 how impurity-induced absorption affects the level of transmission at wavelengths below 10 μm, since four-phonon processes should not alter the transmittance in any significant way.

4. Elevated-Temperature Features

4.1 Spectral Transmittance

The temperature dependence of photon absorption at the multiphonon edge of cubic ZnS was first considered by Deutsch [8] and subsequently reinterpreted by Marshall and Mitra [16] in terms of tentative characteristic zone-edge phonons. From a practical point of view, the situation is best summarized as in figure 5, which exhibits long-wavelength spectral transmittance traces for CVD ZnS at temperatures ranging from 22° up to 200°C. These measurements were conducted in the usual fashion, with a small furnace placed close to the focal point of the spectrophotometer; at wavenumbers below 800 cm^{-1}, corrections were made for eliminating spurious contributions originating from the sample's self-emittance.

The behavior of the absorption band at 885 cm^{-1} warrants further investigation: The band broadens and shifts its position to lower wavenumbers as the temperature increases. Considering the results of section 3, this band must be attributed to a three-phonon process, specifically, to a 3 x TO summation with TO referring to a characteristic transverse optic mode of frequency ω_o, at the zone boundary. The data presented in figure 5 then indicate that we have $(1/\omega_o)(d\omega_o/dT) \approx -6 \times 10^{-5} K^{-1}$, or essentially the same type of "mode softening" as reported for optical phonons in ZnSe.[4] In this connection, we note that the temperature dependence of the mode frequency originates mainly from thermal expansion and is given by [18]

$$\omega(T) = \omega(O) \exp\left(-3\gamma \int_o^T \alpha \, dT\right) \tag{7a}$$

or

$$(1/\omega)(d\omega/dT) = -3\gamma\alpha , \tag{7b}$$

where α is the linear coefficient of thermal expansion and γ is the mode Grüneisen parameter. With $\alpha = 7.85 \times 10^{-6} K^{-1}$ [1] and $\gamma \approx 1.8$ [19], it follows that the calculated value of $(1/\omega_o)(d\omega_o/dT)$ should be

4. See, for instance, ref. [17].

on the order of $-4 \times 10^{-5} K^{-1}$ and, thus, consistent with our experimental results. This assumes, however, that the Grüneisen parameter does not show much dispersion, as the work in reference [19] only concerns long-wavelength ($\underset{\sim}{k} \approx 0$) lattice vibrational modes.

4.2 Spectral Emittance

The use of emittance techniques for investigating optical properties of solids is now well established [20] and rests primarily on exploiting the basic emittance equation,

$$\mathbf{E} = \frac{(1-R)[1-\exp(-\beta t)]}{1-R\exp(-\beta t)}, \tag{8}$$

for spectroscopic purposes. An application to CVD ZnS in the 0° to 100°C temperature range is illustrated in figure 6. First, we note that the zinc hydride band at 6 μm exhibits little dependence on temperature, which confirms that we are dealing here with a molecular impurity. Also of interest are the following observations:

(a) In the 8- to 10-μm range, there is virtually no change in emittance with temperature, and the levels involved are sufficiently low to allow us to extract absorption coefficients simply from the $\mathbf{E} = \beta t$ approximation. We thus obtain β's as listed in table 5, which are in satisfactory agreement with values derived from room-temperature spectrophotometry as well as laser calorimetry (see sec. 2).

Table 5. CVD-ZnS absorption coefficients derived from emittance measurements.

IR wavelength (μm):	8.0	9.0	10
Absorption coefficient (cm^{-1}):	0.043	0.074	0.11

(b) The emittance peak at 11 μm reflects the multiphonon (3 x TO) absorption process described earlier, and is seen to shift towards longer wavelengths as the temperature increases, thus confirming the mode-softening trend.

(c) Beyond 14 μm, we note that the emittance reaches a plateau, which is characteristic of an opaque spectral region. In such situations, eq. (8) reduces to $\mathbf{E} = 1-R$ and becomes a function of the index of refraction only. At 0°C, the average emittance of CVD-ZnS specimens originating from three depositions turns out to be 0.87 at 15 μm, which is precisely the amount anticipated for an index ($n = 2.11$) as obtained from eq. (6); at higher temperatures, however, the emittance appears to decrease at a faster rate than predicted on the basis of available dn/dT data [10].

4.3 Temperature Dependence

Around 10 μm, the temperature dependence of the absorption coefficient of CVD ZnS can be established quite accurately by means of laser calorimetry. The results of such experiments, at 10.6 and 9.27 μm, are displayed in figure 7. In conjunction with the 10.6-μm data, we have also plotted some absorption coefficients obtained from the transmittance and the emittance curves of figure 5 and figure 6; note that the IRTRAN-2 data point refers to hot-pressed ZnS and was derived from an emittance measurement [21] by means of the Stierwalt-Potter equation [20].

Consider now a multiphonon-like absorption involving p emitted phonons: If $h\nu$ is the energy of an incident photon, this means that the phonons must have an average energy $\hbar\omega_o = h\nu/p$. Since the probability of a photon absorption resulting in the creation of p "average" phonons is proportional to $[1+N(\hbar\omega_o)]^p$ whereas the probability of a photon emission induced by the destruction of p phonons is proportional to $[N(\hbar\omega_o)]^p$, it follows that, in terms of absorption coefficients we have [6]

$$\beta \propto [1+N(\hbar\omega_o)]^p - [N(\hbar\omega_o)]^p, \tag{9}$$

where N represents the Bose-Einstein function. Furthermore, we take it that the matrix element expressing the transition probability is nearly temperature independent, which leads to the conclusion that eq. (9) can be utilized to specify the temperature dependence of an absorption involving a fixed number of phonons.[5] In figure 7 we show the results of an evaluation of eq. (9) in the three-phonon

5. This approach ignores the temperature sensitivity of normal modes and may not be valid at excessively high temperatures.

regime (upper part), on assuming incident radiation of 10.6 to 12 μm, and for the four-phonon regime (lower part) in the case of photons of 1079 cm^{-1}. The comparison with experimental results confirms that, in the three-phonon region, the absorption is near intrinsic and increases exponentially with temperature as predicted by the model. At 9.27 μm, however, the absorption exhibits a much weaker dependence than intrinsic mechanisms thus demonstrating that, below 10 μm, the bulk of the absorption in CVD ZnS must be due to phenomena involving defects and/or impurities, which are not easily removed through improvements in the deposition procedure.

5. Modulation-Transfer Function

From an image-spoiling point of view, the performance of an optical blank is best specified in terms of a line-spread function because this information immediately yields the transfer function: $\tilde{r}_W = \mathcal{F}\{LSF\}$. The procedure is illustrated in figure 8, which refers to early long-wavelength data for a thick (5/8 in.) slab of CVD ZnS, at near-normal incidence. Note that we are showing here single-pass bulk material data as obtained after removal of diffraction, detector, and target-aperture effects on the convolution. The width of the line-spread tracing at the 15 percent points is 47 μrad and measures the size of the window-material blur spot in the sense that, on assuming Gaussian distributions, this spot contains 84 percent of the transmitted energy [22]. Since this fraction corresponds to the diameter of the first dark ring of the Airy disk, $2\rho_1 = 2.44(\bar{\lambda}/D)$, it follows that the "resolution" of CVD ZnS as displayed in figure 8 is equivalent to the theoretical diffraction blur of a 20-in. diameter aperture, at an average wavelength of 10 μm. However, it should be emphasized that Gaussian fits such as

$$LSF = \exp(-z^2/2\sigma_W^2) \tag{10 a}$$

and

$$\tilde{r}_W = \exp(-2\pi^2\sigma_W^2 f^2) \tag{10 b}$$

do not provide an accurate description of CVD-ZnS image-spoiling features at high spatial frequencies ($f > 5$ cy/mr).

Actually, recent progress in establishing process conditions leading to optimized CVD material has resulted in the production of large blanks of ZnS, which exhibit essentially no spoiling. As evidenced in figure 9, the presence of a 10-in. diameter window at the entrance aperture of an MTF test system does not have any significant effect on the contrast transmittance, even at spatial frequencies as high as 20 cy/mr, which correspond to the optics cutoff of our system. This is in sharp contrast to the situation experienced with large-diameter germanium components, which have been reported to inject additional losses of some 40 percent in the MTF of long-wavelength thermal imaging devices [23].

In this context, we have also examined some independent index-variation measurements involving 10.6-μm interferometry (see table 6). This typical set of data points to Δn's in general accord with the refractometry work done at NBS [10], which indicates that two specimens of CVD ZnS prepared under quite dissimilar conditions exhibit differences in Δn of at most 1×10^{-4}, throughout the useful wavelength range. Root-mean-square Δn's obtained from Δn "maps" show an interesting pattern in the sense that the $(\Delta n)_{p/v}:(\Delta n)_{rms}$ ratios are always close to 4.5, as seems to be the case for many IR transmitting materials [24]. Wavefront distortions caused by index inhomogeneities are best expressed in terms of

Table 6. Index homogeneity and wavefront distortion (8-in. diameter, 5/8-in. thick CVD-ZnS disk).

Index homogeneity:	$(\Delta n)_{p/v}$	$= 1.3 \times 10^{-4}$
	$(\Delta n)_{rms}$	$= 0.29 \times 10^{-4}$
Wavefront distortion:	$(OPD)_{p/v}$	$= 0.20^*$
	$(OPD)_{rms}$	$= 0.044^*$
Strehl ratio:	i	$= 0.92$

*In wave units at a wavelength of 10.6 μm.

optical path differences (OPD) across the specimen and are most conveniently measured in wavelength units, $OPD = (t/\lambda)\Delta n$. In table 6 it is seen that our windows are in fact diffraction limited, both in the sense of Rayleigh $[(OPD)_{p/v} < \lambda/4]$ and in the sense of Maréchal $[(OPD)_{rms} < \lambda/14]$. Furthermore, since optical designers often assess the effect of solid windows on the system performance in terms of Strehl ratios,

$$i = 1 - [2\pi (OPD)_{rms}]^2, \tag{11}$$

we may point out that a Strehl of 0.92 (see table 6) should not degrade the MTF by more than a few percent, at any resolution frequency, and in accord with direct evidence produced in figure 9.

Refractive index variations derived by means of interferometry represent Δn variations averaged over the thickness of the optical blank. If one assumes that these "average" Δn's reflect local, in-plane variations in density, the connection can be established via the Lorentz-Lorenz law, which states that [24] the fractional change in density that causes an index inhomogeneity Δn is given by[6]

$$\frac{\Delta\rho}{\rho} = \frac{6n}{(n^2-1)(n^2+2)}\Delta n \quad . \tag{12}$$

In this light, it would appear that, for $n = 2.19$, we may anticipate a relationship such as $\Delta\rho/\rho \approx \Delta n/2$. Preliminary indications on density fluctuations in CVD-ZnS material originating from three different deposits shows that $\rho = (4.08335 \pm 0.00020)$ g · cm^{-3} or $\Delta\rho/\rho \approx 5 \times 10^{-5}$. We conclude that index inhomogeneities should be on the order of 1×10^{-4}, which is definitely compatible with the bulk of available evidence on Δn in CVD ZnS.

6. Conclusion

The optical properties of CVD ZnS are of considerable importance in contemporary IR technology, and suitable test facilities have been established in order to monitor the production of large-size blanks. For instance, the significant factors that determine the performance of CVD-ZnS windows in a thermal-imaging application include the transmittance, emittance, and image-spoiling characteristics of the window material, in the 8- to 12-μm wavelength region. This paper gives an account of work that has been carried out in this context, particularly with regard to assessing lattice-absorption processes.

- Room-temperature absorption coefficients derived from spectrophotometer tracings, emittance spectroscopy, and laser calorimetry are in good agreement, throughout the wavelength range of primary interest.
- Both wavenumber and temperature dependence of the absorption demonstrate that intrinsic multi-phonon phenomena control the transmittance/emittance at wavelengths above 10 μm.
- A total of 16 two-phonon summation bands has been identified at wavenumbers less than $2 \times LO(\Gamma) = 704$ cm^{-1}; a critical-point analysis yields zone-boundary phonon frequencies in excellent accord with dispersion data obtained by other methods.
- Three-phonon processes evidenced at the lattice-absorption edge of massive ZnS deposits evolve from four (4) major singularities in the density-of-states spectrum; the strong absorption band at 885 cm^{-1}, in particular, can be attributed to a summation of three (3) characteristic TO phonons.
- Line-spread functions of state-of-the-art CVD-ZnS blanks demonstrate that scattering and other potential image-spoiling properties of this material do not inject any detectable degradation in system MTF, at spatial frequencies of relevance in contemporary high-resolution thermal imaging applications.
- Index-homogeneity maps generated by CO_2-laser interferometry confirm that the transfer function of full-size CVD-ZnS windows is indeed diffraction limited in the 8- to 12-μm spectral region.

6. This assumes that the wavelength of interest is sufficiently removed from both absorption edges, which is indeed the case for ZnS at 10.6 μm, and, furthermore, that the material is free of strain and/or second-phase inhomogeneities.

7. References

[1] diBenedetto, B., Pappis, J., and Kohane, T., Proc. IRIS 20, 543 (1977). This paper is unclassified.

[2] Klein, C. A., in Proc. 1976 Infrared Imaging Meeting (ERIM, Ann Arbor), p. 37. This paper is unclassified.

[3] Lloyd, J. M., Thermal Imaging Systems (Plenum, New York, 1975), chap. 5.

[4] Reynolds, L. H., Infrared Phys. 8, 233 (1968).

[5] Vagelatos, N., Wehe, D., and King, J., J. Chem. Phys. 60, 3613 (1974).

[6] Spitzer, W. G., Semiconductors and Semimetals 3, 17 (1967).

[7] Lipson, H.G., Appl. Optics 16, 2902 (1977).

[8] Deutsch, T., in Proc. 1962 Int. Conf. Physics of Semiconductors (Institute of Physics, London), p. 505.

[9] Nilsen, W. G., Phys. Rev. 182, 838 (1969).

[10] Dodge, M. J., in Proc. 1977 Symp. Laser-Induced Damage in Optical Materials (USGPO, Washington), p. 83.

[11] Bendow, B., Lipson, H., and Yukon, S., Phys. Rev. B 16, 2684 (1977).

[12] Harrington, J. A., in Proc. 1976 Symp. Laser-Induced Damage in Optical Materials (USGPO, Washington), p. 45.

[13] Johnson, F.A., Progress in Semiconductors 9, 181 (1965).

[14] Irwin, J. C., Can. J. Phys. 48, 2477 (1970).

[15] Birman, J. L., Phys. Rev. 131, 1489 (1963).

[16] Marshall, R. and Mitra, S., Phys. Rev. 134, A 1019 (1964).

[17] Skolnik, L., Lipson, H., Bendow, B., and Schott, J., Appl. Phys. Letters 25, 442 (1974).

[18] Barker, A. J., Wilkinson, G.R., Massa, N. E., and Mitra, S.S., in Proc. 1975 Int. Conf. Optical Properties of Highly Transparent Solids (Plenum, New York), p. 45.

[19] Mitra, S., Postmus, C., and Ferraro, J., Phys. Rev. Letters 18, 455 (1967).

[20] Stierwalt, D.L. and Potter, R.F., Semiconductors and Semimetals 3, 71 (1967).

[21] Hatch, S.E., Appl. Optics 1, 595 (1962).

[22] Dippel, C. E., Proc. IRIS 18, 51 (1973). This paper is unclassified.

[23] Lidwell, M. O., Opt. Acta 22, 317 (1975).

[24] Bennett, H. E., Bethke, J. W., and Norris, W. P., in Proc. 1977 High Power Laser Optical Components and Component Materials Meeting (AFML, Dayton/Ohio), p. 328.

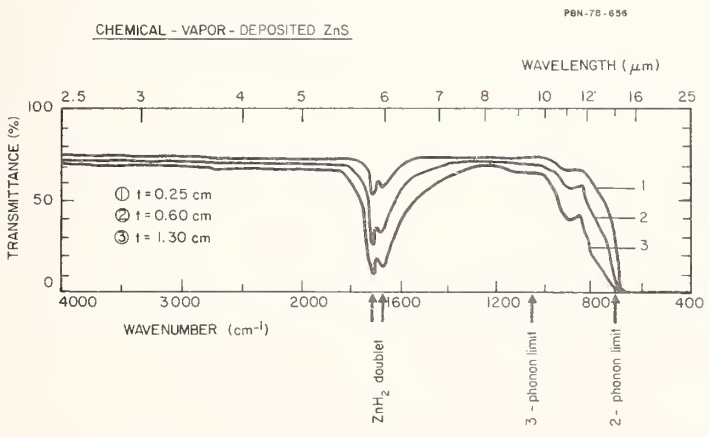

Figure 1. Spectral transmittance profile for three specimens of chemical-vapor-deposited zinc sulfide of differing thickness. Cutoff markers for multiphonon absorption are based on a Raman-phonon frequency of 352 cm^{-1}.

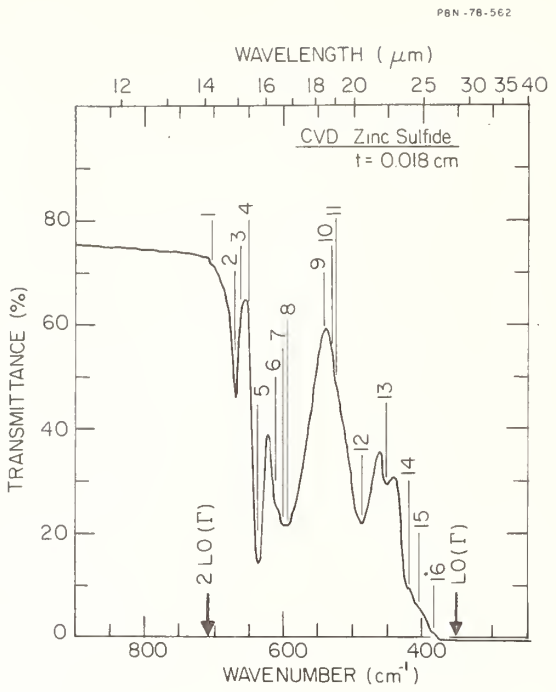

Figure 2. Two-phonon absorption region in chemical-vapor-deposited zinc sulfide. Structural features are identified and assigned to critical-point phonons, in table 2.

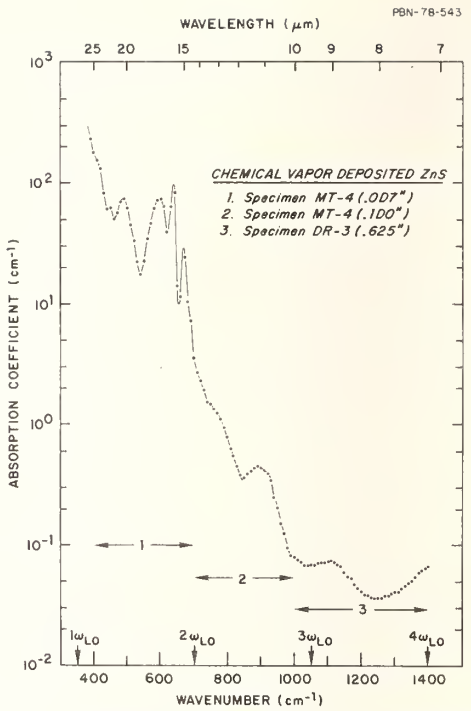

Figure 3. Wavenumber dependence of the absorption coefficient of chemical-vapor-deposited zinc sulfide at frequencies corresponding to phonon multiplicities of 2, 3, and 4. Data points are as obtained from transmittance tracings for three specimens of increasing thickness.

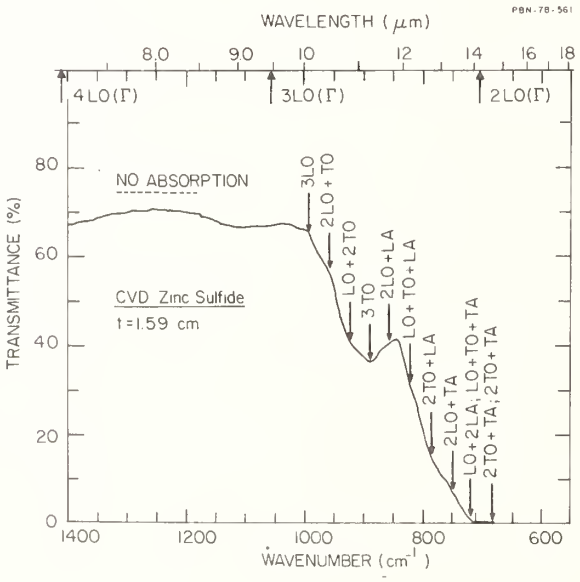

Figure 4. Three-phonon absorption edge in chemical-vapor-deposited zinc sulfide of engineering thickness. Assignments reflect combinations of characteristic phonons as obtained from the density-of-states calculation in reference 5.

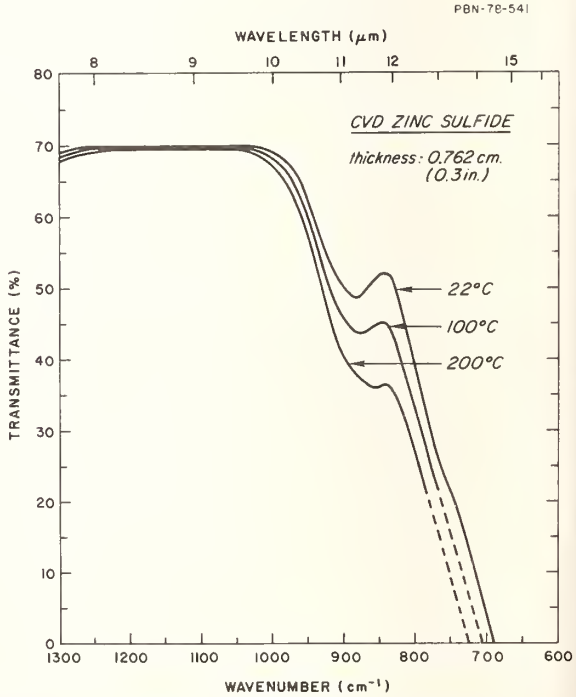

Figure 5. Spectral transmittance profile of chemical-vapor-deposited zinc sulfide at elevated temperatures. Contributions originating from self-emittance mask features occurring at far-infrared wavelengths.

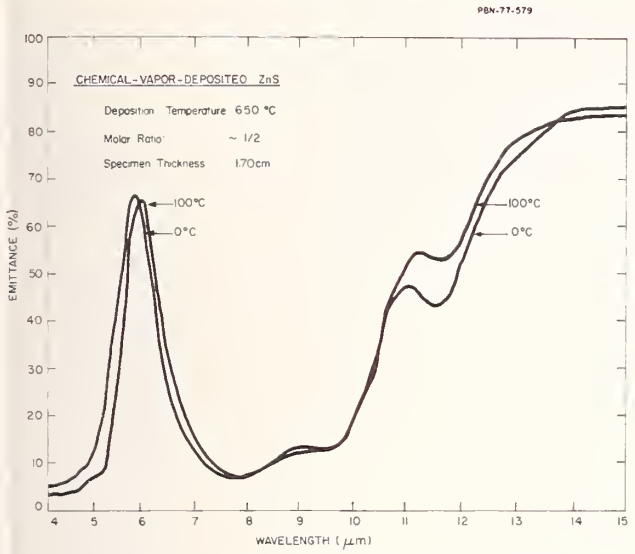

Figure 6. Sepctral emittance of chemical-vapor-deposited zinc sulfide. Note the temperature-dependence behavior in the 8- to 12-μm wavelength region.

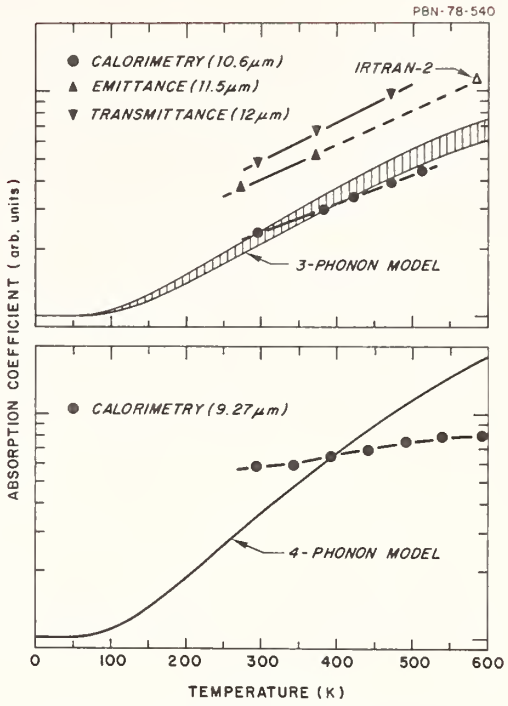

Figure 7. Temperature dependence of the absorption coefficient of chemical-vapor-deposited zinc sulfide, in the 8- to 12-μm region. Calculated dependencies are as derived from a model involving a fixed number of "average" phonons.

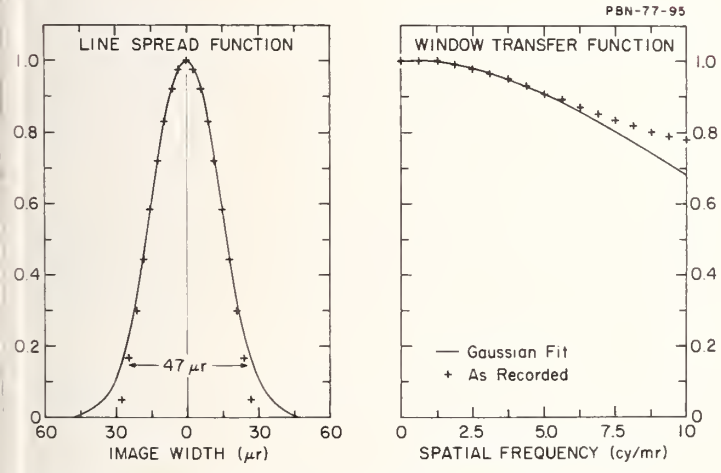

Figure 8. Image-spoiling characteristics of chemical-vapor-deposited zinc sulfide. The data refer to long-wavelength measurements on a full-size window and point to non-Gaussian distributions at high spatial frequencies.

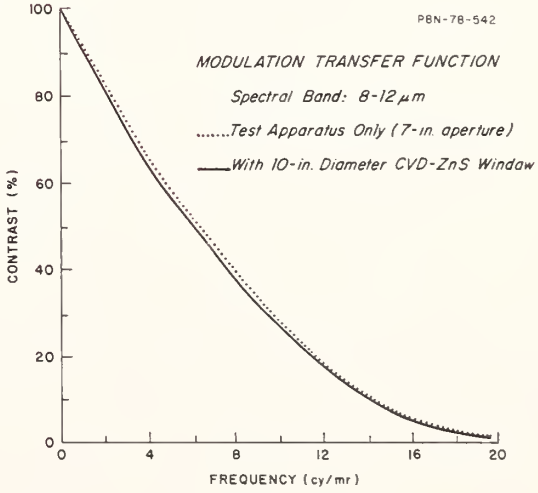

Figure 9. Contrast transmittance as a function of spatial frequency in the presence and the absence of a chemical-vapor-deposited zinc sulfide window at the entrance aperture of the test system. There is no significant effect on the modulation-transfer function.

Discussion

It was pointed out that low temperature measurements of the absorption spectrum would be useful in identifying which phonon processes were dominant in the absorption process.

The speaker was also asked if CVD samples of ZnS could be prepared which would be a free of absorption in the visible ("water-white") as the best conventionally prepared samples. He indicated that the preparation of such samples was planned but had not yet been carried out.

LASER INDUCED DAMAGE IN FLUORIDE GLASSES: A STATUS REPORT*

S. E. Stokowski, D. Milam, M. J. Weber
University of California
Lawrence Livermore Laboratory
Livermore, California 94550

Bulk and surface damage thresholds of fluorophosphate and fluoroberyllate glasses have been measured for 1-ns 1064-nm laser pulses. For crystal-free samples, threshold values for fluoride glasses are comparable to those measured in optical quality fused silica and borosilicate glasses. However, for many samples investigated the presence of solid inclusions results in low damage thresholds. Some examples of solid inclusions are shown and discussed. Surface damage thresholds in FK-51 fluorophosphate glass are uniformly high and exhibit an approximate square root dependence on pulse duration in the range of 0.1-1.0 ns.

Key words: Damage thresholds; fluoroberyllate glass; fluorophosphate glass; inclusions; pulse duration.

1. Introduction

Fluoride glasses have the smallest linear and nonlinear refractive indices of optical glasses. These glasses can therefore be used for optical components in high power laser systems, such as the proposed Nova laser at LLL, to minimize beam self-focusing [1]. Components include i) transmitting elements such as lenses, windows, and substrates and ii) active elements such as rare-earth doped amplifier glass and Faraday rotator materials. Because of their large transparency range--from approximately 160 nm (BeF_2) in the ultraviolet to 4000 nm in the infrared--fluoride glasses are potentially useful for many laser applications, particular in the UV.

Low-index fluoride glasses are also of interest to test empirical scaling laws for the dependence of laser damage on refractive index [2]. Damage threshold data for a large class of transparent dielectric materials indicate that damage thresholds are inversely proportional to the index of refraction [3,4]. Because of their low indices, fluoride glasses, pure BeF_2 in particular, have promise as very damage resistant materials.

Fluoride glasses include i) pure fluoride glasses based upon BeF_2 or ZrF_4 as the glass network former and ii) oxyfluoride glasses, such as fluorophosphate, fluorosilicate, and fluoroborates. Development of fluoride glasses has been rapid over the past two years. For example, Nd-doped fluorophosphate glass is now melted and cast routinely in sizes up to 40 X 80 X 8 cm, and fluoroberyllate glass has been cast in 20-cm diameter by 3-cm thick disks. Here we report the first measurements of the optical damage thresholds of these glasses for 1-ns 1064-nm laser pulses.

A primary motivation for developing fluoride glasses was to obtain materials with lower nonlinear refractive indices. The intensity-dependent contribution to the refractive index of a material is given by γI, where γ is the nonlinear refractive index coefficient. It has been found that low index, low dispersion materials also have small γ values [5]. An empirical expression [6] relating γ to the linear index n_D and Abbe number $\nu[(n_D - 1)/(n_F - n_C)]$ has been successfully employed in predicting γ values. Computed lines of constant γ are plotted as a function of n_D and ν in figure 1.

General regions of oxide and fluoride optical glasses are indicated in figure 1. Because the principal contribution to the refractive index in common silicate glasses arises from oxygen and polarizable, high atomic number cations, the replacement of oxygen by fluorine results in lower linear and nonlinear refractive indices. The lowest index glasses are those with beryllium fluoride as the glass network former. The measured γ value of pure BeF_2 was, as predicted by the empirical expression, the lowest yet found for any solid [7]. The glasses studied in this investigation are located in the clear areas labeled fluorophosphate and fluoroberyllate.

Until recently, fluorophosphates such as Schott's FK-51 and FK-52, and similar glasses made by other companies, had the lowest refractive index of commercially available optical glasses. These are designated as Group I in Table 1 which gives manufacturers, linear indices, and Abbe numbers. Optical and Nd-doped fluorophosphates with smaller oxygen content and lower indices have now been

*Work performed under the auspices of the U.S. Department of Energy under contract No. W-7405-ENG-48 and the Materials Sciences Program.

produced. These new glasses, designated fluorophosphates II, are also listed in Table 1. The γ-values of fluorophosphate II glasses are 2-3 times less than for silicate laser glasses. For reference, the corresponding properties of two standard optical materials, BK-7 borosilicate glass and fused silica, are included in Table 1.

The design of the Nova Nd:glass laser at LLL calls for damage thresholds of $\gtrsim$25 J/cm^2 on bare surfaces at normal incidence for 1-ns pulse durations. Operation at other pulse durations in the range 0.1-10 ns is also contemplated. Glasses such as FK-51 have demonstrated damage resistance comparable to BK-7 and fused silica, which is adequate for the above design. Our interest is in the newer, lower index fluorophosphate II glasses and the beryllium fluoride glasses.

2. Samples

Samples consisted of commercial BK-7 glass, optical grade fused silica, and FK-51 glass; the remaining glasses in Table 1 were from experimental melts by the sources indicated. The general compositions of the fluoride glasses are given in Table 2. The principal differences between the Group I and Group II fluorophosphate compositions are a reduction of the oxygen/fluoride ratio and an increase in the proportion of low atomic number cations, both of which result in a lowering of n_D and γ.

The fluorophosphate samples in most cases were polished using cerium oxide and standard finishing techniques. However, for surface damage measurements some samples were polished with ZnO, which produces excellent surfaces on fluorophosphate glasses [8]. The beryllium fluoride glasses were rough polished with 0.5 μm diamond powder and ethylene glycol on a pellon pad. The final polish was achieved using tin oxide and ethylene glycol on a lap made of a 1:1 mixture of 64 and 73 Gulgoz pitch. With good temperature control, satisfactory optical polish can be obtained. High-purity cerium oxide was also tried, but was too hard and did not yield a good surface. Finished samples had areas >1 cm^2.

The fluorophosphate samples were obtained from both small (<1 liter) and large (10-20 liter) melts poured from platinum crucibles. The fluoroberyllate glass was melted in a graphite crucible-mold. Beryllium fluoride glass from UCLA was vacuum distilled to improve purity and to remove water. Because of the hygroscopic nature of BeF_2, the surfaces of this material were susceptible to water contamination. The other fluoroberyllate glasses, however, have satisfactory chemical durability in normal atmospheres.

3. Measurement Techniques

Damage measurements were made using procedures described in detail previously [9,10]. One-ns 1064-nm pulses were obtained by gating out a portion of a 30-ns Q-switched Nd:YAG laser pulse. Pulses were subsequently amplified in a series of Nd:glass rod amplifiers. A collimated beam of 2-3 mm diameter (e^{-1}) was incident on the samples. The spatial profile of the beam at the sample was recorded for each shot using a vidicon and video disk recorder. Absolute flux was computed by an on-line data reduction system [11]. The waveform of each pulse was recorded to insure constancy of pulse shape. All measurements were made at room temperature.

Bulk damage was detected by observation of induced light emission during irradiation, and by permanent alteration of bulk scattering levels. Samples with high bulk damage thresholds were examined by Nomarski microscopy to determine surface damage thresholds.

Samples were initially irradiated at flux levels of 4-6 J/cm^2. If damage was induced on the first firing at this level, the test was discontinued except in instances where a parameter study such as water content or scattering was involved. Therefore, thresholds were not actually measured for many samples; it was simply determined that the threshold was less than some small value. If the sample failed to damage at 4-6 J/cm^2, the test was continued until a threshold was determined.

4. Results

4.1. Damage Threshold

Threshold data for bulk and surface damage are summarized in Table 3. For BK-7, SiO_2, and fluorophosphate I the results represent typical values; for the fluorophosphate II, BeF_2, and fluoroberyllate glasses, the best values measured to date are given. For the latter group of fluoride glasses, large variations in bulk damage thresholds were seen. For example, the flux levels at which bulk damage is observed in fluorophosphate II glasses, plotted in figure 2, range over a factor of ten.

Bulk damage in the fluoride glasses is evidenced by the presence of tracks in the region exposed to the laser beams. These tracks for a fluorophosphate glass are illustrated in figure 3 and are caused by scattering from a large number of spherical inclusions. A photomicrograph of a damaged center is shown in figure 4. The center is an ≈2 μm sphere with some evidence of surrounding glass fracture. Identification of the center has not been made as yet because of the difficulty in isolating it on the surface for X-ray analysis. The refractive index of these centers is lower than the glass matrix, however [12]. This observation suggests that they are gas or vacuum bubbles resulting from heating of the glass by laser energy absorbed at microscopic centers.

In silicate laser glasses platinum inclusions were a severe damage problem [13]. However, employing the techniques of X-ray fluorescence and emission spectroscopy, little evidence of Pt in fluorophosphate glass has been seen. Analyzed levels of Pt in the fluorophosphate glasses are <1 ppm; one analysis gave <70 ppb [14].

In early samples of fluoroberyllate glasses the presence of seeds, solid inclusions (including graphite particles), and high stress fields resulted in low damage thresholds of $\lesssim 7$ J/cm^2. The use of vitreous carbon crucibles and better melting techniques has yielded excellent fluoroberyllate glasses with no inclusions visible by optical microscopy and the high thresholds reported in Table 3. In the case of glassy BeF_2, the presence of transition metal impurities and poor surface quality due to the hygroscopic nature of this material contributed to low damage threshold; this is not believed to be indicative of the "intrinsic" limits for this material.

Several of the fluorophosphate and beryllium fluoride glasses were examined by optical and electron microscopy for possible damage inducing defects [15]. Some examples of observed seeds (bubbles), and crystals are shown in figure 5. Star-shaped crystallites were common and in some cases were high in Ca and low in P. Variation in the composition of the crystallites has been observed, thus different crystals have grown in the glass. Some needle-shape voids are present in the vicinity of crystal growth; this can cause considerable enhancement of the optical field, thereby leading to damage at low intensities. In addition, the crystal-glass interface is a region of compositional gradient or discontinuity. It may contain impurities, which along with associated voids and stress fields, are deleterious for damage.

At this time we do not know what impurities and/or melt conditions nucleate the crystal growth. The effect of water content in the glass, as monitored by IR absorption, on the bulk damage thresholds values of fluorophosphate II glasses was checked but no correlation was found. Identification of the crystal composition would aid in finding approaches to eliminate bulk damage.

5. Pulse Width Dependence

The Nova laser will be operated in a pulse width range of 0.1 to 10 ns, therefore it is of interest to know the pulse dependence of surface damage thresholds in fluorophosphate glass. This data was obtained on FK-51 (fluorophosphate I) and is compared with data on fused silica [16] in figure 6. The results indicate that in the region 0.1-1.0 ns, high quality fluorophosphate glass exhibits the approximate square root of pulse duration dependence of damage threshold found for the other optical glasses [2].

6. Conclusions

1. Fluorophosphate and fluoroberyllate glasses with high damage thresholds sufficient for current fusion laser applications have been observed.

2. Reproducible preparation of large melts of inclusion-free damage-resistant glasses is needed to render these glasses useful for high power laser applications. A bulk damage problem was encountered in fluorophosphate I glasses and solved [17] by a suitable modification of melting techniques. A similar effort is underway for the newer fluoride glasses.

3. The internal quality and surface finishes of the present fluoride glass samples are insufficient to test the validity of the empirical rule that low index materials should have high damage thresholds.

4. Damage threshold data as a function of pulse duration data indicates that high-quality fluorophosphate glasses exhibit an approximate square root of pulse duration dependence in the 0.1-1.0 ns time domain.

7. Acknowledgments

We thank the following people for providing test samples: Fluorophosphate glasses - K. Mader, N. Neuroth - Schott Optical Glass, Inc.; G. Dubé and P. Vergano, - Owens Illinois, Inc., Inc.; T. Izumitani, D. Segawa - Hoya Optics, U.S.A. Beryllium fluoride glasses - D. Morgan, Corning Glass Works, Inc.; C. Baldwin - University of California, Los Angeles; C. Cline, D. Kingman - Lawrence

Livermore Laboratory. We are grateful to R. Maney for polishing the beryllium fluoride glasses and to R. Landingham for optical and electron microscopy. Helpful discussions with W. Haller of the National Bureau of Standards are also gratefully acknowledged.

8. References

[1] S. E. Stokowski, R. A. Saroyan, M. J. Weber, and W. F. Hagen, Proc. Electro-Optics/Laser 77 Conference, Anaheim, CA, October 1977 (Industrial and Scientific Conference Management, Inc., Chicago) p. 29.

[2] J. R. Bettis and A. H. Guenther, "Scaling Laws for Damage" in Optical Materials for High Power Lasers (Academic Press) - to be published.

[3] J. R. Bettis, A. H. Guenther, and A. J. Glass, "Laser Induced Damage in Optical Materials; 1974," NBS Special Publication 414, U. S. Government Printing Office, Washington, D.C. (1974), A. J. Glass and A. H. Guenther, editors, p. 214.

[4] J. R. Bettis, R. A. House, A. H. Guenther, and R. R. Austin, "Laser Induced Damage Optical Materials. 1975," NBS Special Publication 435, U. S. Government Printing Office, Washington, D. C. (1975), A. J. Glass and A. H. Guenther, editors, p. 289.

[5] For a review see M. J. Weber, D. Milam and W. L. Smith, Opt. Engineering, 17, 463 (1978) and references cited therein.

[6] N. Boling, A. J. Glass, and A. Owyoung, IEEE J. Quantum Electronics, QE-14, 601 (1978).

[7] M. J. Weber, C. F. Cline, W. L. Smith, D. Milam, D. Heiman, R. W. Hellworth, Appl. Phys. Letter 32, 403 (1978).

[8] N. J. Brown and R. T. Maney, "Optical Fabrication of Fluorophosphate Laser Glasses," LLL Report No. UCRL-81081 (1978).

[9] D. Milam, Appl. Opt. 16, 1204 (1977).

[10] D. Milam, Proc. SPIE Technical Symposium East

[11] W. L. Smith, A. J. DeGroot and M. J. Weber, Appl. Optics (in press).

[12] W. Haller, private communication.

[13] Hopper, R. W. and Uhlmann, D. R., J. Appl. Physics, 41, 4023 (1970).

[14] P. Vergano, private communication.

[15] R. Landingham, private communication.

[16] D. Milam, Laser Program Annual Report-1976, Lawrence Livermore Laboratory, UCRL-50021-76.

[17] K. Mader, private communication.

[18] O. Deutschblein, M. Faulstich, W. Hahn, G. Krolla, and N. Neuroth, Appl. Opt. 17, 228 (1978).

Table 1. Refractive index and Abbe number of representative glass types included in this study.

Glass	Type	Source	n_D	ν
Borosilicate	BK-7	Schott	1.517	64
Fused silica	4000	Dynasil	1.459	68
Fluorophosphate				
Group I	FK-51, LG-800	Schott	1.487	84
	E-123	Owens Illinois	1.485	84
Group II	FK-54, LG-812	Schott	1.431	93
	LHG-10	Hoya	1.459	90
	E-309	Owens-Illinois	1.436	90
Beryllium Fluoride				
BeF_2	-	UCLA, LLL	1.275	107
K-Ca-Al-BeF_2	-	Corning	1.341	104
Al-Mg-Ca-Ba-BeF_2	-	Corning	1.38	~100

Table 2. Approximate compositions of fluoride glasses in mol. %.

Compound	Fluorophosphate I	Fluorophosphate II	Fluoroberyllate
AlF_3	20	32	10
LiF	12	-	-
NaF	1	12	-
KF	-	-	27
MgF_2	7	8	-
CaF_2	16	27	16
SrF_2	23	8	-
BaF_2	12	8	-
$Al(PO_3)_3$	7	5	-
Al_2O_3	2	-	-
BeF_2	-	-	47

Table 3. Observed damage thresholds for 1.0-ns 1.064-nm laser pulses incident at 10° from normal.

Material		Damage Threshold - J/cm^2 Bulk	Rear Surface	Comments
Borosilicate	BK-7	>40	20	PH-4 quality
Fused silica	-	>40	22	Optical grade
Fluorophosphate I	FK-51	>20	20 ± 3	
Fluorophosphate I	LG-802	>20	13	40 J/cm^2 at 40 ns (ref. 18)
Fluorophosphate II	E-309	>25	16 ± 2	Small melt
Glassy BeF_2	-	6 ± 1	_	Impurities; hygroscopic
Fluoroberyllate	-	>25	12 - 15	Free of solid inclusions; poor surface finish

REFRACTIVE INDICES AND DISPERSION OF OPTICAL GLASSES

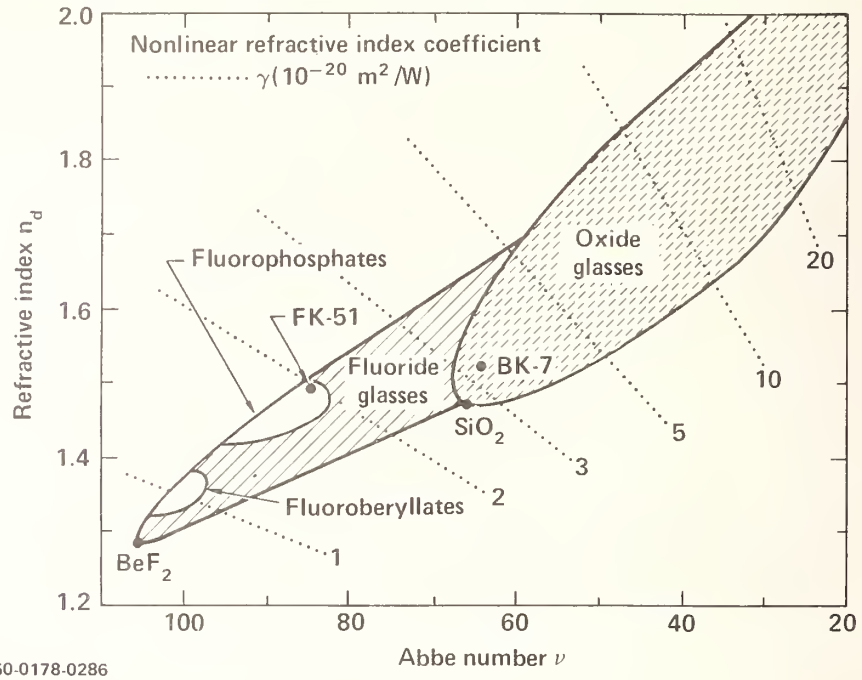

Figure 1. Refractive index, Abbe number, and nonlinear refractive index coefficients of known optical glasses. The fluoride glasses investigated have values in the clear areas indicated.

MEASURED BULK DAMAGE THRESHOLDS OF FLUOROPHOSPHATE GLASSES FOR 1.0 ns 1064 nm LASER PULSES

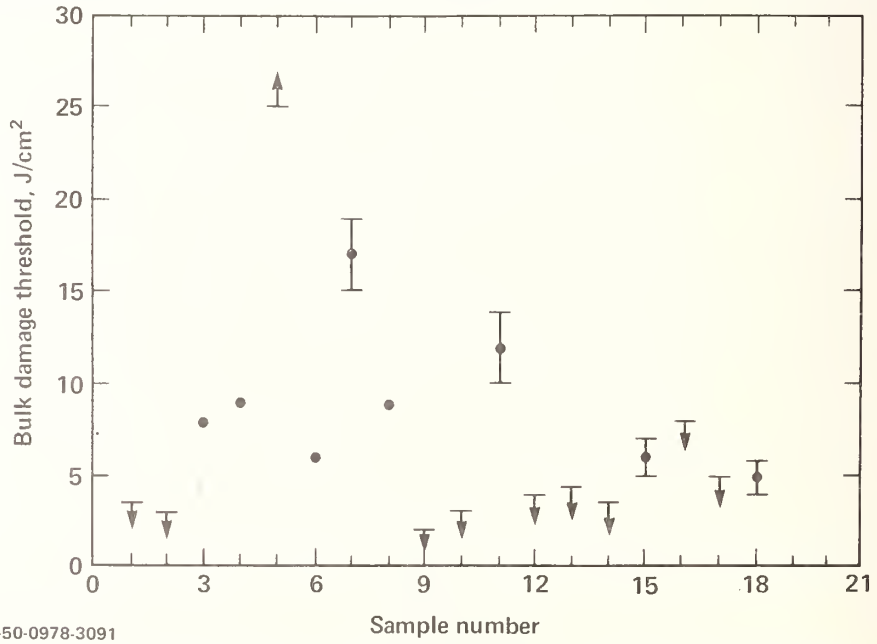

Figure 2. Record of the bulk damage thresholds for Group II type fluorophosphate measured with 1.0-ns 1064-nm laser pulses.

Figure 3. Laser-induced damage tracks in fluorophosphate glass.

OPTICAL MICROGRAPH OF A DAMAGED CENTER IN FLUOROPHOSPHATE GLASS

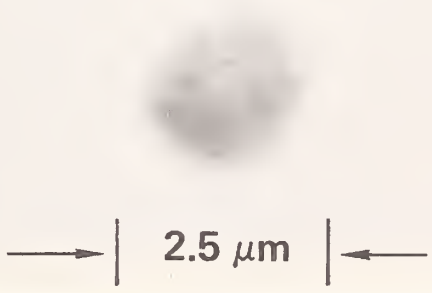

Figure 4. Photomicrograph of a damage center in fluorophosphate glass. The center is ~2.5 μm in diameter and shows evidence of glass fracture around it. The glass was subjected to a 5 J/cm^2 1-ns 1064-nm pulse.

Figure 5. Optical and SEM micrographs of crystals in fluorophosphate glass.

a. Interior of a 1-mm diameter polycrystalline region.

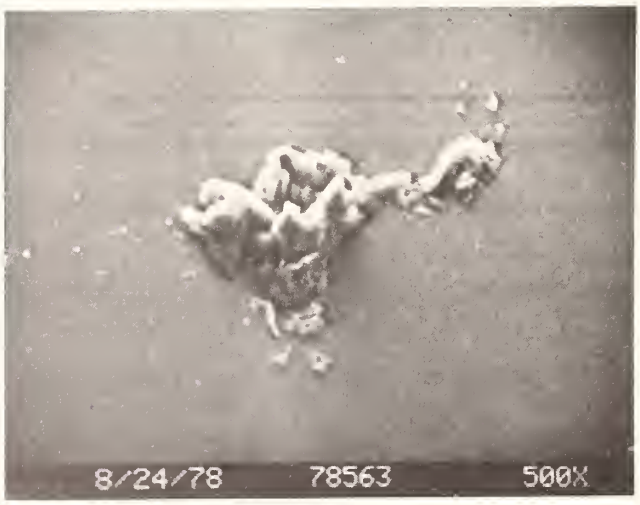

b. Crystalline regions as detected by SEM on a freshly fractured surface.

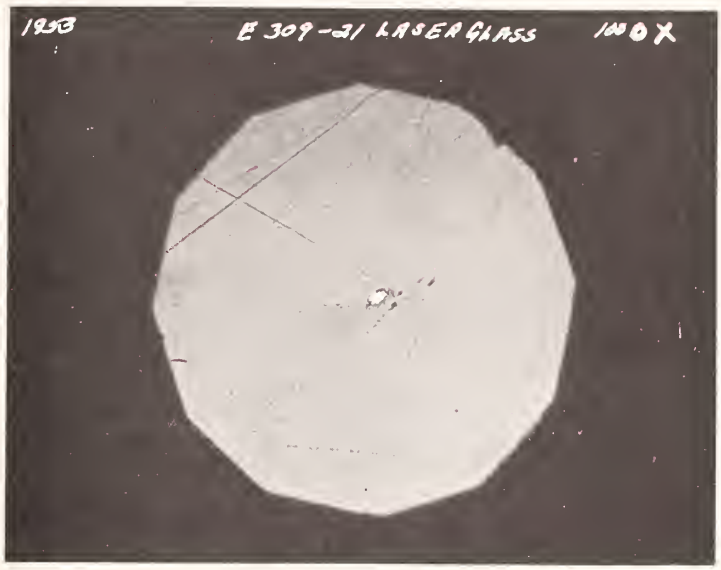

c. 2-3 μm sized crystal at the surface of a highly-scattering piece of fluorophosphate glass.

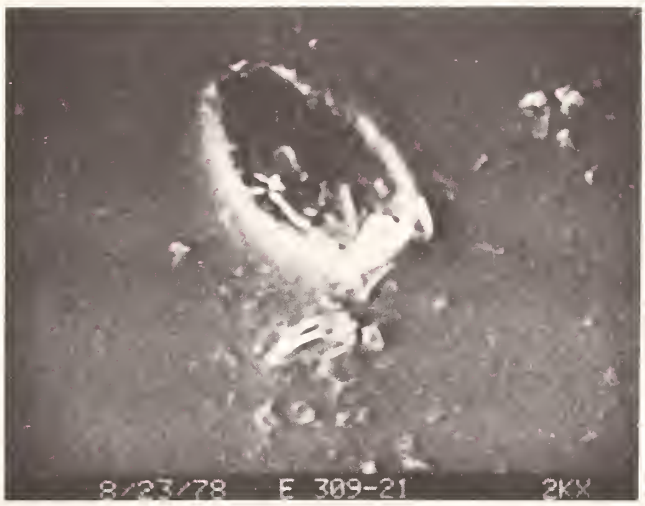

d. Ellipsoidal inclusion (~15 x 30 μm) examined by SEM; crystals are evident.

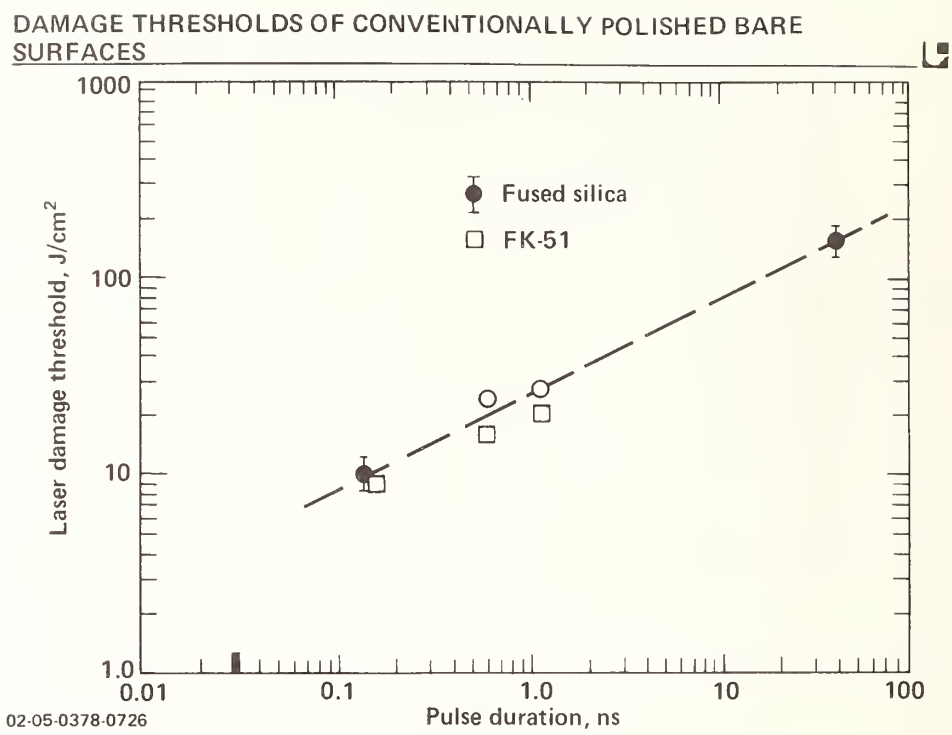

Figure 6. Damage thresholds of conventionally polished base surfaces as a function of 1064-nm laser pulse duration. The dashed line corresponds to a square root of pulse duration dependence of the damage threshold.

Discussion

The speaker was asked if the polishing compound used on fluorophosphate glass led to a reduction in surface damage threshold. He replied that the observed thresholds were comparable to those seen in BK-7 surfaces.

LIQUIDS FOR HIGH REPETITION RATE GLASS LASER SYSTEMS

James M. Rinefierd, Stephen D. Jacobs, David C. Brown,
Joseph A. Abate, Owen Lewis, and Henry Appelbaum
Laboratory for Laser Energetics
University of Rochester
Rochester, New York 14623

We present physical properties data for a number of liquids currently being used for cooling and/or index matching of components in high peak power, low repetition rate Nd: glass laser systems. Liquids examined include saturated water solutions of $ZnCl_2$ and $ZnBr_2$, TCP, benzene, DMSO, glycerol, ethylene glycol, FC-104, Dow-Corning 710, and Cargille 5040 and 5610. Thermal properties (conductivity, diffusivity), mechanical properties (viscosity, density), chemical properties (pH, materials compatibility), and optical properties (refractive index, Abbé value, nonlinear index, dn/dT, optical transparency) are tabulated and compared to projected liquid properties requirements for high repetition rate systems.

Key words: Abbé value; coolants, dn/dT; index matching liquids; Neodymium glass lasers; nonlinear refractive index; thermal conductivity; viscosity.

1. Introduction

A variety of liquids serve as important components of current moderate repetition rate glass laser systems. Specifically, these liquids find application as coolants and as index matching mediums in amplifiers and electro-optic isolation systems. In addition, future systems may have other uses for liquids such as in liquid electrodes for electro-optic devices.

It is the intent of this paper to provide data on the physical properties which are important for the selection of the most appropriate liquid for a given application. In what follows we identify the materials currently in use or proposed for use in large glass laser systems, and the physical properties of interest. We then give a description of the various measurment techniques utilized, followed by a tabulation of data. Finally, a discussion of results including advantages/disadvantages of certain liquids in particular applications is presented.

2. Liquids

A dozen liquids were chosen for inclusion in this study. These liquids are identified by manufacturer, grade, lot number, and use in table 1.

Table 1. Liquids of interest

Liquid	Manufacturer	Grade/Lot#	Description
Distilled H_2O			Coolant
Ethylene glycol	Mallinckrodt	AR/EGK	Coolant
Tricresyl phosphate	J. T. Baker	515303	Index match - from mixed cresols
Glycerol	Mallinckrodt	AR/WRDN	Index match
Dimethyl sulfoxide	Eastman	Reagent/B44	Index match
Benzene	Fisher	AR/714259	Index match
$ZnBr_2$ (aq)	Cargille	optical/551	Index match
$ZnCl_2$ (aq)			Index match - prepared @ LLE with Fisher solid $ZnCl_2$ AR/746575
DC-710	Dow-Corning	BFC345	Index match - silicone oil
C5040	Cargille	"ND 1.495 @ 10,600Å"	Index match - immersion liquid, hydrogenated terphenyl and mineral oil
C5610	Cargille	"ND 1.495 @ 10,600Å"	Index match - immersion liquid, silicone oil
FC-104	3M	526	Fluorochemical flashtube coolant

$ZnBr_2$ and $ZnCl_2$ are both highly acidic and corrosive; they do however exhibit stability under intense UV flashlamp irradiation. The Cargille liquids 5040 and 5610 can be obtained from the manufacturer

mixed to a desired refractive index of between 1.46 and 1.56. These Cargille liquids possess an extremely low water content, and are resistant to high voltage breakdown, making them compatable with KD*P in Pockels cell devices. Liquids such as benzene, tricresyl phosphate, and dimethyl sulfoxide pose health hazards [1][1].

3. Measurements and apparatus

The physical properties discussed in this paper fall into four categories: optical, thermal, thermo-optic, and mechanical. Specific properties studied include the following: refractive index at λ = 1.064μm, 0.6328μm, 0.6563μm(n_C), 0.5876μm(n_d), 0.4861μm(n_F); Abbé value ν_d; spectral transmittance from 0.2μm to 1.4μm; absorption coefficients at a variety of wavelengths; a calculated value for n_2 the nonlinear refractive index; the temperature coefficient of refractive index dn/dT; thermal conductivity, density and viscosity. Table 2 gives a listing of measurement apparatus and experimental precision obtained for the above.

Table 2. Measurement apparatus and precision

Measurement	Apparatus/Technique	Precision
Refractive index	Hilger-Chance Refractometer [2]	±.0005
Abbé value, ν_d	"	±7% low Abbe values ±50% high Abbe values
Nonlinear refractive index, n_2	"	±8% large values n_2 ±50% small values n_2
Absorption coefficient α	Cary 14 spectrophotometer	±.015 cm^{-1}
Spectral Transmittance	"	
Temp. coeff. of ref. index, dn/dT	Minimum angle of deviation	±5%
Thermal conductivity, k @ 25°C	Thermal comparator [3]	±3%
Density, ρ @ 38°C	Gay-Lussac pyncometers	±.003 gm/ml
Viscosity, kinematic, v @ 21°C	Cannon-Fenske viscometers	v, ±5%
Viscosity, absolute, V @ 38°C	ASTM sizes 25, 100, 200, 450	V, ±3%

Refractive index is determined using a Hilger-Chance refractometer [2], constructed of BK-7 and calibrated with Hoya BSC-7 glass. The device has a range of 1.25-2.0. Yag, HeNe, and dye laser sources are used to provide the wavelengths necessary to generate the index data.

The Abbé value, ν_d is calculated from the standard formula,

$$\nu_d = \frac{n_d - 1}{n_F - n_C} \tag{1}$$

Figure 1 gives a plot of n_d versus ν_d.

The electronic part of the nonlinear refractive index, n_2^e, which causes self-focusing of optical beams [4], is calculated using ν_d, n_d and the following relationship:

$$n_2^e(10^{-13}\text{esu}) = \frac{68(n_d - 1)(n_d^2 + 2)^2}{\nu_d \left\{1.517 + \left[(n_d^2 + 2)(n_d + 1)\nu_d\right]/6n_d\right\}^{\frac{1}{2}}} \text{ [5]} \tag{2}$$

Figure 2 gives a plot of n_d versus n_2.

A Cary spectrophotometer provides the spectral transmittance of each liquid from 0.2μm to 1.4μm. Absorption coefficient data is similarly obtained from this instrument. For spectral scans the samples are contained in a quartz cell with an optical pathlength of 3.7 cm. Measurements are made at a scanning rate of 50Å/sec. These scans are presented in figures 3-8. Absorption coefficients have been calculated for five wavelengths (1.34μm, 1.064μm, 1.054μm, 0.6328μm, 0.3550μm) using the relationship

[1]Figures in brackets indicate the literature references at the end of this paper.

$$\alpha_{cm^{-1}} = \frac{\text{(optical density)} + 2\log_{10}(1-R_1) + 2\log_{10}(1-R_2)}{L(\log_{10}e)} \qquad (3)$$

where L = length of cell = 1.0 cm

R_1 = reflectivity - quartz/air interface = $\left(\frac{n_{quartz} - 1}{n_{quartz} + 1}\right)^2$

R_2 = reflectivity - quartz/liquid interface = $\left(\frac{n_{quartz} - n_{liquid}}{n_{quartz} + n_{liquid}}\right)^2$

n = refractive index at appropriate wavelength.

The temperature coefficient of refractive index, dn/dT, is measured via a minimum angle of deviation technique at λ = 1.06μm near room temperature. The liquid is placed in a hollow glass prism (vertex angle 30°50'); the deflection of a laser beam passing through the liquid at minimum angle of deviation is determined as the liquid temperature is changed from 29°C to 23°C. Temperature is monitored by a thermocouple placed within a capillary tube inside the prism. The value of dn/dT is calculated from the following equation

$$\frac{dn}{dT} = \frac{\cos \tfrac{1}{2}(\alpha + \theta)}{2 \sin \tfrac{1}{2} \alpha} \frac{d\theta}{dT} \qquad (4)$$

where α = calibrated angle of prism = 30°50'

$\theta = 2 \sin^{-1}(n_{1.064} \sin \alpha/2) - \alpha$

$\frac{d\theta}{dT} = \frac{\text{(beam displacement in mm)}}{\text{(path length in mm) } (\Delta t)}$

Δt = temperature change in °C

Beam displacements are typically 10-20 mm for path lengths of 15-18 meters.

Thermal conductivity, important for heat flow calculations, is measured at room temperature for each liquid with a thermal comparator [3]. This instrument records the rate of cooling of the tip of a probe heated to 9°C above ambient upon contact with the teflon membrane of a liquid sample cell. A thermocouple pair responds to the temperature change by generating a microvolt signal which can be converted to thermal conductivity by calibration with reference standards. Figure 9 gives a thermal conductivity plot established with such standards. Thermal conductivity values for the samples are determined from this calibration curve with the microvolt signals obtained.

Density at 38°C is determined per ASTM D369-67 using Gay-Lussac type pyncometers. The filled pyncometers are heated to 38°C±.1°C in a water bath whose temperature is controlled using a Thermomix 1460 [6]. Mass determinations are made with a Sartorius 2474 analytical balance [7]. The volume of the pyncometers is obtained using a standard value for the density of H_2O at 38°C [8].

Viscosity at 21°C and 38°C is determined using Cannon-Fenske type viscometers. Each viscometer comes with a factory calibration at 38°C and is experimentally calibrated at 21°C. Temperature is maintained at 38°C using the Thermomix and at 21°C by using a large water bath at room temperature. The kinematic viscosity, v in centistokes, is found as v = Ct where C is the calibration constant of the viscometer and t is the efflux time of the travel of the liquid meniscus under the pull of gravity between two etched marks on a capillary tube. Absolute viscosity, V in centipoise, is expressed as V = vρ where ρ is the density of the liquid at the appropriate temperature. The absolute viscosity is determined at 38°C using density values measured at 38°C and the kinematic viscosity found with the viscometer calibration at this temperature. Kinematic viscosity is determined at 21°C only, because no density data was determined at this temperature.

4. Results

The data generated in this investigation are presented in three different forms. Table 3 collects numerical data on the physical properties of interest. Figures 1, 2, and 9 present graphs of n_d versus ν_d, n_d versus n_2, and thermal conductivity versus thermal comparator signal respectively. Figures 3-8 give spectal transmittance scans of the liquids.

Measured values of refractive index range from approximately 1.56 (TCP) to 1.27 (FC-104). The Hilger-Chance technique results in measured values of refractive index in close agreement with published values (generally ±.001). Table 4 lists a number of liquids and compares our data with published refractive index values.

Table 3. Physical properties of liquids for high repetition rate glass laser systems

Property	Water	Ethylene Glycol	Tricresyl Phosphate	Glycerol	Dimethyl Sulfoxide	Benzene	$ZnBr_2$	$ZnCl_2$	Dow-Corning 710	Cargille 5610	Cargille 5040	3M FC-104
Optical												
n_λ Refractive index, λ=1.06μm	1.327	1.424	1.539	1.466	1.468	1.487	1.538	1.523	1.517	1.496	1.498	1.271
n_C λ=.6563μm	1.333	1.430	1.552	1.472	1.477	1.497	1.551	1.532	1.528	1.506	1.506	1.272
n_λ λ=.6328μm	1.333	1.430	1.551	1.472	1.476	1.498	1.552	1.534	1.529	1.508	1.506	1.273
n_d λ=.5876μm	1.334	1.432	1.556	1.474	1.479	1.502	1.555	1.536	1.533	1.510	1.511	1.273
n_F λ=.4861μm	1.338	1.437	1.569	1.480	1.487	1.513	1.567	1.545	1.544	1.520	1.519	1.275
ν_F Abbé value	67	62	33	59	48	31	35	41	33	36	39	91
n_2 Calculated nonlinear index (10^{-13}esu)	.6	.9	3.6	1.1	1.6	3.1	3.2	2.4	3.2	2.7	2.3	.25
$\alpha_{1.34\mu m}$ Absorption coeff. cm^{-1}	5.029	.669	.128	.738	.105	.162	1.208	1.013	.093	.093	.104	.005*
$\alpha_{1.064\mu m}$	.153	.205	.029	.242	.046	.028	.091	.080	.023	.023	.051	.006*
$\alpha_{1.054\mu m}$	.162	.214	.026	.254	.035	.028	.102	.087	.027	.023	.057	.006*
$\alpha_{.6328\mu m}$	.014*	.019	.015*	.040	.015*	.017	.020	.021	.021	.021	.021	.013*
$\alpha_{.3550\mu m}$	.005*	.007*	.222	.040	.017	.016	.107	.145	.327	.231	2.503	.006*
Approx. UV edge μm (O.D.=1.0 for 3.7cm cell)	<.200	.210	.345	.250	.280	.280	.290	.280	.330	.330	.375	.210
Thermo-Optic												
dn/dt Temp. coeff. ref. index (10^{-4})/°C	-1.2	-2.7	-3.3	-2.2	-3.6	-5.7	-2.6	-2.5	-3.1	-3.1	-3.6	-3.8
Thermal												
K, thermal conductivity cal/cm-sec-°C(10^{-3})	1.45	.52	.26	.38	.34	.35	.59	.45	.24	.22	.24	.23
Mechanical												
ρ Density @ 38 °C gm/cm^3	.99299 [8]	1.101	1.152	1.250	1.082	.859	2.447	2.097	1.089	1.049	.897	1.727
Viscosity @ 38 °C, centipoise	.69	10.23	30.0	320	1.62	.52	15.22	81.9	248	89.5	10.74	1.02
Kinematic viscosity @ 21 °C, centistokes	.98	15.8	62	915	1.97	.74	10.5	101	566	156	21.0	.77

*>99% transmission.

Table 4. Refractive index measurements compared to literature values

Liquid	Measured values	Values from other sources
H_2O	n_C = 1.333	n_C = 1.331 [9]
	n_d = 1.334	n_D = 1.333 [9]
	n_F = 1.338	n_F = 1.337 [9]
		n_D = 1.333 [10]
Ethylene glycol	n_d = 1.432	n_D = 1.432 [10]
		n_D = 1.429 [8]
Tricresyl phosphate	n_d = 1.556	n_D = 1.556 [9]
Benzene	n_d = 1.502	n_D = 1.501 [9]
		n_D = 1.501 [10]
		n_D = 1.498 [8]
Glycerol	n_d = 1.474	n_D = 1.473 [9]
FC-104	$n_{1.06}$ = 1.271	1.271, λ unspecified [11]
	n_C = 1.272	
	$n_{.6328}$ = 1.273	
	n_d = 1.273	
DC-710	n_d = 1.533	1.533, λ unspecified [12]

The Abbé value which was calculated using refractive index data requires some explanation. It is seen that large Abbé values have errors of approximately ±50% while small Abbé values have calculated errors of ±7%. Because a high Abbé value indicates low dispersion while a low Abbé value indicates large dispersion; it follows that for low dispersion as seen in FC-104 and water, the limit of $n_F - n_C$ as $n_F \rightarrow n_C = 0$. Hence, ν_d is large and any small change in n_F, n_C, or n_d can have a large effect on ν_d.

The absorption coefficients and the spectral transmittance scans indicate wavelength regions in which transmission through thick samples of certain liquids would not be advisable due to strong absorption losses. Liquids exhibiting the strongest IR absorption are water, aqueous $ZnCl_2$ and $ZnBr_2$, ethylene glycol and glycerol. All the test liquids are highly transparent in the visible. Differences in absorption coefficients at .3550μm can be attributed mainly to the effect of the UV edge for the different liquids as indicated in table 3. The importance of the UV edge in relation to flashlamp degradation will be discussed later. It is noteworthy that H_2O and ethylene glycol which absorb in in the IR near 1.06μm also have the lowest UV edges (with FC-104) of the liquids tested.

The temperature coefficient of refractive index for water, 1.34 x 10^{-4}/°C is clearly substantially lower than dn/dT for any other liquid tested. The measured dn/dT values for liquids are approximately 10^2 times larger in magnitude than dn/dT values for glasses at 1.06μm [13]. All the liquids exhibit negative dn/dT values in that the refractive index decreases as the liquid temperature increases. From a product information sheet on Cargille immersion liquids [14], dn/dT values for 15-35°C average -3.3 x 10^{-4}/°C which are close to measured values for C5040 and C5610 of -3.6 x 10^{-4}/°C and -3.1 x 10^{-4}/°C respectively.

Thermal conductivity values fall between 1.45 cal/cm-sec-°C x 10^{-3} for water to approximately .25 cal/cm-sec-°C x 10^{-3} for TCP, DC-710, C5040, C5610 and FC-104. The plot in figure 9 of absolute signal versus thermal conductivity is a least squares fit of the data for calibration standards CCl_4, toluene, ethanol, methanol, and H_2O [3]. This plot has a coefficient of determination r^2 = .96. Little conductivity data is available for liquids other than the calibration standards. Product literature gives conductivity data for FC-104 and DC-710. FC-104 has a reported conductivity of .15 cal/cm-sec-°C x 10^{-3} [11] versus a measured value of .23 cal/cm-sec-°C x 10^{-3}. For DC-710 the published value is .35 cal/cm-sec-°C x 10^{-3} [12]; the measured value is .24 cal/cm-sec-°C x 10^{-3}. For these two liquids

the percentage difference between published and measured values is large. It should be noted however, that $ZnBr_2$ and ethylene glycol were measured at two different times using the same technique with resultant conductivity values within the stated precision of ±3%.

Measured viscosity and density exhibit a wide range of values. Viscosity is low for H_2O, benzene, FC-104 and DMSO; it is two orders of magnitude higher for DC-710 and glycerol. Density values range from approximately .9 gm/ml for benzene and C5040 to 2.4 for $ZnBr_2$. It is interesting to note that benzene and FC-104 have kinematic viscosities which are practically identical but density differences result in the absolute viscosity of FC-104 being twice that of benzene at 38°C.

There is generally good agreement between measured and published values of viscosity and density. Table 5 compares those values for water, benzene, glycerol, ethylene glycol, FC-104 and DC-710.

Table 5. Measured values of density and viscosity compared to other sources

Liquid	Measured values	Data from other sources
Water	V_{38} = .69cp	ρ_{38} = .99299 gm/ml [8]
	v_{21} = .98cs	V_{38} = .678cp [8]
		V_{38} = .681cp [9]
		v_{21}* = .980cs [8]
		v_{21}* = .983cs [9]
Benzene	ρ_{38} = .859 gm/ml	V_{40} = .503cp [8]
	V_{38} = .52cp	V_{30} = .561cp [9]
	v_{21} = .74cs	v_{21}* = .742cs [8]
		v_{21}* = .737cs [9]
Ethylene glycol	ρ_{38} = 1.101 gm/ml	ρ_{30} = 1.106 gm/ml [15]
	V_{38} = 10.23cp	v_{25}* approx. = 15.6cs [9]
	v_{21} = 15.8cs	v_{20}* = 19.0cs [15]
Glycerol	ρ_{38} = 1.250	v_{20}* = 1182cs [8]
	V_{38} = 320cp	v_{20}* = 848cs [9]
	v_{21} = 915cs	
DC-710	ρ_{38} = 1.089 gm/ml	ρ_{25}** = 1.107 gm/ml [12]
	V_{38} = 248cp	v_{25} = 500cs [12]
	v_{21} = 566cs	
FC-104	ρ_{38} = 1.727 gm/ml	ρ_{25} = 1.75 gm/ml [11]
	V_{38} = 1.02cp	v_{25} = .8cs [11]
	v_{21} = .77cs	

* Kinematic viscosity computed from reported absolute viscosity by: $v = V/\rho$. Density determined by multiplying specific gravity values [11] by density of water at reference temperature.

** In product literature specific gravity given at 25°C. Density determined by ρ DC-710 = (spec $grav_{25}$) x (ρ H_2O_{25}).

5. Considerations regarding n_2

In this paper we have considered liquids which may be applicable to high repetition rate Nd: glass lasers. Accordingly, one parameter of great interest is the nonlinear refractive index, n_2, important for the propagation of high peak power laser pulses. The electronic part n_2^e of n_2 has been calculated according to the method of Boling, Glass and Owyoung [5], and can be written

$$n_2^e\ (10^{-13}\text{esu}) = \frac{K(n_d - 1)(n_d^2 + 2)^2}{\nu_d\left\{1.517 + \left[(n_d^2 + 2)(n_d + 1)\nu_d\right]/6n_d\right\}^{\frac{1}{2}}} \tag{5}$$

where K is an adjustable parameter (taken to be K = 68 here). The results for liquids in table 1 are given in table 3 and figure 2, where n_2^e has been plotted versus the linear refractive index n_d. As is the case for glasses, a low nonlinear index is generally correlated with a low linear index of refraction. In figure 1 we show n_d plotted versus ν_d, and it is apparent that large Abbé values also correlate with liquids having low calculated values of n_2^e.

Although there is a paucity of data concerning experimentally determined n_2 values in liquids, we have been able to compare our calculated values of n_2^e for benzene with those found in the literature. The third order susceptibility $\chi^{(3)}_{1111}$ for a liquid or glass is related to the total n_2^T, through the relationship

$$n_2^T = \frac{12\pi}{n_d}\,\chi^{(3)}_{1111} \tag{6}$$

where

$$n_2^T = n_2^e + n_2^n \tag{7}$$

Here n_2^n is the nuclear contribution to n_2^T, and is usually in the range of 20-30% of n_2^T in glasses, but in liquids can be much larger. In this paper we concentrate strictly on n_2^e; the nuclear contributions to n_2^T for liquids will be the subject of a separate publication. If we write $\chi^{(3)}_{1111}$ as a sum of electronic (χ^{3e}_{1111}) and nuclear (χ^{3n}_{1111}) parts

$$\chi^{(3)}_{1111} = \chi^{(3e)}_{1111} + \chi^{(3n)}_{1111} \tag{8}$$

then n_2^e is given by

$$n_2^e = \frac{12\pi}{n_d}\,\chi^{(3e)}_{1111} \tag{9}$$

Levenson and Bloembergen [16] have reported a value for $\chi^{(3e)}_{1111}$, as has Owyoung [17]. Using eq. 9 to calculate n_2^e we arrive at the results shown in table 6 below.

Table 6. Calculated vs. experimental values for n_2^e in Benzene

$n_2^e\ (10^{-13}\text{esu})$ (calculated)	$n_2^e\ (10^{-13}\text{esu})$ [16]	$n_2^e\ (10^{-13}\text{esu})$ [17]
3.1	4.62	5.02

Owyoung [18] has determined that n_2^e is approximately 20% of n_2^T in benzene, and that $n_2^T = 14 \times 10^{-13}$esu; hence the nuclear part is $n_2^n \simeq 10 \times 10^{-13}$esu. Our value for n_2^e is in fair agreement with both of the reported values, and will probably show better agreement once a data base has been established and the adjustable constant K in eq. 5 has been recalculated for liquids. Thus the data given in table 3 and figure 2 should be treated in a first order sense at present.

This is, to our knowledge, the first application of the Boling, Glass, Owyoung theory [5] to the liquid state, and gives the electronic contribution n_2^e to the total nonlinear refractive index. Extension of this work to other liquids for which the total nonlinear refractive index is known will allow the separate contributions of electronic and nuclear susceptibility to be determined.

6. Discussion

Optimum characteristics for an index matching liquid or a coolant may be considered to be the following: low viscosity, high thermal conductivity, low absorption in important spectral regions, low dn/dT and low n_2.

Low viscosity is an important property where liquid flows are considered. For example, glycerol exhibits relatively good values for n_2, thermal conductivity and dn/dT which might lead one to consider glycerol as a coolant. However, the extremely large viscosity of glycerol would put a severe strain on any pumping system.

Heat removal considerations for cooling applications optimally require liquids with high thermal conductivities. A comparison of H_2O and FC-104 will serve as an example of this factor. Both liquids have low viscosities, low n_2 values, similar UV edges and FC-104 has lower absorption than H_2O, especially in the near-IR region. However, on the basis of thermal properties alone, H_2O would be the superior choice for a coolant as its thermal conductivity is 6 times greater than FC-104 and dn/dT for H_2O is approximately 1/3 lower. Another important thermal property is thermal diffusivity, defined as $K/(\rho C_p)$ where K = thermal conductivity, ρ = density, and C_p = specific heat at constant pressure. The specific heat of these liquids, not yet measured, is required to calculate this quantity. Another thermal measurement to be performed on these and other liquids at a later date is an examination of the coefficient of thermal expansion in the region around room temperature.

Characteristics other than those specifically mentioned above may come into play in an application decision. For example, silicone oils are quite difficult to dissolve with normal solvents. Hence, any cleanup of these materials can be a monumental task. Also silicones and TCP are examples of liquids which degrade in UV radiation. The UV edge of these liquids shifts towards the visible with exposure to intense UV from flashlamps. Care must also be used in choosing coolant/index matching liquids that are chemically compatible with materials used to contain them. $ZnCl_2$ (aq) is corrosive to aluminum and stainless steel, but does not react with 70/30 brass [19].

7. Conclusion

A wide range of values for refractive index, n_2, dn/dT, thermal conductivity, density, viscosity, pH, and spectral transmittance is observed for the liquids examined in this work. The data generated in this investigation should aid in a system designer's decisions in choosing a particular liquid for a given application. Further investigation is planned of other useful properties including: thermal expansion, specific heat, thermal diffusivity, and $n_{1.15\mu m}$. This work will be expanded to consider additional liquids such as deuterated water, toluene, ethyl alcohol, cyclohexane, CCl_4, and acetone.

8. Acknowledgements

This work was partially supported by the Laser Fusion Feasibility Project, which is sponsored by: Exxon Research and Engineering Company, General Electric Company, Northeast Utilities Company, Empire State Electric Energy Research Company, and New York State Energy Research and Development Administration.

9. References

[1] N.I. Sax, Dangerous Properties of Industrial Materials, 4th ed. VanNostrand Reinhold Co., 1975.

[2] J.V. Hughes, J. Sci. Inst., 18, 234 (1941).

[3] Lafayette Instrument Co., Lafayette, Indiana.

[4] R.W. Hellwarth, Phys. Rev., 152, 156 (1966).

[5] N.L. Boling, A.J. Glass, A. Owyoung, L^3 report UCRL 75628 (1974).

[6] B. Braun Melsungen A.G., San Mateo, Calif.

[7] Sartorius-Werke GMBM, Göttingen, Germany.

[8] R.C. Weast ed., Handbook of Chemistry and Physics, 52nd ed., Chemical Rubber Co., (1971).

[9] J. Dean ed., Lange's Handbook of Chemistry, McGraw-Hill Book Co., 11th ed., 1973.

[10] L. Meites, ed. Handbook of Analytical Chemistry, McGraw-Hill Book Co., 1st ed., 1963.

[11] Product information on Fluorinert liquids, 3M Co., St. Paul, Minn.

[12] Bulletin #22-281 (6/1974), Dow-Corning Corp., Midland, Mich.

[13] D. Brown, S. Jacobs, J. Abate, O. Lewis, J. Rinefierd, Laser Induced Damage in Optical Materials: 1977, NBS special pub., 509, 416.

[14] Cargille Laboratories, Cedar Grove, NJ.

[15] M. Windholz ed., The Merck Index, 9th ed., Merck & Co. Inc., 1977.

[16] M.D. Levenson and N. Bloembergen, Phys. Rev. B, 10, 4447 (1974).

[17] A. Owyoung, Optics Comm., 16, 266 (1976).

[18] A. Owyoung, App. Phys. Lett. 26, 168 (1975).

[19] LLE Annual Report 1977.

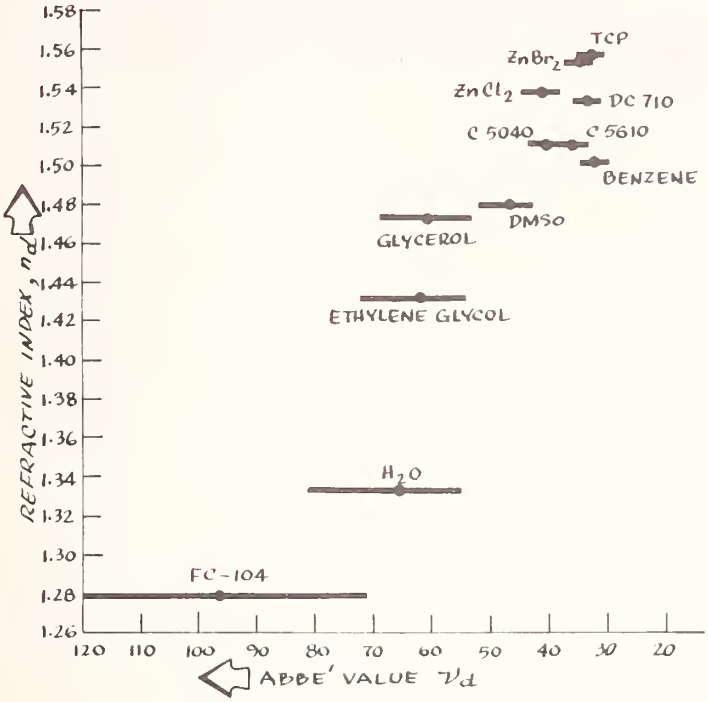

Figure 1. Abbe value versus refractive index.

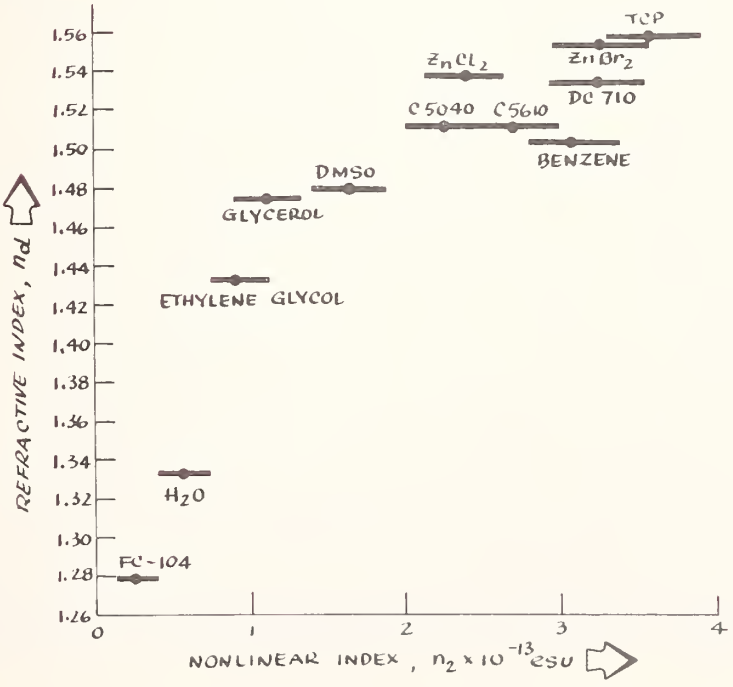

Figure 2. Calculated nonlinear refractive index versus linear refractive index.

Figures 3-8 Spectral transmittance of liquids under study. All liquids scanned in 3.7 cm quartz cells at 50 Å/sec.

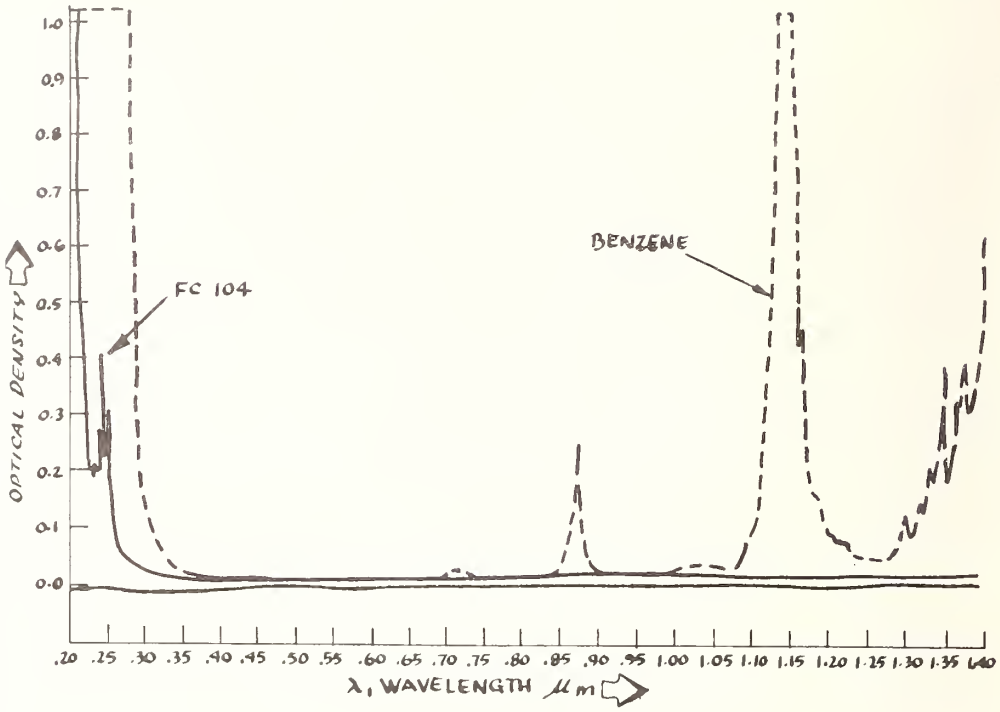

Figure 3. Spectral transmittance of FC-104 and Benzene.

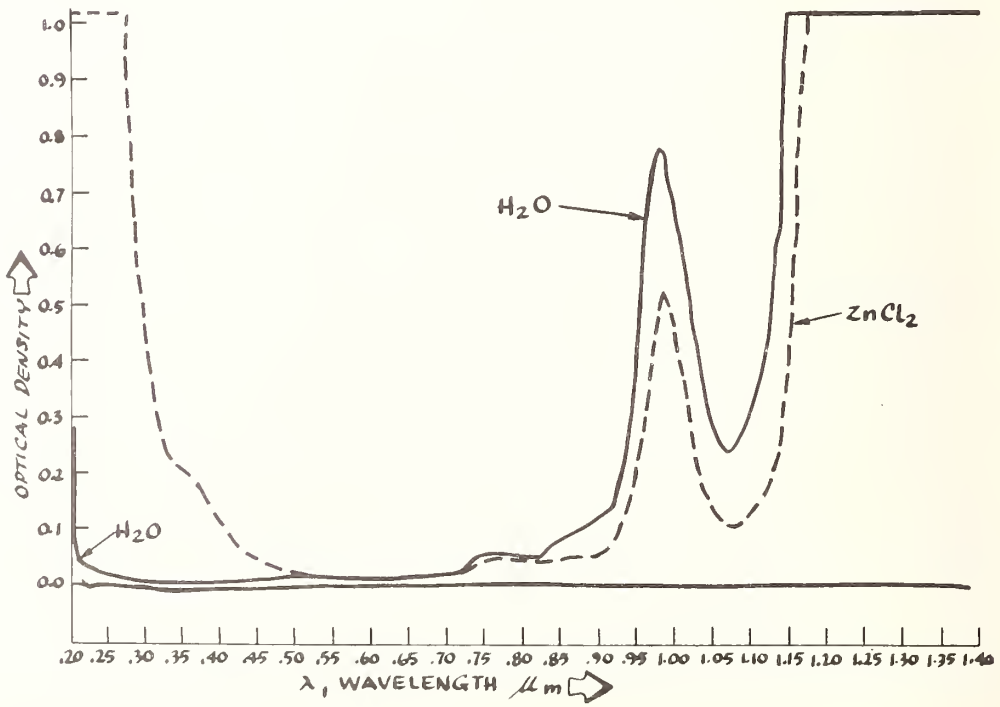

Figure 4. Spectral transmittance of H_2O and $ZnCl_2$.

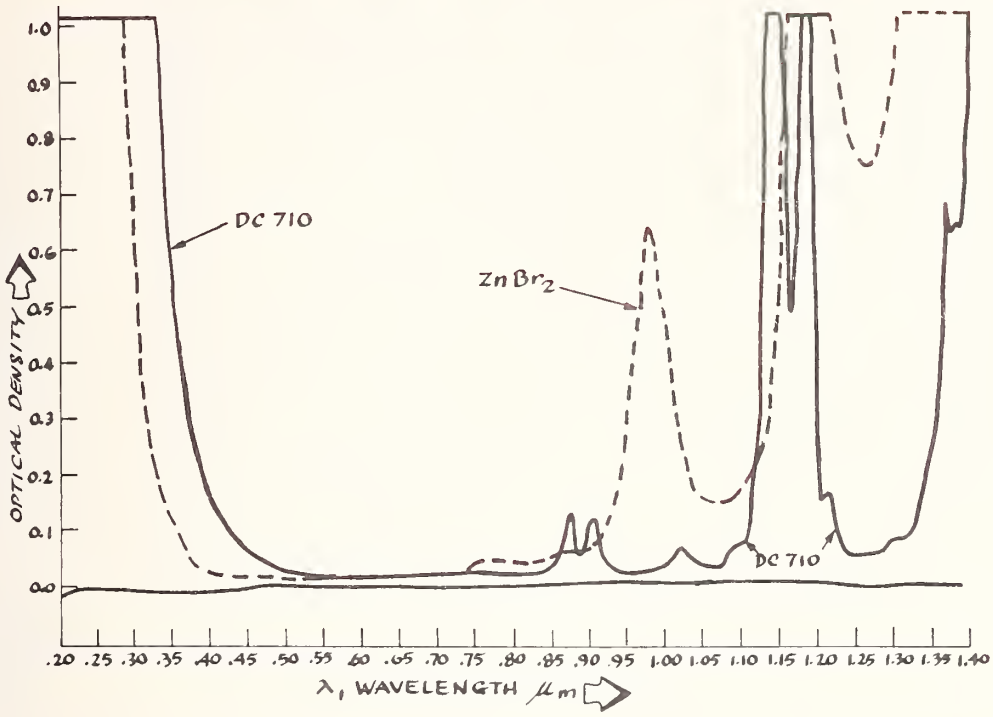

Figure 5. Spectral transmittance of $ZnBr_2$ and DC-710.

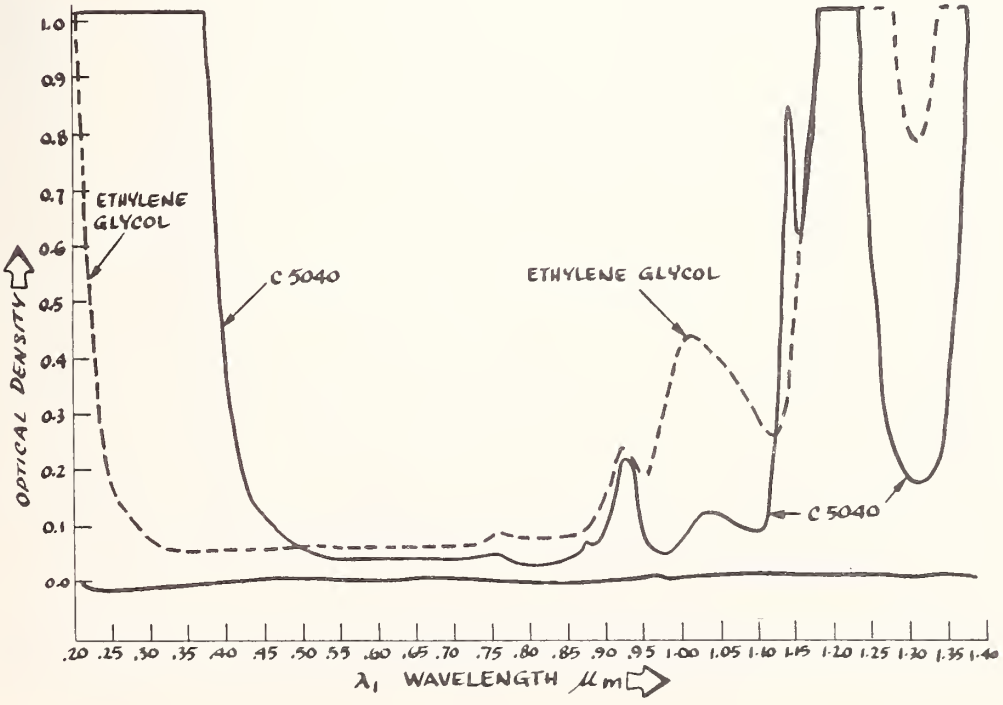

Figure 6. Spectral transmittance of Ethylene glycol and C5040.

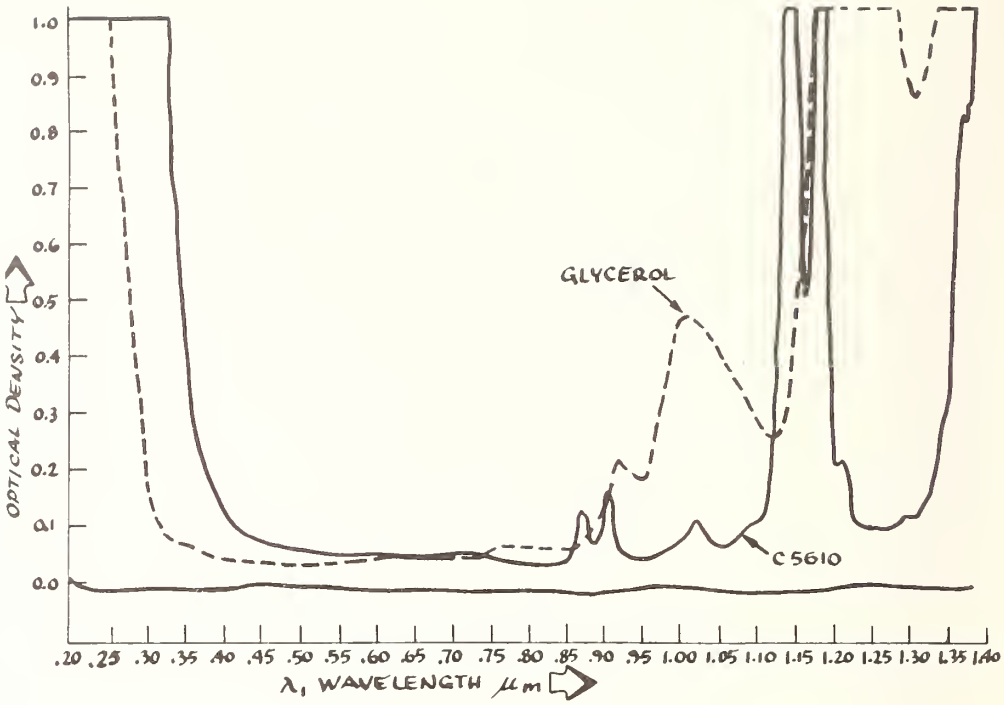

Figure 7. Spectral transmittance of glycerol and C5610.

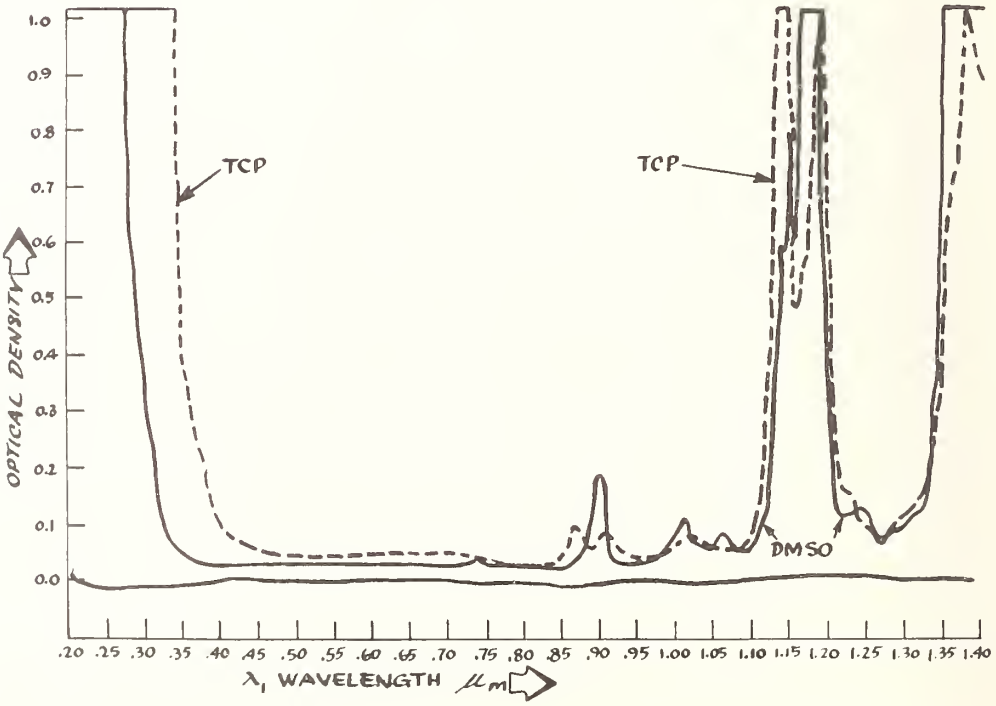

Figure 8. Spectral transmittance of Dimethyl sulfoxide and Tricresyl phosphate.

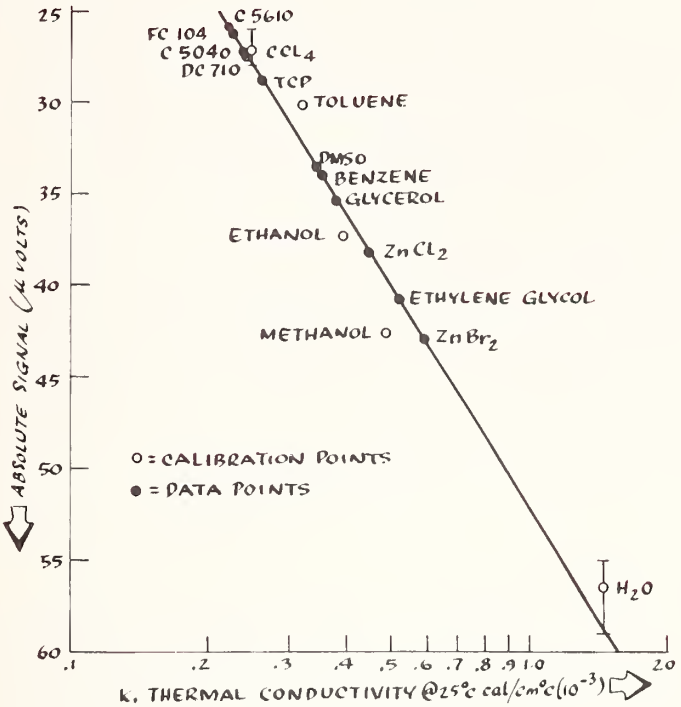

Figure 9. Thermal comparator signal versus thermal conductivity.

PHYSICAL AND OPTICAL PROPERTIES OF SURFACES GENERATED BY DIAMOND-TURNING ON AN ADVANCED MACHINE

D. L. Decker and D. J. Grandjean
Michelson Laboratory, Physics Division
Naval Weapons Center, China Lake, CA 93555

A superprecision, two-axis, air-static bearing, diamond-turning machine of advanced design has been previously described at this Conference and is now operational. The microtopography and other physical characteristics of surfaces turned by this machine will be examined in detail. Some effects of machining parameters will be briefly discussed. The ability of this machine to turn surfaces with very small slope errors ($< 10^{-3}$) and small rms roughness (~ 10 Å) is discussed with relation to the resulting optical absorption, scattering, and laser damage resistance. The characteristics of the machine which permit these high quality surfaces are identified, and some projections are given to the future application of diamond-turned optics at near infrared or visible wavelengths.

Key words: Absorption; diamond-turning; scattered light; surface roughness.

This paper describes some significant advances in the technology of diamond-turning of precision optics with specific emphasis on those results which bear on laser component applications, especially at wavelengths shorter than 10.6 μm. Although state-of-the-art diamond-turned surfaces are adequate for many demanding applications in the 8- to 14-μm wavelength region, the use of such surfaces at shorter wavelengths is hampered by limitations of both finish and figure. A paper by the first author of this paper was given at this Conference in 1976 which described details of the design of an advanced all air-bearing, two-axis lathe at the Naval Weapons Center (NWC) [1][1]. This machine is completed and is now mechanically operational. Optical and physical characteristics of plane surfaces turned on this machine are presented as examples of present capability.

The work at NWC has not only included systematic study and optimization of the effects of the machining process on the optical properties of turned surfaces, but also significant advances in machine technology. Slides, slide drives, and servo controls have received particular attention. The results at this point are significant and very encouraging. Surface roughness has been a first concern and, by a somewhat empirical, iterative approach, has been reduced to ~ 10 Å rms on bare OFHC copper measured by total integrated scatter (TIS) of visible light. This finish is characterized by maximum slope errors a factor of two to three smaller than previously measured on surfaces from other machines. The measured infrared reflectance of this surface is identical to that of the best evaporated films and is 0.992 at 10.6 μm wavelength. These values have been achieved without the benefit of interferometric servo control, relying on the intrinsic truth of motion of slide and spindle, and by an optimized machining procedure. The NWC machine, which was manufactured by Pneumo Precision, Inc., Keene, New Hampshire, provides slide motion which is much smoother and more accurate than available from any previous machine. A 6-inch-diameter copper mirror has been turned flat to $\lambda/10$ [633 Å peak-to-valley (p-v)] with no servo correction. With the addition of a modern high-speed interferometric servo loop all residual slide errors can, in principle, be corrected to ~ 100 Å p-v, over the full range of motion of the machine.

Figure 1 is an isometric schematic of the NWC machine, showing the arrangement of slides and spindle. The machine base is an air-suspension isolated, granite surface plate.

---

* Work supported by Navy Independent Research and Independent Exploratory Development funds, and the Air Force Weapons Laboratory.

1. Figures in brackets indicate the literature references at the end of this paper.

This arrangement has several advantages over the most common machine configuration, namely, the Moore #3 conversions [2]. All critical components are tied thermally and mechanically to the base in a similar manner, with all critical parts at essentially the same height from the floor. Vertical air temperature gradients are thus less important. Also, the granite surface plate represents a very versatile two-dimensional optical/mechanical bench, allowing changes in components or configuration to take place without extensive redesign or rework. For example, the incorporation of an interferometer to measure slide position is easily accomplished, as is shown in figure 1. It is relatively easy to have the interferometer beam at spindle centerline height, thus minimizing Abbe offset errors. Figure 2 is a photo of the machine showing tool and spindle slides, tool post assembly, chip/coolant guard, and spindle housing. A 6-inch copper flat is being turned. Table 1 is an outline of the machine performance as actually measured. Of particular interest is the maximum slope error associated with slide motion. Figures 3 and 4 give, respectively, examples of the long- and short-period departures from ideal straight line motion in the yaw plane of the tool slide. Similar motion is observed in the pitch plane and for pitch and yaw of the spindle slide. Note, in particular, the magnitude of the maximum slope observed in the short-period motion (1.6×10^{-4}).

Table 1. Actual measured performance data of the NWC diamond-turning machine.

Hydrostatic Air Spindle	
Axial and radial runout	< 3 μin. total indicator reading
Angular (wobble) error	< 0.1 arc sec
Axial stiffness	0.5×10^6 lb/in.
Radial stiffness at nose	0.3×10^6 lb/in.
Load capacity at nose	300 lb
Swing	14 in. over tool carriage
Hydrostatic Air Slides (both x and y)	
Straightness (yaw) and flatness (pitch)	< 3.2 μin. per in. max short range < 8.2 μin. in 8-in. max long range
Stiffness in pitch	0.3×10^6 lb/in.
Stiffness in yaw	0.5×10^6 lb/in.
Axial stiffness	0.4×10^5 lb/in.

The finish achievable on a single-point diamond-turned surface is determined by both the quality of the tool and of the machine, and by the machining technique employed. However, it appears that virtually all of the surface finish imperfection can be ascribed to unwanted machine motion or to the machining process itself rather than the tool, when tools of the highest quality are employed. The ideal surface generated by turning with a radiused nose tool is shown in figure 5. The peak-to-valley roughness δ_{pv} is given approximately by the expression $\delta_{pv} = f^2/8r$, valid if the ratio of the feed/revolution of the spindle, f, to the tool radius, r, is small [3]. Other useful expressions are given in this figure and are computed similarly. A high quality diamond-turned surface has superposed, on the ideal structure just discussed, a wealth of fine scale roughness as a consequence of unwanted tool/workpiece motion or interaction, including tool build-up or chip interaction with the work. Figure 6 is an intercomparison of the surface profile perpendicular and parallel to the machining grooves for surfaces turned at NWC, Battelle Northwest, and Y-12 Union Carbide Laboratories. Of particular interest is the reduced fine scale structure displayed especially by the NWC perpendicular scan but also by the parallel scan. The parallel scans cover a distance of 50 μm, which was cut in a time on the order of 50 μsec. Obviously, there is much structure in all cases with a period of 1 μsec or even less. This time interval is ≈ 4 orders of magnitude smaller than the period of the fundamental resonant frequencies of the spindle axial or slide yaw oscillation. This fine structure and the fine structure displayed in the perpendicular scans is similar in all examples of this figure and is almost certainly a consequence of microscopic variations in the machinability

of the work material or to variations in the flow of the chip away from the work surface. Assuming that this structure was generated by harmonic motion, and assuming an amplitude of 10 Å, one computes a maximum acceleration of 4×10^4 m/sec^2 or 4,000 g. It is clear that since the measured machining tool forces are typically a fraction of a gram weight, only extremely small masses can follow this motion if the reaction forces act on this tool or workpiece. A 1-cm length of copper chip removed with a 10^{-4} inch/revolution feed rate with a 1/8-inch nose radius tool has a computed mass of only 4×10^{-11} g. Hence, it is perfectly reasonable that a small section of chip respond with the amplitude and frequencies observed associated with the very fine scale surface structure. This motion may represent torsional or longitudinal acoustic vibration of a very small length of chip still attached to the work surface. It has been observed empirically that by guiding the chip with a small, vigorous, liquid jet from a hypodermic needle, much of the large scale chip motion observed easily with a low power microscope can be greatly reduced. Subsequently, it was discovered that the effect of this procedure is to produce a considerable reduction in fine scale surface structure. This improvement has a dramatic effect on light scatter especially at short wavelengths. The finish improvement may come about from a chip motion damping effect or from improved lubrication of the chip on the tool. The latter explanation seems most likely since the chip oscillation is possibly driven by variations in tool/chip friction.

The perpendicular scan profiles are superpositions of "snapshots." The cutting profile at the tip of the tool is preserved and is overlayed by the similar profile with successive adjacent passes. Even for the best of the surfaces turned at NWC, significant departure from the ideal surface exists, as is indicated in table 2. This discrepancy has been almost universally observed. Control of the chip or chip/tool interaction is the key to producing very smooth turned surfaces. The measured surface parameters in table 2 were obtained on a 6-inch-diameter copper flat; similar data are compared to the previously discussed Battelle and Y-12 samples in table 3. The NWC sample is characterized by a very small roughness in the parallel direction, and an rms slope in the perpendicular direction a factor of two to three smaller than the Battelle and Y-12 samples. The surface roughness values obtained by TIS must be interpreted with caution. The scattered light originates at structure on the sample surface associated with the turning process or at defects in the basic material exposed by turning. Scattered light is, however, limited by a spatial cutoff length equal to the incident wavelength, so that structure with a correlation length less than the wavelength does not contribute to the scattered light intensity. This is the primary reason for the discrepancy between TIS and profilometer roughness values [4].

Table 2. Comparison of calculated and measured surface finish for a feed rate of 10.9 μm (~ 500 μin.) per revolution and a tool radius of 3175 μm (1/8 in.).

Calculated	Measured
$\delta_{pv} = 46.8$ Å	200 Å
$\alpha_{max} = 1.7 \times 10^{-3}$	10×10^{-3}

Table 3. Quantitative summary of roughness values measured by TIS and by profilometer and slopes measured by profilometer for the surfaces intercompared in figure 6.

	rms Roughness (TIS), Å	rms Roughness (Talystep, parallel to grooves), Å	rms Slope (Talystep, parallel to grooves), Å/μm
NWC, 6-in. dia.	19.0	7.7	43
Battelle, 2-in. dia.	12.3	12.9	85
Y-12, 1.5-in. dia.	20.1	9.7	--

Inclusions and voids occur with surprising concentration even in "high purity" materials. Easily visible in either dark field or Nomarski microscopy, these defects contribute significantly to the light scatter of the surface. For example, the 6-inch NWC copper disc "roughness" of 19 Å rms is substantially due to this origin. If the 90 points at which scatter was measured are ranked, and the highest scatter 50% discarded, the apparent roughness drops to under 10 Å rms. The concentration of scattering centers (primarily voids and microcracks) is on the order of $500/mm^2$. A copper substrate with a much lower concentration of defects was turned with similar machining parameters which had a measured TIS roughness of 10.1 Å, in corroboration of the defect origin of much of the scattered light. Mechanical polishing appears to smear over the microscopic defect structure just described, and so is not discovered by routine examination. Much of the spatial variation of pulsed laser damage thresholds on apparently uniform polished bare metal surfaces is believed to be due to subsurface defects of this sort [5].

The NWC diamond-turned surface in figure 7 displays the very uniform residual turning structure resulting from precise machine geometry and chip control, and also the very low defect concentration of this surface. It is instructive to qualitatively compare the surface structure of turned surfaces coming from several different laboratories in detail. Figure 8 is the autocovariance function for a perpendicular scan of the 6-inch-diameter flat already discussed [6]. The long-period structure displayed here has the effect of producing scatter very near the specular direction. Figure 9 shows the height and slope distribution function for this same surface. Neither the height nor slope distributions are well represented by Gaussian profiles. A Y-12 diamond-turned bare copper surface appears in figure 10, showing a typical concentration of localized defects. Figures 11 and 12 show, respectively, the autocovariance function and height and slope distribution functions for the same Y-12 sample. These distributions are very similar to those of the NWC sample, with slightly larger rms roughness and an rms slope a factor of two larger. The Battelle diamond-turned characteristics shown in figures 13, 14, and 15 are quite different. The surface structure is of much higher spatial frequency, as is indicated by the autocovariance function in figure 14. The rms roughness is intermediate between the NWC and Y-12 results, but the rms slope is significantly larger than the Y-12 case. The Battelle surface possesses a wealth of low amplitude but short-period, high slope structure. The effects of such a surface profile on laser damage remain unknown although the infrared reflectance of this surface is not notably degraded [5].

Much of the larger scale nonideal structure has been demonstrated to be reproducible on a scale of a few hundred angstrom units in the case of modified Moore #3-type lathes [7]. In principle, by calibrating the slides of the machine, and by incorporating this information in the program or tape commanding the machine motion, the systematic unwanted motion can be controlled. However, the servo bandwidth of controllers in current use are typically only a few hertz and, consequently, much high frequency spatial irregularity remains uncorrected. This approach can make significant improvements in gross figure, but has little impact on small scale figure or finish.

To effect small scale figure improvements, two areas must be attacked simultaneously: the spatial frequency of unwanted slide and spindle motion must be reduced, and the servo loop must incorporate a minimum Abbe offset interferometric position/velocity sense and high bandwidth. Nonreproducible slide motion in plain hydrodynamic way lead screw-driven carriages is primarily a consequence of spatial variations in friction. Hydrostatic ways, either air or oil, can result in very significant improvement, since the motion is completely free of stick-slip, and has a friction component only as a consequence of shearing an air or oil film. The drive problem can be addressed by several approaches: 1) superfinished recirculating ball lead screw, 2) a traction drive of some sort, 3) linear induction motor. All three have been implemented and can work. In the present case, a ball screw directly coupled to a dc torque motor provides the carriage motion.

The Hewlett Packard 5501A doppler interferometer system provides a well-documented yardstick for gaging slide motion to a position resolution of $\lambda/80$ (.311 min) and with an absolute accuracy of 0.5 parts in 10^6 and a stability of one part in 10^8. A thoroughly modern phase lock servo loop can make optimum use of the very high bandwidth of the Hewlett Packard system, and being a digital/analog hybrid can possess the very high velocity resolution and stability required to produce a two-axis contouring cut limited primarily by the resolution of the interferometer. These authors hope to report success in this regard

at this Conference a year from now. Since the very high frequency structure, which is a primary contribution to surface roughness, is not a direct consequence of slide motion it should be possible to maintain surface roughness ~ 10 Å rms under these conditions for parts up to the full capacity (0.4-m diameter) of the machine. This machine will thus be capable of producing optical surfaces useful for many demanding visible wavelength applications.

References

[1] Decker, D. L., and Cram, R. E., "Naval Weapons Center Diamond Turned Optics Facility," in *Laser Induced Damage in Optical Materials: 1976*, ed. by A. J. Glass and A. H. Guenther, Washington, D.C., National Bureau of Standards (NBS Spec. Publ. 462), pp. 145-48.

[2] Arnold, J. B., Steger, P. J., and Burleson, R. R., "Slide Position Errors Degrade Machined Optical Component Quality," in *Laser Induced Damage in Optical Materials: 1975*, ed. by A. J. Glass and A. H. Guenther, Washington, D.C., National Bureau of Standards (NBS Spec. Publ. 435), pp. 75-89.

[3] Donaldson, R. R., "Nomograms for Theoretical Finish Calculations With Round Nose Tools," presented at the Society of Manufacturing Engineers Conference, San Francisco, Calif., November 1974.

[4] Decker, D. L., and Bennett, J. M., "Surface Evaluation Techniques for Optical Components," in *Proceedings of the Society of Photo-Optical Instrumentation Engineers*, Vol. 140, June 1978 (in press).

[5] Decker, D. L., Bennett, J. M., Soileau, M. J., Porteus, J. O., and Bennett, H. E., "Surface and Optical Studies of Diamond-Turned and Other Metal Mirrors," Opt. Engr. 17, #2, 160 (1978).

[6] Bennett, J. M., "Surface Evaluation Techniques for Optical Components," this Conference (to be published by Academic Press).

[7] Bryan, J. B., presented in a panel discussion at the Society of Manufacturing Engineers "Precision Machining Workshop" in Williamsburg, Va., June 1978.

Figures

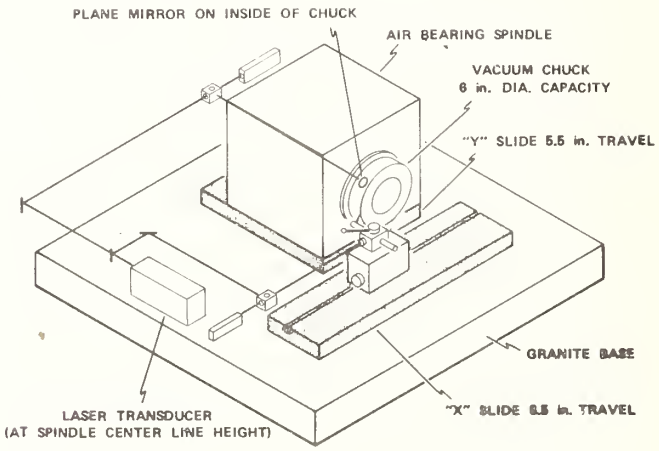

Figure 1. Shown in this isometric schematic of the NWC two-axis diamond-turning machine are the placement of the spindle and tool slides in a "T" base configuration. Also shown is a simple interferometer layout for measuring the primary motion of the slides.

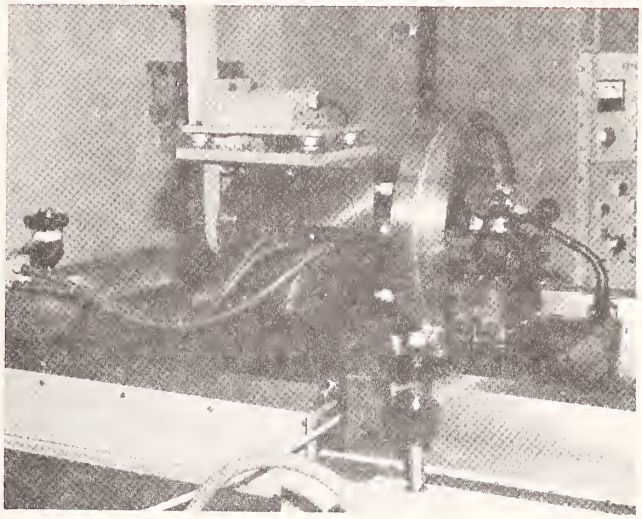

Figure 2. This photograph of the NWC machine shows the tool and spindle slides, the tool post assembly including precision height adjuster, chip/coolant guard, and spindle housing. A 6-inch-diameter copper flat is being machined.

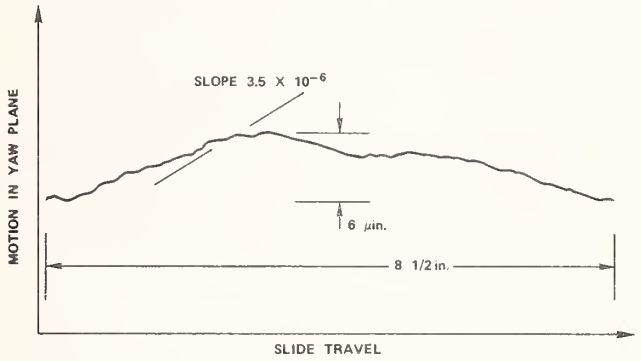

Figure 3. Measured long-period departure from ideal straight line motion in the yaw plane of the tool slide. An electronic gage was run against an optical flat for this measurement.

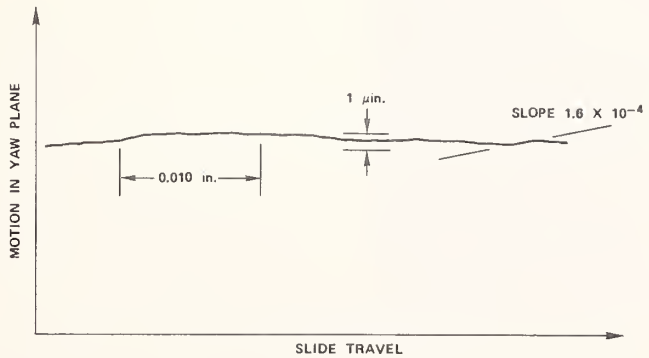

Figure 4. Measured short-period departure from ideal straight line motion in the yaw plane of the tool slide.

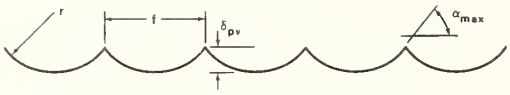

$\delta_{pv} \cong f^2/8r$ ASSUMING THAT $f/r << 1$

$\alpha_{max} \cong f/2r$

OR RMS VALUES:

$\delta_{rms} \cong \delta_{pv}/\sqrt{5}$

$\alpha_{rms} \cong \alpha_{max}/\sqrt{3}$

Figure 5. Ideal finish achieved by machining with a tool of nose radius r, and a feed rate f. Both peak-to-valley (pv) and rms values are given.

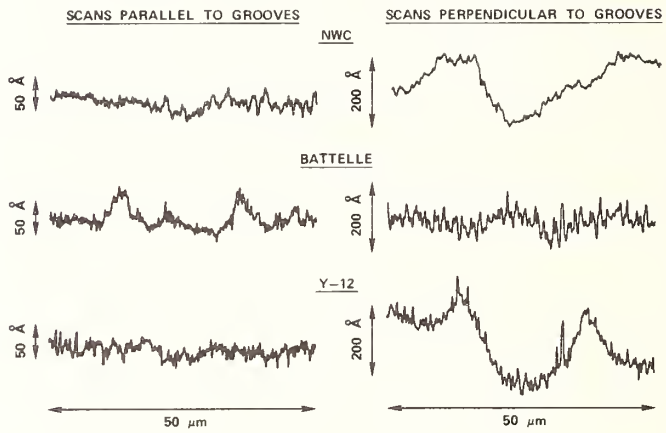

Figure 6. An intercomparison of the surface profiles of several diamond-turned surfaces obtained with a Talystep profilometer with a 0.1-μm radius stylus. Scans both parallel and perpendicular to the residual machining structure are shown. The NWC surface is a 6-inch sample turned at 800 revolutions/minute with a feed rate of 3 x 10^{-4} inch/revolution.

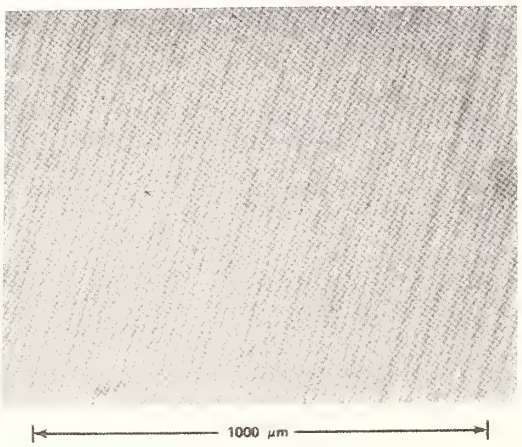

Figure 7. This Nomarski micrograph shows the very uniform residual turning structure on the NWC diamond-turned surface shown in figure 6.

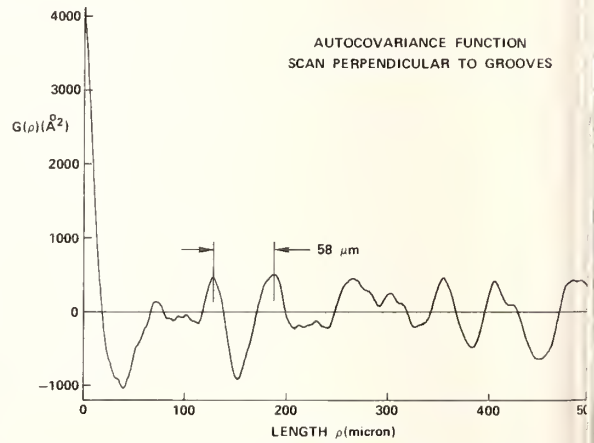

Figure 8. The autocovariance function plotted in this figure is for a scan made perpendicular to the machining grooves of the 6-inch NWC turned copper disc shown in figures 6 and 7.

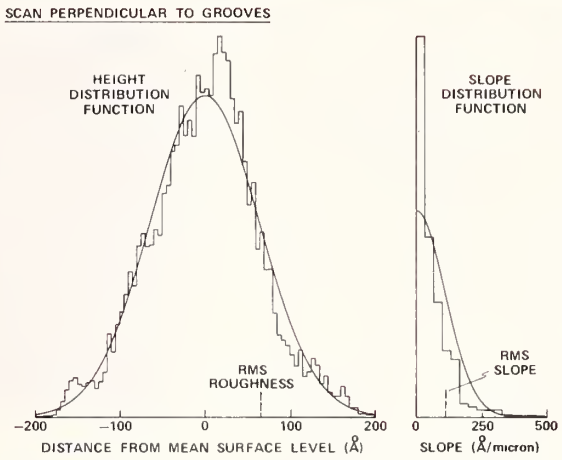

Figure 9. This figure shows the height and slope distributions corresponding to the autocovariance function plotted in figure 8.

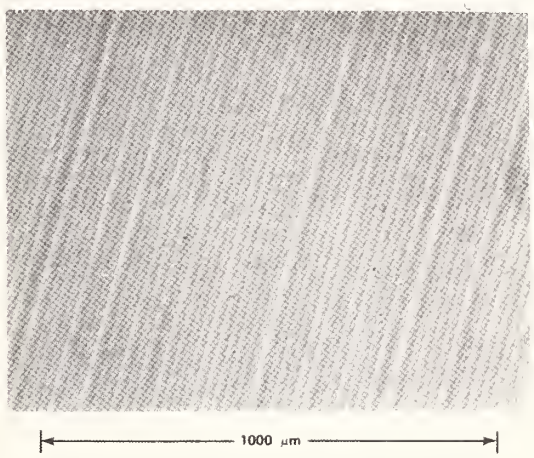

Figure 10. This Nomarski micrograph is of the Y-12 diamond-turned copper surface displayed in figure 6, showing some irregularity of the residual structure and a typical concentration of localized surface defects.

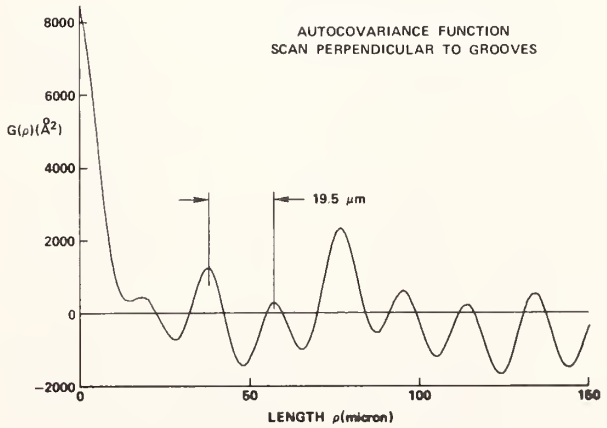

Figure 11. This figure is a plot of the autocovariance function of the Y-12 sample shown in figure 6.

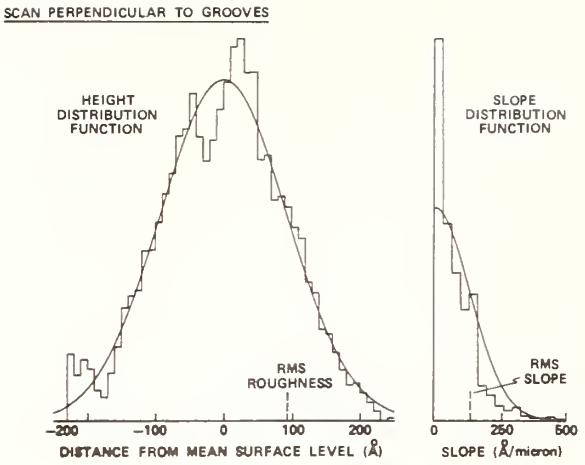

Figure 12. This figure is a plot of the height and slope distribution functions of the Y-12 sample shown in figure 11.

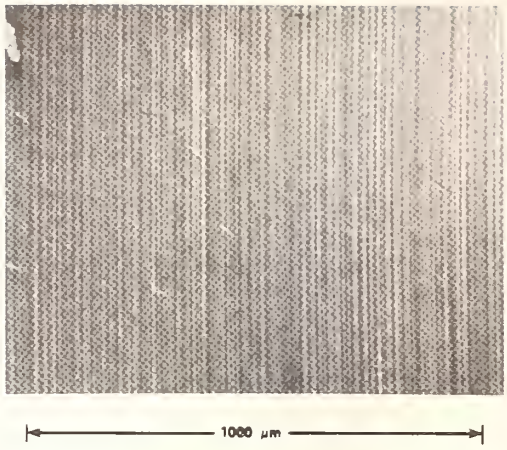

Figure 13. This Nomarski micrograph is of a Batelle Northwest diamond-turned copper surface shown in figure 6, displaying a large variation in the noticeably higher spatial frequency structure of this surface.

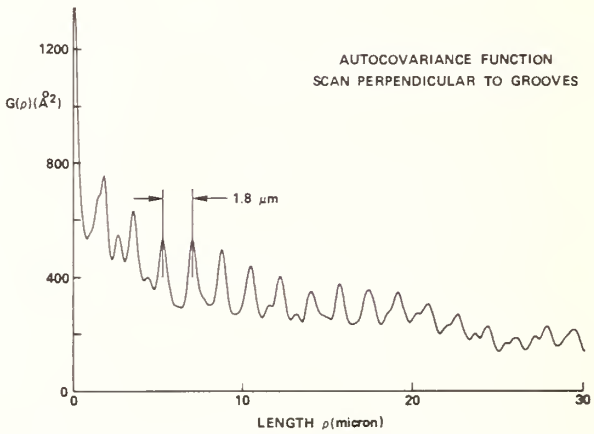

Figure 14. The autocovariance function for the Battelle sample of figure 13. This surface is characterized by very strongly correlated short-period structure.

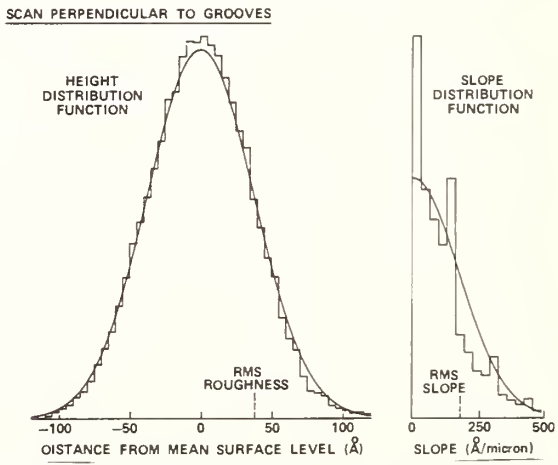

Figure 15. The height and slope distribution functions of the Battelle surface shown in figure 14 have a roughness value intermediate between the NWC and Y-12 values, but with an rms slope considerably larger than the Y-12 value.

Discussion

It was pointed out, that for the present studies, the machine is not temperature stabilized but performs satisfactorily due to its large thermal mass and the relatively short duration (minutes) of the cut. Ultimately, as more precise surfaces are required, cuts will be of longer duration; and thermal stabilization or temperature control of the machine will be required.

It was pointed out from the audience that diamond-turned copper mirrors degrade more rapidly than polished copper in the gas environment of industrial CO_2 lasers. This result is somewhat at variance with past experience with diamond-turned aluminum, which oxidized more slowly than polished aluminum. It should be noted that both the quality of the copper and the cleanliness of the mirror would affect the rate at which it degrades. The effect noted was significant, however, and warrants further investigation.

OPTICAL AND METALLURGICAL CHARACTERIZATION OF MOLYBDENUM LASER MIRRORS*

Shew M. Wong
Rockwell International, Rocky Flats Plant, Golden, CO 80401

George Krauss
Department of Metallurgical Engineering, Colorado School of Mines
Golden, CO 80401

and

Jean M. Bennett
Michelson Laboratory, Physics Division
Naval Weapons Center, China Lake, CA 93555

A study has been performed to determine the correlation between the microstructure, metallurgical processing, and surface finish of eight specially selected molybdenum (Mo) specimens from various sources. Samples of bar and plate stock produced from pure Mo either arc-cast or pressed and sintered, and TZM (Ti-Zr-Mo) Mo alloy were examined in the form of optically polished 1 1/2-inch- (3.86-cm-) diameter discs. Metallurgical characterization included hardness measurements, grain size and shape determinations from polished and etched sections, scanning electron microscopy, and Auger electron spectroscopy. Optical characterization consisted of measurements of total integrated scattering, rms roughness, height distribution functions, and autocovariance. In some cases, the surface roughness of as-polished mirror surfaces could be directly related to grain structure and substructure as revealed by etching. These observations and their implications for the selection of Mo starting stock to be used in the production of low-scatter laser mirrors will be discussed.

Key words: Laser mirror; metallurgical characterization; microstructures; molybdenum; optical characterization.

Introduction

Molybdenum (Mo) is a material of interest for high power laser mirrors because it has good heat conductivity, low thermal expansion, a reasonably high damage threshold, and is sufficiently stiff that thin mirror faceplates can be fabricated and attached to water-cooled backs. The primary drawback to the use of Mo is that it is difficult to obtain low scatter surfaces. Since Mo cannot be diamond-turned using present techniques [1][1], the only way to obtain optical surfaces is by polishing. Either the bulk material can be polished, or a layer of Mo can be sputtered onto a polished Mo surface and the sputtered layer polished. This latter method has the advantage that the sputtered layer can have a very fine grain structure, and hence can be polished to a very smooth finish, of the order of 15 Å rms. However, the sputtered layer may be porous, and the damage threshold for polished sputtered Mo on Mo is lower than that of rougher conventionally polished Mo surfaces. The reason for the lowered damage threshold may be related to porosity in the sputtered layer which can affect the heat transfer and make the film unable to support stresses developed during heating and subsequent thermal expansion. There may also be a contamination film at the interface between the sputtered layer and the bulk material which can adversely affect the damage threshold. More work needs to be done in this area.

---

* Work supported by Defense Advanced Research Projects Agency and NWC Independent Research funds.

1. Figures in brackets indicate the literature references at the end of this paper.

The purpose of this study was to determine the relation, if any, between the grain structure in the Mo and the structure appearing on well polished Mo surfaces. Eight samples, which represented commercially available types of material including arc-cast and powder metallurgy products fabricated into both bar and plate stock, were chosen for the study. Metallurgical analyses were performed on all eight samples and included investigation of the as-polished mirror surfaces, etched mirror surfaces, and polished and etched surfaces cut normal to the mirror surfaces. The microstructures, i.e., grain size, substructure and second-phase particles, and hardness were correlated with the processing of the various samples, as supplied by the manufacturer. Chemical analyses of the various Mo specimens were obtained, and the grinding and polishing compounds used to fabricate the optical surfaces were chemically analyzed for impurity content. The optical characterization consisted of absolute normal incidence reflectance, total integrated scattering (TIS), and surface profile measurements. From the scattering and profile data, rms roughness, rms slope, and autocovariance length information were obtained. In addition, Auger scans were made on one sample to determine surface impurities and to see how these penetrated into the depth of the material. Finally, the metallurgical and optical data were compared, and it was found that there is a direct relation between the grain and subgrain structure in the bulk material and the structure appearing on well polished Mo surfaces.

Mirror Materials

Table 1 lists the identification number, shape, method of preparation, final mechanical and thermal processing, and chemical analysis, where available, of the eight Mo mirrors examined in this investigation. The materials selected represent a good mixture of processing histories that might be expected to affect microstructure and polishing behavior. There are essentially three groups of materials: (1) low carbon, arc-cast Mo, (2) powder metallurgy Mo, and (3) arc-cast Mo TZM alloy. The first type of Mo is produced by vacuum-arc melting of powdered Mo in a water-cooled copper mold, and is expected to be of high purity with a minimum of second-phase particles. The second group of Mo samples is produced from compacted and sintered Mo powder, and is expected to contain some voids and/or oxide particles as a result of this processing approach. The TZM alloy is produced by vacuum-arc melting of carbon-deoxidized Mo with the alloying elements titanium and zirconium in a water-cooled copper mold. The titanium and zirconium additions are designed to produce a dispersion of fine carbide particles that improve strength and high temperature structural stability. The types of Mo described above may be wrought into either bar or plate shapes after the ingot or initial compacted bar is produced. Also included in table 1 is vacuum-arc-cast plate sample 50194, similar to specimen NC7720, that was metallurgically characterized but not optically polished.

Polishing

The first four of the eight Mo samples listed in table 1 were polished by Abe Klugman of the Northrop Corporation, according to the grinding and polishing processes documented in the literature [2]. The surface preparation consisted of (1) blocking all four substrates on a flat aluminum plate, (2) rough grinding with a 100-grit silicon carbide wheel on a surface grinder with water and coolant to bring all four substrates into a plane and to remove rough machining marks from the surface, (3) medium grinding on a conventional optical grinding and polishing machine with 22.5-μm-diameter Al_2O_3 grit in water and a cast iron flat grinding tool to remove all 100-grit marks from the surface, (4) fine grinding with 9.5-μm-diameter Al_2O_3 grit on the same machine, and (5) optical polishing, as described below. For the first 10 hours all four substrates were polished on the same block on a conventional optical polishing machine using a medium-hard pitch lap with 0.3-μm-diameter Al_2O_3 powder in water. The brush feed method (applying the alumina to the lap with a brush) was used. After 10 hours of polishing, the substrates were removed from the block and were polished separately for 13 more hours, still with the same pitch and polishing procedure. Nomarski micrographs were taken at various stages of the grinding and polishing process to show how the surface texture developed.

Chemical analyses of the 22.5- and 9.5-μm-diameter Al_2O_3 grinding compounds and the 0.3-μm-diameter Al_2O_3 polishing compound revealed the impurities shown in table 2. The table shows that the grinding compounds are full of many impurities, the largest amounts being titanium, iron, magnesium, calcium, silicon, cerium, and zirconium. The polishing

Table 1. Processing and composition of molybdenum mirror stock.

Sample	Shape	Alloying and/or melting practice	Final mechanical and thermal processing	Chemical analysis (AMAX)
NC10280	Bar stock	Low C Vacuum Arc-cast	85% Cold work; Stress relief; 930°C, 1 hr.	C-0.005%, Fe-0.002, Ni-<.001, Si-0.001 O_2-0.0001, H_2-<.0001, N_2-<.0001
NC7720	Plate	Low C Vacuum Arc-cast	85% Cold work; Stress relief; 900°C, 1 hr.	C-0.003%, Fe-<.001, Ni-<.001, Si-<.001 O_2-0.0003, H_2-<.0001, N_2-0.0001
NSC9152	Bar stock	Powder Metallurgy Processing	67% Cold work; Stress relief; 930°C, 1 hr.	C-0.001%, Fe-0.002, Ni-.001, Si-0.002 O_2-0.002, H_2-<.0001, N_2-0.0001
NTZM10395	Bar stock	Ti and Zr Alloying (TZM) Vacuum-arc-cast	67% Cold work; Stress relief: 1200°C, 1 hr.	Ti-0.45%, Zr-0.08, C-0.022, Fe-0.001 Ni-<.001, Si-<.001 O_2-0.0008, H_2-<.0001, N_2-0.0001
N243	Bar stock	Low C Vacuum Arc-cast	80% Cold work; Stress relief; 930°C, 1 hr.	C-0.004, Fe-0.001, Ni-<0.001, Si-0.001 O_2-0.0006, H_2- 0.0001, N_2-0.0001
S279	Bar stock	Powder Metallurgy Processing	None available	None available
H218	Plate	Powder Metallurgy Processing	10% recrystal.	None available
AP041	Bar stock	Low C Vacuum Arc-cast	80% Cold work; Stress relief; 930°C, 1 hr.	C-0.003%, Fe-0.001, Ni-0.001, Si-0.001 O_2-0.0009, H_2-<0.0001, N_2-0.0002
50194	Plate	Low C Vacuum Arc-cast	Stress relief; 910°C, 1 hr.	C-0.001, Fe-0.003, Ni-<0.001, Si-0.001 O_2-0.0005, H_2-<0.0001, N_2-0.0001

Table 2. Impurities in grinding and polishing compounds obtained from spark source mass spectroscopy.

Numbers are parts per million by weight.

Impurities	Materials		
	22.5 μm Al_2O_3	9.2 μm Al_2O_3	0.3 μm Al_2O_3
As	1	1	-
B	2	-	2
Ba	160	99	-
Ca	1100	2000	2
Ce	920	1700	-
Cl	70	42	-
Cr	190	230	-
Cu	29	23	-
Fe	3940*	2950*	9
K	320	1600	62
La	180	100	-
Mg	2100	2600	6
Mn	400	490	-
Na	520	640	53
Ni	47	17	-
P	15	18	8
Pb	1	4	-
Pr	82	87	-
S	110	120	67
Si	1100	1400	70
Sr	160	300	-
Ti	20,000	11,000	-
V	75	91	-
Y	8	14	-
Zn	130	40	-
Zr	470	1900	-

* Results obtained by atomic absorption.

compound is very much cleaner, and has appreciable amounts of only silicon, sulfur, potassium, and sodium. There are only 9 ppm of iron in the polishing compound, although iron is the only impurity other than sodium that appeared on the polished surface of one of the Mo samples.

Surface Chemistry

In order to obtain information about what materials are present on Mo surfaces, Auger scans were made on the low carbon, arc-cast plate sample NC7720. The results are shown in figures 1 and 2. Figure 1 shows that on the as-polished surface there are detectable amounts of carbon, oxygen, nitrogen, iron, and sodium. Of these, carbon, oxygen, and nitrogen are present on most surfaces because of adsorption of air molecules. The iron and sodium may have come from the polishing compound, since both are present there in small amounts. After 3 minutes of sputter-etching with argon, during which some material was removed, no iron, sodium, or nitrogen could be detected, even though the gain on the high energy part of the scale was boosted by a factor of 3. The amounts of oxygen and carbon were considerably reduced and the Mo peaks were much more prominent. In order to show how the amounts of contaminants varied in the depth of the material, an Auger depth profile was made, as shown in figure 2. The two major contaminants, oxygen and carbon, dropped after the sputter-etching began, the oxygen decreasing more slowly; the small amount of iron

became an undetectable amount. The proportionate amount of Mo increased as the contaminants were removed. After the sputter-etch stopped, the amount of oxygen on the surface started to increase. The oxygen seems to be tightly bound on the surface layers and, once removed, the fresh Mo surface seems to absorb oxygen quite rapidly.

Optical Measurements and Surface Roughness Characterization

The normal incidence reflectances of the first four Mo samples listed in table 1 were measured shortly after the polishing was completed, and the results are shown in table 3. The precision of the measurements is about ±0.0004 or better and the accuracy is ±0.001. It is seen that the reflectances of the various samples at a given wavelength are within a few tenths of a percent of each other, even the alloy TZM. Thus, the small amounts of titanium and zirconium apparently do not affect the reflectance. The maximum reflectance differences are at the shortest wavelengths in the ultraviolet where the effects of surface films, scattering, etc. would be the largest. Since all the samples scattered about the same amount of light, the constancy of the reflectance indicates that the reflectance is insensitive to the metallurgical form of the Mo, i.e., the grain and subgrain structure.

Surface scans made by a Talystep surface-profiling instrument [3,4] are shown in figures 3-12. These correlate very well with the Nomarski micrographs of the polished surfaces shown in figures 14(a)-21(a). For example, the coarse surface structure of specimens NC10280 and S279 are clearly shown in both the surface scans (figs. 3 and 10) and the Nomarski micrographs [figs. 14(a) and 19(a)]. The scratches on the surface of specimen AP041 shown in the Nomarski micrograph [fig. 21(a)] also appear in the surface scan (fig. 12), although the largest scratches have been avoided. Since this material is similar to that from which specimens NC10280 and N243 were made, it is clear that the polishing technique plays an important role in the surface finish which can be obtained. The Nomarski micrographs do not show the particulates which project 100 to 200 Å above the surface level in the NTZM10395 and N243 specimens. However, these particulates have diameters of 1 to 2 μm, as judged from the surface scans, so they would be close to the limit of resolution of the optical microscope used for the Nomarski pictures. The particles may be inclusions, or, in the case of the TZM, particles of titanium or zirconium carbide.

Table 4 summarizes the optical measurements made on all eight polished Mo specimens. The first column contains rms roughness values for the polished surfaces derived from measurements of TIS made at a laser wavelength of 5682 Å or 6328 Å. A relation predicted by the scalar scattering theory is used: $TIS = (4\pi\delta/\lambda)^2$, where δ is the rms roughness and λ the wavelength [5]. This relation defines an "effective rms roughness," since implicit in the derivation of the relation is the assumption that the distribution of heights of surface features about the mean surface level is Gaussian. This assumption is not satisfied for several of the Mo specimens, as has been determined from measurements of the height distribution function from digitized Talystep surface height data [6]. Figure 13 shows two such non-Gaussian height distributions. Specimen NC10280 had proportionately too many small bumps and too few shallow holes, while specimen NTZM10395 had the only bimodal height distribution yet measured. This distribution may be caused by small carbide particles which either project slightly above the mean surface level or tear out of the surface leaving shallow holes. The remainder of the columns in table 4 contain data obtained from Talystep surface scans. The digitized surface height data are used to calculate the rms roughness, rms slope, and the autocovariance function. The autocovariance length is obtained from the 1/e value of the autocovariance function, and can be thought of as a measure of the separation of surface features. Short correlation distances mean that the features are closely spaced, and, conversely, larger correlation distances mean that they are farther apart. Light scattering from a surface depends not only on the heights of surface features but also on their slopes. A surface with a small rms roughness but large rms slope may scatter as much as a more wavy surface with a much larger rms roughness and very small rms slope. Thus, both light scattering data and surface profile data are necessary to understand the optical behavior of the Mo surfaces.

Table 3. Normal incidence reflectances of polished molybdenum mirrors.

Wavelength (μm)	Low carbon arc-cast bar NC10280	Low carbon arc-cast plate NC7720	Powder met. bar NSC9152	TZM arc-cast bar NTZM10395
0.2600	0.6712	0.6731	0.6772	0.6722
0.2800	0.6564	-	-	-
0.3000	0.6180	0.6190	0.6209	0.6188
0.3200	0.5821	-	-	-
0.3300	0.5740	-	-	-
0.3400	0.5691	-	-	-
0.3500	0.5692	0.5710	0.5705	0.5699
0.3600	0.5648	-	-	-
0.3700	0.5633	-	-	-
0.3800	0.5652	-	-	-
0.3900	0.5671	-	-	-
0.4000	0.5708	0.5711	0.5695	0.5701
0.4200	0.5761	-	-	-
0.4400	0.5868	-	-	-
0.4600	0.6001	-	-	-
0.4800	0.6024	-	-	-
0.5000	0.6046	0.6039	0.6051	0.6043
0.5200	0.6023	-	-	-
0.5400	0.5995	-	-	-
0.5461	0.5981	0.5964	0.5978	0.5970
0.5500	0.5971	0.5959	0.5966	0.5962
0.5600	0.5955	-	-	-
0.5682	0.5936	0.5934	0.5931	0.5909
0.5800	0.5934	-	-	-
0.6000	0.5931	0.5930	0.5928	0.5922
0.6250	0.5955	-	-	-
0.6500	0.5982	-	-	-
0.6750	0.6000	-	-	-
0.7000	0.5984	0.5977	0.5976	0.5971
0.7250	0.5963	-	-	-
0.7500	0.5948	-	-	-
0.7750	0.5930	-	-	-
0.8000	0.5915	0.5921	0.5911	0.5906
0.8250	0.5926	-	-	-
0.8500	0.5919	-	-	-
0.9000	0.6015	-	-	-
0.9500	0.6313	-	-	-
1.0	0.6938	0.6912	0.6922	0.6920
1.2	0.7952	-	-	-
1.5	0.8854	-	-	-
2.0	0.9399	-	-	-
3.0	0.9709	0.9692	0.9700	0.9674
4.0	0.9728	-	-	-
5.0	0.9746	-	-	-
6.0	0.9764	-	-	-
7.0	0.9780	0.9767	0.9778	0.9808
8.0	0.9797	-	-	-
9.0	0.9800	-	-	-
10.0	0.9816	-	-	-
10.6	0.9820	0.9802	0.9818	0.9831
12.0	0.9823	-	-	-
14.0	0.9833	-	-	-
16.0	0.9845	0.9841	0.9847	0.9852
18.0	0.9850	-	-	-
20.0	0.9858	0.9857	0.9863	0.9872

Table 4. Surface statistics of polished molybdenum mirrors.

Sample	rms Roughness (Å)*	rms Roughness (Å)**	rms Slope (Å/μm)**	Auto-covariance length (μm)**
NC10280	15.4	40.2	47.0	24.4
NC7720	17.0	71.4	43.6	14.4
NSC9152	20.7	37.8	59.0	5.3
NTZM10395	21.7	60.6	156.2	2.4
N243	16.3	56.9	131.1	3.0
S279	20.7	64.8	62.3	7.0
H218	23.2	31.0	51.3	3.3
APO41	63.4	31.8***	79.3***	1.9***

* Calculated from total integrated scattering measurements.
** Measured with Talystep surface profiling instrument.
*** Region without deep scratches.

Microstructural Characterization

The results of the metallurgical characterization are summarized in table 5, and micrographs of each of the polished specimens are shown in figures 14-21. In each figure the Nomarski micrograph of the polished mirror surface is designated by (a), while the balance of the pictures are standard light micrographs of metallographically polished or polished and etched surfaces. A few scanning electron microscope micrographs are included in some of the series and are marked as such. In some cases, only the microstructure of normal surfaces could be etched because the mirror surfaces had been coated for high reflectance in the ultraviolet wavelength region subsequent to the optical measurements described in the previous section. The coated specimens are identified in table 5.

The results of the metallurgical characterization show that, in general, elements of the grain structure or the substructure within the grain were revealed on the polished mirror surfaces if good polishing techniques were used [2]. The grain structure in each case was strongly affected by the nature of the mechanical processing. In the bar stock the grains were elongated parallel to the longitudinal axis of the bar, and hence the mirror surface intersects the cross sections of the deformed grains. Figures 18(d) and 21(d) show the elongation of the grains on surfaces normal to the mirror surface, while figures 18(b) and 21(b) show the grain cross sections on the mirror surfaces. For the most part, the grains in bar stock have equiaxed cross sections, but some grain boundaries show a curvature that has developed to accommodate the cylindrical shape of the bar stock. In plate stock, on the other hand, the grains have been flattened by rolling to a plate or pancake shape with the flat, broad grain surfaces intersected by the mirror surfaces [figs. 15(b) and (c)] and the reduced, elongated grain sections parallel to the mirror surface [figs. 15(d) and (e)]. The pronounced elongation and deformation of the grains in all of the specimens is a consequence of the large amounts of cold work introduced during the final reduction stages, 67% to 85%, as noted in table 1, and the fact that the stress relief treatments did not produce recrystallization or a return to an equiaxed grain structure. The stress relief treatment did, however, produce a fine substructure within the grains, as shown best in figures 14(c) and 15(c). Frequently, the scale of the surface relief revealed in the Nomarski micrographs could be directly related to the substructures developed by the stress relief treatment.

An important effect of grain orientation is the difference in the rates of polishing of adjacent grains having different orientations. Evidently, when certain crystal planes are parallel to the plane of polish, they polish much more slowly than do their neighbors, thus producing a noticeable surface relief or roughness directly related to the grain

Table 5. Hardness and microstructural characterization of polished molybdenum mirrors.

Specimen	Hardness KHN (500 gm)	Final mirror surface preparation	Grain size* μm	Microstructures**	
				Mirror surface	Normal surface
NC10280	282.15 ±15.28	Polished and coated with $(HfO_2/MgF_2)_4$/Al	11.5	Unetchable. Layer peeled off at rim. Some inclusions (carbides) visible.	Elongated grains ⊥ mirror surface. Clean microstructure--few inclusions.
NC7720	274.64 ±13.86	Polished	7.0	Pancake-shaped grains as large as 180 μm in width. Substructure within grains appears to correlate features on Nomarski micrograph.	Elongated grain structure ∥ mirror surface. Some inclusions on as-polished surface.
NCS9152	271.39 ±16.10	Polished and coated with $(MgO/MgF_2)_7$/Al	15.0	Unetchable, but circular particles visible. Diameter of particles 0.25 to 2.0 μm.	Elongated grain structure ⊥ mirror surface. Very uniform worked grain structure. Elongated inclusions and/or pores--correlate with powder metallurgy processing (see SEM micrographs).
NTZM10395	326.00 ±15.00	Polished and coated with $(ZrO_2/MgF_2)_4$/Al	22.0	Unetchable. High hardness correlates with alloying.	Elongated grain structure ⊥ mirror surface. Carbide particles about 2.5 μm in diameter.
N243	261.33 ±12.77	Polished	14.0	Duplex grain structure. Finest grain structure correlate with surface features. Mixed grain sizes correlate with larger final bar diameter.	Elongated grain structure ⊥ mirror surface. Comparable metallurgically to AP041--polishing technique varies.
S279	304.33 ±21.49	Polished	55.0	Coarse, equiaxed to pancake-shaped grains with substructure. Many spherical particles on surface. Grain structure correlates with Nomarski micrograph.	Elongated grain structure ⊥ mirror surface. Spherical inclusions, many line up in grain boundaries. High hardness corresponds to oxide dispersion.
H218	279.05 ±18.32	Polished	7.5	Elongated pancake-shaped grains. Some very fine substructures visible. No evidence of recrystallization.	Elongated grain structure ∥ mirror surface. Fine grain size consistent with powder metallurgy processing.
AP041	258.73 ±10.81	Polished	14.0	Highly distorted and curved grains of variable sizes. Scratches and particles on as-polished surface.	Elongated grain structure ⊥ mirror surface. Lowest hardness microstructure as is N243.

* Transverse to metal working direction.
** Etched in 50% NH_4OH - 50% H_2O_2.

structure. This phenomenon is demonstrated on most of the specimens, and figures 18(c) and 21(c) are good examples. The differential polishing effect related to grain orientation is probably the major cause of the surface relief seen in the Nomarski micrographs and the Talystep profiles.

In addition to grain structure and substructure, the metallographic examination showed second-phase particles of various forms consistent with the processing history of the Mo mirror stock. Fine carbides were found in the TZM specimen [figs. 17(c) and (d)], in accord with the alloy carbide dispersion expected in this alloy. The powder metallurgy fabricated specimens showed evidence of elongated oxides and/or porosity. Figures 16(c) and (d) show good examples of the latter features. The source of the oxides is frequently due to the oxides on the Mo powder which is pressed and sintered, and frequently porosity results when theoretical density is not achieved during the pressing, sintering, and subsequent reduction of the powder metallurgy product.

Laser Damage Measurements

Multithreshold laser damage measurements were made at a wavelength of 10.6 μm (100 nsec pulse length) on two of the polished samples, NC10280 and NC7720, using the laser damage facility described previously [7]. The damage profile of vacuum-arc-cast Mo plate specimen NC7720 is shown in figure 22. The threshold for craters is greater than 59.8 J/cm^2, the maximum energy in the laser pulses. The threshold for melting, 15.1 ± 0.4 J/cm^2, is a convenient parameter to use for comparing the performance of different samples. For eight bare Mo samples damage tested, this parameter varied from a maximum of 17.5 ± 2.0 to a minimum of 9.2 ± 0.2 J/cm^2. The lowest value was for a polished Mo specimen onto which a layer of Mo had been sputtered and then polished. The lowest threshold for a polished sample was 11.0 ± 0.3 J/cm^2; this sample was the roughest of those tested, having a roughness of 47.3 Å rms, as measured by TIS. The rest of the samples, which were smoother, also had higher damage thresholds, and sample NC7720 was among the smoothest, and was also among the most damage resistant. Although the surface microstructure was not characterized for the other specimens (except for NC10280), it is probable that a variety of types of structures were represented. Thus, we can conclude that for well polished Mo specimens the damage threshold for melting for pulsed 10.6 μm laser radiation is probably independent of microstructure.

The damage morphology for sample NC7720, shown in figure 23, is typical of that for a well polished Mo surface. Figure 24 shows a portion of the damaged area and a Talystep surface scan made across this area. The white areas in the Nomarski micrograph where the material has melted and recrystallized are appreciably rougher than the undamaged surface.

The damage morphology for film-covered sample NC10280 is shown in figure 25. Since the multilayer $(HfO_2/MgF_2)_4$, designed to enhance the reflectance of the Mo in the ultraviolet, is absorbing at 10.6 μm, the morphology shown in this figure may not be representative of morphology obtained in a region where the films are transparent. However, as the surface scan in figure 26 shows, the films are apparently separating at their interfaces, and there is also melting of the inner MgF_2 layers. Melting and recrystallization greatly increase the roughness of these materials. Failure of film-covered substrates generally occurs at cracks and defects in the films, and occurs at much lower energies than that for the film materials in bulk form or for the substrate material.

Conclusions

In conclusion, Mo samples having metallurgical structures representative of the commercially available types of material have been optically and metallurgically characterized. It has been found that, on well polished samples, there is a close correlation between the grain and subgrain structure in the material and the structure appearing on the polished surface. A major cause of this effect is believed to be associated with variations in hardness, i.e., polishing behavior, of different crystal planes lying parallel to the mirror surface in adjacent grains. On ground or poorly polished samples the grinding and/or polishing marks obscure the grain structure. Different lots of nominally the same material may not have the same metallurgical structure and optical surface structure. Dispersion strengthening elements such as titanium and zirconium that form small particles of

alloy carbides and inclusion particles detract from the polishability of the material and produce small hard particles that project above the surface or pull out, leaving holes. Both holes and bumps produce proportionately much more scattering than the rest of the grain structure of the Mo. More work should be done to determine if it is possible to process Mo in order to get an easily polishable, uniform grain structure which will make possible consistently high quality, low scatter mirrors.

Acknowledgments

The authors would like to thank Russell W. Burman of AMAX Specialty Metals Corporation for providing some of the specimens and for helpful discussions and information about the processing of the specimens, James Capes of Rockwell International, Rocky Flats Plant, for metallographic assistance, and James O. Porteus of the Naval Weapons Center for the laser damage measurements.

References

[1] Arnold, J. B., Morris, T. O., Sladky, R. E., and Steger, P. J., "Machinability Studies of Infrared Window Materials and Metals," Opt. Engr. 16, 324 (1977).

[2] Klugman, A., and Bennett, J., "Polishing of Molybdenum Substrates," in *Proceedings of the High Power Laser Optical Components and Component Materials Meeting*, 3-4 October 1977, Boulder, Colorado, Defense Advanced Research Projects Agency, Arlington, Virginia, December 1977, pp. 163-173.

[3] Elson, J. M., and Bennett, J. M., "Relation Between the Angular Dependence of Scattering and the Statistical Properties of Optical Surfaces," J. Opt. Soc. Am., in press.

[4] Bennett, J. M., "Surface Evaluation Techniques for Optical Components," this conference.

[5] Bennett, H. E., and Porteus, J. O., "Relation Between Surface Roughness and Specular Reflectance at Normal Incidence," J. Opt. Soc. Am. 51, 123 (1961).

[6] Bennett, J. M., and Elson, J. Merle, "Surface Statistics of Selected Optical Materials," in *Laser Induced Damage in Optical Materials: 1977*, A. J. Glass and A. H. Guenther, eds., National Bureau of Standards, Washington, D.C. (NBS Spec. Publ. 509), pp. 142-156.

[7] Porteus, J. O., Jernigan, J. L., and Faith, W. N., "Multithreshold Measurement and Analysis of Pulsed Laser Damage on Optical Surfaces," in *Laser Induced Damage in Optical Materials: 1977*, A. J. Glass and A. H. Guenther, eds., National Bureau of Standards, Washington, D.C. (NBS Spec. Publ. 509), pp. 507-515.

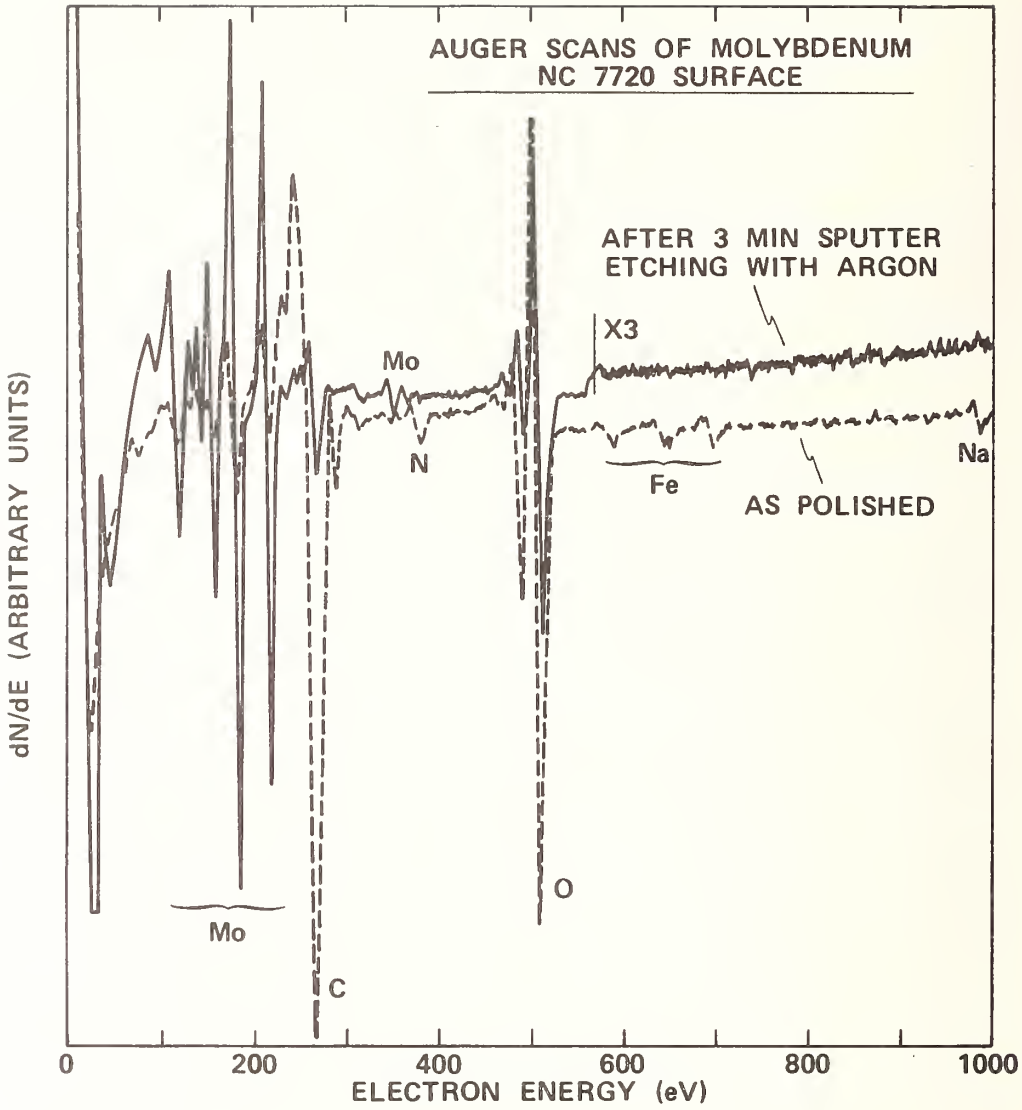

Figure 1. Auger electron spectroscopy scans of the surface of arc-cast Mo plate, specimen NC7720, before and after a 3-minute sputter-etch with argon.

AUGER DEPTH PROFILE OF MOLYBDENUM NC7720 SURFACE

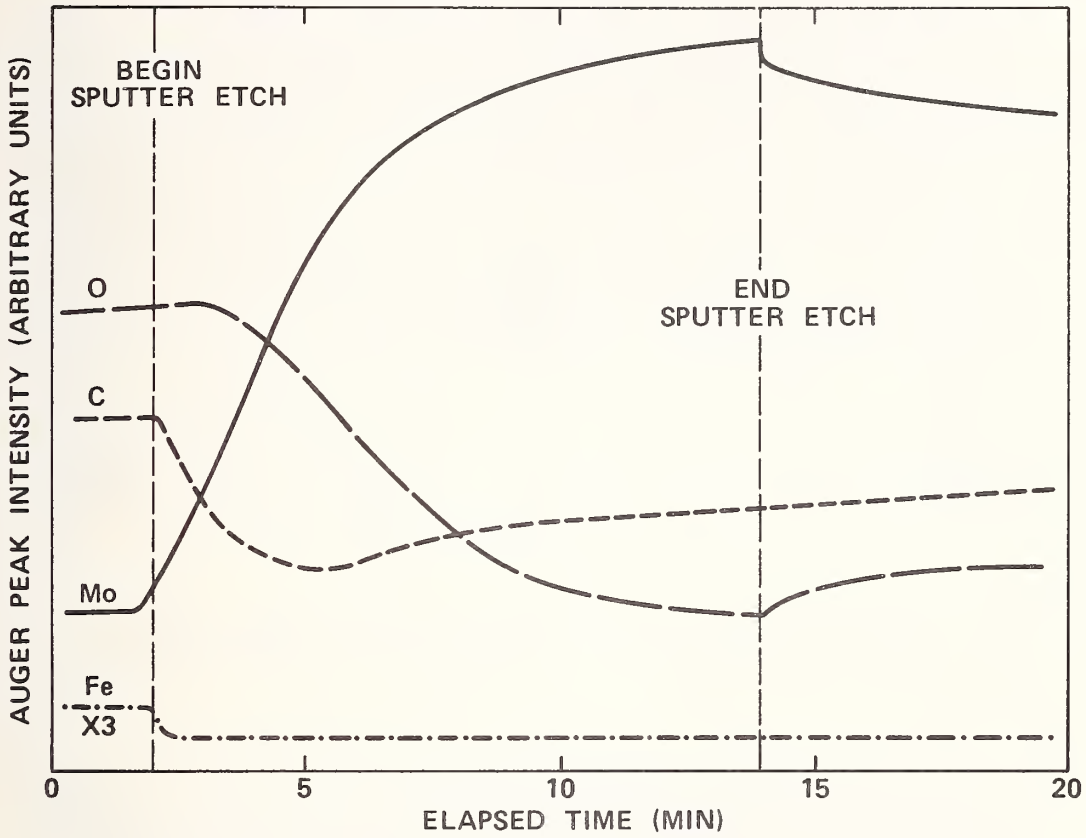

Figure 2. Auger depth profile of the surface of the same Mo specimen as in figure 1.

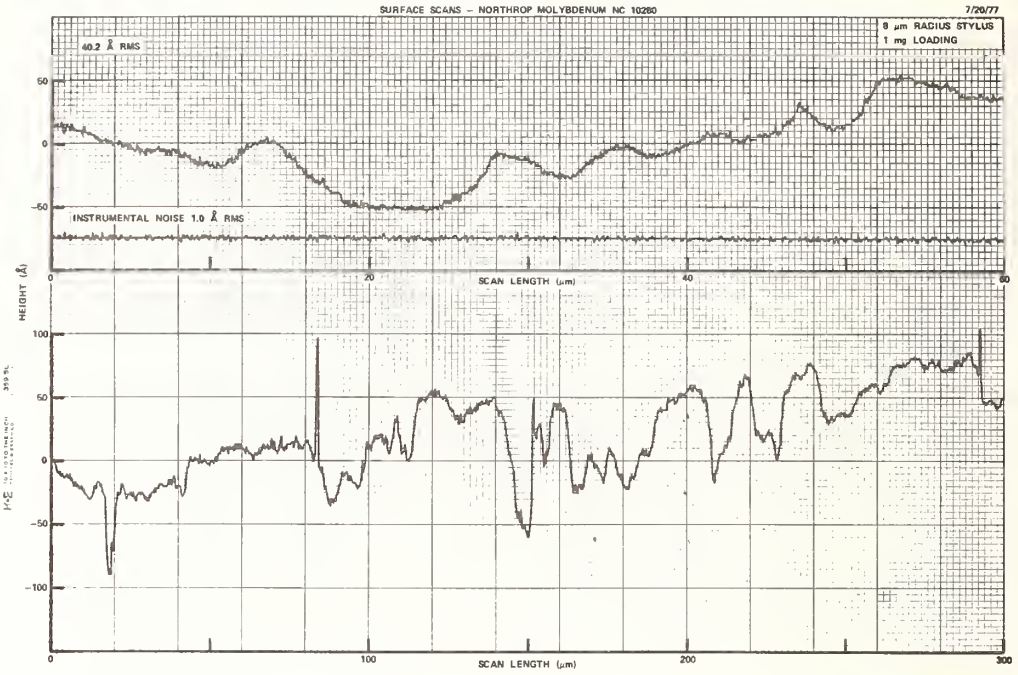

Figure 3. Surface scans of vacuum-arc-cast Mo bar, specimen NC10280.

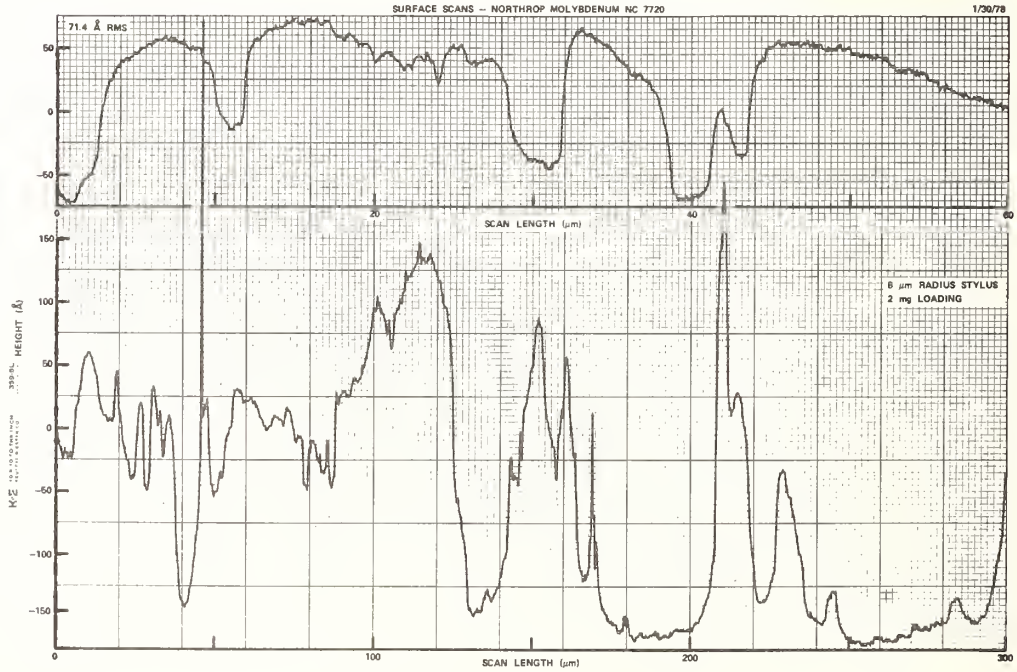

Figure 4. Surface scans of vacuum-arc-cast Mo plate, specimen NC7720.

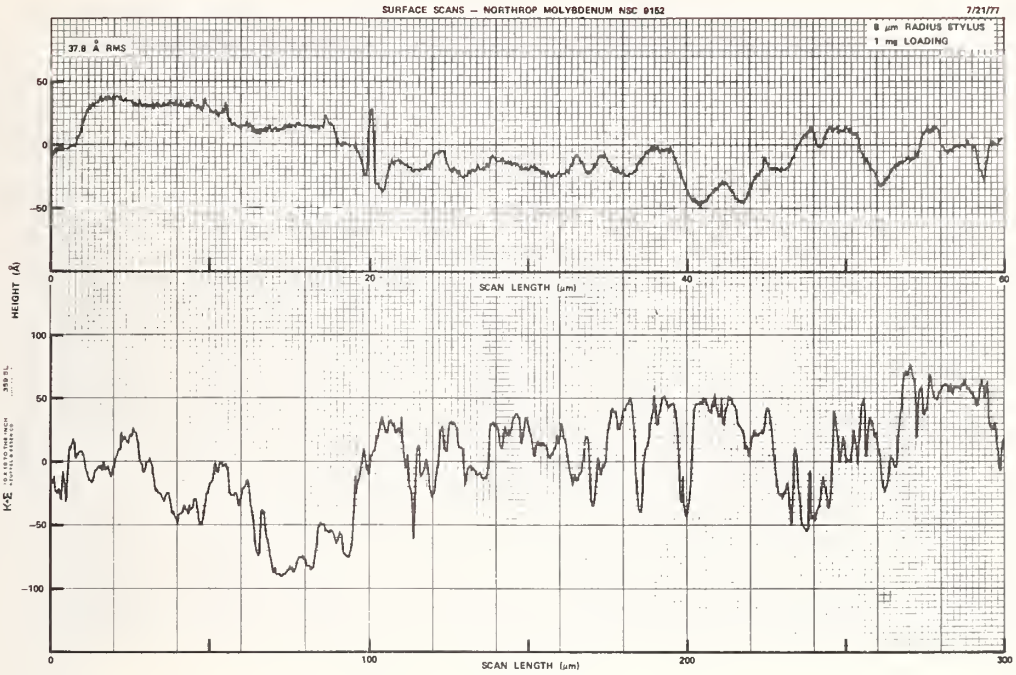

Figure 5. Surface scans of powder metallurgy Mo bar, specimen NSC9152.

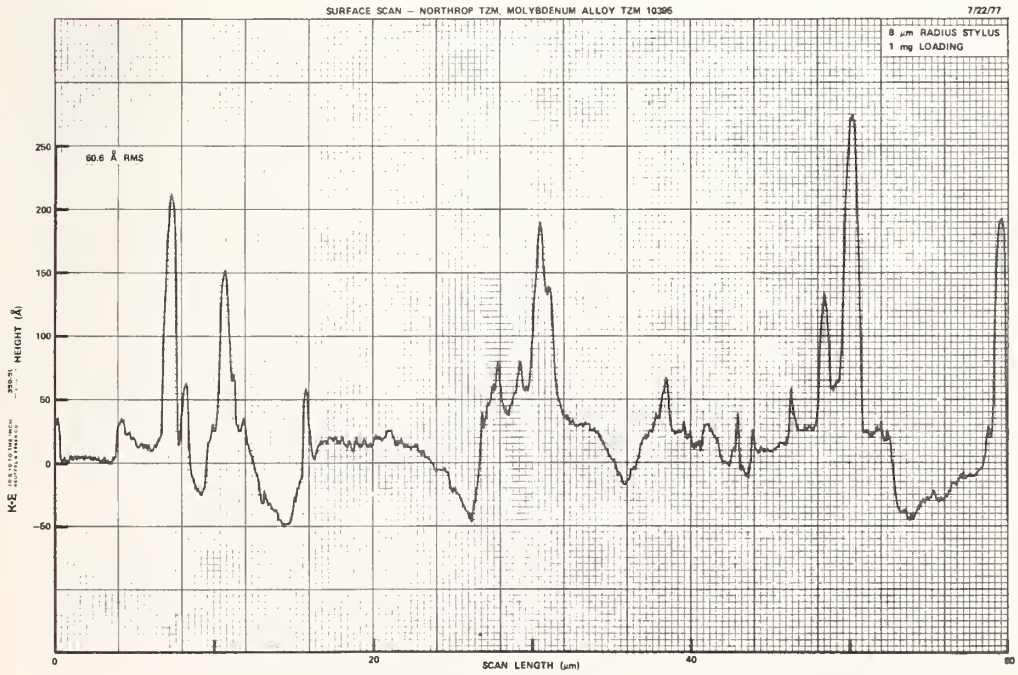

Figure 6. Surface scan of vacuum-arc-cast TZM alloy bar, specimen NTZM10395.

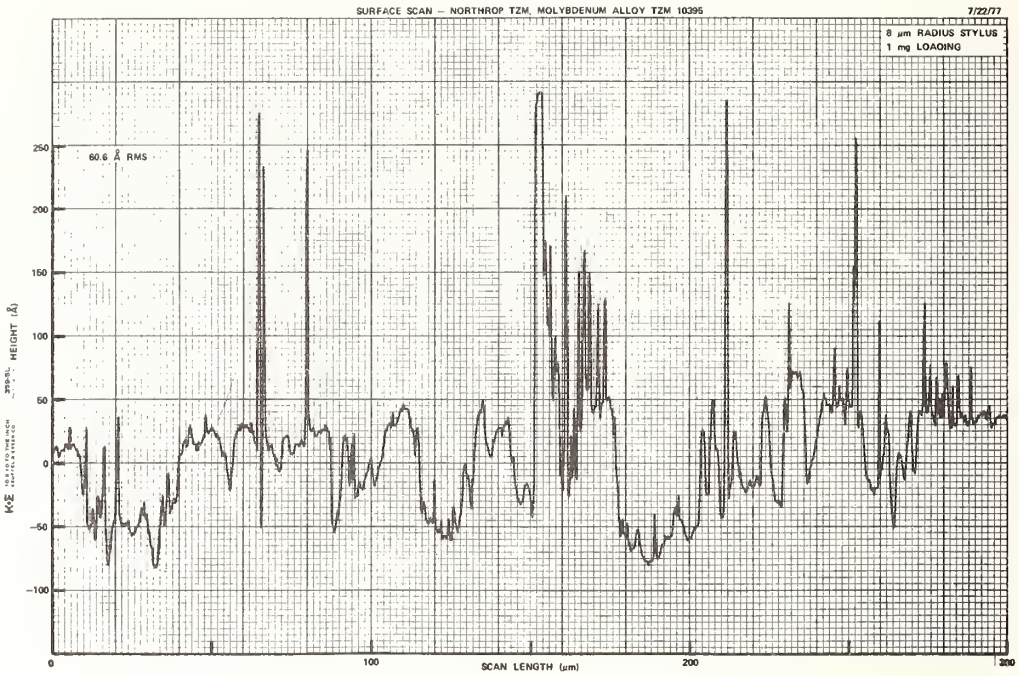

Figure 7. Surface scan of vacuum-arc-cast TZM alloy bar, specimen NTZM10395.

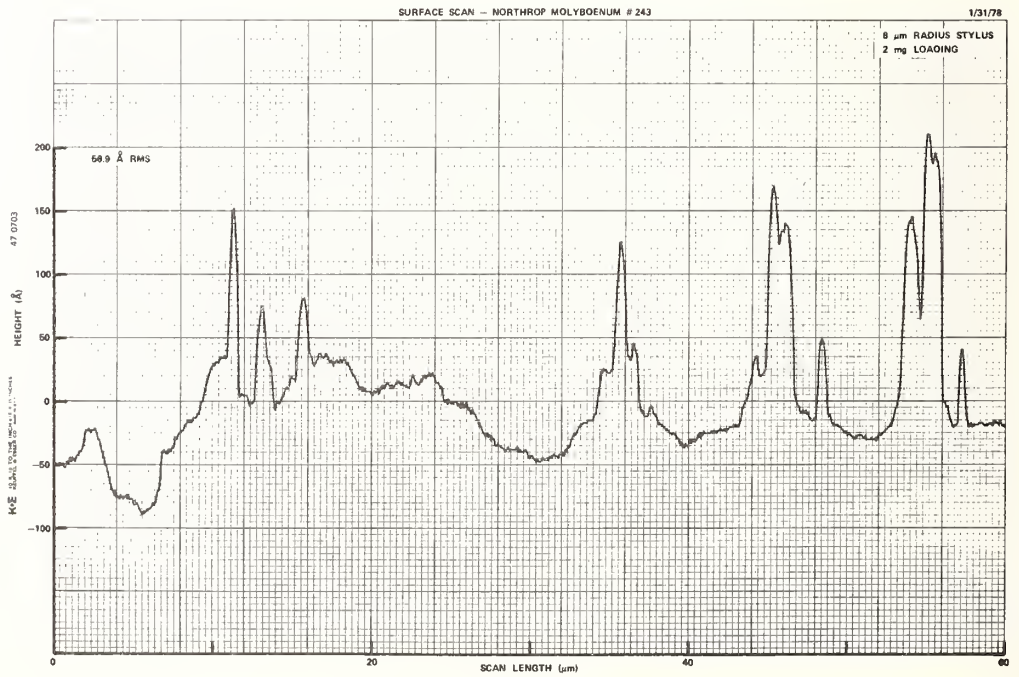

Figure 8. Surface scan of vacuum-arc-cast Mo bar, specimen N243.

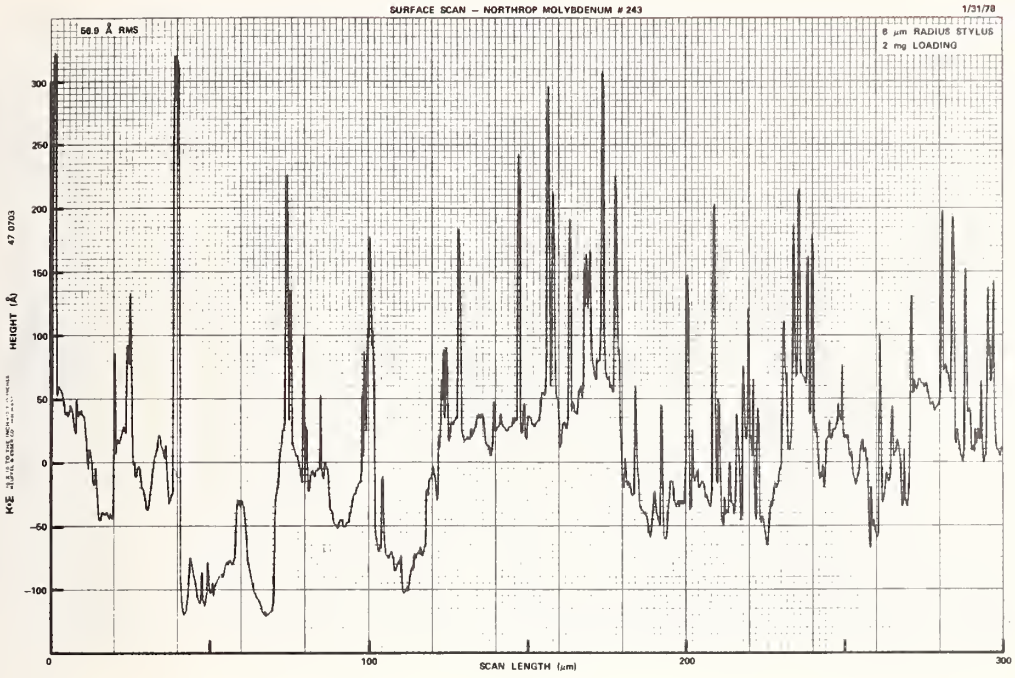

Figure 9. Surface scan of vacuum-arc-cast Mo bar, specimen N243.

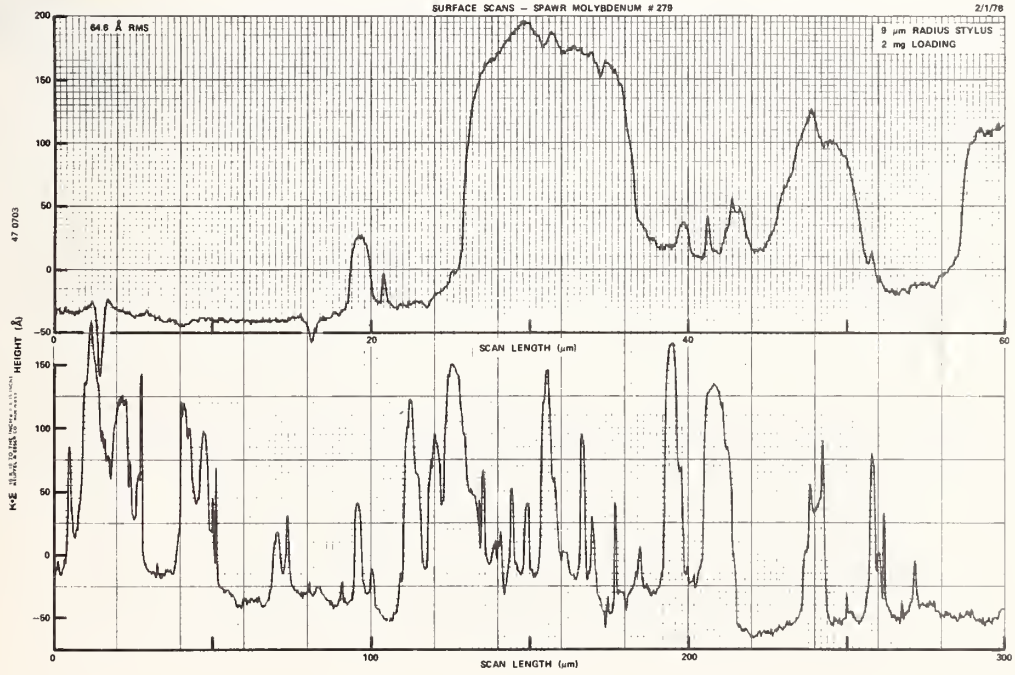

Figure 10. Surface scans of powder metallurgy Mo bar, specimen S279.

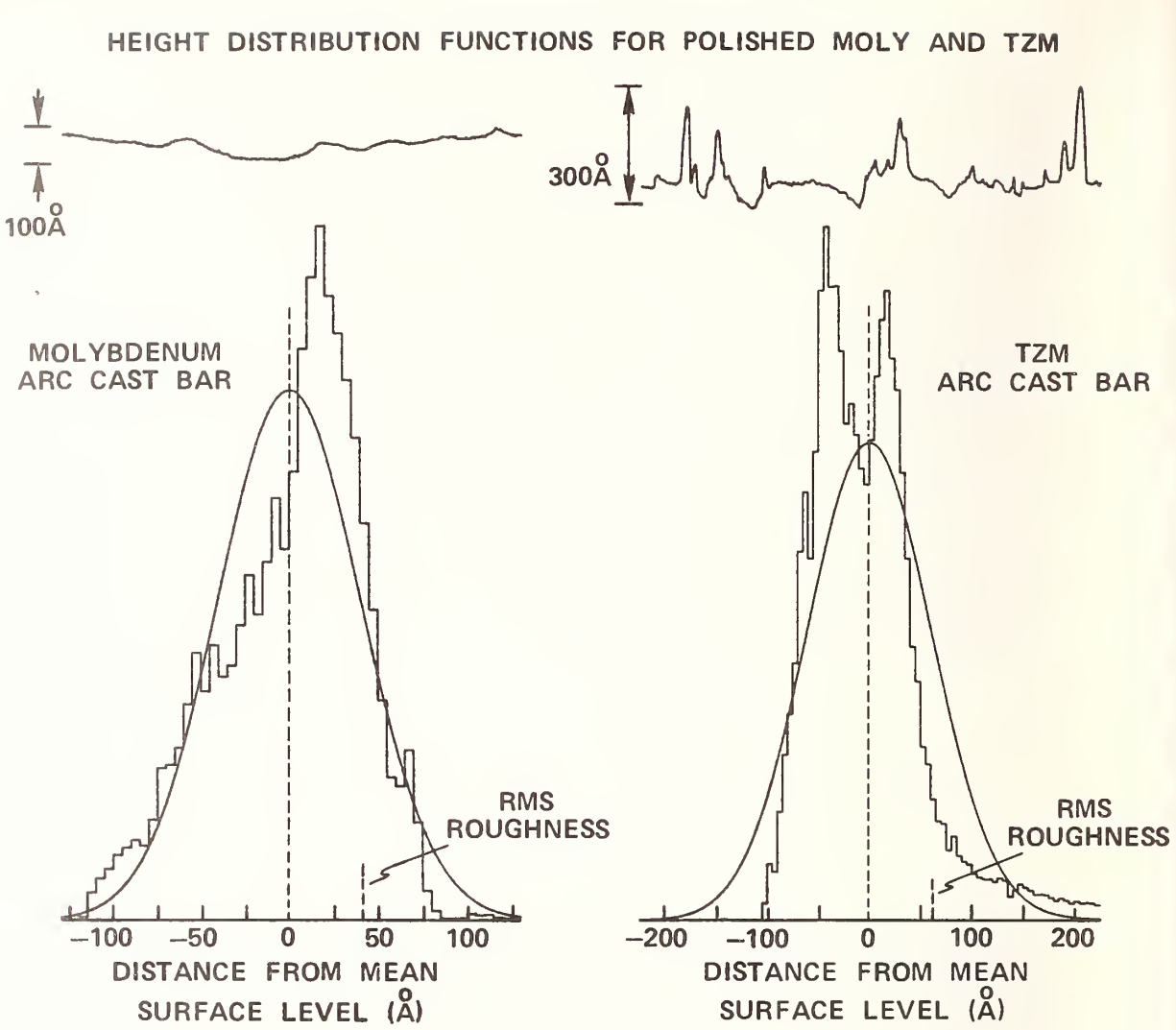

Figure 13. Surface scans and height distribution functions for vacuum-arc-cast bar, specimen NC10280, and vacuum-arc-cast TZM alloy bar, specimen NTZM 10395.

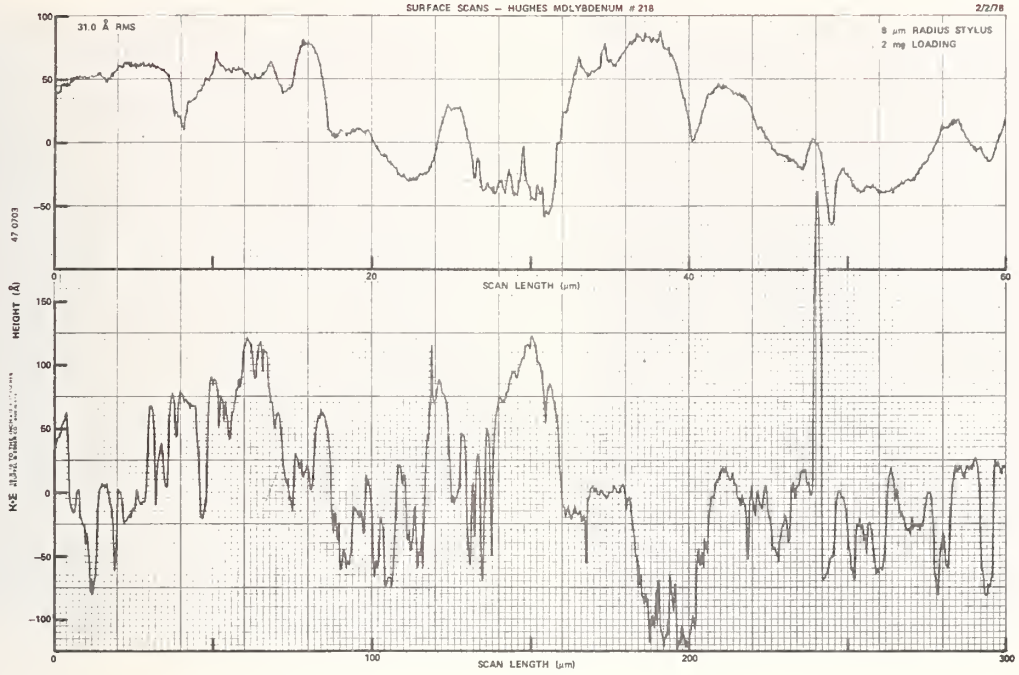

Figure 11. Surface scans of powder metallurgy Mo plate, specimen H218.

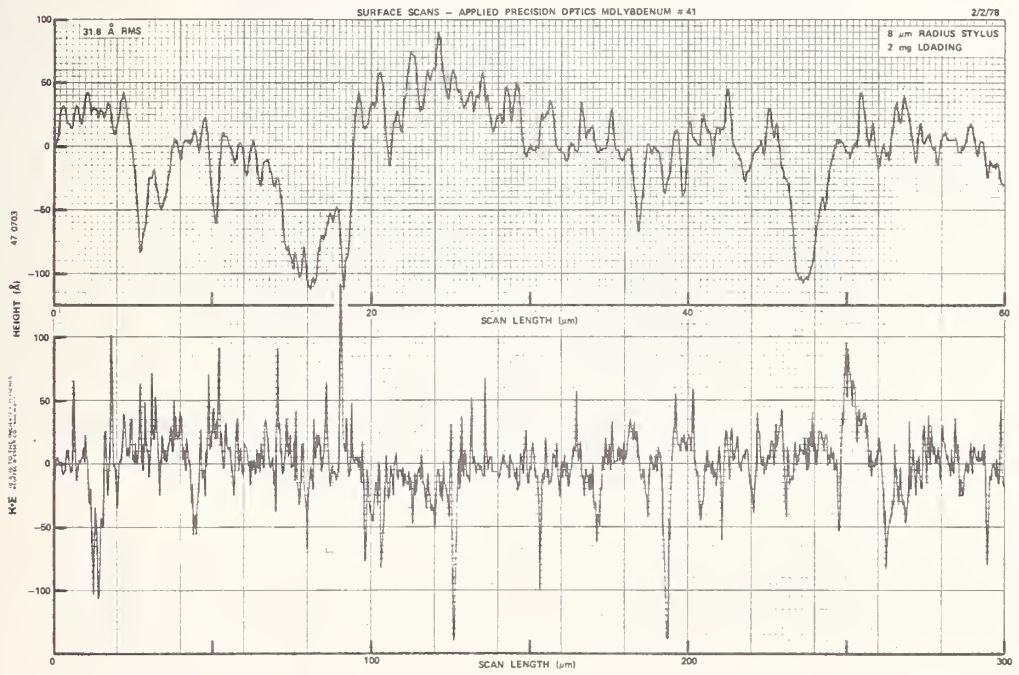

Figure 12. Surface scans of vacuum-arc-cast Mo bar, specimen APO41.

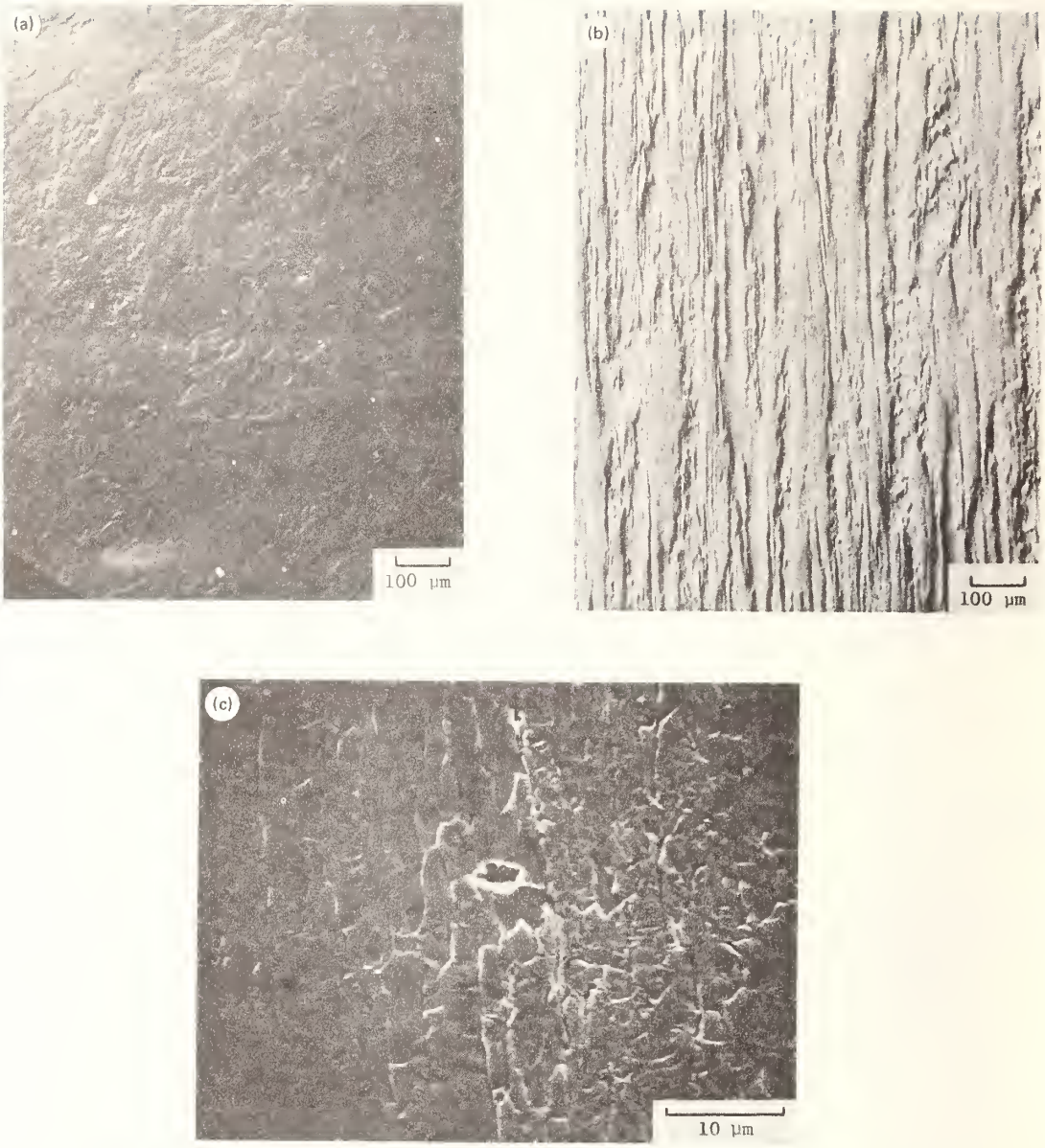

Figure 14. Microstructures of vacuum-arc-cast Mo bar, specimen NC10280: (a) Nomarski micrograph of optically polished mirror surface, (b) micrograph of metallurgically polished normal surface, and (c) scanning electron micrograph of metallurgically polished normal surface.

Figure 15. Microstructures of vacuum-arc-cast Mo plate, (a) to (e) specimen NC7720; (f) and (g), specimen NC50194; (a) Nomarski micrograph of optically polished mirror surface, (b) and (c) micrographs of metallurgically polished and etched mirror surface, the latter with emphasis on substructure, (d), (f), and (g) micrographs of metallurgically polished normal surface, and (e) micrograph of metallurgically polished and etched normal surface.


(d)
100 µm


(f)
100 µm


(e)

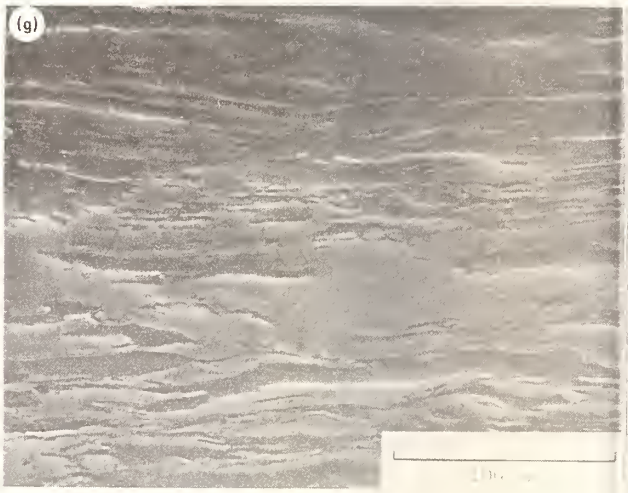
(g)

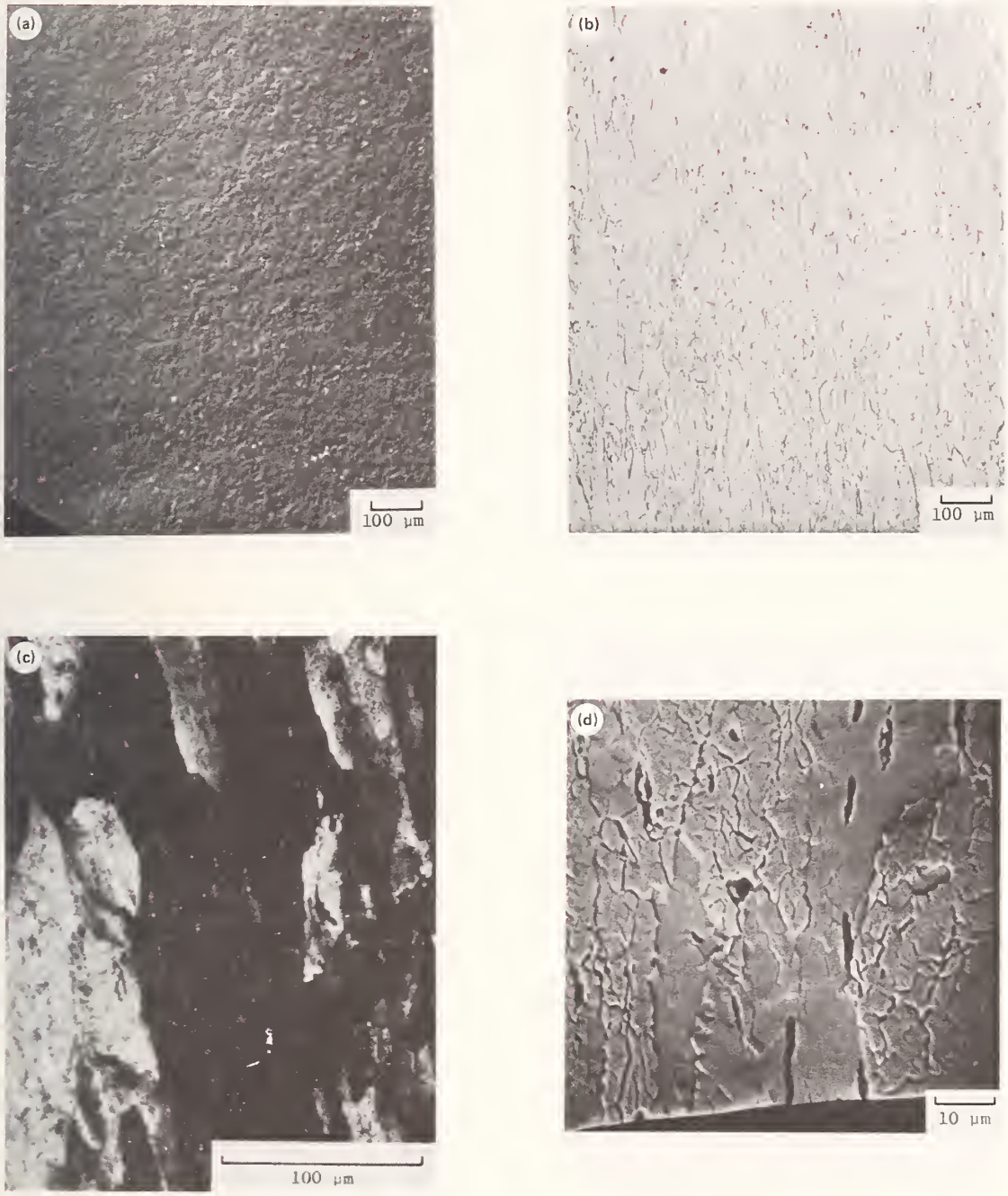

Figure 16. Microstructures of powder metallurgy Mo bar, specimen NSC9152: (a) Nomarski micrograph of optically polished mirror surface, (b) and (c) micrographs of metallurgically polished and etched normal surface, and (d) scanning electron micrograph of etched normal surface.

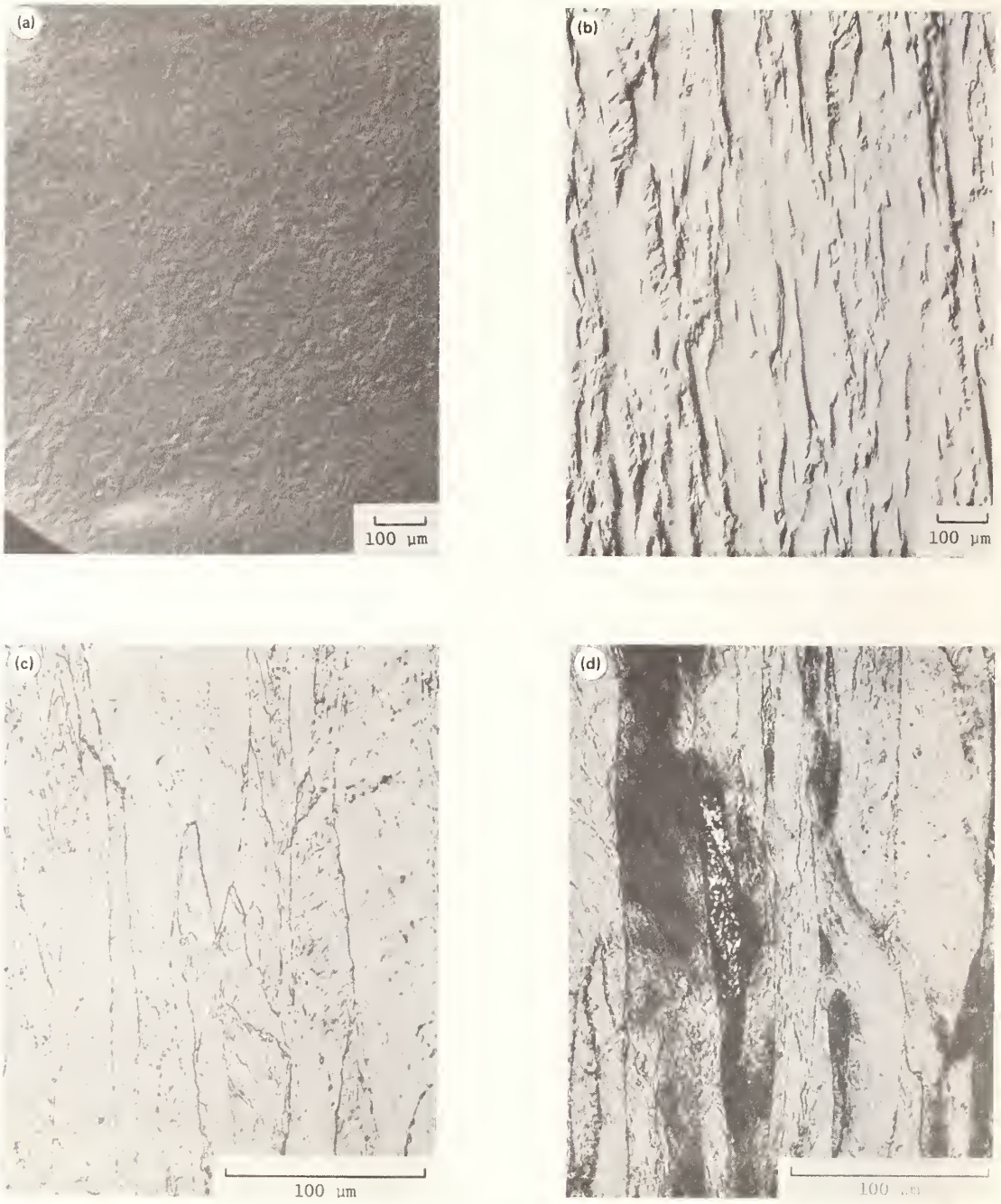

Figure 17. Microstructures of vacuum-arc-cast TZM alloy bar, specimen NTZM10395: (a) Nomarski micrograph of optically polished mirror surface, (b) micrograph of metallurgically polished normal surface, (c) and (d) micrographs of metallurgically polished and etched normal surface.

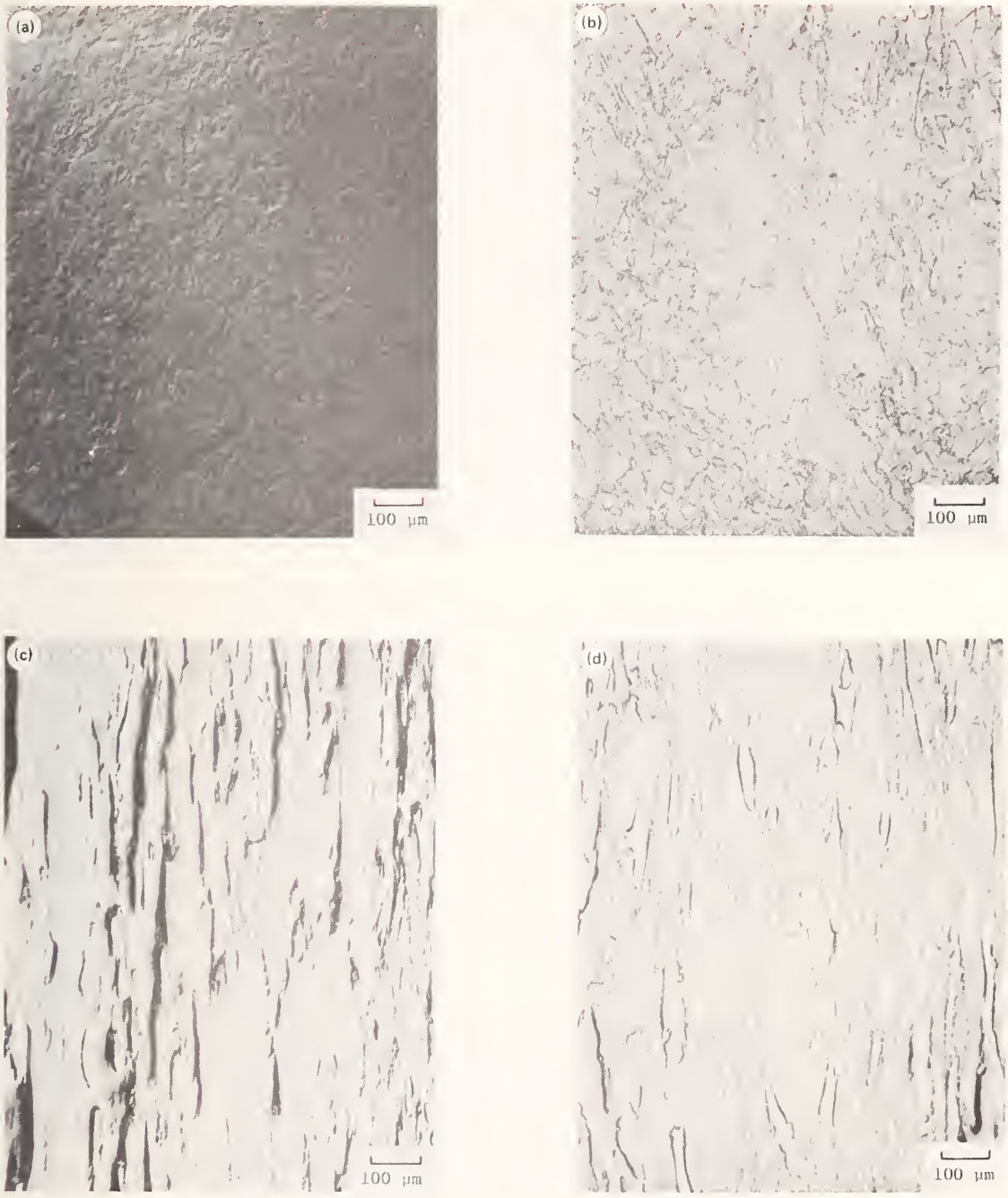

Figure 18. Microstructures of vacuum-arc-cast Mo bar, specimen N243: (a) Nomarski micrograph of optically polished mirror surface, (b) micrograph of metallurgically polished and etched mirror surface, micrographs of metallurgically polished (c) and polished and etched (d) normal surface.

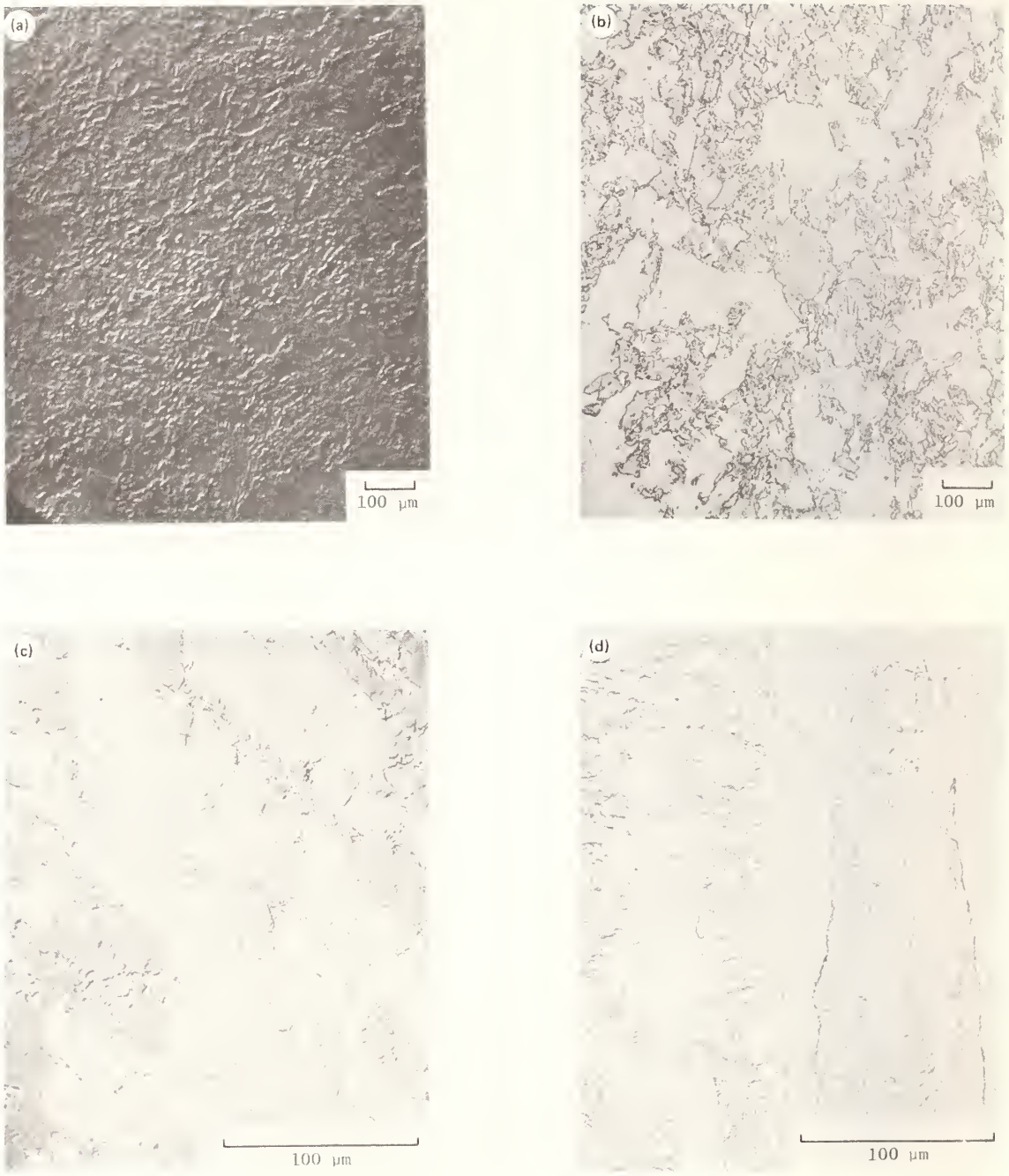

Figure 19. Microstructures of powder metallurgy Mo bar, specimen S279: (a) Nomarski micrograph of optically polished mirror surface, (b) and (c) micrographs of metallurgically polished and etched mirror surface, (d) micrograph of metallurgically polished and etched normal surface.

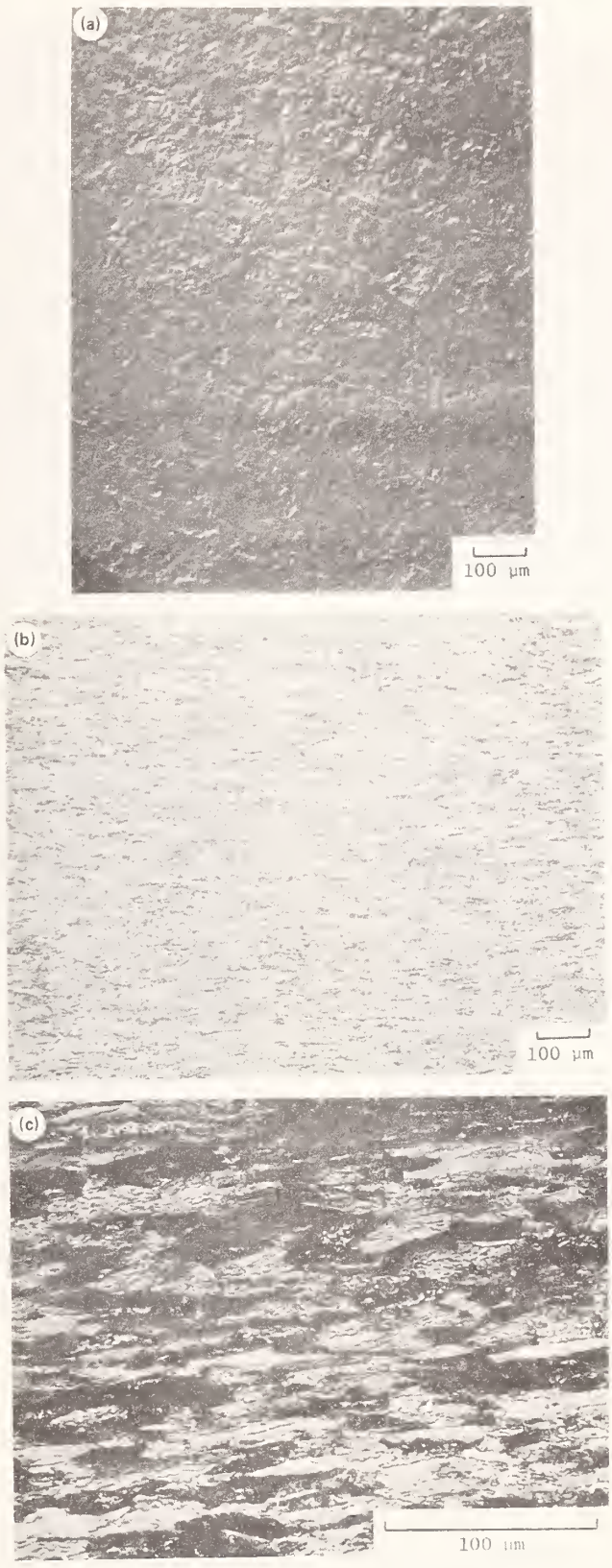

Figure 20. Microstructures of powder metallurgy Mo plate, specimen H218: (a) Nomarski micrograph of optically polished mirror surface, (b) and (c) micrographs of metallurgically polished and etched normal surface.

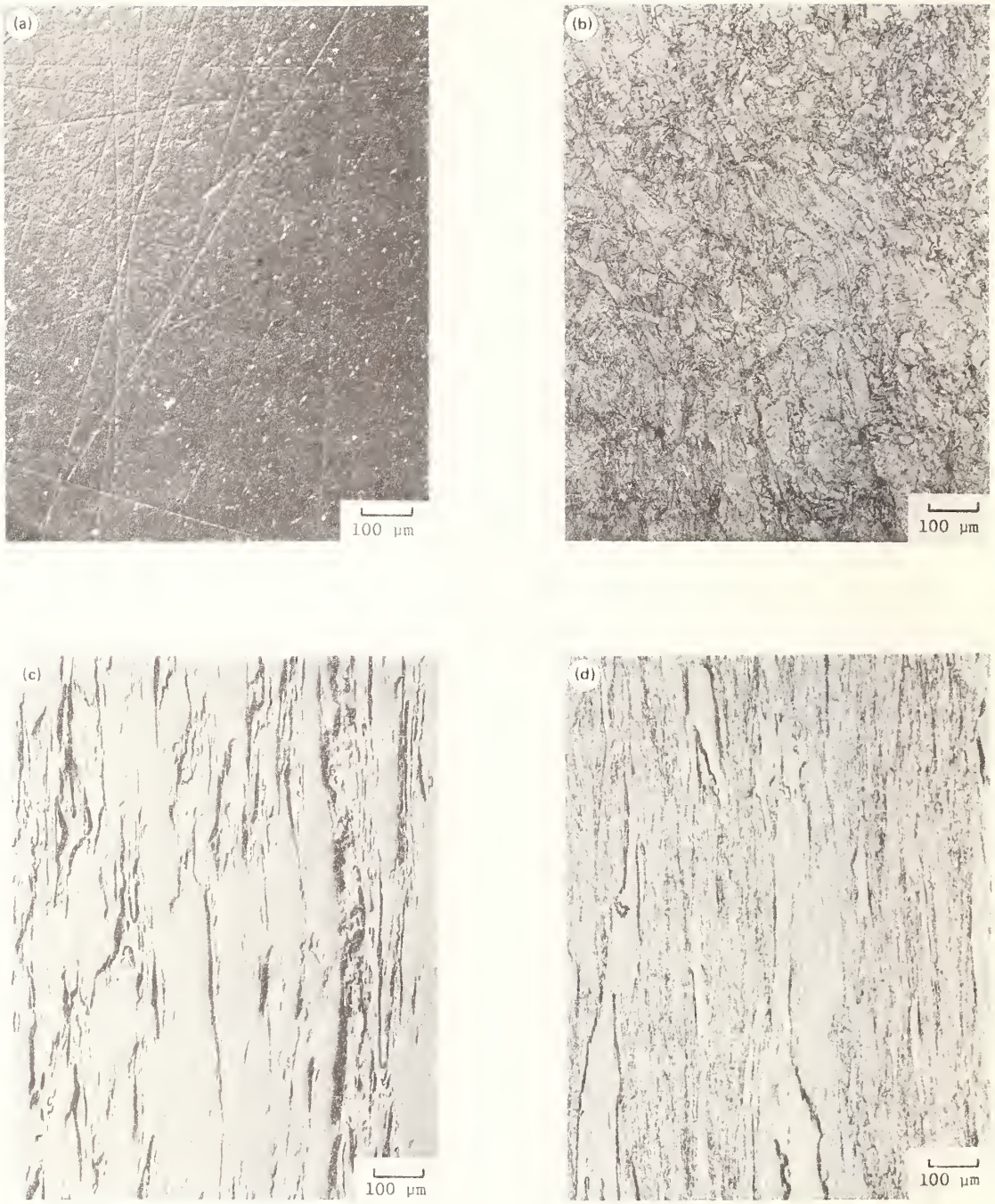

Figure 21. Microstructures of vacuum-arc-cast Mo bar, specimen AP041: (a) Normarski micrograph of optically polished mirror surface, (b) micrograph of metallurgically polished and etched mirror surface, micrographs of metallurgically polished (c) and polished and etched (d) normal surface.

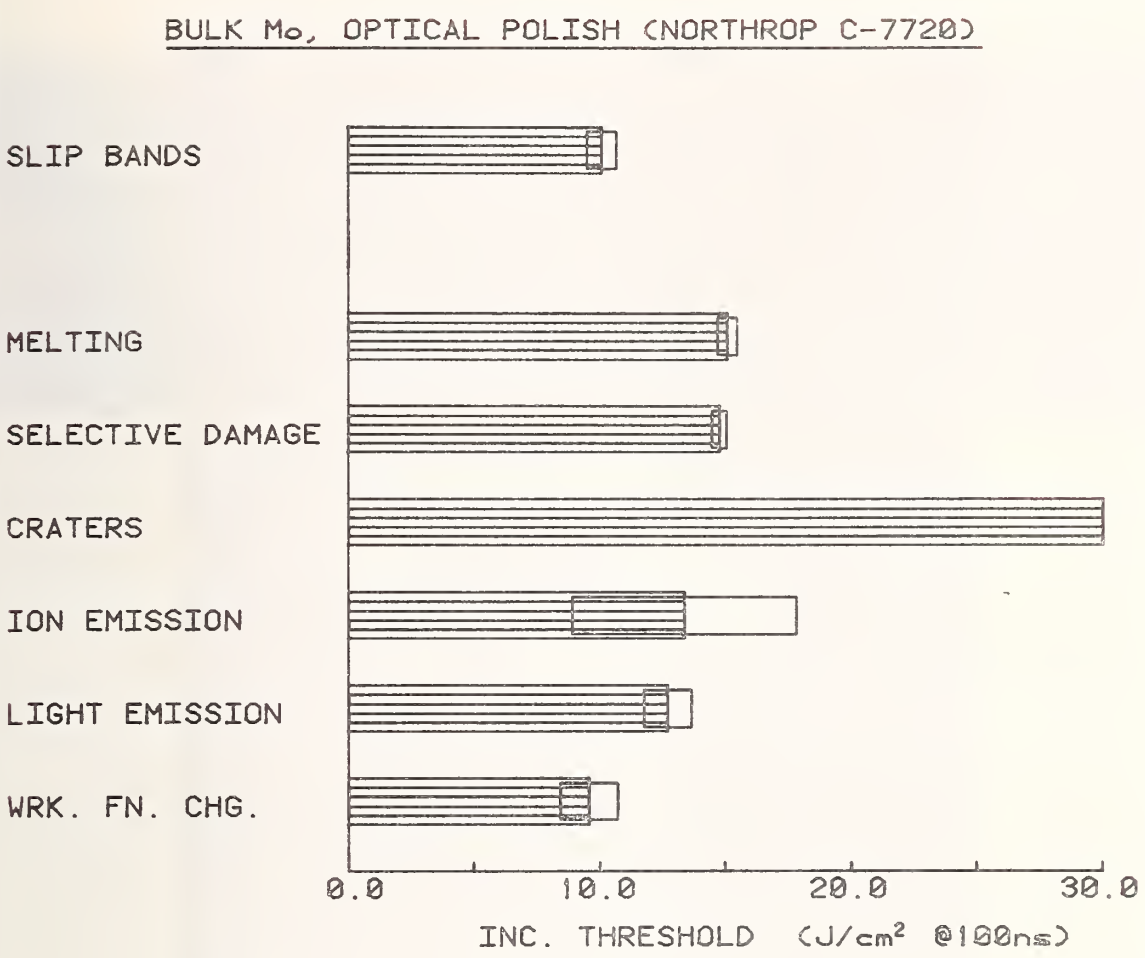

Figure 22. Multithreshold laser damage profile (10.6 μm wavelength, 100 nsec pulse length) for vacuum-arc-cast Mo plate, specimen NC7720.

Figure 23. 10.6 μm laser damaged area on specimen NC7720.

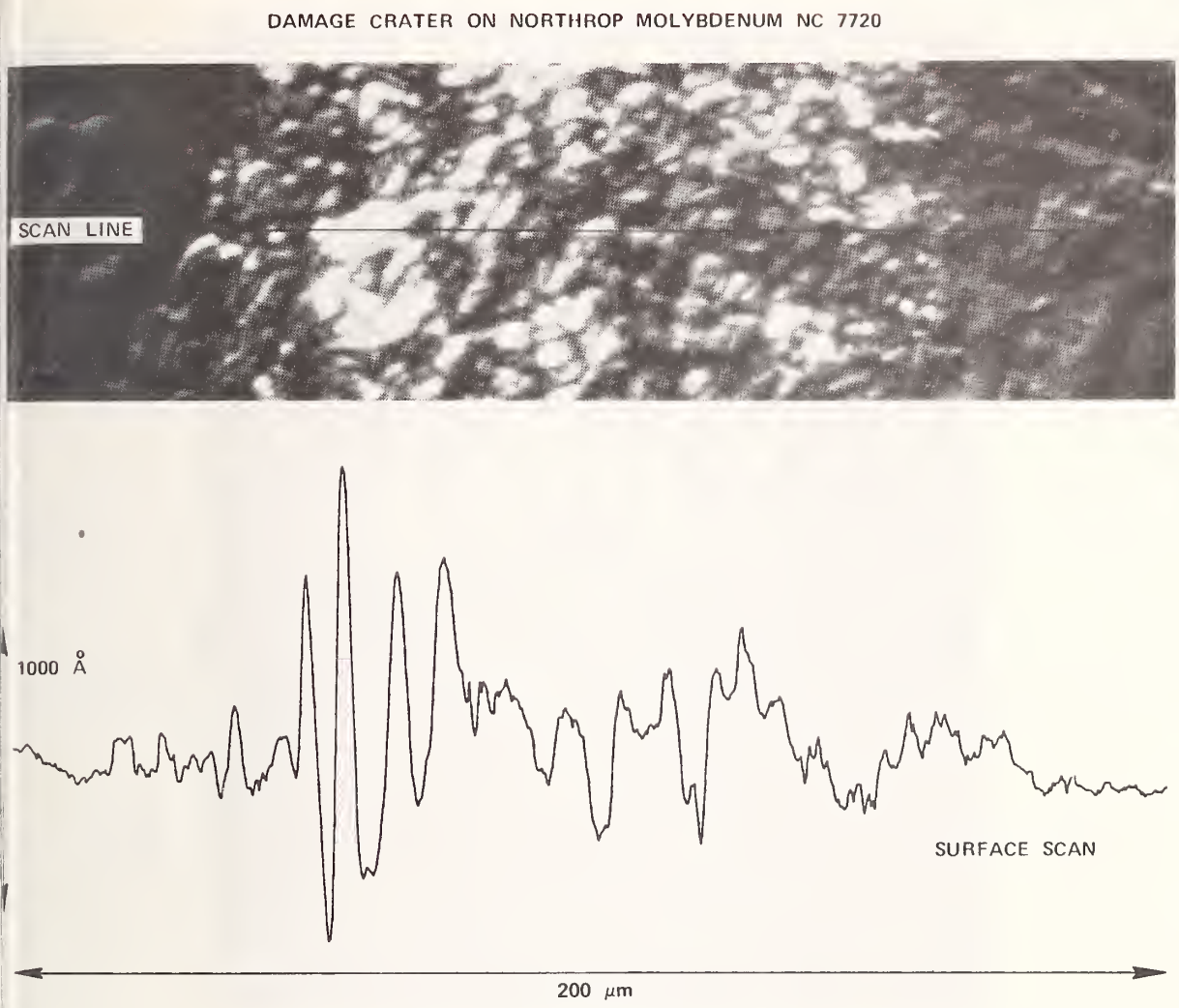

Figure 24. Enlarged portion of damaged area from figure 23, and Talystep surface scan approximately on the line indicated in the photograph.

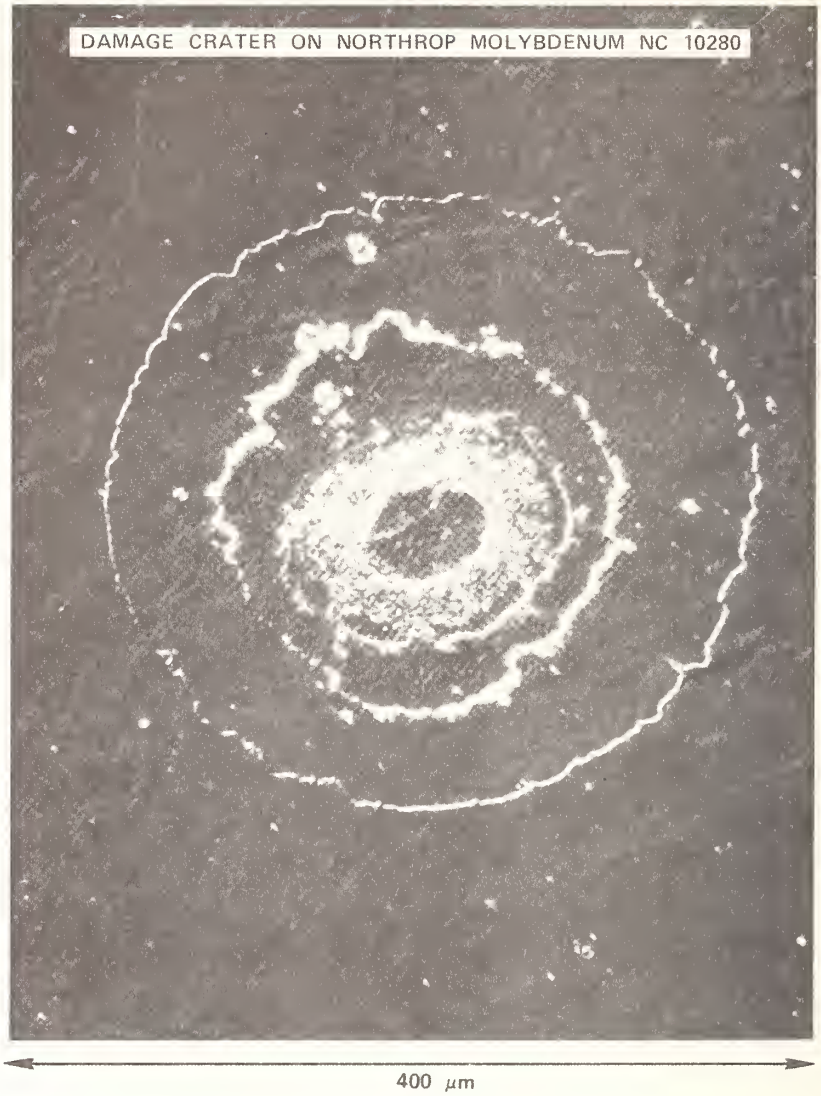

Figure 25. 10.6 μm laser damaged area on vacuum-arc-cast Mo bar, specimen NC10280 covered with multilayer films $(HfO_2/MgF_2)_4$.

DAMAGE CRATER ON NORTHROP MOLYBDENUM NC 10280

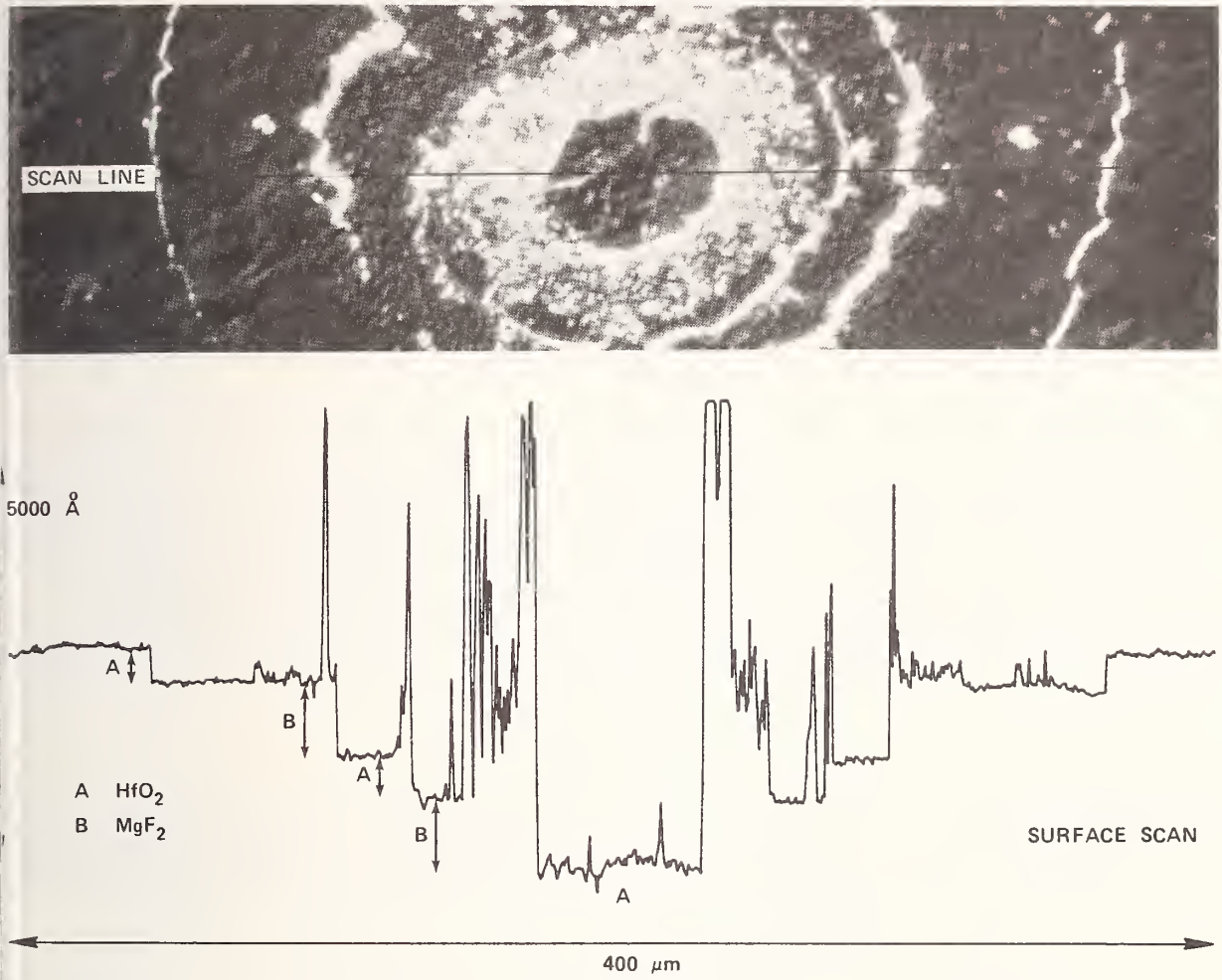

Figure 26. Enlarged portion of damaged area from figure 25, and Talystep surface scan approximately on the line indicated in the photograph.

1064 - NM LASER DAMAGE THRESHOLDS OF POLISHED GLASS SURFACES AS A FUNCTION OF PULSE DURATION AND SURFACE ROUGHNESS*

D. Milam
University of California
Lawrence Livermore Laboratory
Livermore, California 94550

Laser damage thresholds were measured for four polished glass surfaces, using linearly polarized 1064-nm pulses with durations of 0.17 ns, 1.0 ns, 1.6 ns, and 3.2 ns. Thresholds scaled approximately as the square root of pulse duration, but were insensitive to variations in surface roughness when the roughness was <25 Å rms. Careful cleaning increased the damage threshold at 3.2 ns by removing particulates.

Key words: BK-7 glass; fused silica; laser damage; polished surfaces; pulse duration dependence of damage; surface roughness.

1. Introduction

The relationship between surface roughness and laser damage thresholds of polished glass surfaces is not well understood. Extreme roughness, rms roughness >100 Å, caused reductions in damage threshold for 1064-nm pulses of 40 ns [1] and 0.15 ns [2] durations. For relatively smooth surfaces, rms roughness <40 Å, the correlation between roughness and thresholds held at 40 ns [1], but not at .15 ns [2]. This is but one example of what seems to be a systematic difference in damage induced by short-duration and long-duration pulses [3]. If such systematic variations are real, theories of laser damage must be compatible. The question of surface roughness and its influence on damage thresholds is also of practical importance. If smoother surfaces have higher thresholds, additional polishing will be an easy fix for some laser damage problems. We report here additional measurements of damage thresholds on polished surfaces of varied roughness.

2. Threshold Measurements

Entrance-surface and exit-surface thresholds for laser damage on four glass windows were measured using linearly polarized 1064-nm pulses with durations of 0.17 ns, 1.0 ns, 1.6 ns, and 3.2 ns, incident at 10° from the normal. Two lasers were used to make the measurements. A passively mode-locked Nd:YAG oscillator provided the 0.17-ns pulses. The waveform of each pulse was not recorded except by a fast diode/oscilloscope combination which was adequate to detect improper mode-locking. The assigned pulse width 0.17 ns is the mean pulse width most recently recorded for this laser. This mean is stable. It has varied from 0.15 to 0.17 ns during the last two years. However, the shot to shot variation in pulse widths from passively mode-locked lasers is large, typically ± 30% of the mean. Intensity or optical electric field strength cannot be accurately measured for mode-locked oscillators unless the waveform of each pulse is recorded. Pulses at 1.0 ns, 1.6 ns, and 3.2 ns were obtained by gating a portion from a 30-ns pulse produced by a Nd:YAG oscillator operating in a single cavity mode. The waveform for each pulse was recorded to verify pulse duration.

With both lasers, the beam profile in the sample plane was recorded on each firing, and absolute flux computed to within ± 7%. Beam diameter at the sample was 2-3 mm. Details of this measurement procedure are recorded elsewhere [4].

3. Damage Samples

Three samples, designated A, 081, and C18, were BK-7 glass. Sample A was a λ/20, 2"-diameter, 3°-wedged window of grade-A material purchased for use in the damage experiment. It had been used for over two years prior to these tests, and frequently cleaned with acetone or alcohol. Details of its preparation are unknown, except that "absorbing" abrassives, i.e., iron oxide, were not used. Sample 081 was carefully prepared from PH-3 grade material for damage testing. It was ground using progressively smaller alumina grit size; at each size the surface was ground to a depth equal to 3 times the previous grit diameter. Final polish was done with commercially available CeO_2. The surface roughness was 10 Å rms [5], which is extremely smooth for conventionally polished BK-7. Sample C18 had one conventionally polished surface, and one surface finished by bowl-feed polishing. Companion samples to C18 exhibited rms roughness of 7-9 Å on the bowl-feed surfaces [5]. CeO_2 was used to polish C18.

*Work performed under the auspices of the Material Sciences Program of the U.S. Department of Energy and Contract No. W-7405-ENG-48.

One sample of optical grade fused silica was tested. It was a 2-inch diameter window prepared for use in the damage facility. Polishing history is unknown except that iron-oxide was not used as a polishing agent.

All four samples had surfaces which meet or exceed specifications for usable optical components. Two were typical of conventional polishing, with roughnesses of 20-25 Å; two had carefully prepared surfaces and were somewhat smoother.

4. Results and Conclusions

Damage thresholds for the four samples are shown in figures 1-4. The following conclusions can be drawn.

1. The smoothest BK-7 surfaces did not have the highest thresholds. Samples C18 and 081 were carefully prepared yet had thresholds less than that of the routinely polished surfaces on sample A. Some other variable, probably surface absorption, is more important than surface roughness in setting short-pulse thresholds on surfaces with roughness <30-40 Å.

2. Contamination by particulates can lower thresholds at 3.2 ns by as much as 50%. The first experiments on sample A yielded low thresholds. The sample was scrubbed with soap and water, alcohol, and acetone, and retested. Surface scatter was reduced and thresholds increased as shown in figure 1. Scrubbing did not change thresholds on new samples C18 and 081.

3. Thresholds scaled approximately as the square root of pulse duration [6]. Departure from this scaling law was greatest on the surface with the lowest threshold, the rear surface of C18. For that sample thresholds at 1.6 and 3.2 ns were nominally the same.

4. Exit-surface thresholds were less than entrance-surface thresholds, although the ratio was not always as predicted [7] by the ratio of intensities at exit and entrance surfaces,

$$\frac{I_{exit}}{I_{ent.}} = \frac{4n^2}{(n+1)^2}$$

5. Acknowledgments

The author gratefully acknowledges the assistance of G. E. Murphy and S. E. Peluso in maintaining and operating the damage facility, the assistance by W. L. Smith and W. H. Lowdermilk in collecting some of the data, frequent useful discussions with M. J. Weber, and the efforts of Lou Beggio in preparing the manuscript.

6. References

[1] House, R. A., Bettis, J. R.; Guenther, A. H., and Austin, R., "Correlation of laser-induced damage with surface structure and preparation techniques of several optical glasses at 1.06 μm," in Laser-Induced Damage in Optical Materials: 1975, A. J. Glass and A. H. Guenther, eds., Nat. Bur. Stand. (U.S.) Spec. Publ. 435, pp. 305-320 (1975); also R. A. House, "The effect of surface structural properties on laser-induced damage at 1.06 μm," Ph.D. dissertation Air Force Institute of Technology, Wright-Patterson AFB, Ohio, 1975 (now available as report AFWL-TR-76-62, Kirtland AFB, NM 87117); also R. A. House, J. R. Bettis and A. H. Guenther, "Surface roughness and laser damage threshold," IEEE J. Qu. Elect. QE-5, pp. 361-363 (1977).

[2] Milam, D., Smith, W. L., Weber, M. J., Guenther, A. H., House, R. A., and Bettis, J. R. "Effects of Surface Roughness on 1064-nm 150-ps Laser Damage," in Laser Induced Damage in Optical Materials; 1977, A. J. Glass and A. H. Guenther, eds., Nat. Bur. Stand. (U.S.) Spec. Publ., 509, pp. 166-173 (1977).

[3] Milam, D., "Can a Model Which Describes Gas Breakdown Also Describe Laser Damage to the Bulk and Surface of Solid Dielectrics," in Laser-Induced Damage in Optical Material: 1976; eds., A. J. Glass and A. H. Guenther, Nat. Bur. Stand. (U.S.) Spec. Publ. 462, pp. 350-356 (1976).

[4] Milam, D., Laser-Induced Damage at 1064-nm 125-ps; Appl. Opt. 16; 1204 (1977).

[5] J. M. Bennett, private correspondence.

[6] Bettis, J. R., and Guenther, A. H., "Scaling Laws for Damage," elsewhere in this publication.

[7] Crisp, M. D., Boling, N. L., and Dubé, G., "Some Aspects of Surface Damage That Can be Explained With Linear Optics," Appl. Phys. Lett. 21; 364 (1972).

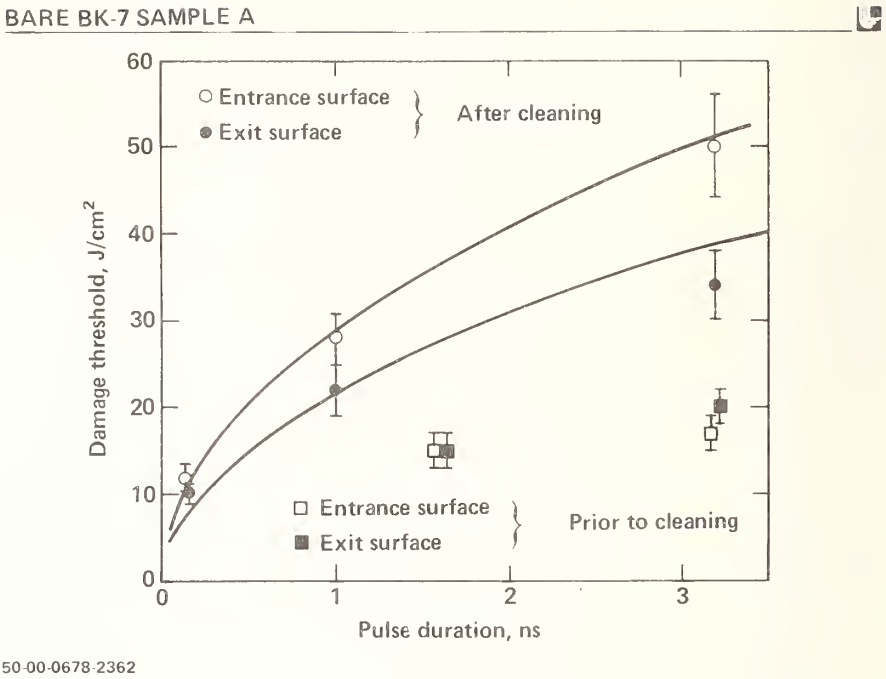

Fig. 1. Surface damage threshold vs. pulse duration, BK-7 sample A. Data indicated by squares was taken prior to a vigorous scrub cleaning. This sample had been used as a splitter prior to these tests. The accumulated particulates could not be removed by less than scrubbing. Curves are best-fit square-root functions.

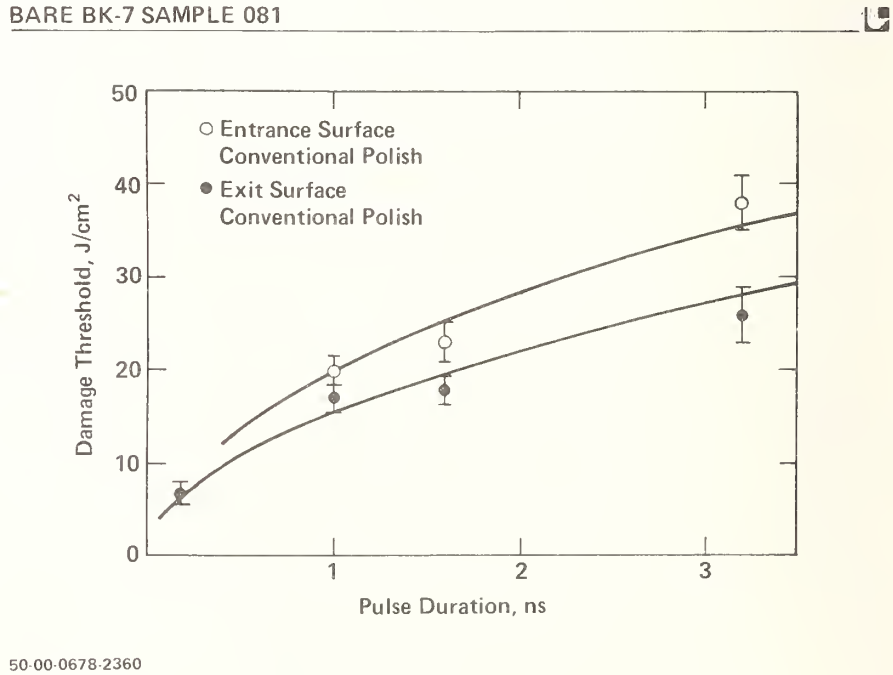

Fig. 2. Surface damage threshold vs. pulse duration, BK-7 sample 081. Curves are best-fit square root functions.

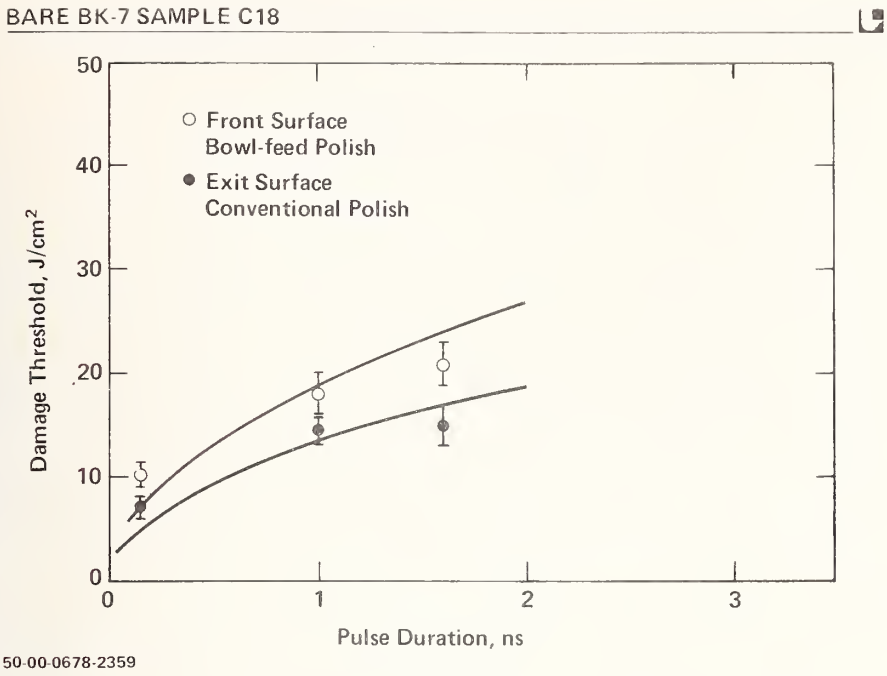

Fig. 3. Surface damage thresholds vs. pulse duration, BK-7 sample C18. This sample was not large enough to allow measurement at all four pulse durations. Curves are best-fit square root functions.

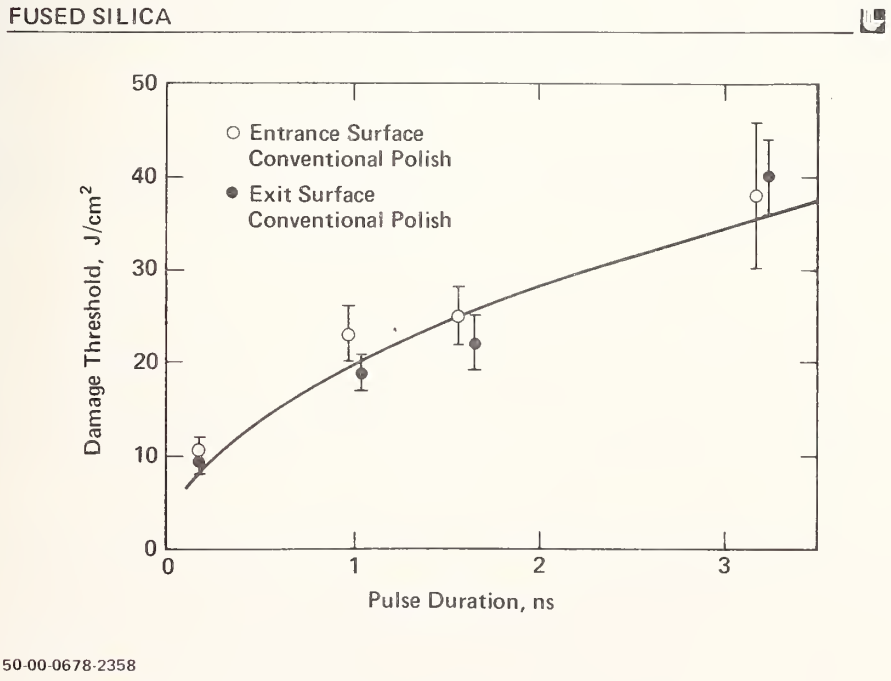

Fig. 4. Surface damage threshold vs. pulse duration, polished fused silica. Curve is a best-fit (to exit surface data) square root function. The error in entrance surface threshold at 3.2 ns is due to site to site variations in the surface, and exceeds the ± 7% uncertainty in flux measurements.

LARGE GIANT AND FREE-RUNNING LASER PULSE ENERGY AND POWER DENSITIES THROUGH OPTICAL FIBERS*

M. J. Landry
Sandia Laboratories
Albuquerque, N. M. 87185

The surface threshold damage levels (STDL) and coupling efficiencies, ε, (ratio of output-to-input energy) have been determined for single and multiple optical fibers of five manufacturers. For giant laser pulses of 30 nsec duration, the largest STDL's were observed in American Optical Company fibers for single and multiple laser shots with values of 48.2 and 31.6 J/cm^2, respectively. For free-running laser pulses of 100 μsec duration, the largest STDL was observed in Corning Glass Works fibers for single laser shots with a value of 4.66 kJ/cm^2. For multiple laser shots increased energy caused the initial damage sites in the binding or fiber cladding materials to increase in size and cause new sites in these materials at lower STDL's than for single laser shots. The giant laser pulses caused the most severe surface damage. There is no evidence to suggest that the observed decrease in ε was caused by other than the increase in damage to the input surface of the fibers.

Key words: Free-running laser pulses; giant laser pulse; optical fiber damage; pulsed Nd^{3+} laser damage; single and multiple element fibers; surface threshold damage.

1. Introduction

Many optical fiber applications being considered by investigators include transmitting multimode giant and free-running laser pulses containing high energy and power. One such application requires propagating short duration, high energy giant laser pulses through optical fibers to initiate secondary explosives [1][1], another requires propagating longer duration free-running laser pulses through optical fibers to initiate primary explosives [2]. The output energy and power handling capacity of optical fibers are limited by optical damage to the fibers [3-8] and by losses in the fibers, which include absorption in the bulk material, scattering at the core-cladding interface, Rayleigh scattering and backward stimulated Raman and Brillouin scattering [9-13].

It is the purpose of this paper to report measurements of the coupling efficiency (output energy/input energy E_2/E_1), input and output energy and power densities, the surface threshold damage levels (STDL's) and the optical damage in optical fibers caused by ∿30 ns and 100 μs duration Nd:glass laser pulses.

2. Experimental Set-Up

2.1 Mechanical and Optical

The mechanical and optical set-up used in studying the threshold damage level of the maximum energy transmitted through optical fibers is shown in figure 1. For giant pulse operation the oscillator (OSC) consists of a 75% reflective (R) output coupler (M_2), Nd^{3+} laser rod (LR) pumped by a double elliptical cavity, a stack glass polarizer (P_2) for horizontal polarization, a 3.87 mm diameter aperture (A_1), and the Q-switch (QS). The QS consists of a Pockels cell (PC) operated at $\lambda/2$ voltage, a stack glass polarizer (P_1) for vertical polarization, and a chip-free knife-edge right angle prism maximum R (M_1). For the free-running operation M_1 replaces PC, eliminating PC and P_1 from the 100 cm long laser cavity. The free-running laser pulse is unpolarized.

The output of OSC is directed through the laser amplified (AMP) and to the input end of the optical fiber by three mirrors (M_3, M_4, and M_5). The AMP built at Sandia Laboratories, consists of a 61 cm long by 1.27 cm diameter, 5% Nd^{3+} ED-2 glass rod, four 50.8 cm by 1.3 cm diameter linear Xenon flashlamps in a close couple pumping

---

* Work supported by the Department of Energy.

1. Figures in brackets indicate the literature reference at the end of this paper.

geometry, and a power supply. The ends of the rod are cut parallel to each other with their normals 6^{o} relative to the geometric axis of the laser rod to eliminate reflection feedback into the OSC. The power supply charges four 275 μF capacitors to 1.7 kJ.

The OSC beam is sampled at station (STA) #0 by a beamsplitter (BS_0). The AMP beam is sampled at STA #1 and STA #2 by two beamsplitters (BS_1 and BS_2), with STA #1 sampling before the aperture (A_2) and STA #2 after. Each STA contains two uncoated quartz beamsplitters (BS_0, BS_1, or BS_2, and BS_3); a 50-50 coated BK-7 beamsplitter (BS_4); a KDl photodiode (D_0, D_1, or D_2) manufactured by Korad; and two linear semiconductor diode arrays (RA) manufactured by Reticon. Beamsplitters BS_0, BS_1, and BS_2 each sample ∿4% of the incident laser beam. Approximately 3.7% of the incident laser beam is directed to a pressed magnesium oxide diffuser (DF). The response of D_0, D_1, and D_2 is calibrated using energy meter (mfg. Quantronic) EM_1, EM_2 with A_2 removed, and EM_2 with A_2 in the beam, respectively. EM_3 measures the energy transmitted through the fibers.

Approximately 0.11% of the incident beam is directed toward the Reticon arrays Model EC-256, EC-384, and EC-512 diodes, which are 1.27, 1.91, and 254 cm long and contained 256, 383, and 512 diodes, respectively. The diodes, each 0.00254 cm on edge, are fixed 0.005 cm on line center. At each station one array displays energy contained in this 0.00254 cm slit height across the laser beam in a horizontal direction (H) and another in a vertical direction (V). Neutral density filters keep the arrays and photodiodes operating in their linear regimes.

Aperture A_2, beamsplitter BS_2, and microscope M are mounted on adapter plates which are kinematically mounted to plate #1. The microscope is also kinematically mounted to plate #2. This mounting technique allows the microscope, which is used to photograph the ends of the fibers (magnification of 35.6 X), and the other components to be removed and repositioned without refocusing or realigning.

The microscope is a Zeiss Model FS-45 trinocular polarizing tube with a Nikon photomicrographic attachment Model EFM containing a relay lens, an eyepiece, and a polaroid adapter.

A telescope (T), aperture (A_3), mirrors (M_6 and M_7), and beamsplitter (BS_5) are used with the Spectra Physics Model 124B laser (He-Ne) to align the OSC, AMP, optical fiber, and other components. Components BS_5 and M_7 are positioned on kinematic mounts for ease of removing and precise repositioning during alignment. All the mirrors which reflect both the He-Ne and the Nd^{3+} laser beams are coated for maximum reflectivity at both 632.8 and 1060 nm.

2.2 Electrical

Figure 2 shows the block diagram of the electrical connections of the laser OSC and AMP, Pockels cell (PC) power supply, oscilloscopes (SCOPE), photodiodes (KDl), Reticon array (H and V), and associated equipment (Generators). The timing sequence for the giant laser pulse experiment is shown in the lower left portion of the figure. A switch closure in the operator's hand initiates the triggers of the Rutherford Generator at $T_0 = 0$.

The trigger T_4 to section B of SCOPES 1, 2, and 3 is adjusted to the giant pulse emission time. Times T_6 and T_5 are adjusted so the arrays are triggered at the beginning of the first graticule of the oscilloscope. The oscilloscope sweep speeds are adjusted so that each array is read out in ten divisions making each scale division 0.127, 0.191, and 0.254 cm for Model EC-256, EC-384 and EC-512 arrays, respectively.

For the free-running laser pulse experiment trigger T_3 is eliminated. Trigger T_4 is adjusted to trigger section B of SCOPES 1, 2, and 3 before the laser free lases.

2.3 Beam Profile

The typical responses of the EC-256 Reticon linear diode arrays at STA #2 for 0.279, 0.439, and 0.508 cm diameter aperture A_2 are illustrated in figures 3A, 3B, and 3C and for a 0.508 cm diameter hole in figure 3D. The upper traces are the response of the arrays which are oriented in the vertical direction (V) relative to the table top and the lower traces in the horizontal direction (H). Each major division (time axis) is calibrated to correspond to 0.127 cm.

Figures 3A-3C illustrates the laser beams centered on A_2 yielding symmetrical response. The shoulders on the RA response in figure 3A-3D are caused by the Sandia AMP operating in its saturation regime [14,15]. The RA response in figure 3D contains concentric rings caused by over filling the AMP rod with the OSC beam. These diode

responses show that the assumption of a plane wave incident onto the optical fibers for the giant pulse experiment is reasonably good for the 0.508 cm diameter aperture.

3. Theory

For a highly collimated laser light source with no area mismatch to the fiber the entire energy is coupled into the fiber except for Fresnel reflection and fiber packing fraction losses (neglecting scattering from the input face), since numerical aperture (NA) is larger than the laser divergence. The coupling efficiency which accounts for losses due to transmission (T), scattering (σ), absorption (α), and fiber packing fraction (f_1) is given as

$$\varepsilon = Tf_1\sigma\alpha = E_2/E_1 \quad , \tag{1}$$

where E_2 and E_1 are the output and input energy of the fiber, respectively. The transmission is given as

$$T \simeq (1-R)^2 = (1-\rho^2)^2$$

$$= [1 - (\eta_0-\eta_2)^2/(\eta_0+\eta_2)^2]^2 \quad , \tag{2}$$

where η_0 and η_2 are the refractive indices of the air and core material, respectively. For long fibers (> several meters) the packing fraction, which consists of the packing density (γ) and the core fraction (f_2), is given by $f_1 = \gamma/f_2$. The maximum packing density is 0.79 or 0.91 for square or hexagonal packed fiber array [16], respectively. If the fibers are loosely packed, these values will be smaller. The core fraction is $f_2 = (a/b)^2$, where a and b are the core and core plus clad diameters, respectively.

For the giant laser pulse tests the length of the fibers used were 1.5 ± 0.1 m and for the free-running laser pulse test they were 0.3 ± 0.01 m. Cladding modes were not removed for these short fibers. For these short, low loss fibers (<20 db/Km) scattering and absorption losses are negligible within ± 1.5%.

4. Experimental Results

In this study we tested optical fibers manufactured by American Optical Co. (AOC), Corning Glass Works (CGW), Fiber Optic Cable Corp. (FOC), Incom Inc. (II), and Valtec (V). The physical and optical characteristics of these fibers are listed in table 1. The fiber bundles were in single and multiple fiber forms. The individual fibers in the II and AOC bundles were hexagonal in shape due to the method used to fuse nearest neighbors. An epoxy binder was used to hold the fibers in the CGW bundles. A silicon type binder was used to hold the fibers in the FOC and V bundles. Ref loss % in table 1 refers to Fresnel reflection losses.

4.1 Giant Laser Pulse Experiment

Figure 4 illustrates the coupling efficiency (ε) as functions of input energy density (ξ_1) and power density (ρ_1) for AOC fibers FN5-FN8 which sustained the largest STDL and maximum ξ_1 and ρ_1 for giant laser pulses. Multiple laser shots ($\sim$20 shots) were incident onto the input end of the fibers with each laser shot containing progressively higher energy. The cross-sectional area of the laser beam A [17] was 1.17×10^{-2} cm^2 for FN5 and 4.58×10^{-2} cm^2 for FN6-FN8. We have $\xi_1 = E_1/A$, $\rho_1 = P_1/A$, $\xi_2 = E_2/A$, and $\rho_2 = P_2/A$ where E_1, E_2, P_1, and P_2 are input and output energy and input and output power, respectively. The power P is E/τ, where E is energy and τ is the laser pulse duration at FWHM.

Both FN5 and FN6 exhibited an $\varepsilon \sim 0.50$ at the onset of the test. For FN5 and FN6 as the laser energy density was increased ε remained approximately constant until the STDL's of $\xi_1 = 10$ and 31.6 J/cm^2 and $\rho_1 = 0.334$ and 1.05 GW/cm^2 were reached, respectively. The coupling efficiency continued to decrease with increasing energy density until at the end of the test an $\xi_1 = 19$ and 44.1 J/cm^2 and $\rho_1 = 0.634$ and 1.47 GW/cm^2 resulted in an $\varepsilon = 0.369$ and 0.368, and maximum energy and power densities out of the fiber of 17.0 and 39.5 J/cm^2 and 0.568 and 1.32 GW/cm^2, respectively. The ξ_2 and ρ_2 were derived assuming absorption and scattering losses were negligible with $\xi_2 = T\xi_1$ and $\rho_2 = T\rho_1$, where $\rho_1 = \xi_1/\tau$.

Fiber bundles FN7 and FN8 were tested differently in that initially each fiber received a laser pulse containing low energy, then FN7 and FN8 received two and one high energy laser pulses, respectively. The measured coupling efficiency was slightly less for the smaller laser pulse. For FN7, the third laser pulse with $\xi_1 = 40.8$ J/cm^2

gave a calculated $\varepsilon = 0.44$. This ξ_1 value failed to exceed the STDL of FN7. A laser pulse with a higher $\xi_1 = 48.2$ J/cm^2 and $\rho_1 = 1.61$ GW/cm^2 gave a calculated $\varepsilon = 0.468$ for FN8. This exceeded the STDL for FN8. The multiple laser shots (LS's) in FN6

Table 1. Physical and optical characteristics of fibers

Fiber No.	Mfg	Core Mat	No. of Fibers	Core dia(μm)	Core† η	Ref Loss %	T	NA
Giant Pulse Laser Exp.								
FN1, FN2	II	Flint*	1	0.635(cm)	1.602	5.35	0.896	0.66+
FN3, FN4	II	Flint**	>600	200	1.608	5.43	0.894	0.66+
FN5, FN6, FN7, FN8	AOC	Flint*	>600	84-90	1.602	5.35	0.896	0.66+
FN9	CGW	Silica++	61	87-96	1.467	3.62	0.929	0.18††
Free-Running Laser Exp.								
FN10-FN17, FN22	V	Silica***	1,7 1	100-140 250	1.449	3.36	0.934	0.30
FN18-FN21	FOC	Silica***	7	210-240	1.449	3.36	0.934	0.30
FN23-FN27	CGW	Silica++	7	87-96	1.467	3.62	0.929	0.18††

* F-2 Schott glass
† Measured at 1060 nm
\+ Calculated at $\lambda = 589.3$ nm, $\eta = 1.62$ (core) and 1.48 (cladding)
** F-7 Schott glass
++ Ge-doped baron doped silica cladding
†† Calculated at $\lambda = 1.060$ nm, $\eta = 1.467$ (core) and 1.459 (cladding)
*** Cladding plastic

caused damage at lower levels than for single LS's, in agreement with observed surface damage in bulk material [18].

The photographs in figure 5 illustrate the increase in surface damage observed at the input end of FN5 (light spots) with increasing ξ_1. Prior to each photograph $\xi_1 =$ 10, 11.3. 14.5, 14.4, 15.6, 16.5, and 19 J/cm^2 was incident on FN5 for figures 5A-5G, respectively. Although a decrease in ε was observed at 10 J/cm^2 in figure 4 for FN5, no apparent optical surface damage is visible in figure 5A which is the photograph of the input end of the fiber after that LS. It is evident that either damage must be occurring in the core even though the damage is not visible or cladding modes are excited thus causing the decrease in ε. The first visible optical surface damage to the input end of FN5 appears between two fibers after the next LS with an input energy of $E_1 = 0.132$ J, which is a STDL of $\xi_1 = 11.3$ J/cm^2 and a $\rho_1 = 0.377$ GW/cm^2 (fig. 5B).

It is believed that the points where damage initiated have the largest stress because of the difference between cladding and fusing materials. As the energy in the laser beam was increased new damage sites appeared and the old ones became larger. This is as expected if the STDL for the entire end of the fiber is constant. As the energy in the laser beam increased its energy density at the center also increased causing more damage at the old sites. As the energy density at the periphery of the beam reached STDL new sites were formed. At the end of the test, the first damage site was the largest.

The photograph in figure 5B shows that initially the STDL was exceeded over an area approximately equal to the diameter of a single fiber (7.2×10^{-3} cm) which is comparable to the diameter of the most intense portion of the triangularly shaped laser beam (5.1×10^{-3} cm shown in fig. 3B). Over this area $\xi_1 = 90$ J/cm^2.

The dimension of the smallest damage structure in figure 5G is (<0.1 fiber core diameter) $<7.2 \times 10^{-4}$ cm. The maximum input energy of $E_1 = 0.222$ J caused damage over a maximum linear dimension of 1.61 cm, which was a slightly larger dimension than that of the laser beam FWHM (0.123 cm), but less than the dimension of the laser beam containing 90% of the energy (0.254 cm). The implication is that the fibers at the periphery damaged at a lower STDL than those in the center.

Figure 5D compared to figure 5C shows that a laser pulse containing the same energy as the previous pulse caused additional surface damage. This is in agreement with observed STDL trends in bulk material which has seen previous laser energy [18].

Fibers FN1-FN4 were tested similar to FN5 and FN6. Within experimental error the ε measured for FN2 (0.895) was equal to T (table 1), since $f_1 = 1$. The lower ε of 0.81 observed for FN1 was attributed to either increases in internal scattering or external scattering at the ends of the fiber due to end fabrication. FN1 and FN2 broke 18 and 17.8 cm from their input ends when $\xi_1 = 4.76$ and 5.63 J/cm^2 and $\rho_1 =$ 0.159 and 0.188 GW/cm^2 were incident on the fibers, respectively. A = 0.1829 cm^2 (as determined using the FWHM method) and the maximum input energy was 1.07 J. The output energy densities $\xi_2 = 3.76$ and 4.67 J/cm^2 and output power densities $\rho_2 = 0.125$ and 0.156 GW/cm^2 for FN1 and FN2, respectively. No damage was observed on the input faces of either fiber.

The values of ε measured for FN3 and FN4 were less than those observed for FN1 and FN2 because $f_1 \neq 1$. The hexagonal packing density was close to optimum so $f_2 \sim 0.93$. Neglecting absorption and scattering losses in the fiber, a calculated value for the coupling efficiency is $\varepsilon(C) = T\gamma f_2 = (0.894)(0.91)(0.93) = 0.75$; however, the coupling efficiency measured was between 0.5 to 0.6 and 0.5 for FN3 and FN4, respectively. The hexagonal shape of the individual fibers in fiber bundle FN3 and FN4 could have caused increased losses which were not accounted for in the calculation. The observed increase in 90° off-axis scattering in FN3 and FN4 compared to FN1 and FN2 is suspected as being caused by core to cladding interface scattering. The STDL's of FN3 and FN4 were measured at 4.02 and 4.62 J/cm^2, respectively. A maximum value of $\xi_1 = 6.78$ J/cm^2 and $\rho_1 = 0.226$ GW/cm^2 was observed for both FN3 and FN4. The corresponding values of ξ_2 and ρ_2 will be less by a factor $\sigma\alpha$, which if taken to be $\varepsilon(C)$ is between 0.20 to 0.33 for FN3 and 0.33 for FN4.

As the energy in the laser beam was increased, new damage sites appeared and the old ones became larger. At the end of the test, the first damage site was the largest.

Prior to testing CGW fibers, we attempted to produce a more spatially uniform laser beam and still retain fairly high energy density by changing aperture A_2 from a 0.279 cm to a 0.439 cm diameter hole. This failed and produced a large laser-to-fiber mismatch for FN9.

In order to reduce the potential future damage to the fibers in determining ε at low input energy, the first ε values was measured using a laser pulse of long duration ($\sim$100 μs pulse length). The ρ_1 is 3×10^{-3} times smaller for the free-running laser pulse compared to the giant laser pulse. Input energies of $E_1 = 0.050$, 0.092, and 0.127 J resulted in $E_2 = 0.0020$, 0.0038, and 0.005 J and $P_2 = 20.0$, 38.0, and 50.0 W with corresponding $\xi_2 = 0.46$, 0.88, and 1.15 J/cm^2 and $\rho_2 = 4.60$, 8.80, 11.5 kW/cm^2 produced $\varepsilon = 0.040$, 0.420 and 0.042, respectively. The low ε values were caused by the laser beam-to-fiber bundle mismatch.

Two relatively high energy pulses (giant 30 ns pulse duration) of $E_1 = 0.790$ and 0.775 J produced $E_2 = 0.036$ and 0.0336 J, respectively. The corresponding $\xi_1 = 6.48$ and 6.35 J/cm^2 and $\rho_1 = 0.216$ and 0.212 GW/cm^2 and $\xi_2 = T\xi_1 = 6.02$ and 5.90 J/cm^2 and $\rho_2 = T\rho_1 = 0.216$ and 0.212 GW/cm^2, if the laser beam area (A = 0.122 cm^2) used in the density calculations is that determined by the FWHM area method. If we consider the core cross-sectional area A(f) of the 60 good fibers the corresponding $\xi_2 = 8.29$ and 7.74 J/cm^2 and $\rho_2 = 0.276$ and 0.258 GW/cm^2 and $\xi_1 = \xi_2/T = 8.92$ and 8.33 J/cm^2 and $\rho_1 = \rho_2/T = 0.297$ and 0.278 GW/cm^2. The ξ and ρ values calculated using A(f) are $\sim$25% higher than those calculated using A. This large difference illustrates the inaccuracy involved in assuming the laser beam to be spatially uniform in calculating ξ and ρ values and in using the FWHM area method in determining the cross-sectional area of the laser beam.

No visual optical surface damage was evident at the input end of FN9 after both high energy laser pulses, nor was there any decrease in ε. It must be concluded that the STDL for single laser shot for FN9 was not reached. Our ξ_1 values were limited by the aperture diameter, the size of the OSC and AMP, and the fact that we wanted to use unfocused optical radiation at the input of the fiber during the giant laser pulse experiment.

4.2 Free-Running Laser Pulse Experiment

In this portion of the experiment free-running laser pulses were transmitted through optical fibers before and after they were exposed to $\geq 10^6$ rad(Si) of gamma radiation. The optical fibers were irradiated at the Sandia Laboratories Gamma

Irradiation Facility using a Co^{60} source. Tests duration were from 9.7 to 11.6 hs.

Table 2 lists the 18 fibers tested using the free-running laser pulses. The maximum calculated output energy density $\xi_2(M) = E_2(M)/A(f)$, where $E_2(M)$ is the maximum output energy and A(f) is the total area of the fiber core or cores and the maximum calculated input energy density $\xi_1(M) = \xi_2(M)/T$. The total number of laser shots transmitted through the fiber at both low and high energy density before or after gamma irradiation (irr) is recorded under No. Laser Shots.

Table 2. Free-running laser experiment energy densities and coupling efficiencies in fibers

Fiber No.	Mfg	No. Fibers	Maximum ξ_2 kJ/cm^2	Maximum ξ_2 kJ/cm^2	ε (Max.)	No. Laser Shots	Irr. Mrad*
FN10	V	7	0.061	0.065	0.160	3	-
FN11	V	7	0.093	0.100	0.107	4	-
FN12	V	1+	0.014	0.015	0.017	5	-
FN13	V	1+	0.739	0.791	0.896	3	-
FN14	V	7	2.766	0.962	0.881	7	10^6
FN15	V	1†	2.450	2.623	0.708	3	-
FN16	V	1†	3.554	3.806	0.887	3	-
FN17	V	1†	0.286	0.306	0.800	3	-
FN18	FOC	7	1.022	1.094	0.788	12	-
FN19	FOC	7	0.135	0.145	0.814	7	10^6
FN20	FOC	7	0.907	0.971	0.852	11	10^6
FN21	FOC	7	0.269	0.288	0.858	1	10^6
FN22	V	1†	0.079	0.085	0.908	5	-
FN23	CGW	7	2.680	2.895	0.792	11	10^6
FN24	CGW	7	0.278	0.300	0.744	4	10^6
FN25	CGW	7	3.978	4.282	0.688	5	10^6
FN26	CGW	7	1.950	4.500	0.295	2	10^6
FN27	CGW	7	0.281	0.303	0.905	6	10^6

* Background 3-5.7 x 10^6 rad(Si)
\+ PC10
† PC5

Fibers FN10-FN16 were aligned relative to the free-running laser pulse using a pointing system, while FN17-FN27 were aligned using a Hadron trinocular viewing system. In the first method a laser burn was made on Hadron "fingerprint" paper placed at the input end of the fiber approximately at the focal point of an 8.09 cm focal length lens (L_1). A pointer was placed at the center of the laser burn. The paper was removed. The input end of the fiber was center to the pointer. A 10X eyepiece was used in positioning the above.

The Hadron trinocular viewing optical system contained a flip-flop mirror which was used in viewing the input end of the fiber and the burn. With the flip-flop mirror up a burn was made on "fingerprint" paper placed at the input end of the fiber approximately at the focal point of the 9.01 cm focal length lens (L_2) of the Hadron trinocular viewing optical system. With the flip-flop mirror down the crosshair of the viewing eyepiece was centered over the image of the burn. The image of the input end of the fiber was centered to the crosshair by moving the input end of the fiber.

Initially the input ends of FN10 and FN11 were placed 0.87 cm before the focal point of L_1. The laser pulse was incident on all 7 fibers of these fiber bundles. The total area A(f) of the 7 fiber cores of FN10 was A(f) = 6.4 x 10^{-4} cm^2. E_2 = 0.038 J resulted in ξ_2 = 0.059 kJ/cm^2, ξ_1 = 0.063 kJ/cm^2, and a low ε = 0.16. From the E_1 = 0.242 J for the same shot and ξ_1 value above, the area of the laser beam A = E_1/ξ_1 = 0.242/0.063 = 3.75 x 10^{-3} cm^2 was calculated. The area of the furrule

containing all the fibers was 2.89 x 10^{-3} cm^2. No visual damage resulted at these low input power levels. A similar calculation for FN11 resulted in a A(f) = 5.58 x 10^{-4} cm^2 and a slightly smaller A = 4.86 x 10^{-3} cm^2.

For both fibers, photographs after each laser shot (LS) show that the binding and cladding materials vaporized and recollected onto the ends of the fiber. This accounts for the observed decrease in ε with increasing number of LS's, as well as the physical change to the input face of the fibers.

A single PC10 V fiber (FN12) was placed 0.38 cm past the focal point of L_1. The area of the fiber core A(f) = 5.27 x 10^{-4} cm^2 while A = E_1/ξ_1 = 0.415/14.5 = 2.86 x 10^{-2} cm^2. Photographs of FN12 in figures 6A-6E, taken after each LS, show that the left side of the core is increasingly overlayed with what appears to be recondensed vapors of the vaporized plastic cladding. This accounts for the observed decrease in ε from 0.017 to 0.0108 with increasing number of LS's. Only the left side of the cladding shows deterioration because the other portion was broken at a slant range away from the plane of the paper such that the laser beam was not incident onto it with as high an ξ_1. The low ε values indicate a large mismatch between the laser beam diameter and the core diameter.

Another single PC10 V fiber (FN13) was used in order to decrease the laser beam to fiber core mismatch. The L_1-to-fiber dimension was increased by another 0.15 cm thus positioning FN13 0.53 cm past the focal point of L_1, as was determined by burn dimensions on "fingerprint" paper as a function of distance from L_1. The 0.53 cm dimension resulted in the smallest burn diameter. The maximum ε value for this fiber position was 0.896. The area of the fiber core A(f) = 5.03 x 10^{-4} cm^2 while A = E_1/ξ_1 = 0.415/791 = 5.25 x 10^{-4} cm^2, which was slightly larger than A(f). The photographs after the LS's do not show any apparent damage to the fiber core yet ε decreased from 0.896, 0.876, to 0.723 for approximate constant ξ_1 values.

The central fiber of FN14 was tested with the same laser beam diameter as used for testing FN13. The ξ_2 and ε values are listed in the upper (kJ/cm^2) and lower numbers in each photograph, in figure 7. The appearance of the input end of the fibers changed gradually until the 4th LS (figure 7), where an abrupt change occurred. More LS's continued to change the physical characteristics of the input face of the fibers.

The high values of ε calculated for FN14 in figure 7 indicate that the laser energy was transmitted through only the central fiber. The central core area A(f) = 1.37 x 10^{-4} cm^2, while the calculated A = 1.45 x 10^{-4} cm^2, which is slightly larger than A(f). For the lower value of ε = 0.426 the calculated A = 3.00 x 10^{-4} cm^2 is slightly larger; however, the laser beam area was not changed for this shot. The larger calculated A indicates that the ξ_1 value was smaller due to the decrease in transmission at the face of the fiber due to vapors recondensing over the entrance or core of the central fiber of FN14. The ratio of the laser areas 1.45 x 10^{-4}/3.00 x 10^{-4} is equal to the ratio of ε's. The conclusion is that all the energy went through the central fiber core.

We placed FN15-FN17 into the test system to determine whether we could couple the laser energy into single fibers of 1.21 to 1.26 x 10^{-2} cm diameter (d). The variations in the observed ε values for these fibers (table 2) are attributed to the uneven breaks in the ends of the fibers. The ξ_2 of 3.554 kJ/cm^2 for FN16 was the highest record for V fibers.

The photographic sequence for FN16 (d = 1.21 x 10^{-2}cm) in figure 8 shows that after the 1st LS containing large input energy density, (ξ_1 = 3.806 kJ/cm^2) figure 8A, slight damage appeared at the input face. This was the 2nd LS into the fiber, the 1st was at ξ_1 = 0.307 kJ/cm^2. The next LS, ξ_1 = 3.768 kJ/cm^2 (figure 8B) increased the damage. At lower ξ_1 values in FN17 (d = 1.21 x 10^{-2} cm) more severe damage occurred after the 3rd LS into the fiber (compare photographs in figure 8C taken after the 1st LS ξ_1 = 0.131 kJ/cm^2, to figure 8D taken after the 3rd LS, ξ_1 = 0.306 kJ/cm^2). The calculated A for FN15, FN16, and FN17 was 1.65, 1.21, and 1.35 x 10^{-4} cm^2, respectively. The A for FN15 and FN16 compare favorably to that calculated for FN14, when the same test configuration was used. The Hadron viewing system was used for FN17 with the fiber at the focus of L_2 (f = 9.01 cm).

The 10^6 rad(Si) of gamma irradiation did not reduce the ξ_2 or ε values observed for V fibers as seen by comparing FN13 to FN14 (table 2).

Both low and high ξ_2 values were calculated for the FOC fibers FN18-FN21. The cross-sectional areas of the central fiber core tested varied from 3.49, 3.49, 4.17, to 4.49 x 10^{-4} cm^2, respectively. The calculated ξ_2 values in table 2 are low since the area used was that of the core of the fiber tested. The laser beam cross-sectional

area calculated from FN17 data was A = 1.34 x 10^{-4} cm^2 or 2.60, 2.60, 3.11, and 3.35 times smaller than the core area of fibers FN18-FN21, respectively. The variations in ε from fiber to fiber is attributed to variations in surface finish of the ends of the fiber.

As a means of determining the area of the laser beam for FN18-FN21 more accurately, a V fiber FN22 with a 1.13 x 10^{-2} cm core diameter (A(f) = 9.94 x 10^{-5} cm^2) was tested. As shown in table 2, the maximum ε value observed was 0.908, but the variation in its value was from 0.881, 0.908, 0.895, to 0.885 for an average of 0.892. If the fiber losses consisted of only Fresnel reflection losses at its ends $\varepsilon = T = 0.929$ (table 1). It can be concluded that the cross-sectional area of the laser beam at the input end of FN22 was equal to the cross-sectional area of FN22 core to ±2%. The A values varied from 1.02, 1.02, 1.04, to 1.08 x 10^{-4} cm^2 for an average value of 1.03 x 10^{-4} cm^2. Using this as the A for FN18-FN21 the calculated ξ_2 and ξ_1 values changed as shown in table 3. These values are A(f)/A = 3.4, 3.4, 4.1 and 4.4 times larger than those listed in table 2 for FN18-FN21, respectively.

Table 3. Free-running laser experiment calculations of ξ_2 and ξ_1 using the average A from FN22

Fiber No.	A(f)/A	Maximum	
		ξ_2 kJ/cm^2	ξ_1 kJ/cm^2
FN18	3.4	3.490	3.675
FN19	3.4	0.453	0.487
FN20	4.1	3.640	3.897
FN21	4.4	1.162	1.245

Figure 9 illustrates two things: (1) the variations in the surface finish of the ends of FOC fibers represented by the speckle appearance or white spots on the ends of the fibers and (2) the optical damage to the central fiber of FN20 after ξ_1 = 0, 0.068, 4.090, 3.974, 4.090, 4.283, 4.100, 4.042, 4.023, 4.071, 4.139, and 4.234 kJ/cm^2 for figures 9A-9L was incident on the fiber for the 1st LS before irr and 1st-10th LS after irr, respectively. There is no drastic change from one photograph to another, but rather, a gradual change takes place in the immediate surroundings of the central fiber between the 12 o'clock and 4 o'clock position, a blistering on the periphery of its core between the 11 o'clock and 1 o'clock position, and an overlayer of recondensed binding or fusing material located over the central core radially inward from the 12 o'clock position. This small change in appearance from start to finish is in agreement with the observed change in ε of about 5.7%.

Again the 10^6 rad(Si) of gamma irradiation did not reduce the ξ_2 or ε values for the FOC fibers (compare FN18 to FN20). Comparable or higher ε values were obtained for before and after irradiation.

The CGW fibers (FN23-FN27) were the final group of fibers tested. Both low and high energy densities were propagated through these fibers. The cross-sectional area of FN23-FN27 A(f) varied from 5.97, 5.97, 6.36, 5.59, to 6.76 x 10^{-5} cm^2, respectively. These fibers had the smallest core diameter of all the fibers tested resulting in the largest ξ_2 values (FN25) as shown in table 2.

A total of five LS's were incident on FN25, three had an ξ_2 of 0.107, 0.107, and 0.121 kJ/cm^2 before irr and the remaining two LS's had ξ_2 of 3.978 and 0.173 kJ/cm^2 after irr. The corresponding ξ_1 values were 0.132, 0.135, 0.135, 4.282, and 4.477 kJ/cm^2. The last ξ_1 value was calculated using A = 8.22 x 10^{-5} cm^2, which was obtained from the E_1 and the ξ_1 values of the previous LS. The low ξ_2 value for the last LS indicates that the fiber was either not aligned or it broke during the shot. Figure 10C shows that after the last LS the central fiber core was broken. Figures 10A-10C are photographs of the input end of FN25 before the 1st LS, after the 1st LS (ξ_1 = 4.282 kJ/cm^2) after irr, and after the 2nd LS (ξ_1 = 4.477 kJ/cm^2) after irr, respectively.

Figures 10D-10F are photographs of the input end of FN26 before the 1st LS, after the 1st LS (ξ_1 = 0.089 kJ/cm^2), and after the 1st LS (ξ_1 = 4.500 kJ/cm^2) after irr, respectively. The area of the laser beam was the same as for FN25. There is evidence in the last photograph (fig. 10F) that the beam could have been larger than the central core since not only it changed in appearance. The cross-sectional area of the damaged area was 5.84 x 10^{-4} cm^2. If this is taken as the area of the laser beam instead of

the cross-sectional area of the central fiber core then, $\xi_2 = 0.187$ kJ/cm^2. Earlier test of FN22 established an upper limit on A = 1.03×10^{-5} cm^2 setting a lower limit of $\xi_2 = 1.05$ kJ/cm^2 for FN26. What looks like burned areas around the central fiber could be recollected blow off of binding material.

At lower ξ_1 and ξ_2 values the input ends of the CGW fibers damaged less severely as is illustrated in figures 11A-11G for the top fiber of FN23. A total of 11 LS's were incident on this fiber. Figure 11A is a photograph before any LS's and figures 11B-11G are for 1st-5th, and 7th LS's after irr with ξ_1 values of 2.750, 2.262, 2.406, 2.895, 0.887, and 2.804 kJ/cm^2, respectively. The low ε calculated for figure 11F indicates that the laser beam was misaligned and causing damage to the surroundings of the top fiber. The inhomogeneous material around the top fiber in figure 11F and 11G appears to be recondensed vaporized binding material.

The ε values were observed to decrease with increasing number of LS's for all fibers whose input ends were damaged. Figure 12 illustrates the decrease in ε values for large ξ_1(AVG) values for FN18, FN20, and FN23 as functions of laser shot No. The decrease in ε values from start to finish were 0.071, 0.059, and 0.173 for FN18, FN20, and FN23, respectively. The erratic behavior of the FN23 ε values is attributed to the laser beam diameter being approximately equal to the fiber core diameter and some varying malalignment between the two.

5. Discussions and Conclusions

5.1 Giant Laser Pulse Experiment

For all nine fibers tested with the giant laser pulse, table 4 lists core material, ξ_1 levels required to produce optical damage in bulk material, ξ_1 and ρ_1 levels required to produce optical damage in fiber material, and the maximum energy and power densities applied and transmitted through the fibers. In the case of FN1 and FN2 the damage was inside, not on the input surfaces. The STDL for the bulk F2 glass was slightly less than for the F7, while the STDL's for these glasses in fiber form were reversed [19]. The F2 or F7 glass used in the core was not the material that damaged initially, but rather, the binding material used between the fibers damaged. For FN3 and FN4 the binding material was the 10μm boron silicate cladding. For FN5-FN8 the binding material was the ASG67 AOC glass around the En-2 glass cladding. The bulk STDL's for these materials are not known. At higher energy levels the STDL of the F2 and F7 fiber core material was exceeded. It is not known whether the STDL of F2 and F7 core material would have been exceeded if the II fibers had stood alone without being bonded to neighbors or if the AOC fibers had stood alone without the ASG67 binding material. The stress in the cladding of the II fibers could have reduced the STDL of the boron silicate cladding material just as stress might also have been involved in the damage of the ASG67 binding glass.

Table 4. Giant laser pulse experiment energy and power densities in bulk and fibers

Fiber No.	Core Mat	STDL			Maximum in Fiber			
		Bulk+	Fiber					
		ξ_1 kJ/cm^2	ξ_1 J/cm^2	ρ_1 GW/cm^2	ξ_1 J/cm^2	ξ_2 J/cm^2	ρ_1 GW/cm^2	ρ_2 GW/cm^2
FN1†	F-2*	2.8	4.76	0.159	4.76	3.76	0.159	0.125
FN2†	F-2	2.8	5.63	0.188	5.63	4.67	0.188	0.156
FN3	F-7*	3.5	4.02	0.134	6.78	6.06	0.226	0.202
FN4	F-7	3.5	4.62	0.154	6.78	6.06	0.226	0.202
FN5	F-2	2.8	11.3	0.377	19.0	17.0	0.634	0.568
FN6	F-2	2.8	31.6	1.05	44.1	39.5	1.47	1.32
FN7	F-2	2.8	40.8	1.35	40.8	36.5	1.36	1.22
FN8	F-2	2.8	48.2	1.61	48.2	43.2	1.61	1.44
FN9	Q++	--	--	--	8.92	8.29	0.297#	0.276

\+ [19]
† Volume damage occurred
* Schott glass
++ Ge-doped fused quartz
\# Calculated from ξ_2 and ρ_2 values

The AOC fibers, followed by the CGW fibers, exhibited the largest STDL for single (FN8) and multiple (FN6) LS's and the largest maximum ξ_1, ξ_2, ρ_1, and ρ_2. For fibers receiving multiple LS's the AOC fiber exhibited the greatest decrease in coupling efficiency.

In all cases, the damage at the input end of the fibers was initiated in the bond between the fused fibers. Increased input energy caused the initial damage site to increase in size and caused new sites to be formed at lower STDL with increasing radial dimension relative to the initial site. The fibers receiving single LS's containing large energy densities (FN7 and FN8) exhibited as large or larger coupling efficiencies with less optical damage than those fibers receiving comparable ξ_1 and ρ_1, but had seen previous laser energy (FN5 and FN6). For multiple LS's into the fibers once optical damage occurred the ε for the fiber decreased with equal or increasing laser energy.

5.2 Free-Running Laser Pulses

As for the giant laser pulse experiment, fibers tested with free-running laser pulses damaged initially at the cladding or binding material used in holding nearest neighbors. Table 5 lists the STDL for 7 of the 18 fibers tested. For multiple LS's two FOC fibers FN18 and FN20 exhibited the largest STDL's followed by two V fibers FN16 and FN14 then by a CGW fiber FN23. For single LS's two CGW fibers FN25 and FN26 exhibited the largest STDL's followed by a V fiber FN15. The STDL for a single LS was not determined for FOC fibers.

Table 5. Free-running laser experiment
STDL in fibers

Fiber No.	Mfg	STDL		No. of Laser Shots
		ξ_1 kJ/cm^2	ρ_1 MW/cm^2	
FN14	V	2.962	29.62	3
FN15	V	>2.623	26.23	1
FN16	V	>3.806	38.06	2
FN18	FOC	3.675	36.75	2
		4.660*	46.60	2
FN20	FOC	3.897	38.97	8
		4.320*	43.20	8
FN23	CGW	2.895	28.95	6
FN25	CGW	4.282	42.82	1
FN26	CGW	4.500+	45.00	1

* A = 1.03 x 10^{-4} cm^2 determined from FN22 test
+ Damaged during laser shot

At lower than STDL many free-running laser pulses can be transmitted through V, FOC, and CGW fibers with only slight decreases in ε ($\Delta\varepsilon$) as shown in table 6.

Table 6. Free-running laser experiment
decrease in ε for
multiple laser shots in fibers

Fiber No.	Mfg	$\Delta\varepsilon$	No. of Laser Shots	Avg ξ_1 kJ/cm^2
FN14	V	0.185	4	2.873
FN18	FOC	0.071	9	1.052
FN20	FOC	0.059	10	0.929
FN23	CGW	0.173*	7	2.605

* Variation, last shot ε largest

The 10^6 rad(Si) of gamma irradiation did not reduce the ξ_2 or ε in V fibers (compare FN14 to FN16 in table 2), in FOC fibers (compare FN18 to FN20), or in CGW fibers. The ε values were approximately the same for both low or high ξ_2 values after gamma irradiation of the fibers as seen for FOC fibers (compare FN19 and FN21 to FN20) and for CGW fibers (compare FN24 and FN27 to FN23, FN25, and FN26).

In general the damage caused by free-running laser pulses was much less severe than that caused by giant laser pulses (compare fig. 5 to fig. 6-11).

For all fibers in which STDL's were reached there was no evidence that the observed decrease in ε was caused by nonlinear optical behavior. It is believed that the decrease in ε was due to increases in observed optical damage at the input face of the fibers.

6. Acknowledgments

I would like to thank H. P. Davis for his competent and diligent assistance in setting up this experiment and, with the help of R. J. Haushalter, acquiring the data. The financial support of AFWL/ELP for the free-running laser experiment is also acknowledged.

7. References

1 Landry, M. J., SLA Report No. SAND78-0602 (1978).

2 Partial support by AFWL/ELP, PO77-134.

3 Brown, R. G., Appl. Optics 6, 1269 (1967).

4 Veinberg, V. B., Kuz'mina, N. P., and Frolev, D. M., Sov. J. Optics Tech. 43, 282 (1976).

5 Davis, F. W. and Shrader, J. E., Boeing Co. Report No. D180-19235-1 (1976).

6 Crow, J. H., Appl. Optics 13, 467 (1974).

7 The method for determining energy density in reference 6, as determined by the energy divided by the area of the damaged area, results in a threshold damage level which is high relative to the threshold level determined by energy divided by the area of the laser beam containing one-half the beam energy.

8 Goldman, J. A. and Meyer, R., Nature 205, 892 (1965).

9 Smith, R. G., Appl. Optics 11, 2489 (1972).

10 Stolen, R. H., Ippen, E. P., and Tynes, A. R., Appl. Phys. Lett. 20, 62 (1972).

11 Ippen, E. P. and Stolen, R. H., Appl. Phys. Lett. 21, 539 (1972).

12 Stolen, R. H. and Ippen, E. P., Appl. Phys. Lett. 22, 276 (1973).

13 Stone, J., Appl. Phys. Lett. 26, 163 (1975).

14 Brannon, P. J., SLA Report No. SC-TM-72-0558A (1972).

15 Palmer, R. E. and Brannon, P. J., SLA Report No. SLA-73-0157 (1973).

16 Holimer, J. P., SLA Report No. SAND75-0610 (1976).

17 The area used in determining the densities is that of a circle whose diameter is equal to the dimension at FWHM of the horizontal Reticon array response at STA #2, see figure 3, which is the polarization direction of the laser beam, hereafter called the FWHM method. The horizontal dimension of the laser beam is about 3% greater than its vertical dimension.

18 Olness, D., J. Appl. Phys. 39, 6 (1968).

19 Neuroth, N., Hasse, R., and Knecht, A., in Proc. 3rd Symp. Damage in Laser Mat's., ed. by Glass, A. J. and Guenther, A. H., (NBS Spec. Pub. No. 356, 1972), pp 3-14.

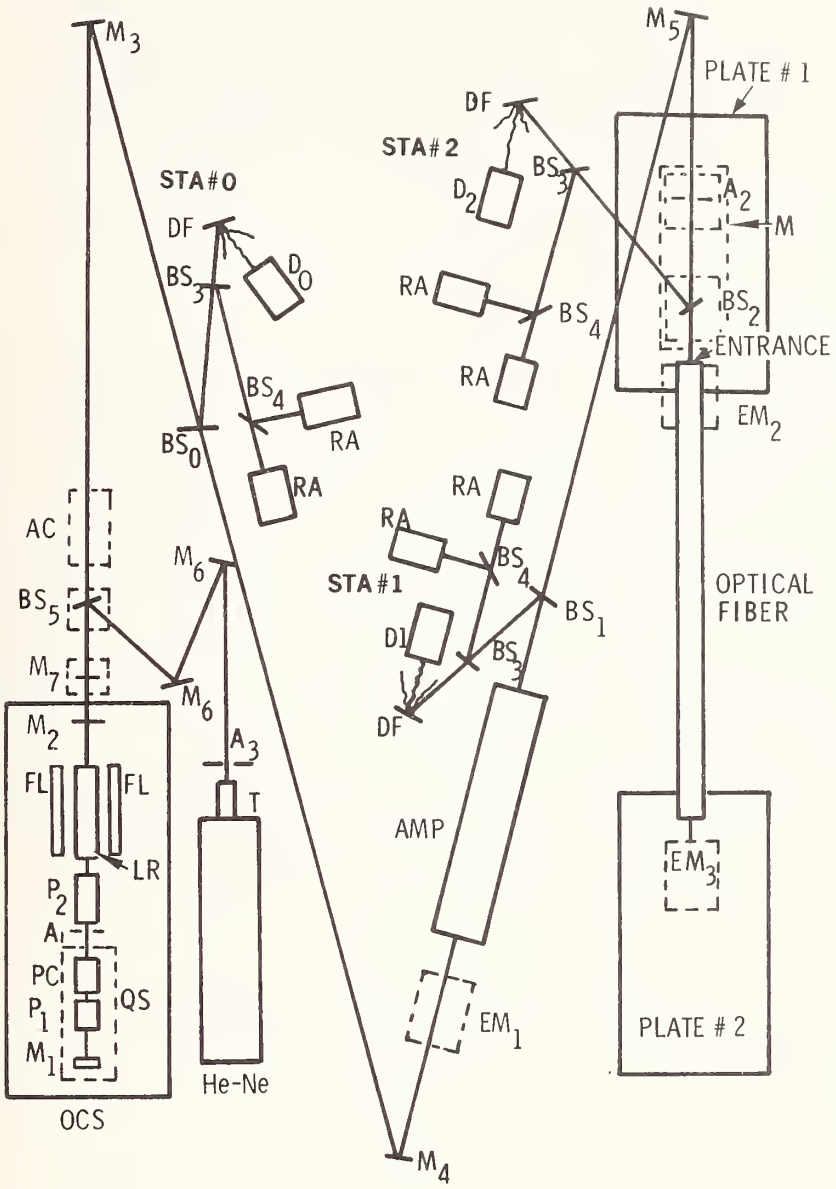

Figure 1. The mechanical and optical set-up used in studying surface threshold damage levels of optical fibers is illustrated. The components are the Nd^{3+} laser oscillator (OSC) and amplifier (AMP), alignment gas laser (He-Ne), beam sampling stations (STA #0, STA #1, and STA #2), energy meters (EM_1, EM_2, and EM_3), microscope (M), optical fiber, directing mirrors (M_3, M_4, M_5, M_6, and M_7), beamsplitters (BS_5, BS_0, BS_1, and BS_2), and restricting apertures (A_1, A_2, and A_3). Each beam sampling station has two beam-splitters (BS_3 and BS_4), a diffuser (DF), a photodiode (D_0, D_1, or D_2), and two linear diode arrays (RA).

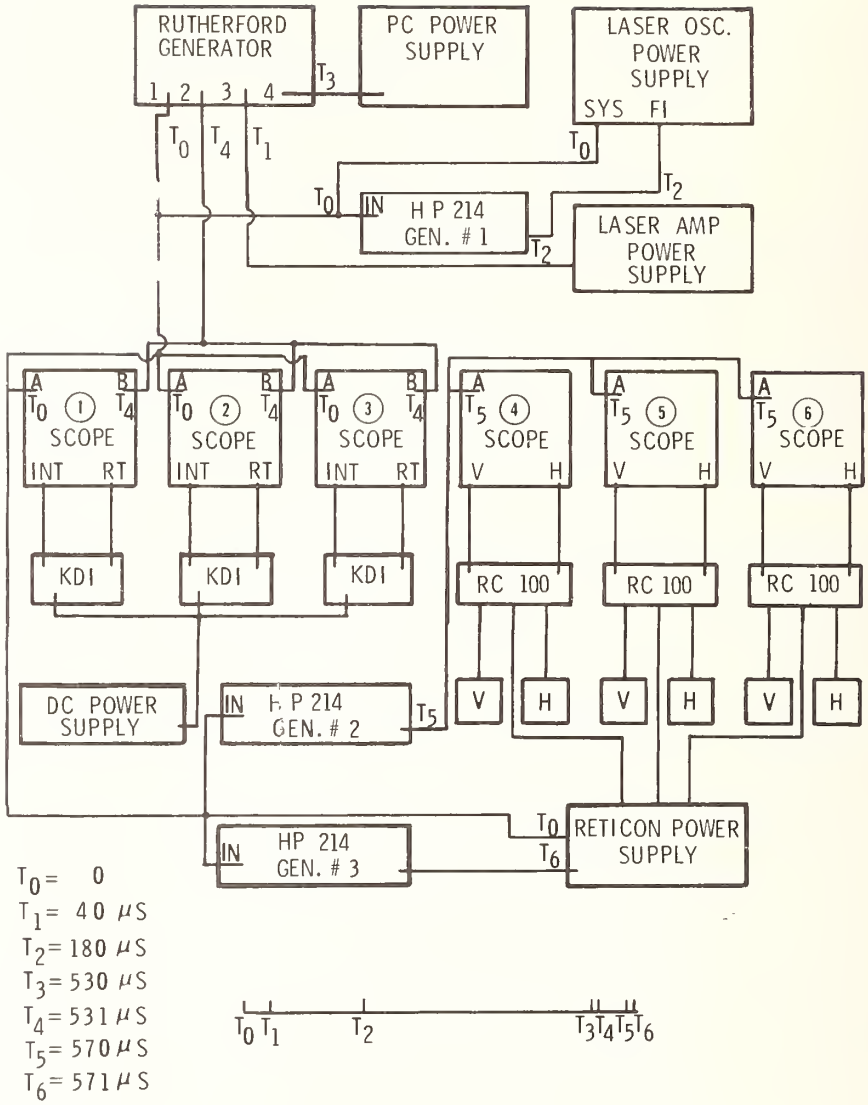

Figure 2. This block diagram illustrates the electrical connections of the laser OSC and AMP, Pockels (PC) power supply, oscilloscopes (SCOPE), photodiodes (KDl), Reticon arrays (H and V), and associated equipment (HP 214 GEN. #1, #2, and #3, Rutherford generator, DC power supply, and Reticon power supply). The relative time sequence is also illustrated.

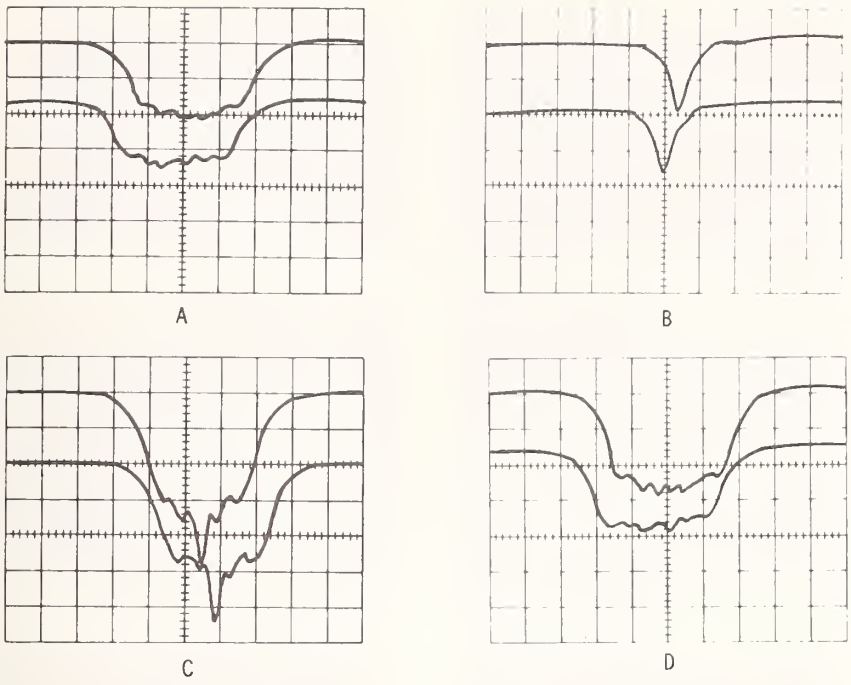

Figure 3. The laser beam profile as observed by Model No. EC-256 Reticon arrays at Sta #2 for apertures with diameters of (A) 0.508 cm, (B) 0.279 cm, (C) 0.439 cm, and (D) 0.508 cm. Full scale deflection in amplitude (vertical) is 5 divisions. Each major horizontal division is 0.127 cm.

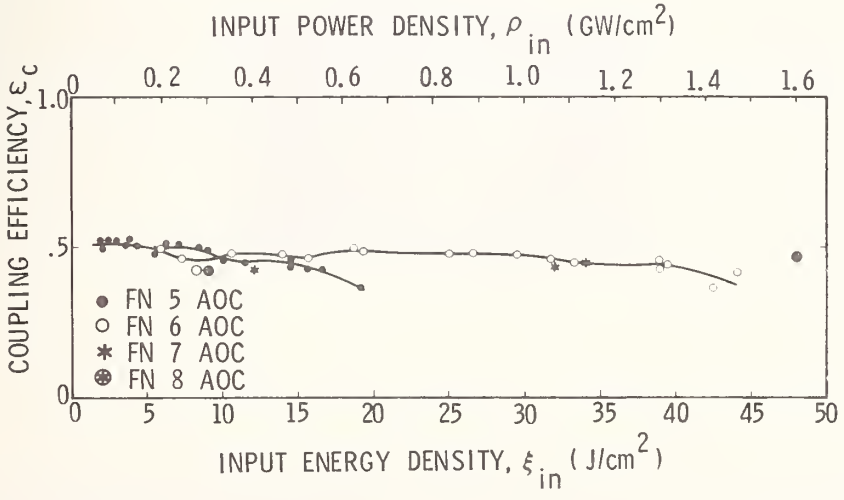

Figure 4. The coupling efficiency (ε) is illustrated as functions of input energy density (ξ_1) and input power density (ρ_1) for four AOC fibers (FN5-FN8).

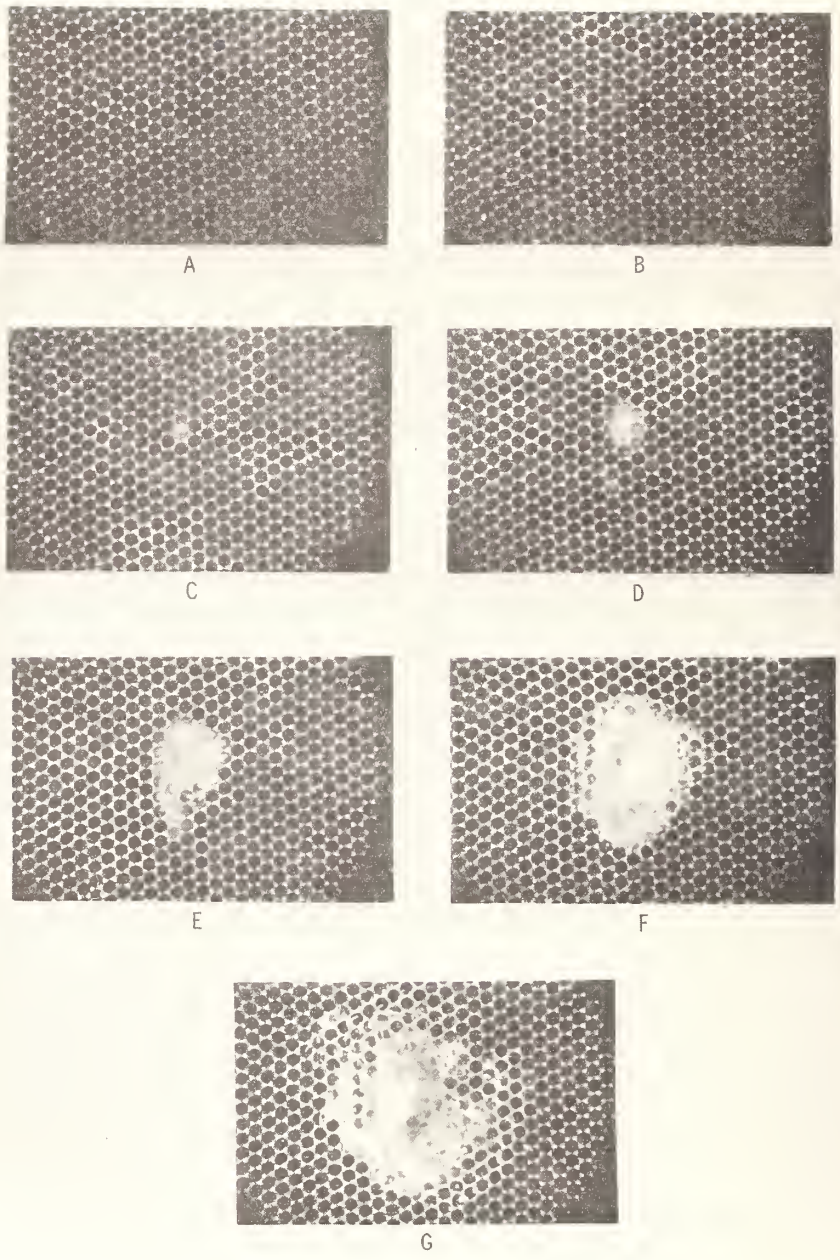

Figure 5. Photographs A-G show the increase in surface damage to the input end of FN5 (AOC fiber) for increase in input energy density (ξ_1) = 10, 11.3, 14.5, 14.4, 15.6, 16.5, and 19 J/cm^2, respectively.

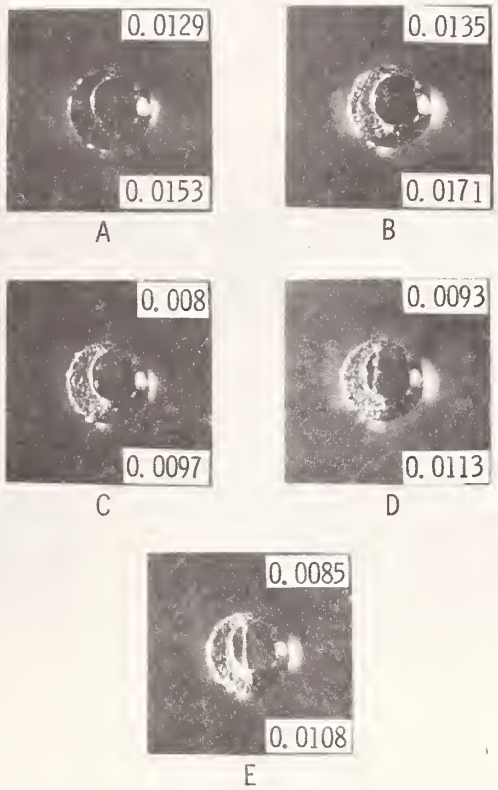

Figure 6. Photographs of the input end of FN12 illustrate its surface damage and decrease in ε (lower no.) for low ξ_2 values (upper no. in kJ/cm^2) with increasing laser shot (LS) no. Photographs A-E were taken after the 1st-5th LS, respectively.

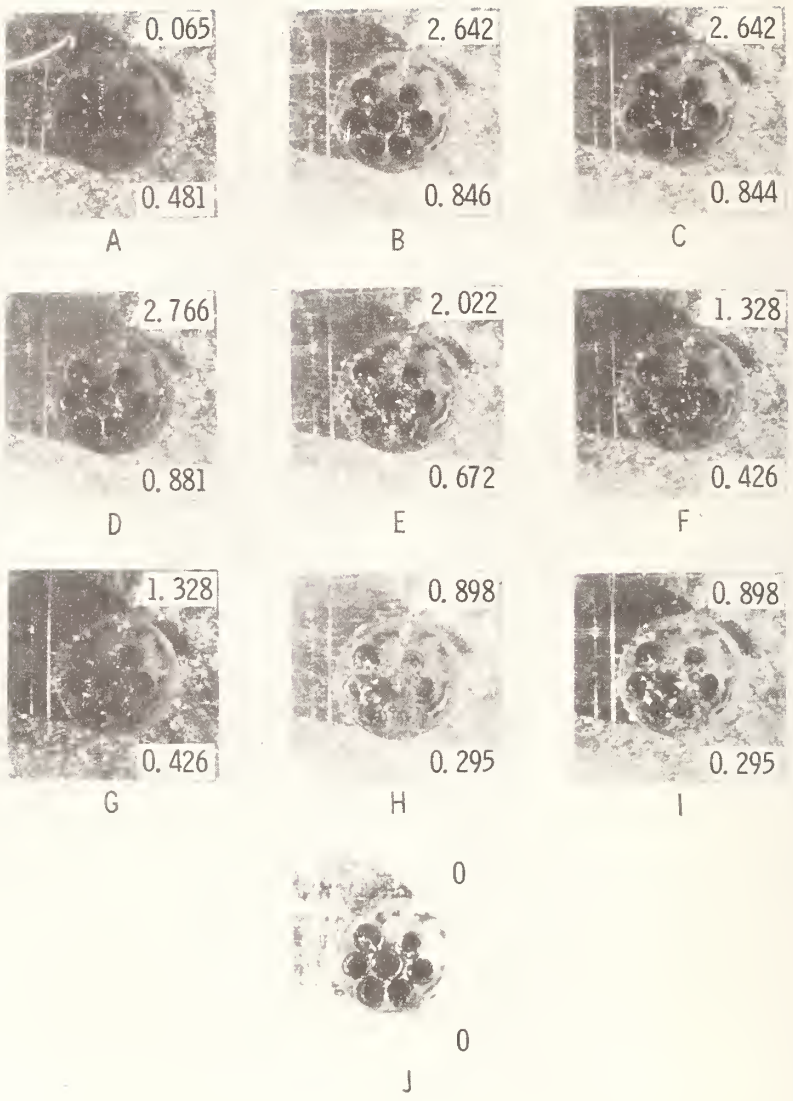

Figure 7. Photographs of the input end of FN14 illustrate the increase in its surface damage and corresponding decrease in ϵ (lower no.) for high ξ_2 values (upper no. in kJ/cm^2) with increasing laser shot (LS) no. Photograph A was taken after the 1st LS. Photographs B-F and H were taken after the 1st-6th LS after irr. Photographs F and G were taken after the 5th LS after irr and H and I after the 6th LS after irr. Photograph J was taken before the 1st LS.

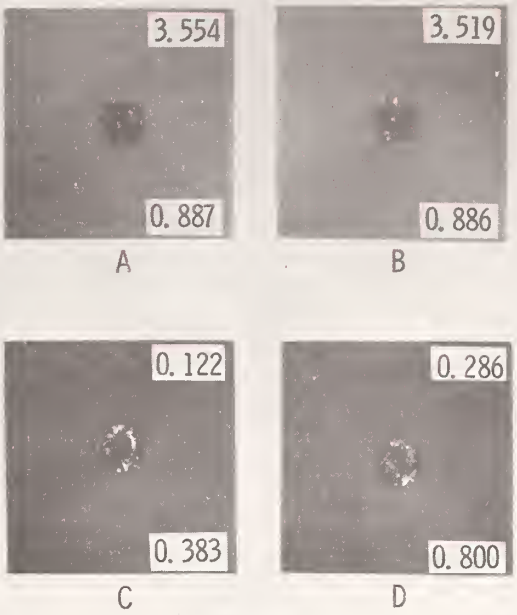

Figure 8. Photographs A and B of the input end of FN16 illustrate the increase in its surface damage after two high ξ_2 value (upper no. in kJ/cm^2) laser shots (LS's). Photographs C and D of the input end of FN17 illustrate the increase in its surface damage after the 1st and 3rd LS for low ξ_2 values.

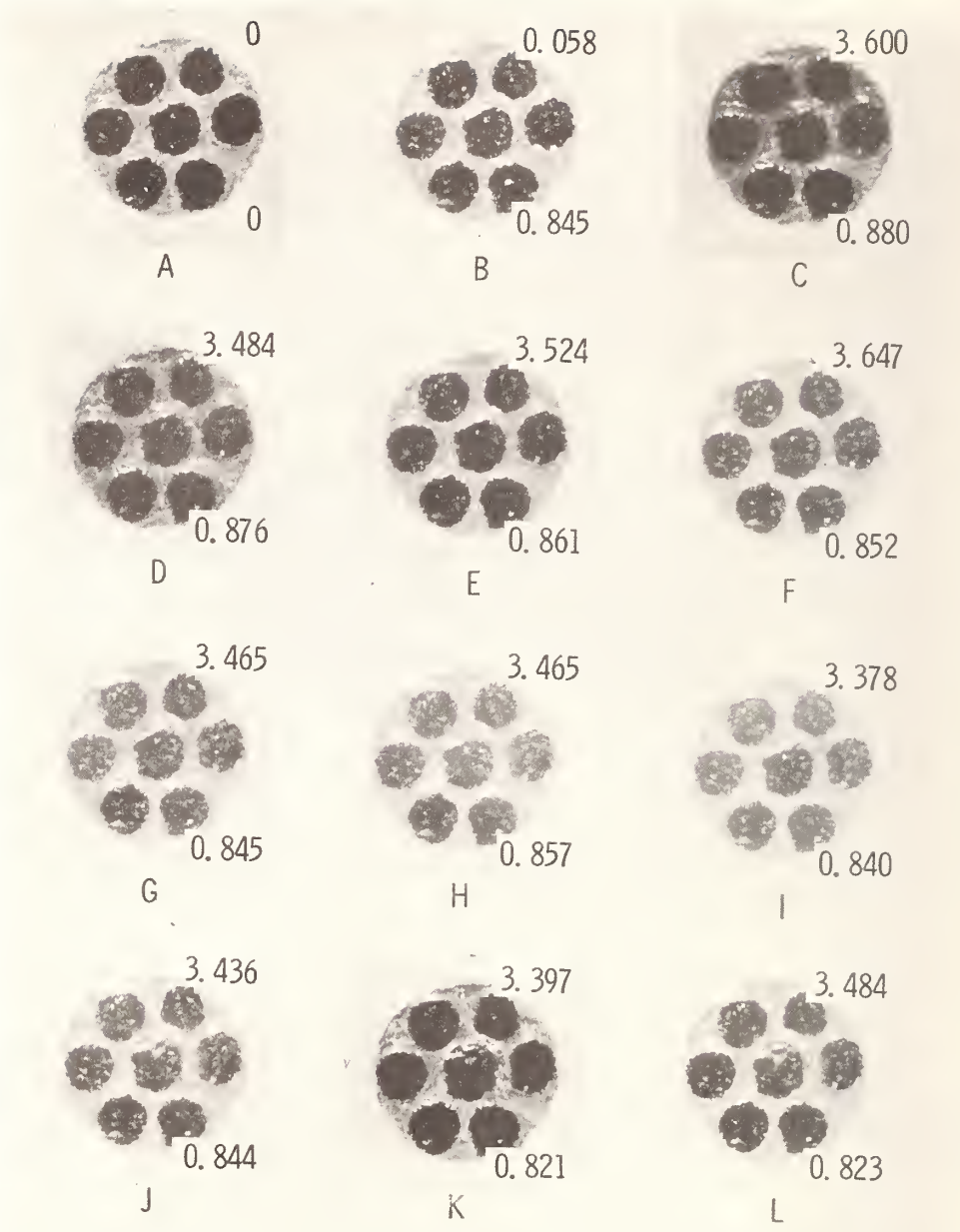

Figure 9. Photographs of the input end of FN20 illustrate the gradual increase in the surface damage to the central fiber and decrease in ε (lower no.) for large ξ_2 values (upper no. in kJ/cm^2). Photograph A is before any laser shot (LS); B is for after the 1st LS; and C-L are for after the 1st-10th LS after irr, respectively.

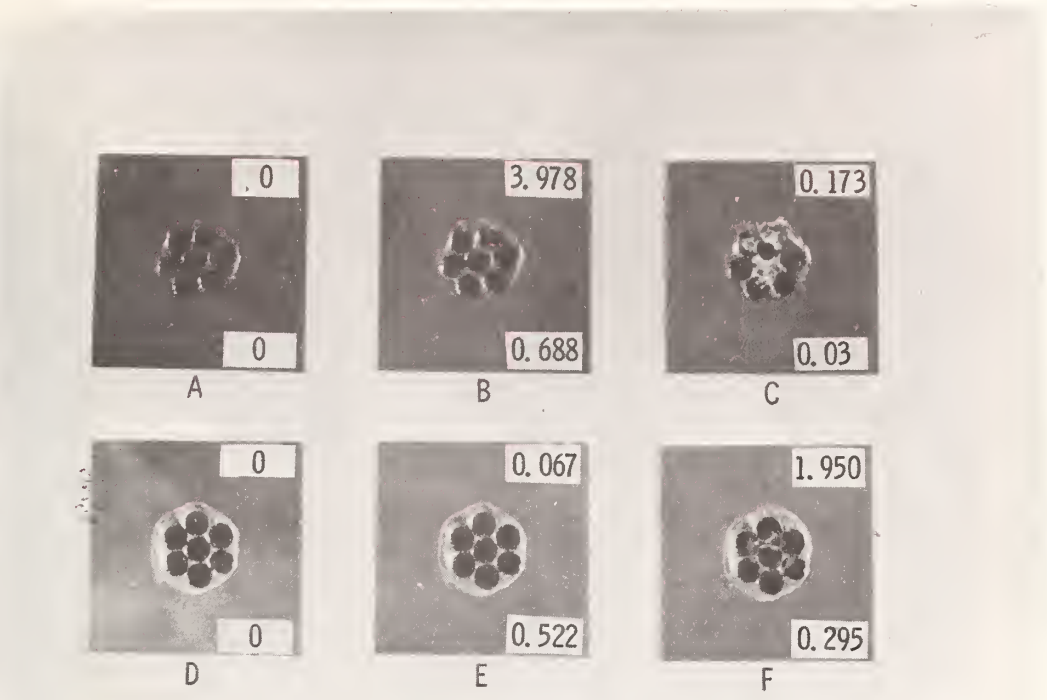

Figure 10. Photographs A-C of the input end of FN25 illustrate the damage to the central fiber during the 2nd LS after irr (C). Photograph B is after the 1st LS after irr. Photographs D-F, are of the input of FN26 before the 1st LS, after the 1st LS, and after the 1st LS after irr, respectively. The ξ_2 values are the upper no. in kJ/cm^2 and the ε are the lower no.

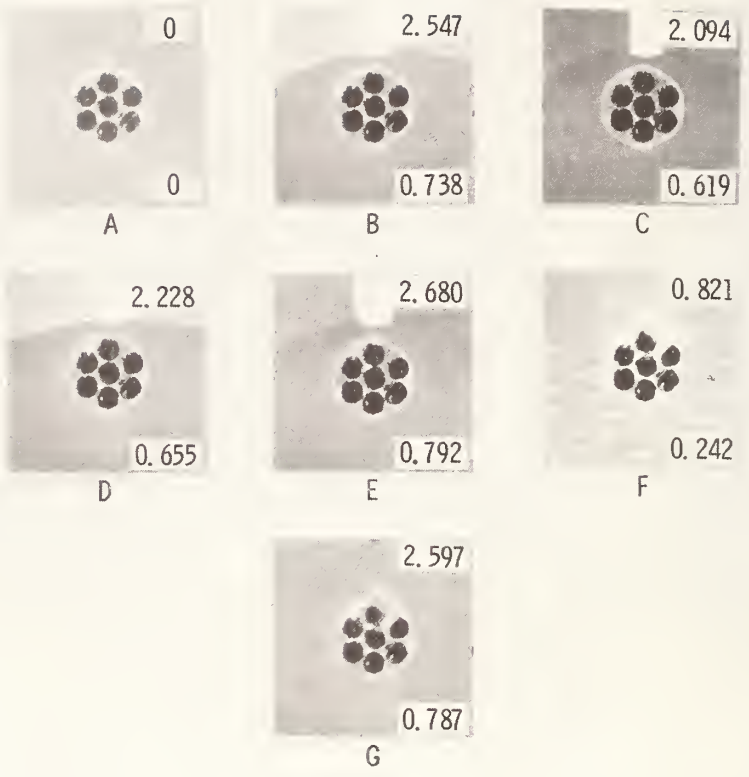

Figure 11. Photographs A-G of the input end of FN23 (CGW fiber) show little changes to the top fiber for large ξ_2 values (upper no. in kJ/cm^2). Photograph A is before any LS and B-G are after the 1st-5th and 7th LS after irr, respectively. The ε values are the lower no.

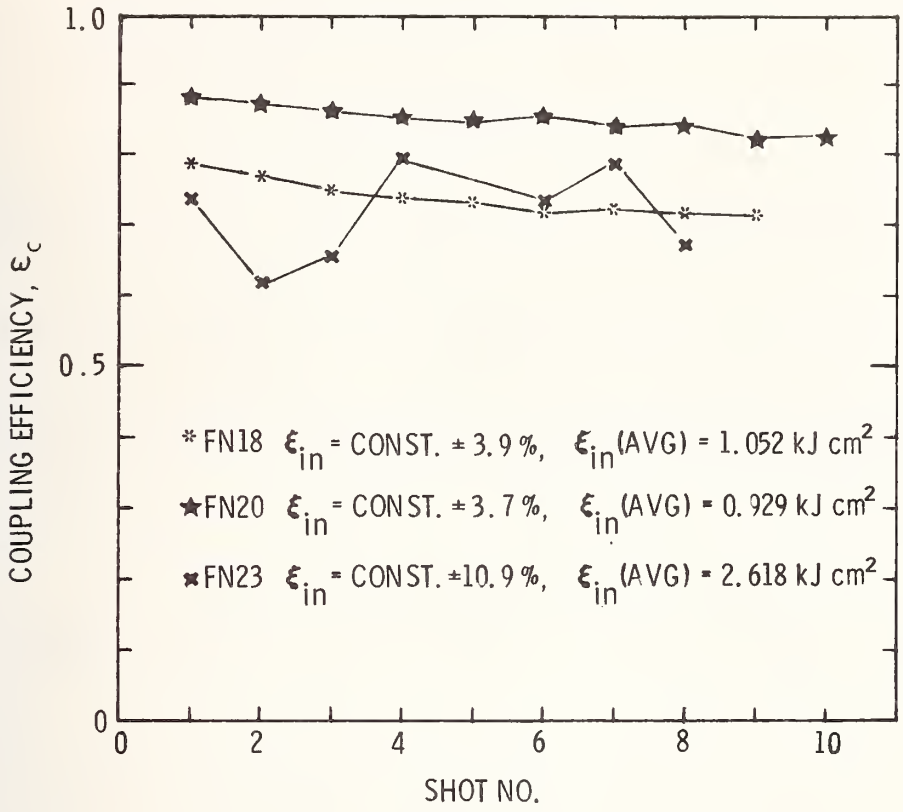

Figure 12. The decrease in ε values is illustrated for three fibers FN18, FN20, and FN23 as functions of laser shot no.

ULTRAVIOLET DAMAGE RESISTANCE OF LASER COATINGS*

Brian E. Newnam and Dennis H. Gill
Los Alamos Scientific Laboratory
Los Alamos, New Mexico 87545

The damage resistance of several thin-film materials used in ultraviolet laser optics was measured at 266 nm and 355 nm. The coatings included single, quarter-wave (QW) layers of NaF, LaF_3, MgF_2, ThO_2, Al_2O_3, HfO_2, ZrO_2, Y_2O_3 and SiO_2, plus multilayer reflectors composed of some of these materials. The substrates were uv-grade fused silica. Single-shot thresholds were obtained with 22-ns and 27-ns (FWHM) pulses at 266 and 355 nm, respectively. One of the samples had previously been tested using 20-ps pulses, providing a pulsewidth comparison.

At 266 nm the coating with the highest damage threshold was a QW layer of NaF at 10.8 J/cm^2 (450 MW/cm^2), whereas for a maximum reflector of Al_2O_3/NaF the value was 3.6 J/cm^2 (154 MW/cm^2). At 355 nm the QW layer of NaF could not be damaged at 38 J/cm^2 (1390 MW/cm^2), and the threshold of the maximum reflector was 12.2 J/cm^2 (470 MW/cm^2).

The results were analyzed to determine correlations with standing-wave electric fields and linear and two-photon absorption. Scaling relationships for wavelength, refractive index and atomic density, and pulsewidth were found.

Key words: damage thresholds; electric fields; laser damage; nanosecond pulses; pulsewidth dependence; standing waves; thin-film coatings; two-photon absorption; ultraviolet wavelength scaling.

1. Introduction

The recent growth in popularity of rare gas-halogen lasers has pointed up the lack of damage threshold data in the ultraviolet. This paper examines a variety of coating materials useful for uv laser optics. Single QW layers and multilayer total reflectors were irradiated at 266 nm (22 ns) and 355 nm (27 ns). Materials evaluated at both 355 nm and 266 nm were NaF, ThO_2, Al_2O_3 and ZrO_2. In addition, LaF_3, MgF_2, HfO_2, Y_2O_3 and SiO_2 were tested at 266 nm. Total reflectors of Al_2O_3/NaF and ThO_2/SiO_2 were tested at both wavelengths, and reflectors of ThO_2/MgF_2 and PbF_2/cryolite were tested at 266 nm. The film and substrate characteristics are listed in table 1. All coatings were deposited by use of an electron gun, except those by rf-sputtering as noted.

Table 1. Coating and substrate characteristics.

Coating Material	Substrate	Substrate Roughness Å rms	Substrate Deposition Temperature ° C	Coating Index of Refraction 266 nm	355 nm	Coating Absorption Edge[a] nm
NaF	Suprasil 2	12	30	1.34	1.33	> 130
SiO_2 (sputtered)	Suprasil 2	12	165	1.52	1.51	> 160
MgF_2	Suprasil 2	12	30	1.39	1.38	> 115
LaF_3	Suprasil 2	12	30	1.61	1.60	> 135
ThO_2	Dynasil 1000	20	200	2.0	1.95	250
Al_2O_3	Suprasil 2	12	30	1.67	1.65	> 140
ZrO_2	Optosil 1	20	200	2.17	1.95	225
ZrO_2 (sputtered)	Suprasil 2	12	175	2.4	2.27	260
HfO_2	Ultrasil	20	250	2.15	2.08	220
Y_2O_3 (sputtered)	Suprasil 2	12	200	2.0	1.79	215
Al_2O_3/NaF	Suprasil 2	12	30			
ThO_2/SiO_2	Dynasil 1000	20	200			
ThO_2/MgF_2	Dynasil 1000	20	200			
PbF_2/Cryolite	Suprasil 2	12	30	2.17/1.37		230/>130

[a] Coating absorption edge was defined where measured absorption was 10%. Values preceded by > are for bulk materials [1][1]; negligible absorption was measured for these coatings down to 200 nm.

* Work performed under the auspices of the U. S. Department of Energy.

1. Figures in brackets indicate the literature references at the end of this paper.

Most of the samples were on identical substrates of Suprasil 2 with approximately a 12 Å rms surface roughness. A few samples were on other types of uv-grade fused silica and had an approximate surface roughness of 20 Å rms. Spectrophotometric traces for the single QW layers are shown in figure 1. Note that some of the layers were not exactly $\lambda/4$ thick at 266 nm. The actual wavelength at which each coating was $\lambda/4$ thick is tabulated in tables 2 and 4.

The NaF single-layer samples were fogged in appearance. This was probably due to the high relative humidity in the coating company's plant (reported to be about 65%). However, Al_2O_3/NaF reflectors were not fogged, probably because the outer layer of Al_2O_3 protected the NaF. The gradual decline in transmission at shorter wavelengths for NaF (fig. 1) was due to scattering losses from the fog. Special note is also made of the short-wavelength transmission of the ThO_2 which did not extend to the expected absorption edge.

2. Experimental Procedure

The experimental arrangement is shown in figure 2. A Nd:YAG laser was Q-switched using Bis (4-dimethylamino-dithiobenzil) nickel dye and 3 etalons inside the cavity. The combination of slow-relaxation-type dye and etalons produced a 35 ns pulse at 1064 nm. This beam was then frequency doubled and subsequently tripled or quadrupled. The 266 nm pulsewidth was nominally 22 ns and the 355 nm pulsewidth was nominally 27 ns. Two dispersive prisms were used to separate out the desired wavelength. Beam pickoffs reflected energy into a fast photodiode (ITT F4014) and a Laser Precision Energy Meter. The photodiode signal was sent to a Tektronix R7912 Transient Digitizer. Another beam pickoff was focused by a 500 mm f1 lens, identical to that in the main beam path, onto a Reticon linear diode array, as shown in figure 2, or onto an aperture in front of another Laser Precision Energy Meter, as shown in figure 3. The Reticon array was used at 355 nm to determine focal spot size; it could not be used at 266 nm due to fluorescence of the array window.

The arrangement shown in figure 3 was used at both wavelengths to determine the peak energy density on the sample. The two apertures were 70 μm in diameter. Aperture 1 and Energy Meter 1 were located at the sample position, which was 450 mm from the 500 mm f1 lens. After the calibration, these were removed and the samples placed at position 1 for the tests. Aperture 2 and Energy Meter 2 remained in position for the entire test. By determing the ratio of the transmitted energy in the two paths, path 2 could be used during the test to establish the energy density at the sample. Since the beam spot size w was 0.15 mm (radius at $1/e^2$ intensity), the beam profile was not completely flat across the aperture. A small correction factor (6.3%) was used to calculate the peak energy density.

Energies from the energy meters, time profiles from the R7912 and (at 355 nm) the spatial profile from the diode array were fed to an on-line computer and data acquisition system for immediate analysis [2]. The calculated peak energy- and power-densities were printed out after each shot for use in plotting the data on a scatter-plot as the test proceeded.

Each sample was irradiated with an average of about 40 shots. Each site was irradiated only once. Damage was determined by visual observation of the irradiated site through a 40X stereo microscope. Two types of illumination were used. A bright white-light source illuminated the entire sample. A He-Ne laser illuminated only the actual irradiated zone. The laser-induced scattering of both light sources was used to determine the occurrence of damage.

3. Results

Table 2 lists the damage thresholds of the various single QW layer materials tested at 266 nm. The ranges quoted in the damage threshold columns are from the lowest values that did cause damage to the highest values that did not cause damage [3]. For each laser shot the computer integrated the photodiode signal and calculated an effective pulsewidth which was then used to calculate the peak power density. Thus the apparent pulsewidth one obtains by dividing energy density by power density is not a constant. The previously quoted pulsewidths of 22 ns for 266 nm and 27 ns for 355 nm are average values for all of the tests.

The peak internal electric field was calculated using a LASL code that computes the E-field distribution within a dielectric stack. The actual thicknesses of each layer were taken into account. The various layers were not exactly a quarter wave at 266 nm, as shown in table 2. Figure 4 shows the relative E-field-squared distribution within two materials, one whose index of refraction is less than the substrate and one whose index is greater than the substrate. The peak E-fields are substantially different for the two cases. Also shown in figure 4 is the effect of testing at 355 nm a coating that is QW thick at 266 nm.

The low index material with the highest damage threshold was NaF, in spite of its fogged appearance. The high index material with the highest damage threshold was LaF_3.

Table 2. Comparison of materials at 266 nm

Material	Thickness λ/4 at (nm)	Damage Threshold Energy Density J/cm²	Power Density MW/cm²	Peak Internal E-Field MV/cm
NaF	266	10.8 ± 1.7	450 ± 70	.37 ± .03
SiO_2 (sputtered)	532	9.4 ± 0.3	410 ± 10	.32 ± .01
MgF_2	266	6.8 ± 0.7	310 ± 30	.30 ± .02
LaF_3	250	6.7 ± 0.6	280 ± 30	.26 ± .01
ThO_2	290	2.8 ± 0.4	122 ± 17	.16 ± .01
Al_2O_3	266	2.6 ± 0.2	106 ± 10	.16 ± .01
ZrO_2	300	1.5 ± 0.1	67 ± 4	.11 ± .01
ZrO_2 (sputtered)	505	1.5 ± 0.1	66 ± 4	.13 ± .01
HfO_2	278	1.3 ± 0.2	68 ± 10	.11 ± .01
Y_2O_3 (sputtered)	374	0.6 ± 0.2	31 ± 10	.08 ± .01
SiO_2 (Suprasil 2) (Front surface)	---	8.0 ± 0.3	350 ± 10	.29 ± .01

Table 3. Comparison of total reflectors at 266 nm.

Material	Damage Threshold Energy Density J/cm²	Power Density MW/cm²	Peak Internal E-Field MV/cm
Al_2O_3/NaF	3.6 ± .4	154 ± 17	.29 ± .02
ThO_2/SiO_2	1.3 ± .1	71 ± 5	.16 ± .01
ThO_2/MgF_2	1.1 ± .3	55 ± 15	.14 ± .02
PbF_2/Cryolite	0.5 ± .1	19 ± 4	.11 ± .01

Table 3 lists the four reflectors tested at 266 nm. The Al_2O_3/NaF reflector was the best by a considerable margin. The threshold of the PbF_2/Cryolite reflector was quite low.

The single-layer materials tested at 355 nm are listed in table 4. It should be emphasized that these are the same, identical samples as those tested at 266 nm. At 38 J/cm² (1.39 GW/cm²) we were unable to damage the NaF thin film. There were only small differences between the other three samples.

The two reflectors tested at 355 nm are listed in table 5. Again, the Al_2O_3/NaF was best by more than a factor of 2. The reflectors tested at 355 nm were not the same as those tested at 266, but rather were maximum reflectors at 355 nm made by the same company on the same day as the maximum reflectors at 266 nm.

All of the materials and reflectors that were tested at both wavelengths are brought together in table 6 for easier comparison. This data is then plotted in figure 5 in terms of energy density and in figure 6 in terms of electric field. Figure 7 is a plot of the data obtained previously [3] on some of the same materials at 1064, 532 and 355 nm. Pulsewidths for this data were 30 ps, 20 ps and 17 ps, respectively. Spot sizes were similar to the present data. The higher damage thresholds at 532 nm compared to those at 1064 nm were observed to be in accordance with the frequency dependence of the electron avalanche mechanism.

Table 4. Comparison of materials at 355 nm.

Material	Thickness λ/4 at (nm)	Damage Threshold Energy Density J/cm²	Power Density MW/cm²	Peak Internal E-Field MV/cm
NaF	266	> 38	> 1390	> .65
ThO_2	290	9.1 ± .2	340 ± 10	.27 ± .01
ZrO_2	300	7.1 ± .2	250 ± 10	.23 ± .01
Al_2O_3	266	5.9 ± .5	210 ± 20	.22 ± .01

Table 5. Comparison of total reflectors at 355 nm.

Material	Damage Threshold		
	Energy Density	Power Density	Peak Internal E-Field
	J/cm^2	MW/cm^2	MV/cm
Al_2O_3/NaF	12.2 ± .9	470 ± 40	.51 ± .02
ThO_2/SiO_2	4.9 ± .1	180 ± 10	.27 ± .01

Table 6. Spectral dependence of damage thresholds.

Material	Damage Thresholds			
	Energy Density (J/cm^2)		Peak E-Field (MV/cm)	
	266 nm	355 nm	266 nm	355 nm
NaF	10.8 ± 1.7	> 38	.37 ± .03	> .65
Al_2O_3	2.6 ± 0.2	5.9 ± 0.5	.16 ± .01	.22 ± .01
Al_2O_3/NaF Reflector	3.6 ± 0.4	12.2 ± 0.9	.29 ± .02	.51 ± .02
ThO_2	2.8 ± 0.4	9.1 ± 0.2	.16 ± .01	.27 ± .01
ThO_2/SiO_2 Reflector	1.3 ± 0.1	4.9 ± 0.1	.16 ± .01	.27 ± .01
ZrO_2	1.5 ± 0.1	7.1 ± 0.2	.11 ± .01	.23 ± .01

4. Discussion

4.1. Electric-Field Correlations

Several experimental studies with short laser pulses (30 ps-10ns) have determined that coating damage occurs first at the locations of internal electric-field maxima [4,5]. Accordingly, the threshold electric fields listed in tables 2-6 have also been computed at the standing-wave (SW) maxima. However, at our relatively longer (20-30 ns) pulses, a complete analysis should include thermal conduction during the pulse which reduces temperature extremes at SW peaks. This is more applicable for coatings which damage by absorption than by avalanche breakdown.

An exact correlation of peak electric fields for 22-ns pulses at 266 nm is found with ThO_2 coatings. A breakdown field of 0.16 MV/cm was measured for ThO_2 both as a single-layer and in the reflector configuration of ThO_2/SiO_2 (table 6). (Damage occurs first in the high-index layer of the reflector).

A correlation of peak fields was not observed in Al_2O_3 coatings, however. The respective threshold fields in single-layer and reflector configurations (Al_2O_3/NaF) were 0.16 and 0.29 MV/cm. There are two apparent explanations for the difference. One is that the Al_2O_3 single layer had greater absorption or was weaker, a fact which would be difficult to specifically measure. The second possibility is that the material adjacent to the Al_2O_3 was influential.

To discuss the latter, we first note that the peak fields in both coating configurations occurred at the interfaces with adjacent material, the fused silica substrate for the QW case and the first NaF layer in the reflector. If absorption is the damage mechanism, then thermal conduction away from the interfaces during the 22-ns pulse must be considered. Since the thermal diffusivity of NaF at 0.070 cm^2/sec (bulk, 300°K) is an order of magnitude greater than that of fused silica (0.0083 cm^2/sec) [6], conduction losses at the interfaces could well have been significantly different. Additionally, coating damage could have resulted from heating of inclusions in the polished surface layer of the silica substrate. Further experiments would be required to determine which is the correct explanation.

4.2. Spectral Dependence

4.2.1. Linear and Two-Photon Absorption

The decline in damage resistance at 266 nm when compared to that at 355 nm (shown in figures 5 and 6) was anticipated. Linear absorption increases rapidly as the absorption band edge is approached. Besides linear absorption, multiphoton absorption also becomes a potential damage mechanism. As can be deduced from the values of absorption edge listed in table 1, two-photon absorption (TPA) is energetically possible for all of the coating materials for 266-nm irradiation. At 355 nm, TPA is also possible for ThO_2, ZrO_2, HfO_2, Y_2O_3 and PbF_2, but 3 photons are required for resonant absorption in the remaining coatings listed.

In a previous study with picosecond pulses at 355 nm, Newnam and Gill [3] suggested that TPA was a plausible damage mechanism for ZrO_2, HfO_2, and SiO_2. This possibility could not be confirmed because TPA coefficients (β) were not known, nor were accurate linear absorption coefficients (α) measured by calorimetric techniques available. Derivation of α from spectrophotometric curves is subject to error when coating inhomogeneity (variation of refractive index with thickness) and scattering losses are not well quantified. Unfortunately, a similar deficiency in film characterization existed in this study. However, recent measurements of TPA coefficients of laser crystals and windows at 266 and 355 nm reported by Liu, et al. [7], allow estimation of the relative role of TPA for a few of the coatings in this study.

In absorption processes, the power absorbed per unit volume, dI/dz, is the quantity of interest. For both first- and second-order absorption,

$$\frac{dI}{dz} = - \alpha I - \beta I^2 \quad . \tag{1}$$

When the plane-wave expressions for I ($= \frac{1}{2}\sqrt{u/\varepsilon}\,|E|^2$) and I_o (incident) are substituted, we obtain

$$\frac{dI}{dz} = - nI_o \left|\frac{E(z)}{E_o^+}\right|^2 (\alpha + \gamma), \tag{2}$$

where

$$\gamma = \beta n I_o \left|\frac{E(z)}{E_o^+}\right|^2, \tag{3}$$

and $|E(z)/E_o^+|^2$ is the standing-wave distribution normalized to the incident field. To heat a material to its melting point (a well-defined damage threshold), the minimum <u>total</u> absorption coefficient α_T (cm^{-1}) is given by

$$\alpha_T = \frac{\rho c_p}{n \mathcal{E}_o} (T_{mp} - 300°K) \left|\frac{E(z)}{E_o^+}\right|^{-2}_{peak}, \tag{4}$$

where ρ is density, c_p is specific heat, and $\mathcal{E}_o$ is the incident energy-density threshold.

From calculations of α_T and γ using experimentally measured damage thresholds, it is possible to determine the relative role of 1- and 2-photon absorption in the damage process, ignoring other possible competing mechanisms. The reported values of β (cm/MW) at 266 and 355 nm for Al_2O_3 are 2.7×10^{-4} and $< 1.6 \times 10^{-6}$. and for fused silica are $\leq 4.5 \times 10^{-5}$ and $< 1.3 \times 10^{-6}$, respectively [7]. Values for other coating materials tested in this study are not available except for ZrO_2 for which β at 694 nm was reported to be 2.4×10^{-3} cm/MW [8]. Corresponding values at uv wavelengths would, of course, be much larger. Computed values of α_T and γ are shown in table 7. For purposes of comparison, typical values of α for thick commercially deposited coatings are presented in table 8.

The primary observation is that for nanosecond pulses 2-photon absorption is not an important damage mechanism for these three materials. Only for picosecond-pulse irradiation of ZrO_2 is it significant. Secondly, nanosecond-pulse damage to ZrO_2 coatings at 266 nm occurred via linear absorption. The value of α_T to cause melting is within the value listed in table 8. At 355 nm, the computed α_T of 900 cm^{-1} for ZrO_2 exceeds that in table 8 (210 cm^{-1}) by a considerable amount. Possibly, absorbing coating defects were damaged at a lower laser intensity.

Table 7. Total and two-photon absorption contributions to uv laser coating damage.

Coating Material (Pulsewidth)	266 nm $\alpha_T(cm^{-1})$	266 nm $\gamma(cm^{-1})$	355 nm $\alpha_T(cm^{-1})$	355 nm $\gamma(cm^{-1})$
	(22 ns)		(27 ns)	
ZrO_2 (E-gun)	3400	> 1	900	> 1
ZrO_2 (sputtered)	2900	> 1	--	--
Al_2O_3	2300	0.03	1000	0.001
Al_2O_3 (in reflector)	700	0.10	200	0.002
SiO_2 (sputtered)	250	0.02	--	--
SiO_2 (substrate)	350	0.02	--	--
			(17 ps)	
ZrO_2 (E-gun)	--	--	2800	> 300
SiO_2 (E-gun)	--	--	1000	< 0.2

Table 8. Typical absorption coefficients for thick uv coatings deposited by electron gun [9]

Coating Material	$\alpha(cm^{-1})$ 250 nm	350 nm
ZrO_2	6000	210
HfO_2	950	270
Al_2O_3	190	150
LaF_3	850	430
PbF_2	900	100

Computed values of α_T for Al_2O_3 are much in excess of typical values. As these coatings were deposited at ambient temperature and with no reactive oxygen atmosphere, the oxidation of the Al probably was not complete, resulting in high absorption.

Finally, linear absorption at 266 nm was probably the operative damage mechanism for the other oxides, Y_2O_3, HfO_2 and ThO_2, although the available evidence is not conclusive.

4.2.2. Wavelength Scaling

The spectral dependence of laser damage in figure 6 suggests an interesting relationship between the electric-field thresholds at 355 and 266 nm. For the coating materials, NaF, Al_2O_3, ThO_2 and ZrO_2, which were tested at both wavelengths, the ratio of the threshold fields is

$$\frac{E_t(355)}{E_t(266)} = 1.73 \pm 0.23 \tag{5}$$

This is surprisingly close to the ratio of the laser wavelengths squared, i.e. $(355/266)^2 = 1.78$!

It is probably permissable to use this wavelength-squared ratio to estimate the 355-nm thresholds of the additional coating materials that were only tested at 266 nm (see tables 1 and 4) since the wavelength range is narrow. However, the relationship $E_t \sim \lambda^2$ observed here is not expected to be a general scaling law for laser damage at ultraviolet wavelengths. Such a dependence is not generally derivable from the theory of optical absorption in dielectrics. That theory predicts that the absorption coefficient at a frequency ν near the center frequency of an absorption band ν_o is of the form

$$\alpha \sim \frac{\gamma^2\nu^2}{(\nu_0^2-\nu^2)+\gamma^2\nu^2} , \tag{6}$$

where γ is a material constant acounting for the breadth of the absorption band [10]. The subject of a wavelength scaling law for uv laser damage merits further consideration.

4.3. Refractive-Index and Atomic-Density Scaling

In a number of laser damage studies of thin film materials used in the visible and near-ir regions, high-index coatings have been found to damage more easily than low-index coatings [11, 12, 13, 14, 15]. Bettis, et al, [14]. have derived a first-principles equation for the macroscopic breakdown electric field in terms of material parameters,

$$E_{th} = \frac{N}{n^2-1} \frac{q_e}{\varepsilon_0} X_{cr} \sqrt{10^{-5}} \tag{7}$$

where N is atomic density (cm^{-3}), n is refractive index, q_e is electronic charge and X_{cr} is the critical separation required to free an optical electron from its atom. The threshold fields for a number of coating materials, when irradiated with 40-ns, 1.06 μm pulses, were shown to follow this relationship fairly well.[14].

The present coating thresholds for 266 nm have been plotted versus $N/(n^2-1)$ (the dominant term in eq. (7)) in figure 8. A straight line provides a reasonable fit to the data with certain exceptions. The threshold for NaF was considered low, due to fogging, MgF_2 is generally an inhomogeneous film with substantial H_2O content, and the single-layer Al_2O_3 had an anomalously low threshold, probably due to high absorption. A least-squares straight-line fit of the data in figure 8, ignoring the points for lossy films of NaF, MgF_2, and single-layer Al_2O_3, provides the equation

$$E_{th}(MV/cm) \sim 0.54 \frac{N}{n^2-1} \tag{8}$$

Certain corrections could be applied to improve the observed correlation. First, the atomic density, N, should be multiplied by the coating packing density since coatings are not as dense as bulk crystals. For example, p = 0.72 for MgF_2 deposited at 30°C before exposure to the atmosphere [16]. Secondly, HfO_2 and ThO_2 coatings were deposited on slightly rougher substrates than the other films (∿ 20 Å rms as compared to ∿ 12 Å rms). House, et al.[17], have demonstrated that increased substrate roughness decreases the damage threshold field as $E_{th} \sim \sigma^{-0.5}$, so the thresholds for HfO_2 and ThO_2 could be

adjusted upward about 25% for comparison purposes.

4.4. Pulsewidth Dependence

A pulsewidth dependence of laser damage at 355 nm for a single-layer coating of ZrO_2 on Optosil 1 is shown in figure 9 in which the present measurements at 27 ns are compared to a previous measurement at $\sim$ 20 ps on the same sample [3]. The laser spot-size radii were slightly different, 120 μm versus 150 μm, but this does not prevent a direct comparison. (For 30-ps pulses, no significant threshold dependence on spot size was measured [3].) The observed $\tau^{1/6}$ dependence for energy-density threshold is much more gradual than the 1/2-power dependence observed for the bulk and surfaces of many window materials [18].

In previous measurements at 694 nm over a pulsewidth range of 12 to 34 ns, a $\tau^{1/2}$ dependence was measured for a single half-wave coating of ZrO_2 only when the occurrence of a photometrically detectable spark was used as the criterion for damage [12]. Using the more sensitive technique of laser-induced scatter as the damage criterion, only a $\tau^{1/3}$ dependence was measured for the same sample. In another study at 694 nm at 20 ps and 23 ns, Bliss, et al. [19], measured the thresholds (J/cm^2) of ZrO_2/SiO_2 reflectors to increase as $\tau^{1/3}$ to $\tau^{1/2}$. In their tests, a spark was visible on most shots causing detectable damage.

From the above and other observations, one may conclude that the energy-density damage threshold of coatings generally increases with pulsewidth at a rate less than or equal to $\tau^{1/2}$. For the ZrO_2 coating tested in this series at 355 nm, a much weaker dependence was measured.

5. Summary

The damage thresholds of a variety of single-layer coatings and multilayer reflectors were measured at 266 nm and 355 nm using 22- and 27-ns pulses, respectively. The coating materials included NaF, cryolite, MgF_2, SiO_2, LaF_3, Al_2O_3, ThO_2, HfO_2, Y_2O_3, ZrO_2 and PbF_2. The principal findings of this study were:

a. Reflectors comprised of Al_2O_3 and NaF layers had the highest thresholds (3.6 J/cm^2 at 266 nm and 12 J/cm^2 at 355 nm). In a fluorine-gas environment a LaF_3/NaF multilayer would be suggested.

b. The single-layer coating with the highest threshold was NaF (11 J/cm^2 or 0.37 MV/cm at 266 nm and 38 J/cm^2 or 0.65 MV/cm at 355 nm), although the coating was fogged by exposure to a humid atmosphere.

c. The electric-field thresholds at the SW maxima in a ThO_2 single layer and in a ThO_2/SiO_2 reflector were equal. A correlation of peak fields for similar Al_2O_3 coatings was not observed, presumably because the coatings had unequal linear absorption or because of the differing thermal diffusivities of the adjacent materials.

d. The electric-field threshold (internal peak value) is related to the atomic density N and the refractive index in the form $N/(n^2-1)$. At 266 nm the relationship was $E_t \sim 0.54\ N/(n^2-1)$.

e. Two-photon absorption was not an important damage mechanism for 20-ns pulse damage at 266 and 355 nm for coatings of ZrO_2, Al_2O_3 and SiO_2. (For 20-ps pulses, however, TPA is substantial in ZrO_2 at 355 nm.) For the other coating materials, measurements of TPA coefficients are required before conclusions are possible.

f. Linear absorption was responsible for damage of ZrO_2 at 266 nm; failure at 355 nm may have occurred at sites of absorbing inclusions. Damage of HfO_2, ThO_2, Y_2O_3 and Al_2O_3 was probably caused by the same mechanisms, although the available evidence was insufficient.

g. A wavelength scaling relationship of $E_t(MV/cm) \sim \lambda^2$ was discovered for several coatings between 266 and 355 nm. Though not derivable from basic theory, it can be useful for estimating relative thresholds in this restricted spectral range.

h. Increased damage resistance at longer pulsewidths was measured at 355 nm for a ZrO_2 coating. From data points at 20 ps and 27 ns, a threshold relationship of $\mathcal{E}(J/cm^2) \sim \tau^{1/6}$ was apparent. This is a much more gradual pulsewidth dependence than $\tau^{1/2}$, which has been observed for uncontaminated laser window materials.

6. Acknowledgements

The authors gratefully acknowledge the technical assistance of John Meier in conducting the damage tests. The following persons and companies supplied thin-film coatings that were used in the tests and provided technical information about the coatings: Joe Latore, Lambda/Airtron; Verne Costich, Design Optics; Alex Shimkunas, Optical Coating Laboratory, Inc.; Jim Larin, Laser Optics; Manfred Grindel, Continental Optical; John Hartmann, Battelle Pacific Northwest; and Philip Baumeister, University of Rochester. The substrates were polished by Laser Optics.

7. References

[1]. Sparks, M., Sen, P.N., Flannery, M., and Loh, Jr., E., Theoretical Studies of High-Power Ultraviolet and Infrared Materials, Final Tech. Report, Contract DAHC15-73-C-0127, p. 225, March 31, 1978.

[2]. Kuckertz, T. H. and Gill, D. H., Proceedings of Eleventh Hawaii Int'l. Conf. on System Sciences, p. 162 (1978).

[3]. Newnam, B. E., and Gill, D. H., NBS Spec. Pub. 462, 292 (1976).

[4]. Apfel, J. H., Matteucci, J. S., Newnam, B. E. and Gill, D. H., NBS Spec. Pub. 462,301 (1976).

[5]. Newnam, B. E., "Laser Induced Damage Phenomena in Dielectric Films, Solids, and Inorganic Liquids," Ph.D. dissertation No. 73-09, 317, University Microfilm, Ann Arbor, Mich.

[6]. Moses, A. J., Handbook of Electronic Materials, Vol. 1: Optical Materials Properties, (IFI/Plenum, New York, 1971), pp. 68,82.

[7]. Liu, P., Smith, W. L., Lotem, H., Bechtel, J. H., Bloembergen, N., and Adhav, R. S., NBS Spec. Pub. 509, 489 (1977).

[8]. Picard, R. H., Milam, D., Bradbury, R. A., and Fan, J. C. C., NBS Spec. Pub. 435, 272 (1976).

[9]. Costich, Verne R., Design Optics, private communication.

[10]. Seitz, F., The Modern Theory of Solids, (McGraw-Hill, New York, 1940), p. 634.

[11]. Turner, A. F., NBS Spec. Pub. 356, 119 (1971).

[12]. Newnam, B. E., and DeShazer, L. G., NBS Spec. Pub. 372,123 (1972).

[13]. Newnam, B. E., and Gill, D. H., NBS Spec. Pub. 435, 254 (1976).

[14]. Bettis, J. R., House, R. A., Guenther, A. H., and Austin, R., NBS Spec. Pub. 435, 289 (1976).

[15]. Smith, W. L., Milam, D., Weber, M. J., Guenther, A. H., Bettis, J. R., and House, R. A., NBS Spec. Pub. 509, 244 (1977).

[16]. Ritter, E., App. Opt. 15, 2318 (1976).

[17]. House, R. A., Bettis, J. R., Guenther, A. H., and Austin, R., NBS Spec. Pub. 435, 305 (1975).

[18]. Bettis, J. R., House, R. A., Guenther, A. H., NBS Spec. Pub. 462, 338 (1976).

[19]. Bliss, E. S., and Milam, D.,NBS Spec. Pub. 372, 108 (1972).

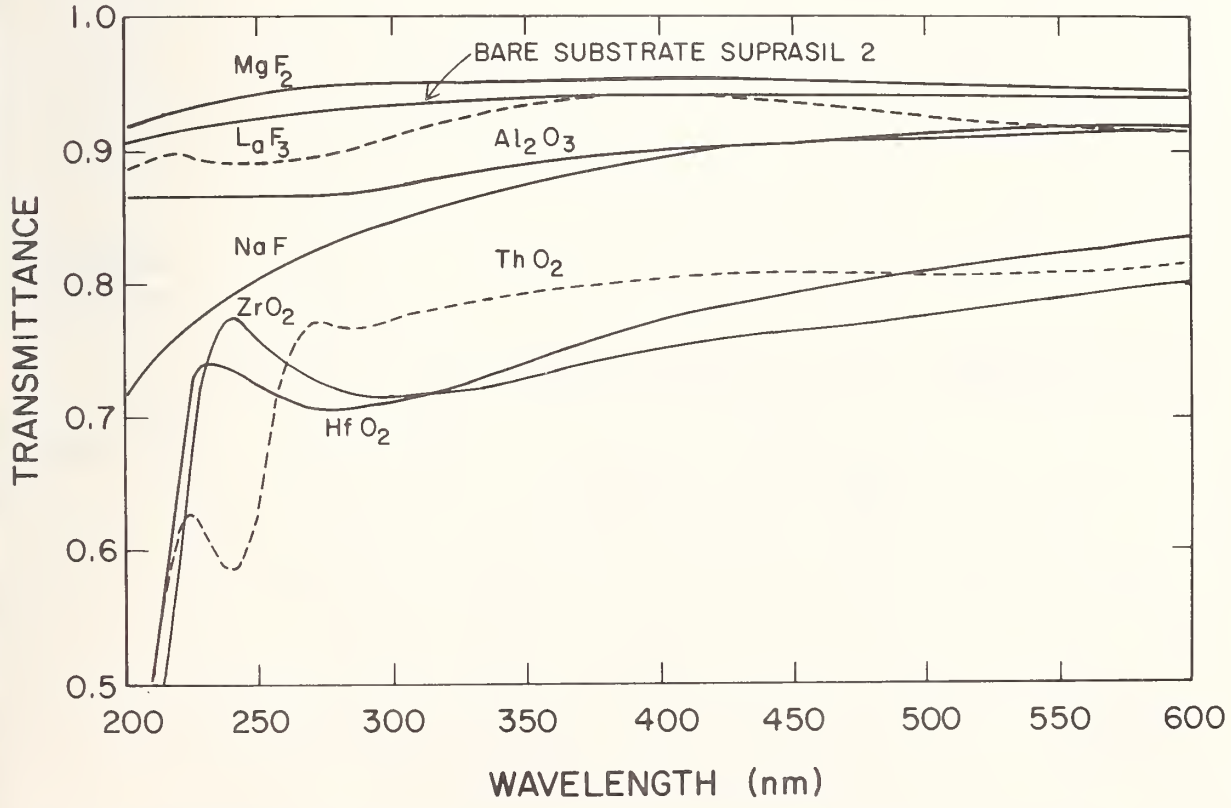

Figure 1. Spectral transmittance for single QW coatings used in laser damage tests.

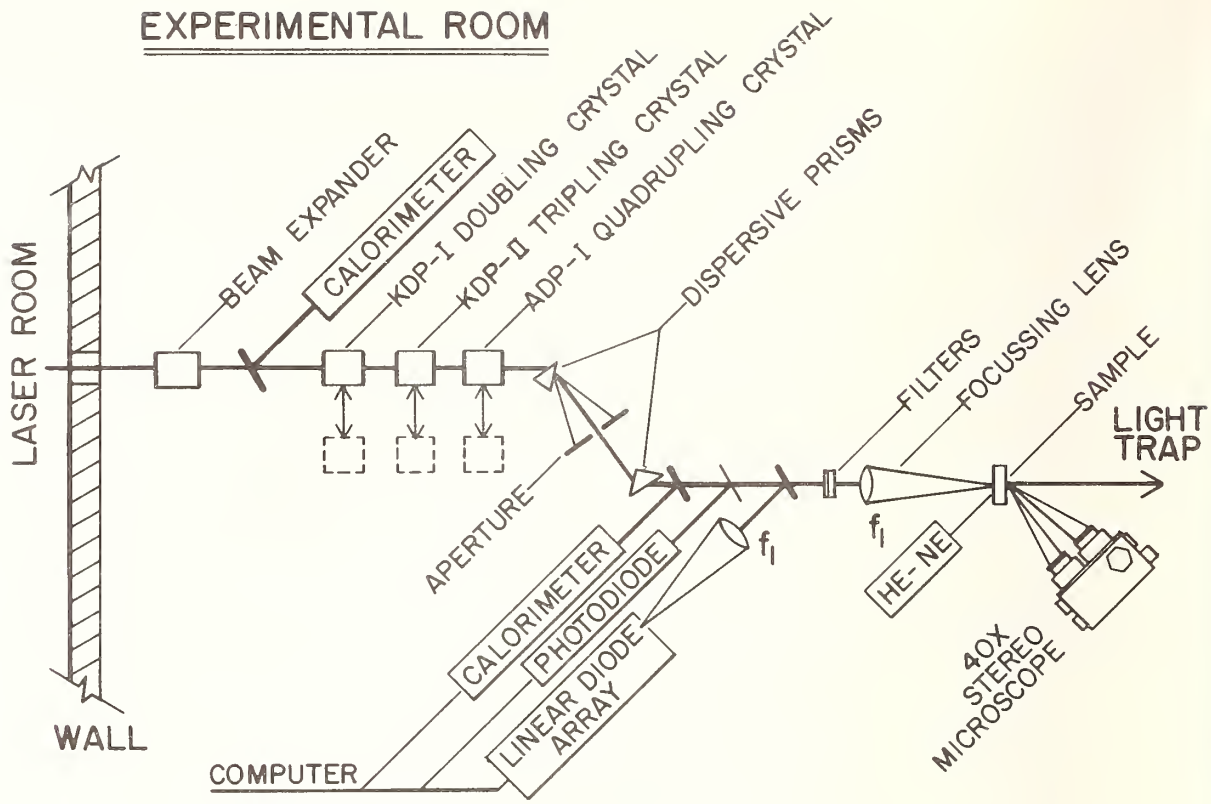

Figure 2. Experimental arrangement for performance of damage tests.

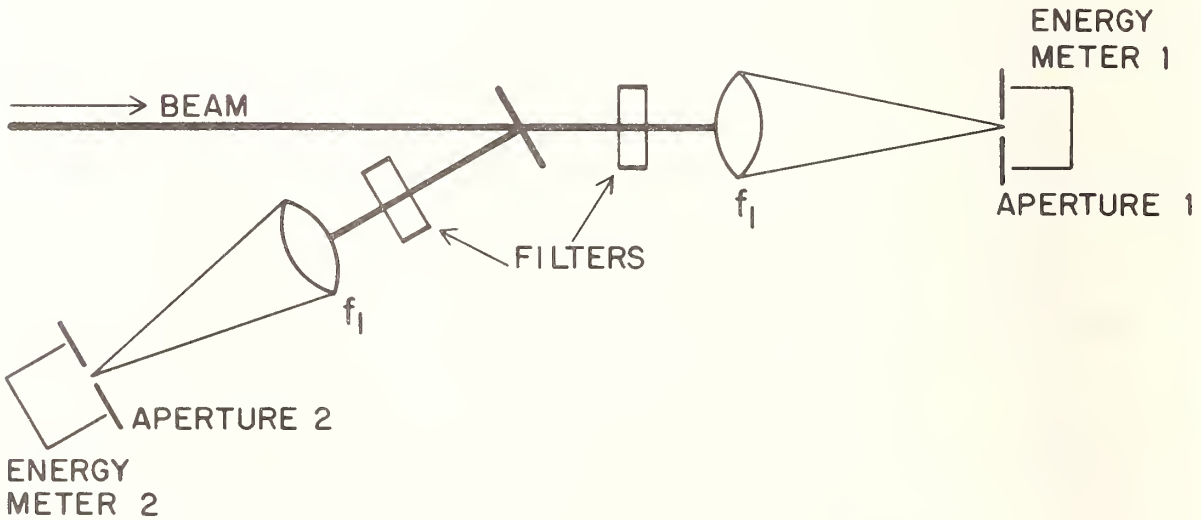

Figure 3. Experimental arrangement for calibration of axial energy density.

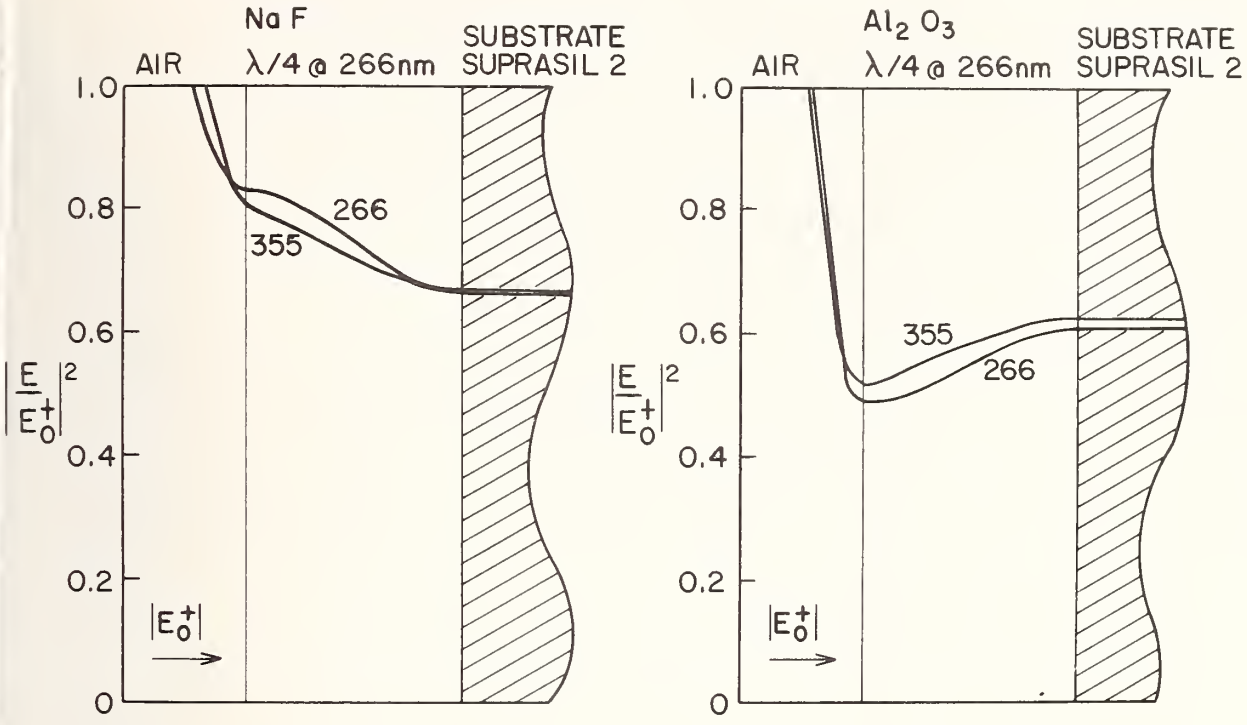

Figure 4. Distribution of standing-wave electric-field-squared in two single QW films, irradiated at 266 and 355 nm.

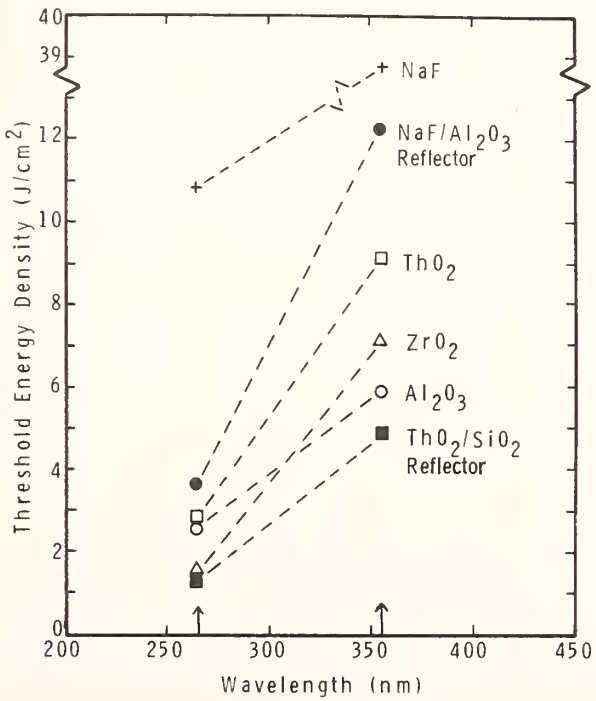

Figure 5. Spectral dependence of energy-density threshold for damage of coating materials and reflectors. Pulsewidths were 22 ns and 27 ns for 266 nm and 355 nm, respectively.

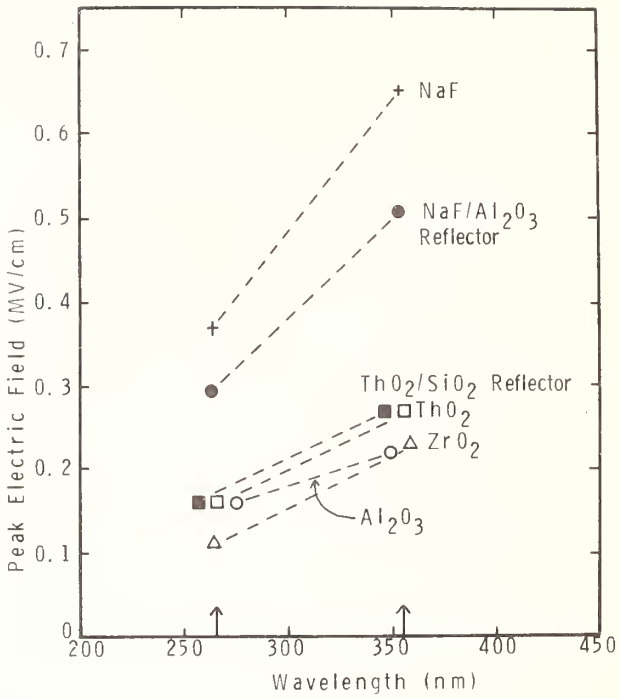

Figure 6. Spectral dependence of electric-field threshold for damage of coating materials and reflectors. Pulsewidths were same as for figure 5.

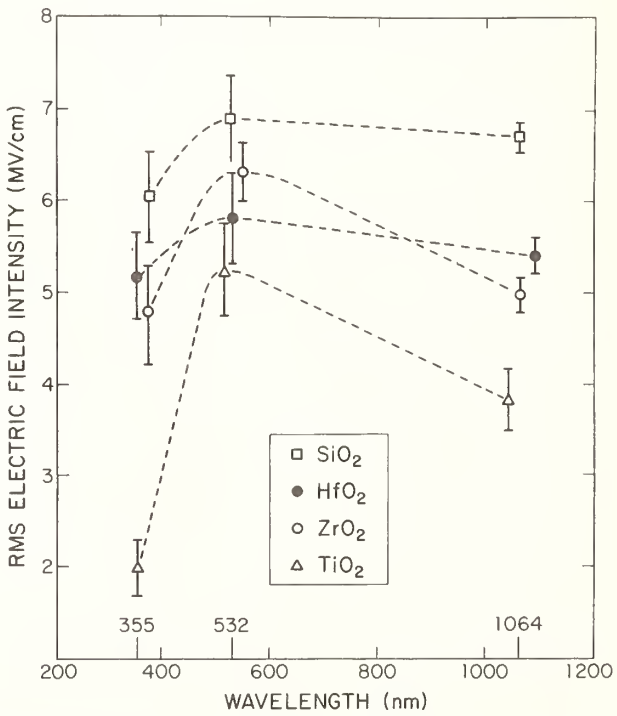

Figure 7. Spectral dependence of electric-field threshold for damage of four coating materials. Pulsewidths were 30 ps, 20 ps, and 17 ps for 1064 nm, 532 nm, and 355 nm, respectively (from Ref. 3).

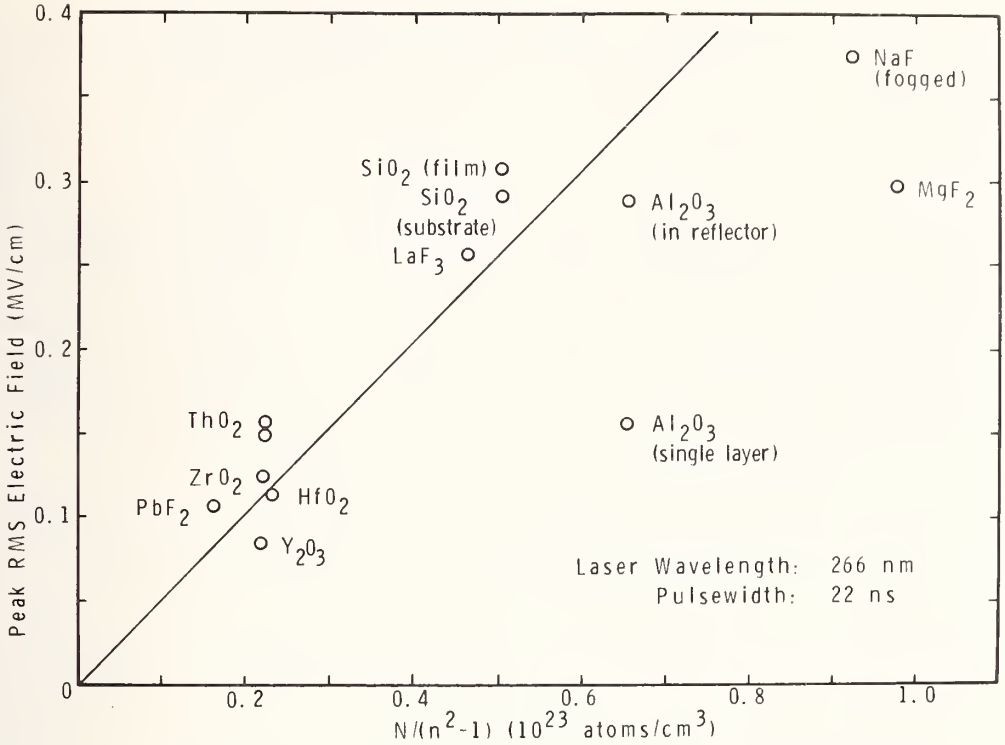

Figure 8. Electric-field threshold versus $N/(n^2-1)$ for optical coatings irradiated at 266 nm.

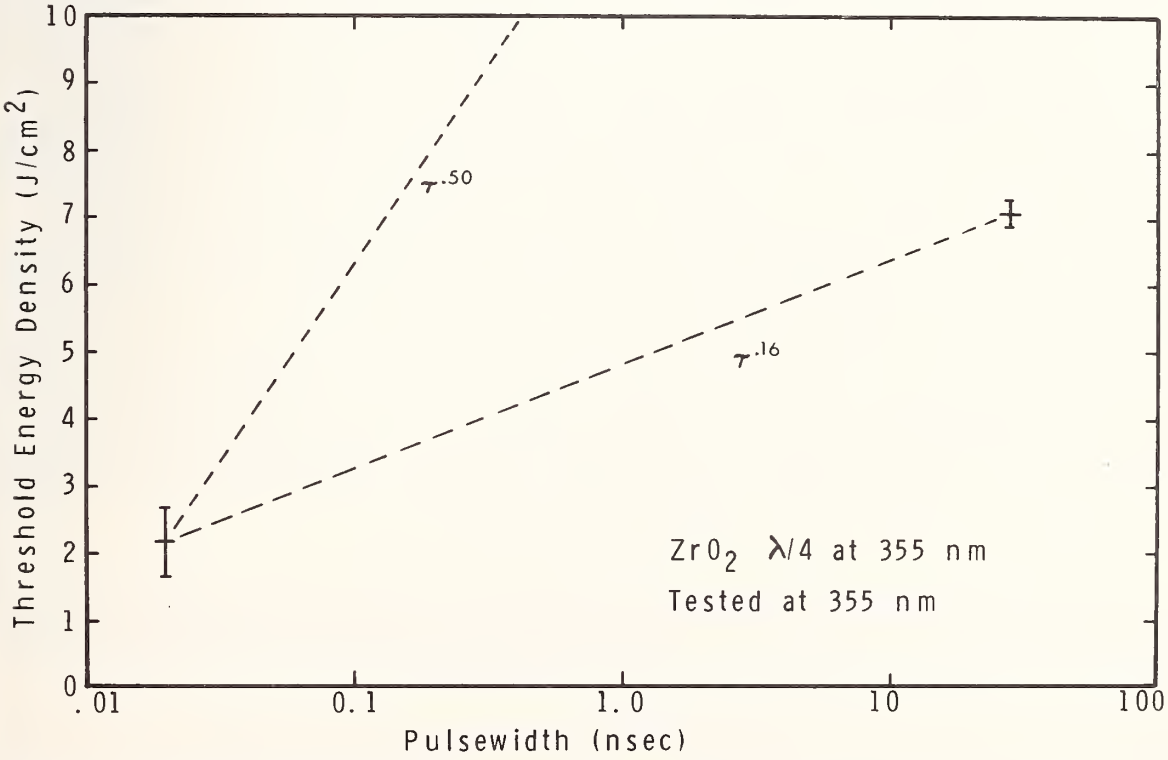

Figure 9. Pulsewidth dependence of threshold energy density for a single QW layer of ZrO_2 at 355 nm. Picosecond data from Ref. 3.

MULTITHRESHOLD EVALUATION OF 100-nsec PULSED LASER DAMAGE TO COATING MATERIALS AT 2.7- AND 3.8-μm WAVELENGTHS*

J. O. Porteus, T. M. Donovan, J. L. Jernigan, and W. N. Faith
Michelson Laboratory, Physics Division
Naval Weapons Center, China Lake, CA 93555

In this time and wavelength regime optical coatings typically fail from thermal damage. Unlike catastrophic damage resulting from dielectric breakdown, one finds disparity among the thresholds for one or more of the following damage characteristics: delamination, cracking, flow, erosion, perforation, ion emission, and light emission. Comparison of the different thresholds provides useful information on how damage proceeds, and how the absorbed energy is distributed in the coating layer. Comparison of multithreshold damage data at the two different wavelengths permits evaluation of the importance of impurities which absorb preferentially at one of the wavelengths, such as water. Comparing thresholds at the two wavelengths after N/1 conditioning provides detection of preferentially absorbing impurities which are laser-desorbed. Complementary information may be obtained from laser calorimetry. The following materials, prepared as single-layer, antireflection coatings, were evaluated: NaF, SiO_x, Al_2O_3, ZnS, As_2S_3, and Si. Samples of the first three were prepared in ultrahigh vacuum, in addition to the usual standard vacuum preparation. Thresholds are expressed in terms of the theoretical energy per unit area in the coating layer in order to permit a practical intercomparison of materials for multilayer coating design.

Key words: Absorption; antireflection coatings; damage thresholds; impurities; laser-induced damage; thermal damage.

Introduction

The pulsed damage threshold of a transparent optical coating is usually well below that of bulk specimens of the same nominal material. Since absorption coefficients are typically several orders of magnitude greater than corresponding bulk absorption coefficients, coatings are more susceptible to heating and thermal damage. As a result, the thresholds for such damage characteristics as delamination, cracking, flow, erosion, perforation, etc. of a given coating often differ, according to the physical properties of coating and substrate, and the conditions of laser irradiation. This contrasts with the catastrophic damage associated with bulk dielectric breakdown, where all characteristics typically share a common threshold. As in the case of metals which was reported last year [1][1], a study of the relative magnitude of the various thresholds for coating damage can reveal the immediate cause of failure. This in turn provides useful information for improving damage thresholds. For example, a susceptibility to thermal stress-related damage is revealed by relatively low thresholds for delamination and cracking. Similarly, spatially nonuniform damage resulting from a highly absorbing interface or an inhomogeneity in composition can be inferred from other threshold relationships, as will be demonstrated. The comparison of multithreshold results at two different wavelengths adds another dimension to the information obtained. Damage resulting from preferentially absorbing impurities, e.g., water, which has an absorption band at 2.7 μm but not at 3.8 μm, becomes evident. Volatile impurities can also be detected by comparing 1/1 with N/1 (conditioned) damage thresholds. Supporting evidence of preferentially absorbing impurities and excessive interface absorption is provided by multiwavelength laser calorimetry [2].

We have used the above methods to evaluate the damage resistance of the following materials: NaF, SiO_x, Al_2O_3, ZnS, As_2S_3, and Si, prepared as single-layer antireflection coatings on sapphire, fused silica, and CaF_2 substrates. A complete discussion of the first three materials is presented here, including inferences concerning damage-related material properties. The As_2S_3 results are more complex and are presented in detail in a separate paper at this conference [3].

Coating Samples

Samples were prepared in two different coating systems: an unbaked "standard" vacuum system and a baked "ultrahigh" vacuum system [3]. The former is pumped with a liquid N_2-trapped 6000 ℓ/sec oil diffusion pump, using an oil which was specially prepared for low backstreaming. Base pressure is

* Work supported by the Defense Advanced Research Projects Agency and Navy Independent Research funds.

1. Figures in brackets indicate the literature references at the end of this paper.

10^{-7} Torr. The second system is ion-pumped during bakeout and has a base pressure of 10^{-9} Torr. During deposition a turbomolecular pump is used and the ion pump is switched off.

Al_2O_3 coatings were electron-beam deposited from pulverized sapphire window material with the substrate at room temperature. NaF coatings were evaporated from a Mo boat containing reactively purified starting material with the substrate at 150°C. SiO_x and SiO_2 were evaporated with the substrate at room temperature, using 4-nines pure SiO in a Knudsen cell and dry oxygen admitted in varying amounts. The SiO_x films (yellow) were produced in 2×10^{-6} and 1×10^{-6} Torr O_2 in the standard and ultrahigh vacuum systems, respectively. The ultrahigh vacuum SiO_2 (clear) was produced in 10^{-4} to 10^{-5} Torr O_2. As_2S_3, ZnS, and Si were each evaporated from starting materials exceeding 4-nines in purity. All coatings were half-wavelength at 2.7 μm in thickness, except for NaF, which was one quarter-wave thick. Spectral scans revealed that the SiO_2 film, which was initially water-free, absorbed water from the atmosphere over a period of hours. Also, multiwavelength laser calorimetry revealed evidence of water in the NaF and SiO_x films [2].

Damage Measurements

Damage measurements were made in a previously described damage facility [4], which is shown schematically in figure 1. The source is a modified Lumonics TE laser [5]. This provides single-mode, multiline radiation centered at either 2.7 or 3.8 μm, depending on the use of either H_2 or D_2, in combination with SF_6, to produce HF or DF lasing. A 1.7-mm spatial filter A_1 eliminates off-axis modes. Pulse energy is controlled by a pair of ZnSe plates reflecting at the Brewster angle. The first plate rotates as a unit with Cu steering mirrors M_4-M_6, which are carefully aligned to prevent off-axis beam walking. This attenuator, when used with aperture A_2, offers the advantage over one previously described [4,5] in eliminating near-axis multiple reflections. A GaP photon drag detector is used to monitor pulse temporal characteristics. The pulse energy is monitored by a calibrated pyroelectric energy meter. The beam is focussed on target by a 12-cm-focal-length ZnSe lens.

Pinhole beam scans performed at the focal point of the lens indicate a highly Gaussian spatial profile with $1/e^2$ full widths of 32.8 μm and 47.5 μm at HF and DF wavelengths, respectively. Thresholds reported here refer to the peak energy density of the Gaussian spatial distribution in each case. The temporal pulse width is nominally 100 nsec. The ratio of peak energy density to peak power density is 126 nsec and 89 nsec at HF and DF wavelengths, respectively.

Emission of light and ions was monitored by a 20-power microscope and impedance-matched ion collector (20-mA/sr detector sensitivity), respectively, mounted in the ultrahigh vacuum test chamber. The Auger analyzer and associated electron imager were used sparingly in order to avoid electron-beam damage, to which many of these coatings are highly susceptible. Postdamage analysis was performed with Nomarski and dark-field optical microscopy at magnifications up to 900.

Multithreshold measurement and analysis procedures have been reported in detail [6]. For 1/1 data, the sample to be analyzed is exposed to one pulse at each of approximately 30 sites, spaced at 1-mm intervals along its surface. Pulse energies, which are measured for each pulse, are uniformly distributed over a range which includes the thresholds for each of the damage characteristics of interest. For N/1 data, the procedure is the same, except that the potentially damaging test pulse is preceded by N - 1 = 5 nondamaging conditioning pulses of equal or lower energy at each site. The energy of all conditioning pulses is nominally the same, and is chosen to be slightly below the 1/1 damage thresholds. The damage observed at each site issummarized by a set of code numbers, each number representing a specific damage characteristic. Damage summaries and corresponding energy densities are entered and the data are computer-reduced, using the threshold algorithm previously described [6]. The result is an average threshold for each damage characteristic, together with its standard deviation, the latter being a measure of the threshold uniformity over the surface. Results are presented in the form of a bar chart called a damage profile. Examples are given below.

A.F. and M.F. Thresholds

In order to make meaningful comparisons of performance between different coating materials, thresholds must relate to energy flow *inside* the sample coating. The total energy per unit area $\phi(x)$ inside a semi-infinite medium (one interface) is related to the energy per unit area incident at $x = 0$ by

$$\phi(x) = n \frac{\langle E^2 \rangle (x)}{\langle E_o^2 \rangle} \phi_o \quad , \tag{1}$$

where $\langle E^2 \rangle$ and $\langle E_o^2 \rangle$ are time averages of the internal and incident electric field squares, respectively, and n is the refractive index. The relationship of ϕ to the irradiance I is

$$\phi_o = \int_o^{t_p} I_o(t)dt \quad , \tag{2}$$

where the integral extends over the pulse length t_p. The absorbed energy per unit area per unit length is

$$-\frac{d\phi(x)}{dx} = \beta\phi(x) \quad , \tag{3}$$

where β is the linear absorption coefficient. Since β is much smaller than the reciprocal wavelength λ^{-1} in any material of practical interest, the attenuation due to absorption is negligible to a depth of the order of a coating thickness, and the damage threshold is expressed unambiguously in terms of $\phi(x) \simeq$ const.

In an actual coating, eq. (1) still applies, but $\langle E^2 \rangle (x)$ and $\phi(x)$ may vary strongly within the coating layer as a result of standing waves resulting from reflections at the second interface. Here the threshold should be expressed in terms of the value of $\phi(x)$ which is physically most appropriate. With a very short pulse, which permits negligible thermal equilibration before damage, ϕ_{max} corresponding to the maximum field $\langle E^2 \rangle_{max}$ in eq. (1) (M.F. threshold) is most appropriate. However, for a long pulse, where thermal damage is preceded by a considerable degree of thermal equilibration within the coating, ϕ_{av}, corresponding to the average field $\langle E^2 \rangle_{av}$ (A.F. threshold) is more appropriate. In quantitative terms the conditions of applicability to thermal damage are $\sqrt{\alpha t_p} \ll \ell$ for the M.F., and $\sqrt{\alpha t_p} \gg \ell$ for the A.F. threshold, where α is the thermal diffusivity and ℓ is the coating thickness. Unfortunately, under present experimental conditions, $\sqrt{\alpha t_p} \sim \ell$, so that neither condition is satisfied. We adopt the A.F. threshold arbitrarily since it leads to more conservative damage thresholds.

Field distributions for applying eq. (1) were computed using a program due to Baumeister [7]. Examples are given in figures 2-4. Conversion factors obtained from such distributions are given in table 1. Only the conversion factors in the first two columns were used to calculate the A.F. thresholds presented in this paper. The second two columns provide the information required to convert to M.F. thresholds.

Table 1. Conversion factors from incident to internal energy/area.

Coating/Substrate	ϕ_{av}/ϕ_o HF	ϕ_{av}/ϕ_o DF	ϕ_{max}/ϕ_o HF	ϕ_{max}/ϕ_o DF
NaF/sapphire	1.026	0.932	1.288	1.192
SiO_x/quartz	0.956	0.932	1.025	1.013
Al_2O_3/quartz	0.974	0.903	1.127	1.082
ZnS/CaF_2	1.053	0.762	1.544	1.254
As_2S_3/CaF_2	1.073	0.742	1.639	1.274
Si/sapphire	0.638	1.273	0.950	2.086

Damage Characteristics

Damage is classified into two general categories, *uniform* or *selective*. The former refers to damage whose spatial distribution is determined strictly by that of the laser intensity, and not by spatial nonuniformities of the coating. The latter category refers to damage spatially "selected" by defects or inhomogeneities in the coating. Specific damage characteristics may fall in either category.

Examples of the characteristics of uniform damage for which thresholds are reported are shown in figure 5. At the damage site on ZnS/CaF_2, massive delamination and cracking of the film has occurred in the outermost damage zone. Sharp regularly spaced interference fringes can be seen here under visual observation. Inside of this zone the substrate is exposed, indicating film perforation. The innermost dark circle represents substrate damage, which is excluded from present considerations. Drop-like formations on the inner edges of the delaminated film are indicative of flow. The damage site on the SiO_x coating shows thickness nonuniformities in the outermost damage zone. Since the surface is not roughened, we infer that flow rather than erosion has occurred. Although interference fringes are apparent, they do not have the sharp, regular character associated with delamination. Between this zone and the dark inner zone of perforation lies a zone of roughening and thinning which exemplifies erosion.

The SiO_x damage site of figure 5 also illustrates selective damage. Just outside the zone of erosion, particularly at the lower left and to the right of center, lie a few isolated damage areas with dimensions ~ 3 μm. Because of the smooth spatial profile of the laser beam, these can be attributed to localized weakness of the coating rather than to intensity "hot spots." No subclassification of selective damage into specific damage characteristics will be made here.

In addition to the characteristics of permanent damage morphology just described, thresholds for the transient characteristics, ion and light emission, are also reported. Because of inadequate spatial resolution of the damage-chamber microscope and ion collector, it is difficult or impossible to categorize these characteristics definitely as either uniform or selective when both categories of permanent damage are present.

Except for delamination and perforation, analogous damage characteristics are observed on bare substrate surfaces. Also, an electron image of the damage site can be obtained on those materials not subject to damage by the 8 keV electron probe beam. The contrast for electron imaging is provided by spatial variations in work function, which is governed by surface composition and topography.

Bare Sapphire Versus Al_2O_3 Coating Material

Thresholds for the onset of the damage characteristics are displayed for comparison in the form of damage-profile bar charts, as previously described. An HF damage profile of a polished bare sapphire surface is shown in figure 6. The equivalence of the thresholds is characteristic of dielectric breakdown, where catastrophic failure is precipitated by the electric field, with no significant thermal damage at lower levels of intensity.

Comparing the damage profile of an Al_2O_3 coating (fig. 7(a)) with figure 6 shows considerably reduced thresholds overall. Also, we find that the threshold for delamination, and possibly for cracking, are smaller than for the remaining damage characteristics. The disparity in this example is evidently related to stress due to differential expansion, compounded by differential heating. It follows from eqs. (1,3) that differential heating can result from differences in both absorption coefficient and refractive index between coating and substrate, although the absorption coefficient usually dominates. In the N/1 profile (fig. 7(b)) the thresholds are somewhat larger and more nearly equal than in figure 7(a). This indicates that the conditioning pulses have done one or more of the following: (1) relieved residual stress, (2) improved the mechanical bond, (3) improved the thermal bond between coating and substrate. DF results (not shown) are qualitatively similar to those shown in figures 7(a) and 7(b).

NaF Coating

From the field plot of the NaF coating (fig. 3) one would expect relatively greater heating at the vacuum-coating interface, as compared to either Al_2O_3 or SiO_x (figs. 2 and 4, respectively). We find evidence of this in the NaF damage profile shown in figure 8(a), where erosion at this interface occurs well below the thresholds for the other damage characteristics. Notice particularly that the energy required for perforation is over three times that required to produce erosion. Another contributing factor to damage, particularly at HF wavelengths, is water, whose presence in the coating has been verified by laser calorimetry [2]. At HF wavelengths one finds higher N/1 (fig. 8(b)) than 1/1 thresholds (fig. 8(a)); whereas, at DF the 1/1 and N/1 results are nearly identical (figs. 9(a,b)). We conclude that water is desorbed by the conditioning pulses, resulting in reduced absorption at HF, which lies in the water band. Percentagewise, the effect is largest for flow, which appears to be superficial, and for erosion, indicating that water is desorbed mainly from the vacuum-coating interface, as one would expect in view of the field distribution.

SiO_x and SiO_2 Coatings

Figure 10(a) shows the HF damage profile of a yellow SiO_x coating, deposited from SiO in the presence of insufficient oxygen to produce typically clear SiO_2. The flatness of the field inside the coating, shown in figure 4, predicts uniform absorption. The equivalence of the thresholds for erosion and perforation agrees with this, in contrast to the case of the NaF coating, discussed above. However, the presence of selective damage (fig. 5) indicates that the absorption is not homogeneous. Another indication of inhomogeneity is the high threshold for ion, as compared to light emission. Light from a plasma formed at an absorbing inclusion is transmitted by the transparent matrix, but the ions are occluded unless the matrix has been sufficiently dispersed, which generally requires more energy.[2]

---

2. An alternative explanation of the observed difference in emission thresholds is plasma formation at the substrate interface as a result of abnormally high interface absorption. Results of 2.7-μm laser calorimetry show relatively little absorption at this interface on a similar sample. Also, the absence of delamination (blistering) supports the interpretation given in the text.

The cooler matrix may also inhibit flow initiated by inclusion heating, an effect which probably explains the relatively high flow threshold. One result, therefore, is that the SiO_x is of inhomogeneous composition extending through the coating.

The DF profile for SiO_x (fig. 10(b)) is strikingly different, showing equivalently high thresholds for all characteristics, including selective damage. This provides a second result; namely, that SiO_x contains material with an absorption band at HF, probably water. SiO_2 coating material, which is discussed below, has a strong affinity for water, as verified by time-lapsed spectral scans made immediately after removal from the coating chamber. This, together with the above evidence, strongly suggests that the SiO_x coating is actually an inhomogeneous mixture of various silicon oxides, including SiO_2. The selective HF damage is believed to be a result of high absorption in small SiO_2-rich regions, which are also rich in water.

Surprisingly, N/1 thresholds for SiO_x at HF and DF are only slightly higher than 1/1 thresholds at both wavelengths, with little evidence for the water desorption effect observed in NaF. The explanation for this may lie in the difference in film structure as determined by transmission electron microscopy. The NaF has an open structure consisting of an aggregate of NaF crystallites, while SiO_x is amorphous with no apparent porosity.

The damage profile of a clear SiO_2 coating is shown in figure 11. The deposition was performed in a baked system using dry oxygen in an effort to minimize water content. In spite of this precaution, however, the coating had incorporated a considerable amount of atmospheric water before the damage experiment. The coating showed no selective damage or other evidence of inhomogeneity. The predominant failure mode was a swelling of the film, classified as flow, followed at slightly higher energy by delamination, erosion, and perforation. The equal thresholds for the last two characteristics indicate that the water is incorporated throughout the coating, rather than being confined to a surface layer. DF thresholds are almost an order of magnitude higher than at HF, except for ion and light emission which are essentially unchanged. Results are consistent with the conclusion that water-rich SiO_2 is incorporated in the SiO_x film.

Standard Versus Ultrahigh Vacuum

To demonstrate that the different vacuum system was not in some way responsible for the differences between the SiO_2 and SiO_x films we prepared a yellow SiO_x film in the baked system also. The damage profile for this film, which is shown in figure 12, is nearly identical to that of the film prepared in standard vacuum (fig. 10(a)), except for slightly lower thresholds overall. This result is typical of similar comparisons made for the Al_2O_3 and NaF coatings. We conclude that films produced in clean, fast-pumped standard vacuum are at least as damage resistant as those produced in a baked system.

Intercomparison of Materials

A comparison of the damage resistance of the various coating materials is shown in figure 13 in terms of the damage characteristic with the lowest threshold in each case. For the materials discussed above, this characteristic can be identified from the damage profiles. The dominating damage characteristic for As_2S_3/CaF_2 is selective damage in the form of delamination at random defects [3]. ZnS/CaF_2 failed primarily as a result of cracking, apparently due to stress, and secondarily, as a result of selective damage at isolated defects. Si/sapphire perforated, apparently as a result of melting and vaporization. As would be expected, materials with higher refractive index tend to have lower damage thresholds. Of the materials evaluated NaF and Al_2O_3 are outstanding performers. SiO_x can also be very damage resistant outside of the water absorption band.

Summary

It has been demonstrated that multithreshold evaluation of optical coating damage at two wavelengths can provide insight regarding properties related to laser damage and other aspects of coating performance. A disparity in the thresholds for the various observable damage characteristics permits a distinction between dielectric breakdown and thermal damage resulting from excessive absorption. Relatively low thresholds for delamination and cracking are indicative of thermal stress and/or adherence failure, which may result from high absorption at the coating-substrate interface. The relationship between thresholds for erosion and perforation indicates the importance of absorption at the vacuum-coating interface. Absorption inhomogeneity, which cannot be ascertained from calorimetric studies, becomes apparent from a disparity in the thresholds for ion and light emission. Comparison of thresholds at different wavelengths is helpful in detecting impurities which display absorption bands, such as water. Comparison of 1/1 and N/1 thresholds at different wavelengths can be used to determine the presence of desorbable impurities. The combined information from these studies can be used to evaluate and improve coating materials. Of the materials evaluated here NaF and Al_2O_3 appear to be the most promising for

damage resistance at 2.7 and 3.8 μm. SiO_x also shows promise at 3.8 μm. The performance of NaF and SiO_2 coatings could be significantly improved at 2.7 μm by eliminating water content. Al_2O_3 coatings can be improved by minimizing residual stress at the substrate interface.

Acknowledgments

The authors are grateful to Dennis K. Burge for figures 2-4, and to Marshall Sparks for contributing to the discussion of threshold definitions. Helpful comments from David Milam and Brian Newnam are also acknowledged.

References

[1] Porteus, J. O., Fountain, C. W., Jernigan, J. L., Faith, W. N., and Bennett, H. E., "Pulsed-Laser Stress Phenomena on Highly Reflecting Metal and Alloy Surfaces," in *Laser Induced Damage in Optical Materials: 1977*, A. J. Glass and A. H. Guenther, eds. Washington, D.C., National Bureau of Standards, 1977 (NBS Spec. Publ. 509), p. 204.

[2] Temple, P. A., Decker, D. L., and Donovan, T. M., "Measured Thin Film Absorption at the Air-Film Interface, the Film Bulk, and the Film-Substrate Interface," this conference.

[3] Donovan, T. M., Porteus, J. O., Jernigan, J. L., and Ashley, E. J., "Multithreshold Damage Measurements on As_2S_3, As_2Se_3, and NaF at HF and DF Wavelengths," this conference.

[4] Porteus, J. O., Soileau, M. J., Bennett, H. E., and Bass, M., "Laser Damage Measurements at CO_2 and DF Wavelengths," in *Laser Induced Damage in Optical Materials: 1975*, A. J. Glass and A. H. Guenther, eds. Washington, D.C., National Bureau of Standards, 1975 (NBS Spec. Publ. 435), p. 207.

[5] Van Stryland, E. W., Bass, M., Soileau, M. J., and Tang, C. C., "Pulsed HF/DF Laser Damage in Window Materials," in *Laser Induced Damage in Optical Materials: 1977*, A. J. Glass and A. H. Guenther, eds. Washington, D.C., National Bureau of Standards, 1977 (NBS Spec. Publ. 509), p. 118.

[6] Porteus, J. O., Jernigan, J. L., and Faith, W. N., "Multithreshold Measurement and Analysis of Pulsed Laser Damage on Optical Surfaces," *op. cit.*, p. 507.

[7] Baumeister, P. W., private communication.

Figures

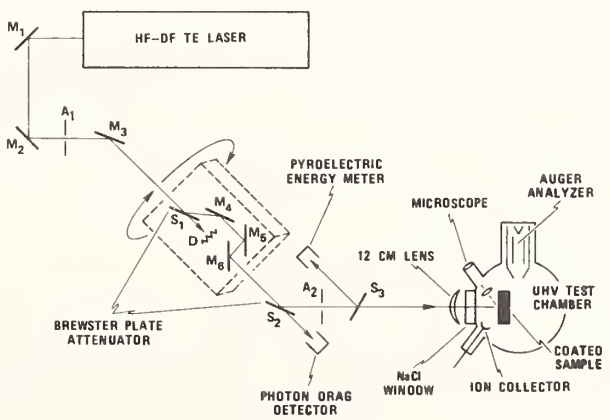

Figure 1. Layout of laser damage facility. M_1-M_6 are beam-turning mirrors, A_1 and A_2 are apertures, S_1-S_3 are beam splitters, and D is a beam dump. The function of the attenuator, which incorporates S_1, S_2, M_4-M_6, A_2, and D, is described in the text.

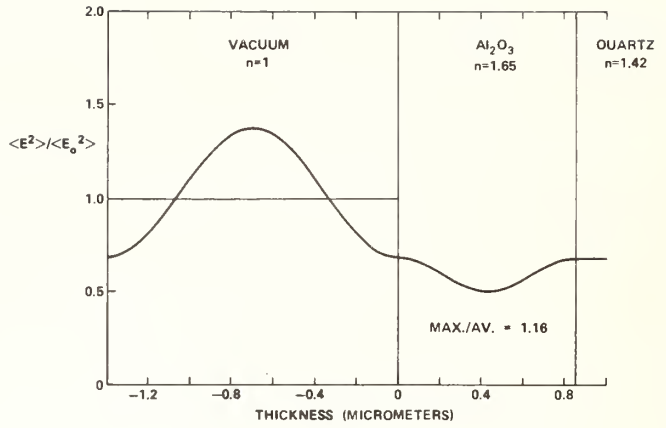

Figure 2. Field plot of $A\ell_2O_3$ coating ($\lambda/2$ at 2.7 μm) on quartz at HF wavelength. The plot at DF wavelength is similar with max/av = 1.20.

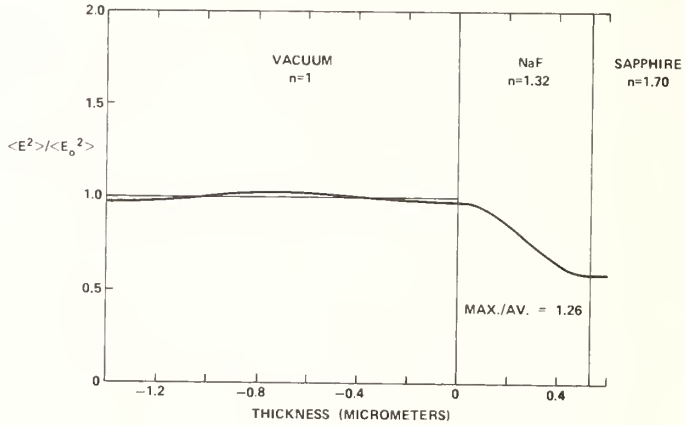

Figure 3. Field plot for NaF coating ($\lambda/4$ at 2.7 μm) on sapphire at HF wavelength. The plot at DF wavelength is similar with max/av = 1.28.

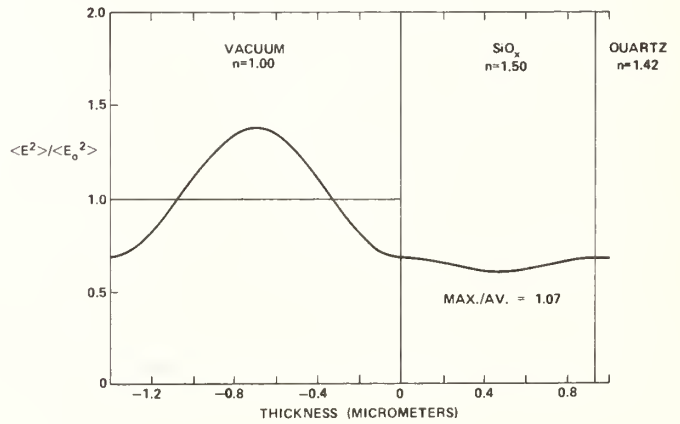

Figure 4. Field plot for SiO_x coating ($\lambda/2$ at 2.7 μm) on quartz at HF wavelength. The plot at DF wavelength is similar with max/av = 1.09.

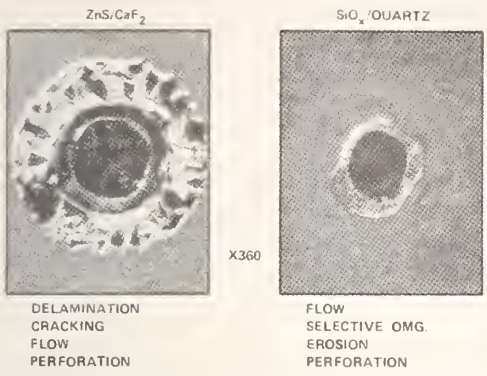

Figure 5. Typical coating damage characteristics observed with Nomarski microscopy. The energies were well above threshold for all illustrated characteristics in each case.

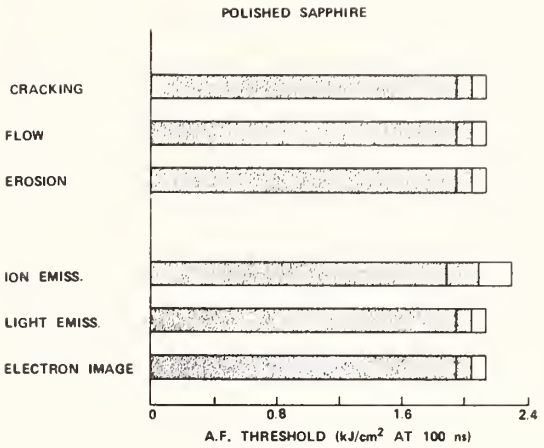

Figure 6. Damage profile of bare sapphire surface: 1/1 at HF wavelength.

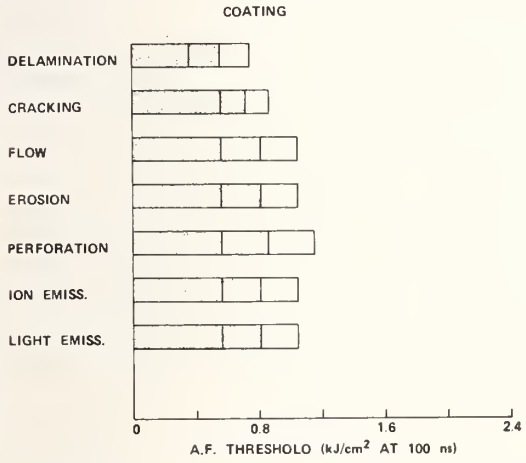

Figure 7(a). Damage profile of $A\ell_2O_3$ coating ($\lambda/2$ at 2.7 μm) prepared in standard vacuum on fused quartz: 1/1 at HF wavelength.

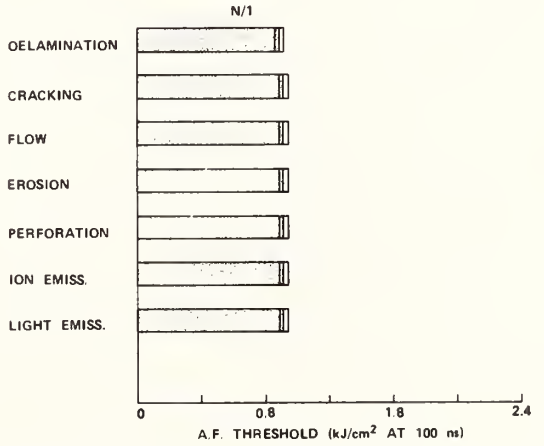

Figure 7(b). N/1 damage profile corresponding to figure (7a).

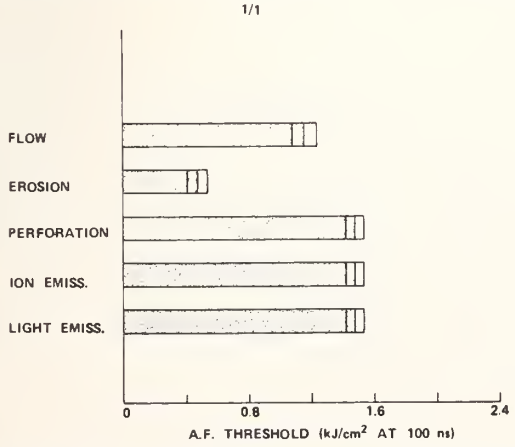

Figure 8(a). Damage profile of NaF coating ($\lambda/4$ at 2.7 μm) prepared in standard vacuum on fused quartz: 1/1 at HF wavelength.

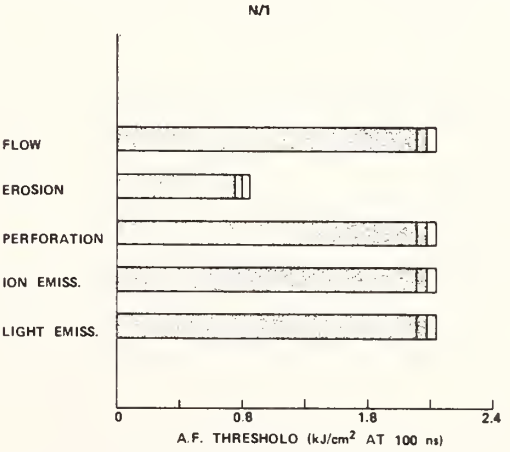

Figure 8(b). N/1 damage profile corresponding to figure 8(a).

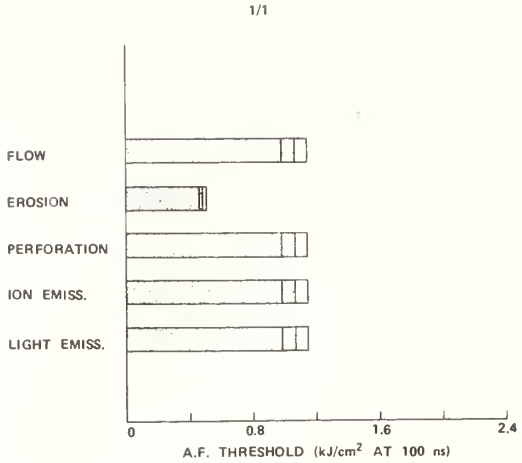

Figure 9(a). Damage profile of NaF coating (λ/4 at 2.7 μm) prepared in standard vacuum on fused quartz: 1/1 at DF wavelength.

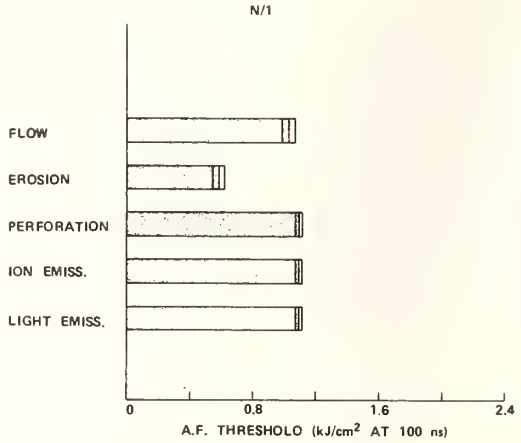

Figure 9(b). N/1 damage profile corresponding to figure 9(a).

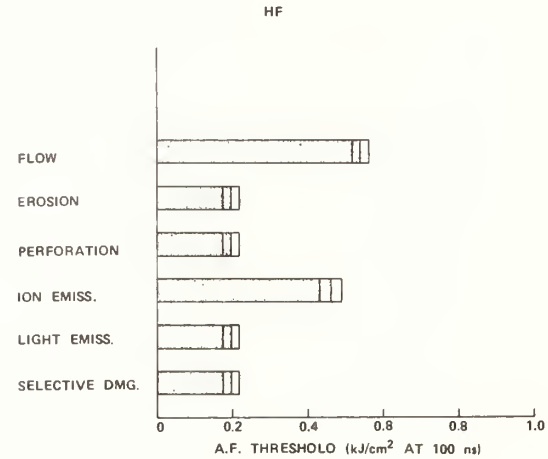

Figure 10(a). Damage profile of SiO_x, $x \leq 2$, coating (λ/2 at 2.7 μm) prepared on fused quartz in standard vacuum: 1/1 at HF wavelength.

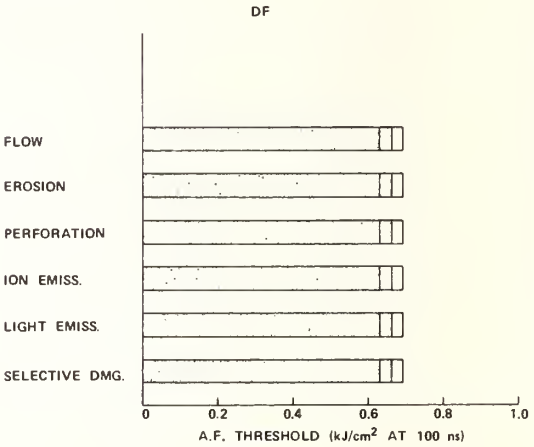

Figure 10(b). DF damage profile corresponding to figure 10(a).

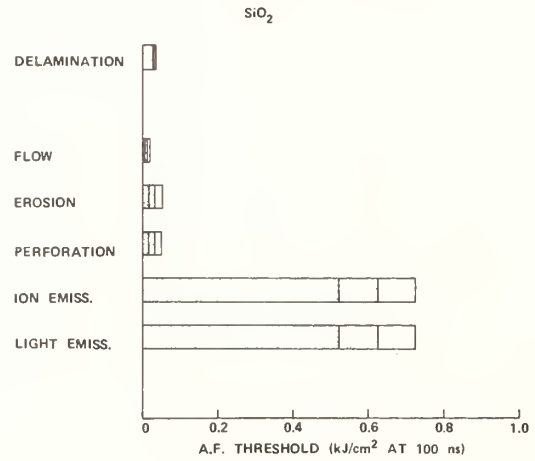

Figure 11. Damage profile of SiO_2 coating (λ/2 at 2.7 μm) prepared on fused quartz in a baked vacuum system: 1/1 at HF wavelength.

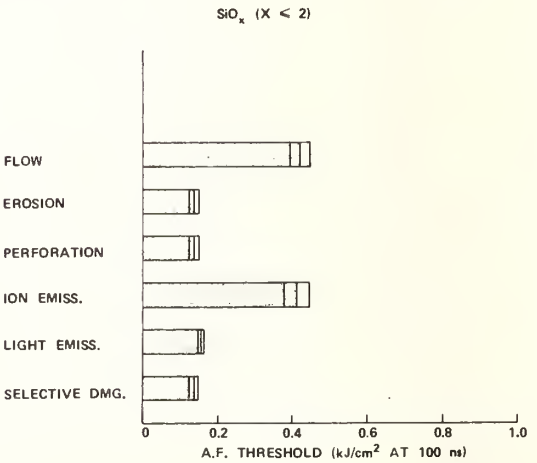

Figure 12. Damage profile of SiO_x, $x \leq 2$, coating (λ/2 at 2/7 μm) prepared on fused quartz in a baked vacuum system: 1/1 at HF wavelength.

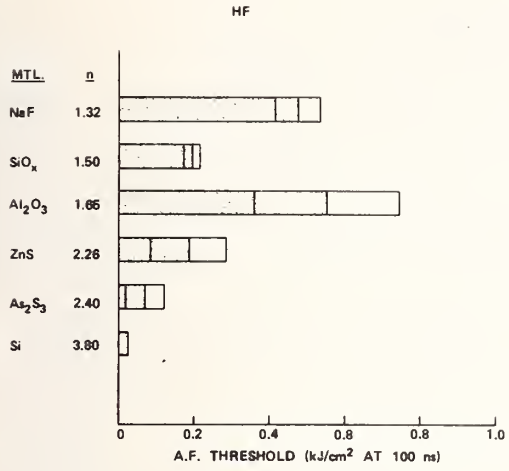

Figure 13(a). Comparison of thresholds for all materials evaluated in terms of damage characteristic with the lowest threshold in each case: 1/1 at HF wavelength. Nominal values of the refractive index n are given for the coating material in each case.

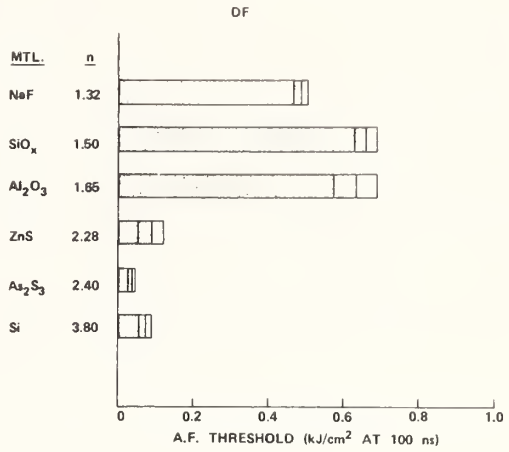

Figure 13(b). Threshold comparison corresponding to figure 13(a) at DF wavelength.

MULTITHRESHOLD DAMAGE MEASUREMENTS ON As_2S_3, As_2Se_3, AND NaF AT HF AND DF WAVELENGTHS*

T. M. Donovan, J. O. Porteus, J. L. Jernigan, and E. J. Ashley
Michelson Laboratory, Physics Division
Naval Weapons Center, China Lake, CA 93555

We previously reported on the deposition, absorption, and CO_2-laser damage threshold for As_2S_3, As_2Se_3, and NaF coatings. It was shown that the damage threshold was much lower for coated than uncoated substrates and that the mechanism for damage was different in the coatings than in the substrates. We speculated that the damage in the coatings was related to the presence of micron-sized crystalline defects distributed in the amorphous chalcogenide matrix. In this paper we report the results of damage measurements on these materials at 2.8 and 3.8 μm and identify two operating damage processes: "uniform" damage, which we associate with the amorphous chalcogenide matrix, and "selective" damage, which we associate with the crystalline defects. For single-layer films, we find that N/1 conditioning generally produces an increase in the damage thresholds. The wavelength dependence of multithreshold results in single-layer coatings of As_2S_3 and NaF suggests that improvement in threshold results from the thermal desorption of contaminating layers of water at 2.7 μm. However, for a dielectrically enhanced reflector containing quarter-wave layers of As_2Se_3 and NaF, N/1 conditioning promoted crystallite growth which resulted in a definite deterioration of N/1 thresholds.

Key words: Absorption; arsenic selenide; arsenic trisulfide; defects; laser damage; sodium fluoride.

Introduction

As_2S_3 and As_2Se_3 films have been evaluated [1][1] for use in three-layer antireflection designs at 10.6 μm. Recent [2] absorption measurements at 2.8 and 3.8 μm indicate that these materials should perform optically well in this wavelength region also. However, relatively low pulsed damage thresholds were observed in these materials and we speculated that the damage was associated with micron-sized crystalline defects imbedded in the amorphous matrix of these films. We have completed preliminary multithreshold damage measurements at HF and DF wavelengths and report observations on possible damage mechanisms.

We observe selective damage on single-layer films which we associate with the crystalline defects. N/1 conditioning with pulses below threshold for actual damage results in an improvement in thresholds for both selective and uniform damage processes, both at HF and DF wavelengths. The improvement appears to be associated with the desorption of surface contamination. Finally, we have fabricated a dielectrically enhanced reflectance multilayer on polished Mo mirrors using As_2Se_3 and NaF as the high and low index layers, respectively. The damage threshold was two times that of a Au-coated, diamond-turned Cu mirror. N/1 conditioning, in this case, leads to defect formation and degradation of the coating resulting in a significant reduction in damage threshold.

Multithreshold Measurements

The details of the multithreshold analysis technique have been described by Porteus [3] and the results of measurements at 2.8 and 3.8 μm on a number of coating materials including NaF are reported [4] elsewhere in this conference. The results of comparing first visible damage on six different materials from the study [4] are shown in figure 1. It is seen that As_2S_3 first damages at an effective fluence of about 50 J/cm^2 while NaF, with a much higher (30X) absorption, damages at about 400 J/cm^2, indicating that absorption alone does not determine the optimum damage resistance.

As further background, figure 2 shows electron micrographs of As_2S_3 and As_2Se_3 films revealing the size and morphology of typical crystalline defects found in these films. The formation, morphology, numbers, and chemical analysis of these defects are described in reference 1.

---

* Work supported by the Defense Advanced Research Projects Agency and Navy Independent Research funds.

1. Figures in brackets indicate the literature references at the end of this paper.

Selective and Uniform Damage

The initial or first observed damage to As_2S_3 films typically occurs in off-axis regions of smaller dimension than the beam diameter; this we refer to as selective damage, or damage which is spatially selected by defects or inhomogeneities in the coating. Figure 3 shows damage resulting from a pulsed CO_2 beam. There is delamination of the film around the damage site and perforation of the film. Figure 4 shows multiple damage sites, interference or ripple patterns, associated with enhanced fields resulting from interference between the incident and scattered beams at a defect [5], and "scrubbing", where the region of the film in the beam is swept free of crystalline defects, which are shown here as small bright spots. This damage we associate with the presence of the type of micron-sized crystalline defect shown in figure 2.

Uniform damage, which includes erosion as well as ion and light emission, occurs uniformly over the area of the incident beam. The spatial distribution is determined then by laser intensity and not by specific inhomogeneities in the film, as in selective damage.

Comparison of HF/DF Damage Thresholds

Selective damage occurs in As_2S_3 at about one half the energy of uniform damage. This is shown in figure 5(a) where the damage for selective processes is compared with uniform processes including erosion, perforation, ion, and light emission. At DF wavelengths [fig. 5(b)] the thresholds are reduced by about a factor of two, except for the threshold for perforation which is reduced slightly. This is different behavior than for films such as SiO_x which contain H_2O impurity [4]. In this case, the thresholds increase on-going from 2.8 to 3.8 μm, as H_2O absorbs strongly at HF (2.8 μm). As_2S_3 and As_2Se_3, on the other hand, have extremely low absorption ($\beta < 0.5\ cm^{-1}$) in the H_2O absorption band at 2.8 μm [2]. The decrease in damage threshold observed here is possibly related to the increase in spot size in going from 2.8 to 3.8 μm.

Conditioning (N/1) Behavior

Figures 6(a) and (b) show multithreshold results for HF damage, both as single-shot and after preconditioning the surface with pulses (typically N = 5, with energy just below that needed for damage) prior to the damaging pulse. It is interesting to note that uniform damage processes show significant improvement while that due to selective damage is increased only slightly. This suggests that conditioning pulses have sufficient energy to thermally remove surface contamination (observed by calorimetry [2], $^{15}N^{++}$ analysis [6], ESCA [1]) but are not effective in reducing defect sites. Defects are "scrubbed" free, as shown in figure 4, but this process occurs only when there is sufficient energy to damage. Detail of the selective damage process and N/1 behavior is shown for DF damage in figures 7(a) and (b). It is of interest to note that ripple patterns or melting is only associated with selective damage processes or crystalline defects. Within the amorphous matrix the film erodes or vaporizes.

$$(As_2Se_3/NaF)^2/Ag/Mo$$

As_2S_3 and NaF were used to fabricate an enhanced reflection design on Ag-coated Mo (R = 0.997 @ 2.8 μm). The damage measurements are compared to those of a Au-coated, diamond-turned, Cu mirror. As can be seen in figure 8(a), the thresholds are slightly greater than 300 J/cm^2 at 100 nsec incident energy and are the same for uniform damage as selective damage. The interesting point is that the threshold is two times that of an uncoated mirror [fig. 8(b)].

N/1 conditioning leads to the creation of crystalline defects and degradation of the surface resulting in "selective" damage at an energy less than damage of the Au-coated Cu mirror [figs. 9(a) and (b)]. The intense HF/DF laser radiation possibly induces local heating which results in the nucleation and growth of recrystallized regions within the coating. Possibly a more uniform and controlled heating process would result in more uniform, defect-free stable coatings.

Conclusions

Preliminary 2.8- and 3.8-μm multithreshold damage measurements have been completed on a single-layer As_2S_3 film deposited on CaF_2 and a multilayer film consisting of quarter-wave stacks of As_2Se_3 and NaF.

1. Two types of damage are observed with As_2S_3: damage that occurs within selected regions of the incident spot which we associate with the presence of micron-sized crystalline defects, and damage that occurs uniformly over the area of the spot and is associated with erosion and other processes within the amorphous matrix.

2. Multilayer films consisting of alternate layers of As_2Se_3 and NaF in an enhanced reflection design on polished Mo have a higher threshold than Au-coated, diamond-turned Cu mirrors. The As_2S_3/NaF-coated mirror degrades significantly during irradiation at energies less than threshold (N/1) at both HF and DF wavelengths. We associate this with the production of micron-sized crystalline defects during the irradiation process.

References

[1] Donovan, T. M., Baer, A. D., Dancy, J. H., and Porteus, J. O., "Defects and Impurities in As_2S_3, As_2Se_3, and NaF Coatings," in *Laser Induced Damage in Optical Materials: 1977*, ed. by A. J. Glass and A. H. Guenther. Washington, D.C., National Bureau of Standards (NBS Spec. Publ. 509), p. 342.

[2] Temple, P. A., Decker, D. L, and Donovan, T. M., "Measured Thin Film Absorption at the Air-Film Interface, the Film Bulk, and the Film-Substrate Interface," this conference.

[3] Porteus, J. O., Jernigan, J. L., and Faith, W. N., "Multithreshold Measurement and Analysis of Pulsed Laser Damage on Optical Surfaces," in *Laser Induced Damage in Optical Materials: 1977*, ed. by A. J. Glass and A. H. Guenther. Washington, D.C., National Bureau of Standards (NBS Spec. Publ. 509), p. 507.

[4] Porteus, J. O., Donovan, T. M., Jernigan, J. L., and Faith, W. N., "Multithreshold Evaluation of 175-nsec Pulsed Laser Damage to Coating Materials at 2.7- and 3.8-μm Wavelengths," this conference.

[5] Temple, P. A., and Soileau, J. M., "Resonant Defect Enhancement of the Laser Electric Field," in *Laser Induced Damage in Optical Materials: 1976*, ed. by A. J. Glass and A. H. Guenther. Washington, D.C., National Bureau of Standards (NBS Spec. Publ. 462), p. 371.

[6] Tombrello, T., private communication.

Figures

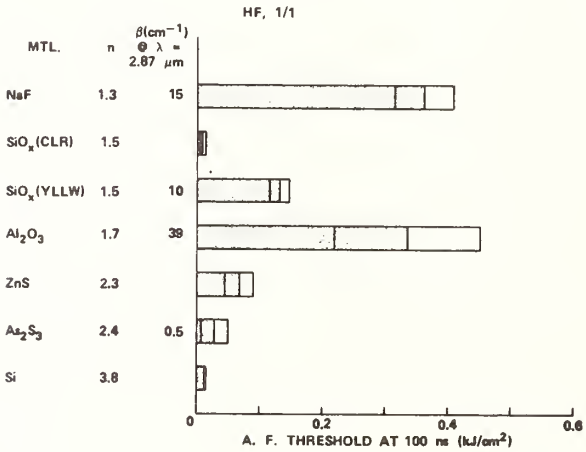

Figure 1. HF first visible laser damage of various single-layer coatings.

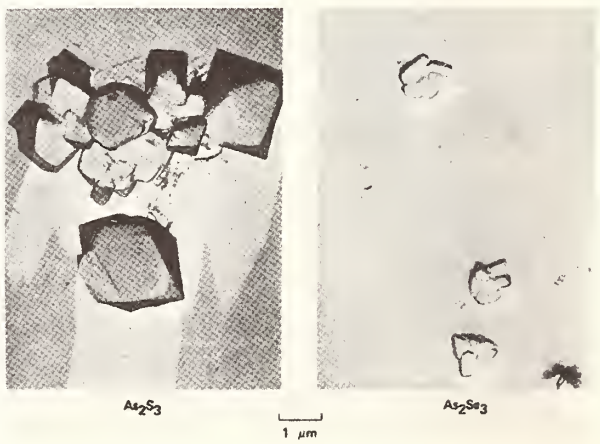

Figure 2. Defects formed on As_2S_3 and As_2Se_3 films.

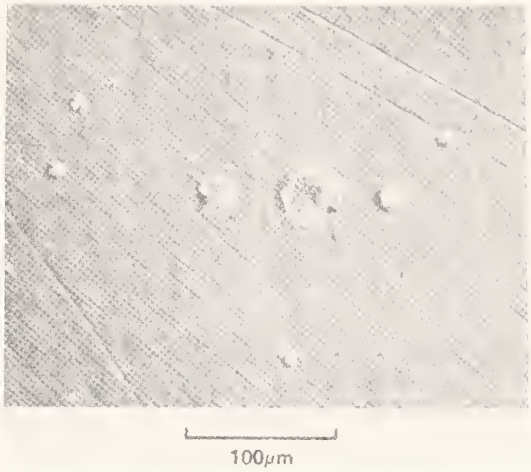

Figure 3. CO_2 laser damage sites showing delamination and perforation.

Figure 4. Multiple CO_2 laser damage sites showing ripple formation and scrubbing effect.

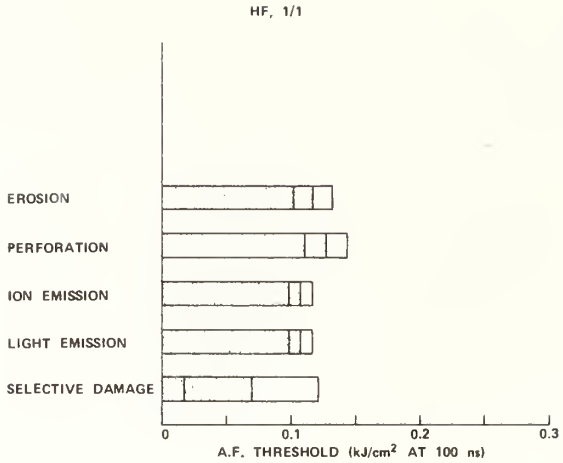

Figure 5 (a). HF laser damage of single-crystal CaF_2 coated with a half-wave of As_2S_3.

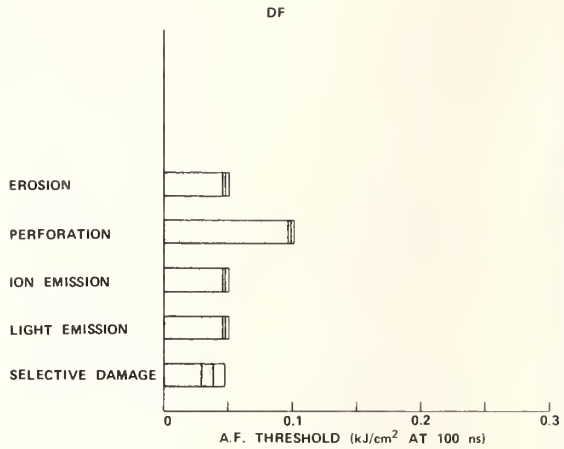

Figure 5 (b). DF laser damage of a half-wave coating of As_2S_3 on single-crystal CaF_2.

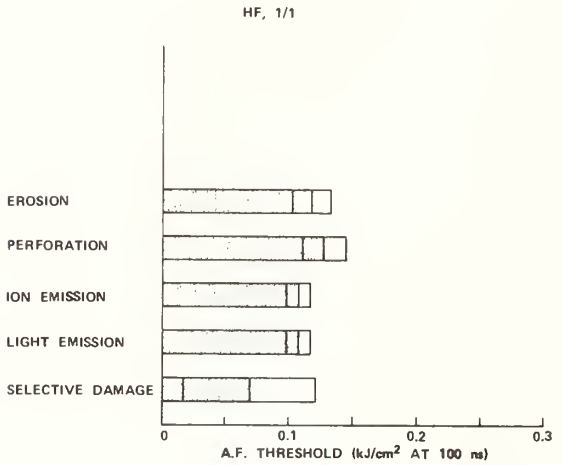

Figure 6 (a). HF laser damage of As_2S_3 film on CaF_2.

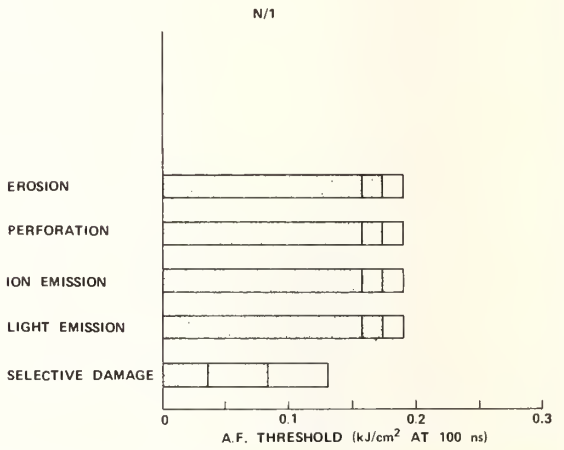

Figure 6 (b). HF laser damage of As_2S_3 film on CaF after N/1 conditioning.

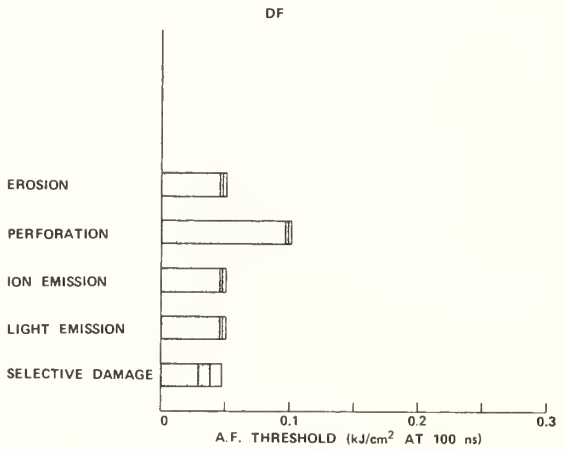

Figure 7 (a). DF laser damage of As_2S_3 film on single-crystal CaF_2.

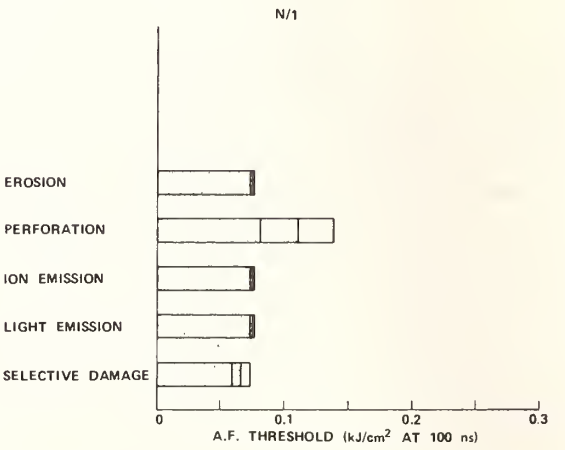

Figure 7 (b). DF laser damage of As_2S_3 film on single-crystal CaF_2 after N/1 conditioning.

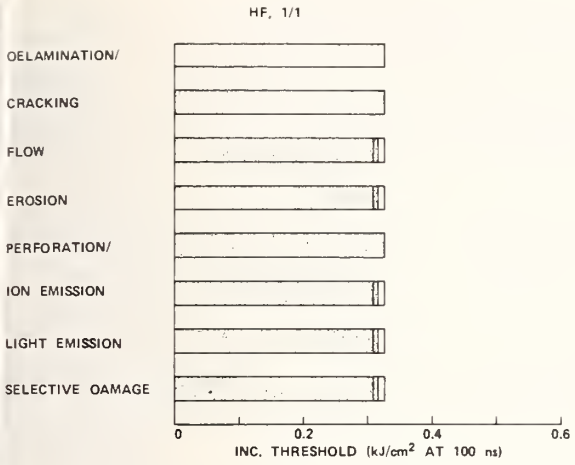

Figure 8 (a). HF laser damage of Ag/Mo mirror (reflectance enhanced with quarter-wave layers of As_2Se_3 and NaF).

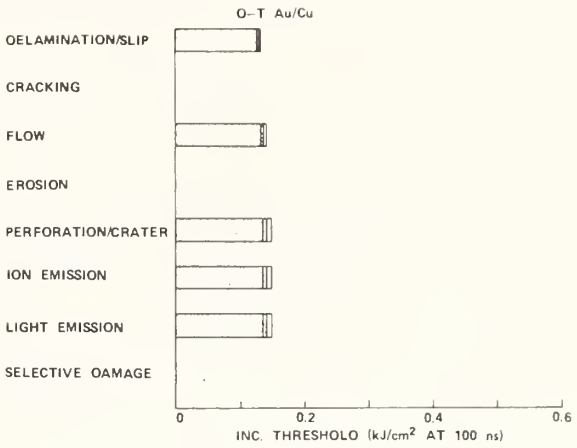

Figure 8 (b). HF laser damage of diamond-turned Au/Cu mirror.

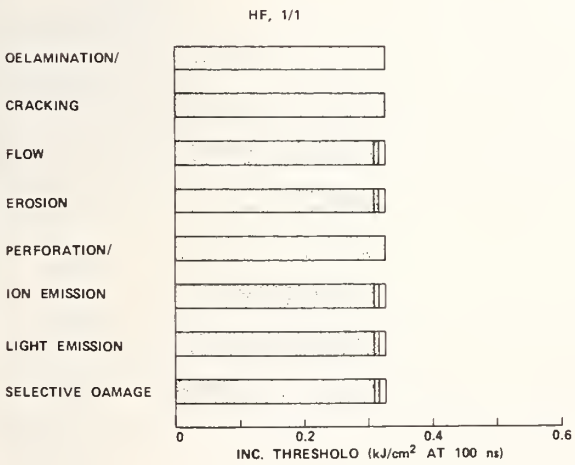

Figure 9 (a). HF laser damage of Ag/Mo enhanced reflectance mirror after N/1 conditioning.

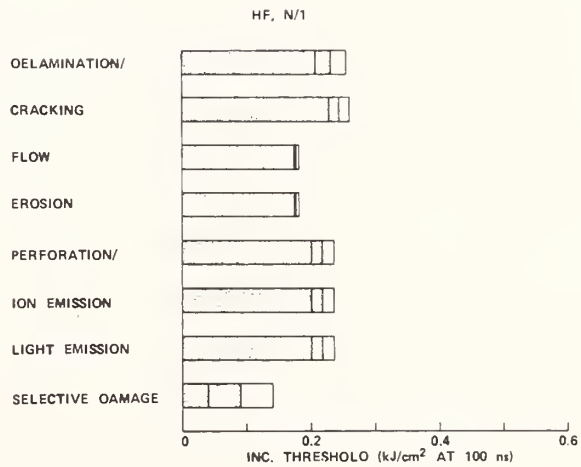

Figure 9 (b). HF laser damage of diamond-turned Au/Cu mirror.

TEM INVESTIGATION OF EFFECTS OF A BARRIER LAYER ON DAMAGE TO 1.064μ AR COATINGS

C. K. Carniglia and Joseph H. Apfel
Optical Coating Laboratory, Inc.
Santa Rosa, CA 95402

and

Gerald B. Carrier
Corning Glass Works
Corning, NY 14830

and

D. Milam
Lawrence Livermore Laboratory
University of California
Livermore, CA 94550

Silica/titania 4 layer AR coatings on BK-7 glass, with and without a half-wave silica barrier layer, have been damaged at 1.064μ by 150 ps laser pulses. The damage sites have been examined by TEM replica techniques at a magnification of 70,000. The size of the damage sites appears to be "quantized." Most sites consist of a 1μ nucleus which leads to a 3μ crater in a fully developed site. The mechanical properties of the films appear to play a role in the morphology of the damage sites. The titania layers seem to fracture while the silica layers seem to melt or tear. A series of micrographs of near threshold damage sites shows the development of the sites from a rupture which appears to occur at or near the substrate surface. Evidence of heating in the substrate is also present, although it is difficult to pinpoint the exact starting point of the damage mechanism.

Key words: Antireflection coatings; electron microscopy; laser damage; optical coatings; thin films.

The low damage threshold of antireflection coatings makes them a limiting factor in the achievement of large laser powers at 1.064μm for laser fusion. The damage threshold for AR coatings is roughly half that of high reflectors in spite of the fact that the electric field intensities in the two types of coatings indicate that the AR coatings should have a higher damage threshold [1]. The purpose of this study is to determine the location of the origin of laser damage in AR coatings using transmission electron microscopy (TEM) to provide detailed pictures of the damage sites. While the results are not conclusive, there are many indications that the damage originates at the interface between the coating and the substrate. However, this conclusion does not answer the question regarding the cause of the damage.

1. Coating Design

The AR coating used for this study is similar to the design used on the larger components of the SHIVA laser system and is referred to here as the SHIVA AR. It is a four layer design consisting of silica and titania. The basic design and electric field intensity are shown in the upper field plot in figure 1. The field is shown for a wave incident from the left in air. The titania layers are shaded. The lower E-field plot in figure 1 shows the same design with an additional half wave barrier layer of silica adjacent to the substrate. Notice that the electric field strength in the four layers of the AR coatings is the same in both cases and also that the field at the substrate interface is the same with or without the barrier layer. Figure 1 shows the spectral performance of the SHIVA AR on both BK7 and fused silica substrate. These curves are similar with or without the barrier layer.

A series of damage tests on the SHIVA AR on BK7 with and without the half wave silica barrier layer has been undertaken previously [2]. The results indicate that for a 0.15ns laser pulse, the threshold for the AR without the barrier layer is between 2.7 and 4.2 joules/cm^2. The presence of a half wave of silica under the same coatings raises the threshold to the range 4.8 to 6.3 joules/cm^2 with a typical improvement in excess of 50%.

There are several possible locations for the origin of the damage. The most likely possibilities are: 1) in the substrate just below the surface, 2) between the substrate and the coating, 3) in the first (thin) titania layer and 4) in the second (thick) titania layer. It is generally accepted that silica has a lower absorption than titania at 1.064μm and thus the damage is not expected to originate in the silica layers. This conclusion is strengthened by the fact that the addition of a thick silica layer raises the threshold.

The large effect of the barrier layer seems to indicate that absorption by surface contamination or by the titania are not sufficient explanations of the damage mechanism. In fact, the success of the barrier layer is difficult to understand in terms of any one damage mechanism taken by itself. It suggests that the titania in contact with the substrate is more damage prone that silica in contact with the substrate. This may be due to an increased absorption caused by an interaction between the titania and the substrate, or due to a better adhesion of the silica. Possible causes of the damage are as follows: a) weakening of the substrate near the surface due to the grinding and polishing process; b) the presence of polishing compound at or below the glass surface; c) contamination left on the surface after cleaning but before coating, resulting either in poor adhesion of the films or in absorption by the contaminants themselves; d) bulk absorption in the titania films.

Further factors that may be relevant to this study are the mechanical and structural properties of the layers. The silica films have a compressive stress while the titania films have a tensile stress. The net stress of the coating is slightly compressive in the case of the SHIVA AR and highly compressive with the barrier layer. The silica layers are amorphous and the titania layers are crystalline. This is verified in the TEM pictures discussed in section 3.

2. Damage Configuration

For this study coatings of the above designs were prepared on 1.5" dia. bowl-feed polished BK7 substrates. The damage testing was done at the Lawrence Livermore Laboratory facility. These samples were subjected to 0.15ns laser pulses at powers well above damage threshold. Sixteen laser pulses were spaced evenly around a 1cm dia. ring in such a way that they did not quite overlap. Generally the damage occurred without the emission of light indicating that the mechanism was linear absorption rather than avalanche breakdown.

Optical microscopy of the damaged areas reveals in most cases a heavily damaged region several hundred micrometers across surrounded by many smaller damage sites. These small damage sites appear to be uniform in size and to decrease in density with distance from the heavily damaged region. It has been previously observed [4] that the density of the individual damage sites is related to the intensity profile of the laser pulse, much as in a photographic image. Thus the sites around the edge of the pulse are expected to be representative of threshold damage. For the same laser pulse energy, the damage to the AR without the barrier layer appears to be more severe, with large regions where the coating is removed completely. The sample with the barrier layer shows a lower level of damage. These observations are consistent with previous findings on other samples regarding the relative damage thresholds of the two coatings.

3. Electron Microscopy

The original intent of this study was to use "over-the-edge" replica techniques to provide a cross section of a near threshold damage site. This technique involves fracturing the sample to be studied and then depositing the replica materials on the top surface of the coating as well as over the fractured cross section of the sample [3]. The replica is then removed and "flattened out" and studied using conventional TEM techniques. Examples of the results of this technique are shown in figures 2 and 3. These micrographs are over-the-edge replicas of the two coatings studied. Figure 2 shows the cross section of the SHIVA AR illustrating the amorphous silica top layer (between single black arrows), the oriented crystalline titania layer (between double white arrows), the thin silica layer (between double black arrows) and the thin crystalline titania layer (between the white-black pair). The single white arrow at the top of the figure indicates the top edge of the sample. The white bar at the bottom of the figure is 1μm in the length. Figure 3 is a similar cross section of the SHIVA AR with barrier layer. The five layers are indicated by pairs of black arrows with the top of the sample to the right as before. A slight etch after fracturing was required to make the boundary between the half wave silica layer and the substrate visible.

The arrangement of the laser shots in a closely spaced ring was intended to improve the chances of fracturing the sample through a damage site. A technique was developed for fracturing the samples radially through the damaged areas. However, away from the heavily damaged region, the density of near threshold damage sites was so low that it was nearly impossible to fracture through one and obtain a cross section. Thus most of the micrographs were taken using standard replication techniques.

All of the electron micrographs are taken from platinum-preshadowed carbon replicas. The platinum-palladium shadowing metal is evaporated from a point source and remains on the sample at nearly the position of impact. The carbon which forms the support film is nearly uniformly thick over the sample surface. The replica is then removed and investigated using TEM. The micrographs are all negative prints. The dark shadowed regions are due to the platinum-preshadowing (corresponding to regions without platinum). The white regions correspond to abrupt steps in the surface contour and are due to the carbon support film. These features are illustrated in figure 4 which is an annotated micrograph of a damage site from the SHIVA AR plus barrier layer. This micrograph illustrates most of the important features of the damage sites. Our interpretation of the features on figure 4 is as follows:

(1) This pair of arrows shows the cross section of the outer silica layer.

(2) This pair of arrows shows the top surface of the outer titania layer where the outer silica layer has separated from the titania layer.

(3) This pair of arrows shows the location of the abrupt step where the outer titania layer cleaved normal to the film surface.

(4) This pair of arrows shows the cross section of the second silica layer.

(5) This pair of arrows shows the surface of the inner titania layer where the second silica layer has separated from it.

(6) This pair of arrows shows the location of the abrupt step where the inner titania layer cleaved normal to the film surface.

(7) This pair of arrows shows the cross section of the innermost silica layer.

(8) This pair of arrows shows a region where the underlying glass has erupted through a portion of the inner silica layer and flowed outward over the silica surface.

(9) This pair of arrows shows the glass substrate. Note that there are a few craters extending down into the glass and that there has been flow of the glass around these craters. Obviously then the glass has been quite hot in the regions of these craters.

(10) Hackle marks - a characteristic feature frequently observed on fractured glass surfaces.

Figures 5a-5 are micrographs of a series of different damage sites from the AR without barrier layer showing a progression in damage level from near threshold to fully damaged site. The fracturing in the center suggests that the damage originates as an explosion beneath the surface which forces the outer layers up and off. The combination of the fracturing in the center and the presence of the large crater suggests that the damage is caused by thermal expansion of the coating beneath the surface according to the model of Duthler and Sparks [5]. It is interesting that the outer edge of the craters have a similar diameter in all cases. This suggests that the damage originates at the same depth within the coating.

Similar micrographs of partially developed damage sites from the sample with the barrier layer are shown in figure 6a and 6b. These suggest a similar damage mechanism namely, an expansion of the material from within the coating. However in this case, there are several different sized craters present. The fractured pattern in figure 6a is larger than those in figures 5a-g indicating that it originated at a greater depth and thus probably at the substrate surface under the barrier layer. The sites in figure 6b are smaller suggesting that they originated within the titania layers. An alternate explanation for the small sites is that they represent the central fracture due to damage originating beneath the barrier layer.

Figure 5g has many of the same features as figure 4, demonstrating that the damage mechanism has many similarities with and without the barrier layer. The substrate appears to have been molten in both cases, suggesting that the hottest area was near the substrate. Figure 7 is an over-the-edge micrograph of the AR without a barrier which is one of the few cases where the fracture goes through one of the damage sites. (The black arrow indicates the fracture edge.) This figure illustrates clearly that the damage extends into the substrate.

The hackle marks which appear in several of the micrographs give further support to the thesis that the damage originates at the substrate interface. Figure 8 is a micrograph of a severely damaged region from the sample with the barrier layer. Near the center bottom of the micrograph are two arrows enclosing a series of hackle marks which occur in the silica barrier layer. These hackle marks indicate that the silica was brittle while the glass substrate was obviously quite fluid. The steps that produce these lines are generally normal to the direction of propagation of the fracture. Thus the lines themselves lie in the direction of propagation. Note that the lines are not parallel, but focus toward a point to the left. It is likely that this focal point is the approximate location of the origin of the fracture.

4. Conclusion

Electron micrographs of laser damage sites on the SHIVA AR with and without a silica barrier layer strongly suggest that the damage is due to thermal expansion of the material at or close to the substrate-film boundary. It appears that the damage is caused by polishing or cleaning residue rather than by absorption in the coating materials themselves. However, this does not explain why the silica barrier layer is so effective in raising the damage threshold. Thus the controlling factors in producing a high damage threshold are not clear from this study. Further studies which could help clarify this point might include 1) using fused silica as a substrate material and 2) using barrier layers of different thicknesses.

5. References

[1] Apfel, J. H., NBS Spec. Pub., 509, 251 (1977).

[2] Apfel, J. H., Enemark, E. A., Milam, D., Smith, W. L., and Weber, M. J., NBS Spec. Pub. 509, 255 (1977).

[3] Carrier, G. B., J. Am. Ceram. Soc., (submitted for publication).

[4] Milam, D., Appl. Opt. 16, 1204 (1977).

[5] Duthler, C. J. and Sparks, M., NBS Spec. Pub. 414, 219 (1974).

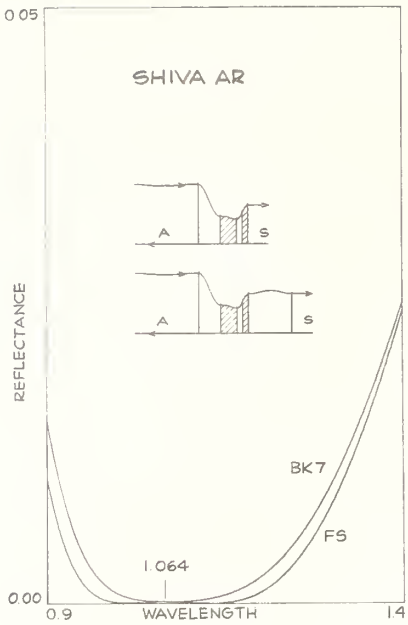

Figure 1. Reflectance versus wavelength of the SHIVA AR on BK7 and fused silica substrate. The electric field profiles for the AR without barrier (upper inset) and with barrier layer (lower inset) are shown.

Figure 2. Over-the-edge replica micrograph of th SHIVA AR showing the four layers. The top surfac of the coating is to the right of single white arrow. White bar indicates 1 micrometer.

Figure 3. Over-the-edge replica micrograph of the SHIVA AR with silica barrier layer. The top surface of the coating is to the right. Single arrow indicates substrate interface.

Figure 4. Damage site from the SHIVA AR with barrier noting the important features as discussed in the text.


5a


5b

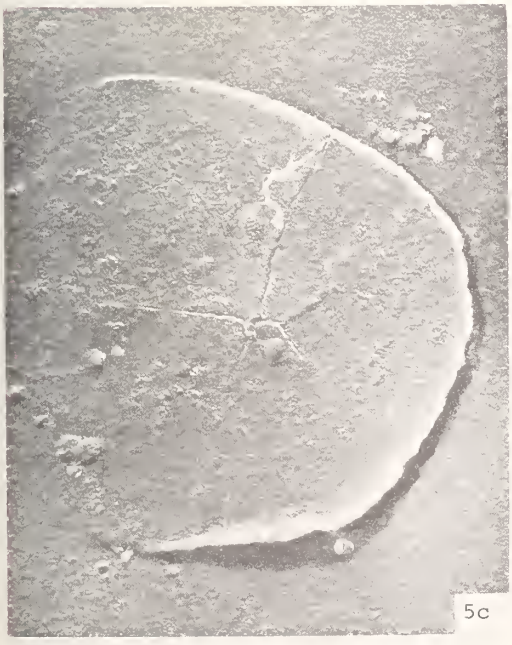
5c


5d

Figures 5a-g. Various damage sites from the SHIVA AR illustrating a progression in damage level from a slightly damaged site (5a) to a fully developed damage site (5g).

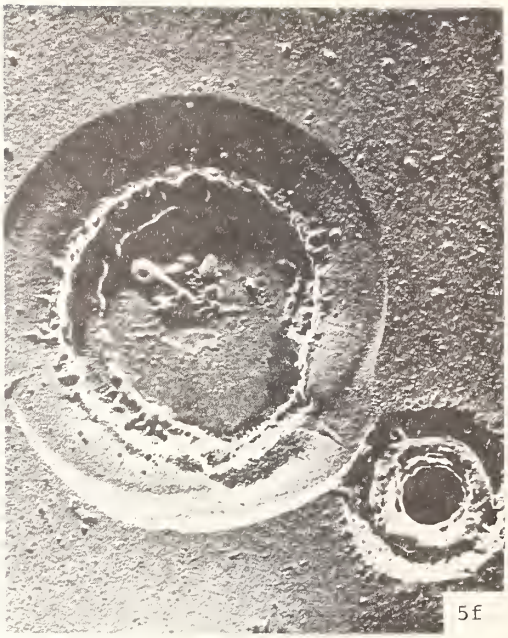

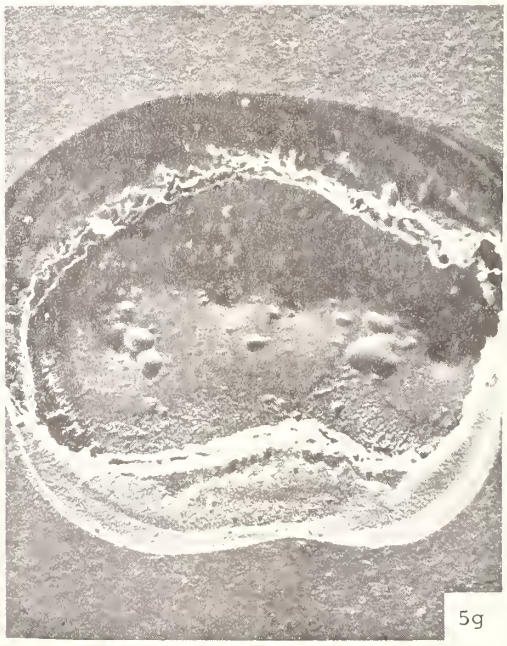

Figures 5a-g. Various damage sites from the SHIVA AR illustrating a progression in damage level from a slightly damaged site (5a) to a fully developed damage site (5g).

6a

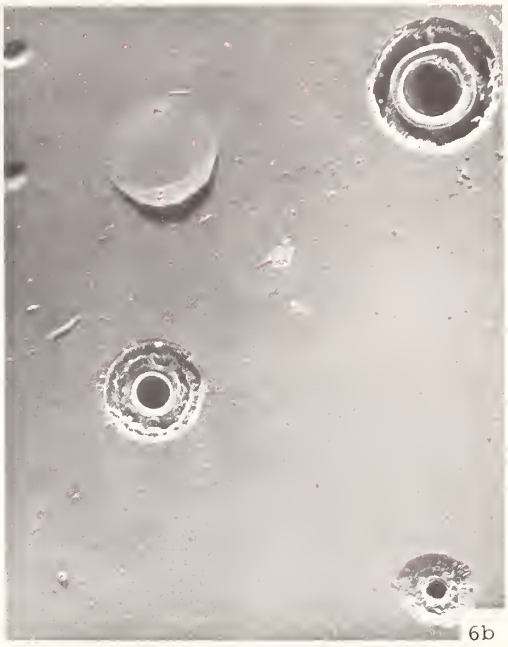

6b

Figures 6a, b. Near threshold damage sites from SHIVA AR with barrier.

Figure 7. Over-the-edge micrograph of a damage site showing that the damage extends into the substrate. Arrow indicates edge of substrate.

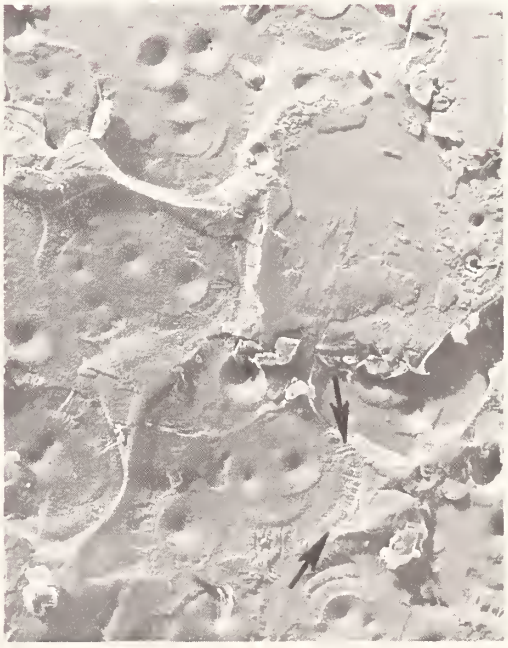

Figure 8. Heavily damaged area from the SHIVA AR with barrier layer illustrating hackle marks between arrows.

OPTICAL TECHNIQUES FOR THE DETERMINATION OF PULSED LASER DAMAGE IN THIN FILMS

T. W. Walker and A. H. Guenther
Air Force Weapons Laboratory
Kirtland AFB, NM 87117

and

P. E. Nielsen
Air Force Institute of Technology
Wright-Patterson AFB, OH 45433

Two techniques, to determine the occurrence of pulsed laser induced damage in thin film dielectric coatings, were compared and evaluated against normally employed methods. One of the new techniques utilized near back scattered radiation from the damaging pulse and proved to be as sensitive as the best existing optical probe method while being experimentally facile. The second new method recorded a time delayed probe pulse which was reflected from the thin film damage site. This method appears to be more sensitive to a local index of refraction change in the thin film rather than increased reflectance/scattering from the damage site. Preliminary test results show that most of the morphological damage occurs after the damaging pulse has passed.

Key words: Laser damage; optical probe technique; radiation scattering; thin films.

1. Introduction

Over the last several years optical probe techniques have been developed to detect the onset of laser induced damage in thin films (1-5). This paper describes a variation of the laser induced scatter (LIS) method (1) which offers several advantages over other proposed techniques. The optical probe arrangement of Alyassini and Parks (2-5) requires specially shaped samples to allow the proper angle of incidence of the probe beam at the film-substrate interface. Furthermore this technique loses sensitivity when the film's index of refraction is higher than that of the substrate. This original LIS method was found not as sensitive for some types of films as the present technique and does not offer a recordable quantitative indication of the damage event.

In making this comparison films of ThF_4, MgF_2 and ZrO_2 were tested. Analysis of the damage to MgF_2 agrees with the result stated in (5); that is, damage in this material can occur after the damaging pulse has passed. This situation also appears to be the case with the ZrO_2 films.

2. Experimental Method

The experimental approach was to compare the intensity of near back scattered radiation from the damaging beam, produced in the thin film, to a reference pulse. The reference pulse was also compared to a time delayed probe pulse which was coincident spacially with the damaging pulse at the thin film/substrate interface. The experimental arrangement is shown in figure 1. The reference pulse was delayed 55 nsec from the damaging pulse, while the probe had an adjustable time delay of 0 to 50 nsec. The three separate pulses of light were collected in one ITT S-20 FW 114A (A) detector. The detector output was dc coupled to a Tektronic R7912 transient digitizer. A separate S-20 (B) detector was used to monitor the transmitted damaging pulse after it exited the sample. A He-Ne probe beam was coincident with the damaging beam and was used for visual LIS detection of damage.

The damaging pulse had a FWHM 18 nsec and a wavelength of 0.53 μm. The beam diameter on target was calculated to be 200 μm at the e^{-1} points and the probe beam was focused to have an equivalent spot size at the target site. Three different thin film materials were tested: MgF_2, ThF_4 and ZrO_2. All films were deposited on fused silica substrates and were of $\lambda/2$ thickness at 1.06 μm.

3. Results and Discussion

Figures 2, 3 and 4 depict the test results for ThF_4 films. Figure 2 exhibits the scattered, probe and reference pulses at an energy well below the film breakdown threshold. The important feature in each test sequence is the ratio of the three peak amplitudes. At low incident laser energies, well below the damage threshold, the ratio of the reference to near back scattered intensity varied somewhat

between different test films, but was essentially constant for different sites on the same films. This low energy pulse ratio for the reference:probe:scattered signals is 1.0 : 0.86 : 0.75. With occurrence of damage the ratio becomes 1.0 : 1.07 : 1.11 which is shown in figure 3. A subsequent return to sub-threshold low energy level is shown in figure 4. The ratio is 1.0 : 1.07 : 1.29. The fact that the relative scattered intensity has increased slightly after the return to low energy level will be commented on later. The morphology of the damaged ThF_4 site is shown in figure 5. The diameter of the site is 1.3 μm and the edge is smooth. There was no detection of damage by the visual LIS method using HeNe illumination. The morphological observations are similar to those described by Alyassini and Parks (5) when they observed damage with their probe technique, but did not detect damage by the visual LIS method.

The results for the MgF_2 films are shown in figures 6 through 9. The initial low energy ratio was 1.0 : 0.69 : 0.69; the ratio at damage was 1.0 : 0.7 : 0.79; the ratio upon a return to low energy level was 1.0 : 0.7 : 1.11. The damage site is shown in figure 9. This damage event was detected by the visual LIS method. This observation is in agreement with Alyassini and Parks (5), probably due to the larger damage site size and its more irregular edge.

Damage tests on ZrO_2 produced the respective low, high, low energy ratios of 1.0 : 1.29 : 0.81, 1.0 : 1.48 : 1.04 and 1.0 : 1.63 : *. The (*) indicates that the scattered signal was so large that the peak was off scale relative to the probe and reference beams. This is shown in figure 12. The relatively large damage site for the ZrO_2 films is shown in figure 13.

The striking difference of the ThF_4 and ZrO_2 film behavior compared with that of MgF_2 film concerns the variation in the probe beam intensity. For the first two film materials there is a definite indication of damage while with MgF_2 the probe beam shows essentially no change before, during or after damage. One possible explanation of this is that the probe beam is a reflected beam. As such it would be more sensitive to a small change in optical thickness, resulting from either a change in refractive index or thickness of the thin film, in a fairly large region around the damage site than it would be to a totally reflective 2-3 μm damage site. In the case of ThF_4 and ZrO_2 films, the reflectance is at a minimum and any local change in the optical thickness of the film would produce an increase in reflectance. The MgF_2 film, on the other hand, is at a maximum of reflectance and any change would effect a decrease in reflectivity. The fact that this does not occur with MgF_2 films may indicate that a local index change does not take place in MgF_2 or that the effect is compensated by increased reflectance from the damage site. The differences in morphology of the three sites can aid in the interpretation. The drastic increase in scattering for ZrO_2 indicates that the near back scattered signal is probably a strong function of the damage site area. Whereas the similar changes in the probe signals for ZrO_2 and ThF_4 films require that the probe signal be at best a very weak function of the damage site size. Thus it would seem that the probe signal increase in ThF_4 film is not due to the damage site itself. Since the MgF_2 film and ThF_4 site sizes are similar in size, whatever is occurring in ThF_4 is not occurring in MgF_2 film. Finally, the ThF_4 damage site has a melted nature while that of the MgF_2 more of a cratered nature, indicating that subtle changes may have occurred around the first site and that changes were more localized at the second site. The degree to which the signal ratio's change for the various films is undoubtedly also a function of the refractive index of the individual films and their difference from the substrate's value.

Another interesting feature is the difference between the ratios at the damaging energy level and at the return to low energy. For ThF_4 film most of the change has occurred during the damaging pulse and is over by the time the probe is incident on the site. The increase in the scattered light signal at the low energy level indicates that some damage has occurred after the damaging pulse but prior to the probe pulse. The MgF_2 and ThF_4 films exhibited a large increase from the high to the low energy levels. This is particularly noticeable in ZrO_2 film and was in evidence in all of the tests on these three materials. Substantial damage evolves in all materials after the damaging pulse has passed through the samples.

The time delay was decreased for the probe in several tests. During this variation there was essentially a constant behavior observed when MgF_2 films were tested. However, there was a small variation in the ThF_4 probe data when the time delay was reduced to 25 nsec, indicating that structural changes may still be occurring to that time. However, the variations were too small ($\sim$ 10%) to be conclusive.

Finally, it was noted that there was no visible spark observed nor any distortion to the transmitted damaging pulse in any of the tests discussed. When a visible spark occurred the scattered

light signal was several orders of magnitude greater than the reference signal. The damage morphology showed several damage sites with diamaters in excess of 10 μm.

4. Summary and Conclusions

We have found that two optical techniques, different from those previously employed, provide a viable technique for determining the occurrence of damage in thin films. Collection and detection of the near back scattered (∿ 5°) light from the damaging pulse and its subsequent ratioing to the incident pulse intensity was the most reliable measure of damage. In the case of MgF_2 and ZrO_2 films, best confirmation of damage is obtained by comparison of the ratio after re-exposure at a low level rather than from ratios obtained during the damaging event. Since most damage experiments are accomplished using a single site-single shot format, this should provide no obstacle other than requiring two additional low energy exposures. The low energy events can be such a level to exclude any conditioning of the film by the laser pulse.

It is not clear why the probe gives a successful indication of damage for ThF_4 but not MgF_2 films. An answer to this point may shed light on why MgF_2 fluoride films do not fit the Bettis, et al. (6) predicted index of refraction dependence on breakdown.

We find that the back scatter method can be more sensitive than the visual LIS method. However, it is only an electronic variation of the same effect. In comparison with the Alyasinni and Parks (5) optical probe, it has more versatility and is much simpler experimentally. Furthermore, it can be made in an objective manner affording a quantitative measure for comparison.

The results found in the backscatter experiment for damage site morphology versus damage detection by visual LIS agree with those of Alyassini and Parks (5).

TABLE I

Relative Changes in the Intensity of Probe and Back Scattered Beams

	Below Damage	At Damage	Return to Below Damage
MgF_2 (p)	0.69	0.7	0.7
(s)	0.69	0.79	1.11
ThF_4 (p)	0.86	1.07	1.07
(s)	0.75	1.11	1.29
ZrO_2 (p)	1.29	1.48	1.63
(s)	0.81	1.04	*

Reference (incident) pulse normalized to 1

p = probe beam
s = scattered beam
* = scattered beam intensity off scale being orders of magnitude greater than level at damage

5. References

(1) B. E. Newnam and L. G. DeShazer, 4th ASTM Symp., Damage in Laser Materials, Edited by A. J. Glass and A. H Guenther, NBS Spec. Pub. 372, 123 (1972).

(2) J. H. Parks and N. Alyassini, 4th ASTM Symp., Damage in Laser Materials., Edited by A. J. Glass and A. H. Guenther, NBS Spec. Pub. 372, 104 (1972).

(3) N. Alyassini, J. H. Parks, and L. G. DeShazer, 5th ASTM Symp., Damage in Laser Materials., Edited by A. J. Glass and A. H. Guenther, NBS Spec. Pub. 387, 133 (1973).

(4) N. Alyassini, Ph.D. Thesis, University of Souther California, 1975 (University Microfilm, Ann Arbor, Mich.).

(5) N. Alyassini and J. H. Parks, Laser Induced Damage in Optical Materials Symp., Edited by A. J. Glass and A. H. Guenther, NBS Spec. Pub. 435, 284 (1975).

(6) J. R. Bettis, R. A. House, A. H. Guenther, and R. Austin, Laser Induced Damage in Optical Materials Symp., Edited by A. J. Glass and A. H. Guenther, NBS Spec. Pub. 435, 289 (1975).

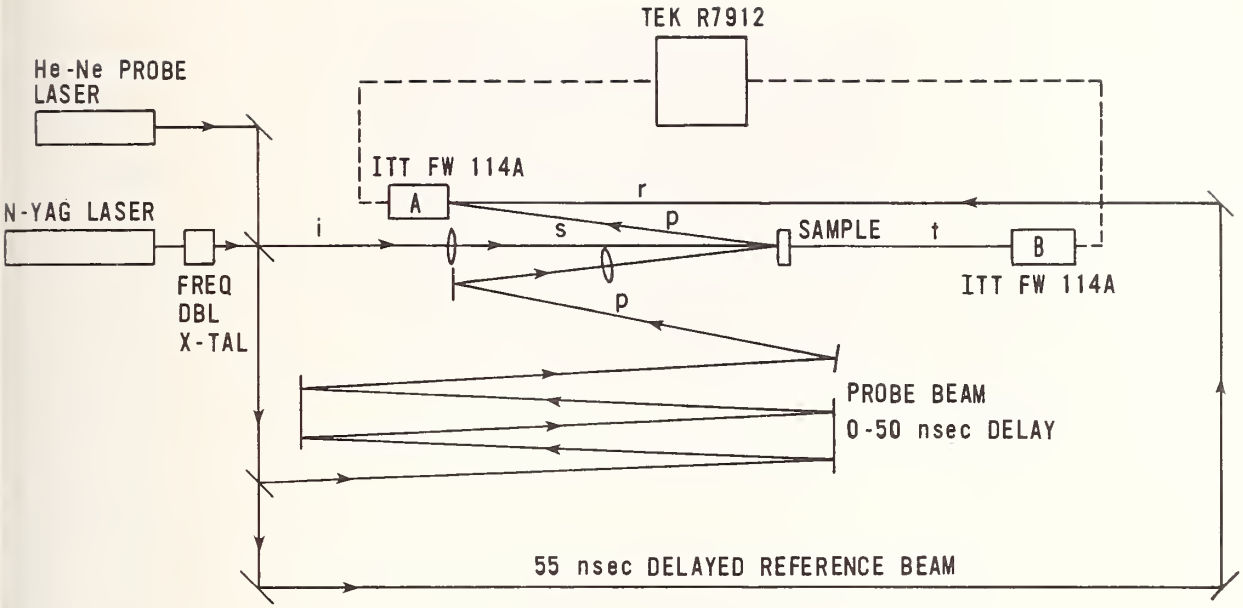

FIGURE 1. EXPERIMENTAL SCHEMATIC

Figure 1. Experimental arrangement for damage experiments employing optical diagnostic techniques. (i, is the incident damaging beam; r, the reference beam; s, the back scattered beam; t, the transmitted beam; and p, the delayed probe beam. The photodiode A records the s, p, and r beams while photodiode B records the t beam.)

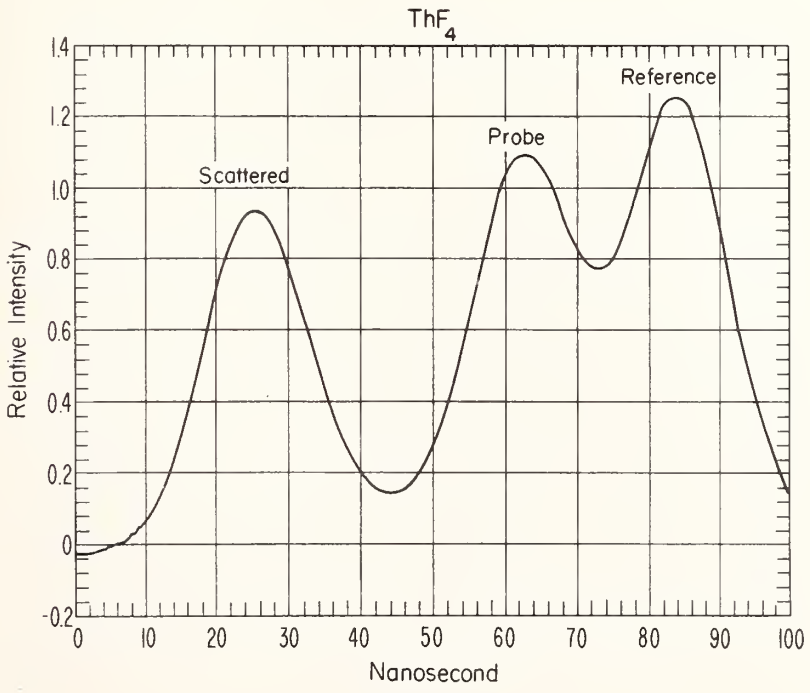

Figure 2. Three pulses at an energy level below the ThF_4 film breakdown threshold. The ratio of peak amplitudes from right to left is 1.0:0.86:0.75.

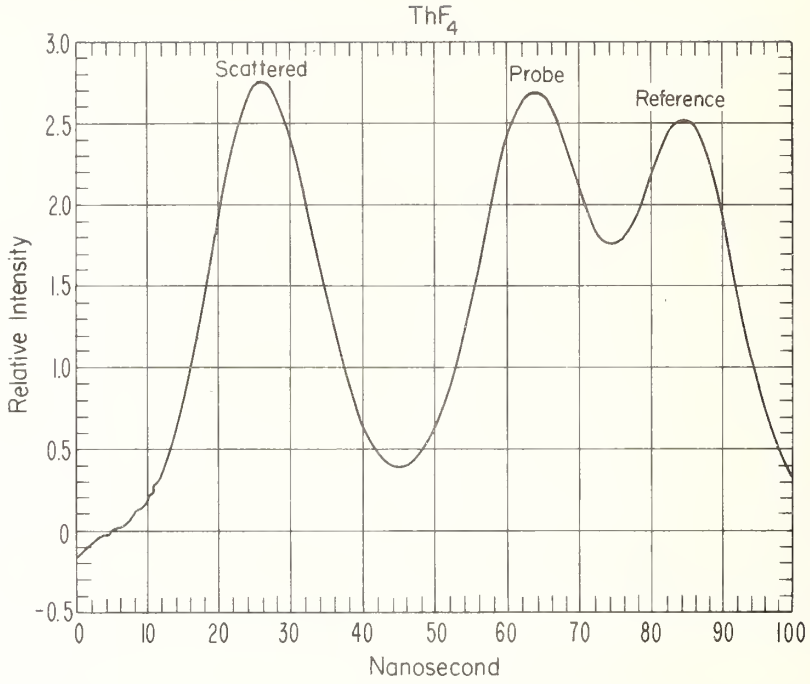

Figure 3. The same three pulses at film breakdown. The right-to-left ratio is 1.0:1.07:1.11.

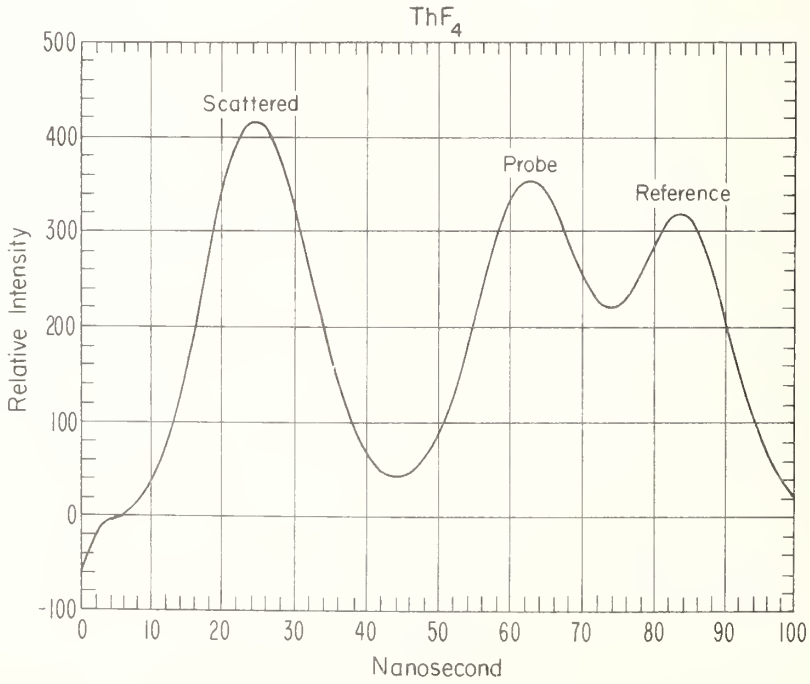

Figure 4. The three pulses upon return to low energy. The ratio is 1.0:1.07:1.29.

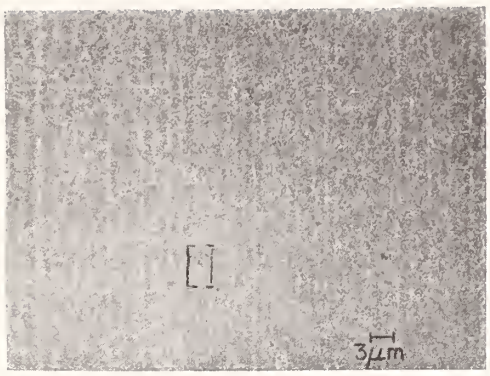

Figure 5. Nomarski micrograph of the damage sit (in brackets) for the ThF_4 film.

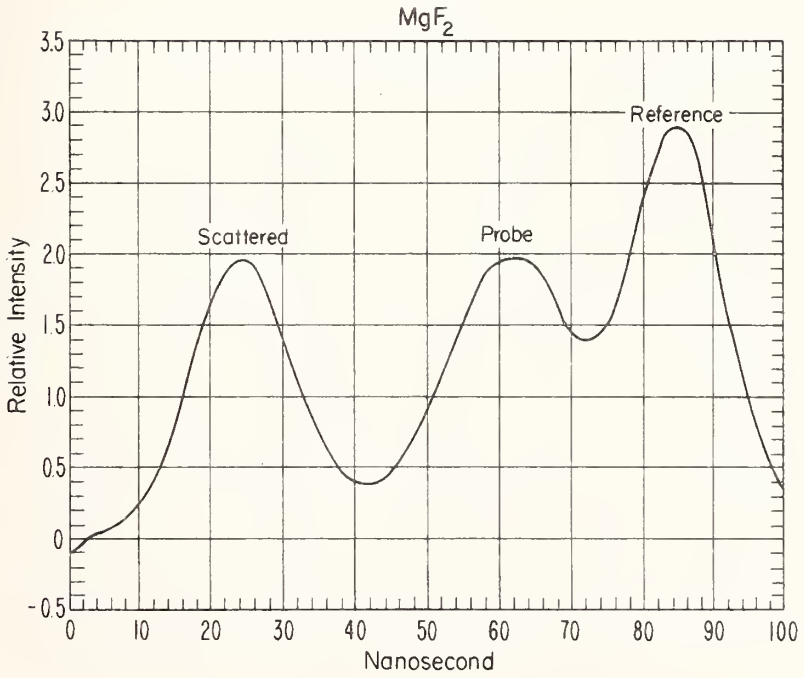

Figure 6. The signal ratio's below film breakdown for MgF_2 are 1.0:0.69:0.69.

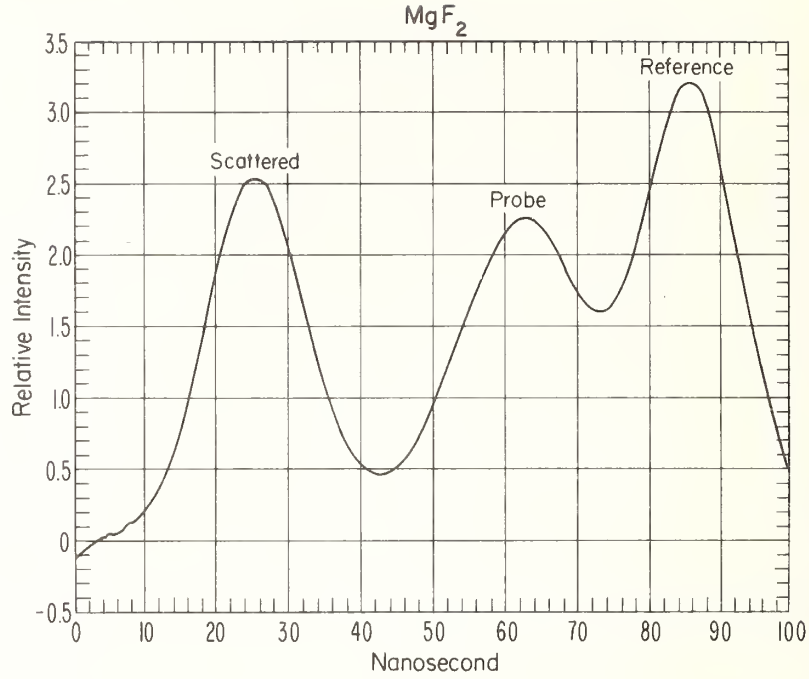

Figure 7. At film breakdown the ratio becomes 1.0:0.7:0.79.

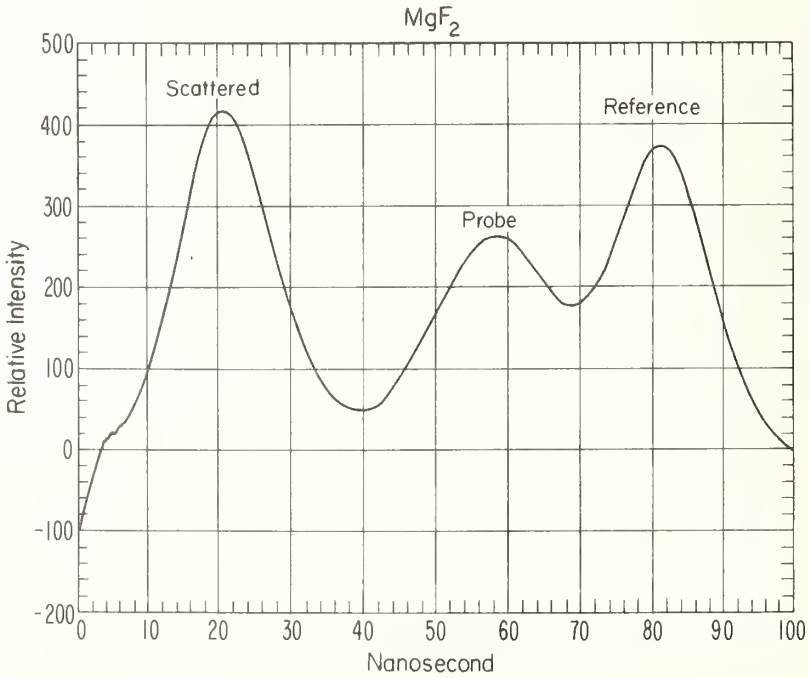

Figure 8. Upon return to low energy the ratio's become 1.0:0.7:1.11.

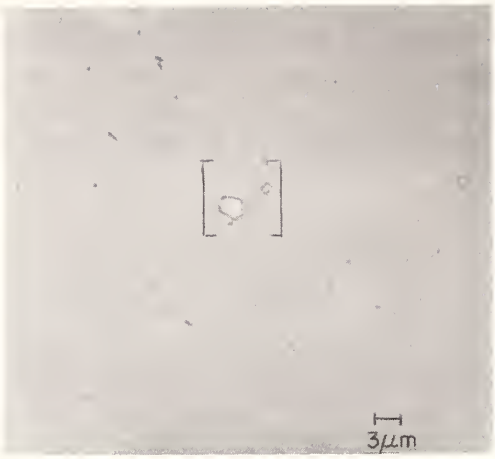

Figure 9. A Nomarski micrograph of the damage site (in brackets) for the MgF_2 film.

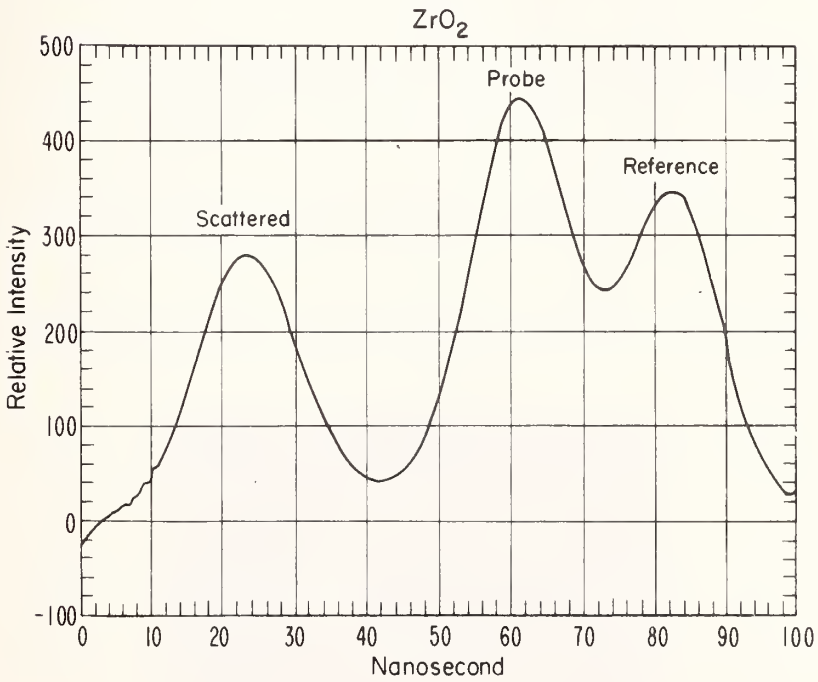

Figure 10. Initial low energy exposure yields ratio's of 1.0:1.29:0.81 for ZrO_2 films.

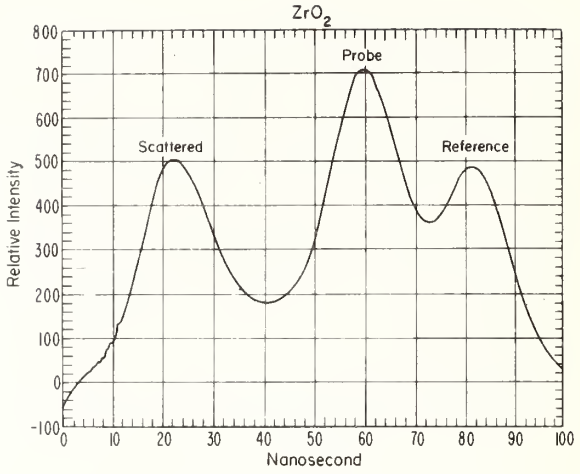

Figure 11. The ratio at film breakdown becomes 1.0:1.48:1.04.

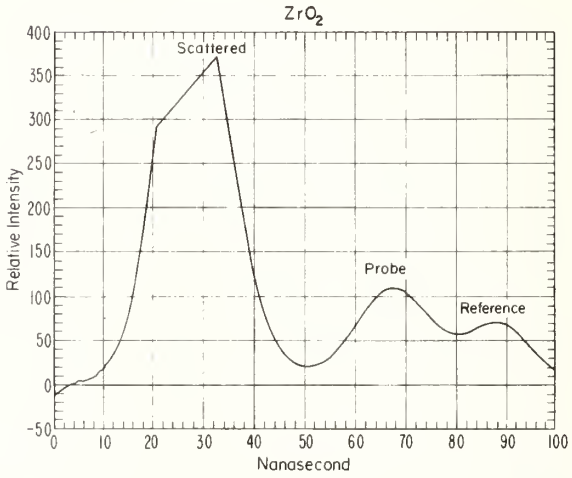

Figure 12. Upon return to low energy the ratio's become 1.0:1.63:*. The (*) indicates that the scattered signal is several orders of magnitude larger than the reference for these ZrO_2 films.

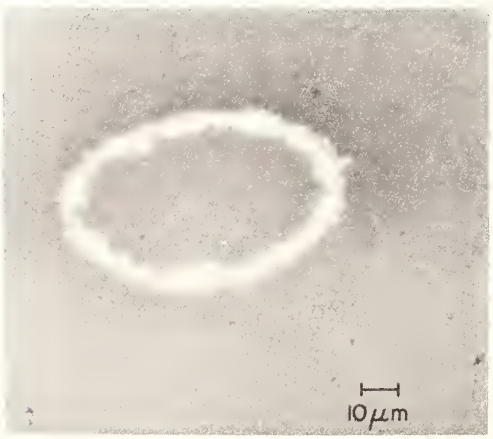

Figure 13. A Normarski micrograph of the damage site in ZrO_2 shown in (brackets).

A STATISTICAL ANALYSIS OF ABSORPTIVE LASER DAMAGE IN DIELECTRIC THIN FILMS*

Aaron B. Budgor and Karen F. Luria-Budgor
University of California
Lawrence Livermore Laboratory
P. O. Box 808
Livermore CA 94550

The Weibull distribution arises as an example of the theory of extreme events. It is commonly used to fit statistical data arising in the failure analysis of electrical components and in DC breakdown of materials.

This distribution is employed to analyze time-to-damage and intensity-to-damage statistics obtained when irradiating thin film coated samples of SiO_2, ZrO_2, and Al_2O_3 with tightly focused laser beams. The data used is furnished by Milam. The fit to the data is excellent; we often obtain least squared correlation coefficients greater than 0.9.

It is found almost universally that statistical models of breakdown, such as the lucky electron theory, oversimplify the damage process by neglecting nonlinear interactions and anisotropies induced by impurities. Thus, the fundamental intensity I relation on pulse length t_p often deviates from the classical $t_p^{-1/2}$ dependence resulting from 2-photon absorption without diffusion, or from linear absorption with diffusion, to dependencies as high as $t_p^{-0.22}$ for the former to $t_p^{-0.44}$ for the latter. This fact, coupled with the experimental nonobservability of higher than 2-photon absorption seems to imply that the avalanche mechanism is the most likely initiator of the plasma requisite for lattice meltdown.

Statistical confidence bands for material survivability as a function of laser intensity and pulse length can be constructed; this lends high practical utility to the Weibull distribution as an engineering diagnostic tool.

Key words: Laser damage; thin films; probability; statistical analysis; Weibull distribution.

*Work performed under the auspices of the U.S. Department of Energy by the Lawrence Livermore Laboratory under contract number W-7405-ENG-48.

1. INTRODUCTION

Laser induced breakdown of solid dielectric films and bulk materials has been a subject of ongoing interest and concern at these symposia. Although the complete theory leading to breakdown will most likely never be understood, i.e., aspects pertaining to imperfections intrinsic and extrinsic to the material, much effort is spent to evaluate two possible physical mechanisms initiating the breakdown process -- avalanche and multi-photon ionization. Both of these theories have been suggested as candidates to provide the requisite number of electrons precursory to lattice melting [1][1].

The avalanche theory propounds the existence of loosely bound electrons derived from shallow traps arising from such structural imperfections as F-centers. These electrons interact with the laser field, become excited, and multiply upon impact ionization with the lattice.

When the laser photon energy is $\geq \frac{1}{n}$ times the bandgap energy E_g n-photon ionization becomes an alternate mechanism for the creation of conduction electrons, but with rapidly diminishing probability as n increases. Thus, the longer the wavelength the laser light is the less effective multi-photon ionization is for exciting valence electrons to the conduction band. For example, a 10.6 cm laser light source requires a 21-photon process to elevate electrons through the NaCℓ F-center bandgap of 2.4 eV.

In reality there is probably some augmentation between multiphoton and avalanche ionization which is dependent on photon energy $\hbar\omega$ and E_g. As the photon energy attains a value $\geq E_g/2$ two photon absorption will quite likely assist the avalanche process, for $E_g/3 \leq \hbar\omega < E_g/2$ three photon absorption may occur, but with reduced probability, etc. Liu et al have set up experiments to detect 3-photon absorption at 355 nm in NaCℓ by direct absorption [2]. Not only were they unsuccessful, but all studies including those by photoconductivity have never been able to discover absorption higher than 5-th order in solids. Apparently the major pitfall is that at the intensity levels of observation breakdown usually intervenes. How to deconvolute this presumed joint dependence of breakdown on both mechanisms is a subject of this paper.

As the total number of such conductive electrons generated depends on the 1) laser pulse duration, 2) photon energy of the laser, 3) energy gap and impurity levels, and 4) ambient conditions there is a great deal of lattitude for interpreting the damage event statistically. Such a point of view has been corroborated by the experiments of Milam et al [3] for dielectric breakdown times of bulk and thin film materials when irradiated at small focal volumes by tightly focused laser beams.

In the following two sections we shall discuss the role and application of the Weibull distribution to the analysis of damage data. This distribution is then fit to data compiled by Picard et al and Milam for various thin film coated samples of SiO_2, $Aℓ_2O_3$, and Zr_O_2 [4,5]. Estimates concerning characteristic lifetimes and breakdown intensities are given as well as a scheme for determining the reliability of those estimates. It is also shown that the dependence of breakdown intensity on laser pulse duration, for the most part, does not deviate markedly from linear or 2-photon absorption. A strong case is then made for the avalanche process.

2. STATISTICS OF FAILURE: THE WEIBULL DISTRIBUTION

The use of statistical failure models to make predictions and deductions about material breakdown in the presence of external forces can be traced to the pioneering work of Griffith in his study of flaws and their correlation to fracture [6]. Griffith theorized that the reason for the difference between calculated and observed values of material strengths resides in the fact that there exist flaws in the body which weaken it. If the flaws are distributed inhomogeneously they will provide a distribution of strengths as a function of material position, each position requiring a different degree of force to produce fracture. When the actual performance of the material is then predicated on its weakest "link" the use of extreme value statistics is in order, that is, the statistics of maxima and minima [7]. Some of the rudiments of this theory are presented in the Appendix.

To pursue the analogy of the foregoing to laser breakdown of optical materials we postulate that a damage event is due to a number of underlying causes. Not only is it a function of laser intensity, impurity concentration, and structural defects, but interposed with these causes is the unifying factor that damage may be the result of cumulative laser pulses. This implies that damage is not necessarily an all or none event but most probably depends on the material's previous history; this includes weakest "links". Inhomogeneities in the material and external fluctuations subsumes the use of extreme value statistics.

---

1. Figures in brackets indicate the literature references at the end of this paper.

An extreme event distribution which has been previously found to fit the failure data of electrical components and of D.C. breakdown of materials is the Weibull distribution [8,9]. Asymptotically it is given by the distribution function

$$F(y) = 1-e^{-(y/\alpha)^{\beta}} \qquad \begin{matrix} y \geq 0 \\ \alpha, \beta > 0 \end{matrix} \tag{1}$$

where y denotes the random variable

$$y = \lim_{n\to\infty} y_n = \lim_{n\to\infty} \min_{n} \left\{ X_1, --, X_n \right\} \tag{2}$$

comprised of the minimum of a large number of independently distributed damage random variables X_j whose distributions are given by (A10). The parameters α and β are respectively defined as scale and shape parameters, with α being a characteristic failure coefficient since it is the 100 x $(1-e^{-1})$ = 63.2 percentile of the distribution for any value of β.

In an attempt to understand the meaning of (1) we examine plots of the density function $\delta(y)$

$$\delta(y) = \beta/\alpha(y/\alpha)^{\beta-1} e^{-(y/\alpha)^{\beta}} \tag{3}$$

in figure 1. For values of β in the range $0 < \beta \leq 1$ $\delta(y)$ is an amodal function of y with mean μ and variance σ^2 (eqs. A2) ranges, respectively, $\infty<\mu\leq 1$ and $(2^{2/\beta} - \beta^{-1/2}) < \sigma^2 \leq 1$. At $\beta = 1$ (1) is exponentially distributed. For values of $\beta<1$, $\delta(y)$ is unimodal, resembling a Gaussian at $\beta \approx 3.6$. The limiting values of μ and σ^2 are

$$\lim_{\beta\to\infty} \begin{cases} \mu = 1 \\ \sigma^2 = 0 \end{cases} \tag{4}$$

In plotting failure data y_i i = 1, .., N, to (1) we rank the y_i's from smallest to largest and assign values to $F(y_i)$ as

$$F(y_i) = \frac{i}{N+1} \tag{5}$$

By placing these points on Weibull graph paper (fig. 2) and drawing a straight line through them rough estimates of α and β can be obtained. The α value is found by entering the probability scale at the 63.2% point and then reading its projection on the abscissa. β is found by drawing a line parallel to the fitted straight line through the point marked origin; the value of its intersection with the vertical shape parameter scale at the left equals β. An alternate and more accurate procedure for determining α and β is to least squares fit a straight line to

$$\ell n \ell n \left[1 - F(y)\right]^{-1} = \beta \ell n y - \beta \ell n \alpha \tag{6}$$

One of the drawbacks to utilizing (1) occurs when failure events pile up at the small values of y. This tends to shift the weight of the distribution to the left, away from the true mode which varies as $N^{-1/\beta}$, resulting in correspondingly poorer fits. This drawback can be remedied by choosing as a variant of (1) the distribution

$$F(z) = e^{-(\alpha'/z)^{\beta'}} \tag{7}$$

z is the random variable defined as

$$z = \lim_{n\to\infty} z_n = \lim_{n\to\infty} \max_{n} \left\{ X_1, --, X_n \right\} \tag{8}$$

the X_j's being independent and identically distributed according to (A18b). α' and β' are the counterparts to the α and β of (1). This distribution is also known as the Pareto distribution after the economist Pareto [10]. Thus, instead of asking what the minimum value of y for which failure occurs is, we now invert the question to the maximum value of z. Pileups of z_i for small values of z

will better the fit to (7). The parameters α' and β' are found by least squares fitting a straight line to

$$\ell n \ell n\, F(z)^{-1} = \beta' \ell n \alpha' - \beta' \ell n\, z \qquad (9)$$

3. DAMAGE STATISTICS OF THIN FILM DIELECTRICS

In this section we apply the formulae of section 2 to damage data compiled by Milam for various sputtered thin film dielectric samples of S_iO_2, Z_rO_2, and $A\ell_2O_3$. These films were prepared on CG7059 electronic substrates with various percentages of sputter bias and sputtering gas (O_2 or A_r) concentrations. The materials were irradiated at a number of separate sites with 20-30 nsec pulses focused to approximately 6 μm focal spots. The pulses were obtained by switching out the central portion of the output from a single longitudinal mode, single transverse mode Q-switched laser by means of a Pockels cell shutter. For a given laser pulse intensity, I, the time delay to damage, or survival time t_d was measured from the width of the transmitted pulse, and beam power from the height of a reference pulse.* These values were obtained to a ±2.5% accuracy. As this I was varied these measurements were equivalent to those of breakdown threshold energy density I_B versus t_p.

A statistical ensemble to which equations (1) and (7) are fit is obtained by ranking all survival times t_d for specific values of I_B, or alternatively by ranking all I_B for specific values of t_d. The results of least squares fitting this data to these distributions are given in tables I-III. Parts A of these tables correspond to distributions in t_d, $F(t_d)$. The first and second columns rowise pair individual breakdown intensities I_B with the N values of t_d (given in parentheses) to be fit to $F(t_d)$ and their respective t_d ranges. The α's denote characteristic sample lifetimes, $\bar{t}_d$. The entries in the parts B tables correspond to distributions in I_B, $F(I_B)$. Now the first and second columns rowise pair individual lifetimes t_d with the N values of I_B to be fit to $F(I_B)$. The α's denote characteristic breakdown intensities, $\bar{I}_B$. For both parts β, r^2, μ, and σ^2 are shape parameter, correlation coefficient squared, mean, and variance. The entries in the α and β columns are not to be literally interpreted as the α's and β's from (1). They may be α' and β' values, depending on whether r^2 was larger for the fit to (9) than it was to (6). This statement is correspondingly true for the calculated mean μ and variance σ^2 values.

The deductions to be drawn from these tables are best summarized as follows:

i) The least squares correlation coefficients r indicate that the fits of thin film damage data to the Weibull distribution are excellent.

ii) Parts A imply that increasingly larger values of I_B lead to decreasingly smaller values of $\bar{t}_d$.

iii) Parts B imply that increasingly larger values of t_d lead to decreasingly smaller values of $\bar{I}_B$; this is true since the sample experiences the damaging pulse for longer times.

iv) The β coefficients from parts B will in general lead to much narrower distributions for $F(I_B)$ than for $F(t_d)$.

v) In some cases the variances σ^2 are not sufficiently broad to distinguish statistics from experimental error.

---

*The relation between laser pulse energy E, intensity I, and power P, is formally given as

$$E = \int\int dx\, dy \int dt\, I(x, y, t)$$

where x and y are coordinates in the plane normal to the light propagation axis. For a constant intensity pulse this reduces to

$$E = I/t_pA$$

where t_p is pulse duration and A is focal spot area.

vi) There may be a stabilization on the range of β values as a function of sputter bias and sputtering gas concentration. More data is needed to investigate this point.

If we now plot for each sample category the median I_B values as a function of $(\bar{\tau}_d)^q$, and least squares fit the result to

$$\ell n\ I = q\ \ell n\ \bar{\tau}_d + C_o \tag{10}$$

the ensuing results for q and r^2 are presented in table IV. By arguing that breakdown occurs when a fixed amount of heat Q_B is deposited per unit volume of the sample, the relevance of these q values can be discerned from the heuristic expression

$$Q_B = K\ I_B\ g(t_d) \tag{11}$$

where K is an effective multiphoton absorption coefficient and the function $g(t_d)$ may be expressed as[4]

$$g(t_d) = \begin{cases} t_d^{-q} & \text{absence of thermal diffusion} \\ t_d^{-2q} & \text{for thin films or long laser pulse durations in the presence of thermal diffusion} \end{cases}$$

Thus, for the samples studied, in the absence of thermal diffusion breakdown incurred by pure multiphoton ionization leads to a maximal 5-photon process. This upper limit is reduced in the presence of diffusion to a 2-photon process. Since the true picture is probably somewhat less than these upper limits due to the availability of conduction electrons from avalanche processes or from other excited states (excitons, for example) we feel that multi-photon events greater than 2 probably play an insignificant role in the damage process.

4. DISCUSSION

As demonstrated in this paper the Weibull distribution is perfectly suited as a statistical tool for the analysis of dielectric breakdown of thin film optical coatings. The authors have performed a similar analysis on gas breakdown for Ar at 500 psi [3,5]. The same excellence of fit was attained, but with the major difference that β was considerably less than those values reported here, consequently leading to much larger values of σ^2. It is the contention of these authors that the Weibull distribution can be utilized to characteristically fit laser induced breakdown of any material. We must wait for experimental verification of this conjecture.

We have shown in section III that characteristic lifetimes $\bar{\tau}_d$ and breakdown intensity $\bar{I}_B$ are determinable from α (or α′). This has high practical significance since with their respective confidence bands delimits on the reliability of the material can be established [11]*. This, of course, enables computation of confidence bands around $\bar{\tau}_d$ and $\bar{I}_B$ for any material under investigation.

In regard to ascertaining the correctness of previous physical or statistical models of breakdown it seems fairly clear that coupled with experimental nonobservability of higher than 2-photon absorption [1] the $I_B\ (\bar{\tau}_d)^{-q}$ fits seem to imply that an avalanche mechanism is the most likely initiator of the plasma requisite for lattice meltdown. These fits also imply that the only other statistical avalanche mechanism for plasma creation, the lucky electron theory, is wrong since this model predicts

---

*A confidence band around a distribution function F(x) provides an interval by interval estimate of F(x). The width of the interval depends upon the confidence level $(1 - \varepsilon) \times 100\%$, $0 \le \varepsilon \le 1$. In terms of the confidence level one can be $(1 - \varepsilon) \times 100\%$ sure that F(x) lies between some upper and lower boundary curves, L(x) and U(x), respectively. For the Weibull distribution these curves are usually found in terms of the relations

$$L(x) = H_x^{-1}(\varepsilon/2); \qquad U(x) = H_x^{-1}\left(\frac{1-\varepsilon}{2}\right) \tag{12}$$

where $H_x(y)$ is the probability distribution function of the beta distribution [12].

a failure distribution Φ which varies on t and the electric field $\mathcal{E} = I^{1/2}$[3,13] as

$$\Phi = 1 - e^{-\Gamma t/\tau_c} \tag{13}$$

where

$$\Gamma = e^{-kI^{-1/2}} \tag{14}$$

k being a constant greater than zero. At damage threshold this implies for a constant value of I_B a linear dependence on t_d, while for a constant value of t_d a Gumble-like dependence on I_B (i.e., $e^{-e^{-I_B}}$) [7]. It seems fairly clear that the linear dependence on t_d is incorrect. The exponential dependence of (11) of I_B, however, often seems to fit our Weibull description for the large values of β obtained. This can be seen upon recasting Γ into the form

$$\Gamma = (I/\gamma)^{\beta} \quad , \tag{15}$$

with $\gamma > I$. Then β must be

$$\beta = \frac{kI^{-1/2}}{\ell n(\gamma/I)}$$

By defining γ as a characteristic damage intensity, $\gamma = \alpha = \bar{I}_B$, then as $I \to \bar{I}_B$, $\beta \to \infty$. Suitable values of I can be found to match the β values we found.

The strong power law dependencies exhibited here may be due to highly nonlinear microscopic mechanisms which in the macroscopic limit are averaged out, once thermal diffusion is included, to produce near linear absorption. Unfortunately it is impossible from the analysis here performed to make any definitive predictions as to the exact microscopic mechanism, other than the improbability of high order multi-photon ionizations.

APPENDIX

The Weibull distribution has frequently been employed as a time to failure model of electrical components and of DC breakdown of materials. It is one of a whole class of distributions arising from the theory of extreme values and is given by the distribution function $\Delta(y)$

$$\Delta(y) = 1 - e^{-(y/\alpha)^{\beta}} \qquad \begin{matrix} y \geq 0 \\ \alpha,\beta > 0 \end{matrix} \tag{A1}$$

$\Delta(y)$ has density function $\delta(y)$, mean μ, and variance σ^2

$$\begin{aligned} \delta(y) &= \beta/\alpha\ (y/\alpha)^{\beta-1}\ e^{-(y/\alpha)^{\beta}} \qquad y \geq 0 \\ &= 0\ , \qquad\qquad\qquad\qquad\qquad \text{elsewhere} \end{aligned} \tag{A2}$$

$$\mu = \alpha\Gamma\ (1/\beta + 1),$$

$$\sigma^2 = \alpha^2\ \left\{\Gamma(2/\beta+1) - \Gamma^2\ (1/\beta+1)\right\}$$

The theory of extreme events poses the following problem:

Given n samples $\left\{ X_1, \ldots, X_n \right\}$ drawn randomly and independently from a population with density function f(x) [distribution function F(x)] let us define y_n such that

$$y_n = \min_n \left\{ X_1 \ldots, X_n \right\} \tag{A3}$$

The distribution function for y_n is formally

$$\begin{aligned} G_n(y) &= \text{Prob}\ (y_n \leq y) \\ &= 1 - \text{Prob}\ (y_n > y) \end{aligned} \tag{A4}$$

From (A3) and the independence of all the X_i, the second equation in (A4) may be rewritten as

$$\begin{aligned} G_n(y) &= 1 - \text{Prob}\ \left(\bigcup_{i=1}^{n} X_i > y \right) \\ &= 1 - [1-F(y)]^n \end{aligned} \tag{A5}$$

For relatively simple distribution functions F(y) such as uniform and exponential distributions, $G_n(y)$ has a rather simple structure. In general, however, it is a fairly complicated function. In the limit as n becomes large it is therefore much more convenient to utilize an asymptotic relation for $G_n(y)$. This is derivable by defining the new random variable

$$\zeta_n = nF(y_n) \tag{A6}$$

such that for any fixed u, $o \leq u \leq n$

$$\begin{aligned} \text{Prob}\ (\zeta_n \leq u) &= \text{Prob}\ \left(nF(y_n) \leq u\right) \\ &= \text{Prob}\ \left(y_n \leq F^{-1}\ (u/n)\right) \\ &= \Delta_n\ (u) \end{aligned} \tag{A7}$$

By virtue of (A4) and (A5) $\Delta_n(u)$ is

$$\Delta_n(u) = 1 - \left(1 - u/n\right)^n \tag{A8}$$

which in the limit as $n \to \infty$ converges in distribution to Δ,

$$\lim_{n\to\infty} \Delta_n(u) = \Delta(u) = 1 - e^{-u} \tag{A9}$$

By now choosing the underlying distribution of the X_j's as a power law

$$\begin{aligned} F(X_j) &= 0 && X_j < 0 \\ &= \left(X_j/\alpha\right)^\beta && 0 \le X_j \le \alpha \end{aligned} \tag{A10}$$

then

$$\begin{aligned} \zeta_n &= n\left(y_n/\alpha\right)^\beta \\ y_n &= \alpha\, n^{-1/\beta}\, \zeta_n^{1/\beta} \end{aligned} \tag{A11}$$

and Δ becomes

$$\begin{aligned} \Delta(y) &= 1 - e^{-(y/\alpha)^\beta} && y \ge 0 \\ &= 0, && \text{elsewhere} \end{aligned} \tag{A12}$$

One should note that when $\beta = 1$, $F(X_j)$ is uniformly distributed and Δ reduces to the Poisson distribution characteristic of the lucky electron theory (as a function of time).

As (A1) is derivable from an asymptotic analysis of minima, a similar procedure given the random variable

$$z_n = \max_n \left\{X_1, \text{--}, X_n\right\} \tag{A13}$$

with distribution function

$$\begin{aligned} H_n(z) &= \text{Prob}\,(z_n \le z) \\ &= \left[F(z)\right]^n \end{aligned} \tag{A14}$$

will upon defining ξ_n as

$$\xi_n = n\left(1 - F(z_n)\right) \tag{A15}$$

result in an asymptotic distribution function $\Lambda_n(v)$, $0 \le v \le n$, of maxima

$$\begin{aligned} \Lambda_n(v) &= \text{Prob}\,(\xi_n \le v) \\ &= 1 - (1 - v/n)^n \end{aligned} \tag{A16}$$

As $n \to \infty$ Λ_n also converges in distribution to

$$\Lambda(v) = \lim_{n\to\infty} \Lambda_n(v) = 1 - e^{-v} \tag{A17}$$

Corresponding to the Weibull distribution, if as our underlying density for the X_j we choose

$$f(X_j) = 0 \qquad X_j \leq 0$$
$$= \beta'/\alpha' \, (\alpha'/X_j)^{\beta'+1} \tag{A18a}$$

then

$$F(X_j) = 1 - (\alpha'/X_j)^{\beta'} \tag{A18b}$$

and

$$\Lambda(z) = e^{-(\alpha'/z)^{\beta}} \tag{A19}$$

ACKNOWLEDGEMENTS

We authors would like to thank R. Mensing, W. L. Smith, and D. Milam for their helpful discussions. Special thanks go to D. Milam for supplying us with the damage data here analyzed.

REFERENCES

[1] Reviews of laser-induced breakdown in optical materials are given in: N. Bloembergen, IEEE J. Quant. Elect. QE-10, 375 (1974); W.L. Smith Opt. Engr. 17, 489, 1978.

[2] P. Liu, W.L. Smith, H. Lotem, J.H. Bechtel, N. Bloembergen, and R.S. Adhav, Phys. Rev. B 1978 (in press).

[3] D. Milam, R. A. Bradbury, and R. H. Picard, in Laser Induced Damage in Optical Materials: 1975 (NBS Special Publication 435), p. 347 (1975).

[4] R. H. Picard, D. Milam, R. A. Bradbury, and J. C. C. Fan, in Laser Induced Damage in Optical Materials: 1975 (NBS Special Publication 435), p. 272 (1975).

[5] Data supplied by D. Milam, private communication.

[6] A. A. Griffith, Phil. Trans. Roy. Soc. 221A, 163 (1920).

[7] E. Gumbel, "Statistical Theory of Extreme Values and Some Practical Applications, Appl. Math. Series 33, NBS (1954).

[8] J. H. K. Kao, Technometrics 1, 389 (1959).

[9] P. H. H. Fischer and K. W. Nissen, IEEE Trans. Elect. Insul. EI-11, 37 (1976).

[10] H. T. Davis, "The Theory of Econometrics (Bloomington, Ind. 1941), p. 23.

[11] G. J. Hahn and S. S. Shapiro, "Statistical Models in Engineering", (John Wiley and Sons, New York, 1968).

[12] J. H. K. Kao, Proc. 6th Nat. Symp. Reliability Quality Control in Electron., pp. 190-201, 1960.

[13] M. Bass and H. H. Barrett, IEEE J. Quant. Electron. QE-8, 338 (1972).

Al_2O_3 TABLE IA

GW/cm^2	N (nsec)		β	$\alpha = \bar{t}_d$	r^2	μ	σ^2
NO BIAS, NO O_2							
$7 \leq I_B \leq 7.4$	$6.8 \leq t_d \leq 10.2$	(12)	7.46	7.84	0.878	7.36	1.36
$7.7 \leq I_B \leq 8.1$	$6.2 \leq t_d \leq 8$	(17)	15.64	6.74	0.864	6.52	0.26
$8.1 \leq I_B \leq 8.5$	$6 \leq t_d \leq 7$	(11)	15.96	6.88	0.885	6.66	0.26
$9.3 \leq I_B \leq 9.8$	$4.6 \leq t_d \leq 7.2$	(10)	7.15	6.17	0.966	5.78	0.91
$10 \leq I_B \leq 10.5$	$4.7 \leq t_d \leq 7.4$	(9)	5.73	5.37	0.939	4.97	1.01
$10.7 \leq I_B \leq 11.3$	$4.8 \leq t_d \leq 6$	(10)	14.05	5.01	0.894	4.83	0.18
10% BIAS, NO O_2							
$6.5 \leq I_B \leq 6.9$	$12 \leq t_d < 19$	(10)	5.61	17.54	0.946	16.21	11.17
$7 \leq I_B \leq 7.4$	$11 \leq t_d < 19$	(10)	6.63	12.68	0.980	11.83	4.37
$7.6 \leq I_B \leq 8$	$9 \leq t_d \leq 16$	(15)	6.50	13.60	0.972	12.67	5.20
$8.6 \leq I_B \leq 9$	$8 \leq t_d \leq 11.2$	(12)	9.47	8.80	0.978	8.35	1.12
$9.2 \leq I_B \leq 9.7$	$6.2 \leq t_d \leq 12$	(10)	5.14	7.41	0.952	6.81	2.32
$10.8 \leq I_B \leq 11.3$	$5 \leq t_d \leq 7.3$	(9)	7.48	5.72	0.948	5.37	0.72
$11.7 \leq I_B \leq 12.4$	$4.3 \leq t_d \leq 7.3$	(8)	5.21	4.62	0.913	4.25	0.98
10% BIAS, 10% O_2							
$8 \leq I_B \leq 8.4$	$10.8 \leq t_d \leq 15.5$	(12)	5.73	12.69	0.971	16.37	10.95
$9.3 \leq I_B \leq 9.8$	$7.2 \leq t_d \leq 15.7$	(12)	5.03	9.01	0.876	8.28	3.55
$11.6 \leq I_B \leq 12.2$	$4.6 \leq t_d \leq 7.6$	(10)	4.93	5.28	0.914	4.84	1.26
$12.3 \leq I_B \leq 12.9$	$3.6 \leq t_d \leq 7$	(12)	5.03	5.92	0.984	5.44	1.53
$13 \leq I_B \leq 13.7$	$3.4 \leq t_d \leq 7.7$	(11)	3.68	4.20	0.913	3.79	1.31

Table I. Thin films of alumina prepared under various sputter bias and sputtering gas conditions.

A. Distributions in t_d: The 1st and 2nd columns rowise pair individual breakdown intensities I_B with the N values of t_d (given in parentheses) to be fit to $F(t_d)$ and their respective t_d ranges. The α's denote characteristic sample lifetimes, $\bar{t}_d$.

B. Distributions in I_B: The 1st and 2nd columns rowise pair individual lifetimes t_d with the N values of I_B to be fit to $F(I_B)$. The α's denote characteristic breakdown intensities, $\bar{I}_B$. β, r^2, μ, and σ^2 are, respectively, shape parameter, correlation coefficient squared, mean, and variance.

Table II. Thin films of zirconia ------. Legend description same as table I.

Table III. Thin films of silica ----. Legend description same as table I.

Table IV. Scaling law for breakdown intensity as a function of laser pulse length.

Al_2O_3 TABLE IB

nsec	N (GW/cm^2)		β	$\alpha = \bar{T}_\beta$	r^2	μ	σ^2
NO BIAS, NO O_2							
$5 \leq t_d \leq 5.3$	$8.7 \leq I_B \leq 11.3$	(13)	11.90	10.68	0.969	10.23	1.09
$5.4 \leq t_d \leq 5.7$	$8.8 \leq I_B \leq 11.2$	(9)	9.62	9.12	0.905	8.66	1.17
$6 \leq t_d \leq 6.3$	$7.9 \leq I_B \leq 11$	(10)	8.70	8.49	0.949	8.03	1.21
$6.7 \leq t_d \leq 7$	$7.4 \leq I_B \leq 10.2$	(22)	13.20	7.89	0.900	7.59	0.49
$7.2 \leq t_d \leq 7.6$	$6.3 \leq I_B \leq 10.3$	(9)	6.18	7.29	0.984	6.77	1.63
10% BIAS, NO O_2							
$7.2 \leq t_d \leq 7.6$	$9.2 \leq I_B \leq 11.7$	(11)	13.21	9.65	0.969	9.28	0.73
$14 \leq t_d \leq 14.7$	$6.5 \leq I_B \leq 8$	(9)	14.35	7.73	0.919	7.45	0.40
10% BIAS, 10% O_2							
$5.5 \leq t_d \leq 5.8$	$11.3 \leq I_B \leq 14.2$	(8)	12.26	12.22	0.963	11.72	1.35
$10.5 \leq t_d \leq 11$	$8.2 \leq I_B \leq 10.5$	(11)	11.20	9.88	0.967	9.44	1.04

ZrO_2 TABLE IIA

GW/cm^2	N (nsec)		β	$\alpha = \bar{t}_d$	r^2	μ	σ^2
NO BIAS, A_r ONLY							
$7 \leq I_B \leq 7.4$	$7 \leq t_d \leq 9.8$	(14)	8.14	8.89	0.933	8.38	1.49
$7.5 \leq I_B \leq 7.9$	$2 \leq t_d \leq 8.8$	(10)	1.99	8.19	0.732	7.26	14.52
$8.3 \leq I_B \leq 8.7$	$4.4 \leq t_d \leq 7.7$	(10)	5.67	5.12	0.993	4.73	0.93
$8.8 \leq I_B \leq 9.2$	$4.2 \leq t_d \leq 5.8$	(13)	10.06	4.70	0.938	4.47	0.29
$9.4 \leq I_B \leq 9.9$	$1 < t_d \leq 5.1$	(9)	7.63	4.09	0.739	3.84	0.36
$9.8 \leq I_B \leq 10.3$	$1 < t_d \leq 4.3$	(11)	1.43	3.72	0.775	3.38	5.75
30% BIAS, NO O_2							
$8.8 \leq I_B \leq 9.2$	$13.5 \leq t_d < 20$	(10)	6.62	15.34	0.956	14.31	6.41
$9.3 \leq I_B \leq 9.8$	$10.5 \leq t_d \leq 17$	(12)	7.33	14.94	0.974	14.01	5.08
$10.1 \leq I_B \leq 10.6$	$7.2 \leq t_d \leq 15$	(23)	5.29	9.63	0.961	8.87	3.72
$10.7 \leq I_B \leq 11.2$	$1 < t_d \leq 10.3$	(16)	4.04	6.08	0.959	5.51	2.35
$11.3 \leq I_B \leq 11.9$	$1 < t_d \leq 9$	(20)	3.10	6.26	0.966	5.60	3.90
$12.1 \leq I_B \leq 12.7$	$1 < t_d \leq 6$	(11)	1.15	4.14	0.818	3.94	11.80
30% BIAS, + O_2							
$9.3 \leq I_B \leq 9.8$	$12 \leq t_d < 20$	(12)	7.95	17.09	0.919	16.09	5.76
$9.9 \leq I_B \leq 10.4$	$13 \leq t_d < 20$	(14)	10.57	14.17	0.953	13.51	2.38
$10.7 \leq I_B \leq 11.2$	$10 \leq t_d \leq 15$	(13)	4.32	9.94	0.984	9.05	5.61
$11.3 \leq I_B \leq 11.9$	$1 < t_d \leq 13$	(11)	0.79	7.92	0.817	9.06	133.9
$12.2 \leq I_B \leq 12.8$	$1 < t_d \leq 10.3$	(13)	1.02	8.35	0.803	8.28	65.94

ZrO_2 TABLE IIB

nsec	N (GW/cm^2)		β	$\alpha = I_\beta$	r^2	μ	σ^2
NO BIAS, A_r ONLY							
$4.1 \leq t_d \leq 4.4$	$8.6 \leq I_B \leq 9.9$	(9)	20.77	9.63	0.976	9.38	0.31
$4.8 \leq t_d \leq 5.1$	$8.1 \leq I_B \leq 9.6$	(9)	19.96	9.07	0.950	8.83	0.30
30% BIAS, NO O_2							
$t_d < 1$	$10.8 \leq I_B \leq 16.7$	(16)	10.49	12.29	0.901	11.72	1.81
30% BIAS, + O_2							
$t_d < 1$	$11.2 \leq I_B \leq 16.3$	(28)	11.10	14.30	0.967	13.66	2.22

SiO_2 TABLE IIIA

GW/cm^2	N (nsec)		β	$\alpha = \bar{t}_d$	r^2	μ	σ^2
NO BIAS, NO O_2							
$7.4 \leq I_B \leq 7.8$	$7 \leq t_d < 19$	(15)	9.27	17.93	0.938	17.00	4.83
$9.6 \leq I_B \leq 10$	$6.2 \leq t_d \leq 11.2$	(15)	6.28	9.36	0.983	8.70	2.61
$10 \leq I_B \leq 10.4$	$2.7 \leq t_d \leq 9$	(13)	2.74	7.78	0.865	6.92	7.44
$11.8 \leq I_B \leq 12.2$	$3.3 \leq t_d \leq 4.8$	(13)	8.90	4.40	0.977	4.16	0.31
BIAS SPUTTERED							
$6.4 \leq I_B \leq 6.8$	$7.7 \leq t_d \leq 10$	(7)	9.19	8.10	0.922	7.68	1.00
$6.7 \leq I_B \leq 7.1$	$7.4 \leq t_d \leq 9$	(11)	17.89	7.81	0.915	7.58	0.27
$9.4 \leq I_B \leq 10.2$	$3.4 \leq t_d \leq 4.5$	(8)	12.20	4.18	0.935	4.01	0.15
BIAS SPUTTERED, + O_2							
$6.8 \leq I_B \leq 7.2$	$8.8 \leq t_d \leq 12$	(11)	10.20	9.69	0.925	9.23	1.19
$9.8 \leq I_B \leq 10.2$	$4.3 \leq t_d \leq 5.8$	(11)	9.96	5.36	0.927	5.10	0.38
$10.9 \leq I_B \leq 11.3$	$3.2 \leq t_d \leq 4.3$	(10)	10.45	4.12	0.919	3.93	0.20
$11 \leq I_B \leq 11.4$	$3.2 \leq t_d \leq 4.3$	(9)	10.14	4.09	0.936	3.89	0.21
$11.7 \leq I_B \leq 12.1$	$2.8 \leq t_d \leq 4$	(11)	10.37	3.56	0.930	3.39	0.16

SiO_2 TABLE IIIB

nsec	N (GW/cm^2)		β	$\alpha = \bar{I}_\beta$	r^2	μ	σ^2
NO BIAS, NO O_2							
$3 \leq t_d \leq 3.3$	$11.3 \leq I_B \leq 13.3$	(10)	19.32	12.89	0.912	12.54	0.64
$3.6 \leq t_d \leq 4$	$11.8 \leq I_B \leq 12.4$	(8)	45.68	12.24	0.895	12.09	0.11
$7.8 \leq t_d \leq 8.2$	$7.2 \leq I_B \leq 10.7$	(8)	25.51	9.92	0.951	9.71	0.22
BIAS SPUTTERED							
$3.8 \leq t_d \leq 4.2$	$9.4 \leq I_B \leq 10.7$	(7)	20.24	9.55	0.834	9.30	0.32
$7.7 \leq t_d \leq 8.4$	$6 \leq I_B \leq 7.2$	(10)	18.26	6.97	0.737	6.77	0.21
BIAS SPUTTERED, + O_2							
$2.8 \leq t_d \leq 3.2$	$11 \leq I_B \leq 13.2$	(11)	19.76	12.56	0.966	12.22	0.59
$3.3 \leq t_d \leq 3.7$	$11 \leq I_B \leq 12$	(8)	30.37	11.81	0.874	11.60	0.23
$4 \leq t_d \leq 4.3$	$10.2 \leq I_B \leq 11.7$	(10)	20.50	11.31	0.853	11.02	0.44
$4.5 \leq t_d \leq 5$	$8.6 \leq I_B \leq 10.8$	(9)	13.00	10.48	0.921	10.07	0.89

TABLE IV

$$g(t_d) = \begin{cases} t_d^{-q} & \text{no diffusion} \\ t_d^{-2q} & \text{diffusion} \end{cases}$$

$I_B\, g(t_d)$	$q =$	$r^2 =$	Maximal multiphoton, no diffusion	Maximal multiphoton diffusion
SiO_2 no bias, no O_2	–0.325	0.992	3	1-2
SiO_2 bias sputtered, no O_2	–0.582	0.997	2	1
SiO_2 bias sputtered, $+O_2$	–0.532	0.993	2	1
ZrO_2 no bias, Ar only	–0.350	0.966	3	1-2
ZrO_2 30% bias, no O_2	–0.221	0.950	5	2
ZrO_2 30% bias, $+O_2$	–0.252	0.740	4	2
Al_2O_3 no bias, no O_2	–0.992	0.940	1	0
Al_2O_3 10% bias, no O_2	–0.442	0.973	2	1
Al_2O_3 10% bias, 10% O_2	–0.408	0.956	2-3	1

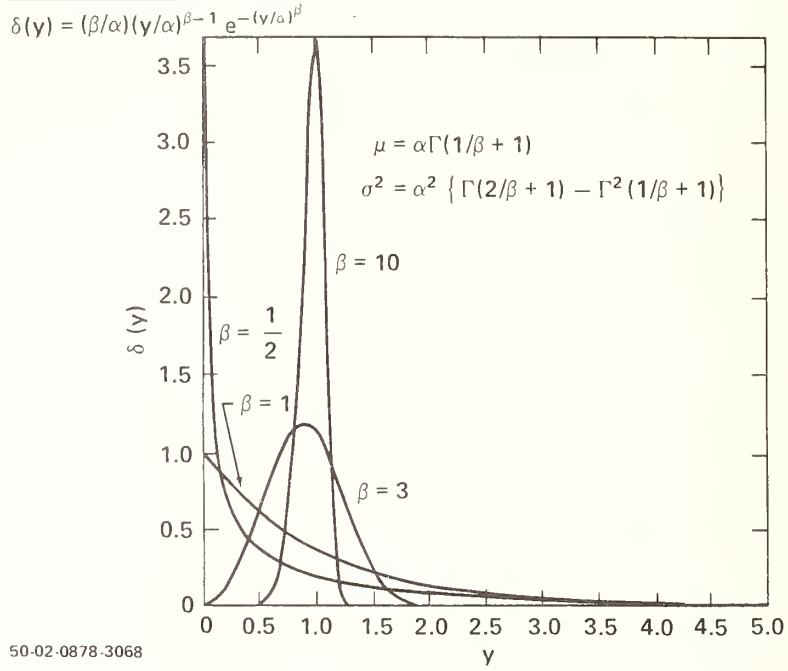

Figure 1. Graphs of the Weibull density function $\delta(y)$ for $\alpha = 1$ and $\beta = \frac{1}{2}$, 1, 3, and 10. μ and σ^2 are, respectively, the mean and variance for this distribution.

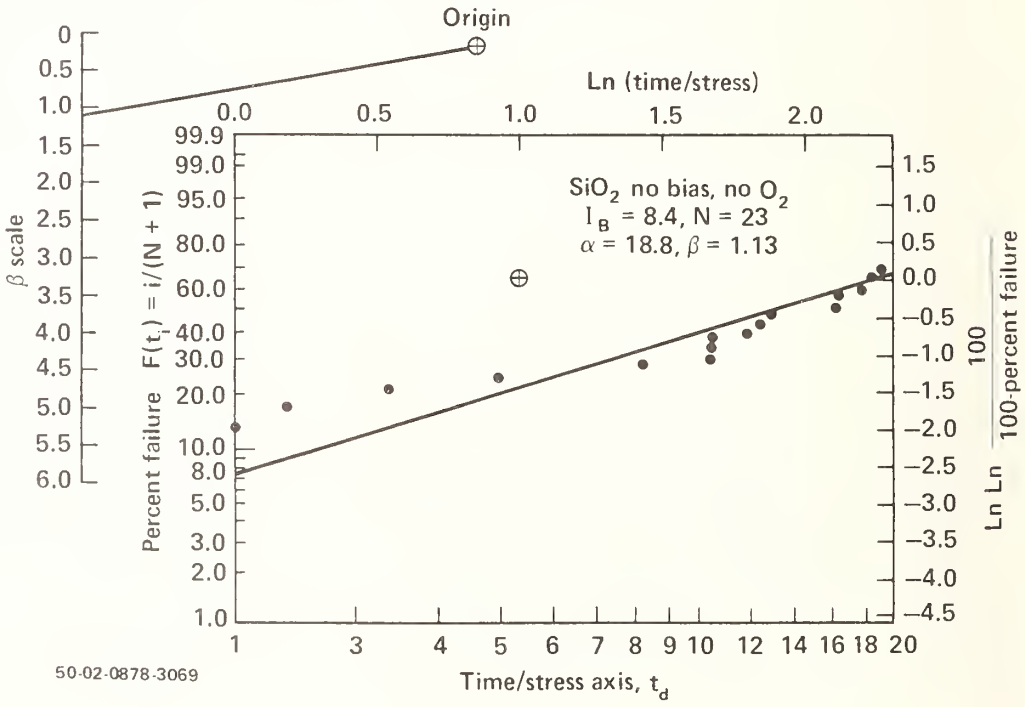

Figure 2. A plot on Weibull graph paper of the cumulative distribution of t_d (in nanoseconds), from smallest to largest, at a fixed breakdown intensity I_B of $\sim$ 8.4 GW/cm^2. The sample irradiated is a SiO_2 thin film deposited without sputter bias or O_2 sputtering gas on CG 7059 substrate. N is the total number of spots irradiated, of which 16 damaged, α is the characteristic sample lifetime, and β the shape fitting parameter.

NEW COATING MATERIALS FOR IR LASER OPTICAL COMPONENTS*

R.C. Pastor, J.A. Harrington, L.E. Gorre, and R.K. Chew
Hughes Research Laboratories
Malibu, California 90265

Six materials (LaF_3, PrF_3, CeF_3, BiF_3, $KGaF_4$, and BiI_3) were prepared and optical evaluated for use as thin film coating materials at 3.8 and 9.27 μm.

Key words: Infrared laser windows; materials purification; Reactive Atmosphere Process (RAP) chemistry; thin film coating materials.

1. Introduction

An optical coating materials purification program was initiated to study new materials which have the potential of producing infrared coatings with improved mechanical and optical properties. The materials studied included three rare-earth fluorides, LaF_3, CeF_3, and PrF_3 along with BiF_3, BiI_3, and $KGaF_4$. Using a purification procedure involving Reactive Atmosphere Process (RAP), it was hoped that an intrinsic bulk absorption coefficient near 0.1 cm^{-1} could be achieved. As will be shown, the bulk absorption of the rare-earth fluorides ranged between 0.6 and 0.9 cm^{-1}.

2. Materials synthesis and purification

2.1 Rare-earth fluorides; CeF_3, PrF_3, and LaF_3

Rare-earth fluorides have long been used as durable coating materials at visible wavelengths. Since their transmission range in the infrared extends to approximately 10 μm, it was felt that highly purified material may be a good thin film material from 3 to 9.5 μm. Each of the three fluorides, CeF_3, PrF_3, and LaF_3 were readily prepared from four- to five-nines pure sesquioxide, R_2O_3 where R = La, Ce and Pr. The oxide was first wet-converted to RF_3 by treatment with an excess of HF(aq) which contained 49% by weight of HF. Teflon wares were used. Since wet conversion is usually only 95% complete, anion purification was completed by dry conversion. The latter step consisted of treating the residue from wet-conversion with a dry mixture of HF/He at 700°C.

These RF_3 powders were compacted by melting (carbon crucible) under HF/He and cooling slowly. Transparent castings, 5-cm diameter, were obtained reproducibly with this technique.

2.2. Bismuth Trifluoride, BiF_3

The starting material was Bi_2O_3, five-nines pure in the cation. The first step in processing was wet conversion, following the same procedure as in the case of RF_3, above. Characterization of the product by x-ray powder pattern shows that the highest phase purity is achieved in the wet-converted material. The material is very white. All attempts to process further under HF/He at a higher temperature led to the gray powder. Hence, DTA characterization of the melting point was not feasible due to the progressive decomposition of the material with each thermal cycling. An open-cup run with the material under a flow of He shows one broad endotherm which starts at 630° or 650°C depending on the conditions of outgas of the apparatus. Such a run is irreversible because the sample volatilizes in the first heatup. With the material bottled inside a platinum capsule, cold-welded in vacuum after a thorough outgassing

* This work was carried out under Contract No. F33615-77-C-5049, under the sponsorship of the Air Force Materials Laboratory, Wright-Patterson Air Force Base (Dayton, Ohio).

[1] [1], two unresolved endotherms at 680° and 745°C result. These results were reproduced after ten consecutive thermal cyclings. It is possible that melting occurs at 680°C and overlaps with boiling at 745°C.

It appears that the published thermal characterization of this material is in an unsatisfactory state. Cubicciotti reports melting at 649 ± 2°C [2], von Wartenberg at 725-730°C [3], and Darnell and McCollum at 755 ± 5°C [4]. Cubicciotti suspects that von Wartenberg's high result stems from oxide contamination. He also points out that Darnell and McCollum used a boron nitride container which is corroded by BiF_3. Our criticism of Cubicciotti's work is that he used a gray powder and makes no mention of a reproducible melting behavior with one sampling. As mentioned above, the DTA run which yields one endotherm in this thermal region is irreversible and is complicated by the overlap of another endothermic process, volatilization.

The problems in materials processing stem from the following behaviors:

1. Corrosive action on metal-oxide ceramics can arise from HF released by the hydrolytic action of outgas H_2O:

$$BiF_3 + H_2O(g) \rightarrow BiOF + 2HF(g). \quad (1)$$

2. Corrosive action on metals is due to free Bi resulting from four possible causes:

   a. Dissociation of the oxide impurity at high T,

$$3\ BiOF \rightarrow BiF_3 + 2Bi + \frac{3}{2}\ O_2. \quad (2)$$

   b. Reduction of the oxide impurity by trace organic matter,

$$4BiF_3 + 3C \rightarrow 4Bi + 3\ CF_4(g), \text{ DOES NOT OCCUR.} \quad (3)$$

$$3BiOF + 3C \rightarrow BiF_3 + 2\ Bi + 3\ CO(g). \quad (4)$$

   c. Free Bi, being below H_2 in the emf series, is not reconverted to BiF_3 by HF,

$$Bi + 3\ HF(G) \rightarrow BiF_3 + \frac{3}{2}\ H_2(g). \quad (5)$$

   d. Free Bi may be formed by disproportionation at high T,

$$5BiF_3 \rightarrow 2\ Bi + 3\ BiF_5. \quad (6)$$

We have not found thermodynamic data in BiF_5 to make an estimate of the lower limit of T for Eq. (6).

These problems of further processing at higher T led us to resort to a procedure for roon-temperature compaction of the wet-converted powder. One-inch diameter billets are conveniently produced by pressing under N_2 at 38,200 psi/30m at 25°C. The density of the compact is 5.36 ± 0.02 g cm^{-3}, which is somewhat higher than the value in the handbook, 5.32 g cm^{-3} [5].

2.3. Potassium tetrafluogallate, $KGaF_4$

This is the only binary system in the group of materials studied. The synthesis recipe which yields the highest anion purity is based on using an equimolar mixture of the nitrates of potassium and gallium. The mixture is gradually heated (decomposed) to 700°C, under HF/He, in a platinum-lined carbon boat.

Depending upon the atom ratio of K:Ga, various stoichiometries (compounds) are possible in the $KF-GaF_3$ system. These compounds and the melting behavior are as follows:

K_3GaF_6 -- Reported to melt congruently at 1012°C [6]. We observe one sharp endotherm at 986°C. The material appears to be quite hygroscopic. Solid-solid transitions are reported at 172° and 239°C [6].

---

1. Figures in brackets indicate the literature references at the end of this paper.

K_2GaF_5 -- Melts incongruently at 600°C (ref. 6).

$KGaF_4$ -- A solid-solid transition at 530°C is followed by incongruent melting at 588°C [6]. We observe two separate endotherms at 534° and 566°C.

Our temperature assignments were based on the following melting-point calibrations of the thermocouple: Au, 1063°C; Ag, 960.8°C; Sb, 630.5°C; Zn, 419.5°C; Cd, 320.9°C; and Sn, 231.9°C.

These compounds are linked to each other by the ease of dissociating of KF. For instance, three consecutive thermal cyclings under Ar yielded a progressive change in the endotherm [7]. This led to the speculation of dissociation,

$$K_3 GaF_6 \rightarrow K_2 GaF_5 + KF. \quad (7)$$

The interpretation appears to be in error, probably due to unsuspected low-level hydrolysis. Our sample of K_3GaF_6 was synthesized under HF/He and the phase purity was substantiated by x-ray powder pattern. Such a sample, bottled in a sealed platinum capsule that has been thoroughly outgassed (cf. ref. 1) shows only one sharp endotherm, which corresponds to melting. This endotherm pattern persisted after seven consecutive thermal cyclings.

Regarding the dissociation linking K_2GaF_5 to $KGaF_4$,

$$K_2GaF_5 \rightarrow KGaF_4 + KF, \quad (8)$$

we observed the appearance of an extraneous phase, identified by x-ray to be K_2GaF_5, in certain preparations of $KGaF_4$. However, in these cases, we also knew that the anion purity of the product was not the highest achievable. When a more rigid control of the HF/He atmosphere and exclusion of oxide impurity was exercised in the preparation of $KGaF_4$, no evidence of K_2GaF_5 was obtained. We still have to resolve the question on whether K_2GaF_5 is a legitimate phase under reactive atmosphere processing.

The preceding discussion indicates that x-ray shows that phase purity in the preparation of $KGaF_4$ is sensitive to anion purity. Under HF/He, we have verified by x-ray that $KGaF_4$ sublimes without decomposition, a feature of interest to film deposition of binary compounds.

Using the platinum-capsule method (cf. ref. 1), we obtained the endograms shown in figure 1. The two endotherms are reproduced after the eighth thermal cycling (not shown). The solid-solid transition at 534°C precludes single-crystal growth. Thus, $KGaF_4$ was compacted as a polycrystalline ingot by melting and crystallizing under HF/He.

2.4. Bismuth Tri-iodide, BiI_3

The starting material is five-nines pure Bi metal. The metal is freed of low-level oxide contamination by trickling through a bed of spectroscopic-grade carbon, using the apparatus scheme shown in figure 2a. The compound (BiI_3) was synthesized by reacting the purified elements in a vitreous-silica ampoule that was sealed off in vacuum. The details of the apparatus are given in figure 2b.

The reported melting point of this material has steadily decreased with the passage of time; presumably, the trend correlates with the improvement in the purity of the material. The usual handbooks up to 1967, report a melting point of 439°C [8]. Cubicciotti and Keneshea report 408.6°C [9]. A more recent handbook (cf. ref. 5, p. B-182) lists 408°C. Darnell and McCollum (cf. ref. 4), report 407.5 ± 1.0°C. These determinations do not comment on the question of reproducibility on one sampling. Again, this issue is pertinent because of hydrolysis by outgas H_2O and the fact that the solid and the melt are volatile. Our DTA measurement, using the sealed platinum-capsule (cf. ref. 1), yields a sharp endotherm corresponding to a melting point at 404°C. This behavior remained unchanged after three thermal cyclings. We realize that our method is a determination of the triple point and

not the melting point. For the present, we do not distinguish between the two characterizations because the pressure difference is less than one atmosphere. The effect of pressure on the fusion temperature is 0.02 to 0.03°C atm^{-1} [4].

Because of volatility problems, single-crystal growth (2-cm diameter) by a vertical-Bridgman mode was carried out in a sealed vitreous-silica crucible. The charge consisted of a polycrystalline ingot, compacted by melting under I_2/He. The crucible was then sealed off at 10^{-2}mm Hg. The melt was soaked at 475°C/1h. Crystal growth was carried out at a constant lowering rate of the crucible. A foliated texture, characteristic of a layer-lattice crystal, resulted at a lowering rate of 7.5 mm/h and at 1.6 ± 0.1 mm/h. To obtain a more coherent texture, the 2-cm diameter crystal cylinder was forged to a 2.5-cm diameter billet at 210°C/ 9400 lbs.

The room-temperature crystal density is 5.79 g cm^{-3}. A value of 5.64 g cm^{-3} is reported [10]. The latter value, also seen in a 1967 compilation (cf. ref. 8), is too low. A value of 5.8 g cm^{-3} is reported in the eleventh edition of reference 8, and 5.78 g cm^{-3} on p. B-182 of reference 5. Our measurement is in good agreement with the later compilation.

3. Optical evaluation of bulk materials

3.1. Rare-earth fluorides

The optical transmission of the three rare-earth fluoride castings is shown in figure 3. From the figure it can be seen that only LaF_3 exhibits no absorption bands between 3 and 10 μm, thus making it the only material of the three that would be a good coating material between 2 to 4 μm. CeF_3 and PrF_3 suffer optically from intense electronic absorption bands between 3.5 to 6 μm due to low lying Stark levels of the Ce^{3+} and Pr^{3+} ions [11]. The multiphonon edges in figure 3 are the high energy side of the reststrahl peak and may be used to estimate the ultimate limiting absorption in the more transparent regions of the solid [12].

To estimate the multiphonon or intrinsic absorption at 9.27 μm, the log of the absorption coefficient β was plotted versus frequency ω. Since $\beta \propto e^{-A\omega}$ [12], interpolation or extrapolation of the data yields the intrinsic β at the wavelength of interest. Figures 4 to 6 are plots of the multiphonon edges for CeF_3, LaF_3, and PrF_3. From these curves, the intrinsic β at 9.27 μm was determined to be CeF_3, 0.84 cm^{-1}, LaF_3, 0.66 cm^{-1}; and PrF_3, 0.9 cm^{-1}. These values are all greater than the desired goal of 0.1 cm^{-1} nevertheless, these materials should still produce low loss thin films at 9.27 μm. No evaluation was made on the LaF_3 at 3.8 μm but this material should be a good film material at the DF laser wavelength owing to the lack of structure in the ir transmission in this region (cf. figure 3).

3.2. BiF_3, $KGaF_4$, and BiI_3

It was not possible to evaluate single crystal BiF_3 because large single crystals could not be fabricated. Therefore, pellets of KBr:BiF_3 were pressed and ir transmission data were taken. The BiF_3 pellets showed generally a featureless spectrum except for one pellet which had an absorption band at 13.5 μm. $KGaF_4$ was evaluated as a translucent solidified mass. There were small absorption bands at 8.9 μm and 10.3 μm. Pellets of $KGaF_4$ exhibited even more structure beyond 16 μm. This structure is somehow associated with the GaF_3 as it shows up in pure GaF_3 pellets too. A thin section of single crystal BiI_3 yields a flat ir transmission from 2.5 to 20 μm.

4. Conclusions

We have synthesized and purified three rare-earth fluorides, LaF_3, CeF3, and PrF_3, BiF_3, BiI_3, and $KGaF_4$ for use as coating materials at infrared laser wavelengths. The rare-earth fluorides have absorption coefficients between 0.6 and 0.9 cm^{-1} at 9.27 μm and only LaF_3 would be a good material of the three rare-earths at 3.8 μm.

While it was not possible to grow large single crystals of BiF_3 of $KGaF_4$, these materials appear to have low absorption at 9.27 and 3.8 μm. BiI_3 looks particularly attractive due to its flat response between 2.5 and 20 μm.

5. Acknowledgments

The authors would like to thank the following for their assistance: M. Robinson for crystal casting the rare-earth fluorides; R. Turk and N. Ramirez for compaction of BiF_3 and BiI_3; A. Timper for x-ray analysis of BiF_3 and $KGaF_4$; K. Arita for casting $KGaF_4$; A. W. Robertson for pellet pressing and ir spectra; and M. Braunstein for overall program management.

6. References

[1] For details of the procedure, see R. C. Pastor and M. Robinson, Mat. Res. Bull. 9, 569 (1974).

[2] D. Cubicciotti; J. Electrochem. Soc. 115 (No. 11), 1138 (1968).

[3] H. von Wartenberg, Z. Anorg. U. Allgem. Chem., 244, 337 (1940).

[4] A. J. Darnell and W. A. McCollum, J. Phys. Chem., 72 (no. 4), 1327 (1968).

[5] "Handbook of Chemistry and Physics," by R. C. Weast (editor), 49th Edition, page B-182 (The Chemical Rubber Co., 1968-1969).

[6] J. Chassang, Rev. Chem. Min. 5, 1115 (1968).

[7] I. V. Tananaev and T. B. Vorotilina, Iz. Akad. Nauk SSSR, Neorg. Mater., 5 (No. 4), 752 (1969).

[8] For instance, see "Lange's Handbook of Chemistry," by N. A. Lange (editor), Tenth Edition, pp. 244-245 (McGraw Hill, 1967).

[9] D. Cubicciotti and F. J. Keneshea, J. Phys. Chem. 63, 295 (1959).

[10] "Comprehensive Inorganic Chemistry," by A. F. Trotman-Dickenson (Executive Editor), Vol. 2, pp. 589-590 (Pergamon Press, 1973).

[11] R. A. Buchanan, H. E. Rast, and H. H. Caspers, J. Chem. Phys. 44, 4063 (1966).

[12] For a review of multiphonon absorption see M. Hass and B. Bendow, Appl. Opt. 16, 2882 (1977).

7. Figures

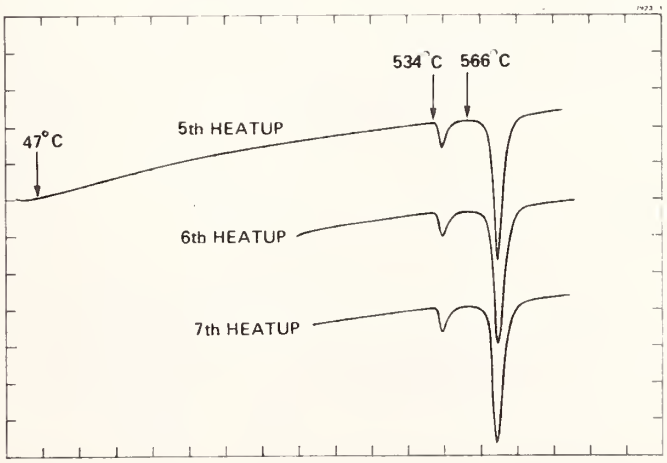

Figure 1. Heatup curves for $KGaF_4$ cold-welded in a platinum capsule at 10^{-6} mm Hg (Ref. 1). The satellite endotherm shows a solid-solid transition; the main endotherm is claimed to be incongruent melting (Ref. 6).

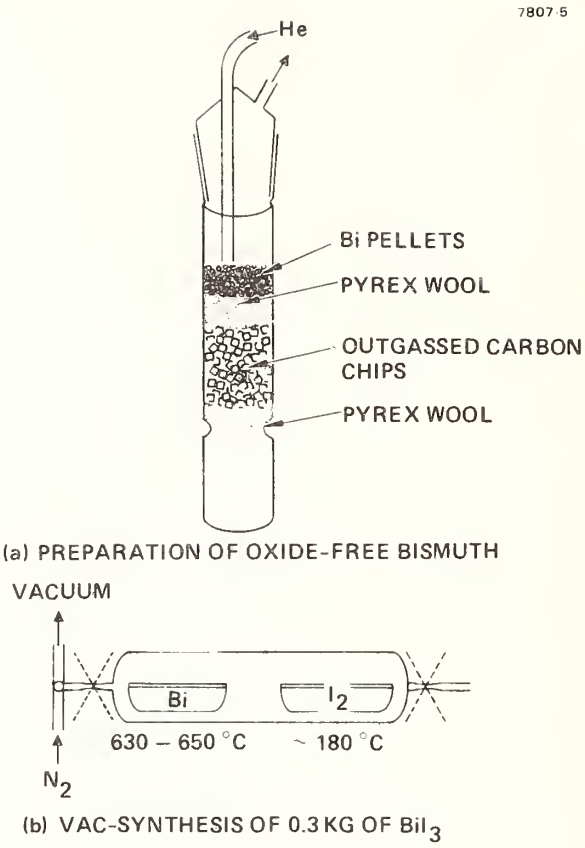

Figure 2. Purification and synthesis of BiI_3. (a) Preparation of oxide-free bismuth. (b) Vac-synthesis of 0.3 kg of BiI_3.

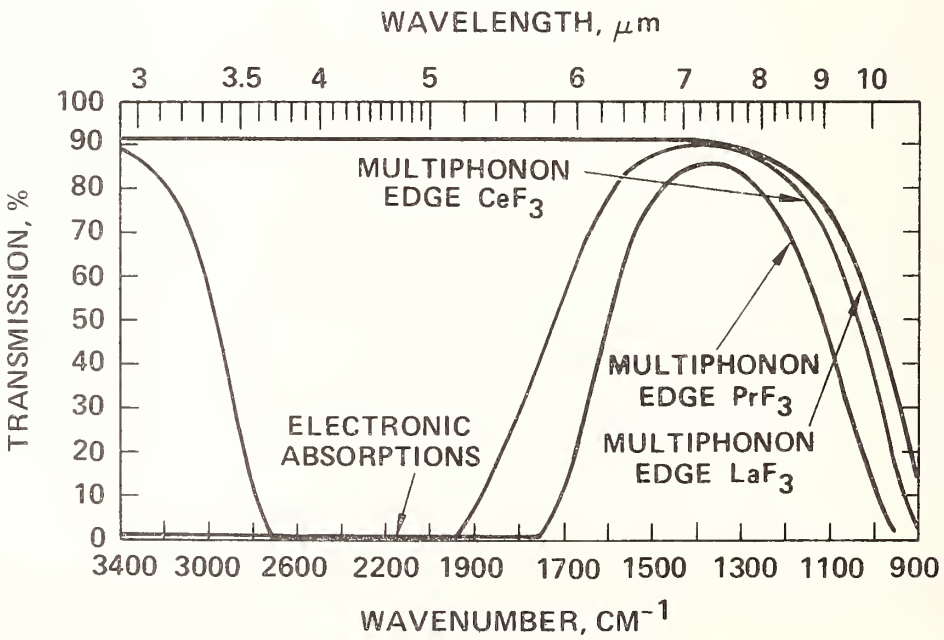

Figure 3. Infrared transmission spectra of rare earth trifluorides.

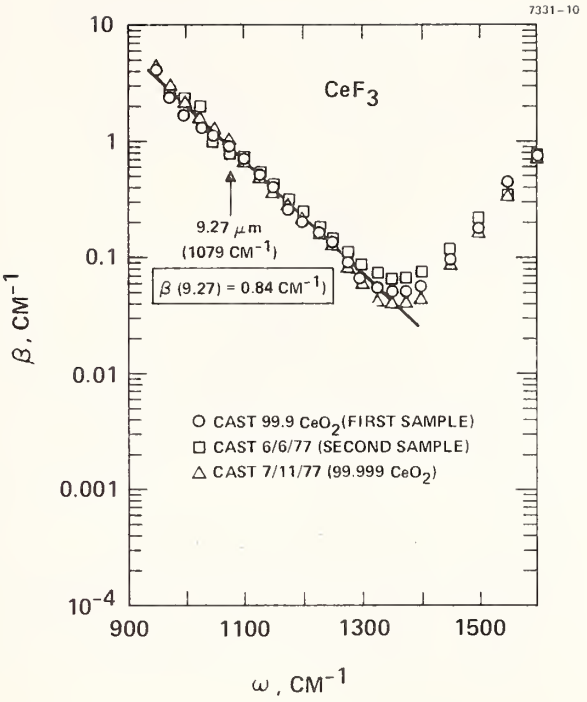

Figure 4. Multiphonon curve of CeF_3 for interpolation of β at CO_2 laser frequencies.

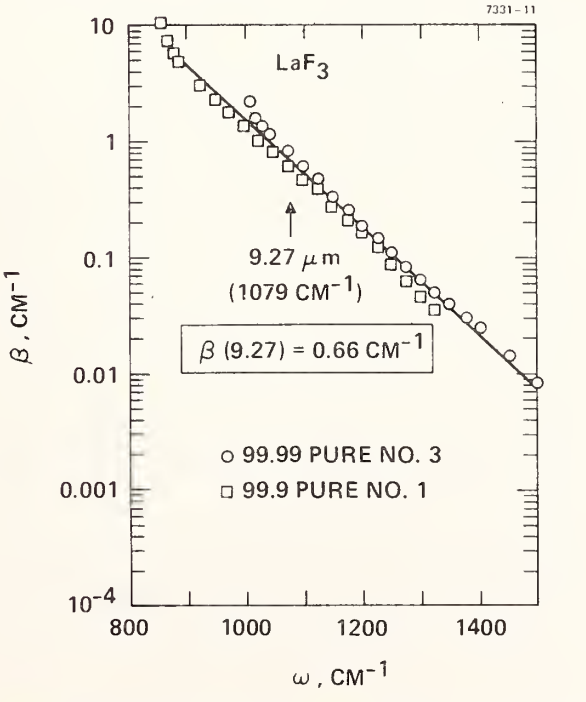

Figure 5. Multiphonon curve of LaF_3 for interpolation of β at CO_2 laser frequencies.

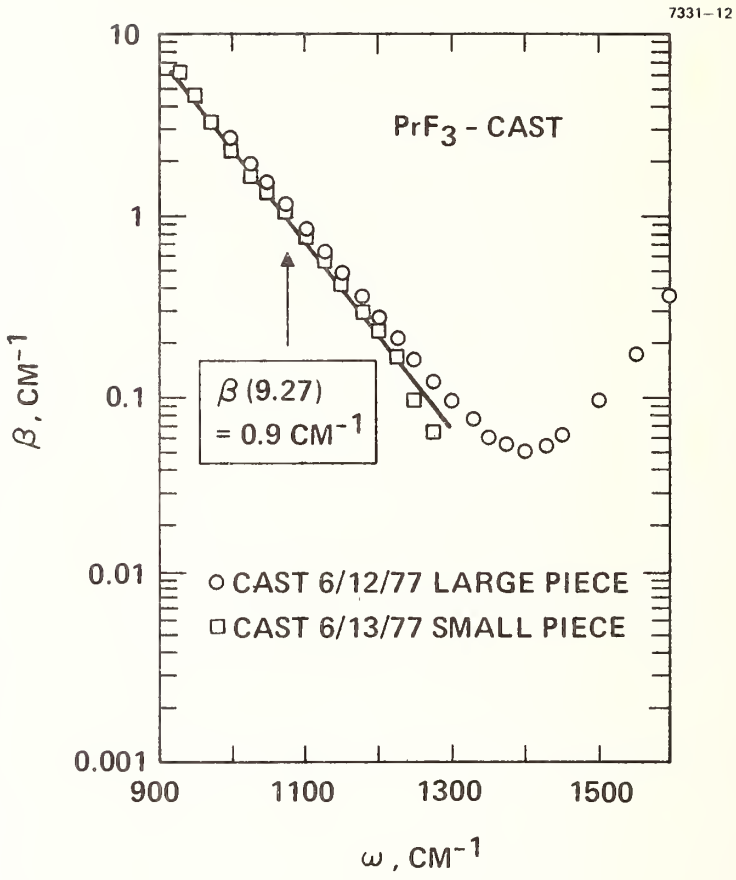

Figure 6. Multiphonon curve of PrF_3 for interpolation of β at CO_2 laser frequencies.

IMPROVED PbF_2 COATINGS FOR THE INFRARED*

P. Baumeister
Aerojet Electrosystems Co.,
Div. of Aerojet-General Corp.
Azuza, CA 91702

and

George P. Arnold and David F. Edwards
Los Alamos Scientific Laboratory
Los Alamos, NM 87545

A technique is described for reproducibly depositing single layer PbF_2 antireflection coatings for CdSe that have a damage threshold of about 50 MW/cm^2 for 2.87 μm laser radiation. This is an 8-fold increase in damage resistance over coatings made by other methods. These same coatings applied to Ge have a damage threshold of about 22 MW/cm^2. The coated Ge value is less probably due to the index mismatch between the PbF_2 and the Ge.

Key words: antireflection coatings, CdSe, coating substrate, damage resistant, Ge, PbF_2, pulsed HF laser.

A technique has been developed for reproducibly depositing PbF_2 antireflection coatings having increased damage resistance. These PbF_2 coatings on CdSe substrates have damage threshold values of about 50 MW/cm^2 for 2.87 μm laser radiation. This is an 8-fold increase over coatings made by previous deposition methods. These damage resistant coatings have also been deposited on Ge test substrates. The technique is also applicable to other substrate materials provided the index matching problems can be surmounted.

The PbF_2 material yielding the highest damage threshold values has been single crystals obtained from Optovac, Inc., N. Brookfield, MA. PbF_2 powder and vacuum fused PbF_2 pellets, with no exceptions gave inferior damage resistant coatings.

Prior to deposition, the CdSe and Ge substrates were polished using a diamond paste on cloth lap resulting in a 20/10 or better scratch and dig surface [1].[1] No attempt was made for surface flatness. The residue of the polishing step was removed by gently scrubbing with a lens tissue and a weak Neodol** solution. The samples are then rinsed with tap water followed by a spectra grade isopropyl alcohol rinse and dried with dry nitrogen. The substrates were given a final cleaning with a glow discharge just prior to cold trapping the evaporation chamber. For this discharge cleaning, argon gas at a pressure of 0.05 to 0.1 torr was bled into the system and a glow discharge (300 ma) was maintained for 10-20 minutes.

Platinum was found to be the best boat material for evaporating the PbF_2. A few depositions were made using a vitreous carbon boat that had a higher outgassing rate than the Pt boat. For this reason and since there was no evidence of chemical reaction between the Pt boat and the crystalline PbF_2, the Pt boat was used for most depositions. A Balzer BA-500 system with thermal evaporation was used for all depositions. With this system pressures of 1 to 3 x 10^{-6} torr are routinely achieved.

The source and substrate holder are located close to the center line of the chamber. The evaporated material impinged on the substrates 4 to 8 degrees from normal.

The PbF_2 was deposited at a rate of about one quarter wave per minute at 632.8 nm which corresponds to a physical thickness rate of about 100 nm/min. To maintain the constant deposition rate the electrical power to the boat required continuous adjustment because the PbF_2 sublimes rather than melts at the deposition temperature. With the Pt boat the chamber pressure remained approximately constant during the PbF_2 evaporation.

The coating thickness was monitored during deposition by measuring the substrate reflectance at 550 nm. Single layer coating of PbF_2 one quarter wave thick at 3 μm was applied to several CdSe and Ge substrates. A few CdSe substrates had thin (about 25 nm) ZnS adhesor layers deposited prior to the PbF_2 layer.

The damage threshold measurements were made at 2.87 μm using the HF oscillator-amplifier system previously described [2]. The samples were placed near the focal plane of the output lens of this laser

* Work performed under the auspices of the U. S. Department of Energy.

** Neodol - Shell Oil Company trade name for ethoxysulfate alcohol detergent.

1. Figures in brackets indicate the literature references at the end of this paper.

system. This lens is used as a 6:1 magnifier to enlarge the beam waist. The laser pulse is near Gaussian with a 120 nsec width (FWHM). The spatial profile has some structure. The beam spot size was measured from a burn pattern on darkened photographic paper. The burn patterns were approximately circular and were from 1.3 to 3.5 mm in diameter depending on the position relative to the focal plane.

For the damage measurements the samples were progressively positioned nearer the focal plane for increased power densities in the samples. The laser spot size changes, but the damage threshold is expected to be spot size independent [3] for 2.87 μm radiation. Both N on 1 and 1 on 1 measurements were made with no apparent difference in the threshold value. Threshold was determined when there was visual evidence of a disturbed layer as viewed by a magnifying glass.

The damage threshold values are shown in table 1. These values indicate that the ZnS adhesor layer had no influence on the damage threshold level. The commercial antireflection coatings on CdSe were multilayers of ZnS and ThF_4 or single layers of PbF_2. The best coatings produced from powdered PbF_2 had damage values as high as 12 MW/cm^2. The best PbF_2 coating on Ge had a damage level about half that of $CdSe/PbF_2$. The reason for this difference is believed to be due to the index mismatch in Ge/PbF_2 resulting in higher electric fields inside the coating. From these data one can see that coatings from single crystal PbF_2 consistently have higher threshold values. Powdered PbF_2 has always formed coatings with inferior damage properties. The presence of the hydroxide, PbOH, is believed to be the cause of inferior coatings made from the powdered PbF_2. The powdered PbF_2 hydrolizes easily to form PbOH which decomposes to form metallic Pb upon heating prior to deposition. Some metallic Pb is then passed to the substrate during deposition. These metallic particles act as heat centers for the laser irradiation. Laser damage nucleates from the microscopic metallic inclusion. Examination of the damage sites using a microscope indicates that metallic inclusions could be the damage mechanism. Crystalline PbF_2 has negligible hydroxide as indicated by the lack of spectral absorption in the 2.7 μm OH band for PbF_2 crystals 2-3 cm in thickness. During the heating of powdered PbF_2 before deposition, small spherical masses are seen in the deposition boat. These are believed to be the metallic Pb particles. These spheres are not formed when crystalline PbF_2 is used as the starting material.

Table 1. Laser damage threshold values for single layer PbF_2 antireflection coatings on CdSe for a laser pulse at 2.87 μm and 120 nsec pulse width.

CdSe uncoated surface	68.5 MW/cm^2
$CdSe/PbF_2$ $\lambda/4$ at 3 μm	50.6 MW/cm^2
$CdSe/PbF_2/1/8\lambda$ ZnS	$\sim$ 50 MW/cm^2
$CdSe/PbF_2$ commercial coatings	6 MW/cm^2
Ge/PbF_2 $\lambda/4$ at 3 μm	22 MW/cm^2

References

[1] Edwards, D. F. and Lazazzera, V., J. of Physics E:Sci. Instr., 3, 156 (1970).

[2] Wenzel, R. G. and Arnold, G. P., Appl. Opt. 15, 1322 (1976); Arnold, G. P. and Wenzel, R. G., Appl. Opt. 16, 809 (1977).

[3] M. J. Soileau, private communication.

GRADED INDEX COATINGS OF CUBIC THALLIUM IODIDE (TlI) AND LEAD FLUORIDE (PbF_2)*

T. J. Moravec and R. A. Skogman
Honeywell Corporate Material Sciences Center
Bloomington, Minnesota 55420

We present a new technique for producing graded index films from alternating very thin layers of two materials. During deposition the thickness of the layers is adjusted so that the resulting average index matches the index of the profile for that total thickness. This method shows great promise for making films with any desired complicated index profile in a very straightforward manner. Results are presented for graded index AR films near 10μm made from TlI and PbF_2. The 10.6μm absorption of these films was similar to that of discrete, multilayer AR films composed of the same materials.

The alternating layer method also takes advantage of the polymorphism of TlI in thin layers to produce films in the cubic phase. We show by X-ray and optical measurements that each TlI layer possesses the CsCl structure at room temperature. It thus appears that each layer of TlI is ignorant of the existence of the previous layer of TlI due to the layer of buffer material (PbF_2).

Key Words: Thin films, Thallium Iodide, Lead Fluoride, graded index, polymorphism.

1. Introduction

Inhomogeneous films with the refractive index graded with a known and prescribed way could have improved optical properties over discrete multilayer optical coatings. By grading the index, the film/film interfaces are eliminated. Laser induced damage to thin film coatings has beem shown to occur at the interface of the films and at the substrate/film interface [1,2,3].[1] The reason is that the effective electric field strength of the light beam is a maximum at interfaces in some multilayer film stack designs. In fact, there is a definite correlation between internal field maxima and damage threshold[3]. One way to increase the damage theshold is to design coatings that minimize electric fields at the interfaces and in the materials that have larger absorption coefficients [4,5]. However, this technique has practical limitations [5].

We report here graded index AR films of TlI mixed with PbF_2 on KCl. Initial results of graded index films of this system were reported previously [6]. These two materials were chosen as representing low absorption 10.6μm high and low index, respectively, coating materials for KCl. Laser damage testing of these films has not been done. However, calorimetry measurements showed that the graded index films did not increase β over discrete AR films.

To our knowledge, grading the index from high to low for laser applications has been tried only once before. Austin et al. [7] did it for an order suppression type filter. They did not see an increase in laser damage threshold for the inhomogeneous versus the homogeneous filter. However, they did not analyze the films to see if they were truly inhomogeneous, as we have done and detailed below. We feel that the question of laser damage threshold for inhomogeneous versus homogeneous films is still unresolved.

2. Preparation of Graded Index Films

Jacobsson [8] has introduced a useful method for describing the film grading of two materials, A and B. He defines a parameter α by

$$\alpha = \frac{v_B(o)}{v_A(T)} \qquad (1)$$

where $v_A(o) = 0$, $v_B(T) = 0$, and where $v_j(t)$ is the rate of deposition of material j at time t in Å/sec varying linearly with time from t = 0 to t = T. In our case, A is PbF_2 and B is TlI. This assumes a

*This work was supported by Defense Advanced Research Projects Agency under Contract No. DAHC15-73-C-0464 ARPA Order No. A02416.

1. Figures in brackets indicate the literature references at the end of this paper.

two source evaporation with changing rates to produce the index gradient. Jacobson used simple linear mixing theory and the Clausius Mossotti Lorentz - Lorentz electric field theory to calculate the dielectric constant for the mixture in the inhomogeneous film. From this, he obtains the following expression for the refractive index as a function of distance x from the air interface for a film of total thickness H:

$$n^2(x) = \frac{n_A^2 - \beta n_B^2}{1-\beta} + \frac{\beta(1-\alpha)\,(n_A^2 - n_B^2)}{(1-\beta)\left\{(\alpha-\beta) - (1-\beta)\left[1 + (\alpha^2-1)\frac{x}{H}\right]^{-\frac{1}{2}}\right\}} \qquad (2)$$

where $\alpha = \beta\, a_1/a_2$. The parameters a_1 and a_2 are given by $a_i = (n_i^2 + 2)^{-1}$ (i = A,B).

Jacobsson goes on to develop the electromagnetic theory for the calculation of the reflection and transmission coefficients of inhomogeneous films. He also develops approximate methods and solutions for special cases, such as hyperbolic index profiles. An interesting result of this is that for some values of α the AR minimum is not very sensitive to changes in α. Since this is a difficult parameter to control experimentally, it should not be too difficult to deposit AR inhomogeneous films.

In figure 1 we show the refractive index profiles calculated from equation (2) for the T&I-PbF_2 system for some values of α. The indices used represent those at 10.6μm; 2.40 for T&I and 1.63 for PbF_2. The total thickness is H and the distance measured from the air interface is X. We can also calculate a mean refractive index versus α from these curves. This is shown in figure 2 for the T&I-PbF_2 system.

We have developed a method that will produce graded index films without rate variations. The procedure is as follows. We desire that an inhomogeneous film be made with its refractive index gradient some n(x), where x is the distance measured from the air interface as shown in figure 3. The total thickness of the film is H and the film should have an index of n_{10}(e.g., = 2.4) next to the substrate and n_0 (e.g., = 1.6) next to the air/film interface. To make this film by our method, we divide up the film into steps, for example of width H/10, with each step having an average index determined by the particular form of the gradient, n(x), such as exponential, hyperbolic, etc. The gradient could be very complicated and could possess oscillatory behavior extending over several periods The average index for step 10 in our example is 2.2. We produce this average index for thickness of increment width H/10 by evaporating first one layer that is d_{10} thick of material with index n_{10} (=2.4). This is followed by one layer of thickness (H/10 - d_{10}) of material with index n_0 (=1.6) such that

$$d_{10}n_{10} + \left(\frac{H}{10} - d_{10}\right) n_0 = \langle n_{10}\rangle \left(\frac{H}{10}\right) \qquad (3)$$

or

$$d_{10} = \frac{3}{4}\left(\frac{H}{10}\right) \qquad (4)$$

This is shown schematically in figure 4.

Thus for all $\langle n_i\rangle$, i = 10 to 1, the average indices, the thicknesses required of the discrete layers of the two materials are given by

$$d_i n_{10} + \left(\frac{H}{10} - d_i\right) n_o = \frac{H}{10}\ \langle n_i\rangle;\ i = 10 \text{ to } 1 \qquad (5)$$

This can be generalized for M increments in H as

$$d_i n_o + \left(\frac{H}{M} - d_i\right) n_M = \left(\frac{H}{M}\right) \langle n_i\rangle;\ i = M \text{ to } 1 \qquad (6)$$

Thus the sequences of high and low index materials are repeated from substrate to air interface each time the appropriate thickness of the two layers is adjusted, so that the average index is equal to n(x) for that value of x in the index profile. Obviously, a smoothly varying index profile can be approximated very well by small increments (say H/1000 or ~10Å for typical optical coatings). Most films discussed in this paper were produced with M = 50 to 100.

The advantage of this method over ones that vary the rates of the two sources, or mix the materials together before evaporation, is that very complicated index profiles n(x) can be easily reproduced. This is so because accurate control of the two rates is not required as it would be for methods that vary the rates to obtain inhomogeneous coevaporated films. This method also lends itself easily to automated control via feedback from a thickness monitor coupled with an automated shutter. We have found that it is not necessary that the individual layer thicknesses be very accurate. Because each step is much smaller than the wavelength of light used, the effect is that of an inhomogeneous gradient index film.

3. ESCA Depth Profiling

Films prepared by the above method were subject to ESCA depth profiling to insure that the films were graded in composition. ESCA was used instead of Auger spectroscopy because of severe charging effects with dielectrics.

Figure 5 shows a profile of a typical graded index film 0.2μm thick made by the step method. It can be seen that the films appear smoothly graded. This result is reassuring, for it means that our step method does make graded composition films within the accuracy of the ESCA method. Some films showed O at the film/substrate interface. It is not known if O is a contaminant here, or if it was adsorbed on the surface during measurement.

4. Experimental Results

An optical monitor was used to determine the end of the deposition run. A 5 watt continuous CO_2 laser operating at 10.6μm was used for the light source. When the transmission maximum was reached the deposition was stopped. A considerable improvement in accuracy of AR minimum could be obtained by development of an optical monitor that could operate at shorter wavelengths than the design wavelength.

Figure 6 shows the near infrared reflectivity for two graded index TlI-PbF_2 films on KCl taken with a prism on the back surface to remove that reflection. Curve 1 is a 2.5μm thick film with $\alpha \sim 1.0$ made by the step method and curve 2 is a 2.6μm film made by varying the rates with a mechanical shutter[6]. The curves are fairly similar with their minima displaced due to different thicknesses and possibly to variation in the gradation. The interesting feature is that every minimum besides the one near 10μm is very antireflecting. This agrees with theory [9]. All the graded index films had vurves similar to these. This spectra can be compared to that of a two layer AR coating that has only one AR minimum as can be seen from figure 7. Curve 2 is the two layer, and curve 3 (film produced by mechanical shutter) the graded index reflectivity in the near infrared.

Following Jacobsson [9], we can make the rough assumption that the minima of curve 2 in figure 6 are separated by $\bar{n}H/2$, where H is the thickness, and $\bar{n}$ is the average index. The $\bar{n}$ is calculated to be about 2.11 for this film. From figure 2, this gives a value of $\alpha = 1.4$, which is plotted in figure 8. This value of α is about what we might expect from a varying rate mechanical shutter arrangement for making the graded index films.

With the step method, however, profiles with different α's can easily be made. Figure 9 compares the reflectivity of sample 801191 ($\alpha \sim 1.0$) with sample 802041 where we attempted to make $\alpha = 0.2$. From the minima positions, $\bar{n}$ is calcualted to be 1.91, making $\alpha = 0.5$. The agreement is considered to be good, since the $\bar{n}$ calculation is an approximation and the run is usually terminated when the optical monitor reaches a peak in transmission regardless of where this occurs in the step sequence.

As was pointed out previously, it was difficult to determine the cutoff of the deposition using the 10.6μm optical monitor. This resulted in a range of minima between 8μm and 13μm in the films that were produced. In order to compare the width of the minima, figure 10 shows the experimentally measured minimum near 10μm of several films in which the minima were all shifted to reference to the same point and values of α. $\alpha = 0.2$ (2) is graded TlI to PbF_2 to air, while $\alpha = 0.2$ (3) is graded TlI to PbF_2 to TlI to air, which mimics a three layer design. We note the interesting result that the lower α values have broader AR minima.

Many samples were made of two layer, three layer, and graded index films of TlI and PbF_2 to determine the effect, if any, upon β of the various AR coatings. The results of these measurements are listed in ref. 10. The 10.6μm average absorption for 2 and 3 layer films was 0.717%/surface and that for the graded index was 0.548%/surface. Overall, the values are fairly high and we believe this to be due to impurities in the PbF_2 part. The source material for PbF_2 was cerac optical grade powder without further treatment. Some transmission spectra did show inorganic absorptions, but no clear pattern could be found. It would be interesting to have samples of homogeneous and inhomogeneous film design tested for laser damage threshold.

5. Physical Characteristics of TlI Films

TlI films on KCl and other alkali halides scatter visible light. The exact nature and peculiarities of this phenomenon have been explained previously [11]. Briefly, the mechanism causing the scattering is inherent in the way TlI forms on KCl. TlI nucleates and grows epitaxially on KCl. On and near the KCl (100) plane the TlI (004) plane grows parallel to the KCl surface. The TlI $\langle b_o \rangle$ direction then lies parallel to the KCl $\langle 110 \rangle$ direction lying nearest the KCl substrate surface. On the exact KCl (100) plane two KCl $\langle 110 \rangle$ directions lie directly in the surface. The orthorhombic TlI nucleates along both of these KCl $\langle 1\bar{1}0 \rangle$ directions. The result is two orientations of TlI grains whose $\langle b_o \rangle$ directions are parallel to the two orthogonal KCl $\langle 110 \rangle$ directions. Optical scattering results from the refraction of light between adjacent birefringent TlI grains whose optic axes are at right angles from one grain to the next.

These characteristics of TlI on KCl have always been observed in films of interest for infrared wavelength applications, i.e. with films of physical thickness between 0.5μm to 2.0μm. Blackman and Khan observed that thin layers of TlI <∿100-200Å had the cubic CsCl structure temperature [12]. Furthermore, Khan reported that thin layers of TlI always possessed the CsCl structure when deposited onto cleavage faces of alkali halides at room temperature [13] and at -180°C when deposited onto amorphous substrates (Formvar) [12]. Work reported by M. Shiojui et al. may offer an explanation for this phenomenon [14]. They grew TlI crystals in silicon hydrogels and found that TlI crystals always nucleated in the cubic phase. After growing to a critical size, the crystals transformed to the stable orthorhombic phase. Since the cubic orthohombic transformation in TlI proceeds by simple shear, they concluded that the gels may prevent the cubic crystals from changing to the orthohombic by shear. The same mechanism may hold for thin films of TlI held from shearing by the alternating layers of a different material.

Samples of TlI-PbF_2 step graded films were examined in our x-ray diffractometer. Table 1 shows results for a typical film. No orthorhombic TlI lines are observed. The two diffraction lines that could not be attributed to β-PbF_2 indicate the presence of cubic β-TlI with α_o = 4.21Å agrees well with that reported by Khan [13] for cubic TlI.

Figure 11 shows two photos taken in transmitted light between parallel polarizers. The left hand side represents a two-layer TlI-PbF_2 AR coating on a KCl substrate. The right hand side represents a 180 alternating layer TlI-PbF_2 graded index AR coating on KCl. The two-layer film scatters light while the laternating layer film does not.

Figure 12 shows photos taken with the polarizers crossed to extinguish the light. The left side is the two layer film and is very birefringent. The right side is the alternate layer film and is not birefringent. None of the graded index films exhibited any birefringence.

6. Conclusions

A unique technique for graded index films has been developed that shows great promise for making films with any desired index profile. The technique was used to make several films AR near 10μm. The absorption of these films was similar to absorption of discrete multilayer AR films composed of the same materials.

The alternating layer method produces films of TlI in the cubic phase. This is confirmed by x-ray analysis. Since the films are cubic they should not be birefringent. Polariscopic examination shows that they are, indeed, not birefringent. Finally, since the TlI is not birefringent, it cannot scatter light by the mechanism mentioned previously. Films of TlI prepared by this new method do not scatter light and are very clear.

Table 1. Identification of observed x-rays diffraction lines from graded index sample 801253

Observed		β-PbF_2		Cubic TlI	
d(Å)	I*	d(Å)	hkl	d(Å)	hkl
3.4	m	3.428	111		
2.95	m	2.97	200	2.97	110
2.43	f			2.428	111
2.10	s	2.10	220	2.103	200
1.78	s	1.791	311		
1.72	m	1.715	222	1.717	211
1.485	m	1.485	400	1.487	220
1.36	m	1.362	331		
1.327	m	1.328	420	1.33	310
1.215	m	1.212	422	1.214	222
1.14	m	1.143	511		
1.12	w	forbidden line for βPbF_2		1.12	321
1.05	m	1.050	440	1.052	400
1.005	m	1.0043	531		
0.99	m	0.9903	600	0.991	330
0.93	m	0.9394	620	0.94	420
0.906	f	0.9059	533		

*Intensity: s = strong, m = medium, w - weak f = faint.

6. References

1. A. J. Glass and A. H. Guenther, "Laser Induced Damage of Optical Elements - A status Report," Appl. Optics 12, 637 (1973).
2. D. Milam, "Laser-Induced Damage at 1064nm, 125 psec," Appl. Optics 16, 1204 (1977).
3. B. E. Newnam, D. H. Gill, and G. Faulkner, "Influence of Standing-wave Fields on the Laser Damage Resistance of Dielectric Films," in Laser Induced Damage in Optical Materials, NBS Special Publication 435 (1975).
4. J. H. Apfel, J. S. Matteucci, B. F. Newnam, and D. H. Gill, "The Role of Electric Field Strength in Laser Damage of Dielectric Multilayers" in Laser Induced Damage in Optical Materials, NBS Special Publication 462, (1976).
5. J. H. Apfel, "Optical Coating Design with Reduced Electric Field Intensity," Appl. Optics 16, 1880 (1977).
6. T. J. Moravec and R. A. Skogman, "Heavy Metal Halide Optical Coatings on KCl: BiF_3, BiI_3, PbF_2 and PbI_2", Proc. High Power Laser Optical Components and Components Material Meeting, 1977.
7. R. R. Austin, R. Michawd, A. H. Guentl.er, and J. Putnam, "Effects of Structure Composition and Stress on the Laser Damage Threshold of Homogeneous and and Inhomogeneous Single Films and Multilayers," Appl. Optics 12, 665 (1973).
8. R. Jacobsson, in Physics of Thin Films, ed. G. Hass, M. H. Francombe, and R. W. Hoffman, 8, 51-98 (1975).
9. R. Jacobsson, "Optical Properties of a Class of Inhomogeneous Thin Films," Opt. Acta. 10, 309 (1963).
10. E. Bernal G., R. H. Anderson, K. M. Leung, T. J. Moravec, J. F. Ready, R. A. Skogman, D. Wertman, Honeywell Final Technical Report on ARPA Contract DAHC15-73-C-0464, 31 March, 1978.
11. R. A. Skogman, Laser Induced Damage in Optical Materials , NBS Special Publication 462, (1976).
12. M. Blackman, and I. H. Khan, "The polymorphism of Thallium and Other Halides at Low Temperatures," Proc. Phys. Soc. London, 77, 471 (1961).
13. I. H. Khan, "On the Polymorphism of the Thallium Halides", Proc. Phys. Soc. London, 76. 507 (1960).
14. M. Shiojir, C. Kaito, Y. Saito, M. Muraham, and J. Kawanota, "Growth of Thallium Iodide Crystals in Silicon Hydrogels," J. Cryytal Growth 43, 61 (1978).

7. Addendum

Subsequent to the preparation of this manuscript, an article was noted on the preparation of gradient index films from small steps of homogeneous films by V. N. Yadova, Shiv. K. Sharma, and K. L. Chopra, Thin solid Films 21, 297 (1974). Their approach is similar to ours in that alternating thin layers of two materials (in their case, ZnS and MgF_2) are deposited sequentially to produce a film that performs as a gradient index film. However, their technique is different in that each small increment is composed of symmetrical thickness pqp layers (p=MgF_2, q = ZnS). Our technique utilizes increments of pq layers (p = TlI, q = PbF_2) and the concept of an average refractive index to produce the gradient. Although the resultant optical properties of the multilayer gradient index film are similar, the theoretical techniques for calculating the individual increments are different.

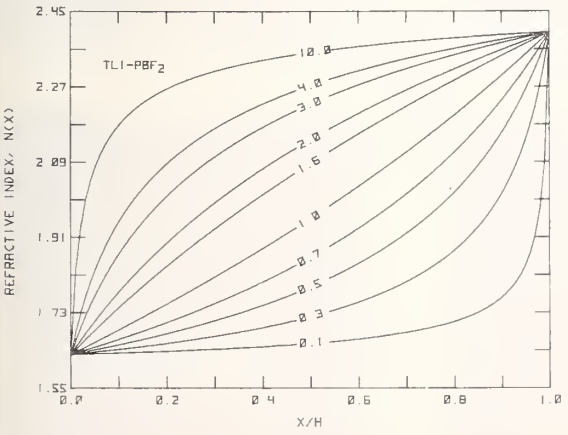

Figure 1. Refractive index profiles for the TlI-PbF_2 system as a function of α noted in the center of each curve.

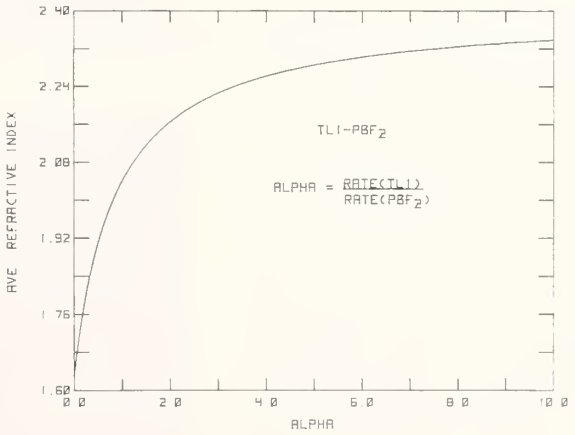

Figure 2. Average refractive index versus α for the TlI-PbF_2 system.

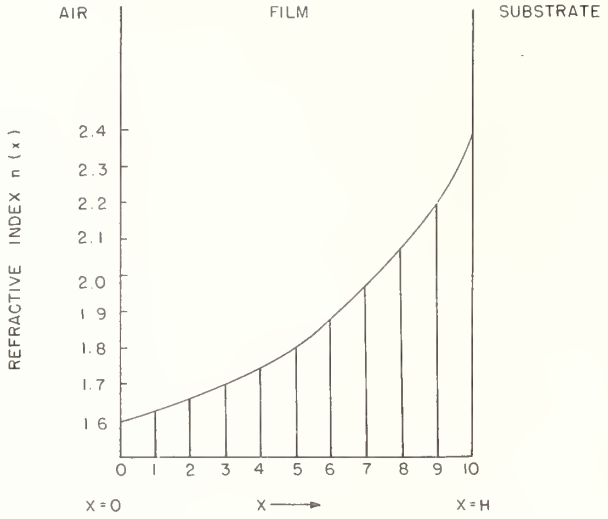

Figure 3. n(x) versus x for graded index film divided up into ten equal increments.

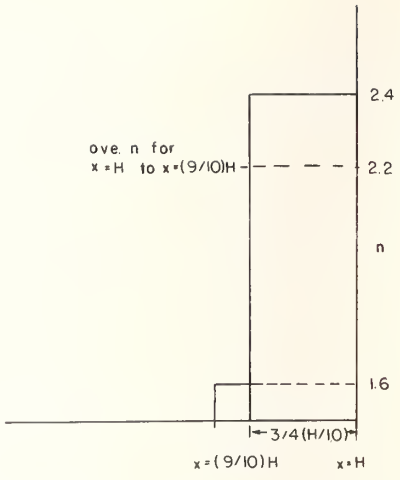

Figure 4. Schematic of first step layer to produce index profile of figure 3 by sequential evaporation of material n_{10} of thickness 3/4 (H/10) followed by material n_0 of thickness 1/4 (H/10).

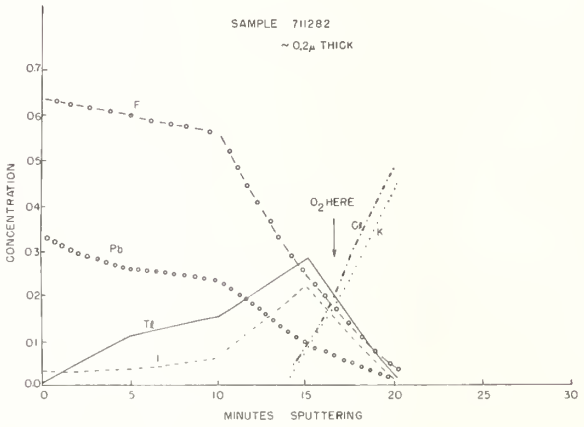

Figure 5. ESCA Profile of Graded Index Film 2000 Å Thick. The following peak heights were used: Tℓ $4f_{7/2}$, I $3d_{5/2}$, Pb $4f_{7/2}$, F 1s.

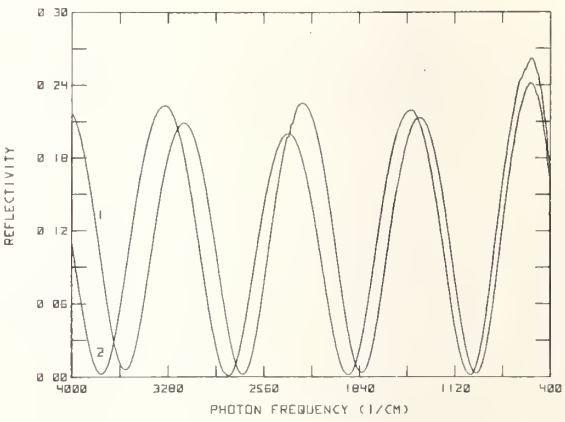

Figure 6. Near infrared reflectivity for graded index TℓI-PbF_2 films on KCℓ. Curve 1: step graded with $\alpha \sim 1$, 2: Varying rates with $\alpha \sim 1$.

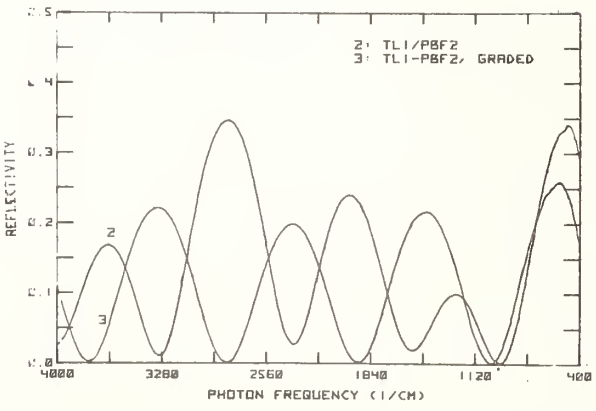

Figure 7. Near infrared reflectivity of graded index film (curve 3) compared with two-layer AR film (curve 2).

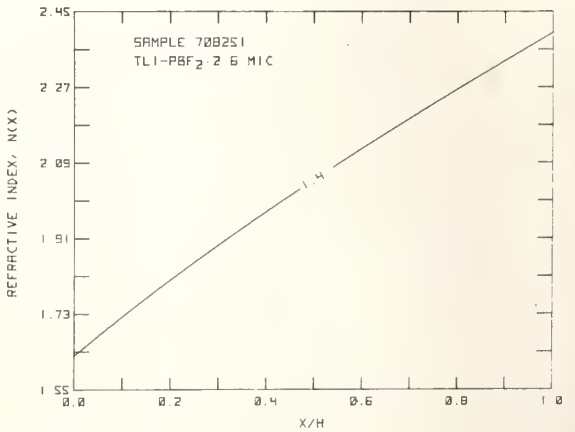

Figure 8. Refractive index profile for TℓI-PbF_2 graded index film with $\alpha = 1.4$.

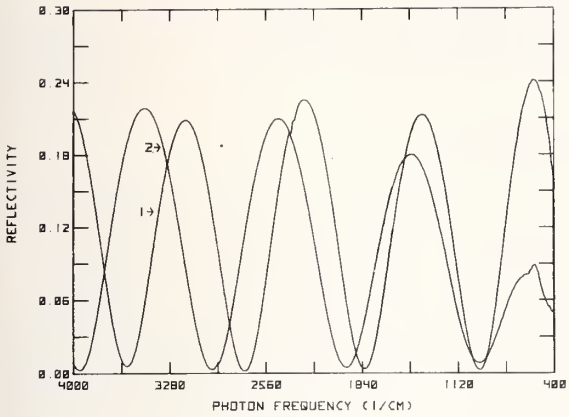

Figure 9. Near infrared reflectivity of two graded index T&I-PbF_2 films made with $\alpha \sim 1$ (curve 1) and $\alpha \sim 0.5$ (curve 2).

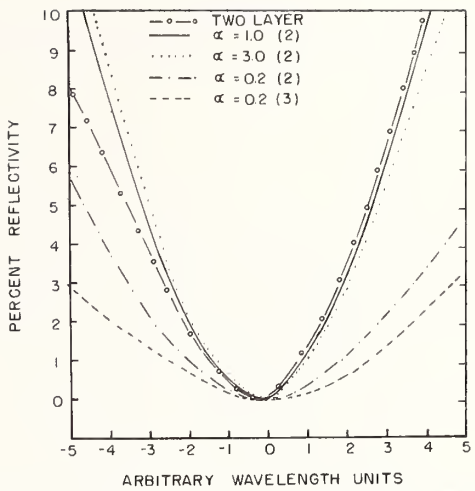

Figure 10. Comparison of experimentally measured AR minima of two-layer film with several graded index films for several α. All minima have been adjusted to go through zero percent reflectivity and zero wavelength units.

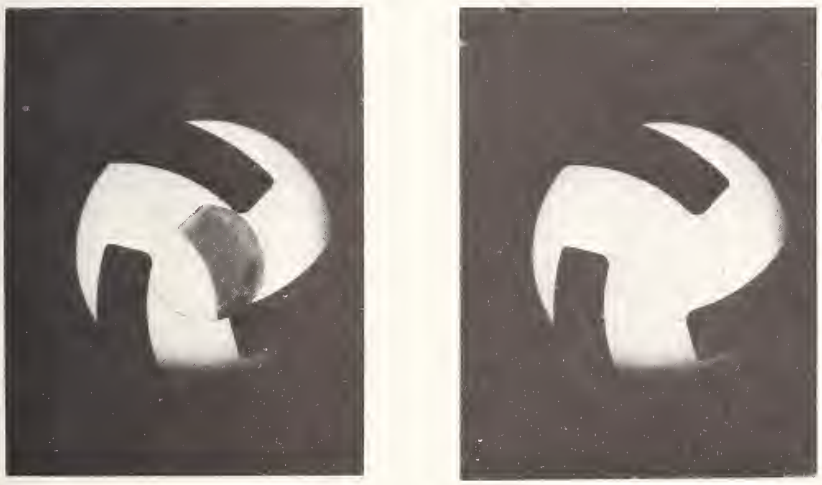

Figure 11. Left-hand side: Two-layer T&I-PbF_2 AR film on half coated KC& shown in transmitted white light. Coated part is on right side of sample and scatters light to give dark appearance. Right-hand side: Step graded T&I-PbF_2 AR film on half coated KC& shown in transmitted white light. Coated area is on bottom part of sample.

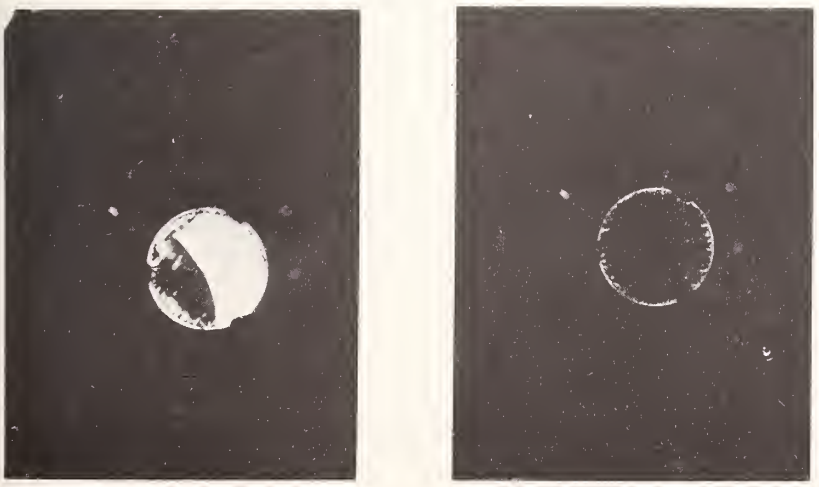

Figure 12. Left-hand side: Corresponding sample of figure 11 shown through crossed polarizers with same sample orientation. Note birefringence of coated (right side) part. Right-hand side: Corresponding sample of figure 11 shown through crossed polarizers. Note no birefringence.

SIMPLE EXPRESSIONS FOR CALCULATING THE EFFECT OF VOLUME OR INTERFACE ABSORPTION IN THIN FILMS ON THE PERFORMANCE OF HIGH REFLECTANCE OR ANTIREFLECTANCE MULTILAYER COATINGS*

H. E. Bennett and D. K. Burge
Michelson Laboratory, Physics Division
Naval Weapons Center, China Lake, CA 93555

Approximate closed-form expressions are developed for predicting the effect of volume and interface absorption in thin films on the performance of quarter-wave multilayer coatings. For highly reflecting coatings on dielectric substrates the volume absorption expressions are equivalent to those obtained by Sparks using a perturbation approach. The results are extended to metal substrates by introducing the concept of a generalized substrate index. An approximate expression for scattering losses for high reflectance coatings is included. Multiple quarter-wave antireflectance coatings are also analyzed using admittance theory. A technique for experimentally separating and determining interface and volume absorption in single-layer films has recently been reported. The expressions developed in this paper make it possible to predict the performance of high reflectance and antireflectance multilayer stacks from these single-film measurements without recourse to a computer.

Key words: Absorption; antireflectance coatings; high reflectance coatings; interface absorption; multilayer films; scattering.

Introduction

The development of very high reflectance, low absorption multilayer coatings on dielectric or metal substrates is a continuing problem in optical coating technology. If the individual films were truly nonabsorbing, as assumed in typical multilayer calculations, reflectances arbitrarily close to zero or unity could be achieved by simply using enough layers. In practice, however, the individual layers absorb slightly and may also scatter light, some of which is absorbed. In addition, absorption and scattering may occur at film-film or film-substrate interfaces. Although the apparent absorption observed for such thin films is very small, it is typically orders of magnitude higher than would be predicted from the absorption coefficient of the bulk filming material. In only a few cases is the absorption coefficient of the material in thin film form equal to that of the bulk material [1,2][1]. Why additional absorption occurs when materials are deposited as thin films is one of the most interesting questions before the thin film physics community. Whatever its source, it clearly limits the reflectance or transmittance achievable in multilayer film coatings.

A straightforward attack on the optical effects of single or multilayer films on a surface as a boundary value problem results in immensely complicated expressions [3]. The solution to this problem has been to make iterative calculations using impedance theory and matrix mechanics. Although the films are usually assumed to be nonabsorbing, the general theory allows absorption to be present in the films and even at interfaces. The multilayer film problem has therefore been solved numerically. However, the functional relationships between absorption in one or more layers or interfaces and the resultant multilayer performance remains obscure. Fortunately, in the special cases in which the films have optical thicknesses which are exactly a quarter or half wavelength and in which the multilayer film either has a high reflectance or is an antireflection film, a considerable simplification occurs and it is possible to obtain simple closed-form expressions. These allow one to predict, without the aid of a computer, what the approximate maximum or minimum reflectance of a multilayer coating on a dielectric or absorbing substrate will be, and how that reflectance is affected by absorption in the coatings or at the interfaces. Developing these expressions is the subject of this paper.

Generalized Index of Refraction

The complex index of refraction of a medium is chosen to be $\bar{n} = n - ik$, where both n and k are real. If the medium is nonabsorbing then $k = 0$. If the substrate is absorbing, the generalized index of a substrate-single film combination may be made real at a given wavelength by choosing the optical thickness of the film so that the phase change induced by the film adds to that of the substrate to produce a resultant phase change of 0 or π. The normal incidence intensity reflectance R for a single interface is $R = rr^*$ and

$$r = \frac{n_o - \bar{n}}{n_o + \bar{n}} \tag{1}$$

* Work supported by the Department of Energy and the Defense Advanced Research Projects Agency.

1. Figures in brackets indicate the literature references at the end of this paper.

where the asterisk indicates the complex conjugate and n_o and $\bar{n}$ are the indices of refraction of the incident medium and the medium upon which the light is incident, respectively. The admittance is defined as

$$Y = \frac{\vec{H}_a}{\vec{k} \times \vec{E}_a} \quad , \tag{2}$$

where $\vec{H}_a$ is the magnetic field, $\vec{E}_a$ is the electric field, and $\vec{k}$ is the unit vector in the direction of propagation, assumed here to be normal to the surface. From Maxwell's equations $H/E = \bar{n}$ in Gaussian units [4], so that the admittance is equivalent to a generalized single medium index of refraction.

By using symmetrical multilayer films it is possible to simulate, as far as phase change on reflection goes, the index of refraction of a single film at a given wavelength [5]. If the multilayer films are nonabsorbing, this simulated or generalized index of refraction, often called a Herpin index, will be real if the optical thicknesses of all films are a quarter or half wavelength or multiples thereof. It may also be real if they are not quarter-wave films but are symmetrical and are chosen so that the resultant phase change on reflection from the film stack adds to zero or π. Only the quarter-wave case will be considered in this paper. The admittance of a multilayer stack on a substrate of index n_S is given by $Y = b/a$, where [6]

$$\begin{bmatrix} a \\ b \end{bmatrix} = \left\{ \prod_{r=1}^{N} \begin{bmatrix} \cos\delta_r & (i \sin\delta_r)/n_r \\ i\, n_r \sin\delta_r & \cos\delta_r \end{bmatrix} \right\} \begin{bmatrix} 1 \\ n_S \end{bmatrix} \quad . \tag{3}$$

The outermost film has $r = 1$, the film next to the substrate has $r = N$, the phase factor δ_r is associated with each film of index n_r and thickness ℓ_r, and for wavelength λ,

$$\delta_r = \frac{2\pi n_r \ell_r}{\lambda} \quad . \tag{4}$$

If the optical thicknesses of the coatings are each a quarter- or half-wave, then $\delta = \pi/2$ or π, respectively. The characteristic matrix for a quarter-wave film is then

$$\begin{bmatrix} 0 & i/n_r \\ i n_r & 0 \end{bmatrix}$$

and for a half-wave film,

$$\begin{bmatrix} 1 & 0 \\ 0 & 1 \end{bmatrix}$$

Antireflectance Coatings

If there is no reflection from a surface coated with an antireflection film and $n_o = 1$ (air), then from eq. (1) $Y = 1$. For a single antireflection quarter-wave film of index of refraction n_L, then

$$\begin{bmatrix} 0 & i/n_L \\ i n_L & 0 \end{bmatrix} \begin{bmatrix} 1 \\ n_S \end{bmatrix} = \begin{bmatrix} i n_S/n_L \\ i n_L \end{bmatrix} \tag{5}$$

and $Y = b/a = n_L^2/n_S = 1$ giving the well-known result that $n_L = n_S^{1/2}$ for a single perfectly antireflecting film. If the transmitted power equals the incident power, i.e., if $n_o E_o^2 = E^2 Y$, then when $n_o = 1$ the field at the air interface is $E = E_o(n_S/n_L^2)^{1/2}$. Similarly, the field at the substrate interface is $E_o/n_S^{1/2}$ and the average power in the film is $(n_L E_o^2/2n_S)(n_S + 1)$.

For a two-layer, quarter-wave film stack, $N = 2$ in eq. (3), and if the outer layer has index n_L and the inner one has index n_H, then

$$\begin{bmatrix} -n_H/n_L & 0 \\ 0 & -n_L/n_H \end{bmatrix} \begin{bmatrix} 1 \\ n_S \end{bmatrix} = \begin{bmatrix} -n_H/n_L \\ -n_S n_L/n_H \end{bmatrix} \tag{6}$$

so that the requirement for the film to be antireflecting is

$$Y = \frac{b}{a} = \frac{n_S n_L^2}{n_H^2} = 1 \quad . \tag{7}$$

The field at the air-film interface is $E_o/(n_S n_L^2/n_H^2)^{1/2}$, at the film-film interface is $E_o/(n_H^2/n_S)^{1/2}$ and at the substrate interface is $E_o/n_S^{1/2}$. A three-layer all quarter-wave antireflecting film can be worked out in a similar way. A more common three-layer coating, however, is the quarter-half-quarter coating, which has low reflectance over a broader wavelength region than does the equivalent quarter-quarter-quarter coating [7]. Since a half-wave coating has a unit matrix, it does not affect the fields at either boundary. However, the field at the center of the half-wave coating of index n_h will be $E_o/(n_S n_h^2/n_H^2)^{1/2}$, as may be seen by considering the half-wave coating to be two quarter-wave coatings back to back. The field distributions inside the various layers are sinusoidal, as shown in figure 1.

Reflectances of the quarter-wave antireflecting films are obtained by substituting Y for n in eq. (1). For a single quarter-wave antireflection (AR) coating in air the reflectance is then

$$R_1 = \left(\frac{n_S - n_L^2}{n_S + n_L^2}\right)^2 \tag{8}$$

and for a double quarter-wave AR coating or a three-layer coating the middle layer of which is a half-wave in optical thickness

$$R_2 = \left(\frac{n_H^2 - n_S n_L^2}{n_H^2 + n_S n_L^2}\right)^2 \quad . \tag{9}$$

These expressions are exact, provided absorption is negligible.

To obtain the absorption in a film, one utilizes Poynting's theorem, which states that the power dissipated in a medium is proportional to nE^2, where n is the index of refraction of the medium and E is the local field strength. The volume absorption per unit of incident power in a film is then

$$A_v = (\beta \ell)(\overline{nE^2}/E_o^2) \quad , \tag{10}$$

where β is the absorption coefficient in the film of thickness ℓ and $\overline{nE^2}$ is the average power in the film. The interface absorption should in principle be handled in the same way, except that the power at the interface would be used instead of the average power in the film. In fact, interface absorption must occur in a narrow region on either side of the interface. The absorption coefficient is decreasing rapidly on both sides of the interface and the experimentally measured absorption is the integral of the product of the absorption coefficient and the depth on both sides of the interface. If we redefine the absorption coefficient at the interface to be the absorption per unit of optical rather than physical thickness, then n in eq. (10) is absorbed into the interface term and the difficult problem of assessing the fractional contribution to the absorption made by each side of the interface is avoided. We then may express the resultant absorption at an interface A_I between two materials designated 1 and 2 as

$$A_I = A_i(E/E_o)^2 \quad , \tag{11}$$

where

$$A_i = \int_{\ell_1}^{o} n_1 \beta_1 d\ell_1 + \int_{o}^{\ell_2} n_2 \beta_2 d\ell_2 \tag{12}$$

is the interface absorption per unit field and is a parameter which can be determined experimentally from calorimetry [8].

The approximate absorption in an AR film is then obtained by substituting for E^2 or $\overline{E^2}$ in eqs. (10, 11). Since we have assumed the films to be a quarter wavelength in optical thickness, the absorption A_1 in a single-layer quarter-wave AR film becomes

$$A_1 = A_{OL} + \frac{\beta_L \lambda}{8 n_S}(n_S + 1) + \frac{A_{LS}}{n_S} \quad . \tag{13}$$

For a two-layer quarter-wave AR film the average power in the outer (low index) film is

$$\overline{n_L E^2} = \frac{n_L}{2}\left(E_o^2 + \frac{E_o^2 n_S}{n_H^2}\right) = \frac{E_o^2 n_L}{2n_H^2}(n_H^2 + n_S) \tag{14}$$

and in the inner (high index) film is

$$\overline{n_H E^2} = \frac{n_H}{2}\left(\frac{E_o^2 n_S}{n_H^2} + \frac{E_o^2}{n_S}\right) = \frac{E_o^2}{2n_H n_S}(n_H^2 + n_S^2) \quad . \tag{15}$$

The absorption A_2 in a double-layer quarter-wave AR film is then

$$A_2 = A_{OL} + \frac{\beta_L \lambda (n_H^2 + n_S)}{8n_H^2} + A_{LH}\frac{n_S}{n_H^2} + \frac{\beta_H \lambda (n_H^2 + n_S^2)}{8n_H^2 n_S} + \frac{A_{HS}}{n_S} \quad . \tag{16}$$

In a three-layer film in which the middle layer is a half wavelength in thickness the absorption will be A_2 minus the interface contribution A_{LH} plus the contribution from the half-wave film. Proceeding as before we find the absorption of such a three-layer antireflection coating to be

$$A_3 = A_2 + \frac{\beta_h \lambda}{4n_S}\left(\frac{n_S^2}{n_H^2} + \frac{n_H^2}{n_h^2}\right) + \frac{n_S}{n_H^2}(A_{Lh} + A_{hH} - A_{LH}) \quad , \tag{17}$$

where the subscript h represents the half-wave coating.

The approximate performance of antireflectance coatings consisting of quarter-or half-wave films can now be simply determined. The reflectance of a single-layer antireflectance coating is given by eq. (8) and its absorption by eq. (13). Its transmission is unity minus the sum of the reflectance and absorption losses. Similarly, for a two-layer antireflectance coating the reflectance is given by eq. (9) and the absorption by eq. (16). For a three-layer quarter-half-quarter coating the reflectance is given by eq. (9) and the absorption by eq. (17). A comparison of results using these expressions with exact computer results is given in table 1. (No interface absorptions are included.) The theoretical performance of coatings made using various coating materials may thus be compared using experimentally measured single-film values of volume and interface absorption for the various filming materials.

The above equations are also useful as a starting point for developing optimum nonquarter-wave antireflection coating designs. These designs often make possible more perfect matching of impedances using available index materials than do quarter-wave designs, and may sometimes also result in thinner coatings. Two-layer coating designs, of which two exist in most cases for each appropriate pair of materials, are facilitated by using a Schuster diagram [9]. Simple relationships governing the design of three-layer coatings, which can result in significant reductions in absorption relative to two-layer coatings when one of the coating materials has a large absorption coefficient, were derived by Baer [10].

High Reflectance Quarter-Wave Multilayers

The concept of a generalized index can also be applied to high reflectance, nonabsorbing quarter-wavelength multilayer films. The characteristic matrix for each high-low (HL) index pair is

$$\begin{bmatrix} 0 & i/n_H \\ in_H & 0 \end{bmatrix}\begin{bmatrix} 0 & i/n_L \\ in_L & 0 \end{bmatrix} = \begin{bmatrix} -\frac{n_L}{n_H} & 0 \\ 0 & -\frac{n_H}{n_L} \end{bmatrix} \tag{18}$$

so that the characteristic matrix for N such multilayer pairs is this matrix raised to the N^{th} power. The generalized index of this multilayer stack is then

$$Y = (n_H/n_L)^{2N} n_S \tag{19}$$

and the reflectance of the combination is

$$\left[\frac{1 - (n_H/n_L)^{2N} n_S}{1 + (n_H/n_L)^{2N} n_S}\right]^2 \quad , \tag{20}$$

which approaches unity as N becomes large.

In deriving eq. (20) we have assumed that the outermost film has a high index and that the film next to the substrate has a low index. If the multilayer stack is symmetric so that high index films are next to the substrate as well as being the outermost layer, the characteristic matrix becomes

$$\begin{bmatrix} (-n_L/n_H)^N & 0 \\ 0 & (-n_H/n_L)^N \end{bmatrix} \begin{bmatrix} 0 & i/n_H \\ in_H & 0 \end{bmatrix} = \begin{bmatrix} 0 & i/n_H(-\frac{n_H}{n_H})^N \\ in_H(-\frac{n_H}{n_L})^N & 0 \end{bmatrix} \tag{21}$$

and the generalized index of the multilayer-substrate combination is

$$Y = n_H^{2N+2}/(n_L^{2N} n_S) \quad . \tag{22}$$

A simple way to visualize the performance of a multilayer high reflectance stack, each of whose layers is a quarter of a wavelength in optical thickness, was pointed out by Sparks [11]. Assume for the moment that the substrate is a dielectric. A standing wave is formed for a perfect reflector having the characteristics shown in figure 2. If the reflectance is unity, at the outer film interface of each HL index pair the field is zero, whereas at the interface between the high index film and the low index film it is a maximum. Inside each film the field is one-quarter of a sinusoidal standing wave. This standing wave is composed of two traveling waves, one from the left having a field strength E^+, and the other from the right having a field strength E^-. At the outer film-pair interfaces $E^+ + E^- = 0$. On the air side of the film-air interface, the incident field strength $E_o^+ = 1$. Since the mirror is a perfect reflector, $E_o^- = -1$ and $E_o^+ + E_o^- = 0$. However, E_o^- is made up of two parts, one reflected from the air-film interface and one transmitted back through it from the multilayer film stack. Letting the subscript H represent the outermost film, the amplitude reflection coefficient r_{OH} on the air side is

$$r_{OH} = \frac{1 - n_H}{1 + n_H} \quad . \tag{23}$$

The amplitude transmission coefficient from medium 1 to 0 is

$$t_{10} = \frac{2n_H}{1 + n_H} \quad . \tag{24}$$

Then the reflected amplitude E_o^-, which is equal to (-1), is given by

$$E_o^- = -1 = 1 \times \frac{1 - n_H}{1 + n_H} + E_1^- \times \frac{2n_H}{1 + n_H} \quad , \tag{25}$$

where E_1^- is the amplitude of the wave traveling to the left in the outermost film. Solving gives

$$E_1^- = -\frac{1}{n_H} \quad . \tag{26}$$

The wave traveling from left to right in medium 1 is E_1^+. It is composed of the transmitted component of E_o^+ and the reflected component of E_1^-. Then

$$E_1^+ = 1 \times t_{01} + E_1^- r_{10}$$

$$= \frac{2}{1 + n_H} - \frac{1}{n_H}\left(\frac{n_H - 1}{n_H + 1}\right)$$

$$= \frac{1}{n_H} \quad . \tag{27}$$

The amplitude of this wave traveling from left to right is unchanged at the HL interface as a consequence of the boundary conditions on the tangential component of E. At the LH interface the average value of E is zero, the amplitude in the next HL pair is determined by the transmission at the LH interface and will be lower than that of the first HL pair by a factor of n_L/n_H, and so on. In each HL pair the amplitude is decreased by a factor n_L/n_H.

Absorbing Substrate

If the multilayer film is deposited on a metal substrate and the thickness of the layer next to the substrate is not adjusted to compensate for the phase change on reflection introduced by the metal, the reflectance of the metal/film combination can be lower after the first two layers have been deposited than it was for the bare metal. To compensate for this phase change, the first dielectric layer is made thinner (or thicker) than a quarter wavelength in optical thickness. The phase change on reflection introduced by the metal substrate is δ where

$$\tan\delta = \frac{2nk_S}{n^2 - n_S^2 - k_S^2} \quad . \tag{28}$$

Thus, when $n^2 > (n_S^2 + k_S^2)$, δ is in the first quadrant. Otherwise, δ is in the second quadrant using the standard conventions [12,13].

The optical thickness $n_H\ell$ of the first dielectric film on the metal substrate in the high index case would be chosen to be

$$n_H\ell = \frac{\lambda}{4}\left(1 + \frac{\delta}{\pi}\right) \quad . \tag{29}$$

More commonly the low index film is deposited on the metal substrate since a smaller optical thickness is required and hence the coating design is more efficient. In the low index case, the optical thickness $n_L\ell$ is given by

$$n_L\ell = \frac{\lambda}{4}\frac{\delta}{\pi} \quad . \tag{30}$$

In either case, these values are substituted in eq. (3). The iterative relationship for the admittance of the substrate-initial film relation in matrix notation gives the characteristic matrix of the generalized substrate as

$$\begin{bmatrix} \cos\frac{2\pi}{\lambda} n\ell & (i \sin\frac{2\pi}{\lambda} n\ell)/n \\ i\, n \sin\frac{2\pi}{\lambda} n\ell & \cos\frac{2\pi}{\lambda} n\ell \end{bmatrix} \begin{bmatrix} 1 \\ n_S - ik_S \end{bmatrix}$$

where the index of the substrate is now $n_S - ik_S$. The characteristic admittance Y_o of this substrate-film combination is then

$$Y_o = \frac{(n_S - ik_S)\cos(\frac{2\pi}{\lambda} n\ell) + i\, n \sin(\frac{2\pi}{\lambda} n\ell)}{\cos(\frac{2\pi}{\lambda} n\ell) + i \frac{(n_S - ik_S)}{n} \sin(\frac{2\pi}{\lambda} n\ell)} \quad , \tag{31}$$

where n is either n_H or n_L, which makes the imaginary part of the admittance zero when the right-hand side of eq. (29) or (30) is substituted. The generalized substrate consisting of the metal-film combination as seen by the multilayer film is thus effectively transformed into a dielectric. The generalized index of refraction of this dielectric, n_S^+, is given by eq. (31), which reduces to

$$n_S^+ = \frac{n_S}{\left(\frac{1 \mp \cos\delta}{2}\right)\left[\left(\frac{n_S}{n}\right)^2 + \left(\frac{k_S}{n}\right)^2\right] + \frac{1 \pm \cos\delta}{2} \pm \frac{k_S}{n}\sin\delta} \quad , \tag{32}$$

where δ is the phase change on reflection given by eq. (28) and the upper or lower sign is chosen for the low or high index case, respectively.

Volume Absorption in a High Reflectance Multilayer Film

The standing waves shown in figure 2 can be utilized to calculate the absorption of the multilayer stack when the films that compose it are slightly absorbing and there is also a small amount of interfacial absorption. Consider first the contribution from volume absorption. If we assume that the films are homogeneous with a volume absorption coefficient β_L for the low index film and β_H for the high index film, the energy absorbed in the low index film in the i^{th} film pair from volume absorption is $A_L^{(i)}$, where

$$A_L^{(i)} = \beta_L \ell_L (n_L \bar{E}_i^2 / E_o^2) \tag{33}$$

and the optical film thickness $n_L \ell_L = \lambda/4$, where λ is the wavelength of the incident light. The average field $\bar{E}_i = E_{i\ max}/\sqrt{2}$, since within each layer the fields are sinusoidal. A similar expression holds for absorption in the high index layers. But from figure 2, $E_{i\ max} = (1/n_H)(n_L/n_H)^i 2E_o$ so that the absorption in the i^{th} film pair $A^{(i)} = A_L^{(i)} + A_H^{(i)}$ is given by

$$A^{(i)} = (\beta_L + \beta_H)\frac{\lambda}{4} \times \frac{1}{2}\left[\frac{2}{n_H}\left(\frac{n_L}{n_H}\right)^i\right]^2$$

$$= \frac{\lambda}{2}(\beta_L + \beta_H)\frac{1}{n_H^2}\left(\frac{n_L}{n_H}\right)^{2i} \quad . \tag{34}$$

The total volume absorption in a multilayer film stack is then A_V, where

$$A_V = \frac{\lambda}{2}(\beta_L + \beta_H)\frac{1}{n_H^2}\sum_{i=0}^{N}\left(\frac{n_L}{n_H}\right)^{2i} \quad . \tag{35}$$

Making use of the binomial expansion gives for $N \to \infty$,

$$A_{V\ max} = \frac{\lambda}{2}(\beta_L + \beta_H)\frac{1}{n_H^2 - n_L^2} \quad . \tag{36}$$

Equation (34) was first deduced in an equivalent form by Koppelmann [14] and more recently by Sparks [11] using an argument similar to that presented here. It allows us to predict, from the volume absorption coefficients of the filming materials, what the limiting reflectance will be if interface absorption (and scattering leading to absorption) can be neglected and if enough layers are used to make the contribution of the substrate negligible. If the absorption or volume scattering of the films is too high, it is easy to see that a desired reflectance may be unobtainable.

If a smaller number of pairs is used, absorption and scattering in the film decreases, but the substrate contribution increases. Although eq. (35) can be used to calculate the multilayer film volume absorption in this case, a more convenient form, obtained using the expansion in Section V of Sparks' paper, is

$$A_V = \frac{\lambda}{2}(\beta_L + \beta_H)\frac{1}{n_H^2 - n_L^2}\left[1 - \left(\frac{n_L}{n_H}\right)^{2N+1}\right] \tag{37}$$

Interface Absorption

An important source of absorption in multilayer film stacks is related to the HL film interfaces. Reference to figure 2 shows that since the fields are very low at the outer interface and at each LH

interface, contaminants or scattering at these interfaces will not to a first approximation affect film performance. However, contaminants at the HL interfaces, where the field is a maximum, will be important.

The absorption arising from the HL interfaces can be calculated in a manner exactly analogous to that used to calculate volume absorption except that the field involved is $E_{i\ max}$, not $\bar{E}_i$. The contribution of interface absorption from the dielectric pairs is then A_{IF}, where

$$A_{IF} = 4A_I \frac{1}{n_H^2 - n_L^2}\left[1 - \left(\frac{n_L}{n_H}\right)^{2N+1}\right] \tag{38}$$

and A_I is the interface absorption in an optical thickness at the interface which is small enough so that the field is effectively constant. What little data we have on direct interfacial absorption [15] suggest that the interfacial thicknesses involved are ~ 0.1 μm. Scattering leading to absorption should also be most important at the interfaces.

Another interfacial absorption that may have to be considered is A_{IS}, that at the film/substrate interface. It is typically most important when the substrate is a metal. In the dielectric case, it is probably negligible for most highly reflecting films, but for completeness it should be mentioned. If $n_L < n_S$, the film dielectric substrate interface occurs at a node for the $0(HL)^N S$ case, and surface absorption and scattering at this interface can to a first approximation be neglected. However, for a $0(HL)^N HS$ film where $n_H > n_s$, the substrate interface occurs at an antinode. In this case, where the high index film is next to the dielectric substrate, the interface absorption is

$$A_{IS} = 4A_S \frac{n_S}{n_H^2}\left(\frac{n_L}{n_H}\right)^{2N} , \tag{39}$$

where A_S is the absorption by the high index dielectric/dielectric substrate interface.

In addition to absorption in the multilayer film or at the interfaces, some light may also be transmitted into a dielectric substrate. If the low index film is next to the substrate, the power transmitted into the substrate is

$$T_L \cong \frac{4}{n_S}\left(\frac{n_L}{n_H}\right)^{2N} . \tag{40}$$

Alternately, if the high index film is next to the substrate, the transmitted power is

$$T_H \cong \frac{4n_S}{n_H^2}\left(\frac{n_L}{n_H}\right)^{2N} . \tag{41}$$

Equation (41) is also useful for calculating the energy absorbed by a metal substrate coated with a matched low index film. Substituting n_S^+ for n_S, this absorption is then

$$A_S = \frac{4n_S^+}{n_H^2}\left(\frac{n_L}{n_H}\right)^{2N} , \tag{42}$$

which may be compared to the interface absorption at a dielectric substrate [eq. (39)]. Equation (40) could be similarly modified to represent absorption of a metal substrate coated with a matched high index film.

The absorption of a multilayer coated metal mirror having a matched low index first dielectric layer is then

$$(1-R) = \left[\frac{\lambda}{2}(\beta_L + \beta_H) + 4A_I\right]\left[1 - \left(\frac{n_L}{n_H}\right)^{2N+1}\right]\left(n_H^2 - n_L^2\right)^{-1} + \frac{4n_S^+}{n_H^2}\left(\frac{n_L}{n_H}\right)^{2N} \tag{43}$$

If the substrate is a dielectric with both the outer film and the film next to the substrate high index, the expression is the same except n_S is substituted for n_S^+ and A_{IS} [eq. (39)] is added. If a low index film is next to the dielectric substrate, the last term in eq. (43) becomes $(4/n_S)(n_L/n_H)^{2N}$. We thus have a general simple closed-form expression which allows us to calculate approximately what the absorption will be in a multilayer coated metal or dielectric mirror. A comparison of calculations made using eq. (43) with exact calculations is shown in table 2. No interface absorption has been included in these calculations. Also note that for the metal substrate case in the table, the number of layer pairs N is one less than it would be if we had not included the final film into the generalized substrate.

Scattering

Light is scattered at interfaces between multilayer films, at the film-substrate interface, and at the film-air interface. In addition, it may be scattered by defects in the volume of the film itself or in the volume of a dielectric substrate. What little evidence there is suggests that interfacial scattering is usually the most important [16,17], except possibly very near the specular direction [18]. It arises both from microirregularities on the substrate surface, which deposited films contour remarkably well, and irregularities resulting from film formation itself. For example, the print-through of the substrate surface was sufficiently exact in the case of silver films deposited on topaz substrates to permit Koehler to determine interferometrically the 7 Å lattice spacing of topaz [19]. On the other hand, a reliable technique for producing surfaces having varying microroughnesses is to deposit various thicknesses of calcium fluoride at room temperature on superpolished quartz surfaces [20]. In this case, the large crystallites formed by the calcium fluoride result in roughness which is uncorrelated to that on the substrate surface. In the limiting case of microirregularities which are correlated with the substrate, so that each film layer replicates the surface irregularities of the layer below it, Eastman [21] showed that to a good approximation (scalar scattering theory) the ratio of scattered to specularly reflected light from the film-covered substrate is the same as that from the uncoated substrate. The light scattered into all directions by a multilayer film whose microirregularities are correlated with those of the substrate is then approximately ΔR, where [22]

$$\Delta R = R_o(4\pi\delta/\lambda)^2 \tag{44}$$

and R_o is the calculated reflectance of the multilayer film in the absence of scattering. For very high reflectance coatings $R_o \simeq 1$. Here δ is the rms microroughness of the substrate surface, preferably determined by light scattering experiments [23] and λ is the wavelength.

Recent calculations utilizing vector scattering theory suggest that although in most cases the scattering from a correlated multilayer-coated surface will track that from the uncoated substrate, anomalies can occur [24]. Much larger anomalies are expected when the microirregularities at the various interfaces are uncorrelated. If optical thicknesses are close to a quarter wavelength, scattering will be smaller than for the case of correlated irregularities; elsewhere it may be larger [24]. Also, phenomena other than microirregularity scattering are expected to contribute to the observed scattering, particularly in the infrared [23]. Equation (44) thus gives only a first approximation to the scattering loss from the multilayer film.

Summary

Approximate expressions have been developed to predict, from experimentally measurable parameters characterizing the filming materials and substrate, what the performance of a high reflectance or AR quarter-wave film coating will be. These expressions are simple enough so that no computer is required even for multilayer problems. They form part of the basis for choice among various thin film materials and also give a starting point for film design efforts aimed at optimization of reflectance, absorption, transmittance, or laser damage threshold. They may be summarized as follows:

AR coatings

Single layer

$$T_1 = 1 - \left(\frac{n_S - n_L^2}{n_S + n_L^2}\right)^2 - \left[\frac{\beta_L\lambda(n_S+1)}{8n_S} + A_{OL} + \frac{A_{LS}}{n_S}\right] \tag{45}$$

Double layer

$$T_2 = 1 - \left(\frac{n_S - n_S n_L^2}{n_H^2 + n_S n_L^2}\right)^2 - \left[\frac{\beta_L\lambda(n_H^2+n_S)}{8n_H^2} + \frac{\beta_H\lambda(n_H^2+n_S^2)}{8n_H^2 n_S} + A_{OL} + A_{LH}\frac{n_S}{n_H^2} + \frac{A_{HS}}{n_S}\right] \tag{46}$$

Three-layer QHQ

$$T_3 = T_2 - \frac{\beta_h \lambda}{4 n_S} \left(\frac{n_S^2}{n_H^2} + \frac{n_H^2}{n_h^2} \right) - \frac{n_S}{n_H^2} \left(A_{Lh} + A_{hH} - A_{LH} \right) \quad . \tag{47}$$

High reflectance coatings ($R \sim 1$)

Low index next to metal substrate

$$R_L = 1 - \left[\frac{\lambda}{2} \left(\beta_L + \beta_H \right) + 4A_I \right] \left[1 - \left(\frac{n_L}{n_H} \right)^{2N+1} \right] \left[n_H^2 - n_L^2 \right]^{-1}$$

$$- \frac{4 n_S^+}{n_H^2} \left(\frac{n_L}{n_H} \right)^{2N} - \left(\frac{4\pi\delta}{\lambda} \right)^2 \quad . \tag{48}$$

High index next to dielectric substrate

$$R_H' = R_L - 4A_S \frac{n_S}{n_H^2} \left(\frac{n_L}{n_H} \right)^{2N} \quad . \tag{49}$$

Low index next to dielectric substrate

$$R_L' = R_L + \frac{4 n_S}{n_H^2} \left(\frac{n_L}{n_H} \right)^{2N} - \frac{4}{n_S} \left(\frac{n_L}{n_H} \right)^{2N} \quad , \tag{50}$$

where n_S^+ for a metal is given by eq. (32) and the low index layer next to the metal has a thickness given by eq. (30). The various symbols have the following meanings:

Symbols		Subscripts	
R	Reflectance	L	Low index layer
T	Transmittance	H	High index layer
A	Absorptance	h	Half-wave layer
β	Volume absorption coefficient	I	Interface
λ	Wavelength	F	Film
n	Index of refraction	S	Substrate
N	Number of layer pairs	O	Incident medium
δ	rms roughness		
n_S^+	Admittance (real) of substrate/ matching film combination		

To use these equations it is necessary to know the volume absorption coefficients of the materials as thin films, the interface absorptions, and the indices of refraction. The surface microroughness of the substrates should also be known for high reflectance coatings. These parameters may all be determined experimentally for individual films or surfaces. Knowing them the approximate performance of AR or high reflectance multilayer film combinations can then be simply predicted.

References

[1] Donovan, T. M., and Baer, A. D., in *Proceedings of the Fifth Annual Conference on Infrared Laser Window Materials*, C. R. Andrews and C. L. Strecker, eds. (Defense Advanced Research Projects Agency, 1976), pp. 291-300.

[2] Harrington, J. A., Rudisill, E. J., and Braunstein, M., Appl. Opt. 17, 2798 (1978).

[3] Bennett, J. M., J. Opt. Soc. Am. 54, 612 (1964).

[4] Macleod, H. A., *Thin Film Optical Filters* (American Elsevier Publ. Co., Inc., New York, 1969), p. 10.

[5] Macleod, H. A., *op. cit.*, pp. 114-115.

[6] Macleod, H. A., *Thin Film Optical Filters* (American Elsevier Publ. Co., Inc., New York, 1969), pp. 17-20.

[7] Cox, J. T., Hass, G., and Thelen, A., J. Opt. Soc. Am. 52, 965 (1962).

[8] Temple, P. A., Decker, D. L., and Donovan, T. M., "Measured Thin Film Absorption at the Air-Film Interface, the Film Bulk, and the Film-Substrate Interface," this conference.

[9] Cox, J. T., and Hass, G., in *Physics of Thin Films*, G. Hass and R. E. Thun, eds., Vol. 2 (Academic Press, New York, 1964), pp. 249-265.

[10] Baer, A. D., in *Laser Induced Damage in Optical Materials: 1976*, A. J. Glass and A. H. Guenther, eds., National Bureau of Standards, Washington, D.C. (NBS Spec. Publ. 462), pp. 221-229.

[11] Sparks, M., J. Opt. Soc. Am. 67, 1590 (1977).

[12] Bennett, H. E., and Bennett, J. M., in *Physics of Thin Films*, G. Hass and R. E. Thun, eds., Vol. 4 (Academic Press, New York, 1967), pp. 79-85.

[13] Muller, R. H., Surf. Sci. 16, 14 (1969).

[14] Koppelmann, G., Ann. Phys. (Leip.) 7, 388 (1960).

[15] Soileau, M. J., Bennett, H. E., Porteus, J. O., Temple, P. A., and Bass, M., in *Proceedings of the Fifth Annual Conference on Infrared Laser Window Materials*, C. R. Andrews and C. L. Strecker, eds. (Defense Advanced Research Projects Agency, 1976), pp. 392-417.

[16] Kozawa, S., *Proceedings Conference Opt. Instrs. Tech., London 1961*, K. J. Habell, ed. (Chapman and Hall, London, 1962), p. 410.

[17] Tien, P. K., Appl. Opt. 10, 2395 (1971).

[18] Guenther, K. H., Gruber, H. L., and Pulker, H. K., Thin Solid Films 34, 363 (1976).

[19] Koehler, W. F., and Eberstein, A., J. Opt. Soc. Am. 43, 747 (1953).

[20] Bennett, H. E., Bennett, J. M., Ashley, E. J., and Motyka, R. J., Phys. Rev. 165, 755 (1968).

[21] Eastman, J. M., PhD Thesis (unpubl.), University of Rochester, New York, 1974.

[22] Bennett, H. E., and Porteus, J. O., J. Opt. Soc. Am. 51, 123 (1961).

[23] Bennett, H. E., Opt. Engr. 17, 480 (1978).

[24] Elson, J. M., "Diffraction and Diffuse Scattering from Dielectric Multilayers," J. Opt. Soc. Am. (in press).

Table 1. AR coatings: comparison with exact calculations.

	Absorptance		Reflectance		Transmittance	
	Approx.	Exact	Approx.	Exact	Approx.	Exact
Single-layer MgF_2/BK7	1.5×10^{-5}	1.3×10^{-5}	0.012601	0.012601	0.987384	0.987386
Two-layer MgF_2/Al_2O_3/BK7	3.1×10^{-5}	3.0×10^{-5}	0.000940	0.000940	0.999029	0.999030
Three-layer (QHQ) $MgF_2/TiO_2/Al_2O_3$/BK7	7.56×10^{-4}	7.54×10^{-4}	0.000940	0.000935	0.998304	0.998311

MgF_2: $n = 1.38$, $\beta = 0.7\ cm^{-1}$; Al_2O_3: $n = 1.65$, $\beta = 1.0\ cm^{-1}$; TiO_2: $n = 2.25$, $\beta = 30\ cm^{-1}$; BK7: $n = 1.52$; $\lambda = 1.06\ \mu m$

Table 2. Mirrors: comparison with exact calculations.

Infrared, metal substrate $(ZnSe/ThF_4)^N ZnSe(ThF_4/Mo)$

N	A_{film}		$A_{substrate}$		R		
	Approx.	Exact	Approx.	Exact	Approx.	Exact	
0	0.0006	0.0010	0.0062	0.0061	0.9932	0.9929	$\lambda = 10.6\ \mu m$
1	0.0012	0.0013	0.0019	0.0019	0.9969	0.9968	ZnSe $n = 2.41$, $\beta = 1.0\ cm^{-1}$
2	0.0014	0.0014	0.0006	0.0006	0.9980	0.9980	
3	0.0014	0.0014	0.0002	0.0002	0.9984	0.9984	ThF_4 $n = 1.35$, $\beta = 10\ cm^{-1}$
4	0.0015	0.0015	0.0001	0.0001	0.9985	0.9985	
							Mo $n = 10\text{-}44j$

Ultraviolet, dielectric substrate $(HfO_2/SiO_2)^N HfO_2 SiO_2$

N	A_{film}		$T_{substrate}$		R		
	Approx.	Exact	Approx.	Exact	Approx.	Exact	
1	0.0029	0.0025	0.7231	0.5171	0.2740	0.4803	$\lambda = 0.35\ \mu m$
3	0.0042	0.0040	0.1973	0.1783	0.7985	0.8177	HfO_2 $n = 2.088$, $\beta = 276\ cm^{-1}$
5	0.0045	0.0045	0.0538	0.0521	0.9417	0.9434	
7	0.0046	0.0046	0.0147	0.0145	0.9807	0.9809	
9	0.0046	0.0046	0.0040	0.0040	0.9914	0.9914	SiO_2 $n = 1.509$, $\beta = 276\ cm^{-1}$
11	0.0046	0.0046	0.0011	0.0011	0.9943	0.9943	
13	0.0046	0.0046	0.0003	0.0003	0.9951	0.9951	

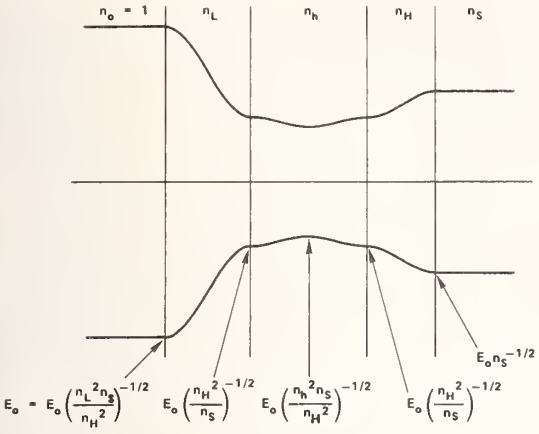

Figure 1.. Electric fields in a quarter-half-quarter antireflection coating.

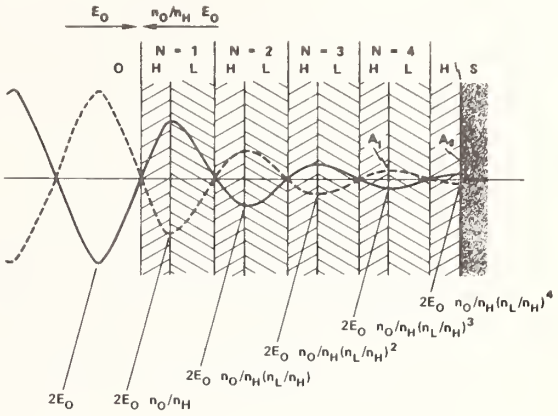

Figure 2. Electric fields in a perfect multilayer reflector (after Sparks [11]).

SIMPLIFIED DESCRIPTION OF DIELECTRIC REFLECTORS

M. Sparks and M. Flannery
Xonics, Incorporated
Santa Monica, California 90401

The spectral reflectance, $R(\omega)$, of a quarter-wave reflector is quite asymmetric in general as a result of absorption. The maximum electric field E in an infinite stack is in the center of the high-index (low-index) layer at the low-frequency (high-frequency) end of the high-reflection band. Thus, the absorptance minimum of a stack having much greater absorption in the high-index material occurs at $\omega > \omega_c$ (band center). Operation at $\omega > \omega_c$ could increase the damage resistance if the high-index material is easily damaged. At ω_c, E decays rapidly. As ω departs from ω_c in an infinite reflector, E penetrates deeper into the coating, with no decay at the band edges. The peak-to-peak distance in an infinite dielectric stack is constant for all frequencies in the band. By using the continuity of E and dE/dz, E can be obtained from E = 0 at the metallic substrate or, in an infinite stack, from E = 0 at the reflector surface for $\omega = \omega_c$ or E = 0 in the center of the high- or low-index layer at the band edges. Simple closed-form approximations for the spectral absorptance and the phase of E are accurate and sufficient for present applications.

Key Words: Dielectric reflectors; spectral absorptance; reflectance, electric-field distribution; theory; asymmetric absorptance; high-power; damage thresholds.

1. Introduction

Multilayer-dielectric-coated metallic reflectors are required in most high-power applications at all wavelengths since the intrinsic absorptance of metals is too great. As shown in figure 1, the lowest available absorptance in the ultraviolet and vacuum-ultraviolet regions is approximately eight to ten percent, and the values of absorptance at the hydrogen-fluoride-laser wavelength, $\lambda = 2.75$ μm, are 0.6, 0.7 and 0.8 percent for silver, gold, and copper, respectively [1]. All of these values are much greater than required values, which are at least as low as 0.1 to 0.01 percent, for high-power systems.

In considering high-power reflectors, it is convenient to consider two scales of reflectance — a fine scale from 0.997 to 1.000 and a large scale from 0 to 1.0. The high-power laser sees the fine-scale reflectance, so to speak. For example, doubling the absorptance from 10^{-4} to 2×10^{-4} doubles the heating, but the difference in the reflectance seen on the large scale is insignificant. Scattering is neglected; thus, the absorptance A is equal to 1 - R, where R is the reflectance, for the infinite-stack reflectors and dielectric-coated-metal reflectors (with zero transmittance).

The large-scale spectral reflectance $R(\omega)$ at normal incidence is shown in figure 2(a) for $(A\ell_2O_3/Si)^\infty$ and $(As_2S_3/GeSe)^\infty$ lossless infinite quarter-wave stacks [2,3]. The notation $Mo(A\ell_2O_3/Si)^3$ indicates three pairs (six layers) of $A\ell_2O_3$ - Si quarter-wave films, with low-index material $A\ell_2O_3$ and high-index material Si, deposited on a molybdenum substrate with an $A\ell_2O_3$ layer adjacent to the substrate. The perfect-reflectance bands (R = 1) of these stacks have full bandwidths $2\omega_c\Delta$ centered at ω_c [4,5]. The values of 2Δ in figure 2 are $2\Delta = 0.428$ for the $(A\ell_2O_3/Si)^\infty$ reflector and $2\Delta = 0.157$ for the $(As_2S_3/GeSe)^\infty$ reflector. As the index ratio n_H/n_L of the layers increases, the bandwidth increases until the perfect-reflectance band extends from $\omega = 0$ to $\omega = 2\omega_c$ as n_H/n_L approaches infinity.

Simple forms of the electric fields in dielectric reflectors will be discussed and used to explain important properties of the reflectors. Apfel and co-workers [6], Apfel [7], Newnam and co-workers [8], Gill and co-workers [9], Sparks [10], and Sparks and Flannery [11], have also investigated effects of the electric-field distributions in dielectric reflectors and other structures. The contents of the paper are as follows: 1. Introduction; 2. Electric Fields; 3. Absorptance and Phase; 4. Summary of Results; and 5. Acknowledgments.

2. Electric Fields

The key to the explanation of the central results for the spectral absorptance and phase shift is the simple form of the electric field in a perfect reflector (R = 1) composed of an infinite number of quarter-wave layers. First consider the center frequency ω_c of the high-reflectance band shown in figure 2. In each layer the electric field is a quarter of a sinusoidal standing wave, as seen in the center curve of figure 3. The amplitude is constant in each pair of HL layers. The electric field E and its normal derivative (slope) dE/dz are continuous everywhere, including the boundaries. Since the slope is continuous at the O-H interface and the wavelength in the high-index (n_H) medium is λ/n_H,

where λ is the wavelength in vacuum, the amplitude of the field is reduced by a factor of n_0/n_H at the O-H interface. Similarly, at the nodes at the L-H interfaces, the amplitude is reduced by a factor of n_L/n_H. The phase ϕ_E must be equal to zero at $\omega = \omega_c$ in order to satisfy the boundary condition at infinity — that the electric field remains finite. If ϕ_E were not zero, then the term $\sim \cos kz$ in the expansion $\sin(kz - \phi_E) = \sin kz \cos\phi_E - \sin\phi_E \cos kz$ would grow to infinity since the nodes would occur at H-L interfaces (and the magnitude of E would increase by a factor of n_H/n_L at every H-L interface).

As $|\omega - \omega_c|$ approaches the band edges, $\omega/\omega_c = 1 \pm \Delta$, the field penetrates deeper into the coating until there is no decay at the edges, as shown in figure 3. At the high-frequency edge, $\omega/\omega_c = 1 + \Delta$, the field has peaks at the centers of the low-index layers and nodes at the centers of the high-index layers, as illustrated in the bottom curve in figure 3. At the low-frequency edge $\omega/\omega_c = 1 - \Delta$, the field has peaks at the centers of the high-index layers and nodes at the centers of the low-index layers, as illustrated in the top curve in figure 3. The stack wavelength Λ, defined as twice the distance between adjacent nodes, remains constant for all frequencies in the band for the infinite stack.

The major differences between the electric fields in the infinite stack (fig. 3) and the finite stack (fig. 4) result from the near-node in the electric field at the metallic surface. Since the fields at the rear of the sixth layer of the infinite stack at $\omega/\omega_c = 1 \pm \Delta$ are far from nodes, while the corresponding fields in the coated-metal reflector have near-nodes at the metal, the metal produces extensive modifications in the fields near the band edges, as shown in figure 4. Other features of the electric-field distribution are summarized in section 4.

3. Absorptance and Phase

In order to develop an approximation to the spectral absorptance $A(\omega)$, consider three cases. First, the absorptance at the center frequency of an infinite quarter-wave stack is [12,13,10]

$$A_c = \frac{\frac{1}{2}(\beta_H + \beta_L)\lambda_c n_0}{(n_H^2 - n_L^2)} = 1.66 \times 10^{-3} \quad , \tag{1}$$

where $\lambda_c = 2\pi c/\omega_c$ is the center wavelength and the numerical value [2] is for $(A\ell_2O_3/Si)^\infty$. Second, the absorptance A_{Nc} at the center frequency of a lossless N-pair dielectric coating on an absorbing substrate in the limit $A_{Nc} << 1$ is closely approximated by the simple result [10,14] $A_{Nc} \simeq (n_L/n_H)^{2N} A_S$, where A_S is the absorptance of the uncoated substrate, $A_S = 2n_{Sr}[(n_{Sr}+1)^2 + \kappa_S^2]^{-1} \simeq 2n_{Sr}/|n_S|^2$. The substrate index is $n_S = n_{Sr} + i\kappa_S$. The approximate equality is satisfied when $A_S << 1$ is satisfied.

Third, the perturbation-expansion for the absorptance of an infinite quarter-wave stack for frequencies near the center frequency is [13]

$$A_\infty(\omega) = A_c + A_1(\omega/\omega_c - 1) + A_2(\omega/\omega_c - 1)^2 \quad , \tag{2}$$

where A_c is given by eq. (1) and

$$A_1 = \frac{(\beta_L n_H - \beta_H n_L)}{(n_H - n_L)(n_H^2 - n_L^2)} \quad , \tag{3}$$

$$A_2 = \frac{n_0 \lambda_c}{8(n_H^2 - n_L^2)^3} \left\{ (\beta_H + \beta_L)[n_H^4 + n_H^2 n_L^2 + n_L^4 - n_0^2 (n_H + n_L)^2] \right.$$

$$\left. + \beta_L n_H [n_H(n_H^2 + 2n_L^2) + 2n_L(2n_H^2 + n_L^2)] + \beta_H n_H n_L (4n_H^2 + 5n_L^2) \right\} \quad . \tag{4}$$

Combining these expressions for $A_\infty(\omega)$ and A_S gives a useful approximation for the spectral absorptance of a dielectric-coated-metal reflector:

$$A(\omega) = A_\infty(\omega)[1 - (n_L/n_H)^{2N}] + (n_L/n_H)^{2N} A_S \quad . \tag{5}$$

The linear perturbation-theory result [13] for the standing-wave electric field phase ϕ_E (which is one half the phase ϕ of the Fresnel reflection coefficient $r = |r| \exp i\phi$) in an infinite stack,

$$\phi_E = \frac{1}{2}\pi n_0(\omega/\omega_c - 1)/(n_H - n_L) \quad , \tag{6}$$

is quite accurate near the center of the high-reflectance band. The phase for an infinite quarter-wave stack reaches its maximum (or minimum) at the high-frequency (or low-frequency) band edge, where the standing-wave electric-field phase is

$$\phi_{Ee} = \pm \tan^{-1}\left[n_0(n_H n_L)^{-1/2} \right] \quad . \tag{7}$$

These results for the edge phases can be found quite easily by using the continuity of E and dE/dz at the O-H interface and the fact that E has a maximum or a node at the center of the first high-index layer. They can also be derived from eqs. (6) through (14) of reference 13 with somewhat more effort.

The high accuracy of the quadratic approximations to $A_\infty(\omega)$ from eq. (2) is shown [15] in figure 5 for three $(ThF_4/ZnS)^\infty$ reflectors which have their losses localized in the low-index layers, uniformly distributed, and localized in the high-index layers. The dashed curves are the exact infinite quarter-wave stack reflectances computed numerically from eqs. (6) through (14) of reference 13. The quadratic approximation provides a good estimate of the absorptance throughout the central part of the high-reflectance band for all three loss distributions.

The asymmetry of the spectral reflectance can be understood by considering the electric fields in the reflector in figure 3. For $\omega_c < \omega$ the fields peak in the low-index layers, while for $\omega < \omega_c$ the fields peak in the high-index layers. Thus the reflector in figure 5(a), with $\beta_H = 0$ and $\beta_L = 2\beta$, has high absorptance for $\omega_c < \omega$ since the peak fields are located in its lossy low-index layers. The reflector in figure 5(c), with $\beta_H = 2\beta$ and $\beta_L = 0$, has high absorptance for $\omega < \omega_c$ since the peak fields are located in its lossy high-index layers.

The high accuracy of the central results (5) and (2) for the spectral absorptance is shown in figure 6 for a practical reflector. The exact theoretical absorptance (heavy solid curve) was calculated by a standard matrix method using eqs. (4) and (9) of Flannery, Sparks, and Loh [13]. The general methods are presented by Lissberger [4] and Heavens [5]. The approximation (5), shown as heavy dots, is in excellent agreement with the exact result. This approximate absorptance is the sum of the approximate infinite-stack absorptance $A_\infty(\omega)$ (dash-double-dot curve) and the approximate substrate absorptance A_{Nc} (light dots). Notice that the substrate absorptance $A_{Nc} \simeq 1.5 \times 10^{-4}$ is much smaller than the absorptance $A_S \simeq 10^{-2}$ of the uncoated substrate. Also, the term $-(n_L/n_H)^{2N} A_\infty(\omega)$ in (5) is negligible in figure 6. Similar results are shown in figure 7 for $Ag(As_2S_3/GeSe)$ reflectors. The reflectance peak occurs at $\omega_c < \omega$ since the high-index layer is lossier, $\beta_L/n_L < \beta_H/n_H$.

4. Summary of Results

Asymmetric spectral-reflectance. The spectral-reflectance curves, $R(\omega)$, of dielectric quarter-wave-stack reflectors are quite asymmetric in general as a result of the absorption in the coating materials. The position of the peak in $R(\omega)$ is shifted from the absorption-free center frequency ω_c by a large amount, typically ten percent, as illustrated in figures 5 through 7. This dependence of $R(\omega)$ on the coating absorptance should be taken into account in designing coatings. The asymmetric spectral reflectance and the other results discussed below are explained in terms of the simple form of the electric field E(z) in a high-reflectance $(1 - R \ll 1)$ coating at normal incidence, as illustrated in figures 3 and 4.

Electric-field distribution. The maximum of E(z) in an infinite-stack reflector occurs in the center of the high-index [or low-index] material at the low-frequency end of the band [or the high-frequency end], as seen in figure 3. Thus, the absorptance minimum of a stack having greater absorption in the low-index material occurs at $\omega < \omega_c$, as seen in figures 5(a) and 6.

At the center frequency ω_c the electric field decays rapidly, reducing in amplitude by a factor of n_L/n_H at every node (at the L-H interfaces), as seen in the center curves in figures 3 and 4. As ω departs from the center frequency in an infinite reflector, the field penetrates deeper into the coating until it approaches a constant amplitude as ω approaches the edges of the reflectance band, at which frequencies the peaks of E are in the low-index and high-index material as discussed above. As seen in figure 3, the stack wavelength Λ, which is the peak-to-peak distance in an infinite dielectric stack, is constant for all frequencies in the band.

The electric fields in N-pair dielectric-coated metal reflectors that satisfy the condition $(n_L/n_H)^{2N} \ll 1$ are similar to those in the corresponding infinite quarter-wave stack for frequencies near ω_c. But the stack wavelength Λ is not constant as a function of frequency, and the fields decay quite rapidly even near the band edges, as seen in figure 4. The electric fields are insensitive to

changes in the small values of the absorptance of the coating materials, in contrast to the large changes in the fine-scale spectral reflectance.

It should be possible in general to improve the performance of a dielectric reflector by changing the layer thicknesses to change the relative values of the nominal center frequency ω_c and the laser frequency. For example, the value of ω_c could be chosen to center the laser band in the lowest absorptance region (at $\omega = 0.91\ \omega_c$ in figure 6, for example). An alternate choice of ω_c could be used in reflectors that are limited by laser damage to one of the layers — usually the high-index layer [16]. For example, by choosing ω_c less than the laser frequency ω, the electric field in the high-index material can be reduced, as seen in the bottom two curves of figures 3 and 4.

Obtaining the electric-field distribution. The electric-field distribution is easily obtained from the continuity of E and dE/dz when the phase ϕ_E of E is known. The electric-field distribution at any frequency in the high-reflectance band of a dielectric-coated metal reflector with metallic absorptance $A_S << 1$ can be obtained to excellent accuracy by starting with E = 0 at the metallic substrate and using the continuity of E and dE/dz at the interfaces and boundaries. Simple relations that are useful in matching E and dE/dz at the surface and interfaces are given by Sparks and Flannery [11]. For an infinite-stack reflector, the electric field is easily obtained for $\omega - \omega_c \tilde{<} \Delta\omega_c/3$, typically, and for ω at the band edges, $\omega = \omega_c(1 \pm \Delta)$, since the phases are known for these frequencies. Specifically, the fields can be plotted by starting at E = 0 at the surface or in the center of the low-index or high-index layer for $\omega = \omega_c$, $\omega_c(1 - \Delta)$, or $\omega_c(1 + \Delta)$, respectively, and using the continuity of E and dE/dz.

Simple closed-form approximation to the absorptance. The simple approximation (5), with $A_\infty(\omega)$ given by (2), developed for the spectral absorptance $A(\omega)$ of an N-pair absorbing stack on an absorbing substrate is sufficiently accurate for present applications when $A(\omega)$ is small. In (5), $A_\infty(\omega)$ is the spectral absorptance of the corresponding infinite absorbing stack, and A_S is the absorptance of the uncoated substrate. The term $(n_L/n_H)^{2N} A_S$ is the absorptance of the substrate with the incident irradiance reduced by the dielectric coating by the factor $(n_L/n_H)^{2N}$. The term $-(n_L/n_H)^{2N} A_\infty(\omega)$ corrects for the absorptance in the missing layers from 2N to infinity.

The expression for A_S and a simple approximation for the case of $A_S << 1$ are given under eq. (1). The infinite-stack spectral absorptance $A_\infty(\omega)$ is well approximated by the quadratic perturbation expansion (2). The accuracy of (2), which is sufficient for present applications, is good for all frequencies in the band that are not near the band edges, as seen in figures 5, 6, and 7. The infinite-stack absorptance $A_\infty(\omega)$ is approached as more pairs are added. Values of $A_\infty(\omega)$ can be calculated exactly, with a moderate amount of computation, from eqs. (6) through (14) of Flannery, Sparks, and Loh [13]. However, using the exact value of $A_\infty(\omega)$ in the approximation (5) for the dielectric-coated-metal-reflector absorptance may not give a great improvement over the simpler approximation (5) with $A_\infty(\omega)$ given by eq. (2), as seen in figures 5, 6, and 7. Finally, the exact value of $A(\omega)$ can be obtained numerically, with a considerably greater amount of computation, by the matrix method, using eqs. (4) and (9) of Flannery, Sparks, and Loh [13] or the general results as presented by Lissberger [4] or Heavens [5].

Simple closed-form approximation to the phase. The standing-wave electric-field phase ϕ_E in an infinite stack is zero at the center frequency ω_c. The simple expression (7) for the band-edge phases is easily obtained by using the continuity of E and dE/dz at the reflector surface and using the zeros of the electric field in the center of the high-index and low-index materials. The perturbation-expansion approximation to the phase ϕ_E given in (6) is accurate for frequencies near $\omega = \omega_c$. Extrapolating between (6) for ω near ω_c and (7) for $\omega = \omega_c(1 \pm \Delta)$ gives sufficiently accurate results for infinite stacks for many applications. Numerical calculations of ϕ_E using eqs. (6) through (14) of Flannery, Sparks, and Loh [13] can be used if greater accuracy is required.

5. Acknowledgments

This research was supported by the Defense Advanced Research Projects Agency with technical administration by the Naval Weapons Center, the Air Force Office of Scientific Research, and the Air Force Weapons Laboratory with technical administration by the University of Dayton Research Institute.

6. References

[1] The data from which figure 1 was plotted is from the following references: Aluminum and gold: Jean M. Bennett and E. J. Ashley, Appl. Opt. 4, 223 (1965), and H. E. Bennett, M. Silver, and E. J. Ashley, J. Opt. Soc. Am. 53, 1093 (1963); copper: High Energy Laser Mirrors and Windows, Semiannual Report No's. 7 and 8, Naval Weapons Center, China Lake, Ca., July 1976, p. 59, and H. E. Bennett, M. J. Soileau, and P. C. Archibald in Proceedings of a Symposium on Laser Induced Damage in Optical Materials, NBS Spec. Publ. 435, edited by A. J. Glass and A. H. Guenther, Boulder, Colo., July 29-31, 1975; silver: Jean M. Bennett and E. J. Ashley, op. cit., and High Energy Laser Mirrors and Windows, Semiannual Report No. 3, Naval Weapons Center, China Lake, Ca., Mar.-Sept. 1963, p. 79; gallium, mercury, and sodium: American Institute of Physics Handbook, third edition (McGraw-Hill, New York, 1972); molybdenum: High Energy Laser Mirrors and Windows, Semiannual Report No. 6, Naval Weapons Center, China Lake, Ca., Sept. 1974 - Mar. 1975, p. 9.

[2] Values of parameters for $A\ell_2O_3$/Si in figure 2 are as follows: $n_L(A\ell_2O_3) = 1.733$, $\beta_L(A\ell_2O_3) = 100\ cm^{-1}$, $n_H(Si) = 3.436$, and $\beta_H(Si) = 8.1\ cm^{-1}$ at $\lambda = 2.75\ \mu m$; $A_S = 99.1$ percent for silver at 2.7 to 3.8 μm. Values of n and A_S are from the American Institute of Physics Handbook, third edition, Dwight E. Gray, editor (McGraw-Hill, New York, 1972), pp. 6-40, 6-41, and 6-150. Absorption coefficients β are from P. A. Miles, J. E. Hopson, and W. T. Beauchamp in High Power Laser Optical Components and Component Materials, compiled by James S. Harris and Charles L. Strecker, Boulder, Colo., Oct. 3-4, 1977, p. 257.

[3] Values of parameters for As_2S_3/GeSe at 2.75 μm in figure 2 are as follows: $n_L(As_2S_3) = 2.42$, from American Institute of Physics Handbook, third edition, Dwight E. Gray, editor (McGraw-Hill, New York, 1972), pp. 6-54; $n_H(GeSe) = 3.1$ is an approximate value; $\beta(As_2S_3) = 0.27\ cm^{-1}$, which is a very rough estimate at 2.75 μm, is the $\lambda = 5.3\ \mu m$ value from C. Willingham, D. Bua, H. Statz, and F. Horrigan, Raytheon Research Division Final Technical Report, Contract DAAH01-74-C-0719, Aug. 1975; and $\beta(As_2S_3) = 31\ cm^{-1}$, which is a very rough estimate at 2.75 μm, is from the value $\beta(As_2S_3) = 16\ cm^{-1}$ at $\lambda = 10.6\ \mu m$, from John F. Lewis and Melvin C. Ohmer in Proceedings of a Symposium on Laser Induced Damage in Optical Materials: 1976, NBS Spec. Publ. 462, edited by A. J. Glass and A. H. Guenther, Boulder, Colo., July 13-15, 1976, p. 279.

[4] P. H. Lissberger, Rep. Prog. Phy. 33, 197 (1970).

[5] O. S. Heavens, Optical Properties of Thin Solid Films (Dover, New York, 1965), chapter 4.

[6] Joseph H. Apfel, John S. Matteucci, Brian E. Newnam, and Dennis H. Gill in Proceedings of a Symposium on Laser Induced Damage in Optical Materials: 1976, NBS Spec. Publ. 462, edited by A. J. Glass and A. H. Guenther, Boulder, Colo., July 13-15, 1976, p. 301.

[7] Joseph H. Apfel, App. Opt. 16, 1880 (1977); Appl. Opt. 15, 2339 (1976); in Proceedings of a Symposium on Laser Induced Damage in Optical Materials: 1977, NBS Spec. Publ. 509, edited by A. J. Glass and A. H. Guenther, Boulder, Colo., Oct. 4-6, 1977, p. 251.

[8] Brian E. Newnam, Dennis H. Gill, and George Faulkner in Proceedings of a Symposium on Laser Induced Damage in Optical Materials: 1975, NBS Spec. Publ. 435, edited by A. J. Glass and A. H. Guenther, Boulder, Colo., July 29-31, 1975, p. 254.

[9] Dennis H. Gill, Brian E. Newnam, and John McLeod in Proceedings of a Symposium on Laser Induced Damage in Optical Materials: 1977, NBS Spec. Publ. 509, edited by A. J. Glass and A. H. Guenther, Boulder, Colo., Oct. 4-6, 1977, p. 260.

[10] M. Sparks, J. Opt. Soc. Am. 67, 1590 (1977).

[11] M. Sparks and M. Flannery, to be published.

[12] G. Koppelmann, Ann. Phys. (Leip.) 7, 388 (1960).

[13] M. Flannery, M. Sparks, and E. Loh, Jr., Appl. Opt., in press.

[14] M. Sparks, Theoretical Studies of High-Power Ultraviolet and Infrared Materials, Xonics Eighth Technical Report, Contract DAHC15-73-C-0127, Dec. 31, 1976; M. Sparks and E. Loh, Jr., Theoretical Studies of High-Power Ultraviolet and Infrared Materials, Xonics Final (Eleventh) Technical Report, Contract DAHC15-73-C-0127, March 31, 1978.

[15] The values of $n_L(ThF_4) = 1.527$ and $n_H(ZnS) = 2.24$ at $\lambda = 2.75\ \mu m$ are from M. Sparks, Theoretical Studies of Materials for High-Power Infrared Coatings, Xonics Sixth Technical Report, Contract DAHC15-73-C-0127, Dec. 31, 1975, p. 139; and P. Kraatz in Proceedings of the High Power Laser Optical Components and Component Materials Meeting, compiled by James S. Harris and Charles L. Strecker, Boulder, Colo., Oct. 3-4, 1977, p. 401.

[16] J. R. Bettis, R. A. House, A. H. Guenther, and R. Austin in Proceedings of a Symposium on Laser Induced Damage in Optical Materials: 1975, NBS Spec. Publ. 435, edited by A. J. Glass and A. H. Guenther, Boulder, Colo., July 29-31, 1975, p. 289.

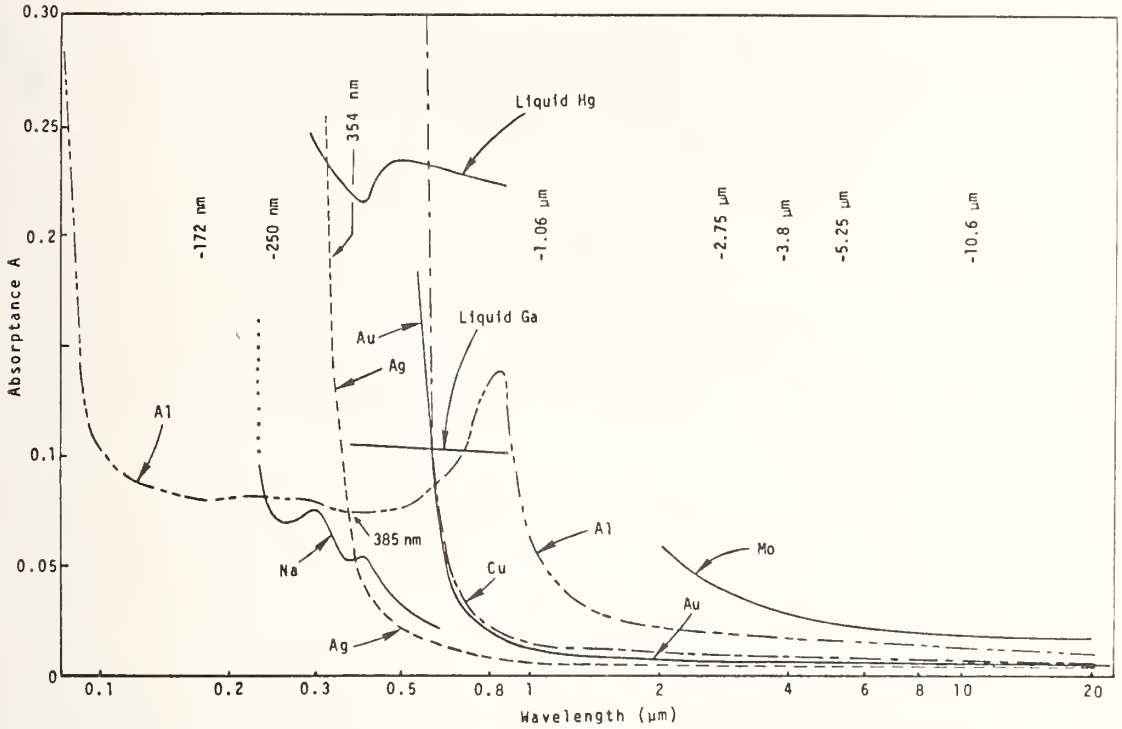

Figure 1. Lowest experimental values of absorptance for several metals. Sources of the data are given in reference 1.

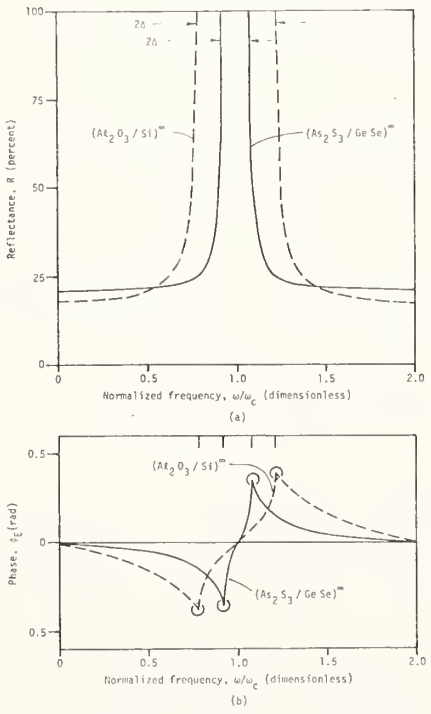

Figure 2. (a) Large-scale spectral reflectance of lossless infinite quarter-wave reflectors showing the perfect reflectance in the high-reflectance band, $1 - \Delta < \omega/\omega_c < 1 + \Delta$, the rapid decrease in reflectance outside the band, and the even symmetry of the curves about the center frequency $\omega_c = 2\pi c(2.75\ \mu m)^{-1}$. (b) Phase of the electric field for the reflectors in (a) showing the zero phase at the center frequency ω_c, the maximum phase amplitudes at the band edges, and the odd symmetry of the curves about ω_c. Data are from references 2 and 3.

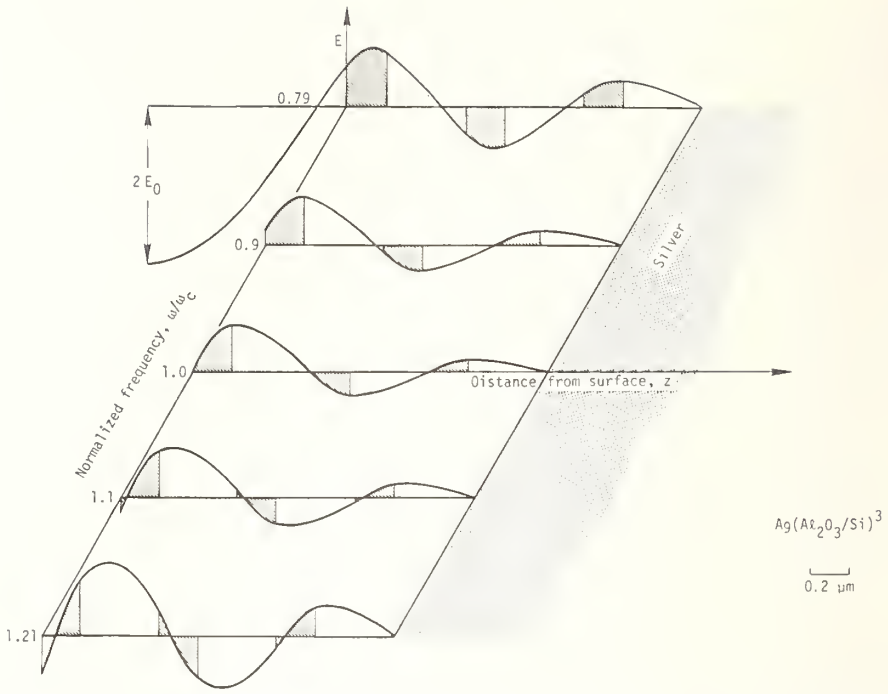

Figure 3. Standing-wave electric fields E in the infinite lossless quarter-wave reflector $(A\ell_2O_3/Si)^{\infty}$ showing: the peak fields at the H-L interfaces for $\omega=\omega_c$ and the peak fields in the centers of the low-index (unshaded) or high-index (shaded) layers at the band edges $\omega/\omega_c = 1\pm\Delta$, respectively; the rapidly decreasing field amplitude for $\omega=\omega_c$; the constant field amplitudes for $\omega/\omega_c = 1 \pm\Delta$; and the constant stack wavelength $\Lambda = \frac{1}{2}\lambda(n_H^{-1} + n_L^{-1})$ for all frequencies in the perfect-reflectance band. Data are from reference 2.

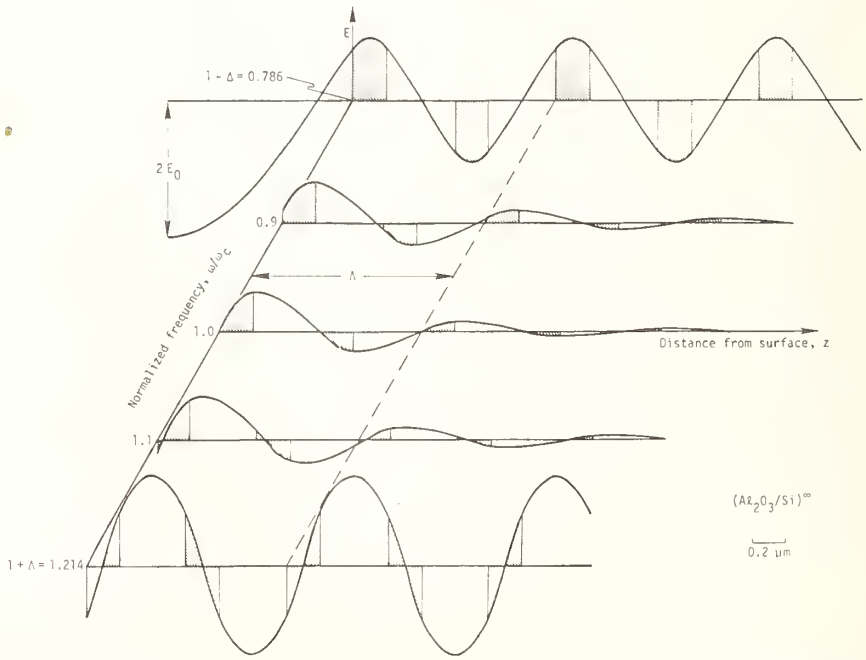

Figure 4. Standing-wave electric fields E in a three-pair quarter-wave coating deposited on a silver substrate showing: the relatively rapidly decreasing field amplitudes even near the band edges, in contrast to the infinite-stack constant-amplitude fields at $\omega/\omega_c=1\pm\Delta$; the change in the stack wavelength Λ with ω, in contrast to the constant Λ for the infinite stack; and the approximate node in the fields near the silver surface at all frequencies. Data are from reference 2.

Figure 5. Fine-scale spectral reflectance for $(ThF_4/ZnS)^{\infty}$. In (a), for loss in L only, A is greater for $\omega_c<\omega$ since E_{max} occurs in L for $\omega_c<\omega$. In (b), for $\beta_H=\beta_L$, A still is greater for $\omega_c<\omega$. The center slope is zero for $\beta_L/n_L=\beta_H/n_H$, from (3). In (c), for loss in H only, A is greater for $\omega<\omega_c$. Data are from references 14 and 15.

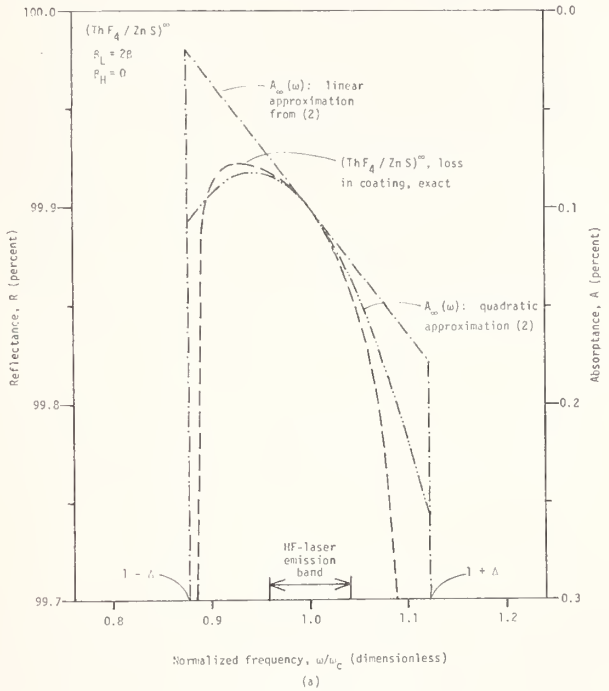

Figure 5 (a).

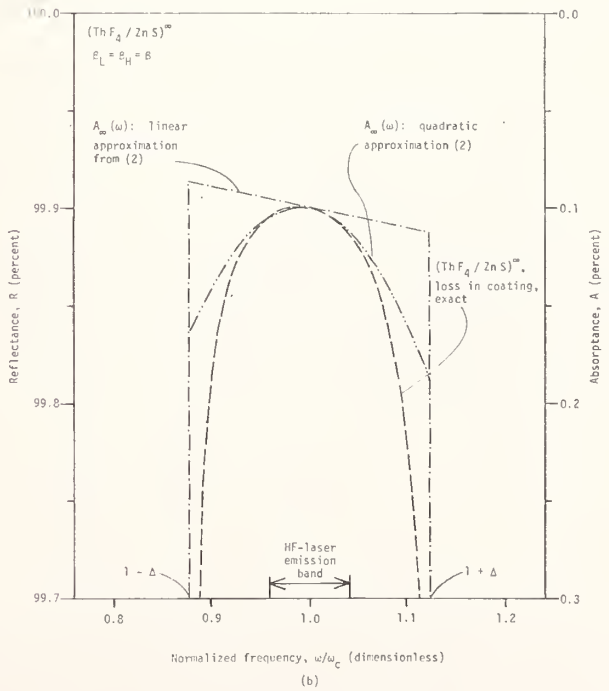

Figure 5 (b).

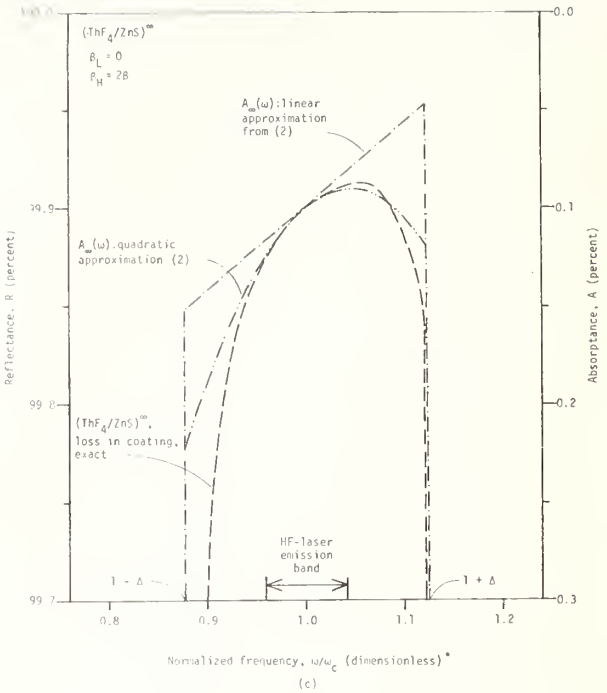

Figure 5 (c).

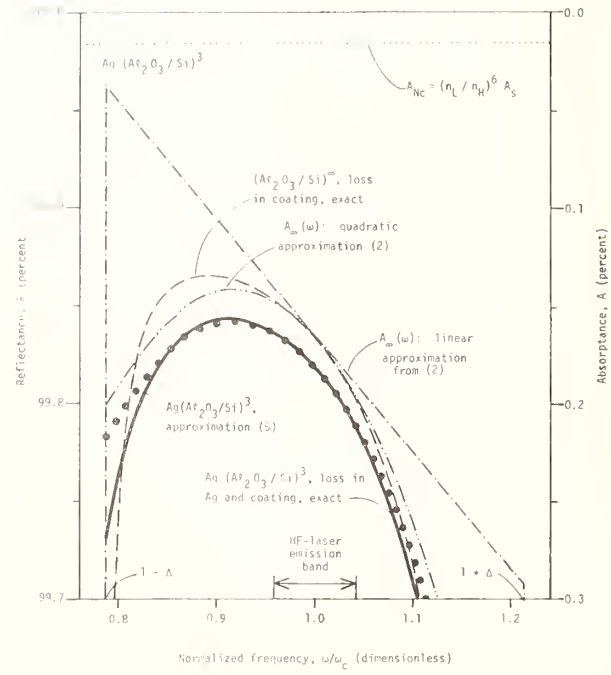

Figure 6. Fine-scale spectral reflectance of a lossy three-pair dielectric stack on silver, $Ag(Al_2O_3/Si)^3$, showing: the approximate absortance $(n_L/n_H)^6 A_S$ of the silver substrate with a lossless three-pair coating (light dotted curve); the good agreement between the exact reflectance for the infinite stack $(Al_2O_3/Si)^{\infty}$ (dashed curve) and the quadratic approximation (2) (dashed-double-dot curve); and the excellent approximations (5) and (2) (heavy dots) to the exact $A(\omega)$ for the $Ag(Al_2O_3/Si)^3$ reflector (heavy solid curve). Data are from reference 2.

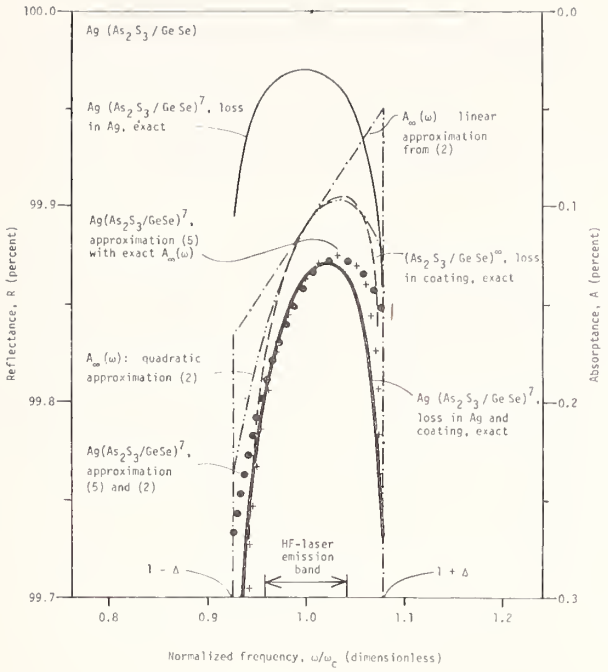

Figure 7. Fine-scale spectral reflectance of a lossy seven-pair dielectric stack on silver, $Ag(As_2S_3/GeSe)^7$, showing: the reflectance of an $Ag(As_2S_3/GeSe)^7$ reflector with no loss in the coatings; the asymmetric reflectance of a lossy infinite stack $(As_2S_3/GeSe)^\infty$; the agreement between the quadratic approximation (2) and the infinite-stack reflectance; the approximations (5) and (2) (solid dots) and (5) with $A_\infty(\omega)$ calculated exactly (plus signs) to the exact $A(\omega)$ for the $Ag(As_2S_3/GeSe)^7$ reflector with loss in the coating; and the lossy infinite-stack approximation (double-dot dashed curve). Data are from reference 3.

Discussion

If this analysis were applied to ultraviolet coatings, the effects of scattering would have to be considered. It was pointed out that uv scattering in multilayer dielectric films is a complicated function of wavelength, due to standing-wave resonances. On another subject, the speaker indicated that in well-designed films, the optimal frequency shift depends only weakly on the number of layers, since the multilayer stack approximates the infinite stack very closely.

ELECTRIC FIELDS NEAR COATED SURFACES: APPLICATION TO DAMAGE PROTECTION

Herbert B. Rosenstock
U. S. Naval Research Laboratory
Washington, D. C. 20375

Damage to transparent materials from intense light pulses usually begins at the exit surface. This is usually explained by "constructive" interference between incident and reflected waves: The total electric field may exceed the threshold for damage only upon reflection from the exit surface. However, in case of a surface coated with a thin film, interference may either increase or decrease the total electric field. Details depend on the optical constants, thickness, and wavelengths. A film designed to provide protection against excessive electric fields at one wavelength may not do so at other wavelengths. Also, attempts to minimize the field in the material proper may entail novel problems in the film, in which the damage mechanism may be an absorptive one.

Key words:
Damage threshold; Electric fields; Internal reflection; Protective coatings

INTRODUCTION AND SUMMARY

The most common use of optical coatings is to eliminate reflection and resulting losses; the body of literature on such "AR-coatings" is large. Here we consider briefly another use of coatings -- to avoid damage in systems exposed to pulsed laser beams.

Damage to transparent materials exposed to short, intense pulses usually begins at the exit surface [1][1] (not in the bulk or the entrance surface). This is usually explained by the "interference" (more simply put, the addition) of the beams incident on and reflected by the exit surface. For an uncoated material (provided its index of refraction is greater than 1, as is almost always true) elementary electromagnetic theory predicts that the "total" electric field (incident plust reflected) is larger than the incident alone; since it is high electric fields that are believed responsible for damage to transparent material [2] (by avalanche production or a similar process), the damage threshold is first exceeded just above the exit surface.

The main purpose of this note is to show that this argument is not necessarily valid if the exit surface is coated. In that case, the "total" field can, in fact, be smaller than the incident field alone (i.e., coatings can make the interference "destructive" instead of "constructive"). Coating the exit surface of a material can thus protect it against damage from intense pulsed beams.

A related problem that must be considered is the possible damage in the coating itself. The electric field there is not hard to compute theoretically (it is, in fact, the same on the two sides of the material-coating interface), but the damage mechanism in the coating may be different (viz. absorptive), and possibly severe.

TRANSMITTED AND REFLECTED ELECTRIC FIELDS AT A SINGLE INTERFACE

Here, we outline the derivation of needed results for the behavior of an electromagnetic wave at an interface. Our purpose is to provide clear definitions and assurance that the assumptions are few and fundamental. More details can be found in textbooks [3].

1. Figures in brackets indicate the literature reference at the end of this paper.

The boundary conditions for a light beam at an interface are the continuity of the tangential component of both E and H. For normal incidence, the tangential components of E and H are simply E and H themselves. So, following the notation of figure 1, we have $E_0 + E_{refl} = E_{tr}$ and $H_0 + H_{refl} = H_{tr}$. Also, E and H are related by $H_0 = A E_0$, $H_{refl} = -A E_{refl}$ and $H_{tr} = B E_{tr}$. The - sign indicates that either E or H must undergo a phase change of 180 degrees upon reflection since propagation is now in the opposite direction. Eliminating the H's from these expressions gives E_{refl} and E_{tr} in terms of E_0,

$$E_{tr} = 2A E_0/(A+B), \quad E_{refl} = (A-B) E_0/(A+B) \tag{1}$$

and similarly

$$H_{tr} = 2A H_0/(A+B), \quad H_{refl} = -(A-B) H_0/(A+B). \tag{2}$$

Here A and B are the complex indices of refraction,

$$A = n_A - i k_A$$

in the usual notation.

Division of eq. (1) by E_0 now gives the conventional transmission and reflection coefficients for electric fields and similarly, from eq. (2) for magnetic fields:

$$t^E_{AB} = 2A/(A+B) \tag{3}$$

$$r^E_{AB} = (A-B)/(A+B) \tag{4}$$

$$t^H_{AB} = t^E_{AB} \tag{5}$$

$$r^H_{AB} = r^E_{BA} = -r^E_{AB} \tag{6}$$

The energy transported in a beam is given by the mean value of the Poynting vector $\underline{E} \times \underline{H}$; in case of a plane wave this becomes [4] $I = \frac{1}{2}\mathrm{Re}(\underline{E} \times \underline{H}^*)$ or, since E and H are perpendicular, $I = \frac{1}{2}\mathrm{Re}(EH^*)$. Substitution of eqs. (1) and (2) into this expression then gives the transmitted and reflected energies. The transmission and reflection coefficients for energy are then obtained by dividing by the incident energy:

$$\mathcal{T}_{AB} = 4\,\mathrm{Re}(AB^*)/|A+B|^2 \tag{7}$$

$$\mathcal{R}_{AB} = |A-B|^2/|A+B|^2 \tag{8}$$

EFFECTIVE COEFFICIENTS IN THE PRESENCE OF A FILM

We next calculate the effective transmission and reflection coefficients for both fields and energies of a thin film F between two media A and B, as shown in fig. 2. Since the film is thin and reflections therefore coherent, we must calculate the total electric and magnetic fields due to multiple reflections first and then, having added these separately, calculate the energy from the two sums. So let us first go through the calculation for the electric fields. Proceeding step by step in fig. 3 from E_1 to E_2 to E_3 ..., we find

$$E_1/E_1 = 1, \quad E_2/E_1 = \xi, \quad E_3/E_1 = \xi r^E_{FB}, \quad E_4/E_1 = \xi^2 r^E_{FB}, \quad E_5/E_1 = \xi^2 r^E_{FB} r^E_{FA}, \ldots$$

and so forth. In words, $\xi = \exp(-2\pi i F \ell/\lambda)$, where λ is the wavelength in vacuum (in cm) and ℓ the thickness (in cm), appears as a factor whenever the film is traversed once, and the appropriate reflection coefficient (known from eqs. (6) and (4)) appears as a factor upon reflection. Now adding $E_2 + E_6 + E_{10} \ldots$ and summing the resulting geometric series gives

$$\sum_{j=2,6,10,\ldots} E_j = E_1 \xi/\Delta \quad ; \tag{9}$$

similarly, we find

$$\sum_{j=4,8,12,\ldots} E_j = E_1 \xi^2 r^E_{FB}/\Delta \quad ; \qquad \text{with} \quad \Delta \equiv 1 - r^E_{FA} r^E_{FB} \xi^2 \tag{10}$$

The total transmitted field is, from fig. 2, seen to be

$$E_{tr} = t^E_{FB} \sum_{2,6,10,\ldots} E_j = E_1 t^E_{FB} \xi/\Delta$$

where we used eq. (9),
or again looking at fig. 2

$$E_{tr}/E_0 = \xi t^E_{AF} t^E_{FB}/\Delta \, . \tag{11}$$

Similarly for the reflected electric field we find

$$E_{refl} = r^E_{AF} E_0 + \xi^2 t^E_{FA} \sum_{4,8,12,\ldots} E_j$$

or

$$E_{refl}/E_0 = r_{AF} + \xi^2 t^E_{AF} t^E_{FA} r^E_{FB}/\Delta \tag{12}$$

The calculation for magnetic instead of electric fields is quite the same; merely replace E by H both in the field quantities and superscripts, and obtain

$$H_{tr}/H_0 = \xi t^H_{AF} t^H_{FB}/\Delta^H \tag{13}$$

instead of eq. (11), and

$$H_{refl}/H_0 = r^H_{AF} + \xi^2 t^H_{AF} t^H_{FF} r^H_{FB}/\Delta^H \tag{14}$$

instead of eq. (12). Here $\Delta^H = 1 - r^H_{FB} r^H_{FA} \xi^2$ is analogous to eq. (10), and from eq. (6), therefore $\Delta^H = \Delta$. (15)

Let us next get rid of the r^H_{ij} and t^H_{ij} coefficients in favor of r^E_{ij} and t^E_{ij}.

With eqs. (5), (6) and (15), eq. (13) becomes

$$H_{tr}/H_0 = \xi\, t^E_{FA}\, t^E_{BF}/\Delta \tag{16}$$

and eq. (14), using eq. (15) for Δ, eq. (5) for t, and eq. (6) for r, becomes

$$H_{refl}/H_0 = -r^E_{AF} - \xi^2 t^E_{FA} t^E_{AF} r^E_{FB}/\Delta \tag{17}$$

or

$$H_{refl}/H_0 = -E_{refl}/E_0.$$

Knowing the total reflected and transmitted electric and magnetic fields, we can now use eq. (13) to get the reflected and transmitted energies, and define the coefficients $\tau_{AB} = I_{tr}/I_0$, $\rho_{AB} = I_{refl}/I_0$. These then turn out to be

$$\tau_{AB} = |\xi/\Delta|^2 \operatorname{Re}\left(t^E_{AF} t^E_{FB} t^{E*}_{FA} t^{E*}_{BF}\right) \tag{18}$$

$$\rho_{AB} = \left|r^E_{AF} + \left(\xi^2 r^E_{FB} t^E_{FA} t^E_{AF}/\Delta\right)\right|^2 \tag{19}$$

TOTAL FIELD ABOVE AN INTERFACE

We now show that the total electric field may be increased or decreased by reflection at a surface, while the net energy flow is always decreased.

It is easy to show from our formalism that when the surface is bare (no film on it), the total field increases. Consider eqs (1a) and (2a)

$$E_{refl} = \frac{A-B}{A+B} E_0, \qquad H_{refl} = -\frac{A-B}{A+B} H_0$$

when both A and B are real (no absorption) and A is greater than B (back surface). Then E_{refl} is in the same direction as E_0 and

$$E_{tot} = E_0 + E_{refl} \tag{20}$$

is greater than E_0. The opposite is true for the front surface where A < B, and the opposite again for H. The total energy (3) is, with (1) and (2),

$$I = \tfrac{1}{2} \operatorname{Re}\left[\left(1 + r^E_{AB}\right)\left(1 - r^E_{AB}\right)^* E_0 H_0^*\right]$$

and can be written

$$= I_0 \operatorname{Re}\left[1 - r_{AB} r^*_{AB} + \left(r_{AB} - r^*_{AB}\right)\right].$$

Since the last ( ) is purely imaginary, we find simply

$$I = I_0\left[1 - r_{AB} r^*_{AB}\right]$$

which, since rr* is positive, is always smaller than I_0.

The situation is less simple when a film is on the surface. We develop a general expression for this situation, and show that E_{tot} can be either greater or smaller than E_0, depending on circumstances. The reflected electric and magnetic fields are now given by (12) and (17) which we write as

$$E_{refl} = E_0 g(A, B, F, \xi^2), \qquad H_{refl} = -H_0 g(A, B, F, \xi^2)$$

where

$$g = r^E_{AF} + \xi^2 t^E_{AF} t^E_{FA} r^E_{FB} / \Delta . \tag{21}$$

We need the total field (incident plus reflected - see fig. 3),

$$E_{tot} = E_0 (1 + g) \tag{22}$$

and find after a little algebra, that we can write

$$E_{tot} = (1 + \xi^2 r^E_{FB}) t_{AF} E_0 / \Delta, \qquad H_{tot} = (1 - \xi^2 r^E_{FB}) t_{FA} H_0 / \Delta \tag{23}$$

or even simpler

$$E_{tot} = 2 E_0 / (1 + \sigma), \qquad H_{tot} = 2 H_0 \sigma / (1 + \sigma) \tag{24}$$

where

$$\sigma = (1 - \gamma) F / (1 + \gamma) A, \qquad \gamma = \xi^2 r^E_{FB} \tag{25}$$

Again the fact that $I_{tot} < I_0$ can be established at once from (3) and (23):

$$\begin{aligned} I_{tot} &= \tfrac{1}{2} \mathrm{Re}\,(E_{tot} H^*_{tot}) \\ &= I_0 \mathrm{Re}[(1+g)(1-g)^*] \\ &= (1 - g g^*) I_0 \end{aligned}$$

which is smaller than I_0 always.

Evaluation of $|E_{tot}|$ for all values of the parameters is a little more involved. We will later show some numerically calculated examples, but first consider some special cases analytically to show directly that this quantity can be either greater or smaller than E_0. We consider three cases:

CASE I. $\xi^2 = 1$ or $\ell/\lambda = j/2 n_F$ (j = integer)

with $k_F = 0$, nonabsorbing film.

CASE II. $\xi^2 = -1$ or $\ell/\lambda = (j + \frac{1}{2})/2 n_F$

with $k_F = 0$, nonabsorbing film.

CASE III. $\xi^2 = 0$, fully absorbing film, $k_F \ell/\lambda \gg 1$.

CASE I. (21) becomes, after a little algebra,

$$g = (A - B)/(A + B) \tag{26}$$

which, by (1), we recognize as the reflection coefficient in absence of a film. So if the thickness is such that $\xi^2 = +1$, the film has no effect at all. If A > B, E_{refl} is in phase with E_0 and E_{tot} therefore greater than E_0.

CASE II.

In this case, (22) becomes, again with a little straightforward algebra,

$$g = (AB - F^2) / (AB + F^2), \tag{27}$$

which can be negative, zero, or positive depending on the values of A, B, or F. The value zero is attained then $F = \sqrt{AB}$, the familiar result for an anti-reflection coating [5] The total electric field is, by (23), given by

$$E_{tot} = E_0 \, 2AB / (AB + F^2) \tag{28}$$

which can be either less or more than E_0.

CASE III. $\xi^2 = 0$, fully absorbing film

We see from (21) that $g = (A-F)/(A+F)$ and

$$E_{tot} / E_0 = 2A/(A+F)$$

with F now purely imaginary. So again E_{tot} can be either larger or smaller than E_0, depending on the values of A and F.

Turning next to magnetic field, we see from sec. III that

$$H_{refl} / H_0 = - E_{refl} / E_0 \tag{29}$$

so that, in the notation of (21),

$$H_{refl} = - H_0 g \tag{30}$$

and so analogous to (23)

$$H_{tot} = H_0 (1 - g) \tag{31}$$

So for Case I it again follows (from (24) and (6)) that the film has no effect at all. For Case II, (31) gives

$$H_{tot} = H_0 \, 2F^2 / (AB + F^2) \tag{32}$$

which again can be $\gtrless 0$ depending on whether $E_{tot} \lessgtr E_0$.

Some graphs depicting special cases and showing how $|E_{tot}| / E_0$ can vary as a function of film thickness and optical constants are shown in fig. 4. In each case shown, total fields below the incident are attainable for some film thickness. (For k = 0, continuation of the plot would be periodic in D/λ.)

Finally, we should note explicitly that the total electric field as plotted is the same just above and just below the material-film interface. (This follows directly from the boundary conditions on which sec. III is based.) A film of optical constant and thickness appropriate to the optical constant of the material and the expected wavelength of the impinging radiation can therefore not only reduce the total field in the material, it will also produce a smaller field in the film. However, since the damage mechanism in the film may be of a different nature (i.e., absorptive), a new set of problems may arise from its presence.

ACKNOWLEDGMENTS

Some of the calculations reported here were begun in connection with experimental work of Drs. E. D. Palik, N. Ginsburg and R. T. Holm [6]. I am grateful to Dr. M. Hass for many discussions.

REFERENCES

[1] M. D. Crisp, N. D. Boling and G. Dubé, Appl. Physics Letters 21, 364 (1972).

[2] M. Sparks, Proc. Symposium (Boulder, Colorado 1975) NBS Special Publication #435 (A. Guenther and A. J. Glass, eds., April 1976).

[3] O. S. Heavens, Optical Properties of Thin Films (Dover, New York, 1965); A. Vasiček, Optics of Thin Films (North Holland, Amsterdam, 1960).

[4] M. Born and E. Wolf, Principles of Optics, fourth edition (Pergamon, Oxford, 1970), page 33.

[5] Reference [4], page 64.

[6] E. D. Palik , N. Ginsburg, H. B. Rosenstock and R. T. Holm, Applied Optics (in print, 1978).

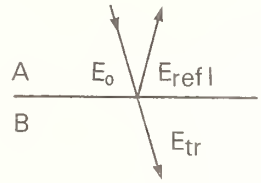

Figure 1. Field at one interface.

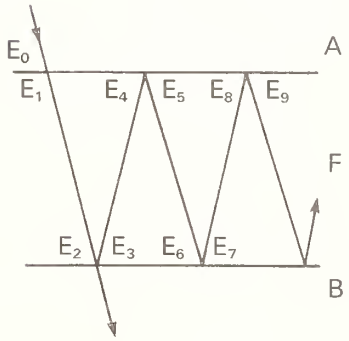

Figure 2. Multiple reflections in a film.

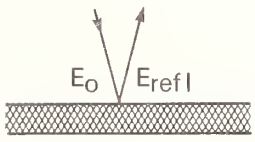

Figure 3. Summary of figure 2.

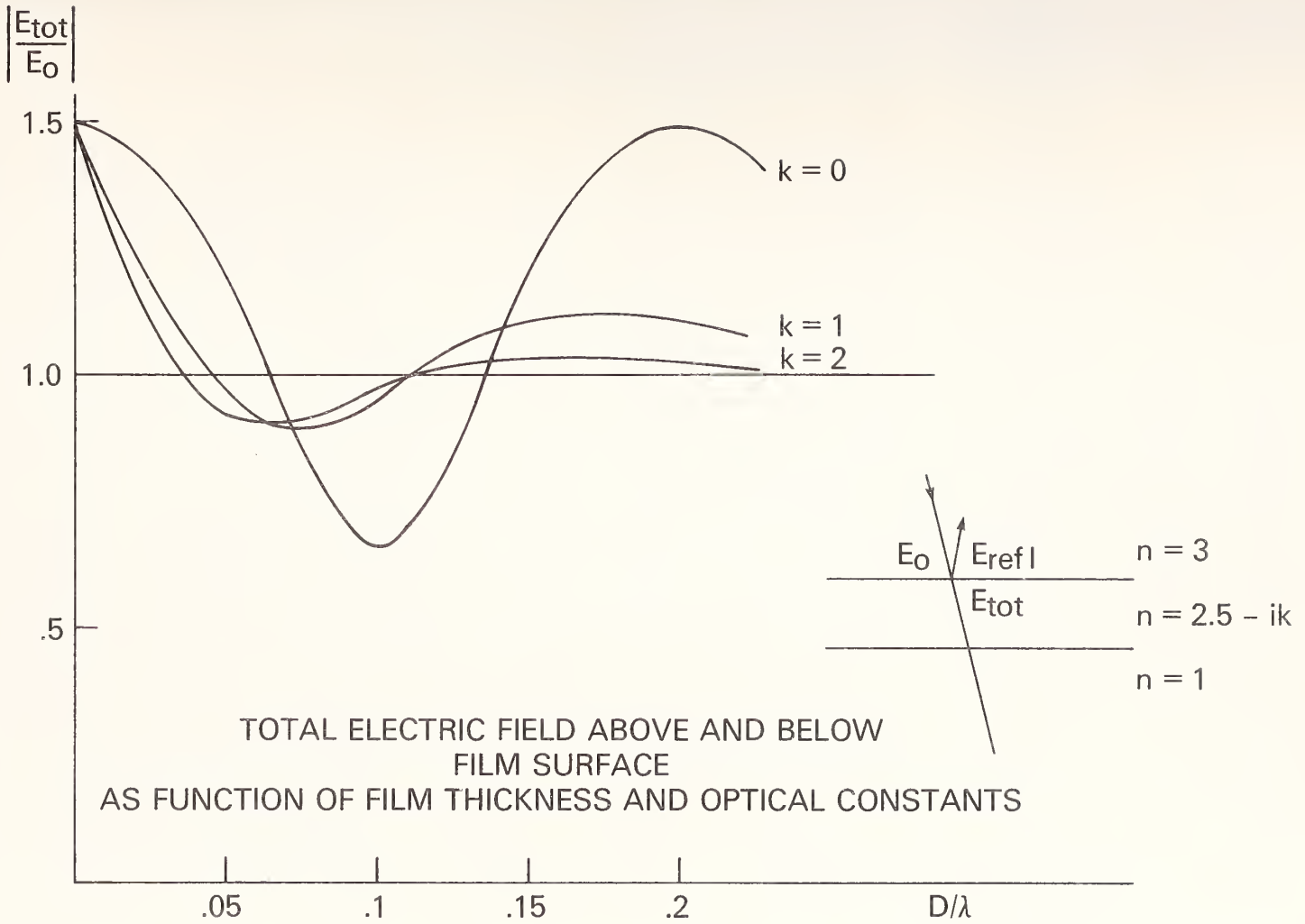

Figure 4. Total field vs. film thickness, for various optical constants.

COMPUTER SIMULATION OF LASER DAMAGE MORPHOLOGY IN THE ALKALI-HALIDES

P. Kelly and D. Ritchie
Physics Division, National Research Council
Ottawa, Ontario K1A 0S1

and

P. Bräunlich and A. Schmid
Washington State University
Pullman, Washington 99163

A numerical model of the spatio-temporal behaviour of a pico-second laser pulse has been developed which allows the study of the interaction of macroscopic photons with electrons in an alkali-halide lattice. Trajectories of the photons are computed. Gradients in the refractive index change the direction of the photons and this can lead to focusing or defocusing of the pulse. Rotational symmetry is assumed for both the pulse and background. Results obtained to date will be presented.

On behalf of my colleagues, I present our progress to date on the investigation of the spatial extent of damage produced by pico-second pulses in the Alkali-Halides. I refer first to our work presented at this symposium last year (1), and subsequently published (2), wherein we showed that spatio-temporal analysis was warranted and that the inclusion of the refractive index appeared as an important element in analysis.

I also call to your attention the excellent work of Smith et al. (3), who presented interesting measurements of the damage morphology.

They showed, that with a 21 psec (FWHM) doubled Neodynium pulse, damage in NaCl consisted of spatially distinct damage vestiges along the propagation axis of $\approx 1\mu$ in diameter and defined the flux, F, as the threshold F_{TH}. With $F \sim 1.5\ F_{TH}$ the damage vestige extends $\sim 100\mu$ by $\sim 2\mu$.

Can the polaron model of damage explain such behaviour? This is the question to which we now address ourselves. The non-linear behaviour of the interaction of such a monopulse with NaCl dictates computer simulation of the problem (while, nevertheless, we still look for analytic solutions).

COMPUTER MODEL

The choice of computer model is based on a new computer technique developed by Elliott and Henderson (4). Therein, the theoretical background has been supplied as well as applications to various physical problems. Their corpuscle - in-medium treatment is more fully described by Düdder and Henderson (5) in a macroscopic photon in cell (MPIC) computer code.

To date a modified version of the MPIC method has been used to simulate the experimental conditions of Smith et al. (3), where the interaction is between a monopulse and a polaron gas. Starting then with the MPIC program, the following changes have been made:

1. the refractive index, $n(\omega)$, is given by photon-optical phonon-polaron interaction (2),

2. the group velocity is calculated from

$$V_g = V_p \Big/ \left(1 + \frac{\omega}{\partial n^2} \frac{\partial n^2}{\partial \omega}\right)$$

where $V_p = c/n$ (and is equivalent to that of Elliott and Henderson (3) when $\varepsilon_i \ll \varepsilon_r$).

3. the equation of motion of a macroscopic photon is given by

$$\frac{d}{ds}(n\vec{\tau}) = \nabla n$$

so that,

$$\Delta\vec{\tau} = (\vec{\tau}_{\perp} \cdot \nabla n)\, \vec{\tau}_{\perp}\, \Delta S$$

with $\Delta S = V_g \Delta t/n$

4. the ionization fraction is defined as

$$g \equiv n_p/N_v(0)$$

where n_p is the generated polaron concentration and $N_v(0)$ is the initial valence band concentration and $\dot{g} = (1\text{-}g)R$ where $R = \sigma_4 F^4$ (instead of a Keldysh mechanism).

5. The grid was 50x50 with 8096 particles, i.e., 4 per active cell.

6. A full Gaussian pulse was employed with clipping at the $1/e^2$ points.

7. Shrinking and stretching of the grid in the radial direction was allowed but no particles were allowed to be "lost".

8. A 21 psec FWHM Gaussian pulse of 2.33 eV photons was focused by a 2.54 cm focal length lens to vacuum focal spot located 0.2 cm inside a NaCl crystal.

9. Rotational symmetry of the pulse and medium was assumed.

10. The initial energy of the pulse was 157x that of Smith et al. (3), to produce maximum fluxes of the same order as F_{TH} (in our cells).

A series of slides was presented illustrating the behaviour of the power density in cells located above the propagation direction and the corresponding profile of the ionization fraction. The focal volume is in front of the vacuum focal spot. Figures 1-6 are representative of the series. The MPIC program (presently) places a grid over the pulse travelling through the medium, which for this case produces a severe lack of resolution.

From the work to date it is clear that it will be practical to consider placement of the grid over an "interaction volume" in the NaCl sample with a spacing which should yield the morphology to micron size. Of course, refraction at the interface, as well as, absorption by the beam will then be included in the analysis.

(1) A. Schmid, P. Kelly and P. Bräunlich, 465 (1977) "Laser Damage in Optical Materials: 1977", NBS special publication 509, US Government Printing Office, Washington, D.C.

(2) A. Schmid, P. Kelly and P. Bräunlich, Phys. Rev. B, 16, 4569 (1977).

(3) W.L. Smith, J.H. Bechtel and N. Bloembergen, "Dielectric Breakdown Induced by Picosecond Laser Pulses", Tec. Report 685, Harvard University, Cambridge, Massachusetts (1976).

(4) C.J. Elliott and D.B. Henderson, J. Appl. Phys. 46, 354 (1975).

(5) H.D. Düdder and D.B. Henderson, Comp. Phys. Comm. 10, 155 (1975).

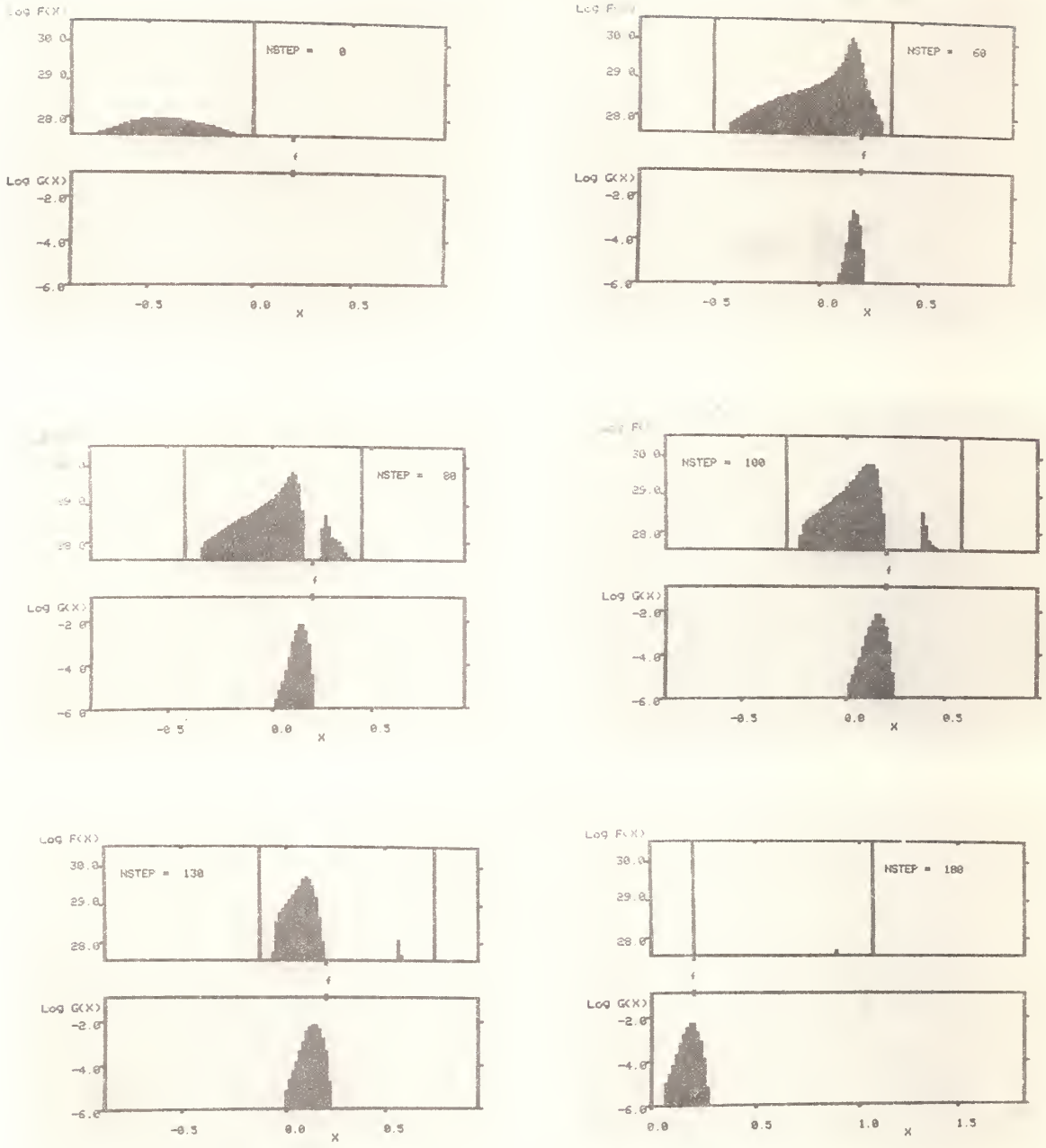

Figures 1-6. Top: Plots of the intensity profile from cells along the propagation axis, as a function of actual penetration of a 21-psec (FWHM) monopulse into NaCℓ.

Bottom: Corresponding ionization fraction profiles. f - Locates geometric focus (in cms).

Discussion

The speaker indicated that the model currently does not conserve energy in the presence of absorption and that, as presented here, it does not model avalanche but could be modified to do so. The assumed four-photon absorption is intended to model experiments carried out with doubled neodymium laser irradiation.

THE RELATIVE ROLE OF IMPACT AND MULTIPHOTON IONIZATION MECHANISMS IN LASER INDUCED DAMAGE OF TRANSPARENT DIELECTRICS

B. G. Gorshkov, A. S. Epifanov, and A. A. Manenkov
Lebedev Physical Institute
Moscow, USSR

The results of a theoretical analysis of the electron avalanche process at high frequencies of the electromagnetic field are presented. The dependence of the avalanche rate on radiation intensity and of the critical field on frequency are obtained for nanosecond and picosecond pulse durations. The relative role of electron avalanche and multiphoton ionization in laser damage of transparent dielectrics is discussed and it is shown that it is strongly influenced by the pulse widths.

Key words: Damage threshold; electron avalanche; frequency and pulse width dependencies of the critical field; multiphoton ionization.

1. Introduction

Impact and multiphoton ionization are expected to be the main fundamental processes limiting the resistance of transparent dielectrics to high intensity laser radiation. The role of these processes in laser induced damage in real optical materials of different types, ionic crystals in particular, has been extensively studied during the last decade. This especially refers to the impact ionization process (usually referred to as the electron avalanche mechanism.) Recently rather detailed theoretical and experimental investigations have been carried out in the Lebedev Physical Institute [1-5]. (The results of these investigations have been discussed by Manenkov at the IX Damage Symposium [6].) It has been found that the frequency and temperature dependencies of the damage threshold observed in some highly resistant samples of alkali halide crystals are in rather a good agreement with the theoretical predictions, giving a reasonable estimate of the electron-phonon collision frequency ($\nu \simeq 6 \times 10^{14}$ sec^{-1} for NaCl). However, some experimental results concerning, particularly, the temperature dependence of the damage thresholds observed at low and high radiation frequencies have not been explained by the avalanche ionization theory. It has been supposed that the disagreement between the observed and theoretical temperature dependences at high frequencies (λ = 0.53 μm) might be attributed to multiphoton ionization as an effective mechanism for generation of free carriers.

These facts motivated us to investigate theoretically the peculiarities of the avalanche ionization process in more detail for high frequency radiation, and to analyze the relative role of the impact and mult oton ionization mechanisms in the laser damage of transparent dielectrics. The principal results ot this work are briefly described in this paper.

2. Results of Theoretical Analysis

The relative contribution of these two processes to the free carrier generation rate, which is characterized by the avalanche and multiphoton rate parameters, γ and W_n respectively, has to be strongly influenced by the dependence of γ and W_n upon the intensity (E^2) and frequency, Ω , of the electromagnetic radiation. From consideration of the multiphoton transitions, it follows that in the pulse duration range of $\tau = 10^{-7} - 10^{-11}$ sec the rate W_n is proportional to E^{2n} if $n \leq 10$.

As far as the intensity dependence of the avalanche rate is concerned, it can be considerably stronger. As has been shown in previous papers [1-3], for electromagnetic breakdown in the nanosecond pulse duration range, the coefficient γ depends on radiation intensity exponentially. For breakdown in the picosecond range of pulse widths, the $\gamma(E)$ dependence is expected to be considerably weaker. Therefore, in order to elucidate the question of which of the two free-carrier generation mechanisms, impact ionization or multiphoton ionization, is predominant, one has, first of all, to study in detail the intensity dependence of the avalanche rate over a wide range of pulse durations and frequencies of the electromagnetic field. In order to find the $\gamma(E)$ and $E_c(\Omega)$ dependences (E_c is the breakdown critical field strength) the quantum kinetic equation for the electron distribution function [5] which satisfactorily describes the avalanche process at relatively low radiation frequencies ($\hbar\Omega \ll I$, where I is the effective ionization potential [1-3],) has been solved without the diffusional approximation.

The solution has shown that in the nanosecond pulse duration range, for relatively large radiation quanta ($I/\hbar\Omega = n$, $n \lesssim 4$), $\gamma \sim E^{2(n+1)}$, whereas for the smaller quanta ($n > 4$), γ becomes an exponential function of E [1-3]. To illustrate such behavior, the $\gamma(E)$ dependences calculated for various photon energies are shown in Figure 1. $\gamma(E)$ dependence has also been calculated for the picosecond range of radiation pulse durations. From the data for $\gamma(E)$, and using a damage

criterion connecting the avalanche rate and the radiation pulse duration [1], we have obtained the frequency dependence of the critical field, which in practice is one of the most important damage characteristics. It has been found that the character of the $E_c(\Omega)$ dependence is rather strongly influenced by the pulse duration. This dependence calculated for two values of τ is shown in Figure 2. One can see that at relatively low frequencies ($h\Omega/I \lesssim 0.15$) the diffusional relationship

$$E_c^2 \sim (\Omega^2 + \nu_{eff}^2) \tag{1}$$

satisfactorily decribes the $E_c(\Omega)$ dependence in for both picosecond and nanosecond pulses, whereas in a high frequency region ($\hbar\Omega/I \gtrsim 0.2$) the behavior of $E_c(\Omega)$ is very different for the two cases: for picosecond pulses the $E_c(\Omega)$ dependence remains similar to the diffusional one whereas for nanosecond pulses, $E_c(\Omega)$ has a nonmonotonic, oscillatory behavior. The latter is due to the oscillatory form of the energy distribution function for hot electrons in high frequency electromagnetic fields.

For elucidation of the relative role of electron avalanche and multiphoton ionization in laser damage, the kinetics of lattice heating due to absorption of laser radiation by free electrons generated in both processes has to be considered. A change of the free carrier density, N, in the conduction band of a crystal is described by the equation

$$\frac{dN}{dt} = \gamma N + W_n - R(N) , \tag{2}$$

where R(N) is the term describing recombination of the carriers.

Solving Eq. (2) together with the coupled equation for the lattice temperature $\theta = T/T_0$:

$$\frac{d\theta}{dt} = \beta\theta^{\kappa} N , \tag{3}$$

where T_0 is the initial temperature of the lattice. κ and β are parameters depending on the electron-phonon interaction [3].

One can obtain a relationship between the pulse width and ionization rates γ and W_n required for a catastrophic temperature rise during a radiation pulse. The final step of this procedure gives the critical field values or the damage threshold intensities.

Figure 3 shows the dependence for the critical field parameter q_c, related to E_c, upon the pulse width for the two mechanisms of free carrier generation, avalanche and multiphoton ionization. One can see that two significantly different cases are possible, depending on the multiphoton generation rate; either the $q_c(\tau)$ curves corresponding to the avalanche and multiphoton ionization are intercepted or not. It means that in the first case there is a competition between the avalanche and multiphoton ionization processes at some pulse widths which can, in general, lie in both the picosecond and nanosecond regions. In other words, in this case the electron avalanche can be the dominant mechanism of laser damage over a wide range of pulse durations, including both the picosecond and nanosecond regions.

In the second case, where the avalanche and multiphoton curves do not intersect each other at any pulse widths, the dominant mechanism of intrinsic damage is associated with multiphoton ionization.

3. Conclusion

The features established in the theoretical study of avalanche and multiphoton ionization concerning, in particular, the frequency and pulse width dependences of the critical field, can be used in experimental investigation to elucidate the dominant mechanism of laser induced damage in optical materials.

4. References

[1] Epifanov, A. S. JETP, 67, 1805 (1974) Soviet Physics JETP 40, 897 (1975).

[2] Epifanov, A. S., Manenkov, A. A. and Prokhorov, A. M., JETP Pis'ma, 21, 483 (1975) . [JETP Letters, 21, 223 (1975)].

[3] Epifanov, A. S., Manenkov, A. A. and Prokhorov, A. M. JETP, 70, 728 (1976). [Soviet Physics, JETP, 43, 377 (1976)].

[4] Gorshkov, B. G. Danileiko, Yu, K., Epifanov, A. S. Lobachev, V. A. Manenkov, A. A. and Sidorin, A. V., JETP Letters, 2, 284 (1976).

[5] Gorshkov, B. G. Danileiko, Yu, K., Epifanov, A. S. Lobachev, V. A. Manenkov, A. A. and Sidorin, A. V., JETP, 72, 1171 (1977).

[6] Manenkov, A. A. NBS Spec. Publ. 509, p. 455 (1977).

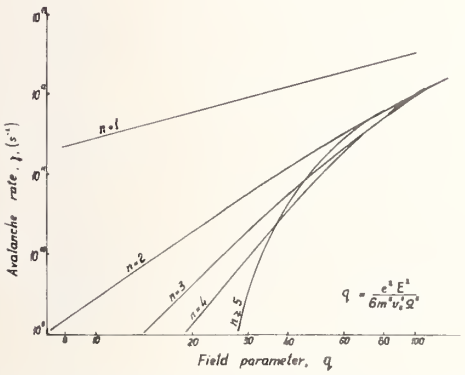

Figure 1. Dependence of the electron avalanche rate on the radiation electric field amplitude at various frequencies (I/ = n). Notations in field parameter q: e and m are the electron change and effective mass, respectively, v_s is the velocity of sound.

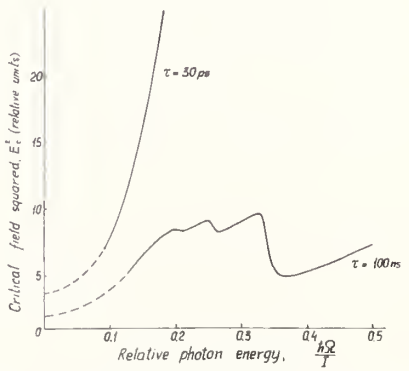

Figure 2. Frequency dependence of the critical field for picosecond and nanosecond pulse durations. The values used in calculation refer to NaCl.

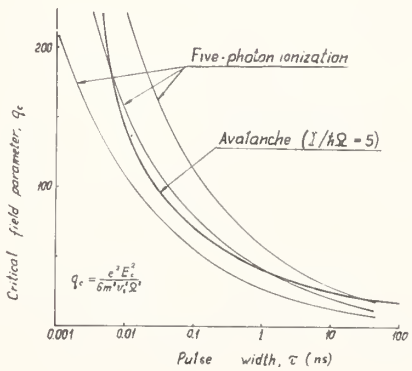

Figure 3. Critical field versus pulse width for the avalanche and multiphoton ionization damage mechanisms. The values used in calculations refer to NaCl.

Discussion

The work of Manenkov, et al., was challenged on two points, both relating to scaling laws. First, it was pointed out that previously reported data taken at Harvard showed the familiar $t^{1/2}$ *dependence for breakdown intensity for pulse durations from 30 psec to 10 nsec. Manenkov's theory would predict a much weaker dependence, but his analysis does not include either electron or thermal diffusion phenomena. Secondly, neither Manenkov's theory nor his data show strong spot-size dependence, although other data reported here and elsewhere do show a threshold decrease with increasing spot size. the speaker agreed that if his experimental results (and theory) refer to intrinsic damage, then a strong spot-size dependence would not be expected.*

THEORY OF LASER DAMAGE IN DIELECTRIC SOLIDS*

Steven Brawer and W. Lee Smith
University of California
Lawrence Livermore Laboratory
Livermore, California 94550

In this theory a new approach to the interaction of conduction band (CB) electrons with damaging radiation is considered. We assume band gaps greater than 4 ev and radiation frequencies greater than 1 ev. Two processes are required for damage. First, the incident radiation rapidly excites a few "primer" electrons from trap levels to the bottom of the CB. Next these primer electrons can either cause enough energy to be absorbed to cause damage without avalanche, or they can trigger an electron avalanche and subsequent damage. In either case a mechanism for the excited-state absorption process is required.

Recent work [1] - [6] on excited-state absorption in dielectrics shows that the low-lying CB states are localized. The applied field can induce dipole-allowed transitions among these levels. Dipole-allowed interband transitions can also occur among more extended states. If avalanche is to occur, the CB electron must gain at least an amount of energy equal to the band gap energy. Since a large number of electronic states are involved, we model the situation by assuming a continuum of possible states and an average transition probability among them. Transitions up this continuum take place by a sequence of one-photon absorptions.

The electron can also "backslide", losing energy by phonon emission. A minimum value of the electron-phonon relaxation time must be inverse (angular) phonon frequency for the dominant phonon, about 5×10^{-15} secs for a 1000 cm^{-1} phonon. This is the average time required to emit one phonon.

Assuming an oscillator strength of unity, the average electron cross section for absorption is about 10^{-15} cm^2. The probability/time that an electron can absorb one phonon, for a field strength of 1 MV/cm and frequency of 1 micron, is about 10^{13}/sec, comparable to the rate of generation of ten phonons. (It requires 10 phonons to backslide an amount of energy equal to one absorption step in this example.)

It is now assumed that when a CB electron gains energy equal to the bandgap energy, it excites an additional electron from the valence band to the CB. After this excitation, both electrons are in the low levels of the CB. In this way, an avalanche is triggered.

These assumptions are sufficient to write equations describing the energy and number of CB electrons as a function of time, and of the heat delivered to the lattice. Damage is presumed to occur when the lattice is heated to the melting point. We come to the following conclusions. (We assume for this discussion that the electron-phonon relaxation time is 5×10^{-15} sec and the absorption cross section is 10^{-15} cm^2. These parameters can vary for each case, so the numbers below are only an indication of the trends and should not be given a rigid, absolute significance.)

1. For a field of 1 MV/cm and pulse duration about 10 ns, about 10^{16} electrons/cc in the CB will absorb enough energy to cause damage. No avalanche is needed.

2. If avalanche occurs, we predict a relation between the pulse duration τ and the threshold electric field E_o. For small fields $\lesssim$ .25 MV/cm the quantity $\frac{d \ln \tau^{-1}}{d \ln E_o}$ is predicted to be about $\Delta/\hbar\omega$ where Δ is the band gap energy, for fields $\gtrsim$ 10 MV/cm the slope becomes smaller than 2.

3. For given pulse duration, we predict that the threshold decreases markedly with increasing frequency for small fields and is nearly independent of frequency for large fields.

These predictions are in qualitative agreement with experiment.

*Work performed under the auspices of the U.S. Department of Energy under Contract No. W-7405-ENG-48 and the Materials Sciences Program.

References

[1] R. T. Williams and M. N. Kabler, Phys. Rev. B9, 1897 (1974).

[2] R. T. Williams, M. N. Kabler, W. Hayes, and J. P. Stott, Phys. Rev. B14, 725 (1976).

[3] R. T. Williams, C. L. Marquardt, J. W. Williams, and M. N. Kabler, Phys. Rev. B15, 5003 (1977).

[4] J. W. Appel in Solid State Physics, vol. 21 (edited by F. Seitz, D. Turnbull, and H. Ehrenreich, Acad. Press, N.Y., 1968).

[5] F. DeMartini, D. Frigione, G. Guiliani, P. Mataloni, and F. Simoni in Nonlinear Spectroscopy (edited by N. Bloembergen, North Holland, Amsterdam, 1977).

[6] R. T. Williams, J. N. Bradford and W. L. Faust, in Optical Properties of Highly Transparent Solids (edited by S. S. Mitra and B. Bendow, Plenum, N.Y., 1975), p.233.

Discussion

It was pointed out that the theory proposed by the speaker is similar to the "cold-electron" model of damage proposed by R. Hellworth at this Symposium in 1972. In order for damage to occur without avalanche, in this theory, a concentration of 10^{15} to 10^{16} impurity or defect centers, capable of single-photon ionization, would be required. It is assumed that these centers are weakly absorbing in the ground state (otherwise the material would be strongly absorbing) but that, when electrons are liberated from these centers, the cross section for absorption is as large as $10^{-15}cm^2$. The speaker noted that, except in the purest semiconductors, impurity concentrations of parts per billion are commonly found. Dr. Peter Braunlich of Washington State University pointed out that one could test the model using a material with a large number of impurity or defect states, at low temperature, by comparing its conductivity, or damage threshold, with and without the liberation of electrons from the impurity centers via uv radiation. One can also look for different statistics of damage onset in the two cases.

LASER-INDUCED DAMAGE IN SEMICONDUCTORS

Yu.K. Danileiko, A. A. Manenkov, and A. V. Sidorin
Lebedev Physical Institute
Moscow, USSR

The laser-induced bulk breakdown in Ge, Si and GaAs crystals at the 10.6 μm, 2.76 μm, and 2.94 μm radiation wavelengths of the pulsed CO_2, $Ca_2F:Er^{3+}$ and YAG:Er^{3+} lasers is investigated. Generation of free carriers has been observed and their kinetics studied by the dc and microwave photoconductivity measurement techniques. In Si and GaAs, the laser-induced bulk damage has been observed and the damage threshold measured. In Ge, the damage was not observed due to a self-defocusing effect associated with the negative contribution of nonequilibrium electrons in the refractive index. Mechanisms of free carrier generation and laser-induced damage are discussed.

Key words: Laser induced breakdown; laser-induced damage threshold; nonequilibrium carriers; semiconductors, Ge, Si, GaAs.

1. Introduction

Electric breakdown in semiconductors has been extensively investigated in dc and microwave fields, but has not been completely studied in laser fields. However, investigation of laser produced breakdown may be of considerable interest for both the fundamental physics of semiconductors, and the application of these materials in the high power lasers.

This paper is concerned with some first results of our experimental investigation of bulk breakdown in Ge, Si, and GaAs crystals, under high power, IR-laser radiation. In order to elucidate the role of free carriers in laser damage, along with the standard damage threshold measurements, we have studied the kinetics of dc and microwave photoconductivity. The data obtained in the photoconductivity experiments can also be of more general interest for understanding the excitation mechanisms of nonequilibrium carriers in semiconductors.

2. Experimental Conditions

In the experiments we have used pulsed CO_2, $Ca_2:Er^{3+}$ and YAG:Er^{3+} lasers operating in single, TEM_{00} mode. The radiation wavelengths and pulse widths were 10.6 μm, 2.76 μm, 2.94 μm, and 60 ns, 90 ns, and 10 μsec, for the CO_2, $CaF_2:Er^{3+}$ and YAG:Er^{3+} lasers, respectively. Excitation of samples was produced in both parallel and focused beam geometries. For beam focusing, a 10 mm focal length Si lens was used. Special attention was paid to lens aberrations, which are very important in order to obtain correct measurements of beam intensities inside the sample.

For detection of dc and microwave photoconductivity kinetics, due to generation of nonequilibrium carriers, a conventional experimental arrangement with a microwave oscillator (klystron), operating at the 3.2 cm wavelength, was used.

Identification of laser-induced damage inside the sample, and the damage morphology studies, were done with an IR-microscope. The typical characteristics of the samples investigated were the following. Si: Dislocation free, with room-temperature resistance, $\rho \simeq 10^4 \Omega$ - cm; GaAs; 1) Undoped, with 10.6 μm absorption coefficient $\alpha \simeq 1$ cm^{-1}. 2) Semi-isolating, $\alpha \simeq 10^{-2}$ cm^{-1}. Ge: Dislocation-free, $\rho \simeq 40\Omega$ - cm.

3. Results

In Ge, we have observed generation of nonequilibrium carriers, under excitation of samples by radiation, with all the lasers used. The characteristic decay times of the microwave photoconductivity kinetics signal varied over the range of 0.1 to 1.0 msec, depending on the excitation geometry and sample size. In the case of tight focusing of the laser beam inside large samples, the decay time is longest, and determined by the bulk recombination of the carriers.

Because of the higher mobility, the observed photoconductivity was mainly attributed to the electrons (the contribution of the holes is expected to be negligible).

With 2.76 μm and 2.94 μm excitation, the carrier generation is due to two-photon ionization. We have measured the two-photon absorption coefficient, β, at 2.76 μm, to be equal to 7.5×10^{-2} cm/MW.

With 10.6 μm excitation, the nature of the carrier generation mechanism is no longer clear. In order to elucidate this question, we have measured the carrier concentration at various excitation levels using dc photoconductivity techniques. It was found that generation becomes detectable at a relatively low laser radiation intensity, $I \simeq 10^5$ W/cm^2, and the electron-hole pair concentration reaches a value of $N \simeq 10^{16}$ cm^{-3} at $I \simeq 10^7$ W/cm^2.

The relatively weak N(I) dependence observed (at high intensities $N \sim I^{1.7}$, as is seen in Figure 1) calls into question the interpretation of carrier generation in Ge by 10.6 μm radiation, on the basis of the impact ionization mechanism, because the theory of this process [1] predicts the exponential growth of N with intensity. We have considered other, alternative possibilities to explain the carrier generation in Ge under 10.6 μm excitation. Among them are thermal ionization, connected with lattice heating by the laser pulse, and photoionization by a hot inclusion existing in the sample. The estimates have shown that neither mechanism can contribute sufficiently to the carrier generation process, so that the question of the nature of this process is open, and requires further investigation.

An interesting result of our studies of Ge at 10.6 μm is that we did not succeed in obtaining laser damage, even at very high incident beam powers, and with tight focusing of the beam inside the Ge samples. We have explained this result as due to self-defocusing of the beam, arising from the negative contribution of nonequilibrium electrons to the refractive index of the sample. Consideration of self-defocusing of tightly focused beams in the solid state electron plasma, of the type which exists in our experimental conditions in Ge, has shown that the intensity in the focal region is limited to a definite value, depending on the focusing geometry and the carrier generation rate. For our particular experimental conditions, we estimate that $I \simeq 100$ MW/cm^2, and $N_{max} \simeq 3 \times 10^{17}$ cm^{-3}. Note that if the self-defocusing effect is not taken into consideration, the intensity in our experiments would reach very high levels of about 10^{11} W/cm^2, at which damage should probably occur.

In Si and GaAs, damage has been observed at all three wavelengths, with rather high thresholds (see Tables 1 and 2) especially at 10.6 μm.

Table 1 Bulk laser damage threshold intensities Jd (GW/cm^2) and effective critical fields E_{eff} (MV/cm) in Si and GaAs

Material	Wave Length, μm					
	(10.6)		(2.76)		(2.94)	
	Jd	E_{eff}	Jd	E_{eff}	Jd	E_{eff}
Si	5.0	0.75	2.3	0.5	0.15	0.13
GaAs	16.5	1.4	0.8	0.3	0.08	0.1

Table 2 Bulk laser damage threshold intensity J_d (GW/cm^2) and effective critical field E_{eff} (MV/cm) for different GaAs samples at 10.6 μm

Sample	Absorption coefficient cm^{-1}	Jd	E_{eff}
Semi-isolating			
1	0.03	1.3	0.4
2	0.035	14.5	1.3
3	0.03	12.4	1.2
4	0.02	10.3	1.1
Undoped			
1	0.9	16.5	1.4
2	0.9	53.6	2.5

In order to understand the mechanism of laser-induced damage in Si and GaAs, we have compared the critical fields E_{eff}, calculated from the laser damage threshold intensities measured, with the field E_o for dc electric breakdown, which is close to 2×10^5 v/cm [1, 2]. Since $E_{eff} > E_o$, especially in the undoped GaAs samples, one can suppose that electron avalanche is the mechanism of laser damage in Si and GaAs at 10.6 μm. Using the relationship

$$E_{eff} \simeq E_o(\Omega^2 + \nu_{eff}^2)^{1/2} , \qquad (1)$$

which avalanche theory predicts [3, 4], we have estimated the value of the effective electron-phonon collision frequency ν_{eff}. The estimated value is $\nu_{eff} = 5 \times 10^{13}$ sec^{-1} for Si, which is close to the well-determined, cold electron collision frequency. Although the reasonable correlation between the laser-induced damage and the dc breakdown data makes it attractive to attribute the laser damage in Si and GaAs at 10.6 μm to the electron avalanche mechanism, we think that additional data are needed to confirm that conclusion. At least, the role of defects of different types in laser

damage has to be cleared up, because our studies have shown "inclusion-type" damage morphology, even in the high threshold samples. We have observed simialr morphology in both Si and GaAs samples at 2.76 μm and 2.94 μm (see Figure 2) which indicates that defects undoubtedly affect the damage process.

Notice also, that in contrast to Ge, the nonequilibrium carriers in Si and GaAs have been detected only at intensities at which damage occurs.

3. References

[1] Aladinsky, V. K., FTT (Fizika tverdogo tela), 7, 1813 (1965).

[2] Aladinsky, V. K., Salomikova, M. V., Electron technics, serija II, No 2, 45 (1973).

[3] Epifanov, A. S., Manenkov, A. A. Prokhorov, A. M. JETP Pis'ma 21, 483 (1975). Soviet Physics JETP Letters 21, 223 (1975).

[4] Epifanov, A. S. Manenkov, A. A., Prokhorov, A. M. JETP 70, 728 (1976) Soviet Physics JETP 43, 377 (1976).

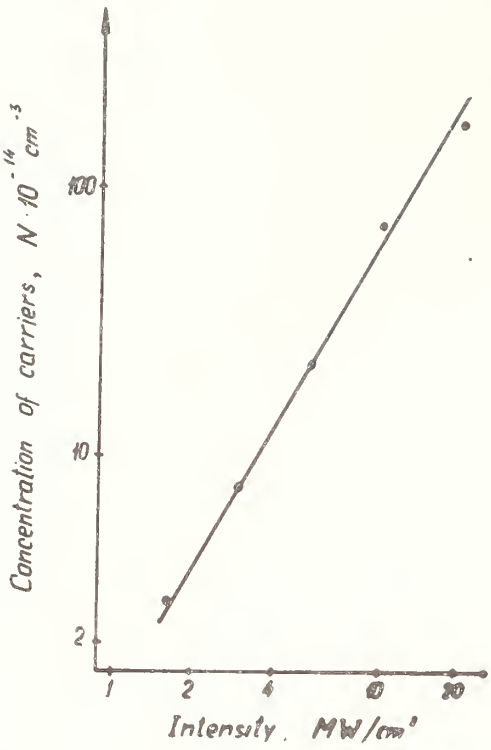

Figure 1. Concentration of nonequilibrium carriers in Ge versus CO_2 laser intensity.

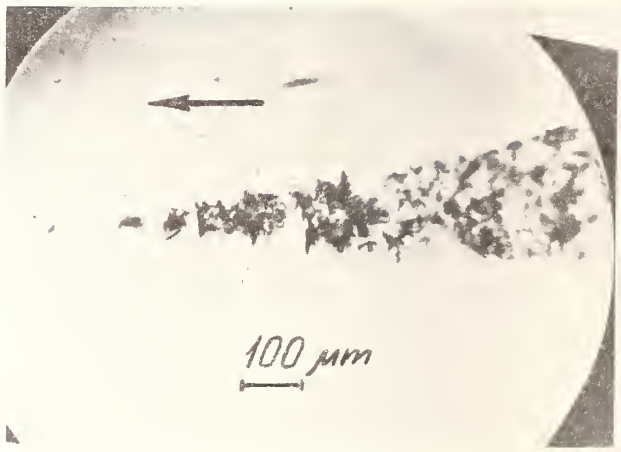

Figure 2. Bulk damage produced by $CaF_2.Er^{3+}$ laser in GaAs (= 2.76 m) at the intensity of 1000 times above threshold, J_{th} = .8GW/cm^2. Arrow shows the direction of incident laser beam propagation.

Discussion

The speaker was questioned on several aspects of this work relating to the competition of intrinsic and extrinsic damage. The observed damage thresholds in GaAs did not show any correlation with measured bulk absorption coefficients. Also, the observed threshold damage morphology consisted of small damage sites of 1 to 2 μm in diameter. The speaker was asked about the work of Austin and Shank, previously reported, in which a strong decrease in carrier lifetime was observed in Ge at high concentrations. He replied that, in his work, this concentration-induced decrease in carrier lifetime was not observed. He felt that near the surface, where high carrier concentrations can be created, carrier lifetimes are already shortened by surface defects and impurities.

FREQUENCY DEPENDENCE OF BREAKDOWN FIELDS IN SINGLE-CRYSTAL NaCl AND KCl*

M. J. Soileau
Michelson Laboratory, Physics Division
Naval Weapons Center, China Lake, CA 93555

and

M. Bass and E. W. Van Stryland
Center for Laser Studies
University of Southern California, Los Angeles, CA 90007

In this paper new observations of the breakdown fields in single-crystal NaCl and KCl are reported. Measurements were made of the wavelength and focal spot radius dependence of breakdown fields in NaCl and KCl at optical frequencies. The measurements at different focal spot radii were used to establish empirical scaling laws for these two materials over the range of focal spot radii studied. Correct application of these scaling laws gives directly comparable fields at all frequencies. The results indicate little dispersion in breakdown fields over the wavelength range of 10.6 to 0.53 μm. The ratio of the NaCl and KCl breakdown fields are found to depend on frequency and this implies that extrinsic phenomena were being probed by these experiments.

Key words: Breakdown fields; KCl; NaCl; spot-size dependence.

Introduction

Measurements were made of the wavelength and focal spot radius dependence of the pulsed laser damage fields in NaCl and KCl. The damage irradiations were performed with pulsed CO_2, HF, and DF lasers with total powers less than 1/18 of the critical powers for self-focusing by tightly focusing the Gaussian laser beams. At 10.6 and 2.7 μm, the CO_2 and HF wavelengths, a single triangular pulse was used; however, at 3.8 μm, the DF wavelength, a double pulse was obtained because the laser oscillated on several lines simultaneously. The measurements at different focal spot radii were used to establish empirical scaling laws for these two materials over the range of focal spot radii studied. These scaling laws are then applied to both current data and previous data to determine the damage threshold as a function of frequency for a common focal spot radius. The results indicate little dispersion in damage threshold over the wavelength range of 10.6 to 0.53 μm.

Background

The objective of this work was to investigate the mechanisms for laser-induced breakdown in highly transparent solids. Emphasis is placed on determining the frequency dependence of the breakdown thresholds of selected alkali halide crystals. Although this problem has been explored by many workers, the detailed mechanism for breakdown is not well understood [1][1] and considerable discrepancies in experimental data exist. Early measurements of breakdown fields in the alkali halides by Yoshiyoki *et al.* [2], indicated that the thresholds for 0.69 μm radiation were nearly the same as those for ordinary impulse breakdown and were affected little by the band gap energy of the crystals. This evidence led the authors to suggest that breakdown was an avalanche process initiated by electrons excited to the conduction band from traps within the gap.

Yablonovitch found that the rms breakdown fields for various alkali halides at 10.6 μm were approximately equal to the DC breakdown fields and had the same systematic variation with band gap [3]. Fradin and Bass [4] found that this systematic variation of thresholds extended to 1.06 and 0.6943 μm. Such evidence led many workers to conclude that the alkali halide breakdown thresholds were due to an intrinsic propriety of the lattice [1]. However, subsequent measurements on very pure KCl crystals at 10.6 μm showed that the systematic differences in the thresholds observed by Yablonovitch at 10.6 μm did not always hold [5,6]. Additional measurements by Yasajima *et al.* [7] for various alkali halide breakdown fields at 1.06 and 0.6943 μm showed that the thresholds were not dependent on the band gap energy. Their measurements of temperature dependence of laser-induced breakdown and photoconduction at prebreakdown optical fields provided additional evidence that laser-induced breakdown was due to extrinsic processes.

Figure 1 shows the results of attempts by Sparks [8] to model the results of Yablonovitch, Fradin, and Bass [3,4]. Recent results by Manenkov [9] are also given in figure 1. The top curve in this

* Work supported by ONR Project No. RR02202, Task RR0220202, Dr. A. M. Diness, Program Manager.

1. Figures in brackets indicate the literature references at the end of this paper.

figure is obtained from a modified version of the Yablonovitch dielectric breakdown model. The Sparks model differs from the Yablonovitch model in that it is assumed that (a) starting electrons are provided by multiphoton excitation of defect states, (b) losses to acoustical phonons are significant, and (c) the value of t_p, the electron collision time with optical phonons, is much larger than that assumed by Yablonovitch. The top curve was adjusted to fit the 10.6 μm data and so predicts a strong frequency dependence over the 10.6 to 1.06 μm wavelength range. The bottom curve in figure 1 results from the Sparks-Holstein model which assumes tight binding of electrons in the conduction band. This model is based on energy transfer from the laser field to the crystal via the Holstein photon-electron-phonon interaction. When first postulated, the Sparks-Holstein model had the attractive features that it fit the then available data quite well and used no adjustable parameters. The Sparks-Holstein model predicted little frequency dependence over the 10.6 to 1.06 μm range. To the problem of selecting data and models, one must now add the possibility that the measured threshold may depend on focal spot radius, w, as was pointed out by Bettis *et al.* [10]. Measurements in the 1.06 to 0.53 μm region are usually made with very small w (on the order of 10 μm radius), whereas, the 10.6 μm measurements are made with larger w (on the order of 50 μm radius). In the present paper, variables such as the focal spot radius are removed from measurements of damage threshold and a clearer determination of the breakdown fields in alkali halides is reported.

Experiment

In the damage measurements a transversely excited HF (or DF) pulsed chemical laser and a TEA CO_2 laser were used as irradiation soruces. The output of the HF laser was multiline and centered about 2.7 μm; the multiline DF output was centered about 3.8 μm. The only change made in the system to go from HF to DF lasing was to switch H_2 to D_2 gas. The power supply, laser cavity, and all other optics remained the same. The HF/DF and CO_2 lasers are described in detail in previous work [6,11,12,13].

The occurrence of laser damage was determined by (1) viewing a change in scattering of a coaxial HeNe beam in a twenty power microscope, (2) observing a visible flash and/or fracture in the sample, and (3) monitoring the transmitted waveform distortion. In this study, it was found that all three of these effects occurred simultaneously, i.e., when damage occurred the HeNe laser scatter increased, a visible flash and fracture were observed, and the transmitted waveform was abruptly truncated. In this research the threshold was defined to be that flux which produced damage in 50% of the sites when each site was irradiated only once.

The laser output was attenuated by either a pair of Brewster angle ZnSe plate polarizers used in reflection [4], or by two pairs of Brewster angle ZnSe plate polarizers used in transmission [11]. The orientation of the ZnSe polarizers were such that the polarization in the beam reaching the target remained constant. Unless otherwise noted, all data reported here were taken using the reflection attenuators.

A narrow slit was used to scan the focal planes of the three uncoated, meniscus, ZnSe lenses used in these experiments at each of the three laser wavelengths investigated. The measured focal spot radii were then corrected for the finite slit width [11]. The results of these measurements are summarized in table 1. The radii of the unfocused beams at the position of the focusing lens were 0.55 cm for CO_2 and 1.01 cm for HF and DF.

Table 1. Focal spot radii.

Lens No.	Focal length at 10.6 μm (cm)	Lens diameter (cm)	Focal spot radius ($1/e^2$ in intensity) (μm)		
			HF	DF	CO_2
1	2.54	2.54	9.55	10.60	20.50
2	6.35	2.54	12.55	13.55	45.00
3	12.70	5.08	26.50	28.50	85.00

The temporal pulse waveform was monitored at two points, one before the focusing lens and one after transmission through the sample. The CO_2 laser produced a train of partially mode-locked pulses with an envelope having full width at half maximum (FWHM) of 60 to 110 nsec (fig. 2). The HF laser produced a triangular pulse with some irregular spiking which had a FWHM of 100 to 140 nsec (fig. 3). The DF laser produced the double pulse waveform shown in figure 4. Damage occurred during the second part of the DF pulse as observed by monitoring the waveform distortion upon transmission through the sample. The ratio of the area under the second DF peak (fig. 4) to the total area of the waveform is equal to the fraction of the total energy in the second part of the pulse. The damaging peak power is then the energy in the second part of the pulse divided by the FWHM of the second part of the pulse. An equivalent pulse width is then defined as the FWHM of a triangular pulse containing total pulse energy but having the same peak power as the second part of the pulse. Equivalent pulse widths of 70 to 100 nsec were found for these experiments. The pulse shapes from these lasers are sensitive functions of various operating parameters (i.e., gas mix, pressure, repetition rate, and discharge voltage) and so pulse width was carefully determined for each damage threshold measurement. The range of pulse widths given above are for different sets of measurements. The variation of pulse widths for a given threshold measurement was less than 10%.

The total energy of each pulse was monitored after the attenuator with a pyroelectric energy meter. After each set of threshold measurements (i.e., a given specimen at a given wavelength and focal spot radius), the energy monitor was calibrated using a thermopile calorimeter. The calibration was performed at the threshold value to avoid any questions concerning nonlinear response of the monitor detector.

The specimens used in this work were single-crystal NaCl and KCl from Harshaw Chemical Company [14]. The specimens used were free from visible (0.6328 μm) scattering and were not limited by linear absorption.

Data Reduction

The intensity thresholds were determined from the measured energy which caused damage in the following way. The total energy Q is given in terms of the energy density, $\mathcal{E}(r)$, at the focal plane by

$$Q = \int_0^\infty \mathcal{E}(r) 2\pi r dr \quad . \tag{1}$$

For the Gaussian beams used in these experiments

$$\mathcal{E}_o = \frac{2Q}{\pi w_o^2} \quad . \tag{2}$$

$\mathcal{E}_o$ is the peak-on-axis energy density and w_o is the radius at which the intensity has fallen to $1/e^2$ of its peak value on-axis. This gives the damage threshold in J/cm^2. The intensity damage threshold I in $watts/cm^2$ is given by

$$I = \frac{2Q}{\pi w_o^2 t_p} \quad , \tag{3}$$

where t_p is the laser pulse width (FWHM). The rms electric field corresponding to the peak-on-axis intensity is given by [6],

$$E(volts/cm) = 19.41 \left[\frac{I(watts/cm^2)}{n}\right]^{1/2} \quad , \tag{4}$$

where I is the peak on-axis intensity and n is the index of refraction of the specimen.

The total energy Q used in the above equations is related to the total energy incident on the focusing lens by

$$Q = Q_{input} T_L T_s \quad , \tag{5}$$

where T_L is the transmission of the focusing lens and T_s is the transmission of the entrance surface of the specimen.

Data

The following tables summarize the data from this work. The numbers quoted are the so-called 1-on-1 thresholds (one irradiation at each site). The thresholds given here are for what has been called intrinsic damage, i.e., damage which occurred at the focal position and near the peak of the laser pulse when irradiated with flux levels which caused damage in 50% of the sites tested.

The bulk thresholds could not be measured at 10.6 μm using lens 3. The samples always failed at the surface even though the laser was focussed in the bulk of the material. This was due to the relative low damage thresholds of the surfaces and the relatively high f-number (f/12) of lens 3 at 10.6 μm. The numbers listed for lens 3 at 10.6 μm in tables 2-5 are the highest values for which front surface damage (or bulk damage) did not occur. Thus, these numbers represent a lower bound for the bulk damage threshold.

The energy threshold divided by the intensity threshold gives the pulse width for the particular laser and focal spot radius.

Since the pulse widths are not the same for all the data points, one might question whether the data are pulse-width dependent for this pulse-width region. There is some dispute about the pulse-width dependence for pulse widths of the order of several to hundreds of nanoseconds. Some workers claim there is a dependence [10] and others claim no dependence on pulse width [15]. We tested specimen 78-NC-6 at 10.6 μm using lens 2 with t_p = 60 nsec and t_p = 107 nsec. The resulting thresholds were the same to within ±3.5%, which was well within experimental error. Thus, we found no pulse-width dependence for these experimental conditions.

Six specimens of KCl were tested. Specimen 78-KC-15 had visible scattering centers when viewed with a 20X microscope with a focused HeNe laser for illumination. The data for this specimen are included for completeness, but are not used in the analysis of breakdown fields or for the development of scaling laws.

Specimen 78-KC-15 exhibited damage characteristics at 10.6 μm, similar to what is usually referred to as "extrinsic" damage. Near threshold the specimens would damage at one or more of the scattering centers which were often off-axis and not in the lens focal plane. The damage sites were very localized, and the transmitted pulse showed only slight distortion or no distortion at all. The 10.6 μm threshold was approximately 10 times smaller than for the other five KCl specimens tested. However, at HF and DF wavelengths the specimen had "intrinsic"-like behavior, i.e., damage at threshold occurred in the lens focal plane and at the peak of the pulse, the transmitted pulse was abruptly truncated, and a large fracture and flash were observed. Thus, the visible scattering centers which initiated damage at 10.6 μm had little or no effect at 2.7 and 3.8 μm.

Analysis

The focal spot radius dependence of the peak on-axis intensity damage threshold of NaCl and KCl were found from the data given in tables 3 and 5 (excluding specimen 78-KC-15). The data for each specimen was normalized to the threshold at the minimum focal spot radius and the results were plotted as a function of the inverse focal spot radius. Figure 5 is such a plot for NaCl at 2.7 and 3.8 μm. The straight lines in these plots are the inverse radius dependence proposed by Bettis *et al.* [10]. Note that some of the samples fall on this line while others deviate considerably and some samples have a different dependence at different wavelengths. Points above the line derived from the Bettis model have a radius dependence of $(1/w)^p$, where p is < 1.0; whereas, for points below the line p is > 1.0. The stars within the black circles are the average values of normalized damage threshold intensity for the five specimens investigated. The average values are below the Bettis model line indicating a stronger dependence than 1/w. Note that the average values show about the same dependence at the two wavelengths.

In figure 6 we plot the spot-size dependence of the threshold averaged over the five specimens of NaCl and KCl. An attempt was made to fit a linear and quadratic dependence of intensity threshold on inverse focal spot radius. The quadratic dependence gave the best fit. We emphasize that the upper-right corner of these plots are the points of normalization and thus must be included as data points in any attempts to fit the data to an analytical function.

The origin of the $(1/w)^2$ dependence is not understood. Such a dependence would seem to indicate that the damage was dependent on total power and that self-focusing was responsible for the damage [16]. However, this is not the case since for the worst case (highest total power at 2.7 μm) the total power was a factor of 18 or more below the critical power for self-focusing.

A possible explanation for the focal spot radius dependence is that the thresholds are determined by defects within the focal volume. A strict dependence on focal volume leads to an intensity threshold proportional to $(1/w)^4$. However, for an avalanche process initiated by electrons excited to the conduction band from defect states the threshold should be only weakly dependent on the number of defects present, as long as at least one defect is in the focal volume.

Let V_f equal the focal volume for which the probability of finding a single defect approaches one. For focal volumes smaller than V_f a strong dependence on focal spot radius is expected since the probability of finding a defect is porportional to the focal volume. As V_f is approached little or no dependence on focal volume (and thus focal spot radius) is expected. Figure 5 is suggestive of this since the focal spot radius dependence in the small focal spot region seems steepest.

The scaling laws shown in figure 6 were applied to our data and to that presented by Manenkov in 1977 [9] to scale all the data to a common spot size. Manenkov's results were for so-called "high optical resistance samples," the 20% or so ofsamples which he reported to have had high thresholds. The average thresholds for our samples at 10.6 μm are as high as those quoted by Manenkov for the so-called high damage threshold samples. While we realize the danger of applying empirical scaling laws derived from our samples to the Manenkov results, the agreement at 10.6 μm (the only point for which direct comparison can be made) lends some confidence for using the scaling laws on his data as well as ours.

In figures 7 and 8 we plot the frequency dependence of the breakdown field (rms field corresponding to the peak on-axis intensity) for NaCl and KCl. In these plots we have scaled our results and Manenkov's results to a common focal spot diameter. The top curves involve the least scaling. The 2.7 and 3.8 μm points were measured at this spot size. Manenkov's data for 1.06, 0.69, and 0.53 μm were taken with focal spot diameters of 17, 14, and 16 μm, respectively ($1/e^2$ full width in intensity). Our data at 10.6 μm was scaled from measurements with a 41 μm focal spot diameter.

The most significant feature on the information displayed in figures 7 and 8 is the very small dispersion of breakdown field over the 10.6 to 0.53 μm wavelength range when all data are scaled to the same focal spot diameter. In figure 7 there appears to be a negative slope for the data scaled to the 41 μm diameter spot. This is probably not significant since if one puts on the error bars of ±15%,

Table 2. Bulk energy density thresholds for NaCl (J/cm^2).

Specimen	78-NC-S1	78-NC-S2	78-NC-4	78-NC-5	78-NC-6
Lens 1 HF	9527	7479	7444	3828	8163
DF	11520	9802	7218	4410	5439
CO_2	3613	5170	3596	1444	2561
Lens 2 HF	5174	5531	4911	1844	3340
DF	8043	5398	5712	2203	3282
CO_2	592	626	630	511	434
Lens 3 HF	2060	2490	1952	916	1851
DF	1945	2427	1785	1057	1848
CO_2	>257	>138	>238	>213	>282

Table 3. Intensity thresholds for NaCl ($x10^9$ watts/cm^2).

Specimen	78-NC-S1	78-NC-S2	78-NC-4	78-NC-5	78-NC-6
Lens 1 HF	73.3	53.3	51.4	32.0	65.4
DF	121.0	125.0	83.0	53.8	53.6
CO_2	33.5	87.7	46.7	19.7	30.5
Lens 2 HF	39.3	47.8	44.5	15.6	28.9
DF	92.9	64.2	63.4	19.0	29.0
CO_2	7.40	7.73	6.62	6.13	7.11
Lens 3 HF	17.4	22.8	17.2	7.87	15.0
DF	19.1	33.9	17.9	11.1	30.9
CO_2	>3.1	>1.9	>2.4	>2.4	>3.4

Table 4. Bulk energy density thresholds for KCl (J/cm^2).

Specimen	78-KC-S1	78-KC-S2	78-KC-S3	78-KC-14	78-KC-15	78-KC-16
Lens 1 HF	3283	2865	3417	3783	3787	3749
DF	3306	5802	3173	4579	3980	4439
CO_2	1071	1366	1226	976	108	1136
Lens 2 HF	1841	2309	2141	2182	2000	2229
DF	1639	1774	2260	2167	1516	2178
CO_2	283	412	370	379	13.6	369
Lens 3 HF	1660	1521	1540	1437	1236	1559
DF	1227	1362	1362	1772	1086	1371
CO_2	>84	>225	>253	>176	0.25	>217

Table 5. Intensity density thresholds for KCl ($x10^9$ watts/cm^2).

Specimen	78-KC-S1	78-KC-S2	78-KC-S3	78-KC-14	78-KC-15	78-KC-16
Lens 1 HF	31.3	27.3	30.5	26.3	30.8	32.4
DF	32.2	70.2	31.1	54.1	43.5	48.8
CO_2	13.6	14.5	16.1	12.1	1.50	15.0
Lens 2 HF	15.6	19.8	16.1	18.2	18.3	17.4
DF	16.4	18.5	22.2	27.8	19.4	25.7
CO_2	4.72	4.96	5.07	4.25	0.21	5.39
Lens 3 HF	12.3	11.8	12.8	12.8	9.30	12.8
DF	14.0	16.9	14.4	30.3	11.4	14.8
CO_2	>1.2	>2.8	>3.1	>1.9	>0.003	>2.6

one could fit any one of the three curves within the resulting band. Note that the Sparks-Holstein model would fit the NaCl data (fig. 3) for the 72 μm spot diameter quite well, but fails to fit the data for the 19 μm spot diameter. The modified version of the simple avalanche model proposed by Sparks would fit the 19 μm spot size data quite well at 1.06 μm, but would fit the 10.6, 3.8, and 2.7 μm data only if much smaller values of electron relaxation time are used. The multiphoton absorption by polarons model proposed by Schmid, Kelley, and Bräunlich [17] would nearly fit the data for the 72 μm spot diameter at 1.06, 0.69, and 0.53 μm, but predicts a much stronger wavelength dependence than observed here and thus would fail to fit the 10.6 μm data for any of the spot sizes shown here.

Note that the threshold field at 2.7 μm for NaCl and KCl is consistently below the best fit frequency dependence shown in figures 5 and 6. This could be associated with increased absorption at 2.7 μm due to $(OH)^-$ in the crystal. Corresponding increases in linear absorption have been reported in hygroscopic crystals such as NaCl and KCl [18].

One can fit a linear dependence of breakdown field with laser frequency and extrapolate the results to get an estimate of the DC breakdown field. Figure 9 is a plot of such a linear fit for the data using the 71 μm spot diameter. The agreement of the predicted values with the measured DC values [19] is reasonable. As can be seen in figure 9, the ratio of NaCl to KCl threshold is not constant with frequency.

Conclusions

Measurements of the focal spot radius dependence of the pulsed laser damage thresholds of NaCl and KCl have shown considerable variation from sample to sample as well as variation with laser wavelength. The average intensity thresholds of the specimens studied had a $(1/w)^2$ dependence. The 10.6 μm average thresholds measured in this work are in good agreement with those reported by Manenkov for his "high optical resistance samples." This agreement lends confidence for using the empirical scaling laws derived in this work to scale our results and Manenkov's results to common focal spot radii. The results indicate little dispersion in damage threshold over the wavelength range of 10.6 to 0.53 μm. The lack of strong frequency dependence is suggestive of avalanche breakdown as the mechanism of failure in these materials. However, the ratio of the thresholds of the two materials studied is not constant with frequency. This implies that an extrinsic property of the material is being measured.

Acknowledgments

The authors acknowledge the support of the staff at the Naval Weapons Center in conducting these measurements, especially J. O. Porteus, J. L. Jernigan, W. N. Faith, and J. W. Bethke. We are thankful for the help in data-taking given by S. T. Wu and Kassem Moravvej of USC.

References

[1] Reviews of the proposed mechanisms for laser-induced damage in transparent materials can be found in the following references: Bloembergen, N., "Laser-Induced Electric Breakdown in Solids," IEEE J. Quantum Electron. QE-10, 375 (1974); Smith, L., "Fundamental Mechanisms of Ionization," these proceedings.

[2] Yasajima, Y., *et al.*, Japan. J. Appl. Phys. 7, 552 (1968).

[3] Yablonovitch, E., Appl. Phys. Lett. 19, 495 (1971).

[4] Fradin, D. W., and Bass, M., Appl. Phys. Lett. 22, 206 (1973).

[5] Allen, S. D., *et al.*, in *Laser Induced Damage in Optical Materials: 1974*, A. J. Glass and A. H. Guenther, eds., National Bureau of Standards, Washington, DC (NBS Spec. Publ. 414, 1974), p. 66.

[6] Soileau, M. J., *et al.*, in *Proceedings of the Fifth Annual Conference on Infrared Laser Window Materials*, 1975, C. R. Andrews and C. L. Strecker, eds. (Defense Advanced Research Projects Agency, Arlington, VA, 1976), p. 391.

[7] Yasajima, Y., *et al.*, Japan. J. Appl. Phys. 14, 815 (1975).

[8] Sparks, M., in *Laser Induced Damage in Optical Materials: 1975*, A. J. Glass and A. H. Guenther, eds., National Bureau of Standards, Washington, DC (NBS Spec. Publ. 435), p. 331.

[9] Manenkov, A. A., in *Laser Induced Damage in Optical Materials: 1977*, A. J. Glass and A. H. Guenther, eds., National Bureau of Standards, Washington, DC (NBS Spec. Publ. 509), p. 455.

[10] Bettis, J. R., *et al.*, in *Laser Induced Damage in Optical Materials: 1976*, A. J. Glass and A. H. Guenther, eds., National Bureau of Standards, Washington, DC (NBS Spec. Publ. 462), p. 338.

[11] Van Stryland, E. W., *et al.*, in *Laser Induced Damage in Optical Materials: 1977*, A. J. Glass and A. H. Guenther, eds., National Bureau of Standards, Washington, DC (NBS Spec. Publ. 509), p. 118.

[12] Soileau, M. J., *et al.*, in *Laser Induced Damage in Optical Materials: 1976*, A. J. Glass and A. H. Guenther, eds., National Bureau of Standards, Washington, DC (NBS Spec. Publ. 462), p. 149.

[13] Porteus, J. O., *et al.*, IEEE J. Quantum Electron. QE-13, 84D (1978).

[14] Harshaw Chemical Co., 6801 Cochran Rd., Solon, OH 44139.

[15] Manenkov, A. A., private communication, Sept. 1978.

[16] Fradin, D. W., IEEE J. Quantum Electron. QE-9, 954 (1973).

[17] Schmid, A., *et al.* in *Laser Induced Damage in Optical Materials: 1977*, A. J. Glass and A. H. Guenther, eds., National Bureau of Standards, Washington, DC (NBS Spec. Publ. 509), p. 465.

[18] Hass, M., and Bendow, B., Appl. Opt. 16, 2882 (1977).

[19] Von Hippel, A., J. Appl. Phys. 8, 815 (1937); Phys. Rev. 54, 1096 (1938).

Figures

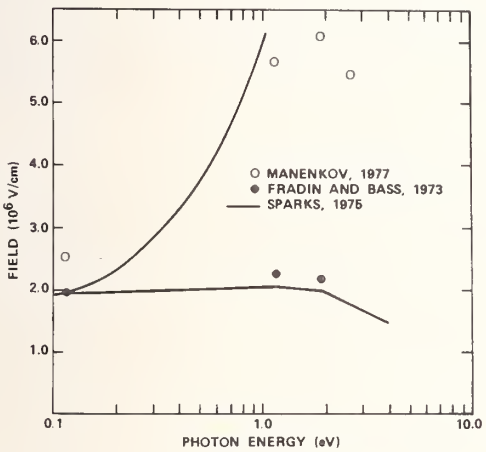

Figure 1. Frequency dependence of breakdown field in NaCℓ. Solid lines are fron Sparks [8]; open circles are from Manenkov [9]; solid circles are from Fradin and Bass [4].

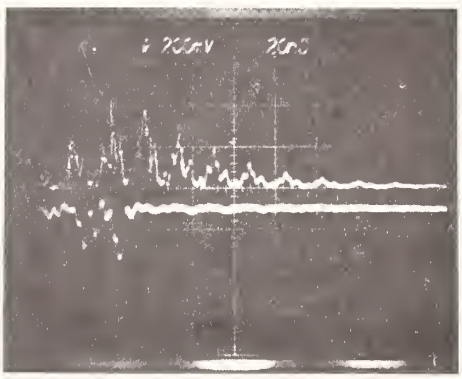

Figure 2. Laser waveforms related to the occurrence of bulk damage in NaCℓ at 10.6 μm. The top trace is the reference and the bottom trace is the truncated transmitted beam observed when damage occurs.

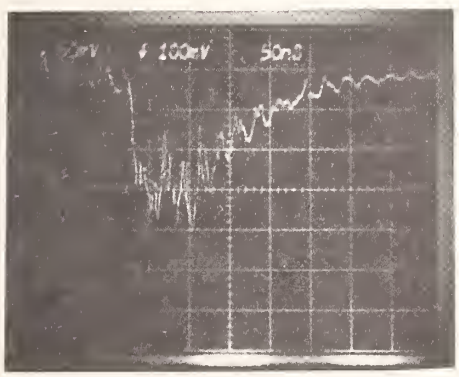

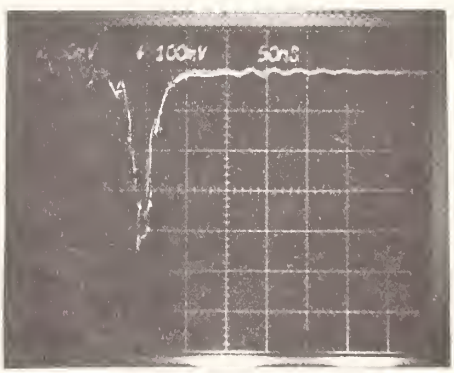

Figures 3a and 3b. Laser waveforms related to the occurrence of bulk damage in NaCℓ at HF wavelengths. The left trace is the transmitted pulse which did not cause damage. The right trace is the transmitted pulse when damage occurred near threshold.

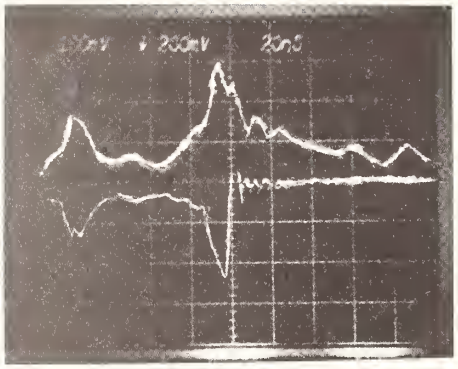

Figure 4. Laser waveforms related to the occurrence of bulk damage in NaCℓ at DF laser wavelengths. The top trace is the reference pulse and the bottom trace is the transmitted pulse. In this case, the damage is near the threshold value and occurs at the peak of the second pulse.

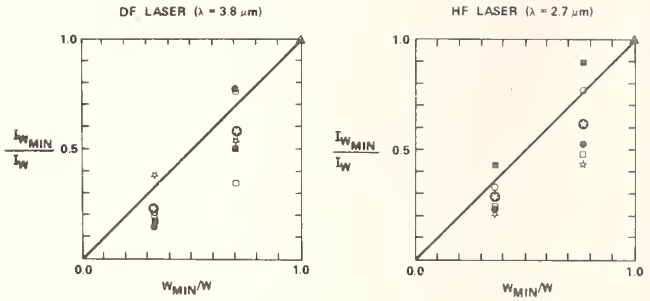

Figure 5. Spot-size dependence in NaCℓ. The white stars in the dark background are the average threshold values of five separate specimens. The other symbols correspond to the thresholds of the individual specimens. The large triangles are points of normalization and must be included in any atempt to fit these data to an analytical function.

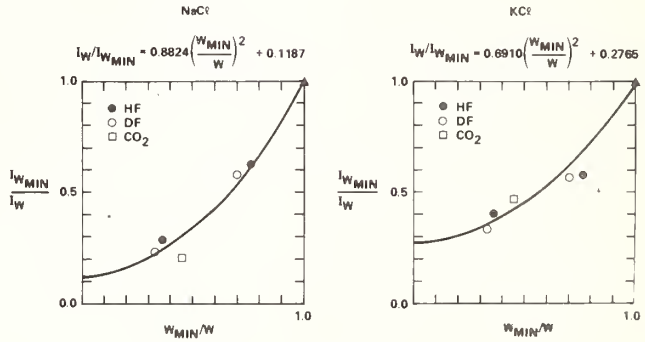

Figure 6. Spot-size dependence in NaCℓ and KCℓ. The above curves are the best fit of the spot-size dependence of the average thresholds for five NaCℓ and five KCℓ specimens. Note that the upper-right corners of the plots are the points of normalization and thus must be included as data points in any attempt to fit the data to an analytical function.

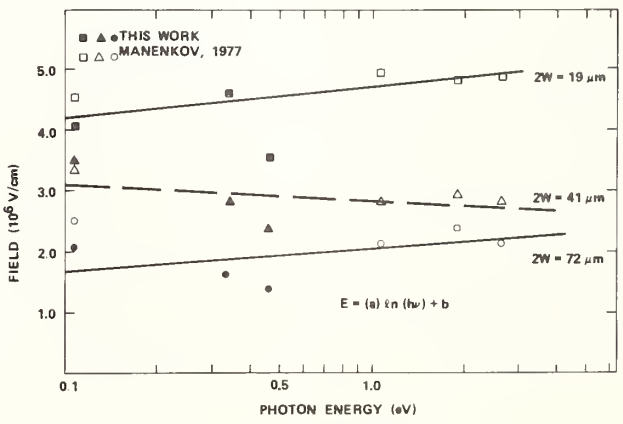

Figure 7. Frequency dependence of NaCℓ breakdown field. The fields given here are the rms electric fields corresponding to the peak on-axis intensity thresholds.

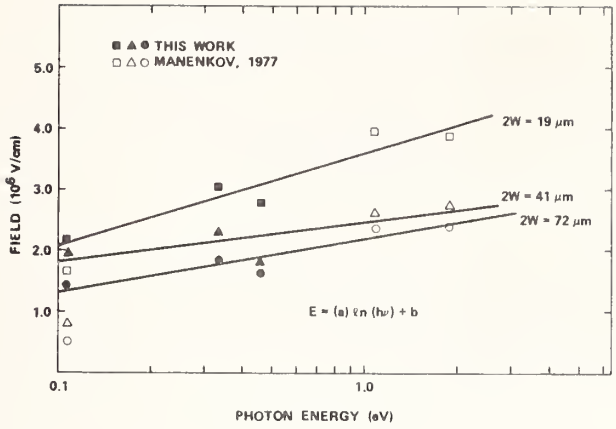

Figure 8. Frequency dependence of KCℓ breakdown field. The electric fields given here are the rms fields corresponding to the peak on-axis intensity thresholds.

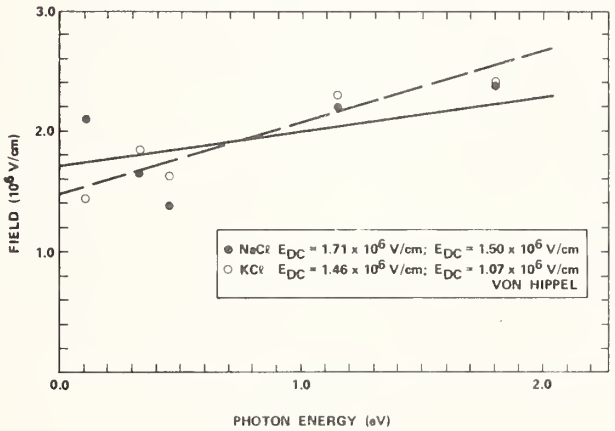

Figure 9. Linear fit to frequency dependence (2w = 72 μm). The DC data given here are from reference [19].

INVESTIGATION OF SURFACE BREAKDOWN MECHANISM IN IR-OPTICAL MATERIALS

V. I. Kovalev, F. S. Faizullov
USSR Academy of Sciences
Leninsky Prospect 53
Moscow, USSR

It has been found that with a decrease in ambient gas pressure, there takes place a decrease of surface breakdown threshold in IR-optical materials under TEA CO_2-laser radiation. To explain this fact, a new mechanism of the breakdown has been proposed, which is connected with evaporation of adsorbed water. The breakdown stage has been experimentally investigated and a theoretical analysis has been performed. The dependence of the surface breakdown in NaCl on ambient gas pressure, spot size, frequency and time have been studied. The dependence on the quantity of adsorbed water (surface absorption) has been studied as well. The breakdown thresholds have been measured with a calibrated, photon drag detector by the amplitude of the transmitted pulse. The results obtained are in good agreement with the proposed model.

Key words: Adsorbed water; breakdown mechanism; IR window materials; NaCl; pulsed TEA CO_2 laser surface breakdown; pressure; spot size; surface absorption; frequency and time dependence of breakdown thresholds; transmitted pulse.

1. Introduction

Surface breakdown threshold in IR-optical materials is determined by adsorbed water, as was found earlier in spectroscopic and mass spectroscopic investigations [1]. To avoid the influence of processes taking place in the ambient gas on the breakdown plasma luminescence at the surface, the investigations have been performed with the samples placed in vacuum.

Breakdown threshold measurements in vacuum have shown that the threshold values are 1.5 to 2 times smaller in comparison with those observed at atmospheric pressure of the ambient gas. The results of these measurements are listed in Table 1.

Table 1 Surface breakdown thresholds (MW/cm^2) in some IR-optical materials in air and vacuum, and ratio between them.

Material	Air	Vacuum	Air/Vacuum
NaCl	65	32	2.0
ZnSe	55	35	1.6
KRS-5	60	32	1.9
KRS-6	40	28	1.5
Ge	50	33	1.5

The method of measuring the threshold is described in detail in paper [2], and is based on measuring the pulse amplitude of the TEA CO_2 laser radiation transmitted through the sample, at the moment when breakdown appears (moment of nontransparency). The pulse amplitude measurement was performed with a photon drag detector calibrated on power. Pulse risetime was 150 ns. Spot size of the incident radiation on the samples surface was measured by the autocalibration method and reached 5.0 mm.

The observed influence of ambient gas pressure on breakdown threshold may be explained by making the assumption that the evaporation of adsorbed water from the surface takes place before the breakdown.

Theoretical analysis of the water evaporation mechanism shows that, in our case, water evaporation is the result of volume boiling of the adsorbed water layer. In this process, a certain part of the threshold energy which is close to the evaporation heat is absorbed (this energy corresponds to an incident energy density $W_{min} \simeq 2.5$ J/cm^2). The water is evaporated under conditions close to critical ($\rho_{cr} = 0.329$ g/cm^3; $T_{cr} = 647$ K^o; $P_{cr} = 225$ atm). As the result of gas-dynamical expansion, the vapor density decreases, and the breakdown conditions in this vapor are fulfilled, according to the Paschen curve (see Figure 1). This, briefly, is the breakdown mechanism. We next present a number of experimental results confirming the proposed model.

2. Pre-breakdown Stage Study

An experimental study of the pre-breakdown stage was performed with the help of schlieren photography in ruby laser light (Figure 2). The spot size of the incident beam of CO_2 laser on the samples was ~ 6 mm; the flux density was about half of the threshold. Typical schlieren photos are shown in Figure 3. Exposure time is 10 nsec. The surface of the sample is horizontal; the radiation is falling from above. The photos were taken with 1.3, 3.6, and 6 μsec delay of the probing pulse in relation to the beginning of the CO_2 laser pulse. It is seen that as a result of water vapor expansion at pre-breakdown intensity, a plane shock wave is formed which propagates in the air from the surface.

Figure 4 shows a typical schlieren photochronogram of the shock wave motion, which was taken with a streak camera in the light of a ruby laser (free oscillation regime), and the corresponding x, t-diagram. During the first microsecond the velocity of the shock wave is 700 m/sec. Thus, the evaporated water may be considered to be the plunger, leading to compression of the ambient gas. In its turn, the ambient gas influences both the density distribution in the expanding vapor, and the vapor expansion velocity.

Figure 5 demonstrates experimental results which show the influence of nitrogen density on the shock wave velocity, when the free water and NaCl surfaces were under the action of the laser pulse. The results of theoretical calculation of the dependence of the shock wave velocity on the ambient gas density is presented here as well. These calculations were carried out using a model of vapor expansion in a centered expansion wave, taking into account the back pressure of the ambient gas [3,4]:

$$D = (\gamma_g + 1)\, U(\rho_g)/4 + C_g\left\{1 + [(\gamma_g + 1)\, U(\rho_g)/4C_g]^2\right\}^{1/2} , \tag{1}$$

$$P_o[1 - (\gamma_v - 1)\, U/2C_v]^{2\gamma_v/(\gamma_v-1)} = (3\gamma_g + 1)\, P_g/(\gamma_g + 1) + (\gamma_g + 1)\, U^2\rho_g/2 , \tag{2}$$

where $\left.\begin{matrix}\gamma_g = 1.4 \\ \gamma_v = 1.33\end{matrix}\right\}$ are adiabatic indices of the ambient air and vapor

C_g and C_v = sound velocities

P_o = initial vapor pressure,

U = velocity contact discontinuity.

In the case of free water, the experimental results are in good agreement with theory. In the case of NaCl, the difference between the absolute value of the velocity and the theoretical prediction is due to a small amount of adsorbed water, but the character of the dependence of the velocity on the ambient gas density remains the same.

3. Breakdown in Water Vapor

Due to expansion, the vapor near the surface has a density which is determined by the formula

$$\rho_v(\rho_g) = \rho_o[1 - 0.167U(\rho_g)/C_v]^6 , \tag{3}$$

where $U(\rho_g)$ is obtained from Eq. (2), and ρ_o is the initial vapor density.

In this vapor region, breakdown may occur. The condition for breakdown development in the water vapor corresponds to the requirement that the rate increase of the energy of the electrons in the field of laser radiation with intensity J must exceed the maximum rate of energy loss by electrons, due to elastic collisions with neutral molecules. This condition may be written as [3]:

$$\frac{\partial\varepsilon}{\partial t} = \left(\frac{4\pi e^2}{mc}\, J\, \frac{\nu}{\omega^2 + \nu^2} - \frac{2m}{M}\, \nu\Delta\right) > 0 , \tag{4a}$$

or $$J > \frac{m^2 c \Delta}{2\pi M e^2}\,\omega^2\left(1+\frac{\nu^2}{\omega^2}\right) \simeq 2.65 \times 10^7\left(1+\frac{\nu^2}{\omega^2}\right)\left(\frac{W}{cm^2}\right), \tag{4b}$$

where m = mass of the electron

e = electron charge

M = mass of the molecule

C = sound velocity

Δ = ionization potential

ω = the laser frequency

$\nu = \rho_v u_e \sigma / M$ = frequency of electron collisions with neutral particles,

where u_e = mean electron velocity

σ = cross section of electron collisions with molecules

It can be seen that the dependence of the threshold intensity goes as $\nu \sim \rho_v$.

Figure 6 demonstrates the $J(\rho_v)$ dependence calculated from Eq. (4). This formula usually describes the dependence of the gas breakdown threshold well at high pressures, when $\nu > \omega$, but it is not valid for low pressures. In gases, when $\nu < \omega$, the threshold increases with a decrease in pressure, because electron losses due to diffusion from the interaction volume become significant. To check the validity of these estimates, we have performed measurements of the breakdown threshold of water vapor as a function of pressure. The results of the measurements are shown in the diagram by dots. As seen from the figure, breakdown in water vapor may actually take place at intensities which lead to surface breakdown.

4. Surface Breakdown Mechanism in IR-Optical Materials

By substituting $\rho_v(\rho_g)$ in Eq. (4), we obtain the dependence of the breakdown threshold on the ambient gas density in the following form:

$$J(\rho_g) \gtrsim 2.65 \times 10^7\left\{1 + [\nu_0^2/\omega^2][1 - 0.167U(\rho_g)/C_v]^{12}\right\}, \tag{5}$$

where $\nu_0 = \nu(\rho_0)$

Figure 7 illustrates the results of calculation by this formula in relative units. Experimental results combined with the theoretical dependence at the point corresponding to atmospheric pressure are presented here. The agreement of calculation and experiment is satisfactory.

It should be pointed that Eq. (5) is necessary for breakdown, but it is not sufficient. Actually, Eq. (5) will, at the same time, be sufficient when the ionization frequency in the radiation field $\nu_i = \Delta^{-1}(\partial\varepsilon/\partial t)$ exceeds the probability of diffusion drift of the electrons out of the interaction zone, $\nu_D = D/\Lambda^2$, where D is the diffusion coefficient, $\Lambda^{-2} = 23d^{-2} + 10\ell_v^{-2}$, d is the spot diameter in the lens focus, and ℓ_v is the dimension of the vapor region along the direction of incident radiation, i.e., it expresses the dimensions of the steady state and transient flows in the expansion wave. In the present case $d \simeq 5 \times 10^{-2}$ cm $\gg \ell_v \leq 10^{-3}$ cm; hence, $\Lambda^2 \simeq 0.1\ell_v^2$, i.e., diffusion losses, and hence, the breakdown threshold, do not depend on spot size.

Taking into account Eq. (4), the avalanche condition ($\nu_i > \nu_D$) may be written as follows:

$$\frac{4\pi e^2}{mc\Delta} J \frac{\nu}{\omega^2 + \nu^2} \gg \frac{10D}{\ell_v^2} \tag{6}$$

For example at $\omega_{CO_2} = \nu$, i.e., in the region of minimum dependence of the vapor breakdown threshold on the density, Eq. (6) will take the form:

$$J >> (mc\Delta D\omega_{CO_2})/(0.4\pi e^2 \ell_v^2) \ . \qquad (7)$$

Inserting values of the constants, we have: $J >> 3 \times 10^6$ W/cm^2.

In fact, the threshold intensity for the water vapor which is found from Eq. (5) significantly exceeds the value in the right-hand part of the inequality. Thus, for our experiments, Eq. (5) is not only necessary, but also sufficient.

On the other hand, the right-hand side of Eq. (7) is proportional to ℓ_v^{-2}, where $\ell_v \sim \ell_w$, is the equivalent thickness of the water film adsorbed at the surface. Reducing the film thickness should result in the violation of Eq. (7), at intensities defined by Eq. (5), and hence, in an increase of the breakdown threshold. This explains the breakdown threshold increase at the surface of IR-optical materials under the action of pulsed CO_2 laser radiation as a result of laser cleaning, chemical etching and improving the technology of mechanical treatment, which has been reported [2,6,7].

5. Some Specific Features of the Breakdown Due to Absorbed Water

The proposed mechanism results in some specific properties of the breakdown threshold, when it is determined by adsorbed water:

(a) Dependence of the breakdown threshold on the ambient gas pressure (almost irrespective of the identity of the gas);
(b) Breakdown threshold does not depend on the spot size of the incident radiation;
(c) The relation between surface absorption and breakdown threshold;
(d) The dependence of the breakdown threshold on the wavelength of the incident radiation;
(e) Specific dependence of the breakdown threshold on pulse duration.

5.1 Pressure Dependence

The results of our study of pressure dependence were shown above (see Figure 7). They show good agreement between the calculations and experiment.

5.2 Spot Size Dependence

As follows from the analysis of the breakdown mechanism (see above), the threshold, determined by the breakdown in adsorbed water vapor, must not depend on the spot size of the incident radiation. Experimental verification of this conclusion has been performed using a pulsed CO_2 laser, with the radiation focused on a NaCl sample surface with a lens having 12 cm focal length. The spot diameter in the lens focus was 0.5 mm. The spot was enlarged up to 2.5 mm, by means of an increase in the distance between the lens and the surface. Here, to avoid breakdown of the ambient gas at the focal point, the sample was placed in an evacuated chamber, so that the lens focus was in vacuum. We have also measured the breakdown threshold when the spot was $\sim$ 200 μm (lens focus, 5 cm). Table 2 summarizes our experiments.

Table 2 The dependence of surface breakdown on the spot-size of the incident radiation (in vacuum).

Spot Diameter, mm	Breakdown Threshold, MW/cm^2
0.23	36
0.50	35
0.65	36
0.92	36
1.24	35
1.84	37
2.25	36

It can easily be seen that, as was expected, the experimentally measured breakdown thresholds do not depend on spot size. In this case, the irradiated zone morphology corresponded to breakdown near the surface, without catastrophic damage.

5.3 Surface Absorption

As shown above, the damage threshold determined by adsorbed water is inversely proportional to the square value of the equivalent water film thickness ℓ_w, i.e., to the quantity on the surface. Since the absorption constant at 10.6 μm wavelength is $\sim 10^3$ cm^{-1}, naturally, the presence of a considerable quantity of water at the suface must influence the surface absorption. For this reason, we have measured the surface breakdown threshold and the surface absorption on the same sample. Surface absorption was measured by a calorimetric method. Initial measurements were performed on a NaCl surface, which had been prepared by mechanical abrasive polishing, and stored in the open air for a long time. The sample was then exposed for 5 min. to concentrated HCl, then washed in alcohol and dried. We then measured the breakdown threshold and surface absorption and determined the dependence of the breakdown threshold on the duration of exposure of the sample to open air. The results are described in Table 3.

Table 3 Breakdown thresholds and surface absorption in NaCl after chemical etching versus the exposure time in the open area

Air Exposure Time	Breakdown Threshold, MW/cm^2	Surface Absorption, %
Before Chem. Etching	36	1.6
5.0 min. After	220	0.24
20.0 min.	100	0.26
1.5 hrs.	113	0.28
20.0 hrs.	105	0.31
3.0 months	105	-

As seen from the table, there is a direct correlation between the surface breakdown threshold and surface absorption (the quantity of adsorbed water). It should be pointed out that on a surface free of adsorbed water (cleavage and measuring of threshold in vacuum) the surface damage threshold appears to be equal to the bulk breakdown threshold. The surface damage morphology corresponds to damage at impurities.

5.4 Wavelength

It follows from Eq. (4) that the frequency dependence of the breakdown threshold in water vapor is $J_{th} \sim \lambda^{-2}$. An experimental study of the frequency dependence was carried out at 10.6 μm, 3.8 μm, and 2.7 μm by means of CO_2, DF and HF-TEA lasers. The pulse risetime in all these cases was 100 ns. The results are shown in Figure 8. The figure corresponds to the dependence $J_{th} \sim \lambda^{-2}$ when normalized to the breakdown threshold at 10.6 μm. The agreement between the calculation and experiment is satisfactory in this case as well.

5.5 Pulse Risetime

The proposed breakdown mechanism is characterized by two parameters: (1) the minimum energy density W_{min} of the incident radiation which is necessary to boil off the surface adsorbed water layer, and (2) the threshold intensity of the incident radiation (dependent on water vapor density) which is necessary for electron avalanche in the vapor. As follows from a theoretical analysis of the water evaporation mechanism and from experimental results that $W_{min} \simeq 2.5$ J/cm^2. It is clear that with reduced pulse duration, the threshold energy density must tend to W_{min}, and the threshold intensity must increase approximately inversely, since the water boiling off is a necessary condition for breakdown. On the other hand, there also must take place an increase of the threshold intensity with increasing pulse risetime. The following considerations make it possible to understand this fact. In this case when W_{min} is absorbed, the laser radiation intensity will not be sufficient enough for the development of the breakdown in the whole density region of the expanding vapor. When the vapor density near the surface decreases sufficiently, due to gas dynamical expansion, so that one is below the vapor minimum breakdown threshold, (but breakdown does not occur), further expansion leads to an increase of the breakdown threshold, according to the results shown in Figure 6.

We have performed an experimental study of the dependence of the breakdown threshold on pulse risetime. Pulse duration was varied from 75 to 150 ns by changing the working mixture in a CO_2, TEA laser. Due to specific features of the measurement method, the form and duration of pulse "tail" were not significant. We have produced a pulse with a 1500 ns risetime from an ordinary CO_2, TEA laser by means of a cell containing saturable absorber [8] (SF_6 gas). Figure 9 shows typical oscillograms of the incident pulse, with a 1500 ns risetime, and the pulse traversing the sample at surface breakdown. The results of measuring the breakdown thresholds (see Table 4) are in agreement with the above mentioned analysis, and it confirms the proposed model as well.

Table 4 Threshold intensity and energy density at NaCl surface versus the pulse rise time

Pulse Rise Time, ns	Threshold Intensity, MW/cm^2	Threshold EnergyDensity, J/cm^2
1.2	2500	3.0 [7]
75.0	100	3.7
100.0	150	4.0
150.0	80	4.9
1500.0	200	150.0

6. Conclusion

The, mechanism for surface breakdown in IR-optical materials, under the action of pulsed lasers operating in the mid-IR wavelength region, is proposed and experimentally validated in the present paper.

7. References

[1] V. I. Kovalev, F. S. Faizullov, Kvantovaya Elektr., 4, 587 (1977); Sov. J. of Quantum Electronics 7, N3 (1977).

[2] V. I. Kovalev, V. V. Moreozov, F. S. Faizullov, Kvantovaya Electr., 1, 2172 (1974); Sov. J. of Quantum Electronics 4, N10 (1975).

[3] A. N. Tikhonov, A. A. Samarasky, Uravnenniya Matematicheskoy Fiziki, Moscow, Nauka, (1977).

[4] Ya. B. Zel'dovich, Yu P. Raizer, Fizikaudarnykn voln i vysokotemperaturnykh gasodinamicheskikh yavleniy, Moscow, Nauka (1966).

[5] Yu. P. Raizer, Lazernaya iskra i rasprostenie razryadov, Moscow, Naukay (1973).

[6] S. D. Allen, M. Braunstein, C. Giuliano, V. Wang, Laser Induced Damage in Optical Materials, 1974 NBS Spec. Publ. 414, p. 66.

[7] W. H. Reichelt, E. E. Stark. Laser Induced Damage in Optical Materials, NBS Spec. Publ. 387, p. 175 (1973).

[8] H. K. Kleiman, S. Marcus, J. Apply. Phys., 44, 1646 (1973).

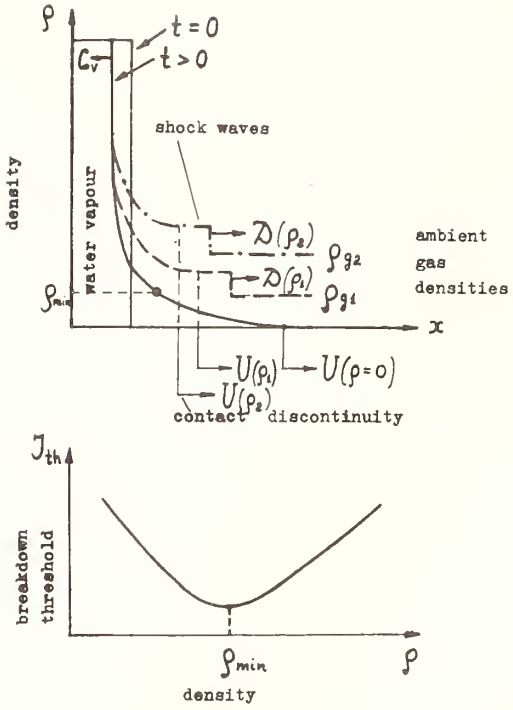

Figure 1. Surface breakdown model.

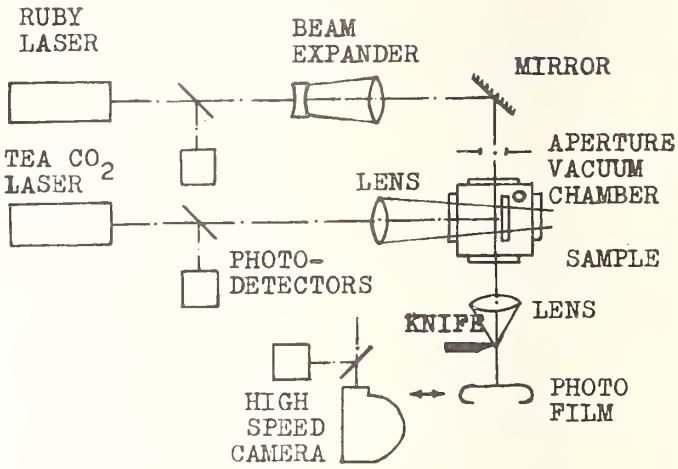

Figure 2. Experimental installation for investigation of surface phenomena in IR-optical materials at the intensity of the incident radiation less than the breakdown threshold.

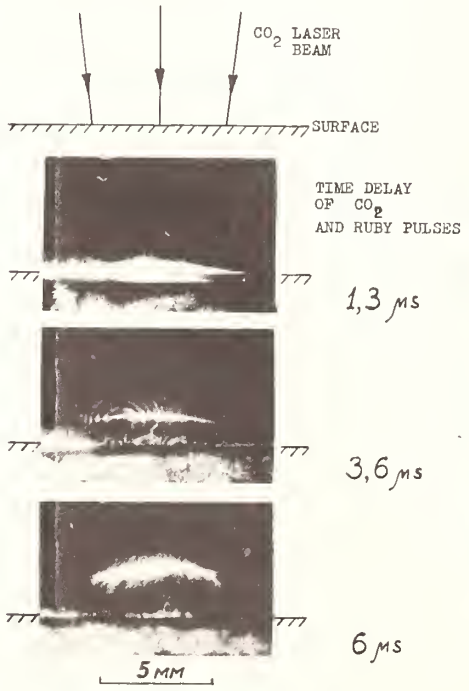

Figure 3. Schlieren-photo of the shock wave near NaCℓ surface. CO_2 and ruby laser pulse time delay is 1.3, 3.6, and 6.0 μsec.

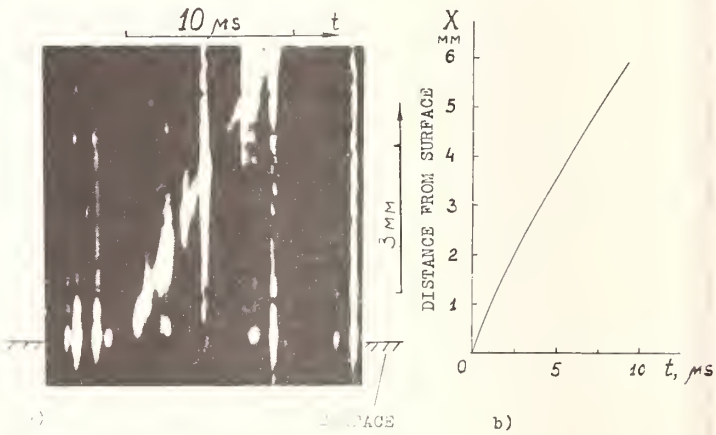

Figure 4. (a) Typical schlieren-photogram of the shock wave motion in the air in the light of ruby laser (true oscillation regime); (b) X,t -diagram.

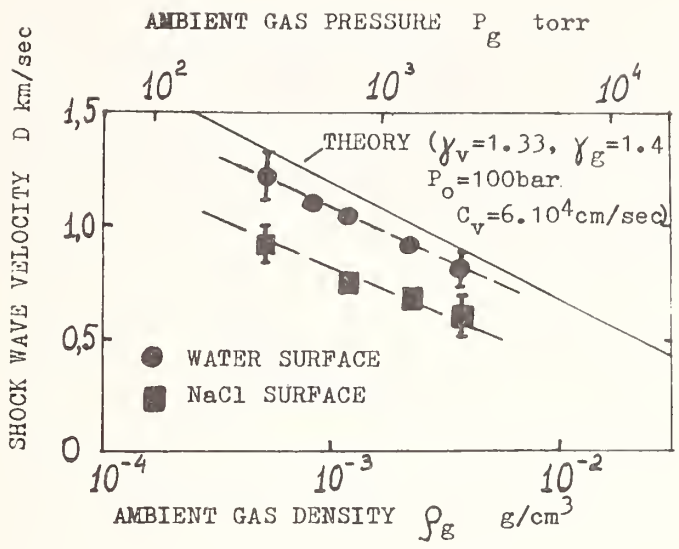

Figure 5. Shock wave velocity versus ambient gas density.

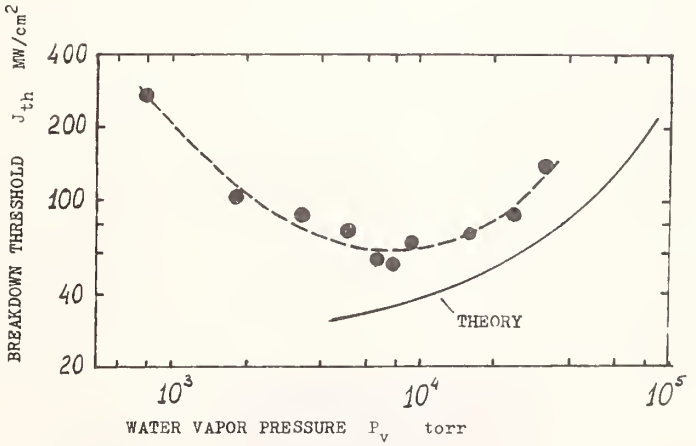

Figure 6. Breakdown threshold in water vapor versus the pressure. Dense curve is calculated by formula (4).

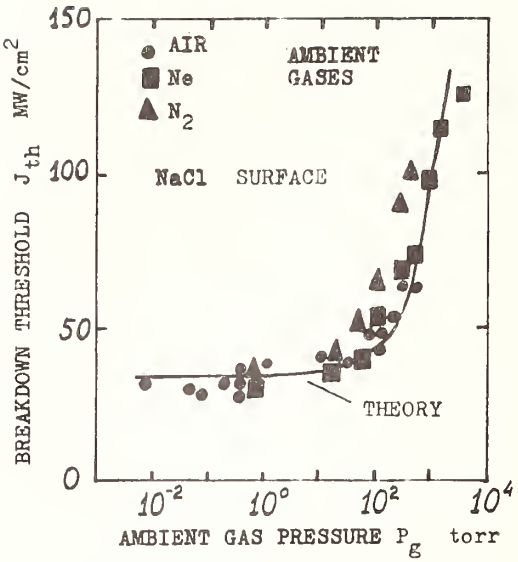

Figure 7. Surface breakdown threshold in NaCℓ versus the ambient gas pressure. Dense curve is calculated by formula (5) in arbitrary units.

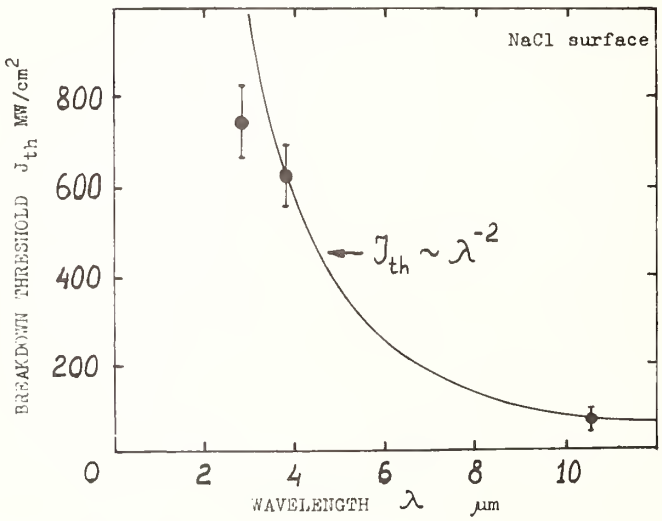

Figure 8. Surface breakdown threshold in NaCℓ versus the wavelength of the incident radiation.

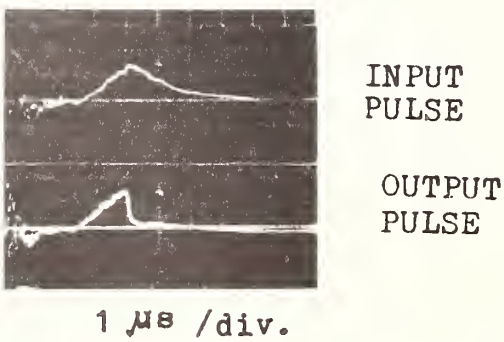

Figure 9. Typical shape of CO_2 laser input (upper) and output (lower) pulses at surface breakdown in NaCℓ.

Discussion

The speaker was asked if any other species besides water evolved from the sample surfaces. He said that only water was seen below the damage threshold but that, when damage occurred, chemical decomposition of the sample was observed. The speaker indicated that the wavelength dependence experiments were carried out with pulses of the same rise time and comparable spot sizes. Finally, the speaker was asked why the observed threshold at 2.7 μm (Fig. 8) was not lowered since the absorption in water vapor is greater at 2.7 μm than at 3.8 μm. The observed breakdown follows the prediction of plasma absorption (Eq. 4) and does not seem to be dependent on molecular absorption for its initiation.

APPENDIX I.

INVITED REVIEW PAPERS

Several invited reviews were presented at the Tenth Annual Symposium on Laser Induced Damage in Optical Materials. These reviews given by the major contributors to this field summarized the state of the art and understanding in the principal sub-areas of optical materials for high power lasers. It is our intention to publish through the auspices of Academic Press, these and other appropriate reviews in a separate volume. For completeness, we list those presented reviews.

The Design of Damage Experiments	M. Bass University of Southern California
Surface and Thin Film Damage	B. Newnam Los Alamos Scientific Laboratory
Scaling Laws for Laser Induced Damage	J. R. Bettis U.S. Naval Academy
	A. H. Guenther Air Force Weapons Laboratory
State of the Art of IR Window Materials	J. Harrington Hughes Aircraft Corp.
UV Materials for High Power Lasers	M. Sparks Xonics Corporation
Thin Film Materials for the IR and UV	M. Braunstein Hughes Aircraft Corporation
Design Consideration in Thin Film Damage	J. Apfel Optical Coating Laboratory, Inc.
Surface Evaluation Techniques for Optical Components	J. Bennett Naval Weapons Center
Metal Mirrors and Diamond Turning	D. Decker J. Porteus Naval Weapons Center
Factors limiting the Energy Transmitted by an Optical Train	H. Bennett Naval Weapons Center
Systems Consideration for Short Pulse, Glass Lasers	J. Trenholme Lawrence Livermore Laboratory
Fundamental mechanisms of Ionization	L. Smith Lawrence Livermore Laboratory
Laser Induced Semiconductor Damage	L. Esterowitz Naval Research Laboratory

APPENDIX II--PARTICIPANTS

S. R. Aiken
Rocketdyne Division
Rockwell International
6633 Canoga Ave.
Canoga Park, CA 91304
(213)884-3346

Susan D. Allen
Center for Laser Studies
University of Southern California
Los Angeles, CA 90007
(213)741-6705

Thomas H. Allen
Optical Coating Laboratory, Inc.
P. O. Box 1599
Santa Rosa, CA 95402

Rogers H. Anderson
Honeywell Corporate Material
Sciences Center
10701 Lyndale Ave. So.
Bloomington, MN 55420
(612)887-4533

Joseph H. Apfel
Optical Coating Laboratory, Inc.
P. O. Box 1599
Santa Rosa, CA 95402
(707)545-6440

Philip C. Archibald
Michelson Laboratory, Code 3818
Naval Weapons Center
China Lake, CA 93555
(714)939-2869

Yoshiyuki Asahara
Hoya Corporation
572, Miyazawa-cho, Akishima-shi
Tokyo, JAPAN

William A. Barletta
L-389
Lawrence Livermore Labs.
Livermore, CA 94550
(415)422-5081

Norman Barnes
Los Alamos Scientific Lab.
P. O. Box 1663
Los Alamos, NM 87545
(505)667-7732

Michael Bartosewcz
Bldg. 201 Dept. 52-54
Lockheed R α D Labs.
3251 Hanover St.
Palo Alto, CA 94034
(415)493-4411 Ext.45750

Michael Bass
Center for Laser Studies
University of Southern California
Los Angeles, CA 90007
(213)741-7994

Pat Beauchamp
Advanced Products Development
Optical Coating Lab., Inc.
P. O. Box 1599
Santa Rosa, CA 95402
(707)545-6440

Harold E. Bennett
Code 38101
Naval Weapons Center
China Lake, CA 93555
(714)939-2869

Jean M. Bennett
Code 38103
Naval Weapons Center
China Lake, CA 93555
(714)939-2869

John S. Bessey
Technical Products Division
Optical Coating Lab., Inc.
P. O. Box 1599
Santa Rosa, CA 95402
(707)545-6440

Jerry Ray Bettis
U. S. Naval Academy
C-3 Perry Circle, USNA
Annapolis, MD 21402
(301)267-7497

Gordon Boultbee
Optical Coating Lab., Inc.
2789 Giffen Ave.
Santa Rosa, CA 95402

Peter Braunlich
Dept. of Physics
Washington State University
Pullman, WA 99164
(509)335-4946

Morris Braunstein
Hughes Research Lab.
3011 S. Malibu Canyon Rd.
Malibu, CA 90265
(213)456-6411

Steven Brawer
Lawrence Livermore Labs.
Livermore, CA 94550
(415)422-8094

David C. Brown
Lab. for Laser Energetics
University of Rochester
250 E. River Rd.
Rochester, NY
(716)275-4446

Dorothy Bruce
STEWS-TE-AG, Bldg. 1676
White Sands Missile Range, NM 88002
(505)678-2812

Richard Bruce
Perkin-Elmer Co.
Main Street M/S 283
Norwalk, CT
(203)762-6366

Aaron Budgor
Lawrence Livermore Labs.
P. O. Box 808 L-464
Livermore, CA 94550
(415)422-5059

David L. Burdick
Naval Weapons Center Code 3813
China Lake, CA 93555
(714)939-2898

Dennis Burge
Naval Weapons Center, Code 3816
China Lake, CA 93555
(714)939-2869

Charles K. Carniglia
Optical Coating Lab., Inc.
P. O. Box 1599
Santa Rosa, CA 95402

George E. Chamberlain
Division 724.02
National Bureau of Standards
Boulder, CO 80303
(303)499-1000 Ext.3706,4208

Verne R. Costich
Design Optics
155 Moffett Park Dr.
Sunnyvale, CA 94086

Terrence F. Deaton
Lawrence Livermore Labs. L-465
Livermore, CA 94550
(415)422-6059

Donald L. Decker
Physics Div., Code 3816
Naval Weapons Center
China Lake, CA 93555
(714)939-3247

David J. Dentz
Airtron Div. of Litton Ind.
200 E. Hanover Ave.
Morris Plains, NJ 07950
(201)539-5500

John A. Detrio
Univ. of Dayton Research Inst. KL
541
300 College Park
Dayton, OH 45469
(513)229-3527

Marilyn J. Dodge
Div. 565
A251 Materials Bldg.
National Bureau of Standards
Washington, DC 20234
(301)921-2033

T. M. Donovan
Naval Weapons Center, Code 3812
China Lake, CA 93555
(714)446-2115

William K. Downing
Design Optics
155 Moffett Park Dr.
Sunnyvale, CA 94086

David F. Edwards
MS-564
Los Alamos Scientific Lab.
Los Alamos, NM 87545
(505)667-7102

David Eimerl
Lawrence Livermore Labs.
P. O. Box 808
Livermore, CA 94550
(415)422-7505

James D. Evans
USAF Materials Lab.
WPAFB
Dayton, OH 45433
(513)255-2066

F. Faizullov
Leledev Physical Institute
53 Lewin Prospect
Moscow, USSR

Albert Feldman
Div. 565, A251 Materials Bldg.
National Bureau of Standards
Washington, DC 20234
(301)921-2840

Nils C. Fernelius
Univ. of Dayton Research Inst.
300 College Park Ave.
Dayton, OH 45469
(513)255-4474

Douglas Flint
Dept. 535
ITEK Corp. - Opt. Sys. Div.
10 Maguire Road
Lexington, MA 02173
(617)276-3491
William G. D. Frederick
AFML/LPO
AF Materials Lab.
Wright-Patterson AFB, OH 45433
(513)255-4098

Dennis H. Gill
Group AP-2
Los Alamos Scientific Lab.
Mail Stop 564
Los Alamos, NM 87545
(505)667-6610

Joseph Giove
Large Laser Components Div.
ILC Technology
399 Java Dr.
Sunnyvale, CA 95014
(408)745-7900

Alexander J. Glass
Lawrence Livermore Labs.
P. O. Box 5808
Livermore, CA 94550
(415)422-5354

Ann T. Glassman
Univ. of Dayton Research Inst.
KL102
300 College Park
Kettering, OH 45469
(513)229-3724

William T. Goosey
Optics Development 144
Apparatus Division - Hawk-Eye
Eastman Kodak Company
Rochester, NY 14650
726-6442

Arthur W. Guenther
Air Force Weapons Lab/CA
Kirtland AFB, NM 87117
(505)264-8561

Yu H. Hahn
CVI Laser Corporation
P. O. Box 11308
Albuquerque, NM 87192
(505)296-9541

W. Haller
Glass Section
National Bureau of Standards
Washington, DC 20234

Robert M. Hardesty
WPL R45X9
NOAA/ERL
Boulder, CO 80303
(303)499-1000 Ext. 6743

James A. Harrington
Hughes Research Labs.
Malibu, CA 90265
(213)456-6411

Marvin Hass
Naval Research Lab., Code 5504
Washington, DC 20375
(202)767-3387

R. B. Hemphill
Vought Corp, Adv. Tech. Ctr.
P. O. Box 6144
Dallas, TX 75222
(214)266-3179

Terry Holcomb
Hughes Aircraft Co.
Centinela α Teale
Culver City, CA 90230
(213)391-0711 Ext. 2970

Samuel J. Holmes
Orgn. 345/T-60
Northrop Research α Technology Ctr.
One Research Park
Palos Verdes Peninsula, CA 90274
(213)377-4811 Ext. 482

T. R. Holt
AFWL/LRE, Bldg. 401
Univ. of Dayton Research Inst.
Kirtland AFB, NM 87117
(505)242-2667

Alan K. Hopkins
Air Force Materials Lab.
Wright Patterson AFB, OH 45433
(513)255-4474

Richard S. Hughes
Naval Weapons Center, Code 3815
China Lake, CA 93555
(714)939-3855

Thomas Humpherys
AFWL/LRE USAF
Kirtland AFB, NM 87117
(505)264-1776

Stephen D. Jacobs
Lab. for Laser Energetics
University of Rochester
250 E. River Rd.
Rochester, NY 14623
(716)275-4837

G. T. Johnston
AFWL/LRE, Bldg. 401
Univ. of Dayton Res. Inst.
Kirtland AFB, NM 87117
(505)242-2667

Milton N. Kabler
Naval Research Lab., Code 5580
Washington, DC 20375

Thomas Kardos
Broomer Labs. Inc.
23 Sheer Plaza
Plainview, NY 11813
(516)249-1544

Paul Kelly
Physics Div., NRC
Montreal Road
Ottawa
Ontario, CANADA

Claude A. Klein
Research Div., Raytheon Company
28 Seyon St.
Waltham, MA 02154

Philipp H. Klein
U. S. Naval Research Lab., Code 5222
Washington, DC 20375
(202)767-3671

Paul Kraatz
Orgn. 345/T-60
Northrop Research α Technology Ctr.
One Research Park
Palos Verdes Peninsual, CA 90274
(213)377-4811 Ext. 482

George Krauss
Dept. of Metallurgical Engineering
Colorado School of Mines
Golden, CO 80401
(279-0300)

Melvin R. Kruer
Optical Science Div.
Naval Research Lab., Code 5554
Washington, DC 20022
(202)767-3276

David J. Krus
Crystal and Elect. Prod. Dept.
Harshaw Chemical Co.
6801 Cochran Rd.
Solon, OH 44139
(216)248-7400

Harald Kuster
Institut fur Angewandte Physik
Technische Universitat Hannover
One Welfengarten
3000 Hannover
WEST GERMANY
Ph. 05M-762/4894

Nils Laegreid
231-Z, 200 West
Battelle Northwest Labs.
Richland, WA 99352
(509)942-2417

Murphy J. Landry
Sandia Labs. 1556
Albuquerque, NM 87185
(505)264-8548

Rene Lenfant
Lab. de Marcoussis CR.C.G.E.
Route de Nozay
91460 Marcoussis
FRANCE
Ph. 901-20-02

Kang M. Leung
Corporate Material Sciences Ctr.
Honeywell
10701 Lyndale Ave. So.
Bloomington, MN 55420
(612)887-4530

Steven R. Lindle
AFWL/LRE
Kirtland AFB, 87117
(264-1776)

Herbert G. Lipson
RADC (ESE)
Hanscom AFB, 01731
(617)861-3297

A. Louderback
Litton Systems MS/87
5500 Canoga Ave.
Woodland Hills, CA 91364
(805)887-2783

W. Howard Lowdermilk
Lawrence Livermore Labs.
P. O. Box 5508 L-465
Livermore, CA 94550
(415)422-5498

Ron W. MacPherson
Electro-Optics Div.
Centre de Recherches pour la Defense
Valcartier
P. O. Box 880
Courcelette, Quebec
CANADA G0A 1R0
(418)844-4350

A. A. Manenkov
LeBeden Institute
53, Leninsky prospect
Moscow, USSR

Peter Martin
Materials Dept.
Box 999 200 W. Area/231Z Bldg.
Battelle Northwest Labs.
Richland, WA 99352
(509)942-2305

Howard McCollister
Materials Research
Owens-Illinois Inc.
1035 Toledo
Toledo, OH 43666
(419)247-9494

Jerry R. Meyer
Naval Research Lab., Code 5554
Washington, DC 20375
(202)767-3276

David Milam
Lawrence Livermore Labs.
Box 808
Livermore, CA 94550
(415)422-5499

Perry A. Miles
Raytheon Co.
Hartwell Ave.
Bedford, MA 01730
(617)274-7100 Ext. 4515

Thomas J. Moravec
Honeywell Inc.
10701 Lyndale Ave. So.
Bloomington, MN 55420
(612)887-4309

Dennis Morelli
Technical Products Div.
Optical Coating Lab., Inc.
P. O. Box 1599
Santa Rosa, CA 95402
(707)545-6440

Jacques Mouchart
Laboratoires de Marcoussis C.R. C.G.E.
Route de Nozay
Marcoussis, FRANCE 91460

C. T. Myers
Northrop Corp., Electromechanical Div.
Dept. 6620
500 E. Orange Thorpe Ave.
Anaheim, CA 92801
(714)871-5000 Ext. 361

Brian E. Newnam
Group AP-2
Los Alamos Scientific Lab.
MS 546, P. O. Box 1663
Los Alamos, NM 87545
(505)667-7751

David B. Nichols
Mail Stop 88-46
Boeing Aerospace Co.
P. O. Box 3999
Seattle, WA 98124
(206)773-8938

Philip E. Nielsen
Dept. of Physics, AFIT/ENP
Air Force Institute of Technology
Wright-Patterson AFB, OH 45433
(513)255-2012

Arthur R. Ondrejka
724.04
National Bureau of Standards
Boulder, CO 80303
(303)499-1000 Ext. 3309

Alexander C. Parker
M.I.T. Lincoln Laboratory
P. O. Box 73
Lexington, MA 02173
(617)862-5500

Walter T. Pawlewicz
Battelle-Pacific Northwest Labs.
P. O. Box 999
Richland, WA 99352
(509)942-2537

Bruce J. Pierce
AFWL/LRE, Bldg. 401
Univ. of Dayton Research Inst.
Kirtland AFB, NM 87117
(505)242-2667

Ben C. Platt
AFWL/LRE, Bldg. 401
Univ. of Dayton Research Inst.
Kirtland AFB, NM 87117
(505)242-2667

J. O. Porteus
Naval Weapons Center, Code 3817
China Lake, CA 93555
(714)939-2771

David W. Porter
Air Force Weapons Lab. CA
Kirtland AFB, NM 87117
(505)264-9856

Ronald F. Prater
Defense Advanced Research Projects
Agency/STO
1400 Wilson Blvd.
Arlington, VA 22209

Frank Rainer
Lawrence Livermore Labs. L-465
P. O. Box 5508
Livermore, CA 94550
(415)422-4376

James D. Rancourt
Advanced Products Development
Optical Coating Lab., Inc.
P. O. Box 1599
Santa Rosa, CA 95402
(707)545-6440

John F. Ready
Honeywell Corporate Material
Sciences Center
10701 Lyndale Ave. So.
Bloomington, MN 55420
(612)887-4430

Dennis K. Rice
Orgn. 345/T-60
Northrop Research α Technology Ctr.
One Research Park
Palos Verdes Peninsula, CA 90274
(213)377-4811 Ext. 595

James M. Rinefierd
Laboratory for Laser Energetics
University of Rochester
250 E. River Rd.
Rochester, NM 17623
(716)275-3418

Paul M. Rushworth
Martin-Marietta Corp. MP-276
P. O. Box 5837
Orlando, FL 32805
(305)352-2373

Gregory M. Sanger
Lawrence Livermore Labs. L-140
P. O. Box 808
Livermore, CA 94550
(415)422-8907

Marion L. Scott
AFWL/LRE, Bldg. 401
Univ. of Dayton Research Inst.
Kirtland AFB, NM 87117
(505)242-2667

C. Y. She
Physics Dept.
Colorado State Univ.
Ft. Collins, CO 80523
(303)491-6261

Glenn H. Sherman
II-VI Incorporated
Saxonburg Blvd.
Saxonburg, PA 16056
(412)352-1504

Alex Shimkunas
Advanced Products Development
Optical Coating Lab., Inc.
P. O. Box 1599
Santa Rosa, CA 95402
(707)545-6440

Dominique Sicard
CEA-Limeil
BP 27
91 - Villeneuve St. Georges
FRANCE
569-96-60 Ext. 6836

Philip A. Simpson
Div. 724.02
National Bureau of Standards
Boulder, CO 80303
(303)499-1000 Ext. 3789

Richard A. Skogman
E-O Dept.
Honeywell Corporate Materials
Sciences Center
10701 Lyndale Ave. So.
Bloomington, MN 55420
(218)887-4533

David H. Sliney
Attn: HSE-RL-L
U. S. Army Environmental
Hygiene Agency
Aberdeen Proving Ground, MD 21010
(301)671-3932

James G. Sliney, Jr.
Optical Engineering Dept.
Aerojet ElectroSystems Co.
P. O. Box 296
Azusa, CA 91702
(213)334-6211 Ext. 7112

W. Lee Smith
Laser Program L-465
Lawrence Livermore Labs.
Box 5508
Livermore, CA 94550
(415)422-8209

Steven R. Snyder
FTD/TQTD
Air Force Systems Command
3042-K Jewel Stone Dr.
Dayton, OH 45414
(513)257-3158

M. J. Soileau
Center for Laser Studies/Code 3817
USC and/or NWC
University Park
Los Angeles, CA 90230
(213)741-6790

John B. Sonderman
L-140
Lawrence Livermore Labs.
P. O. Box 808
Livermore, CA 94550
(415)422-8907

Marshall Sparks
Xonics Inc.
1333 Ocean Ave.
Santa Monica, CA 90401
(213)451-9916

James L. Stanford
Physics Div., Code 3818
Naval Weapons Center
China Lake, CA 93555
(714)939-3306

James L. Stapp
AFWL/LRE
Air Force Weapons Lab.
Kirtland AFB, NM 87117
(505)264-1776

Joe Starling
MN10-1864
Honeywell Ceramics Ctr.
1885 Douglas Dr. No.
Golden Valley, MN 55422
(612)542-7196

Alan F. Stewart
Center for Laser Studies
University of Southern California
University Park
Los Angeles, CA 90007
(213)741-6790

C. Martin Stickley
Office of Laser Fusion
U. S. Dept. of Energy
Mail Stop C404
Washington, DC 20545
(301)353-3462

Thomas Stoebe
326 Roberts Hall FB-10
University of Washington
Seattle, WA 98195
(206)543-7090

Stan Stokowski
Lawrence Livermore Labs. L-465
University of California
P. O. Box 808
Livermore, CA 94550
(415)422-5875

Charles L. Strecker
LPO
Air Force Materials Lab.
WPAFB
Dayton, OH 45344
(513)255-4474

H. C. Sullivan
Laser Development
R α D Assc.
Box 9377 ATO
Albuquerque, NM 87119
(505)264-3013

Paul M. Sutton
Res. Lab. Bldg. Δ2
Aeronutronic Division
Ford Aerospace Corp.
Ford Road
Newport Beach, CA 92663
(714)755-5852

Paul A. Temple
Naval Weapons Center Code 3816
China Lake, CA 93555
(714)939-3307

James H. Tillotson
Laser Dept.
Maxwell Labs., Inc.
8835 Balboa Ave.
San Diego, CA 92123
(714)279-5100

Marvin J. Weber
Lawrence Livermore Labs. L-465
P. O. Box 808
Livermore, CA 94550

Michael F. Weber
Optical Engineering
Aerojet Electrosystems
P. O. Box 296
Azusa, CA 91702
(213)334-6211 Ext. 7112

Robert Weeks
Lumonics Res.
105 Schneider Rd.
Ottawa, Ontario
CANADA K2K1Y3
(615)592-1460

Paul E. Werner
Div. 724.02
National Bureau of Standards
Boulder, CO 80303
(303)499-1000

Thomas W. White
521-109-BA33
Rocketdyne, A Division of
Rockwell International
6633 Canoga Ave.
Canoga Park, CA 91304
(213)884-2620

Richard T. Williams
Naval Research Lab. Code 5581
Washington, DC 20375
(202)767-2768

C. B. Willingham
Research Div.
Raytheon Co.
28 Seyon St.
Waltham, MA 02154
(617)899-8400 Ext. 3765

James M. Wimmer
Univ. of Dayton Research Inst.
300 College Park Ave.
Dayton, OH 45469
(513)229-3527

Harry V. Winsor
DARPA/MSO
1400 Wilson Blvd.
Arlington, VA 22209
(202)694-3031

G. Richard Wirtenson
Univ. of California
Lawrence Livermore Labs. L-465
Box 5508
Livermore, CA 94566
(415)422-1332

Shew M. Wong
B/779, Rocky Flats
Rockwell International
P. O. Box 464
Golden, CO 80401
(303)497-2080

R. M. Wood
G.E.C. Ltd.
Hirst Research Centre
East Lane
Wembley, ENGLAND
Ph. 01-904-1262

Matt Young
Div. 724.04
National Bureau of Standards
Boulder, CO 80303
(303)499-1000 Ext. 3223

Robert W. Zimmerer
Scientech, Inc.
5649 Arapahoe Ave.
Boulder, CO 80303
(303)444-1361

Robert R. Donaldson
Lawrence Livermore Labs. L-332
P. O. Box 808
Livermore, CA 94550

Robert M. Pixton
Developmental Optics Facility
International Laser Systems, Inc.
International Airport Box 9316
Albuquerque, NM 87119
(505)264-1778

Thomas W. Walker
AFWL/CA USAF
Kirtland AFB, NM 87117
(505)264-7368

Durand M. Smith
Room 360V3
General Electric, RESD
P. O. Box 8555
Philadelphia, PA 19101
(215)962-2465

Chang H. Chi
High Energy Laser Lab.
MS 6/D137
Hughes Aircraft Co.
Centinela α Teale St.
Culver City, CA 90230
(213)391-0711 Ext. 7121

Eric Johnson
Optical Electronic Metrology
Electromagnetic Technology Div.
National Bureau of Standards
Boulder, CO 80303
(303)499-1000

Aaron Sanders
Optical Electronic Metrology
Electromagnetic Technology Div.
National Bureau of Standards
Boulder, CO 80303
(303)499-1000

Walter Reichert
L-10 M.S.532
Los Alamos Scientific Lab.
Los Alamos, NM 87545
(505)667-7833

A. Vaidyanathan
AFWL/CA
Kirtland AFB, NM 87117
(505)264-3982

Herbert B. Rosenstock
Naval Research Laboratory Code 55045
Washington, DC 20375
(202)767-2225

John B. Trenholme
Lawrence Livermore Labs.
P. O. Box 5508, L-463
Livermore, CA 94550
(415)422-5489

Thomas J. Gilmartin
Lawrence Livermore Labs.
Y-Division
P. O. Box 5508 L-463
(415)422-0400

E. A. Enemark
Optical Coating Lab., Inc.
P. O. Box 1599
Santa Rosa, CA 95402

S-114A (REV. 5-78)

U.S. DEPT. OF COMM. BIBLIOGRAPHIC DATA SHEET	1. PUBLICATION OR REPORT NO. NBS SP 541	2. Gov't Accession No.	3. Recipient's Accession No.

TITLE AND SUBTITLE

aser Induced Damage in Optical Materials: 1978

5. Publication Date

December 1978

6. Performing Organization Code

AUTHOR(S)

dited by Alexander J. Glass and Arthur H. Guenther

8. Performing Organ. Report No.

PERFORMING ORGANIZATION NAME AND ADDRESS

NATIONAL BUREAU OF STANDARDS
DEPARTMENT OF COMMERCE
WASHINGTON, D.C. 20234

10. Project/Task/Work Unit No.

7240580

11. Contract/Grant No.

Sponsoring Organization Name and Complete Address (Street, City, State, ZIP)

lectromagnetic Technology Division, National Bur. of Stand., oulder, CO 80303, American Society for Testing & Materials, hila., PA 19103, Dept. of the Navy, Office of Naval Research, rlington, VA 22217, Defense Advanced Research Project Agency, Washington, D.C. 20234, Dept. of Energy, Washington, D.C. 20545.

13. Type of Report & Period Covered

14. Sponsoring Agency Code

SUPPLEMENTARY NOTES

ABSTRACT *(A 200-word or less factual summary of most significant information. If document includes a significant bibliography or literature survey, mention it here.)*

The Tenth Annual Symposium on Optical Materials for igh Power Lasers (Boulder Damage Symposium) was held at the National Bureau of Standards n Boulder, Colorado, from 12-14 September 1978. The Symposium was held under the auspices F ASTM Committee F-1, Subcommittee on Laser Standards, with the joint sponsorship of BS, the Defense Advanced Research Project Agency, the Department of Energy, and the ffice of Naval Research. About 175 scientists attended the Symposium, including repre- entatives of the United Kingdom, France, Canada, Japan, West Germany, and the Soviet nion. The Symposium was divided into sessions concerning the Measurement of Absorption haracteristics, Bulk Material Properties, Mirrors and Surfaces, Thin Film Damage, oating Materials and Design and Breakdown Phenomena. As in previous years, the emphasis f the papers presented at the Symposium was directed toward new frontiers and new evelopments. Particular emphasis was given to materials for use from 10.6 μm to the uv egion. Highlights included surface characterization, thin film-substrate boundaries, nd advances in fundamental laser-matter threshold interactions and mechanisms. The caling of damage thresholds with pulse duration, focal area, and wavelength were also iscussed. In commemoration of the Tenth Symposium in this series, a number of compre- ensive review papers were presented to assess the state of the art in the various acets of laser induced damage in optical materials. Alexander J. Glass of Lawrence ivermore Laboratory and Arthur H. Guenther of the Air Force Weapons Laboratory were co- hairpersons of the Symposium. The Eleventh Annual Symposium is scheduled for 30-31 ctober 1979 at the National Bureau of Standards, Boulder, Colorado.

KEY WORDS *(six to twelve entries; alphabetical order; capitalize only the first letter of the first key word unless a proper name; separated by semicolons)*

aser damage; laser interaction; optical components; optical fabrication; optical aterials and properties; thin film coatings.

AVAILABILITY

[X] Unlimited

[ ] For Official Distribution. Do Not Release to NTIS

[ ] Order From Sup. of Doc., U.S. Government Printing Office Washington, D.C. 20402, SD Stock No. SN003-003-02052-4

[ ] Order From National Technical Information Service (NTIS) Springfield, Virginia 22161

19. SECURITY CLASS (THIS REPORT)	21. NO. OF PAGES
UNCLASSIFIED	362
20. SECURITY CLASS (THIS PAGE)	**22. Price**
UNCLASSIFIED	$5.50

USCOMM-DC 66650-P78

☆ U.S. GOVERNMENT PRINTING OFFICE: 1979 O—281-067 (94)

NBS TECHNICAL PUBLICATIONS

PERIODICALS

JOURNAL OF RESEARCH—The Journal of Research of the National Bureau of Standards reports NBS research and development in those disciplines of the physical and engineering sciences in which the Bureau is active. These include physics, chemistry, engineering, mathematics, and computer sciences. Papers cover a broad range of subjects, with major emphasis on measurement methodology, and the basic technology underlying standardization. Also included from time to time are survey articles on topics closely related to the Bureau's technical and scientific programs. As a special service to subscribers each issue contains complete citations to all recent NBS publications in NBS and non-NBS media. Issued six times a year. Annual subscription: domestic $17.00; foreign $21.25. Single copy, $3.00 domestic; $3.75 foreign.

Note: The Journal was formerly published in two sections: Section A "Physics and Chemistry" and Section B "Mathematical Sciences."

DIMENSIONS/NBS

This monthly magazine is published to inform scientists, engineers, businessmen, industry, teachers, students, and consumers of the latest advances in science and technology, with primary emphasis on the work at NBS. The magazine highlights and reviews such issues as energy research, fire protection, building technology, metric conversion, pollution abatement, health and safety, and consumer product performance. In addition, it reports the results of Bureau programs in measurement standards and techniques, properties of matter and materials, engineering standards and services, instrumentation, and automatic data processing.

Annual subscription: Domestic, $12.50; Foreign $15.65.

NONPERIODICALS

Monographs—Major contributions to the technical literature on various subjects related to the Bureau's scientific and technical activities.

Handbooks—Recommended codes of engineering and industrial practice (including safety codes) developed in cooperation with interested industries, professional organizations, and regulatory bodies.

Special Publications—Include proceedings of conferences sponsored by NBS, NBS annual reports, and other special publications appropriate to this grouping such as wall charts, pocket cards, and bibliographies.

Applied Mathematics Series—Mathematical tables, manuals, and studies of special interest to physicists, engineers, chemists, biologists, mathematicians, computer programmers, and others engaged in scientific and technical work.

National Standard Reference Data Series—Provides quantitative data on the physical and chemical properties of materials, compiled from the world's literature and critically evaluated. Developed under a world-wide program coordinated by NBS. Program under authority of National Standard Data Act (Public Law 90-396).

NOTE: At present the principal publication outlet for these data is the Journal of Physical and Chemical Reference Data (JPCRD) published quarterly for NBS by the American Chemical Society (ACS) and the American Institute of Physics (AIP). Subscriptions, reprints, and supplements available from ACS, 1155 Sixteenth St. N.W., Wash., D.C. 20056.

Building Science Series—Disseminates technical information developed at the Bureau on building materials, components, systems, and whole structures. The series presents research results, test methods, and performance criteria related to the structural and environmental functions and the durability and safety characteristics of building elements and systems.

Technical Notes—Studies or reports which are complete in themselves but restrictive in their treatment of a subject. Analogous to monographs but not so comprehensive in scope or definitive in treatment of the subject area. Often serve as a vehicle for final reports of work performed at NBS under the sponsorship of other government agencies.

Voluntary Product Standards—Developed under procedures published by the Department of Commerce in Part 10, Title 15, of the Code of Federal Regulations. The purpose of the standards is to establish nationally recognized requirements for products, and to provide all concerned interests with a basis for common understanding of the characteristics of the products. NBS administers this program as a supplement to the activities of the private sector standardizing organizations.

Consumer Information Series—Practical information, based on NBS research and experience, covering areas of interest to the consumer. Easily understandable language and illustrations provide useful background knowledge for shopping in today's technological marketplace.

Order **above** *NBS publications from: Superintendent of Documents, Government Printing Office, Washington, D.C. 20402.*

Order **following** *NBS publications—NBSIR's and FIPS from the National Technical Information Services, Springfield, Va. 22161.*

Federal Information Processing Standards Publications (FIPS PUB)—Publications in this series collectively constitute the Federal Information Processing Standards Register. Register serves as the official source of information in the Federal Government regarding standards issued by NBS pursuant to the Federal Property and Administrative Services Act of 1949 as amended, Public Law 89-306 (79 Stat. 1127), and as implemented by Executive Order 11717 (38 FR 12315, dated May 11, 1973) and Part 6 of Title 15 CFR (Code of Federal Regulations).

NBS Interagency Reports (NBSIR)—A special series of interim or final reports on work performed by NBS for outside sponsors (both government and non-government). In general, initial distribution is handled by the sponsor; public distribution is by the National Technical Information Services (Springfield, Va. 22161) in paper copy or microfiche form.

BIBLIOGRAPHIC SUBSCRIPTION SERVICES

The following current-awareness and literature-survey bibliographies are issued periodically by the Bureau:

Cryogenic Data Center Current Awareness Service. A literature survey issued biweekly. Annual subscription: Domestic, $25.00; Foreign, $30.00.

Liquified Natural Gas. A literature survey issued quarterly. Annual subscription: $20.00.

Superconducting Devices and Materials. A literature survey issued quarterly. Annual subscription: $30.00. Send subscription orders and remittances for the preceding bibliographic services to National Bureau of Standards, Cryogenic Data Center (275.02) Boulder, Colorado 80302.